NATIONAL AERONAUTICS AND SPACE ADMINISTRATION

*Technical Report 32-884*

# *Mariner Mars 1964 Project Report: Television Experiment*

## *Part I. Investigators' Report*

# Mariner IV Pictures of Mars

*Robert B. Leighton, Bruce C. Murray, Robert P. Sharp*
*California Institute of Technology*

*J. Denton Allen, Richard K. Sloan*
*Jet Propulsion Laboratory*

N68-16106

FACILITY FORM 602

N68-16106 (ACCESSION NUMBER) (THRU)

242 (PAGES) 1 (CODE)

CR-92682 (NASA CR OR TMX OR AD NUMBER) 30 (CATEGORY)

GPO PRICE $ _____

CFSTI PRICE(S) $ _____

Hard copy (HC) 3.00

Microfiche (MF) .65

ff 653 July 65

JET PROPULSION LABORATORY
CALIFORNIA INSTITUTE OF TECHNOLOGY
PASADENA, CALIFORNIA

December 15, 1967

NATIONAL AERONAUTICS AND SPACE ADMINISTRATION

*Technical Report 32-884*

*Mariner Mars 1964 Project Report: Television Experiment*

*Part I. Investigators' Report*

# Mariner IV Pictures of Mars

*Robert B. Leighton, Bruce C. Murray, Robert P. Sharp*
*California Institute of Technology*

*J. Denton Allen, Richard K. Sloan*
*Jet Propulsion Laboratory*

JET PROPULSION LABORATORY
CALIFORNIA INSTITUTE OF TECHNOLOGY
PASADENA, CALIFORNIA

December 15, 1967

***TECHNICAL REPORT 32-884***

Copyright © 1967
Jet Propulsion Laboratory
California Institute of Technology

Prepared Under Contract No. NAS 7-100
National Aeronautics & Space Administration

# Preface

On November 28, 1964, *Mariner IV* was successfully launched on a trajectory that would take it within 150,000 miles of Mars. On December 5, 1964, the spacecraft performed a successful midcourse maneuver, altering its flight path so that it would pass within 6118 miles of the planet. The flight took approximately 7½ months, during which time a great deal of scientific information was gathered concerning the environment of both near-Earth and interplanetary space. On July 14, 1965, *Mariner IV* photographed the surface of Mars and telemetered to earth the most advanced scientific and technical data regarding the planet yet recorded.

The *Mariner* Mars 1964 Project has been documented in a series of reports (see next page). The present report is in two parts. Part I presents the *Mariner IV* pictures of Mars together with the investigators' report thereon. Part II consists of numerical printouts of the picture intensities in matrix form. The report describes the design, construction, calibration, and operation of the television subsystem; outlines the procedures followed in the acquisition, handling, and reduction of the digital data; presents the calibrated and sharpened pictures in several forms convenient for study; and discusses some of the preliminary results obtained.

It is believed that the techniques, procedures and results documented herein are important contributions to the exploration of space and the advancement of science.

W. H. Pickering, *Director*
*Jet Propulsion Laboratory*

L. N. James, *Deputy Assistant Laboratory Director for Flight Projects*

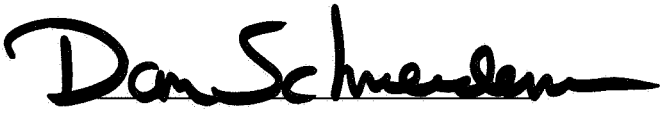

D. Schneiderman, *Project Manager*
*Mariner Mars 1964*

## Elements of the *Mariner* Mars 1964 Project Report

The *Mariner* Mars 1964 Project Report consists of the following volumes:

*Mariner* Mars 1964 Project Report, Mission and Spacecraft Development, Volume I: From Project Inception Through Midcourse Maneuver (TR 32-740, Vol. I)

*Mariner* Mars 1964 Project Report, Mission and Spacecraft Development, Volume II: Appendixes (TR 32-740, Vol. II)

*Mariner* Mars 1964 Project Report, Mission Operations (TR 32-881)

*Mariner* Mars 1964 Project Report, Spacecraft Performance and Analysis (TR 32-882)

*Mariner* Mars 1964 Project Report, Scientific Experiments (TR 32-883)

*Mariner* Mars 1964 Project Report, Television Experiment, Part I: Investigators' Report (TR 32-884, Part I)

*Mariner* Mars 1964 Project Report, Television Experiment, Part II: Picture Element Matrices (TR 32-884, Part II)

Tracking and Data Acquisition Support for *Mariner* Mars 1964, Volume II: Cruise to Post-Encounter Phase (TM 33-239, Vol. II)

# Contents


**I. Introduction** . . . . . 1

**II. The *Mariner IV* Television Pictures** . . . . . 3

A. Introduction . . . . . 3

B. Summary Comments on *Mariner IV* Pictures . . . . . 25

**III. Intensity and Color Calibration of Flight Photographs** . . . . . 29

A. Outline of Flight Picture Calibration Procedure . . . . . 32

B. Photometric Accuracy . . . . . 50

C. Correction of Pictures for Haze or Glare . . . . . 52

D. Sine-Wave Response Function of the Camera System . . . . . 57

E. Treatment of Color Overlap Areas . . . . . 59

**Appendix A.** The Spacecraft . . . . . 65

**Appendix B.** Television Camera Subsystem . . . . . 79

**Appendix C.** Flight Sequence and Performance . . . . . 95

**Appendix D.** Design of the Television Experiment . . . . . 103

**Appendix E.** Data Acquisition and Handling . . . . . 125

**Appendix F.** Haze Studies . . . . . 135

**Appendix G.** TV Interpretation Studies . . . . . 141

**Appendix H.** Martian Slopes and Surface Roughness . . . . . 145

**Appendix I.** Martian Surface Processes . . . . . 155

**Appendix J.** Crater Frequency Distribution and Age Implication . . . . . 163

**Appendix K.** Unenhanced Version of the Pictures . . . . . 169

**References** . . . . . 175


## Tables


II-1. Summary compilation of Martian crater data . . . . . 25

III-1. Calibration picture exposure data . . . . . 33

# Contents (contd)

## Tables (contd)


III-2. Tabulation of $I$ vs DN . . . . . 33

III-3. Coefficients $a_{ns}$ of orthogonal polynomials . . . . . 36

III-4. Normalized exposure $x_i$ and orthogonal polynomials $P_n(x_i)$ . . . . . 37

III-5. Picture coordinates (L, E) of fiducial mark corners . . . . . 43

III-6. DN discrimination and random error . . . . . 52

III-7. Sine-wave response data . . . . . 58

III-8. Picture sharpening matrix . . . . . 60

III-9. Relative displacements of overlapping pictures . . . . . 63

B-1. Mars spectral illuminance data . . . . . 90

C-1. Encounter events from DAS time . . . . . 97

C-2. Scan subsystem performance . . . . . 100

D-1. Preliminary values of parameters influencing picture locations . . . . . 111

D-2. Final parameter values . . . . . 115

D-3. Attitude control data . . . . . 116

D-4. Picture locations and related data . . . . . 117

D-5. Latitude and longitude uncertainties for Picture 11 . . . . . 124

I-1. Calculated annual temperatures on Mars . . . . . 156

I-2. Seasonal ranges in average daily temperatures with latitude . . . . . 156

I-3. Diurnal temperature change at southern hemisphere solstice on Mars . . . . . 157

I-4. Martian erosion . . . . . 159

J-1. Integral crater count data, Pictures 7–12 . . . . . 165

J-2. Area of pictures . . . . . 165


## Flight Pictures


Pictures 1 and 2 . . . . . 8

Pictures 3 and 4 . . . . . 10

Pictures 5 and 6 . . . . . 12

Pictures 7 and 8 . . . . . 14

Pictures 9 and 10 . . . . . 16

Pictures 11 and 12 . . . . . 18

Pictures 13 and 14 . . . . . 20

Pictures 15 and 16 . . . . . 22

Pictures 17–22 . . . . . 24

## Contents (contd)

### Figures


III-1. Plot of 2 × 2 averages of DN's for lines 60 and 61 of flat-field calibration pictures . . . . . 30

III-2. Sample flat-field calibration pictures . . . . . 31

III-3. Plot of average DN vs light intensity for 45 flat-field calibration pictures . . . 34

III-4. Plot of fractional sensitivity $\Delta I/I$ per unit DN, as a function of DN . . . . . 35

III-5. Plots showing the residual errors when polynomials of various orders are fitted to the calibration data . . . . . 36

III-6. Plot of the intensity corrections needed to improve the fitting of the calibration data by second-degree polynomials . . . . . 37

III-7. Printout of red filter factor as a function of position . . . . . 38

III-8. Sample printouts of orthogonal polynomial coefficients $A_0$, $A_1$, $A_2$ . . . . . 40

III-9. Spectral responses of visual photometer, vidicon, vidicon with green filter, vidicon with orange-red filter; also shown are relative spectral distributions of the collimator light source and of sunlight . . . . . 44

III-10. Variation of camera sensitivity with temperature . . . . . 46

III-11. Line and element coordinates of the shutter marks for the calibration pictures and the flight pictures . . . . . 47

III-12. Line and element coordinates of fiducial marks for flight pictures . . . . . 47

III-13. Average of green pictures 2, 3, 6, 7, 10, 11, 14, and 15, enhanced such that the brightness range 100–130 spans the DN range 63–0 . . . . . 48

III-14. Average of red pictures 4, 5, 8, 9, 12, and 13, enhanced so that the brightness range 160–220 spans the DN range 63–0 . . . . . 49

III-15. Plot of intensity vs altitude above the planet for the sky area of Picture 1 . . . 52

III-16. Plot of scattered intensity from a vertical column of atmosphere vs the altitude of the bottom of the column above the planet . . . . . 53

III-17. Schematic intensity map of Mars as viewed by the spacecraft . . . . . 55

III-18. Plot of maximum and minimum intensities observed in each picture vs picture number . . . . . 57

III-19. Plot of modulation transfer function . . . . . 58

III-20. Color intensity ratio pictures of overlap areas of Pictures 1–14 . . . . . 61

A-1. *Mariner* Mars 1964 spacecraft: top view . . . . . 66

A-2. *Mariner* Mars 1964 spacecraft: bottom view . . . . . 66

A-3. Spacecraft mechanical configuration: top and bottom views . . . . . 67

A-4. Spacecraft mechanical configuration: top view, solar panels extended . . . . 68

A-5. Spacecraft mechanical configuration: side view, solar panels folded . . . . . 69

# Contents (contd)

## Figures (contd)


A-6. Attitude control gas jet configuration . . . . . 70

A-7. Clock- and cone-angle descriptive diagram: (a) clock angle, (b) cone angle . . . 71

A-8. Data automation system encounter timing . . . . . 73

A-9. Data automation system non-real-time sequencing at narrow-angle acquisition . . . . . 73

A-10. Planetary scan platform relative look angles, shown with platform in pinned position . . . . . 73

A-11. Video recording timing sequence . . . . . 74

A-12. Pre- and postencounter trajectory, ecliptic view . . . . . 75

A-13. Aiming zones: (a) aiming point diagram, (b) trajectories at Mars . . . . . 76

A-14. Near-Mars trajectory parameters . . . . . 77

B-1. Television camera head . . . . . 79

B-2. Television subsystem, functional block diagram . . . . . 80

B-3. Cassegrain reflecting telescope . . . . . 80

B-4. Components of camera head . . . . . 80

B-5. Camera filter and shutter . . . . . 81

B-6. *Mariner IV* television system, block diagram . . . . . 82

B-7. Six views of TV camera head subassembly . . . . . 83

B-8. Vidicon faceplate . . . . . 84

B-9. Vidicon, mechanical construction . . . . . 84

B-10. Flexible mounting of vidicon in camera head . . . . . 85

B-11. Television camera electronics . . . . . 87

B-12. *Mariner IV* vidicon spectral response . . . . . 91

B-13. Mars illuminance curve . . . . . 91

B-14. Vidicon response through red and green filters . . . . . 91

B-15. System responsivity vs temperature . . . . . 92

B-16. High contrast sine-wave test slides . . . . . 93

B-17. Horizontal and vertical frequency response curves . . . . . 94

C-1. Measured and calculated scan subsystem Y-axis output . . . . . 99

D-1. Engineering constraints for July 15 arrival . . . . . 106

D-2. Typical television value contours for July 15 arrival . . . . . 108

D-3. Picture locations . . . . . 110

## Contents (contd)

### Figures (contd)


D-4. Overlapping frames showing the shift of the center of the later picture away from its computed location because of spacecraft rotation within the attitude control limits . . . . . 112

D-5. Vectors showing the shifts between overlapping pictures due to spacecraft rotation . . . . . 112

D-6. Postencounter attitude control data . . . . . 113

D-7. Resolution of picture translations into vector components . . . . . 114

D-8. Interpolated pitch curve and extrapolated yaw and roll curves through the television encounter period . . . . . 115

D-9. Picture format, as seen projected toward the planet . . . . . 116

E-1. *Mariner* Mars 1964 data stream . . . . . 126

E-2. Data modes during the nominal flight sequence . . . . . 127

E-3. Television ground data processing system . . . . . 128

E-4. Spacecraft TV data system, block diagram . . . . . 129

E-5. Television data formats: (a) transmission sequence of events, (b) Types A, B, C formats . . . . . 130

E-6. Television data tabular display . . . . . 132

E-7. Television data decommutation . . . . . 132

E-8. *Mariner IV* Picture 1: (a) with "torn lines," (b) with "torn lines" removed and contrast enhanced . . . . . 133

F-1. Arrangement of TV optics and photomultiplier for veiling glare and simulated Mars transparency scan tests . . . . . 136

F-2. Veiling glare tests . . . . . 137

F-3. Stray light in image as a function of the diameter of the bright source at which the optical system is pointed . . . . . 138

G-1. Spectral response of flight field test TV camera system . . . . . 141

G-2. Step/edge model . . . . . 142

G-3. Laboratory setup for model studies . . . . . 143

G-4. Terrain model of the Bakersfield (California) area . . . . . 143

G-5. TV pictures of Mars . . . . . 143

G-6. VFC system processed model study picture with optimized operation . . . . . 144

G-7. Martian topography, simulated model . . . . . 144

H-1. Parametric variation of haze and level intensity values . . . . . 146

H-2. Profiles of selected craters in Picture 9 . . . . . 147

H-3. Profiles of selected craters in Pictures 9 and 10 . . . . . 148

## Contents (contd)

### Figures (contd)

H-4. Profiles of Crater P10 L126 E148 . . . . . 149

H-5. Profiles of selected craters in Picture 11 . . . . . 150

H-6. Maximum and minimum intensity fluctuations vs picture number . . . . . 151

H-7. Plot of average variance vs $\tan^2 \theta$, where $\theta$ is the solar zenith angle . . . . 152

I-1. Mars surface temperature . . . . . 157

J-1. (a) Sine wave response of *Mariner IV* television system, (b) results of simulation study of model shown in Fig. J-2 . . . . . 164

J-2. Direct and TV photographs of simulation model . . . . . 165

J-3. Integral crater frequency plot of craters recognized in Pictures 7–12 . . . . . 165

K-1. Pictures 1–18: calibrated, unenhanced . . . . . 169

## Abstract

Reduced data obtained from the *Mariner IV* television experiment are presented in numerical and pictorial form. Procedures are described for correcting the original digital data for (1) the intensity and spectral transfer characteristics of the camera system, (2) the geometric distortions introduced by nonlinear effects in the TV-line scan, (3) the modulation transfer function of the camera, and (4) scattered light.

The calibrated pictures are of very low contrast, intensity ranges (minimum to maximum) of from 15 to 30% being typical. The later pictures cover larger percentage ranges. Surface detail is only dimly visible in the pictures unless they are artificially enhanced in contrast.

The calibrated and contrast-enhanced pictures show 300 craters and an additional 300 possible craters, as compared with the less than 100 identified in the preliminary pictures released on July 29, 1965. Observed crater diameters range from 3 to 180 km, and part of a possible crater 350 km in diameter is seen. About 10% of the craters have central peaks, and a like number have a clear polygonal outline. A number of lineations are seen.

Surface features tentatively identified, or possibly identifiable, with previously mapped markings include Propontis I, one or more "canals," and the boundary between the light area Mesogaea and the dark area Mare Sirenum, near Titanum Sinus.

An analysis of overlapping areas of "red" and "green" pictures for local variations in color (as distinct from brightness) shows only relatively small color variations on the parts of Mars photographed. The average color is distinctly reddish, and the light ("desert") areas are somewhat redder than the dark ("mare") areas.

Slopes of crater walls are found to range up to about 12 deg maximum. Topographic relief in excess of 1 km is uncommon. Large-scale surface roughness (slopes) and albedo fluctuations, measured statistically, are found to be about 3 deg rms and 2 percent rms, respectively. These results are consistent with radar measurements of surface slopes, and indicate that the Martian surface, both dark and light, is much smoother than the lunar uplands. Some of the crater floors appear to have a "domed" profile.

The principal processes that modify the Martian surface relief (craters) are suggested to be meteoroidal pelting and the associated rubble mantling, covering by wind-blown dust, and thermal creep of loose surface debris. The probable absence of significant quantities of liquid water in the soil presumably eliminates chemical weathering and freeze-and-thaw as effective erosional processes.

The large surface density of craters seen, approaching that of the lunar uplands, suggests that very ancient physiographic features, perhaps billions of years old, are still visible on Mars.

## Abstract (contd)

The luminous response characteristics of each picture element were determined using 45 uniformly exposed calibration pictures of known exposure value. The relative sensitivity was evaluated with respect to an approximate standard (non-linear) function, using a quadratic least-squares fit. Internal statistical deviations from a smooth curve, principally due to encoding errors, average less than 1%; the intrinsic reproducibility of a given picture element, prior to encoding, was about 0.2%. Sensitivity variations due to electronic shading, optical vignetting, and other causes amounted to about 40% over the field. Relative sensitivity to "red" and "green" light varied by about $\pm 10\%$ across the picture area. The photometric sensitivity is uncertain by about $\pm 15\%$ due to systematic errors and from 1.5 to 3% due to random effects.

Possible causes of the hazy appearance of pictures of the limb and terminator regions were investigated both experimentally and analytically. Significant contributions both from instrumental glare and from scattering by the Martian atmosphere were found. Lower and upper limits on the haze and glare effects of from 20 to 30% were deduced.

Angular resolution of the camera system, including both optical and electronic effects, was approximately characterized by a gaussian point-spread function having a half width of 0.65–0.85 TV line.

## Note

Several JPL people who contributed to the success of the *Mariner IV* television experiment also prepared parts of this volume:

| | |
|---|---|
| D. Schneiderman: | "Introduction" (Section I) |
| J. D. Allen: | "Television Camera" (Appendix B) |
| A. G. Herriman: | "Design of the Television Experiment" (Appendix D) |
| S. Z. Gunter: | "Data Acquisition and Handling" (Appendix E) |
| L. Adams: | "Laboratory Glare Studies" (Appendix F) |
| C. C. La Baw: | "Calibration of the Television Camera" (Appendix B) |
| | "Television Interpretation Studies" (Appendix G) |

Background information presented in Appendix A ("The Spacecraft") and Appendix C ("Flight Sequence and Performance") was condensed from JPL Technical Reports (TR 32-740, TR 32-881, and TR 32-882). Section II, "The *Mariner IV* Pictures," was written jointly by R. P. Sharp, B. C. Murray, and R. B. Leighton (all of Caltech); Section III, "Intensity and Color Calibration of Flight Photographs," by R. B. Leighton; Appendix H, "Slopes and Surface Roughness," by B. C. Murray and R. B. Leighton; Appendix I, "Surface Processes," by R. P. Sharp; Appendix J, "Crater Frequency Distribution," by R. P. Sharp, B. C. Murray, and R. B. Leighton.

The editorial assistance of V. Annigian, D. Maple, P. Shutts, and R. Van Buren (all of JPL) is gratefully acknowledged. R. K. Sloan (JPL) provided valuable administrative and organizational impetus and also contributed to the study of haze effects in the camera system.

PRECEDING PAGE BLANK NOT FILMED.

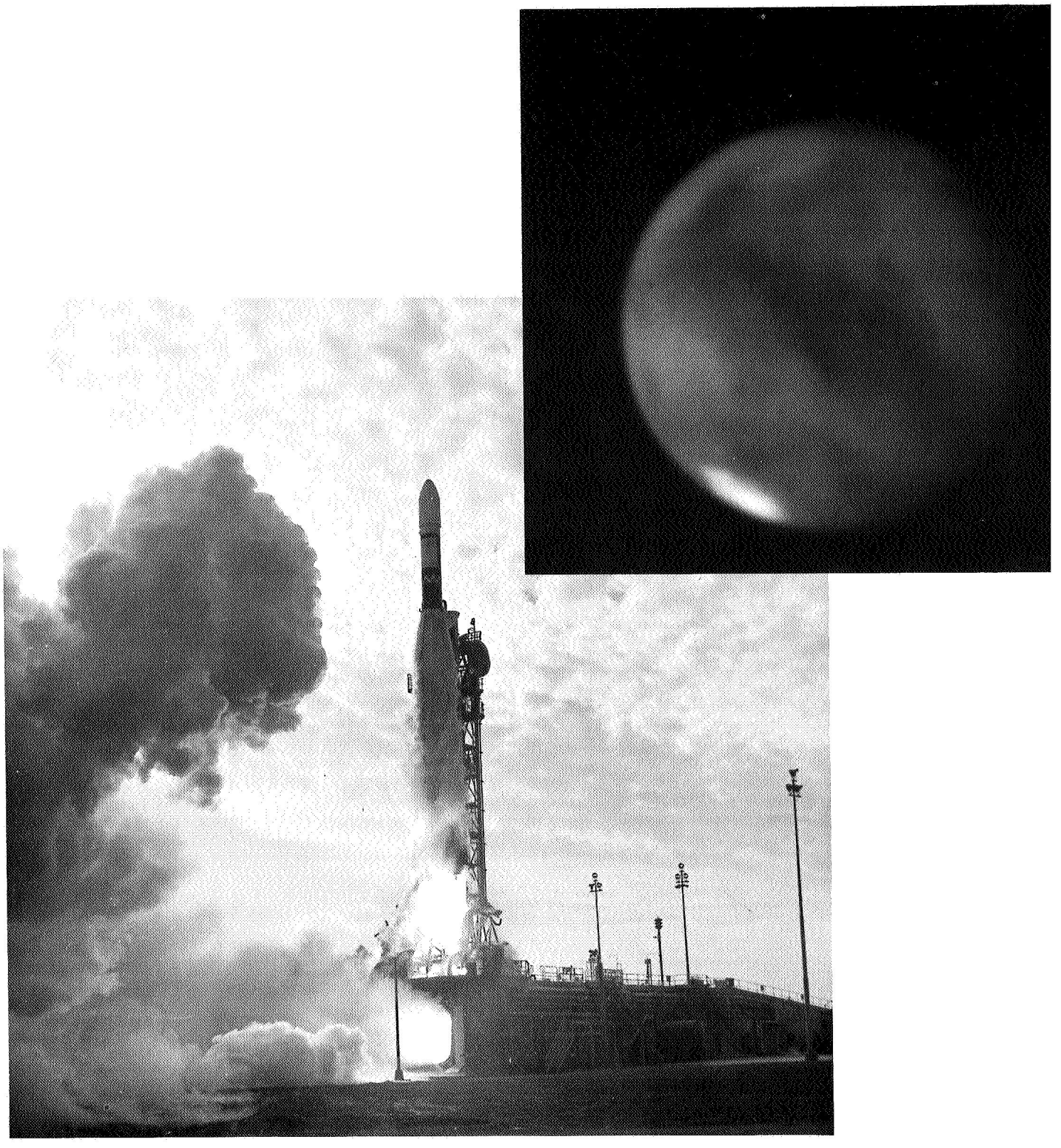

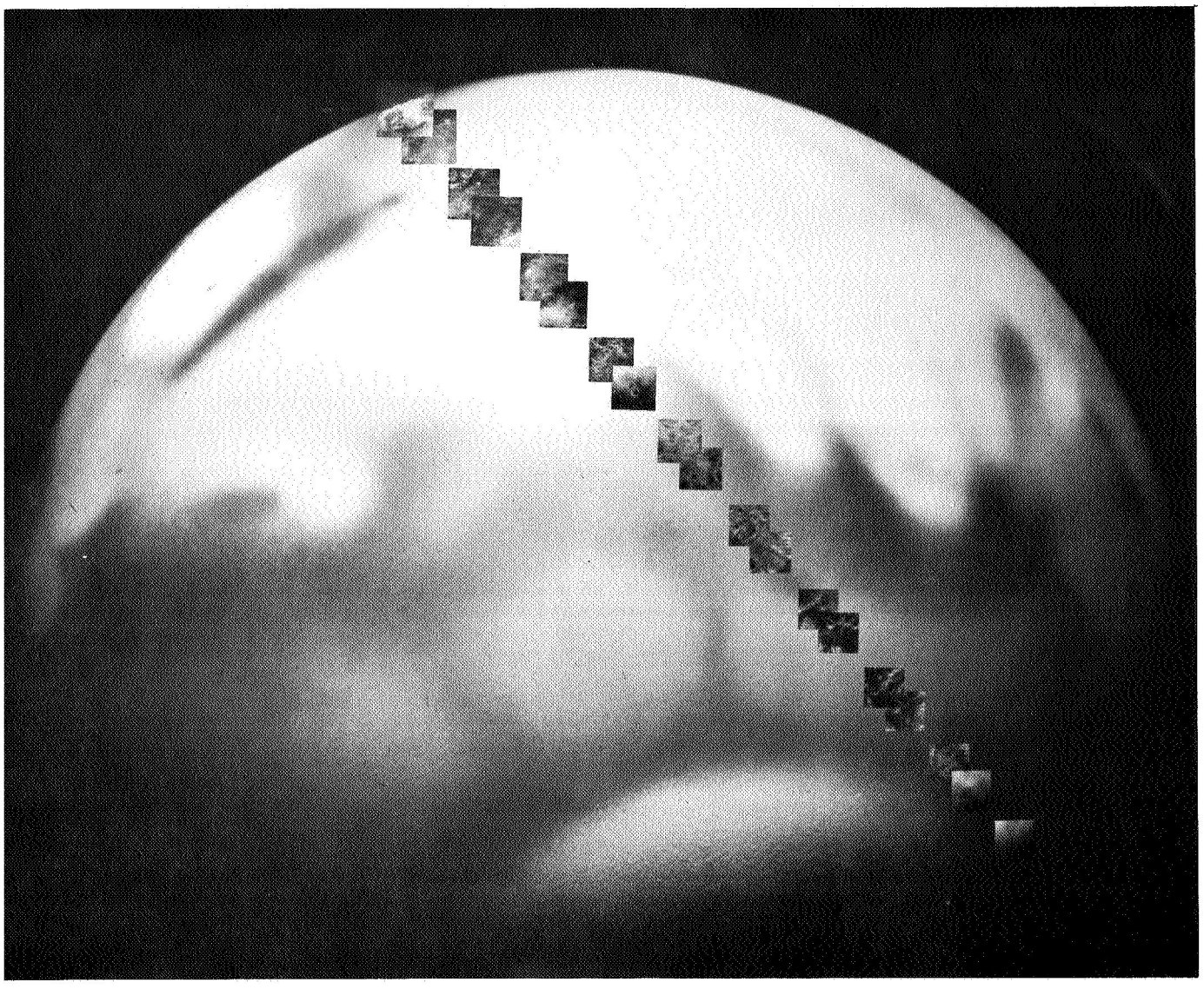

## Frontispiece

**Left:** *Mariner IV* **begins its eight-month journey to Mars on November 28, 1964.**

**Inset: A telescopic view of Mars as seen from earth.**

**Right: A mosaic of the *Mariner IV* pictures superimposed upon a photograph of a hand-painted model of Mars.**

# I. Introduction

The *Mariner* Mars 1964 project was an outgrowth of a 1962 directive by NASA authorizing the Jet Propulsion Laboratory to design and build two spacecraft to be launched toward Mars in the last two months of 1964. JPL was given responsibility for the design, construction, and testing of the spacecraft, for tracking and data acquisition, and for data reduction and processing operations. Lewis Research Center was responsible for the launch vehicle effort.

One proof-test (engineering) model and three flight-qualified spacecraft were built, and one set of selected spare parts was provided. Launch was via the then new *Atlas D/Agena D* vehicle, which would permit spacecraft weight of 260 kg. Mission constraints involved a 28-day launch period, with a 4-hr-maximum launch window each day. Flight time would vary from 220 to 265 days, depending upon the trajectory, with 10 additional days required for each transmission of the tape-recorded data. New techniques involved a capability for performing two trajectory corrections, if required, an S-band (2300-MHz) communications system, use of the sun and the star Canopus as attitude references, and a spacecraft made as automatic as possible, with many redundant functions provided for reliability.

The primary objectives of the mission were to conduct a close-up television reconnaissance of Mars, perform certain field and particle measurements in interplanetary space and in the immediate vicinity of the planet, and transmit the data to earth. Other objectives were to provide experience in flying an attitude-stabilized spacecraft on a long-duration mission away from the sun, and assure a probability of impacting the planet of not more than 1:10,000.

*Mariner III*, first of the two spacecraft scheduled for the 1964 Mars attempt, was launched on November 5, 1964. The plastic shroud failed soon after liftoff and encapsulated the spacecraft, making it impossible to deploy the solar panels. The spacecraft systems were silenced when the battery failed after 8 hr 43 min of flight.

Equipped with a new metal shroud, *Mariner IV* left the launch pad on November 28, 1964. The new *Atlas D/Agena D* vehicle performed well, and injection and separation were normal. Following separation, the four solar panels were extended and the sun was acquired. The spacecraft was allowed to roll gently for the next 15 hr while the magnetometer was calibrated in two axes. Then the star Canopus was acquired, using an optical sensor.

The first attempt at trajectory correction was cancelled when the star sensor lost lock on Canopus, probably because of a sunlit dust particle drifting across the field of view. Later, after this anomaly had occurred several

times, the internal logic of the spacecraft was modified by radio command, solving the problem.

On December 5, the trajectory was successfully changed from a closest approach distance of 251,000 km to one of 9850 km above the south pole of Mars. This required a change in flight angle of less than 1¼ deg and a velocity increment of 16.5 m/sec.

During the first half of the mission, two-way communications were conducted using the low-gain omnidirectional spacecraft antenna. The high-gain, body-fixed, directional antenna was switched on when the beam of the antenna intercepted the earth on March 5, 1965. Thereafter, the earth remained within the antenna beam for the duration of the mission.

On February 11, 1965, the cover protecting the television optical system was removed by radio command, as a precaution against the dislodging of dust particles during the critical encounter phase.

During the long flight, only two failures occurred in critical spacecraft systems. A component failure in the plasma probe in December made its data unintelligible until the switch in data rates in January 1965 effected partial recovery of data for the rest of the mission. The second failure occurred when the Geiger-Mueller tube of the ion chamber recorded a severe solar flare on February 5 and never fully recovered; it ceased functioning completely on March 17, 1965.

*Mariner IV* encountered Mars on July 15, 1965. The planet was in view of the TV subsystem for approximately 20 min, during which time 21 complete pictures were taken and recorded on magnetic tape. As the spacecraft passed behind the planet, it was hidden from earth, and remained so for 54 min, permitting subsequent analysis of the effect of the Martian atmosphere and ionosphere on a radio signal, both while entering and emerging from occultation.

Following encounter, the spacecraft switched to a mode in which the photographs and science data were twice transmitted to earth. Picture transmissions were alternated with intervals of real-time engineering data needed for ground tracking purposes. During the pre-encounter phases, the spacecraft had continuously transmitted a commutated sequence of 280 bits of science data followed by 140 bits of engineering information.

The mission was terminated on October 1, 1965, with the spacecraft over 308 million km from earth. Several radio contacts were achieved after that time. No attempt was made to read telemetry, but the presence of sidebands indicated that the carrier was still being modulated. A successful contact was made on February 3, 1966, with the spacecraft apparently responding to an earth-based signal at a record distance of 344 million km using the new 63-m antenna at Goldstone, California. *Mariner IV* returned within full communications range of the earth in 1967, and operations with the spacecraft were then renewed.

This report is concerned with but one part of the *Mariner IV* mission—the television experiment. Its purpose is to describe in some detail the design, construction, calibration, and operation of the television subsystem; to outline the procedures followed in the acquisition, handling, and reduction of the digital data of the experiment; to present the calibrated and sharpened pictures in several forms convenient for further study; and to discuss some of the preliminary results obtained.

Although the pictures mostly speak for themselves, their full scientific value can be realized only in the context of the many factors that characterized the performance of the TV subsystem and indeed of the whole spacecraft. For this reason a considerable part of the report is devoted to the description of the spacecraft and its operation during the flight as well as to more directly relevant matters such as the spacecraft trajectory, the camera angles of view, and the Martian coordinates of the pictures. Most of these auxiliary data are presented as appendices to the main body of the report.

Because of the relative complexity of the television experiment and the large amount of numerical data it produced, it is impractical to present the raw data and all of the test and calibration information that would be needed for an independent reduction of the picture data to a photometrically accurate form. Instead, only the calibrated pictures are included here, together with a brief description of the steps that were followed in the processing of the data.

In a complex technical enterprise such as the *Mariner* Mars 1964 Mission, it is impossible to acknowledge adequately the important contributions made by the hundreds of persons who participated in it. The scientific investigators are deeply appreciative of their efforts. The undoubted scientific success of the *Mariner* Mars 1964 Mission stands as a tribute to the skill and devotion of each of these many people.

# II. The Mariner IV Television Pictures

## A. Introduction

*In this section are displayed the principal results of* the *Mariner IV* television experiment—nineteen pictures of the Martian surface, ranging from the limb of the planet to the sunset terminator.* The data content of these pictures amounts altogether to 3.75 million bits (counting only the active picture area). In viewing and analyzing them, it is well to recall that, as pictures go, this is not really very much data: an ordinary 10- × 12-cm snapshot taken with a good lens contains about 100 million bits; a single high-quality aerial photograph 30 cm square may contain 10 times this amount. Even comparing the *Mariner* pictures with pictures of the moon, a single earth-based lunar photograph, taken under comparable conditions of surface resolution, would contain 10 to 50 times as much information as the entire set of *Mariner IV* pictures.

On the other hand, in comparison with the previously available photographs of Mars, the *Mariner IV* pictures are outstanding. Even the best of the existing earth-based pictures of Mars contain only about 10,000 bits of data. In addition, because of their far superior linear resolution, the *Mariner IV* pictures add much new information about the present conditions and past history of the Martian surface.

Because of the limited number of pictures, their unique character, and the low contrast of the Martian surface at the resolved scale, it was considered most important that the pictures be calibrated, enhanced in contrast, sharpened in resolution, and geometrically corrected in such ways as to render them quantitatively as well as qualitatively useful. Fortunately, the characteristics of the camera system were such that this could be done with negligible loss of information or introduction of spurious "noise." The calibration and enhancement procedures are outlined in Section III of this report.

In the course of studying various versions of the pictures, as the calibration, enhancement, and sharpening processes were applied, it was found that no single version could be judged "best" in the sense that all features of the scene were more clearly visible on it than in some other versions. This was to be expected, since the ability of the *Mariner* camera to discriminate intensity far exceeds that of the human eye. Further, it was sometimes difficult to distinguish between true features and artifacts introduced in the conversion of the processed data to photographic form. This discrimination was made much easier by identifying the feature in each of two

*Three other pictures, Pictures 20–22, all fall on the nighttime side of the planet.

or more independent pictures. In order that the pictures might be of the greatest scientific use, it was decided that several versions of each picture should be published. This has been done for Pictures 1–16 inclusive. (Pictures 17–22 are presented in one version only.)

It is well known that an experienced observer can discern more detail and sense more subtle relationships in a visual field than can an inexperienced person with equal visual acuity. For this reason, and to exploit more fully the discriminability of the *Mariner IV* camera, various versions of the *Mariner IV* pictures were examined by the professional staff of the lunar mapping section of the Aeronautical Chart and Information Center (ACIC) at Flagstaff, Arizona. This staff rendered the pictures into airbrush drawings showing the Martian surface features in accentuated form. Such an interpretation is, of course, subjective in that it involves personal experience and judgment. The strong lunar orientation of this group may have led to a tendency to sharpen the topographic relief so as to resemble the moon, even though this possibility was consciously recognized and allowed for in the study. There was also a distinct tendency to interpret small-scale shadings as due to surface relief rather than to surface albedo or atmospheric effects. Surface relief was interpreted as primarily the result of cratering, except for lineations and a few other forms that were otherwise interpretable.

Thus, the ACIC drawings must be regarded as an interpretative rendition of what the surface of Mars may look like. It is certainly correct in emphasizing craters as the principal features, but the accuracy of the topographic portrayal, in detail, necessarily must be viewed with some reservation. The drawings are based on repeated consultations between the ACIC staff and the *Mariner IV* experimenters. Even with considerable allowance for error in interpretation, one is left with the clear result that the Martian surface is, in fact, cratered much more densely than was at first believed on the basis of the initial crater counts, and may in places approach the density characteristic of the lunar uplands.

Each picture, then, is represented in the following forms:

(A) The ACIC air-brush rendition.

(B) A calibrated and geometrically corrected version, enhanced in contrast.

(C) The same, but sharpened as well.

(D) A negative version of the calibrated, enhanced picture in the original picture format (not geometrically corrected).

(E) A calibrated, contrast-enhanced version in the original picture format.

(F) A sharpened version of the same.

(G) A "fluctuation plot" in which smooth areas are rendered as dark and locally rough areas are rendered as light.

Details concerning production of the various versions are given in a later section.

The pictures are presented in pairs. The ACIC renditions incorporate the two overlapping pictures of a pair into a single view, but the photographs themselves are presented separately.

Certain technical information and descriptive comments are also included with each picture pair:

(1) The filter used with each picture.

(2) The location on Mars of the center of each picture. These locations were extracted from the more complete table of picture data in Appendix D. The general character of the area covered in each picture is also given.

(3) The approximate dimensions, in km, of the total area included in the picture. More precise data of this kind are also given in Table D-4.

(4) The approximate local solar time and solar zenith angle. The subsolar point was located at approximately 15.3°N, −171.6°E.

(5) The brightness range spanned by each picture. The various picture intensities were converted into integers spanning the range 0-63 by the formula

$$DN = 63\left(1 - \frac{I\text{-}min}{max\text{-}min}\right)$$

where $min < I < max$ is the picture intensity and $DN$ was rounded to the nearest integer. The picture density corresponding to a given integer is indicated by the 64-step gray scales included with each picture. Actual picture intensities are available as numerical matrices in Part II of this report.

The general comments cover the following aspects of the pictures:

(1) The craters appearing in each picture are described as to number, state of preservation, shape, and size. Craters of special interest are discussed individually where appropriate. The crater counts were made from the ACIC renditions and must be used with due regard to the limitations of these renditions discussed above. In general, craters that are in a "good" or "intermediate" condition of preservation will be recognized with little difficulty in the photographs. Craters in a "poor" state of preservation are individually more questionable as to their existence but, taken as a whole, may provide a fair guide as to the crater densities actually present. It is felt that the crater counts as given are probably about right, and are unlikely to be in error by more than a factor of 2 in either direction.

(2) The presence and predominant directions of systems of lineations are described, and the locations of individual lineations are given where appropriate.

(3) The presence and general characteristics of surface albedo variations are pointed out in those cases where these can be distinguished. General relationships of these to known surface features such as "canals" are also discussed.

(4) The character of the surface as to roughness and general texture is pointed out in a few instances.

Particular features of a given picture which are referred to in the text are located by their TV line and element numbers. Thus the location P5 L72 E101 means the 101st element of the 72nd line of Picture 5. If the pictures are viewed with the black mask at the top, the lines are vertical with line number increasing from right to left. Elements are then counted from top to bottom in each line. In the geometrically corrected pictures, single black picture elements at L100 E100, and at points 80 elements removed from this point, mark the corners of the fiducial marks. The lighting in the pictures is such that the sun is behind the camera and at an angle of 60 deg with its axis. The shadow of a point above the surface of Mars would lie on the same TV line and at a larger element number.

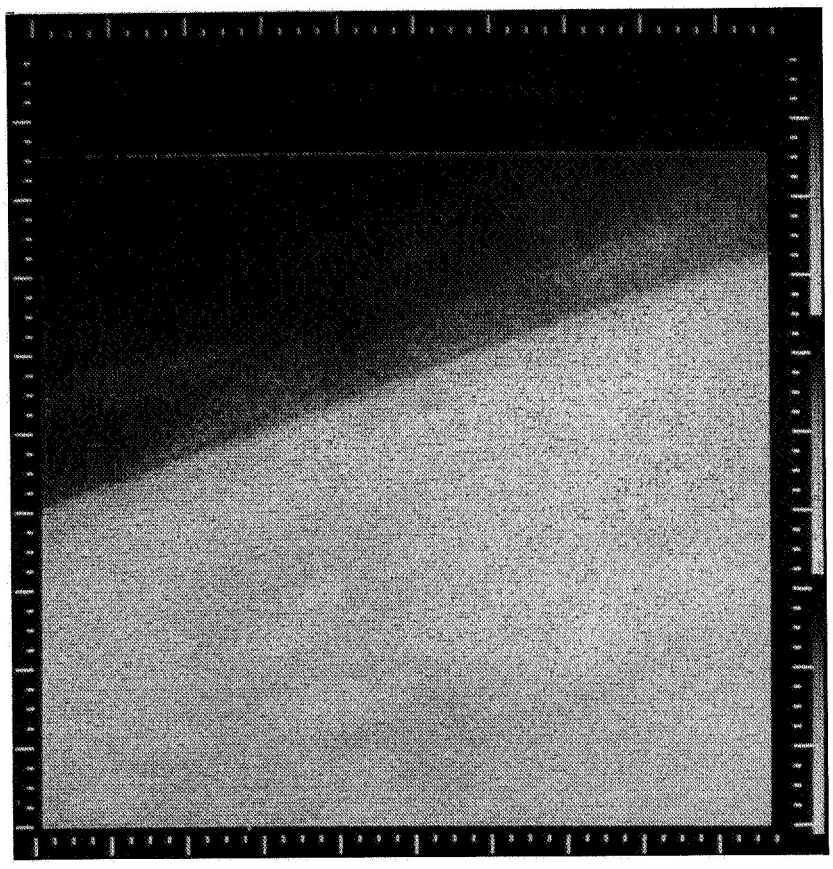

**Picture 1H. Picture 1 processed so as to emphasize the cloud above the limb**

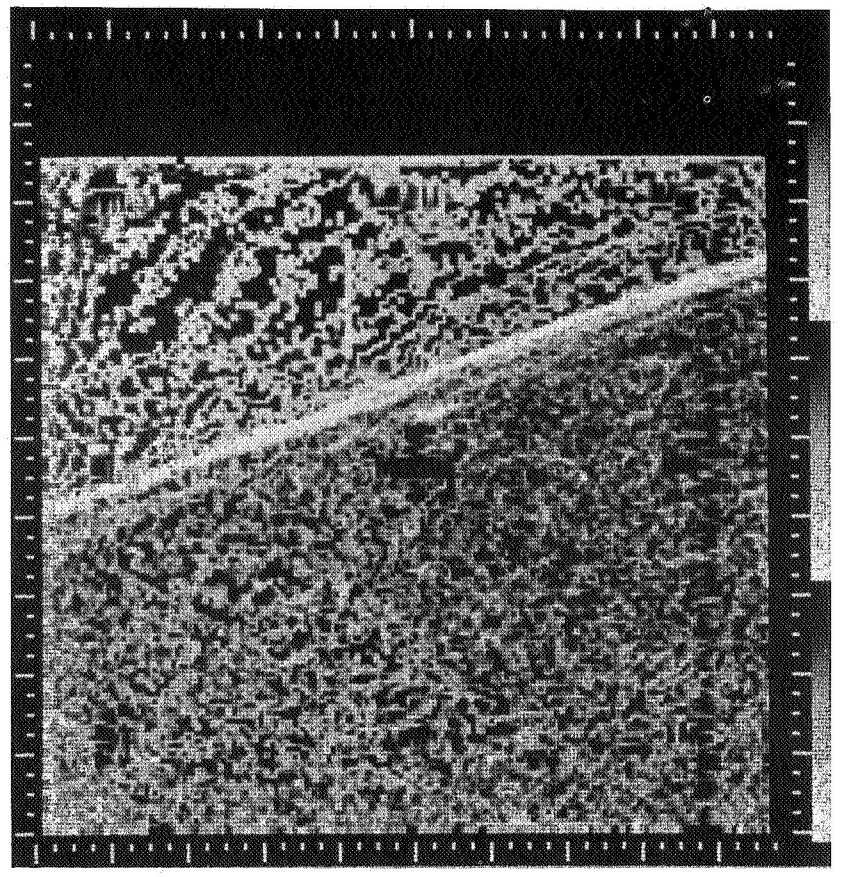

1G. Variance plot

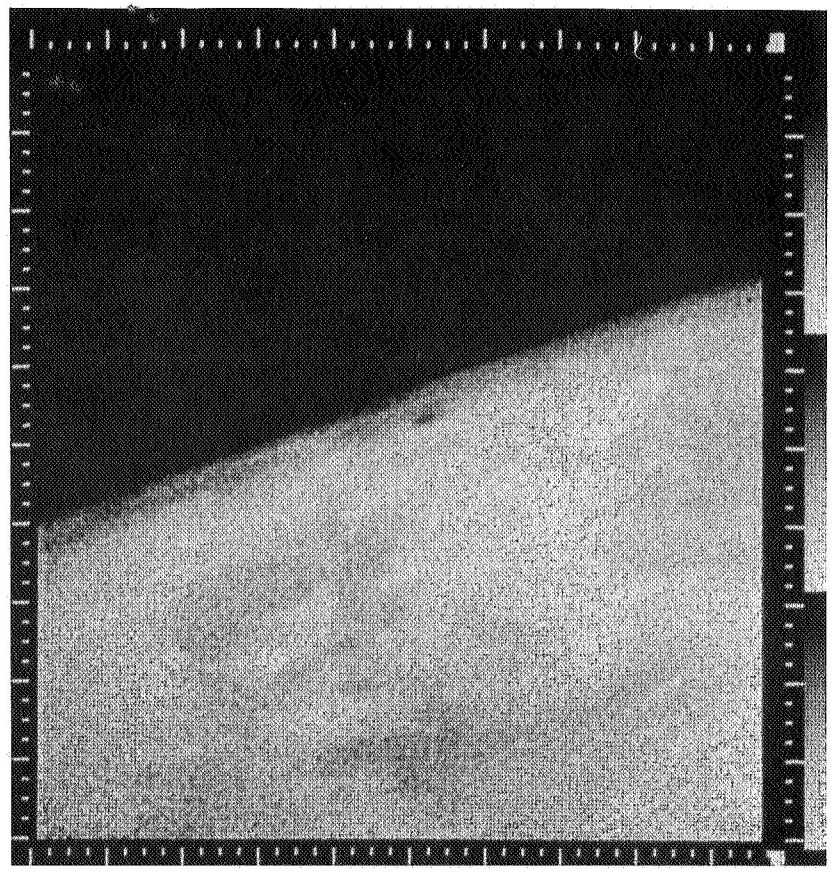

1F. Calibrated, sharpened, and enhanced

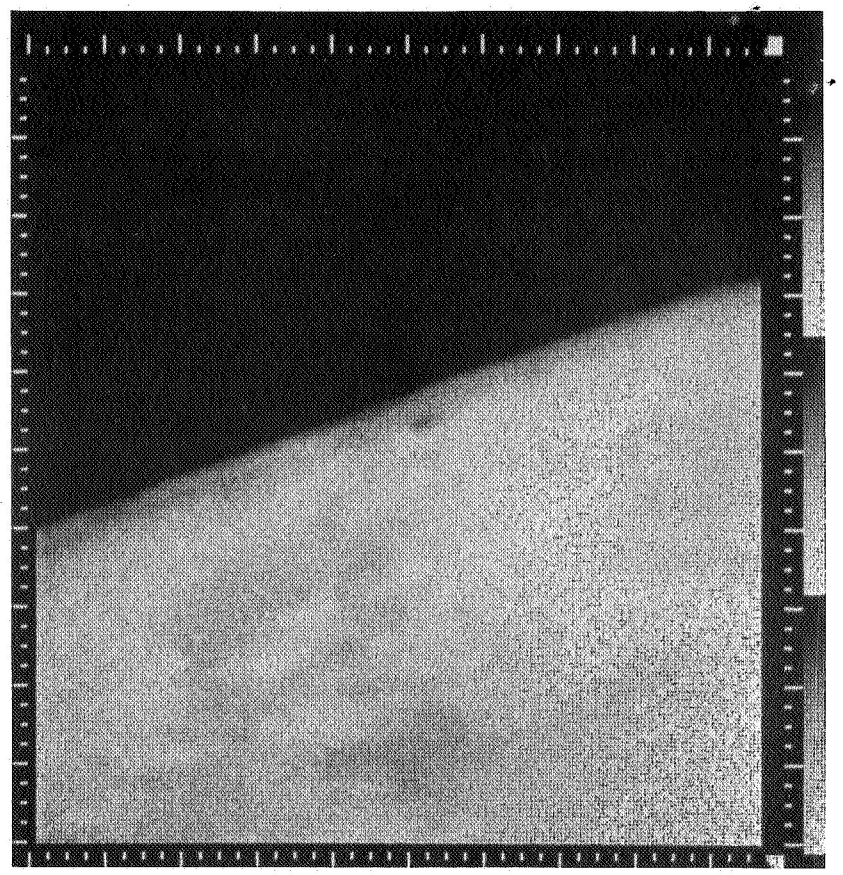

1E. Calibrated and enhanced

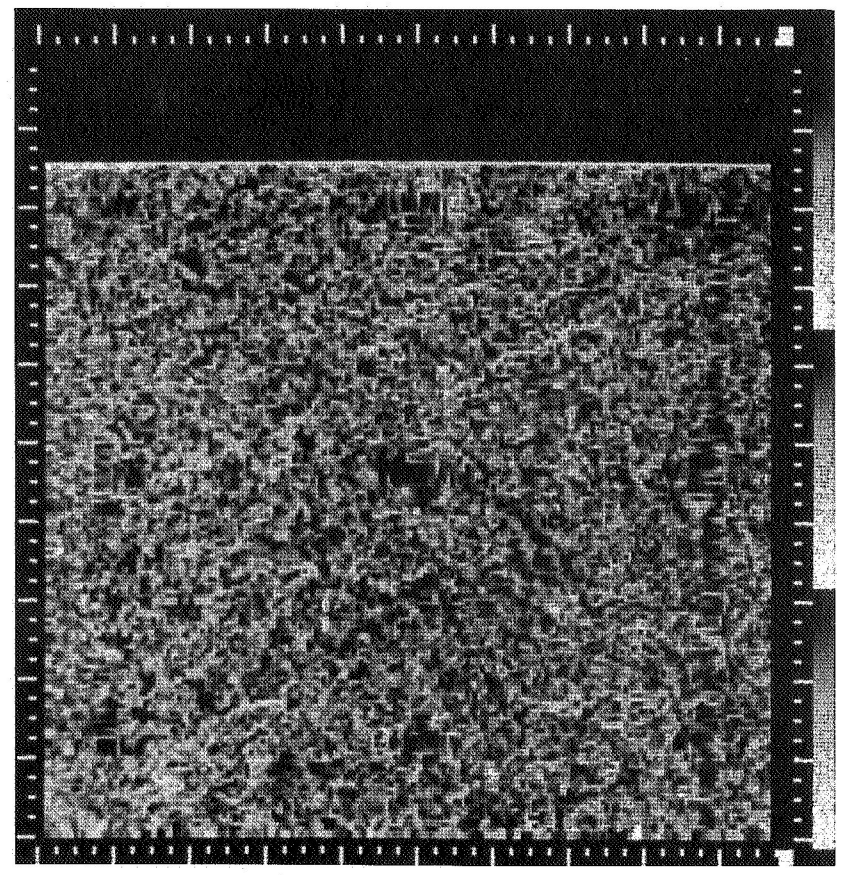

2G. Variance plot

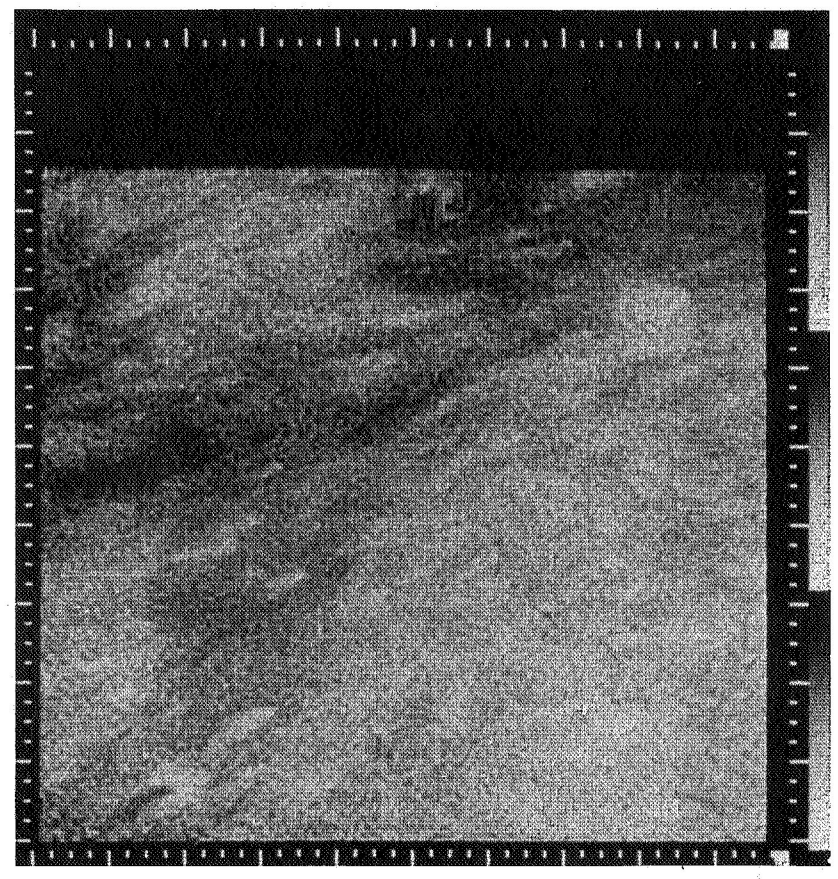

2F. Calibrated, sharpened, and enhanced

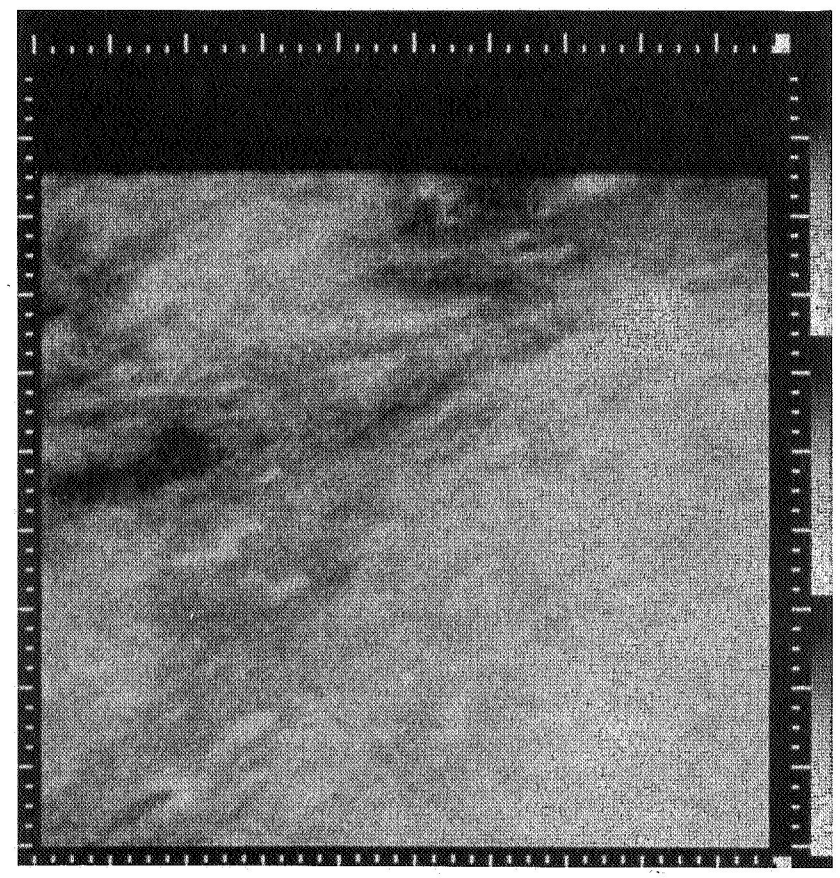

2E. Calibrated and enhanced

## Picture 1

### Filter

Orange

### Location of Picture Center

37°N, 173°E

All of the foreground is bright area and near the limb are the bright regions Phlegra and Azania. The dark spot near the limb is probably Propontis I.

### Dimensions

Picture 1 is about 350 km parallel to the limb; from the limb to the lower edge of photograph is about 1290 km.

### Time and Lighting

The local solar time at the center of the picture is 11:00.

The sun is 27° from the zenith.

### Brightness Ranges*

| Picture 1 | F | E | D | C | B |
|---|---|---|---|---|---|
| Min. | 165 | 165 | 98 | 165 | 165 |
| Max. | 265 | 265 | 265 | 265 | 265 |

### Martian Surface

Aside from some albedo variations involving relatively large, irregular areas and a few linear trends, this photograph provides little information on the nature of the Martian surface. The albedo variations in the SE corner appear also in the NW corner of Picture 2. In order to be visible on the limb, topographic relief would have to be abrupt and on the order of 3–5 km in height.

In addition to the dark spot (Propontis I) near the limb, there is some indication of a faint, dark line parallel to the limb and displaced about 5–7 picture elements from it. This structure is clearly seen in the "fluctuation plot" where it appears as a bright line. It is possible, although it seems unlikely, that this is the true limb, with the lower atmosphere extending 10 km or so above it. Such an effect is commonly seen in photographs of the limb of the earth from orbiting spacecraft. Some Martian maps show faint "canals" Helicon and Gyndes at about this location; the region of Propontis II and Gyndes appeared unusually dark as late as July 19, 1965, according to Capen (1966).

Visible in the sky adjacent to the limb are several faint hazy patches. These are probably thin clouds of dust or frozen $CO_2$ in the Martian atmosphere. These "clouds" are brought out more clearly in Picture 1H, which spans the brightness range 97-265. (The remaining versions of Picture 1 were enhanced so as to emphasize detail on the planet at the expense of suppressing the sky background.)

*Brightness ranges in this section are expressed in "reflectivity units" as described by Eq. (3–15).

## Picture 2

### Filter

Green

### Location of Picture Center

25°N, 175°E

Picture 2 is wholly within the bright region Amazonis, northeast of Trivium Charontis.

### Dimensions

Picture 2 includes 370–550 km east-west and 780–1000 km north-south.

### Time and Lighting

Local time is 11:00.

The sun is 18° from the zenith.

### Brightness Ranges

| Picture 2 | F | E | D | C | B |
|---|---|---|---|---|---|
| Min. | 116 | 119 | 119 | 117 | 121 |
| Max. | 179 | 169 | 169 | 170 | 166 |

### Surface Features

It is probable that a number of craters are shown on this photograph, but they are so faint that no counts or measurements have been made. Several striking contrasts in albedo are recorded, some of irregular outline and others distinctly linear with a northeast trend. A "canal," Erebus, in this region has been mapped by telescopic observation. The direction and location of this feature agree reasonably well with the prominent dark streak in the northern half of the photograph, but positive identification is lacking.

A distinct mottling is evident in the middle and southern part of the picture. The mottles tend to be light with dark borders on their northern edges and sometimes light borders on their southern edges. The shapes and distribution of these mottles seem unlike craters, but more suggestive of clouds. No cloud shadows are seen. If present, these would appear to be displaced along the beam scan direction (toward the south in this picture).

An indistinct, light spot of unknown character is visible near the NE corner of the picture.

REFERENCE COORDINATES

Line and element numbers, as recorded on the original television photographs, are depicted around the perimeter of the imagery for the purpose of identifying and referencing of features.

Element Number . . . . . North to South

Line Number . . . . . East to West

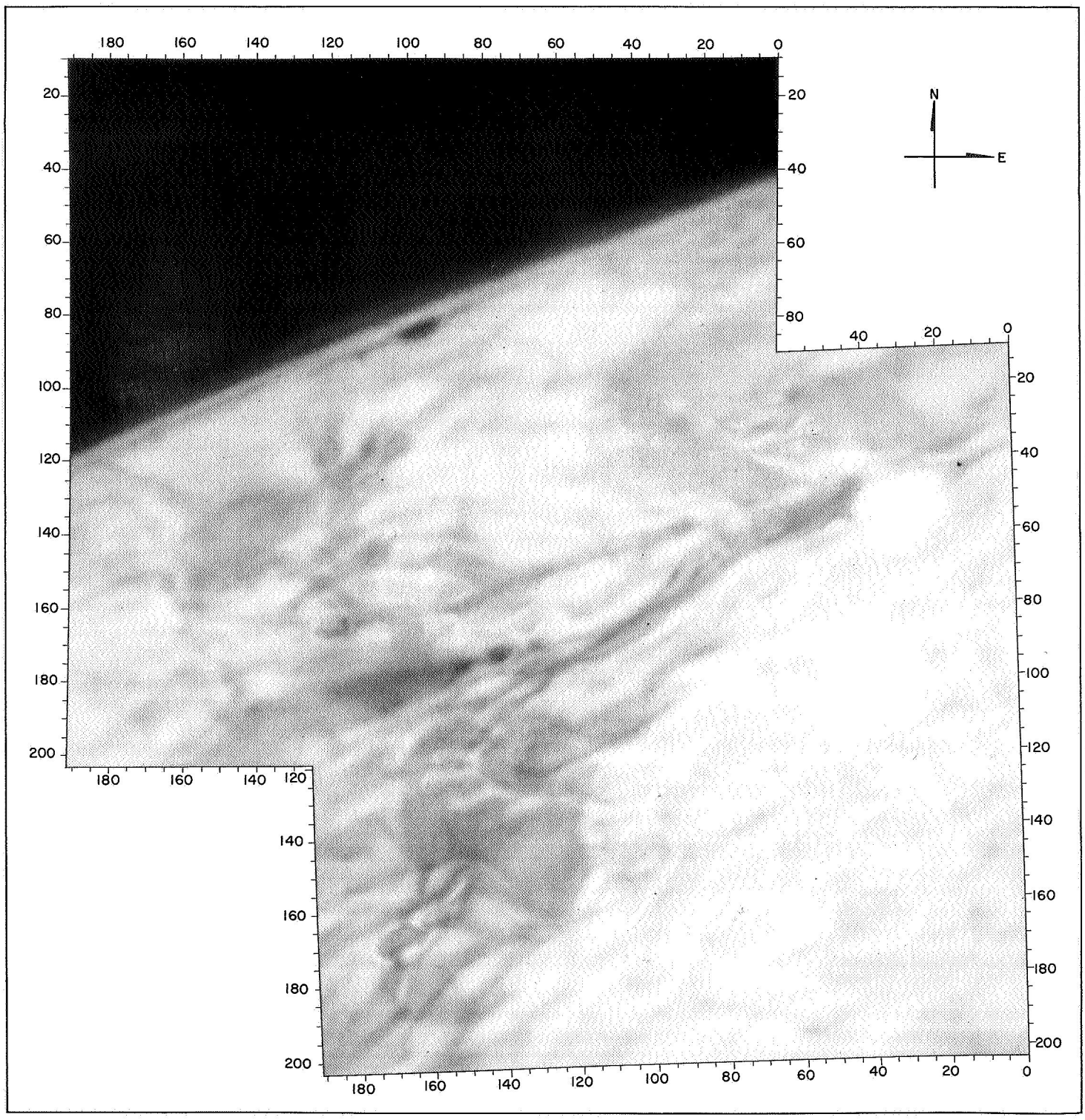


1, 2A. ACIC version



9 B

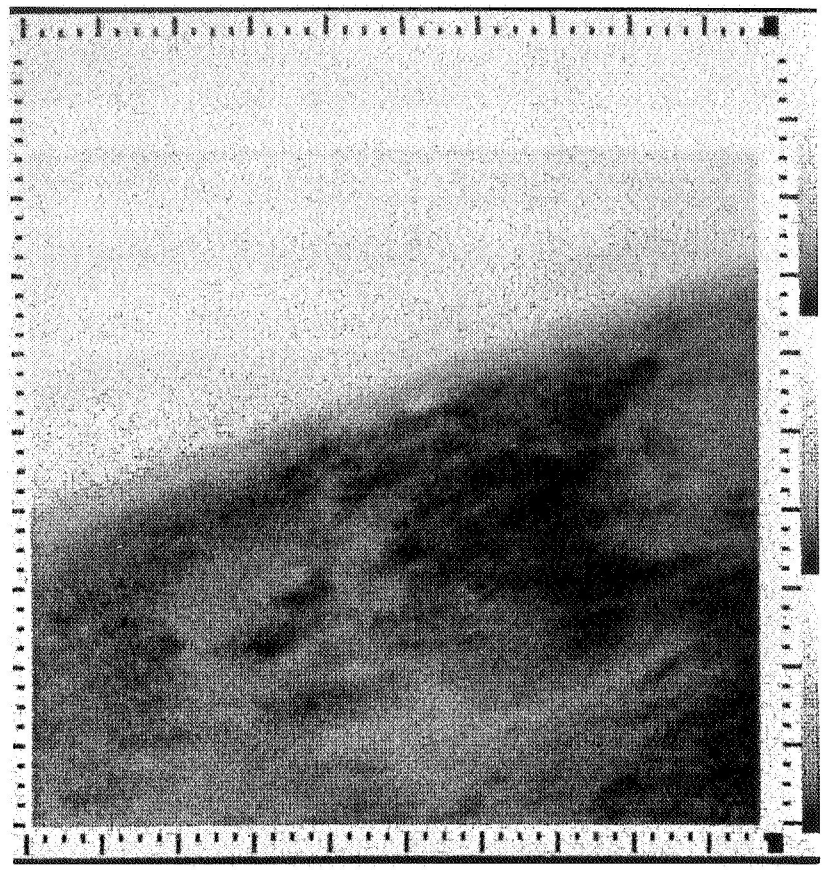

1D. Negative version, calibrated and unsharpened

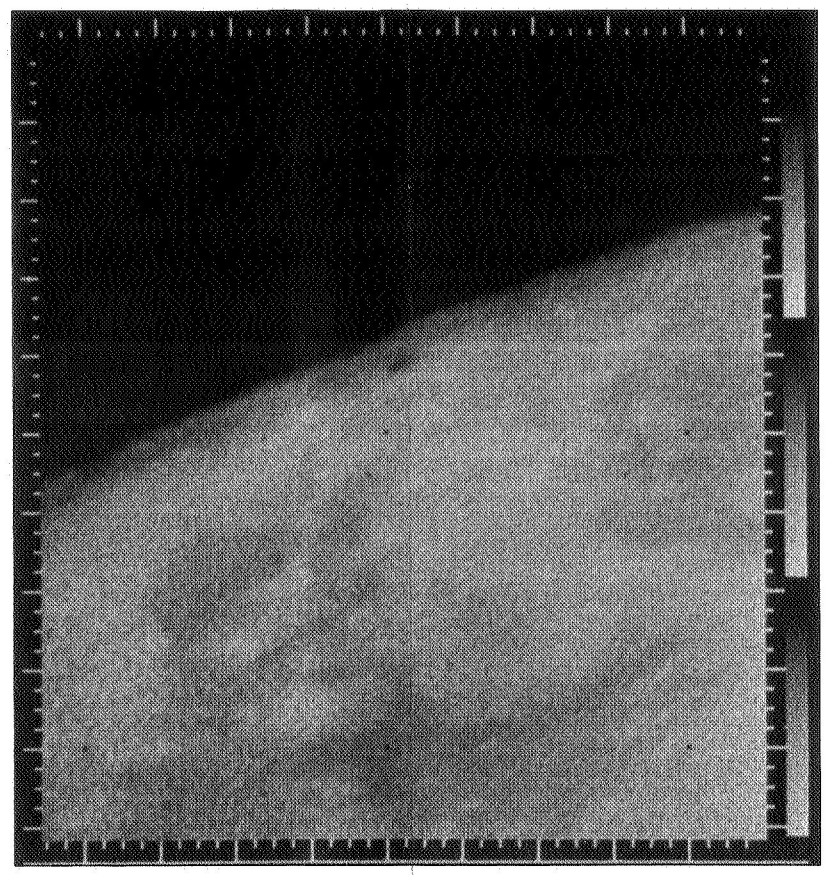

1C. Calibrated, rectified, and sharpened

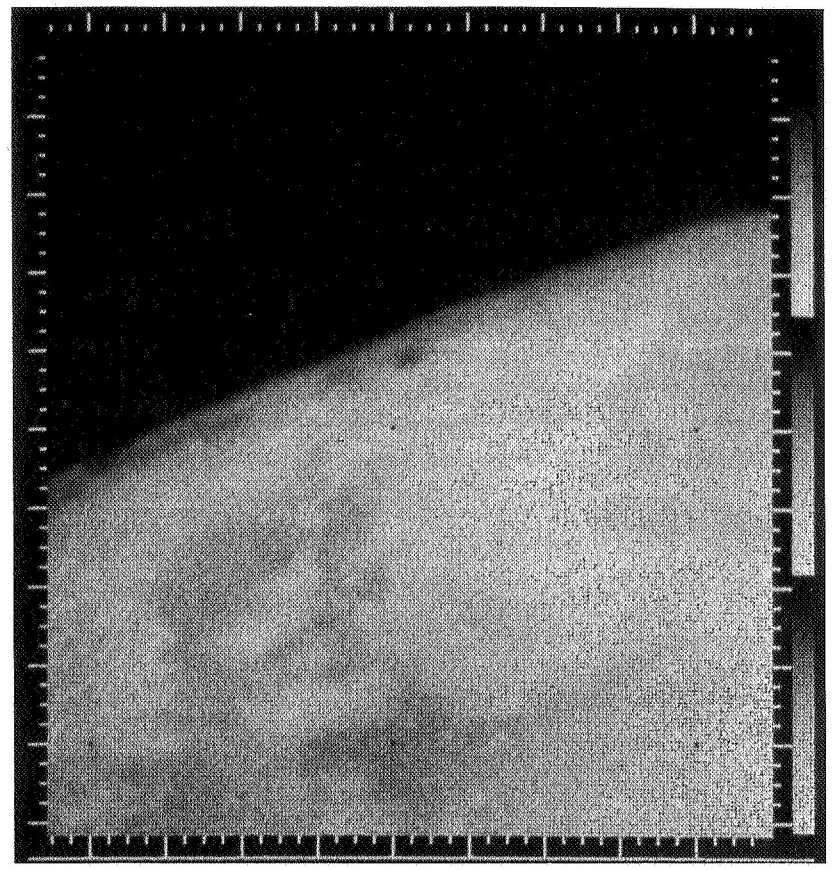

1B. Calibrated and rectified

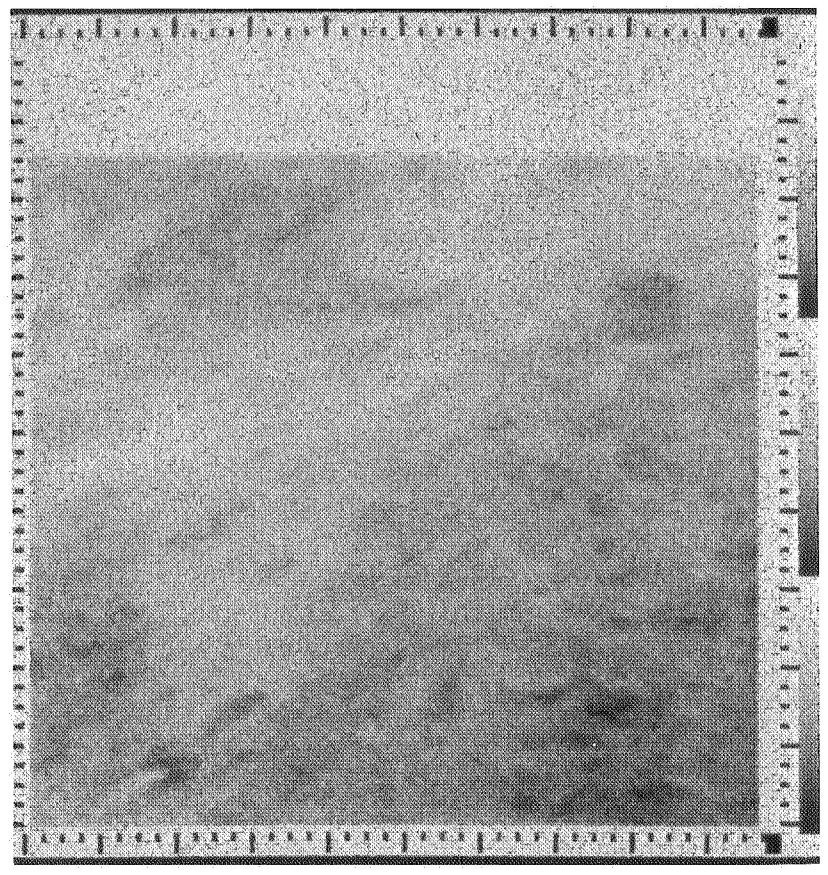

2D. Negative version, calibrated and unsharpened

9-C

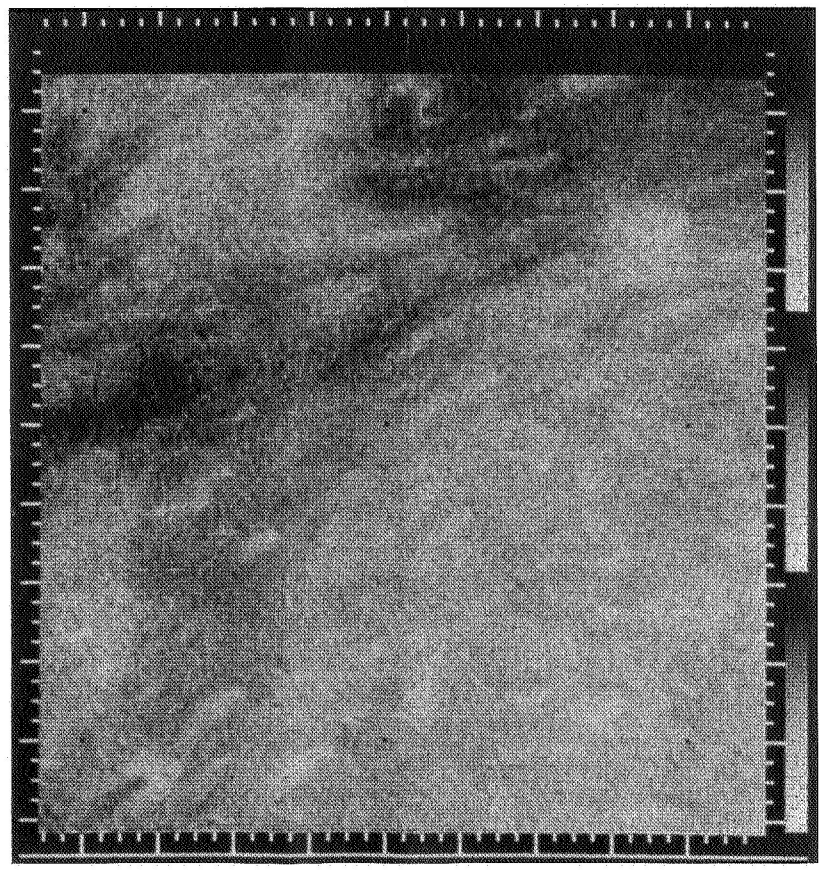

2C. Calibrated, rectified, and sharpened

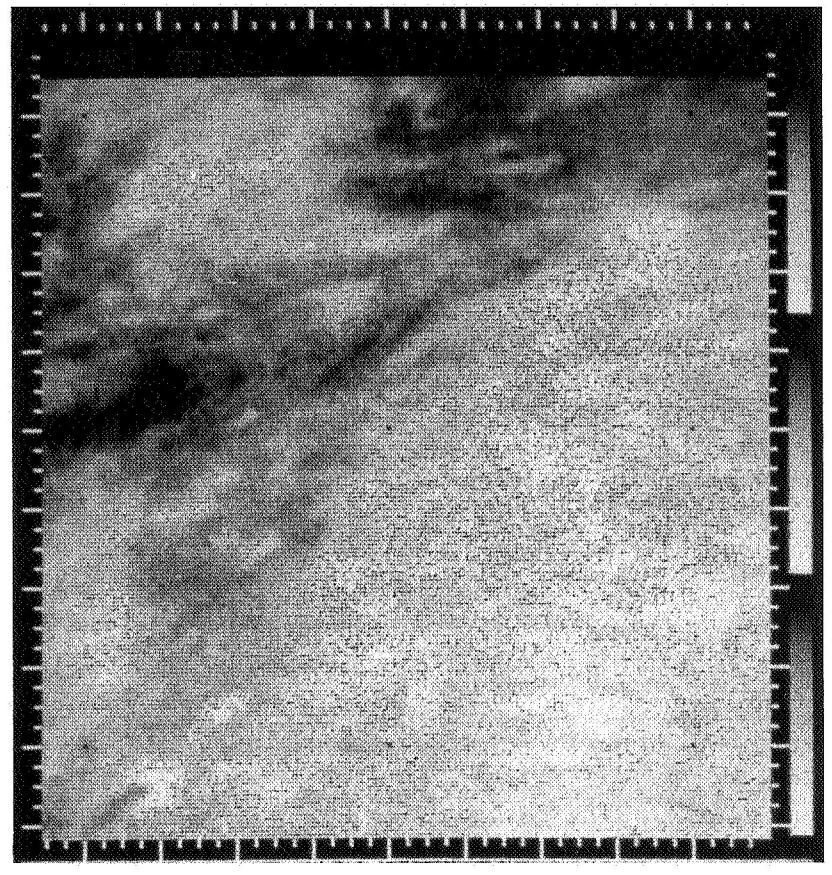

2B. Calibrated and rectified

9-D

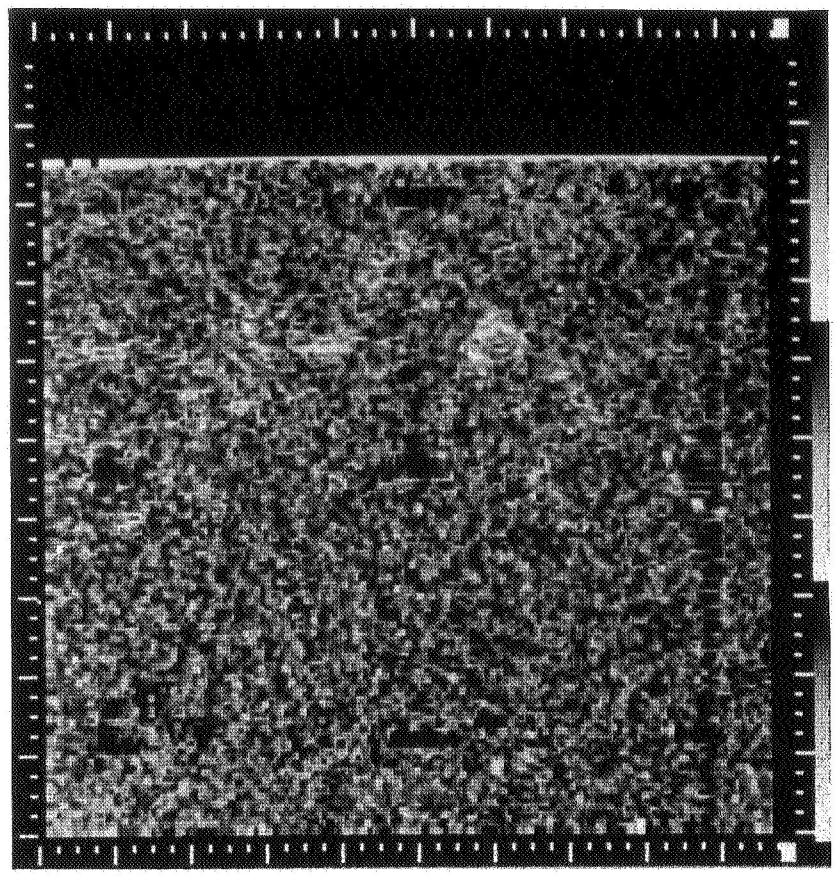

3G. Variance plot

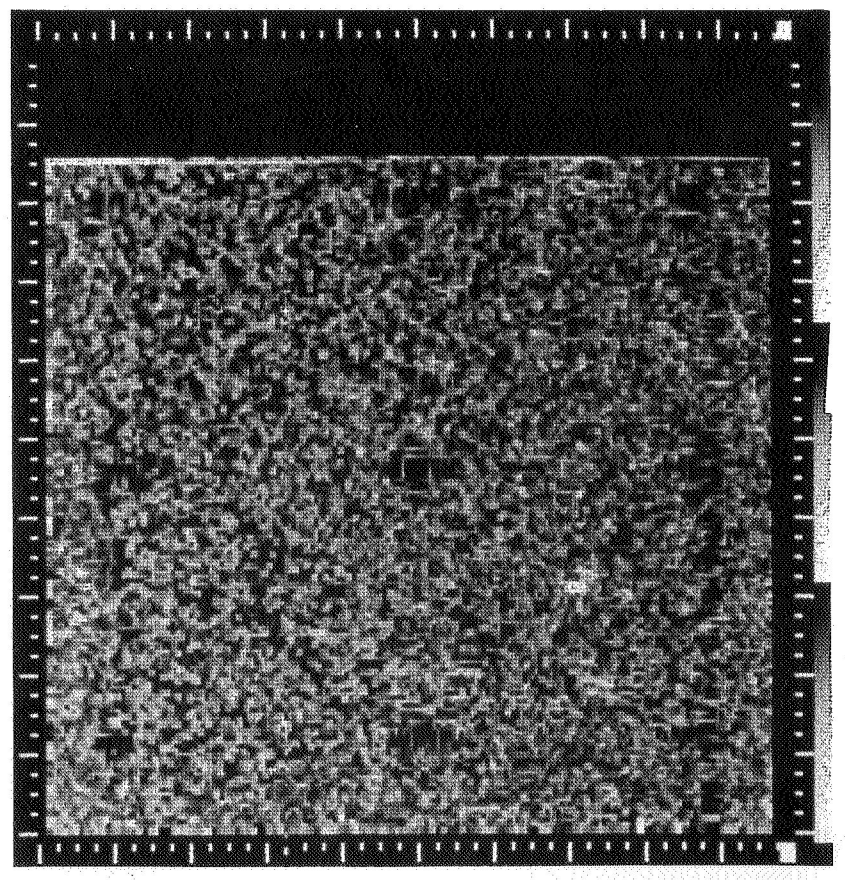

4G. Variance plot

10 - A

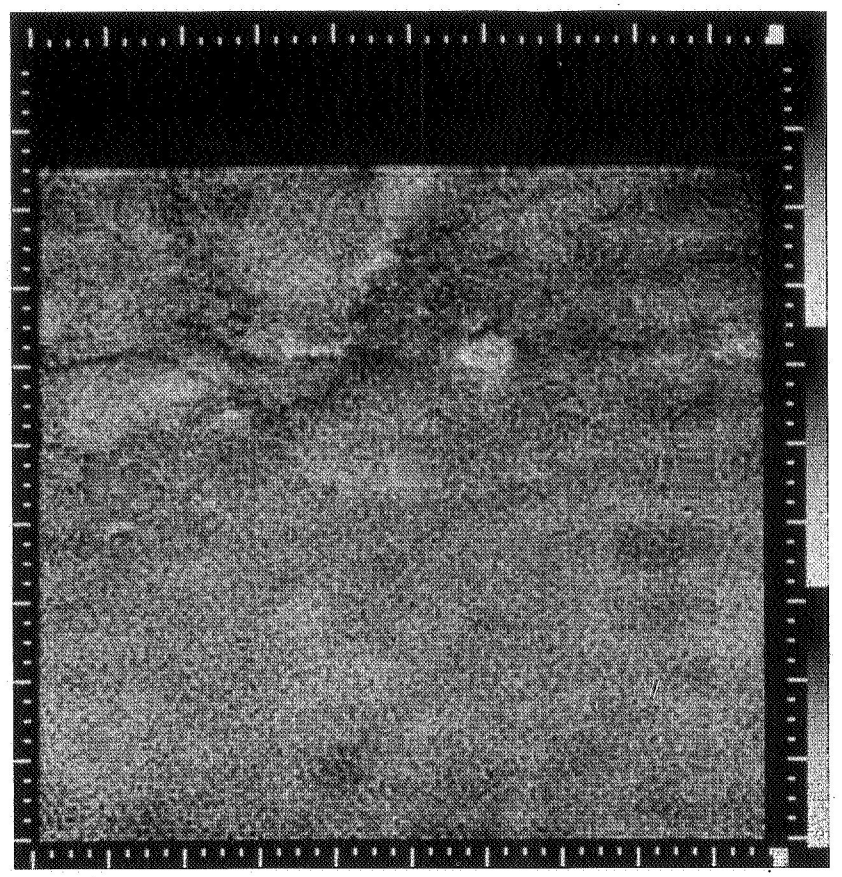

3F. Calibrated, sharpened, and enhanced

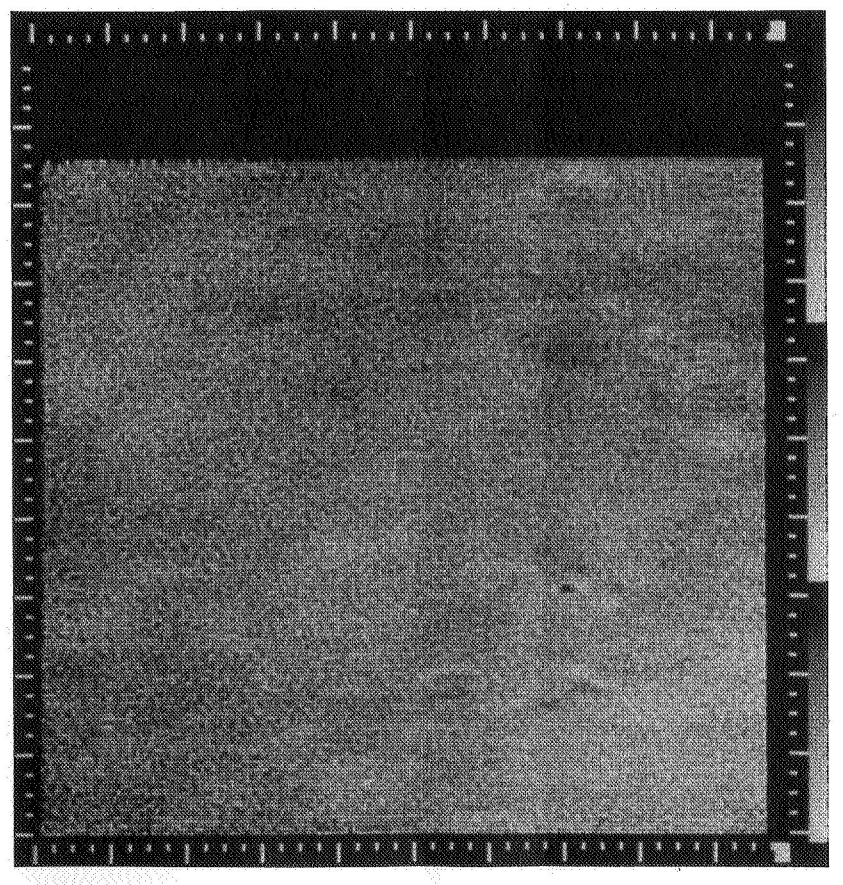

4F. Calibrated, sharpened, and enhanced

10-B

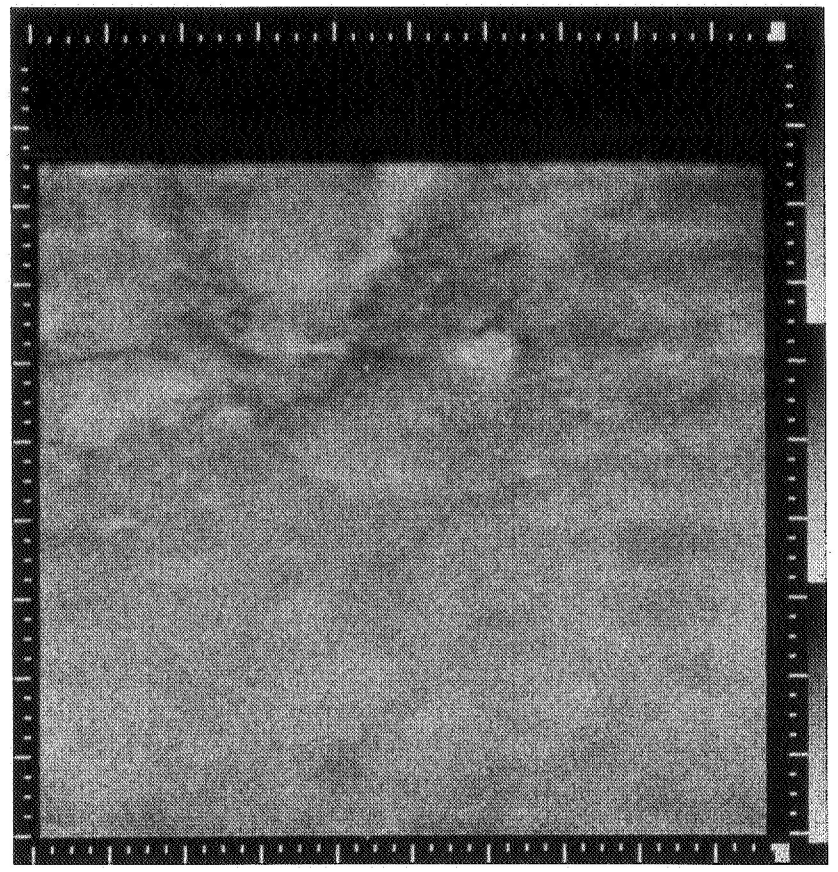

3E. Calibrated and enhanced

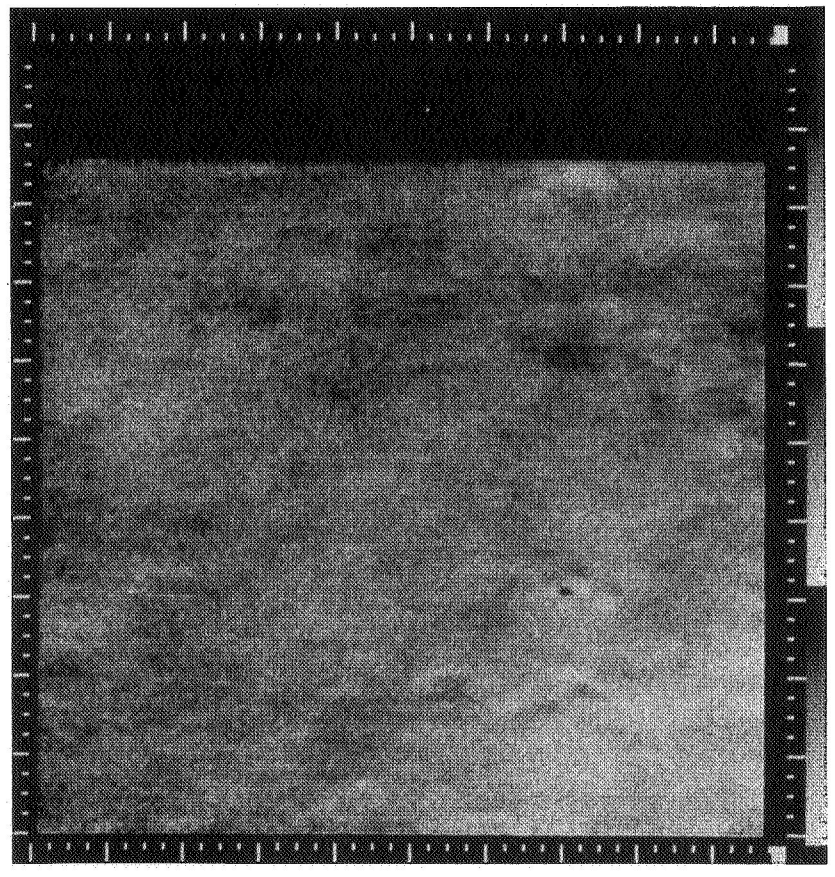

4E. Calibrated and enhanced

10-C

## Pictures 3 and 4

### Filters

Picture 3—green Picture 4—orange

### Location of Picture Center

Picture 3—12°N, 178°E Picture 4—7°N, 179°E

### Dimensions

Picture 3 includes approximately 310 km east-west and 500 km north-south; Picture 4 includes roughly 300 km east-west and 440 km north-south.

### Time and Lighting

The local time is 11:00.

The sun is 14° from the zenith in both pictures. The subsolar point is about 850 km east of the center of Picture 3.

### Brightness Ranges

| Picture 3 | F | E | D | C | B |
|---|---|---|---|---|---|
| Min. | 133 | 128 | 128 | 136 | 141 |
| Max. | 180 | 170 | 170 | 174 | 169 |
| Picture 4 | F | E | D | C | B |
| Min. | 224 | 233 | 233 | 230 | 246 |
| Max. | 300 | 290 | 290 | 294 | 288 |

### Craters

A total of 88 craters or possible craters are recognized on these photos, one with a central peak and none with clear polygonal outline. Of these, 5 are regarded as well preserved, 37 of intermediate and 46 of poor preservation. The largest crater identified is 80 km and the smallest 6 km in diameter. Craters may be considerably more abundant than this, for the high sun angle suppresses the visibility of vertical relief. On the other hand, some of the features interpreted as craters may not actually be such.

### Lineations

Two patterns of lineations, one bearing northwesterly, the other northeasterly, are discernible. Divergences as great as 40° occur in both sets. The complex of lineations in the northwest part of Picture 3 comes close to coinciding with the location and trend of the prominent canal, Orcus, mapped on the Martian surface from earth-based observations. The agreement is not close enough to be more than suggestive.

### Albedo and Surface Texture

The darker albedo in the northwest part of Picture 3 may bear some relation to the greater topographic complexity and possible relief there displayed. Much fine detail is visible in this area, some being greatly enhanced in sharpness and contrast in the sharpened versions of the picture. One's attention is particularly drawn to the narrow, dark lineation entering the west edge of the picture at element 67 (Picture 3B), and the bright spot with a dark edge at L80 E65 (Picture 3B). Some of the mottled appearance in this region may be similar to that noted in Picture 2.

Notable features in Picture 4 are the brighter albedo in the southeast corner, several diffuse dark patches (some of which may be old craters), and a small, especially dark spot at L57 E135 (Picture 4B). This small spot covers four or five picture elements and is about 10% less bright than its surroundings.

D

10-E

REFERENCE COORDINATES

Line and element numbers, as recorded on the original television photographs, are depicted around the perimeter of the imagery for the purpose of identifying and referencing of features.

Element Number . . . . . North to South
Line Number . . . . . East to West

0 20 40 60 80 100 200
km

Orthographic Projection
at 10°39'57"N and 178°26'13"E

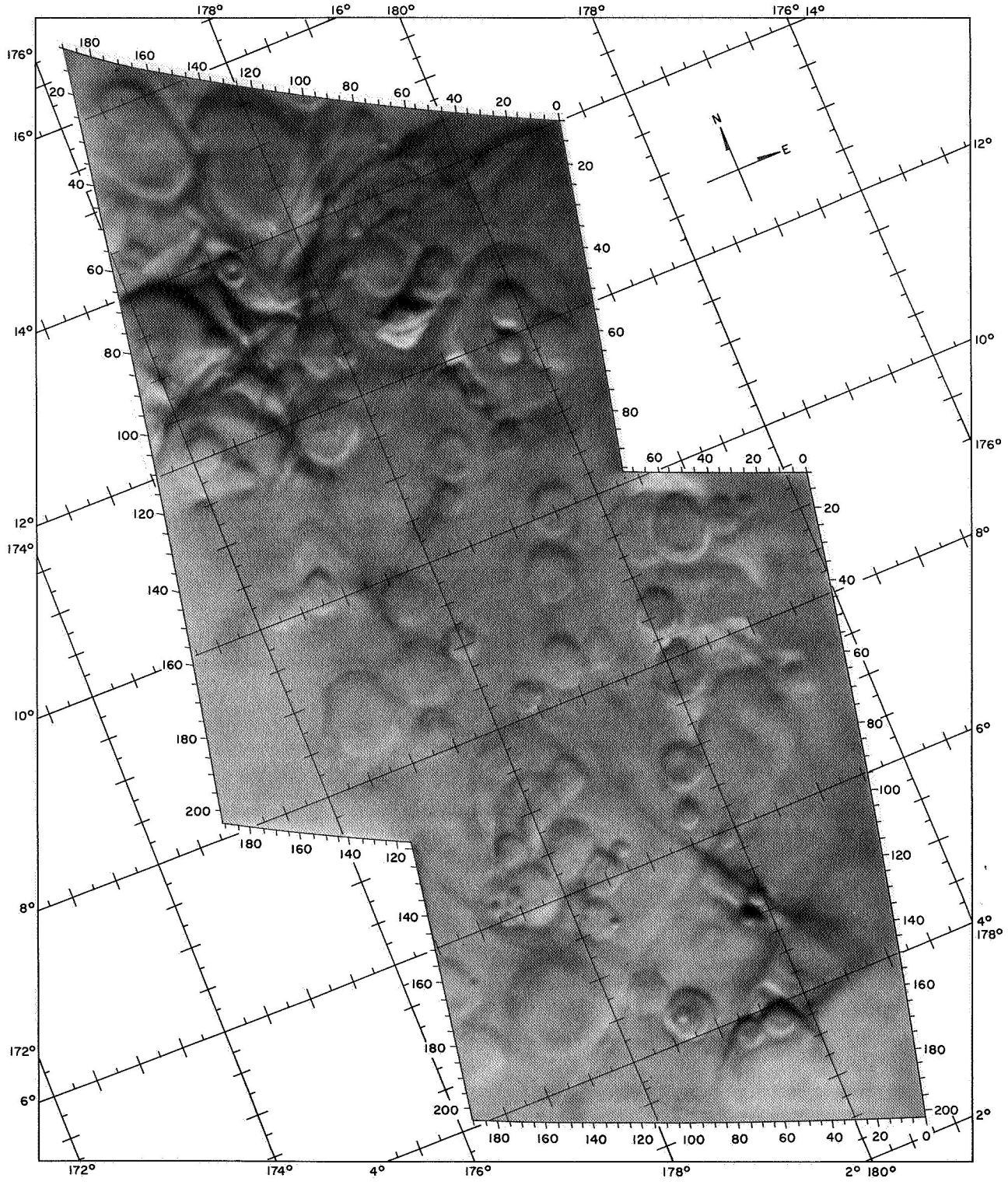


**3, 4A. ACIC version**

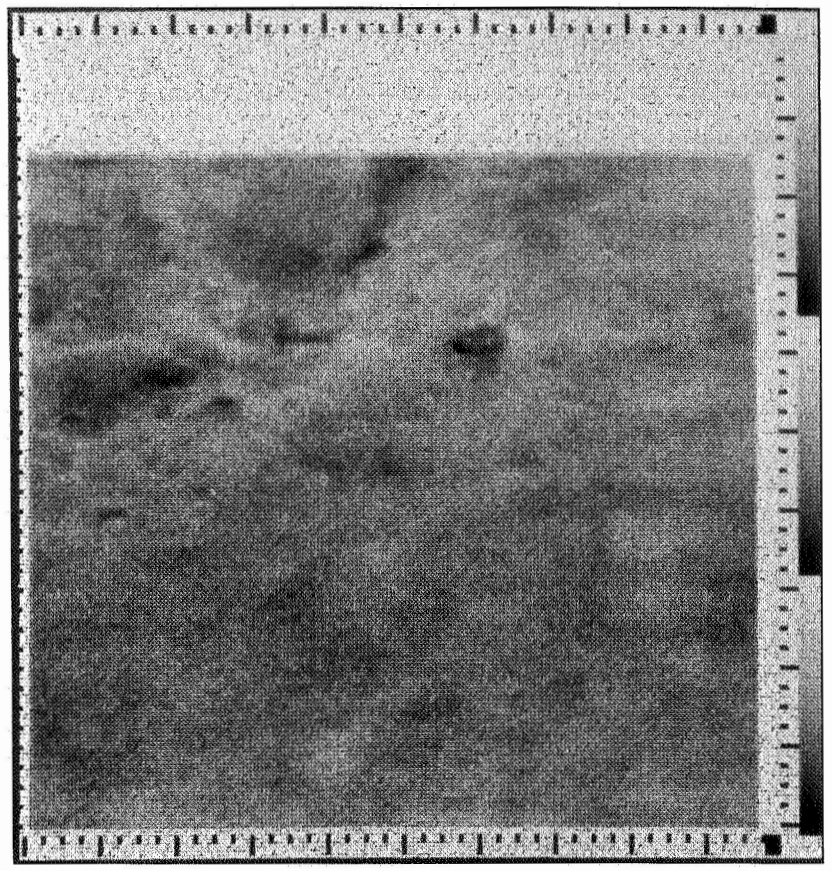

3D. Negative version, calibrated and unsharpened

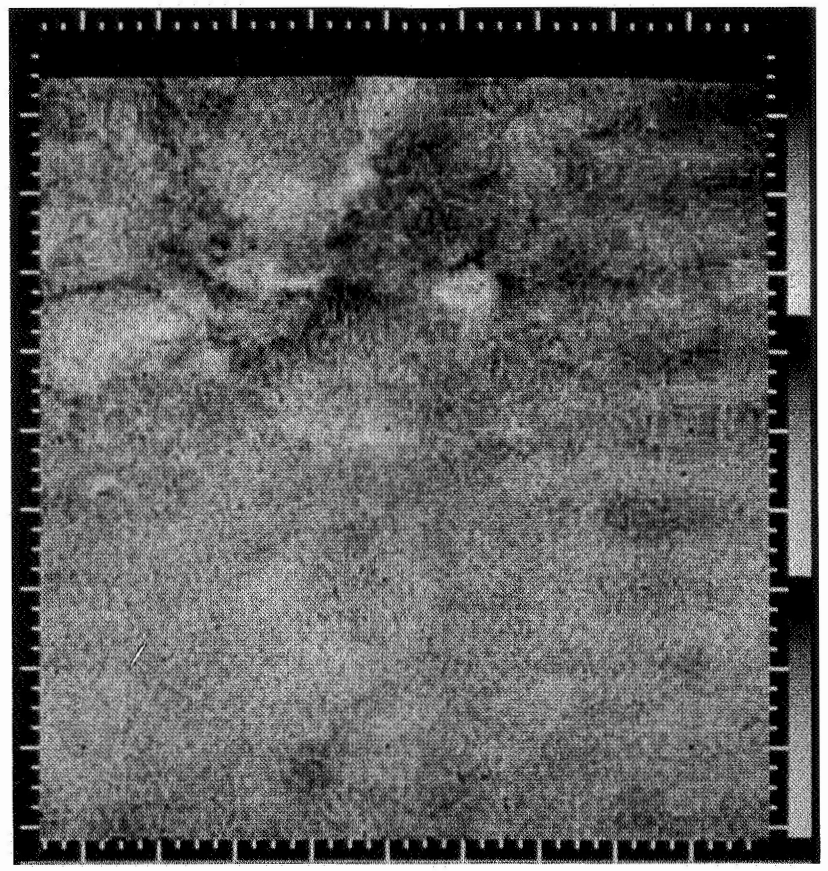

3C. Calibrated, rectified, and sharpened

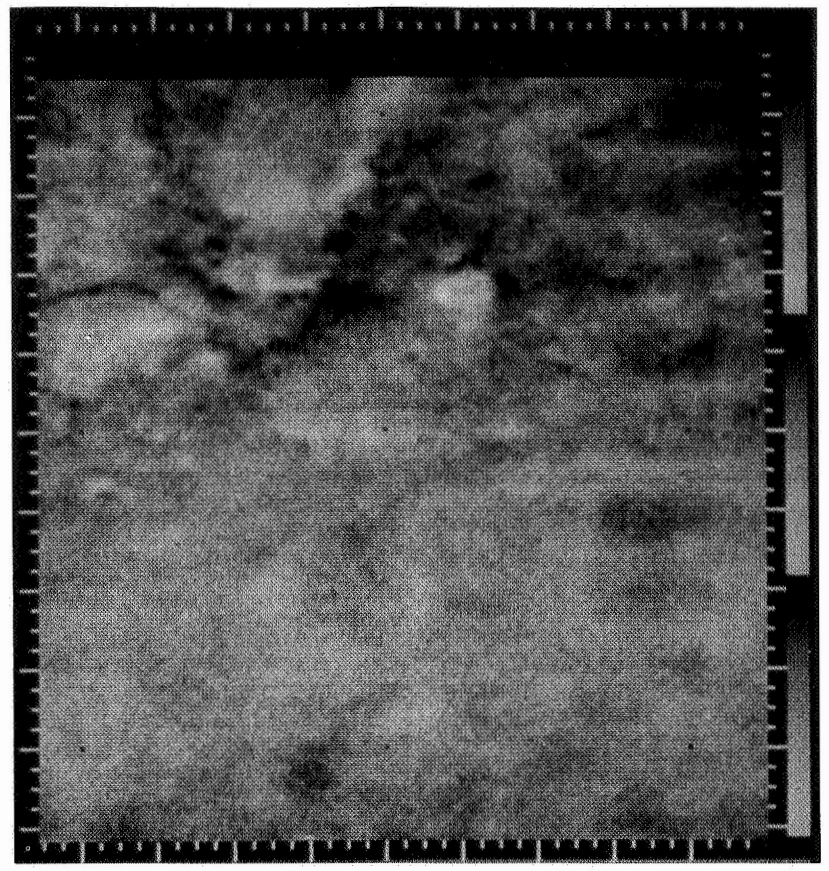

3B. Calibrated and rectified

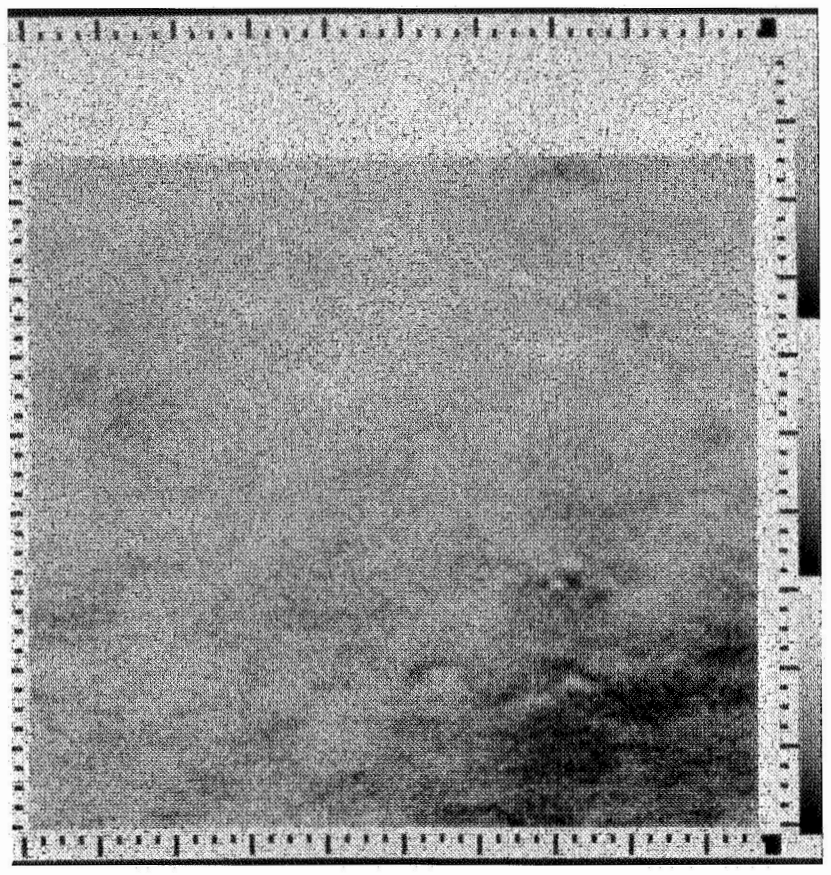

4D. Negative version, calibrated and unsharpened

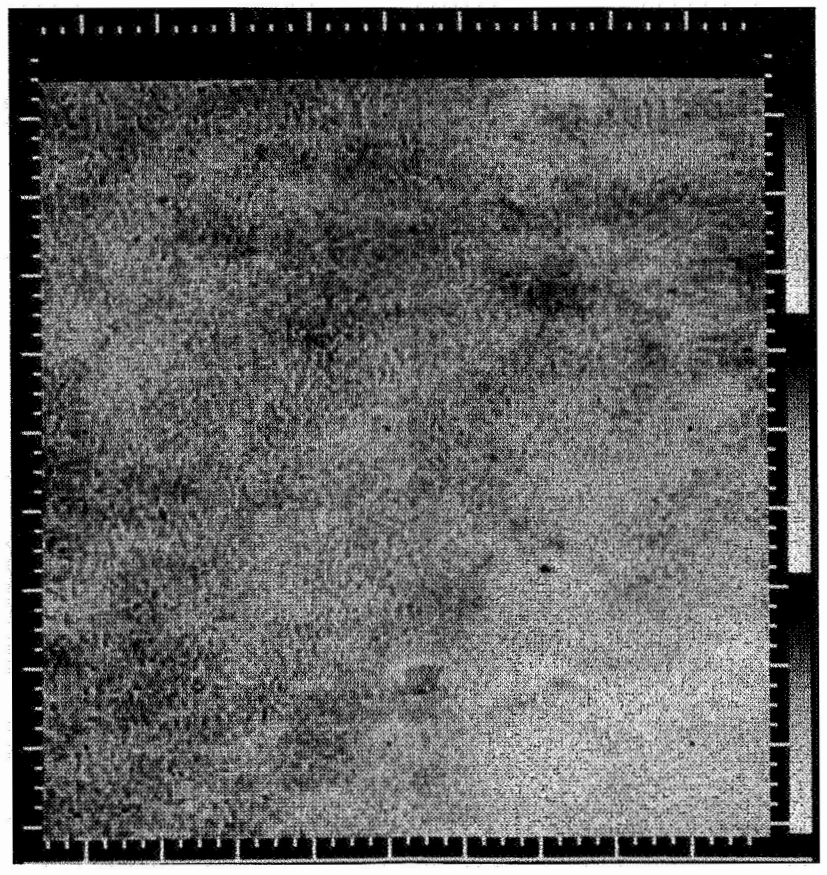

4C. Calibrated, rectified, and sharpened

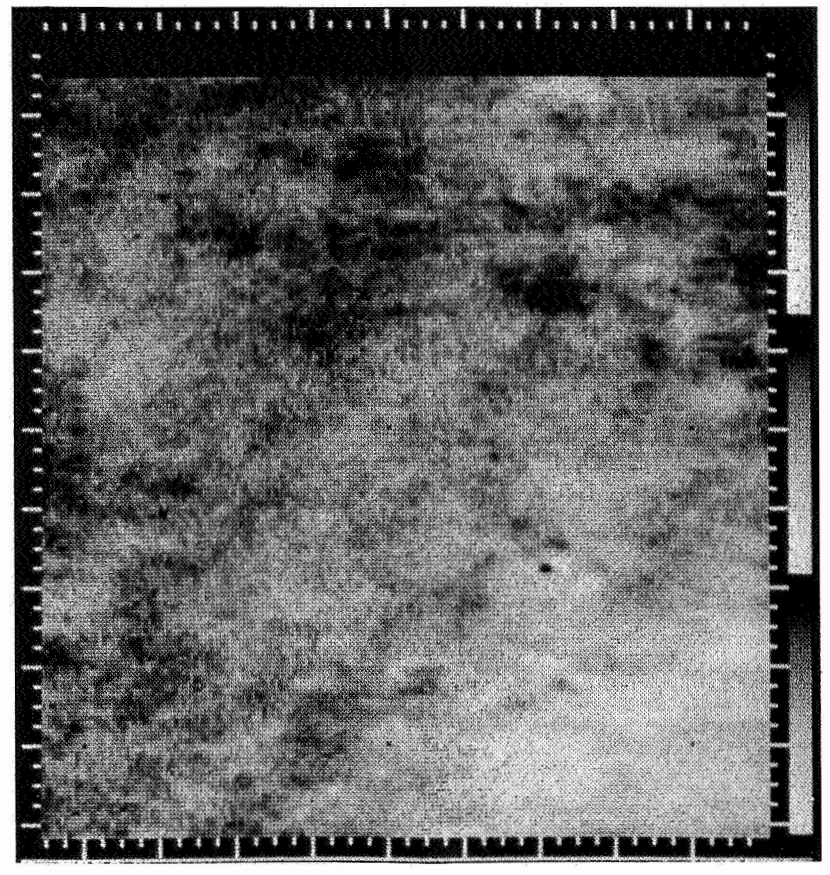

4B. Calibrated and rectified

11-B

11-C

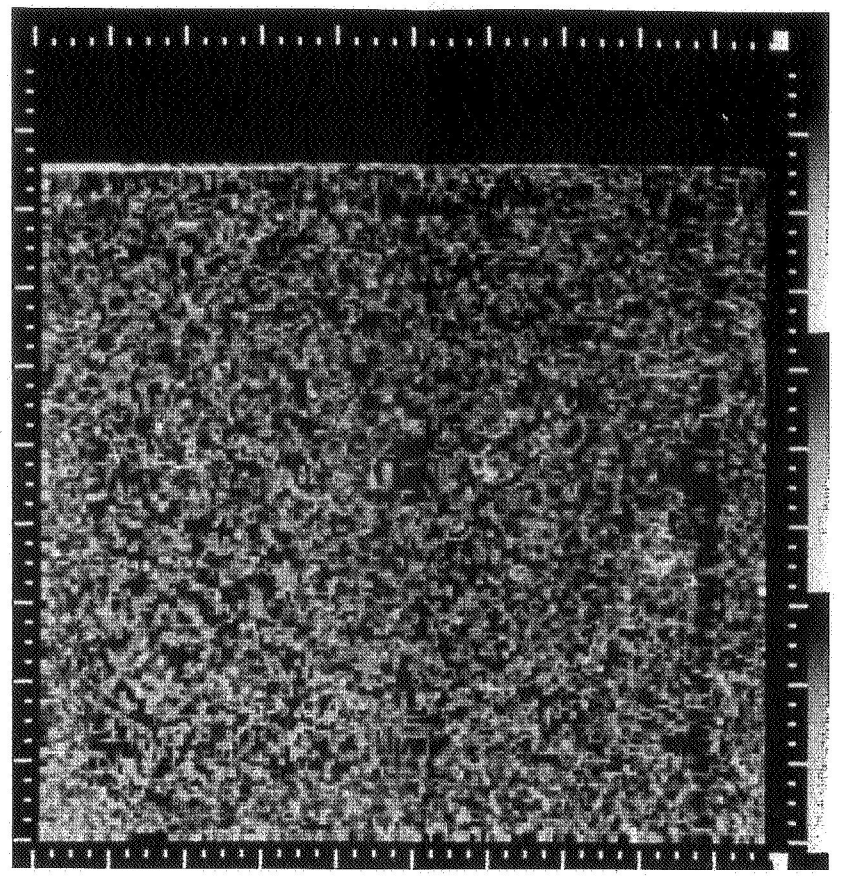

5G. Variance plot

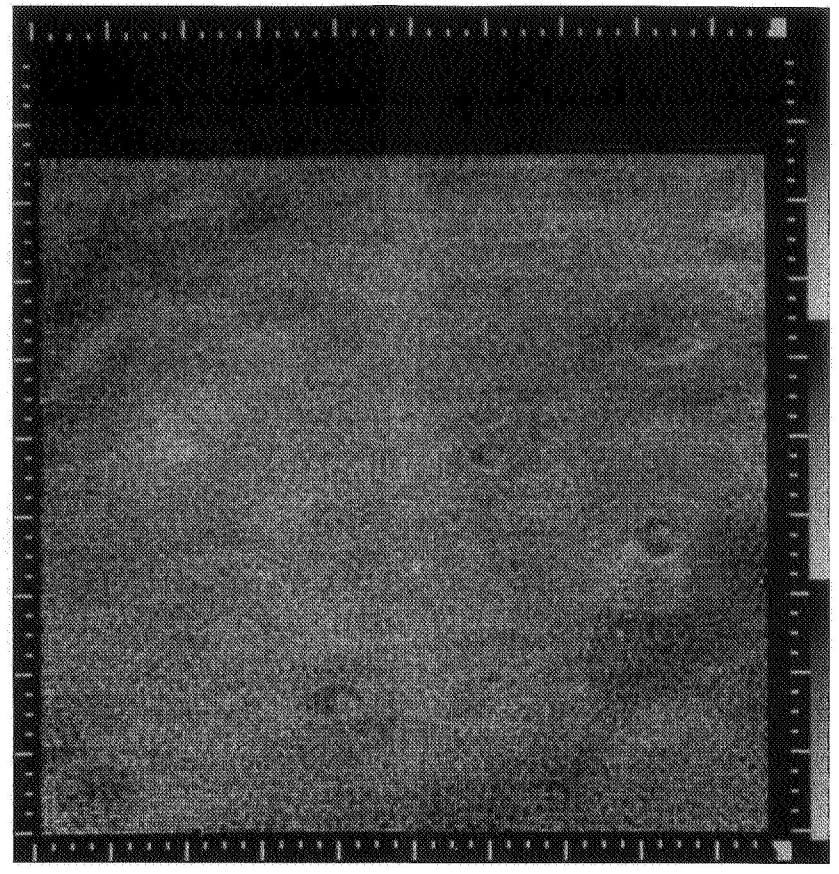

5F. Calibrated, sharpened, and enhanced

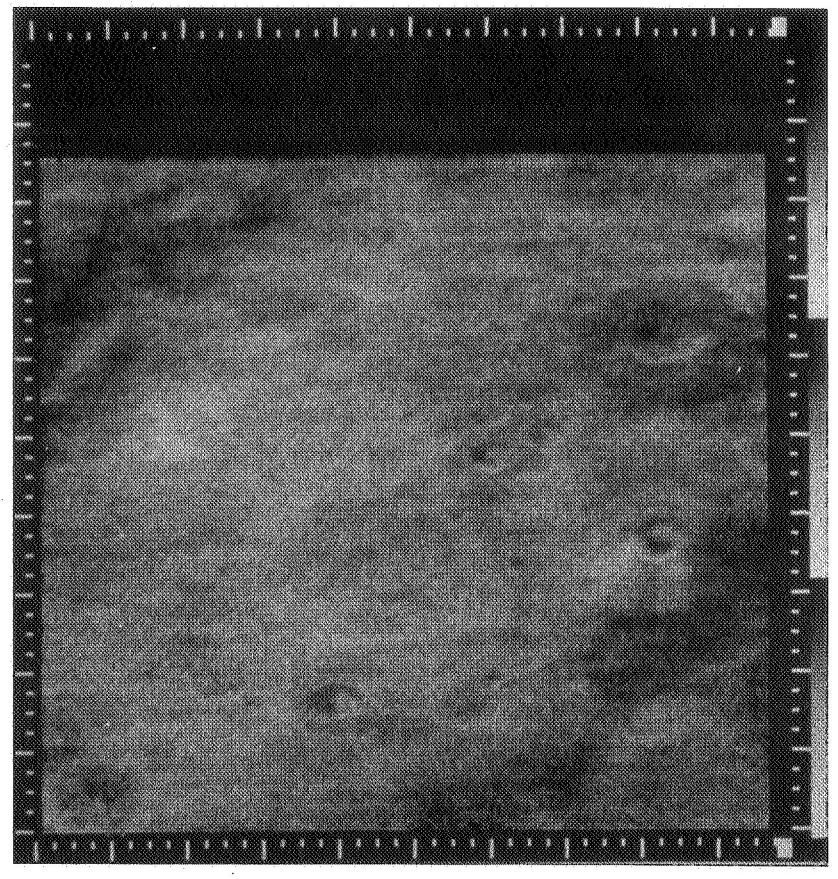

5E. Calibrated and enhanced

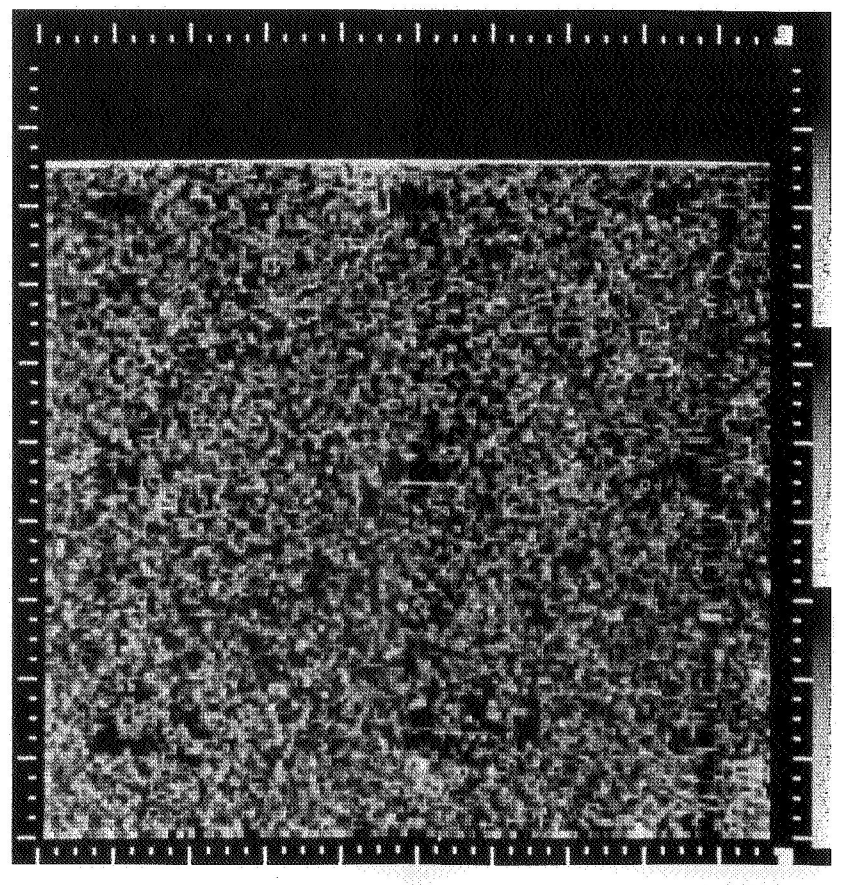

6G. Variance plot

12 - A

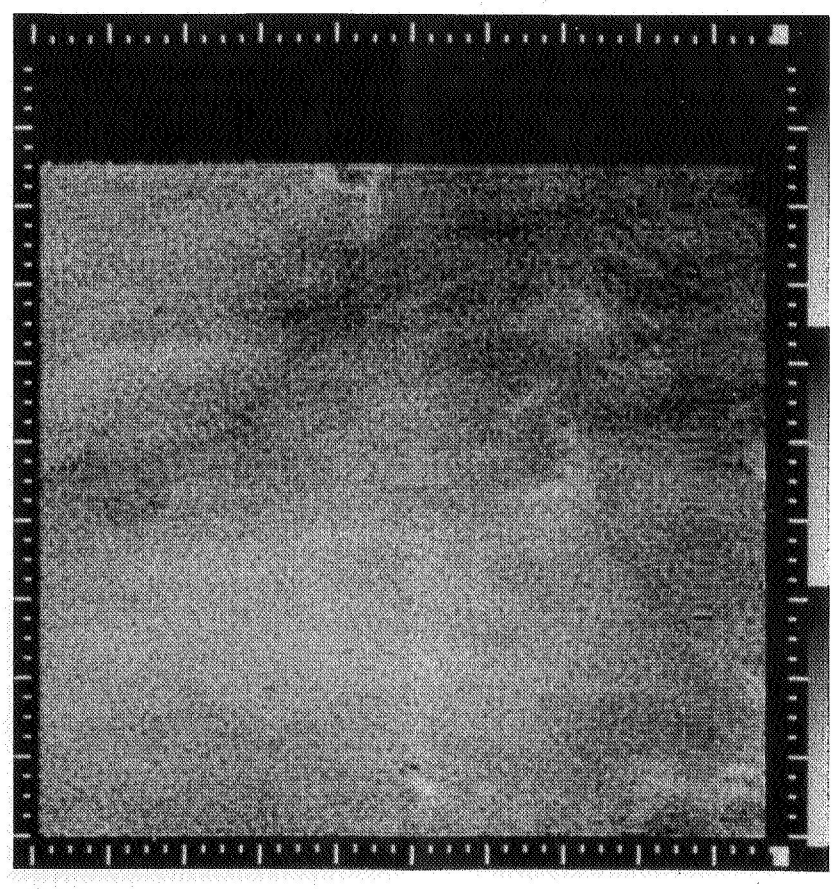

6F. Calibrated, sharpened, and enhanced

12 - B

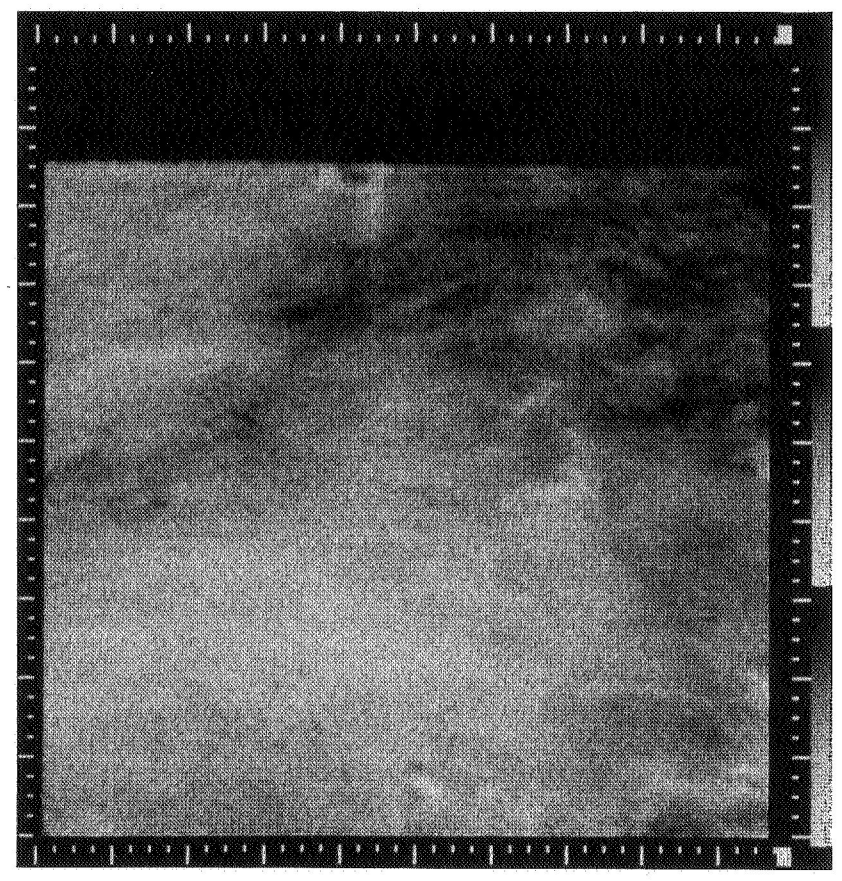

6E. Calibrated and enhanced

12 - C

## Pictures 5 and 6

### Filters

Picture 5—orange Picture 6—green

### Location of Picture Center

Picture 5—2°S, 181°E Picture 6—6°S, 183°E

Both pictures are located between the eastern part of the bright region Zephyria and the western part of the bright region Mesogaea.

### Dimensions

Each picture covers an area approximately 306 km east-west and 322 (for 6) and 354 km (for 5) north-south.

### Time and Lighting

The local time is about 11:30 for both pictures.

The sun is 19° from the zenith in Picture 5 and 22° in Picture 6.

### Brightness Ranges

| Picture 5 | F | E | D | C | B |
|---|---|---|---|---|---|
| Min. | 217 | 231 | 231 | 224 | 233 |
| Max. | 296 | 293 | 293 | 291 | 285 |
| Picture 6 | F | E | D | C | B |
| Min. | 122 | 123 | 123 | 125 | 128 |
| Max. | 171 | 162 | 162 | 169 | 162 |

### Craters

A total of 92 possible craters are recognized on this pair of photos, 6 with a central peak and 2 with good polygonal outline. Nine are classed as well preserved, 40 as of intermediate and 43 of poor preservation. The smallest crater is 5 km and the largest 64 km in diameter. The relatively fewer number of craters recognized and the larger diameter of the smallest crater (5 km compared to 3–4 km on other photo pairs) probably reflects more the elevation of the sun than any true variation on the Martian surface.

### Lineations

Two sets of linear features, trending northeast and northwest respectively, are rather well shown on these photos. Both sets are long, continuous, and somewhat irregular to gently curving.

Quite interesting is the dark, irregular linear zone extending northeasterly across the northwest part of Picture 6 and southeast part of 5. This coincides with a "canal" shown on the ACIC map of Mars (1962). Other Martian maps show different "canal" configurations in this region: the "canals" Avernus, Tartarus, and Saus converge in approximately this area.

An especially narrow, sharp lineation is visible near the northwest corner of Picture 5.

### Albedo and Surface Texture

Although these photos are wholly within a bright area, they show an unusually high albedo contrast, principally because of the irregular dark areas tentatively associated with "canals" in this region. Aside from the craters, which are becoming more visible because of the more favorable illumination angles, the most striking feature of this photo pair is the massive dark area in the northeast part of Picture 6. This marking shows a definite texture of sweeping, curved filaments suggestive of some sort of structure. Some of these filaments become quite narrow in the sharpened Pictures 6C and 6F.

A few light patches are also present: In Picture 5B one sees an irregular mark at L165 E90, a bright fan-shaped area possibly associated with the unusual crater at L32 E123, and a short, bright, westerly bearing lineation near L118 E151. In Picture 6B, the ring-shaped mark centered near L65 E93 is especially noticeable, and a few smaller mottles along the south edge are also present.

REFERENCE COORDINATES

Line and element numbers, as recorded on the original television photographs, are depicted around the perimeter of the imagery for the purpose of identifying and referencing of features.

Element Number . . . . . North to South
Line Number . . . . . East to West

0 20 40 60 80 100 200
km

Orthographic Projection
at 3°31'42"S and 177°48'54"W

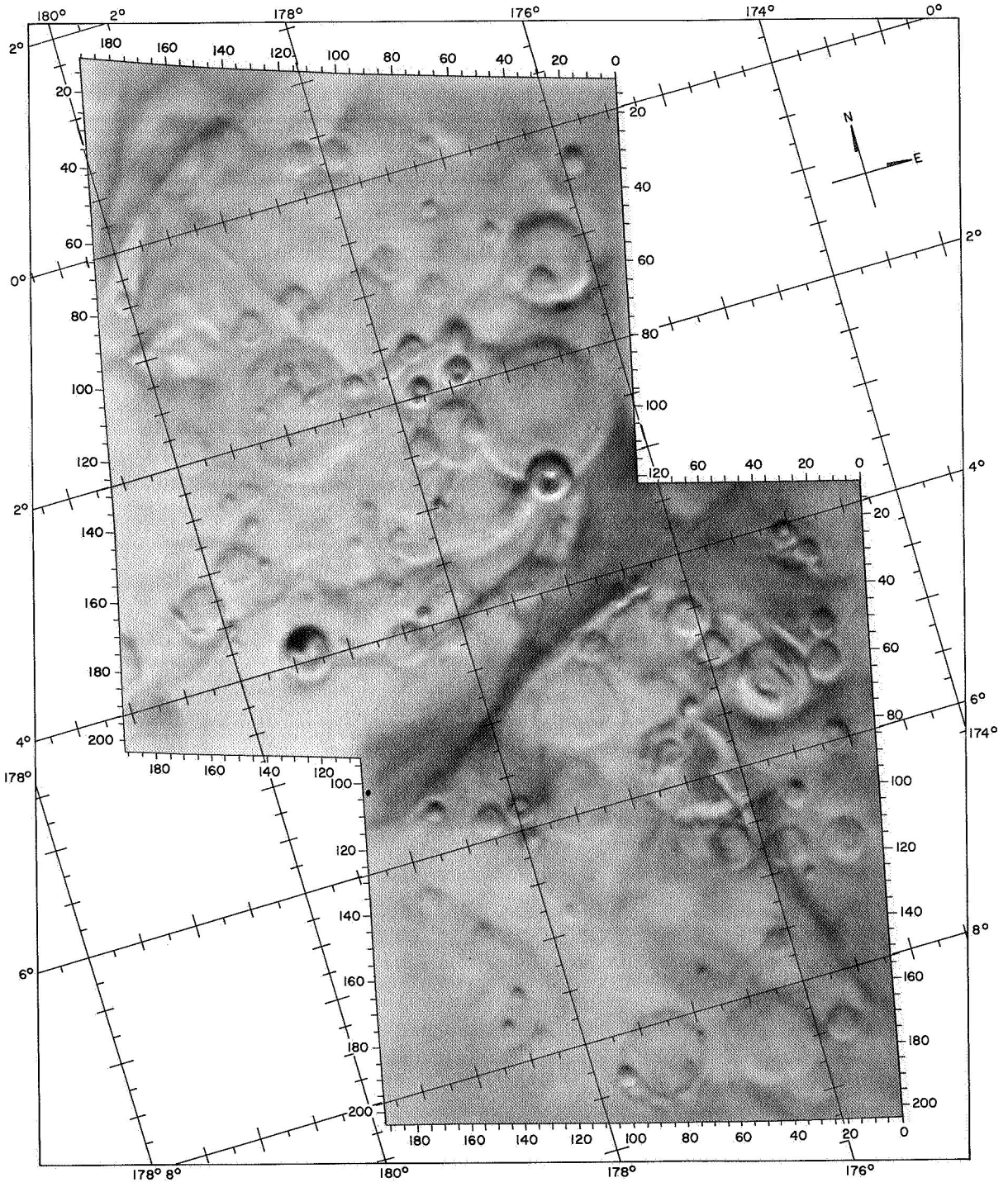


**5, 6A. ACIC version**



13- A

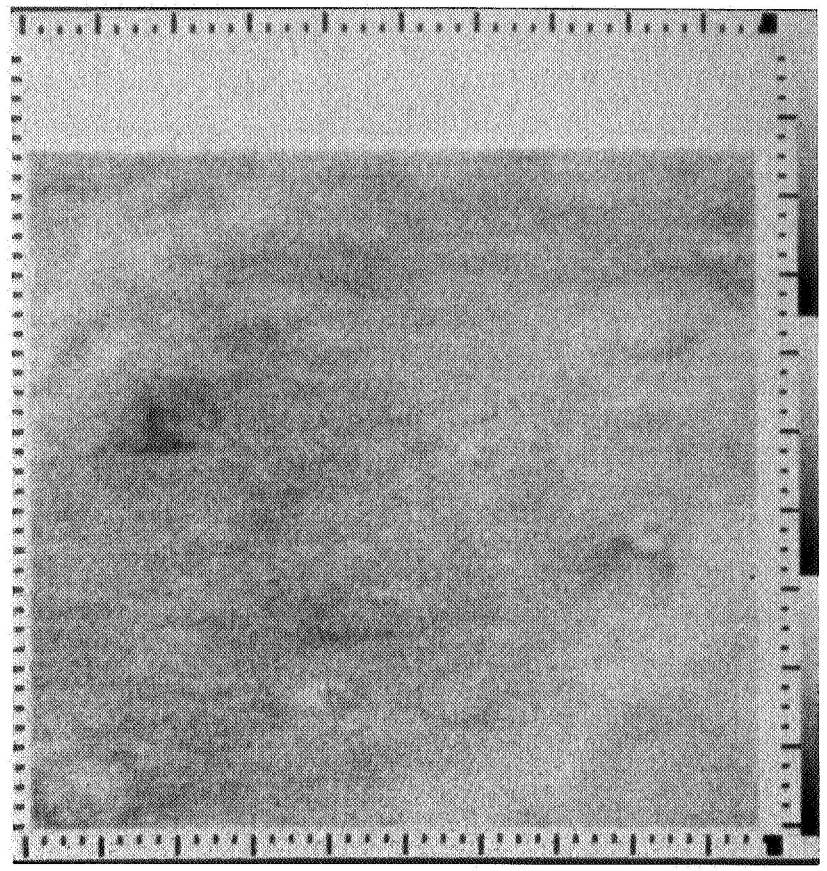

5D. Negative version, calibrated and unsharpened

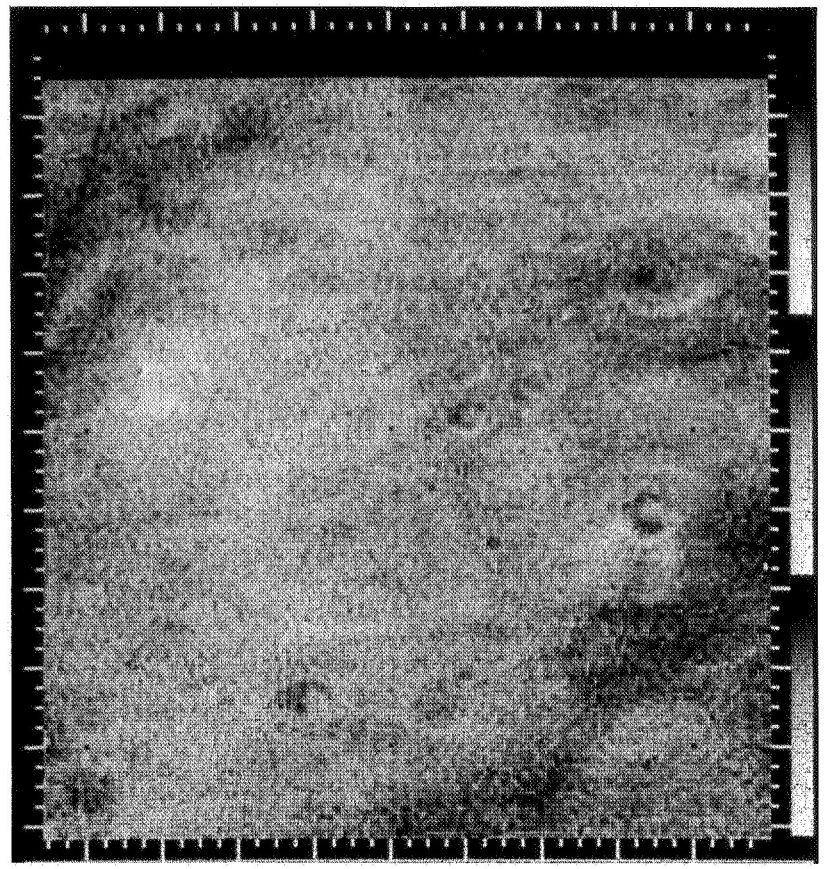

5C. Calibrated, rectified, and sharpened

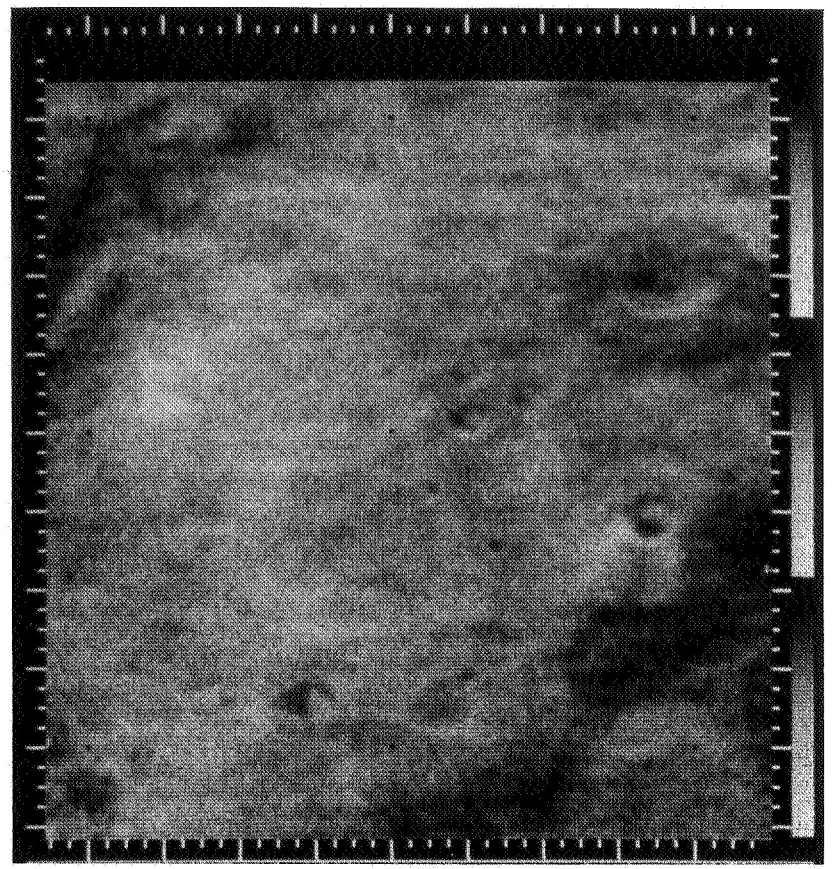

5B. Calibrated and rectified

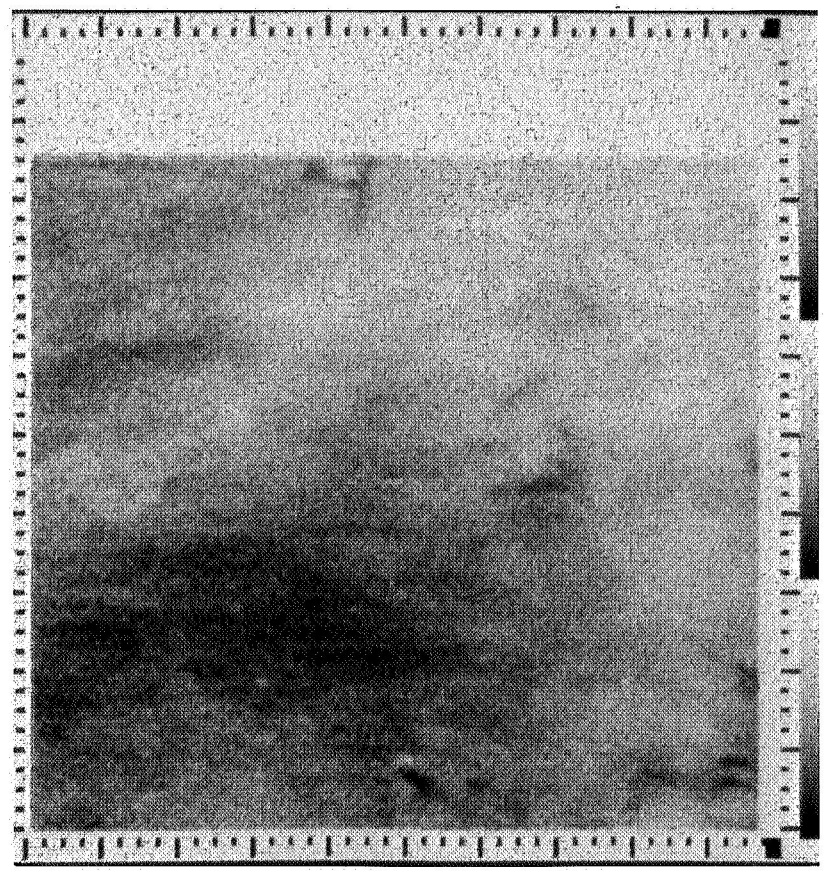

6D. Negative version, calibrated and unsharpened

13 – B

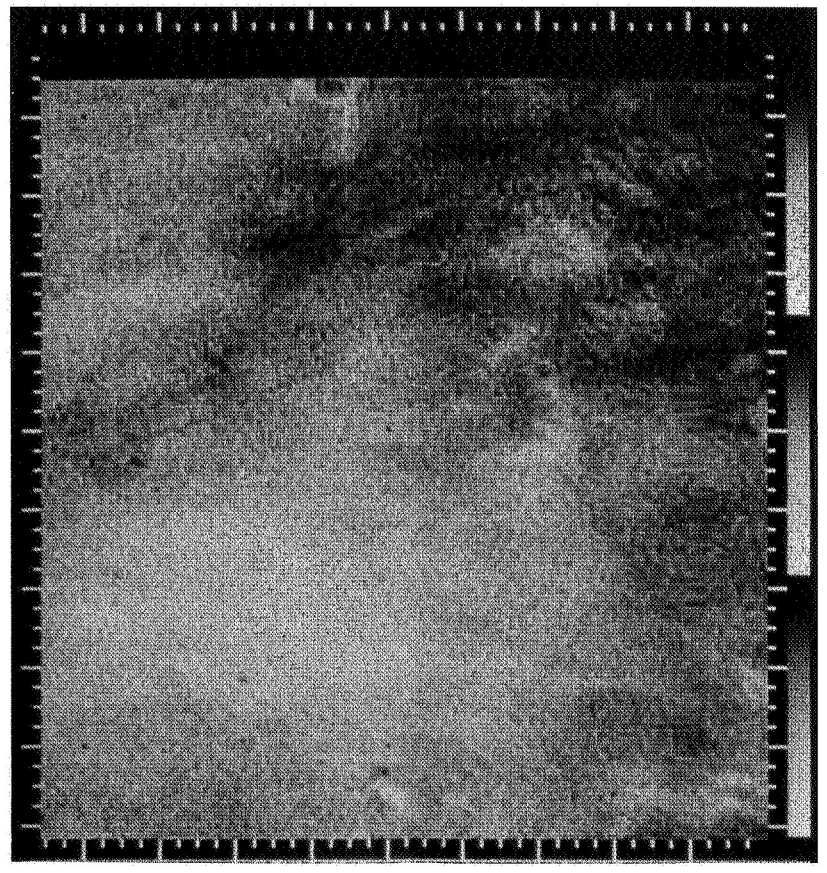

6C. Calibrated, rectified, and sharpened

13 – C

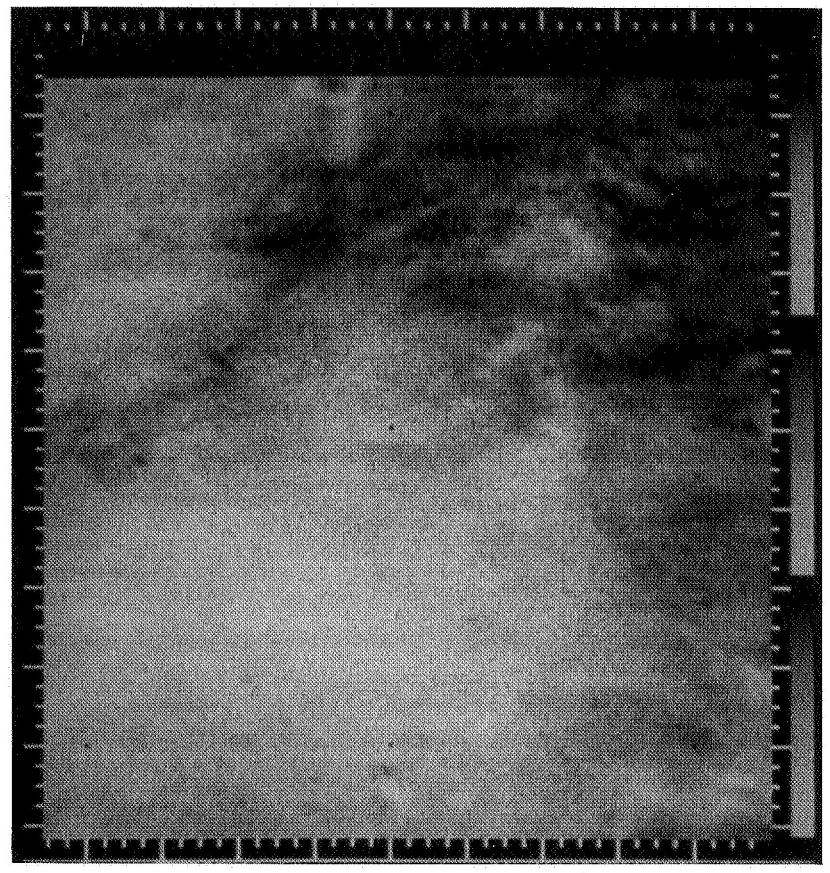

6B. Calibrated and rectified

13 – D

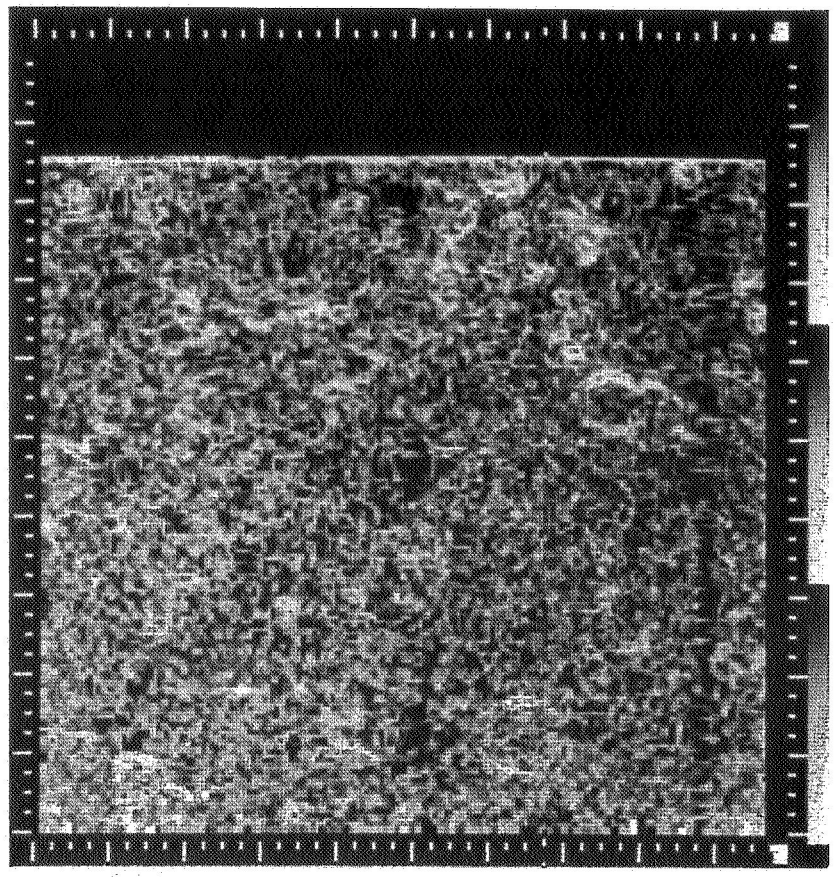

7G. Variance plot

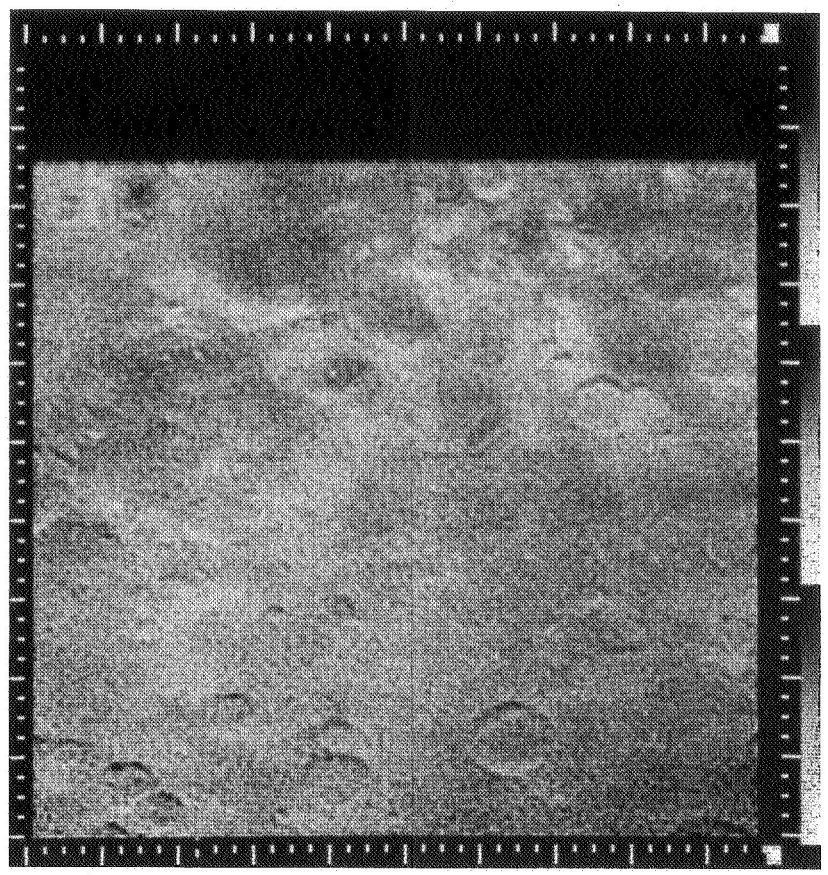

7F. Calibrated, sharpened, and enhanced

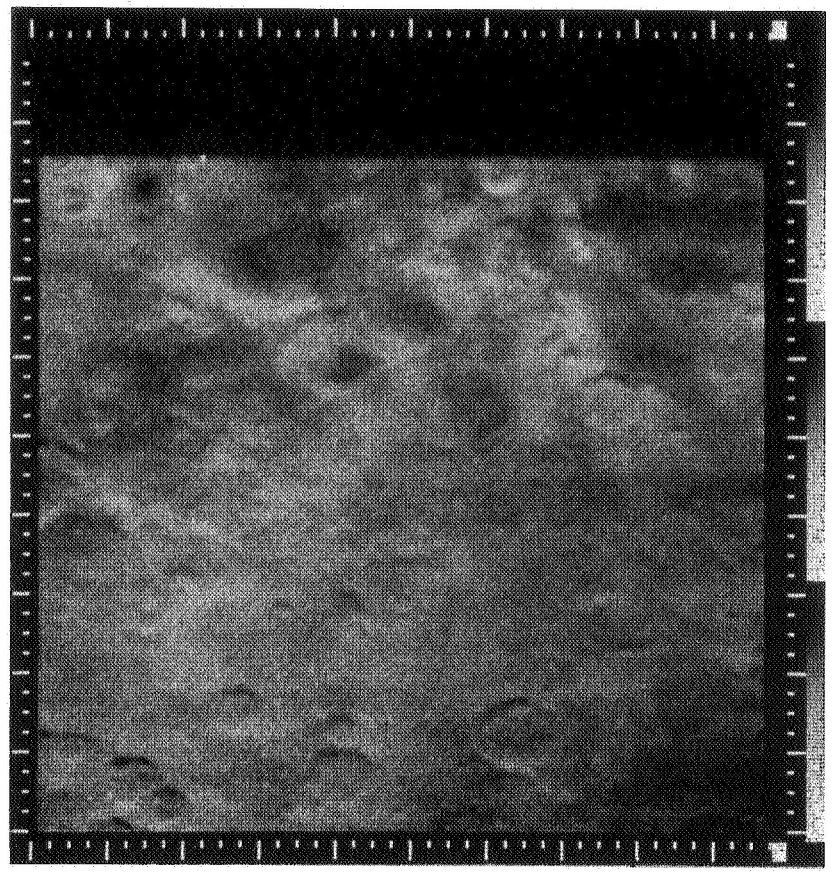

7E. Calibrated and enhanced

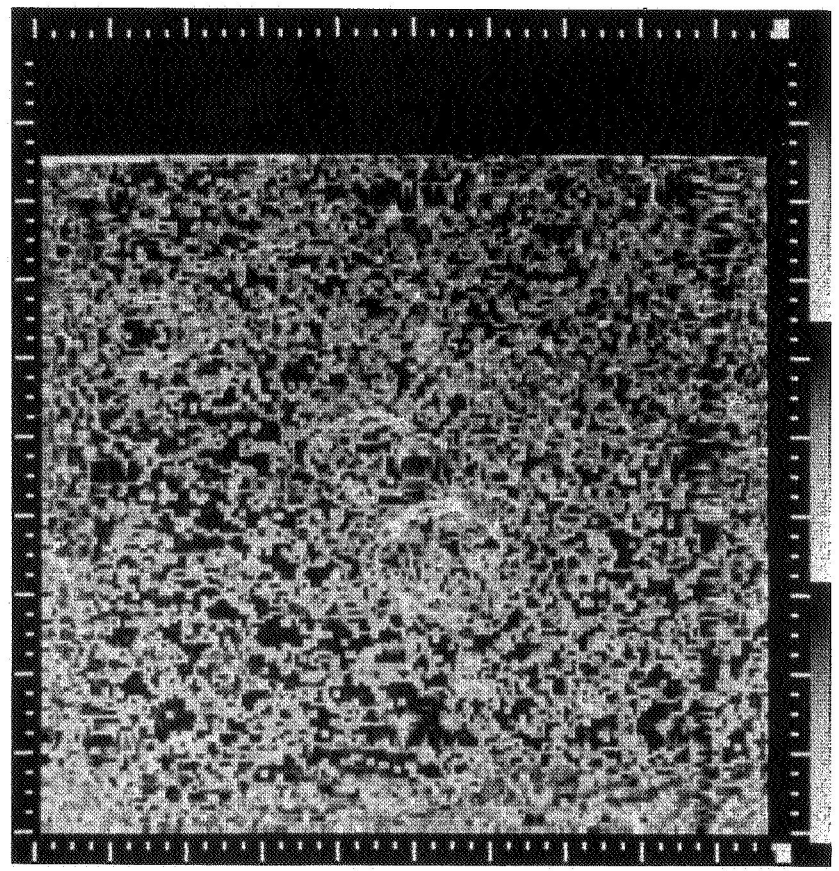

8G. Variance plot

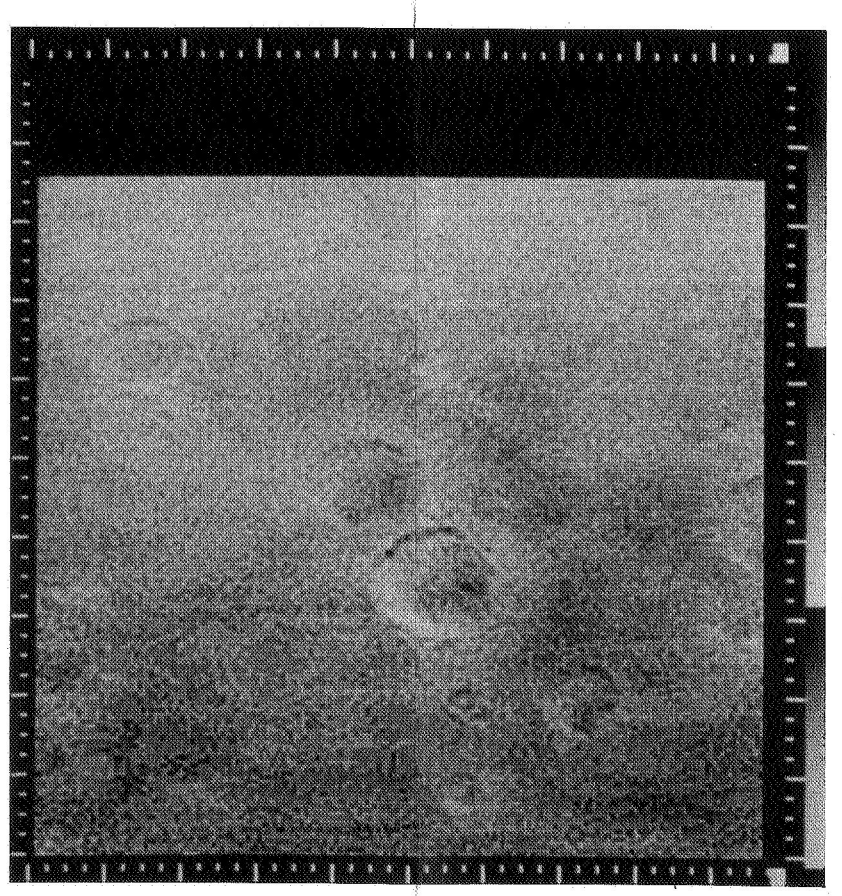

8F. Calibrated, sharpened, and enhanced

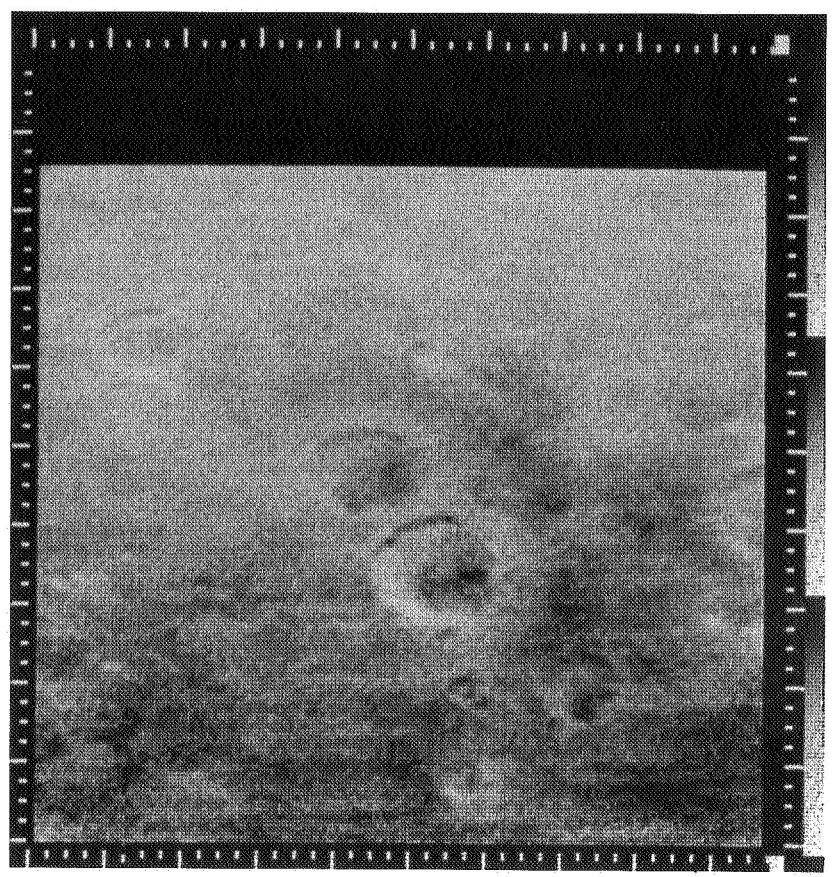

8E. Calibrated and enhanced

14 - A

14 · B

14 - C

## Pictures 7 and 8

### Filter

Picture 7—green Picture 8—orange

### Location of Picture Center

Picture 7—13°S, 186°E Picture 8—17°S, 187°E

Picture 7 is wholly within the southeastern part of the bright region Zephyria, while the border between Zephyria and the dark Mare Sirenum trends across the middle part of Picture 8.

### Dimensions

Each picture covers an area of approximately 290 km east-west and 275 (for 8) to 290 km (for 7) north-south.

### Time and Lighting

The local time is approximately noon.

The sun is 29° north of the zenith in Picture 7 and 32° in Picture 8.

### Brightness Ranges

| Picture 7 | F | E | D | C | B |
|---|---|---|---|---|---|
| Min. | 103 | 106 | 106 | 113 | 113 |
| Max. | 160 | 165 | 165 | 153 | 148 |
| Picture 8 | F | E | D | C | B |
| Min. | 142 | 153 | 153 | 149 | 158 |
| Max. | 228 | 238 | 238 | 223 | 217 |

### Craters

In terms of crater number, this is the second most populous pair of *Mariner IV* photos, after 9 and 10. Of a total count of 115 possible craters, 7 have recognizable central peaks, and 10 have a clear polygonal outline. The degree of preservation of 18 is good, of 45, intermediate, and of 52, poor. The largest crater is 180 km in diameter, and the smallest recognized is 4 km.

Outside the overlap area, Picture 7, wholly in a light area, has 50 craters, and Picture 8, largely in a dark mare, has 53 craters. The craters in Picture 7 appear somewhat better preserved, and the terrain generally appears rougher. This pair of photos provides little if any support to the idea that the difference between light and dark areas is related to topographic features. The topography of Picture 8 appears more subdued, but the crater number is essentially the same.

### Lineations

One long sharp lineation cuts northwesterly across the west half of Picture 7 and possibly extends southeasterly into 8. A pattern of short, less clear lineations bearing northeasterly is faintly visible in both pictures.

### Albedo and Surface Textures

A relatively large irregular area of higher than normal albedo lies in the north central part of 7, and extends through a rough-appearing area toward the southwest. This high-albedo area also appears rougher in the "fluctuation plot," Picture 7G. This roughness is partially due to obvious craters, but partially to irregular, fine-scale fluctuations. The northwest part of the picture appears generally rougher than the southeast part, and there is a suggestion of an abrupt boundary between the rougher and smoother areas, which progresses from the southwest corner, northeasterly toward the north center of the picture, then curving toward the northeast corner.

The northern part of Picture 8 appears less rough than the darker southern part. In this case no abrupt boundary is apparent.

The south or southeast parts of the floors of no less than five of the principal craters in these pictures appear darker than the average. Several craters in Pictures 9, 10, and 11 show a similar effect. Although an explanation in terms of albedo variations seems most likely, the effect is peculiar. It is difficult to imagine an instrumental effect that would lead to such an appearance, but such an explanation cannot be excluded. One must also admit the possibility that this appearance is a true shading effect due to surface slopes, so that the floors of the craters are "domed." Such doming might be produced by isostatic rebound of the Martian crust over a long period of time following a major impact.

14-D

REFERENCE COORDINATES

Line and element numbers, as recorded on the original television photographs, are depicted around the perimeter of the imagery for the purpose of identifying and referencing of features.

Element Number . . . . . North to South
Line Number . . . . . East to West

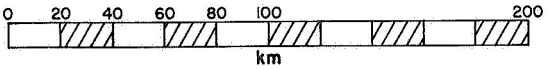


Orthographic Projection
at 25°11'26"S and 168°08'13"W

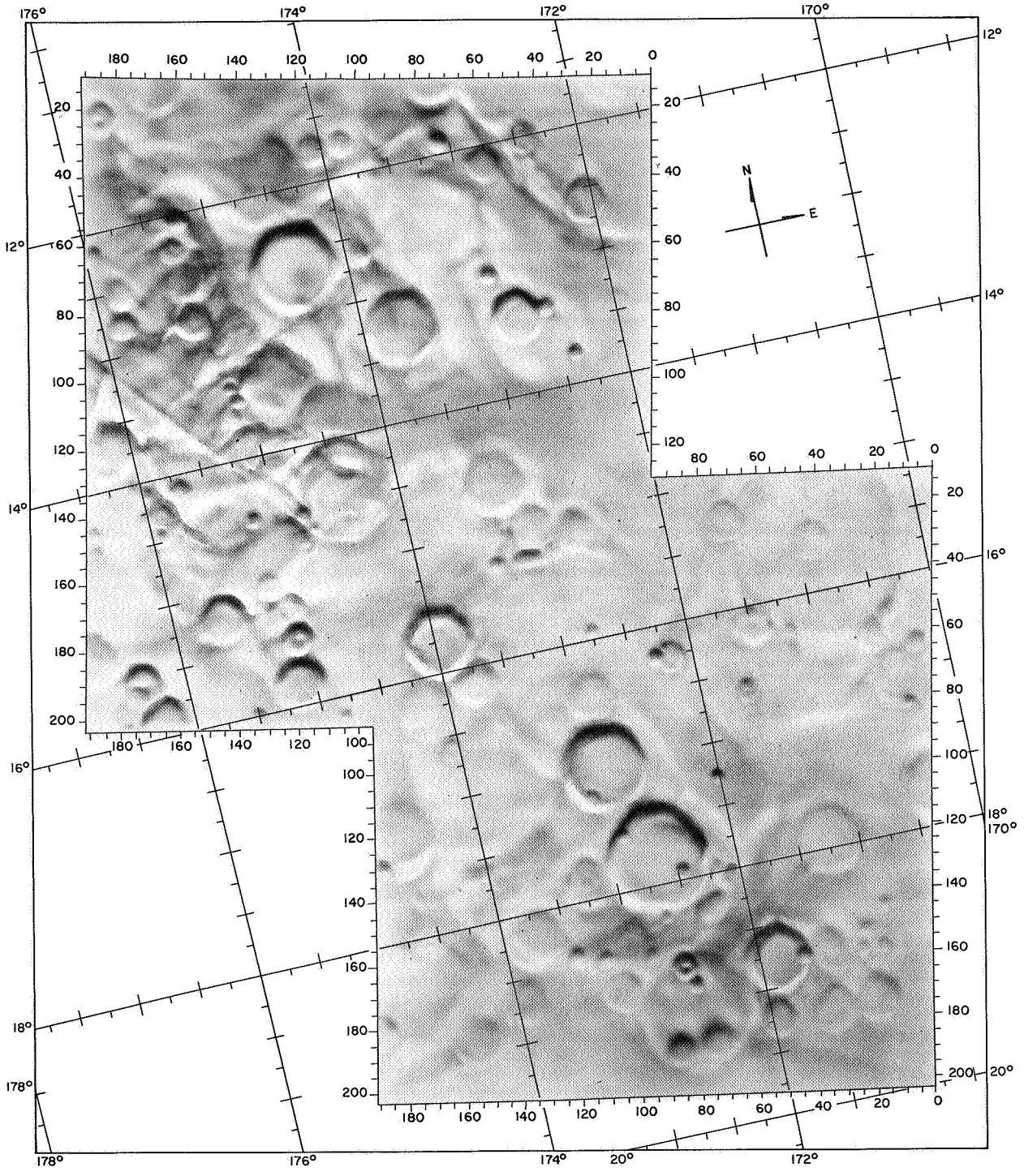


**7, 8A. ACIC version**



15 - A

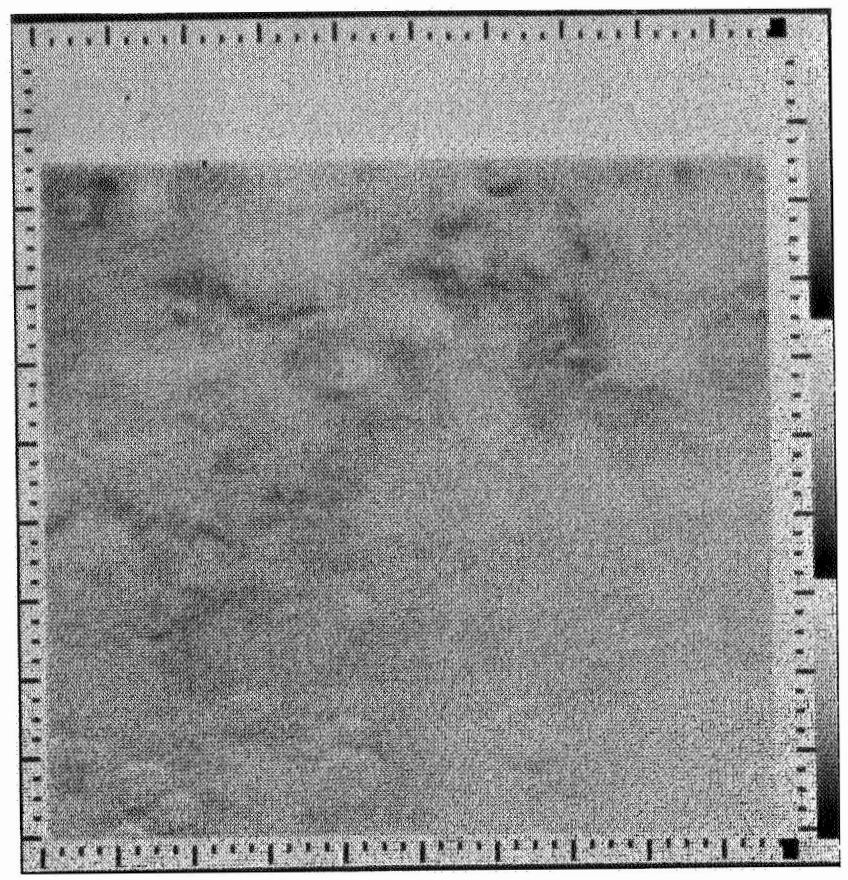

7D. Negative version, calibrated and unsharpened

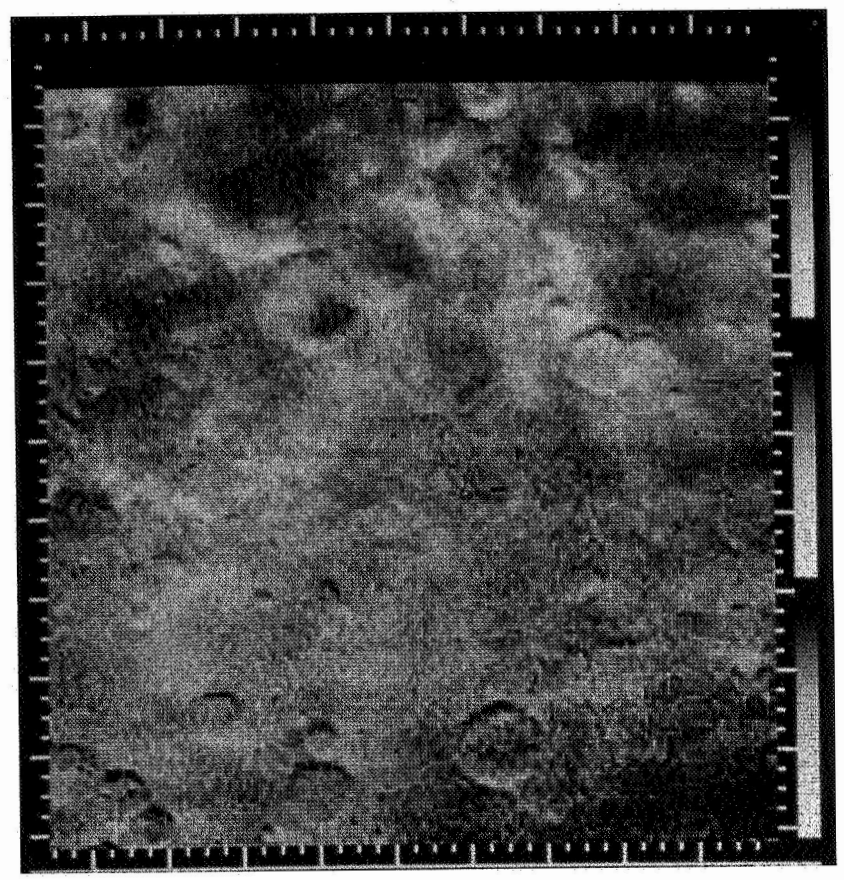

7C. Calibrated, rectified, and sharpened

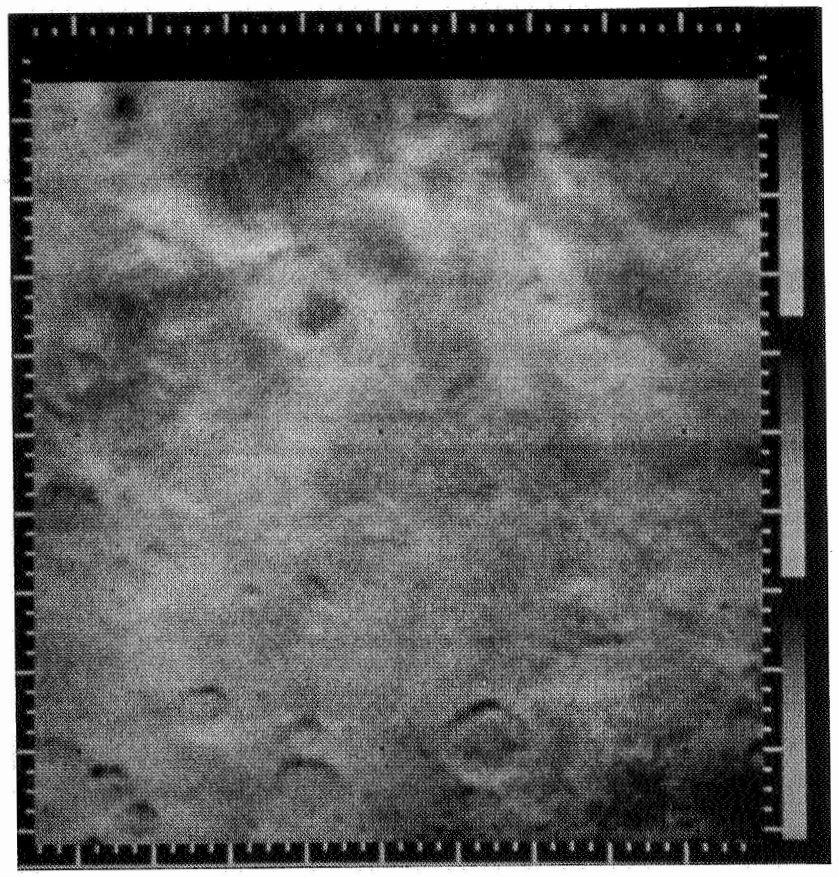

7B. Calibrated and rectified

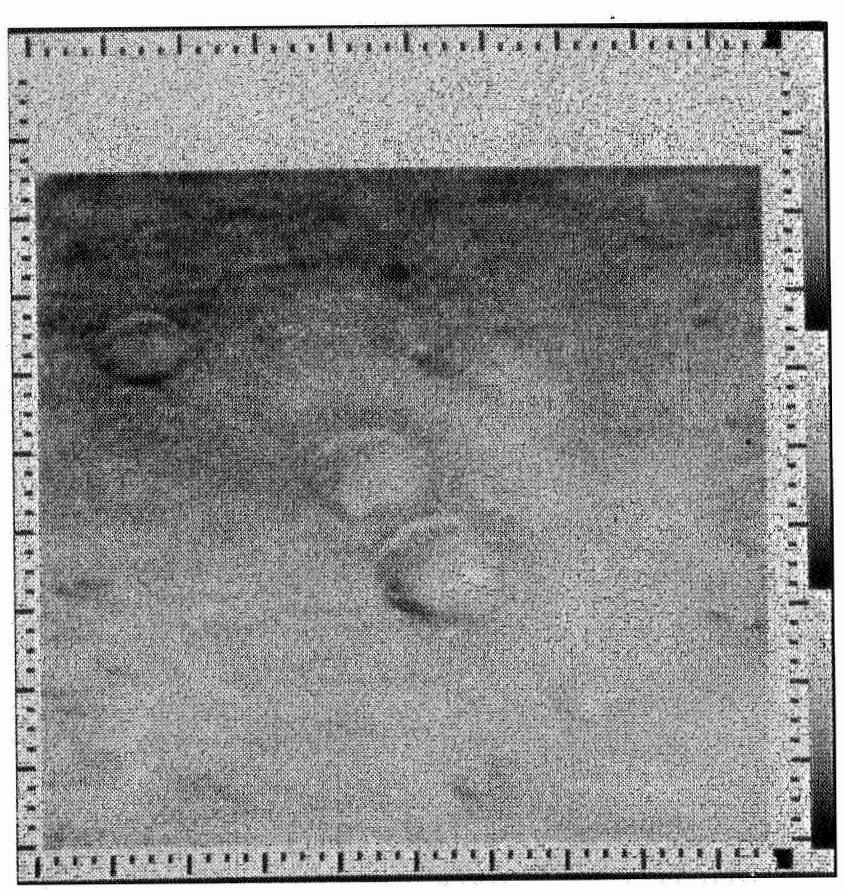

8D. Negative version, calibrated and unsharpened

15-B

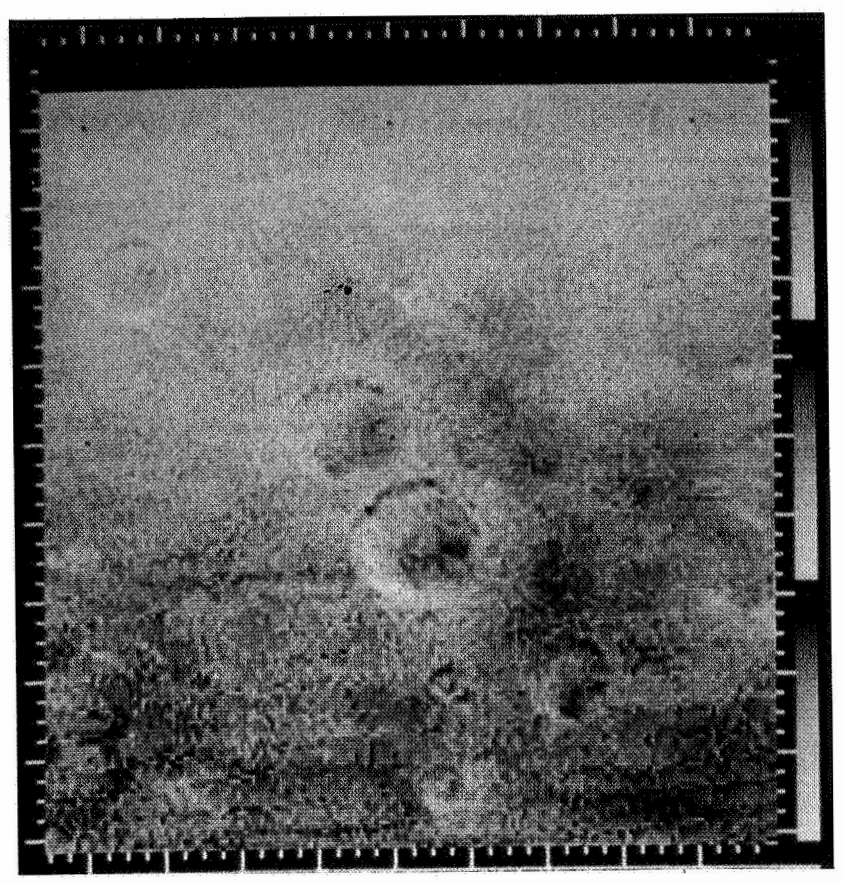

8C. Calibrated, rectified, and sharpened

15-C

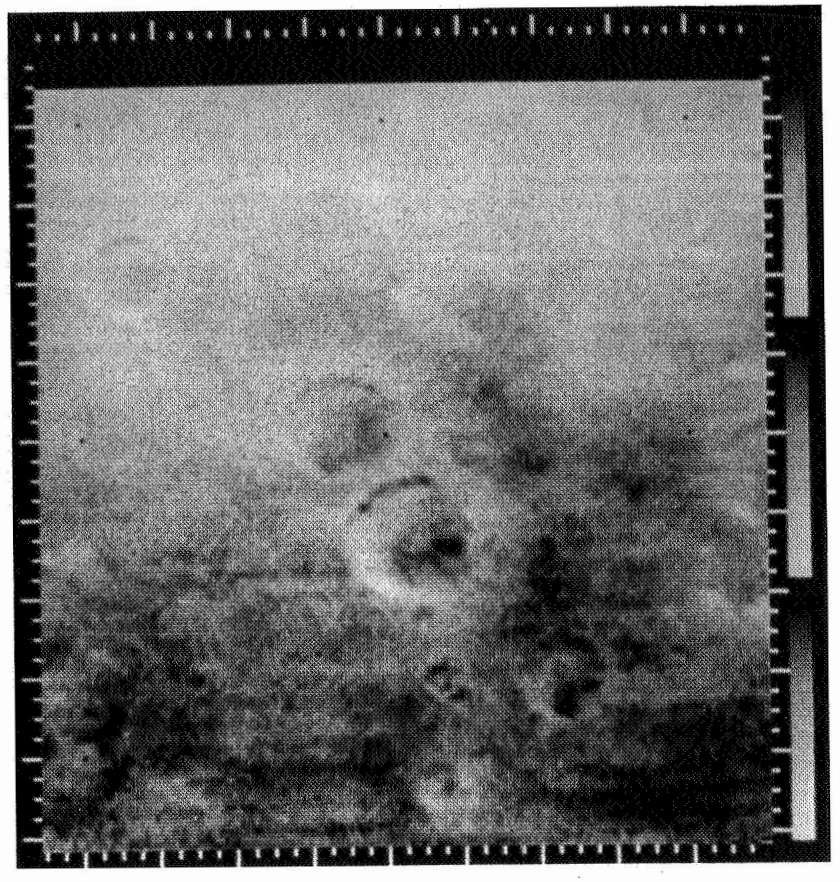

8B. Calibrated and rectified

15

15-D

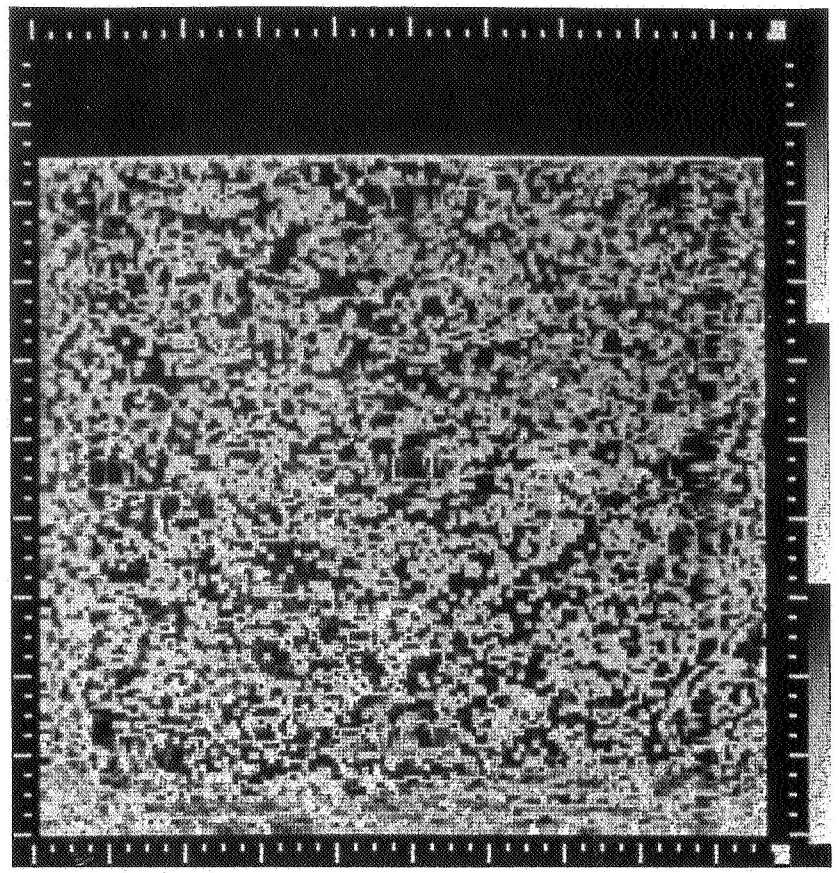

9G. Variance plot

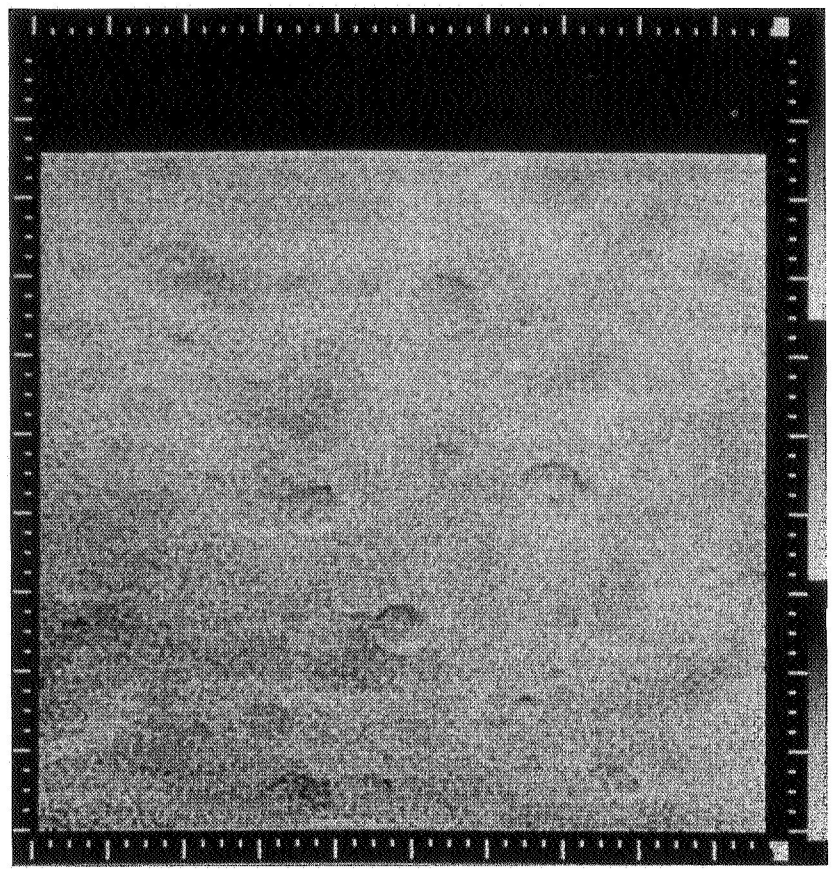

9F. Calibrated, sharpened, and enhanced

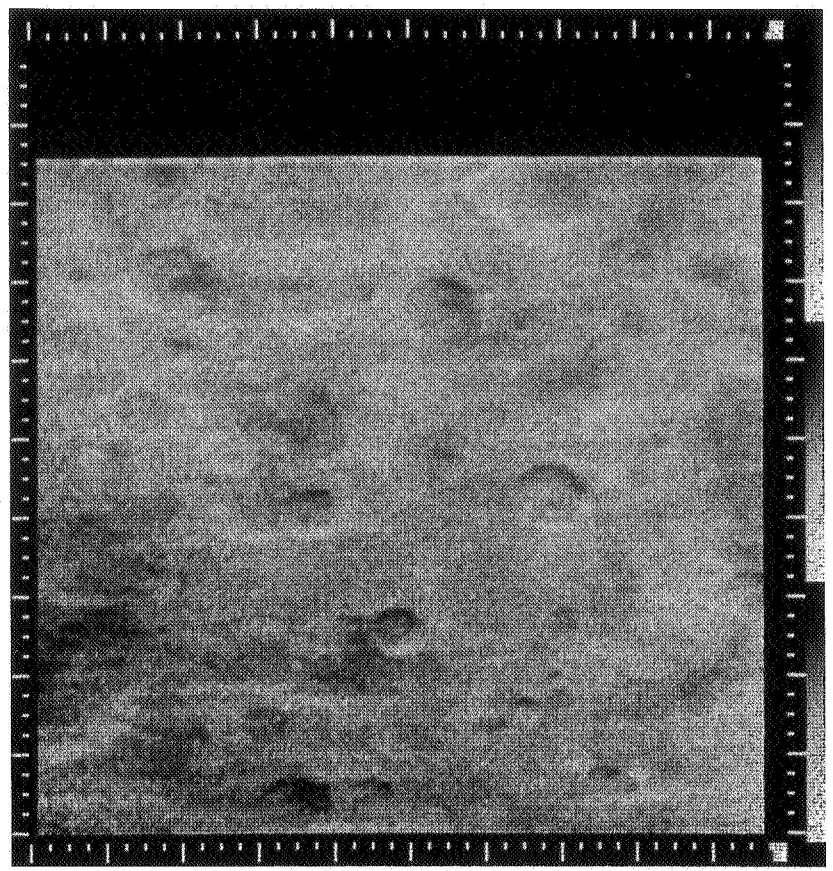

9E. Calibrated and enhanced

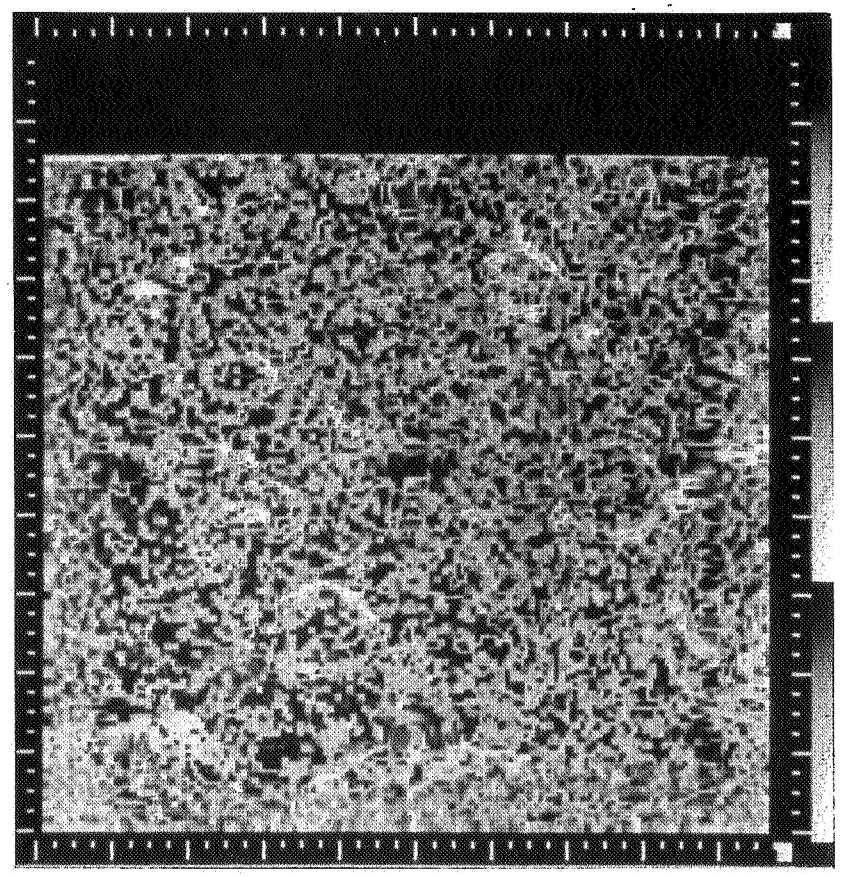

16 - A

10G. Variance plot

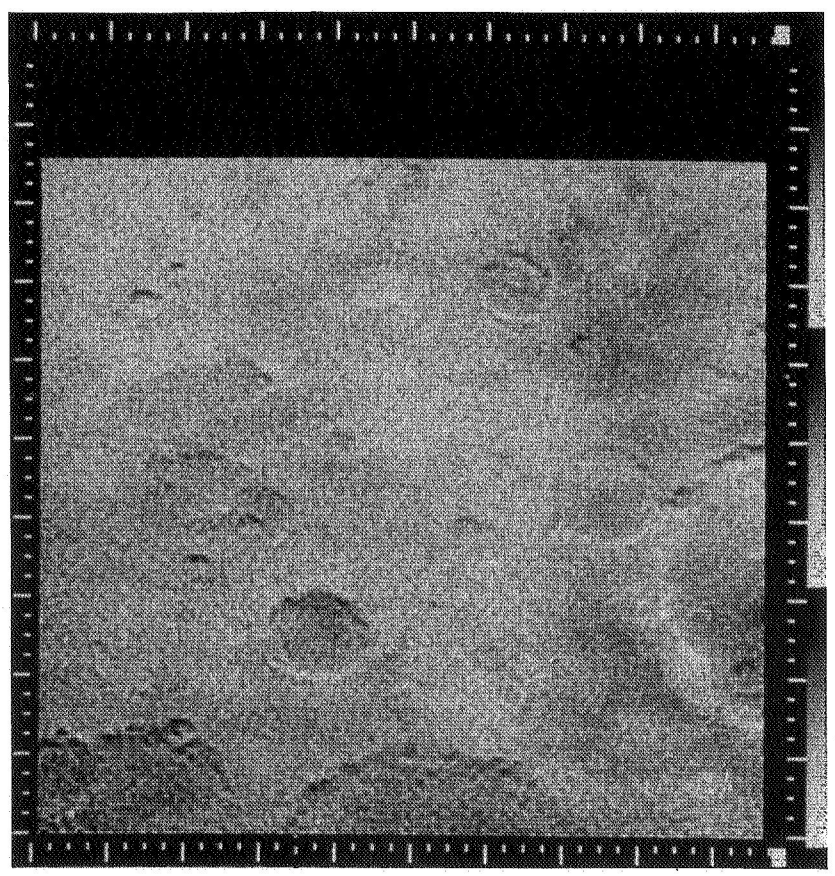

10F. Calibrated, sharpened, and enhanced

16 - B

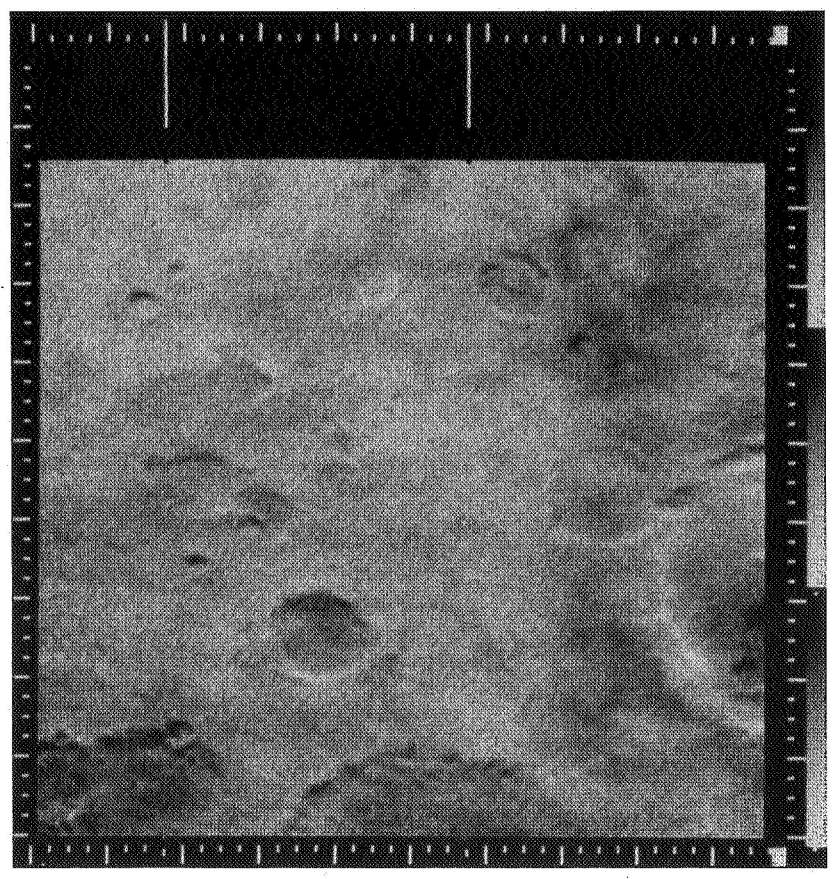

10E. Calibrated and enhanced

16 - C

## Pictures 9 and 10

### Filters

Picture 9—orange Picture 10—green

### Location

Picture 9—24°S, 191°E Picture 10—27°S, 193°E

Pictures 9 and 10 are largely in the dark area, Mare Sirenum, near the light area, Atlantis.

### Dimensions

Each picture covers an area of roughly 275 km east-west and 260 km north-south.

### Time and Lighting

The local time is approximately noon in both pictures; the sun is 39° from the zenith in Picture 9 and 42° in 10.

### Brightness Ranges

| Picture 9 | F | E | D | C | B |
|---|---|---|---|---|---|
| Min. | 100 | 117 | 117 | 112 | 121 |
| Max. | 182 | 184 | 184 | 174 | 169 |
| Picture 10 | F | E | D | C | B |
| Min. | 59 | 69 | 69 | 62 | 70 |
| Max. | 107 | 100 | 100 | 103 | 100 |

### Craters

These two pictures show a greater density of possible craters than any other pair of *Mariner IV* pictures. A total of 132 have been counted, ranging in diameter from 4 to 123 km. Of these, 11 clearly have central peaks and 10 have well-defined polygonal shapes. The smallest crater with a central peak is 11 km diameter and the largest is 27 km. Both central peaks and polygonal form show a direct relationship to the freshness of the crater, suggesting that these features are perhaps more abundant than recognized. Nineteen of the craters are well preserved, 67 are of intermediate preservation, and 46 are poorly preserved. This classification, of course, involves a high degree of subjective judgment. Well-preserved craters are more abundant in the small and medium sizes, many of the larger craters being faint.

The distribution of craters across Pictures 9 and 10 is reasonably uniform aside from local clustering, and no striking alignment of craters is observed.

Larger craters show irregularities on their inner slopes suggestive of slump or mass movements. No consistent variation in albedo between crater floors and surrounding terrain is discerned, although some of the larger craters seem to have darker interiors. The two large craters partially visible at the south edge of 10 seem to have unusually rough and somewhat darkened interiors.

Most of the well-preserved craters of Pictures 9 and 10 have been quantitatively analyzed to obtain slope and elevation information; some detailed results can be found in Appendix H. Several interesting characteristics emerge. First, some large craters, like P10 L29 E111 and the western part of P10 L5 E135 exhibit smoothly filled, relatively flat bottoms, whereas others, notably P10 L72 E44 and P10 L126 E148, have been modified into an irregular array of linear elements. In addition, the northwestern rim of P10 L5 E135 and northeastern rim of P10 L175 E185 are severely distorted by linear gashes and crater chains, similar to certain deformational features on the moon. Finally, some crater bottoms have been partially or entirely covered with dark material which is localized within the crater; P10 L126 E148 and P9 L105 E148 are good examples.

The maximum local relief in Pictures 9 and 10 probably does not exceed 1000 meters, most of the craters displaying very much less. The prominent central peak in P9 L61 E109 rises only about 200 meters above the surrounding floor; its top is 400–500 meters below the general land level in that area. Crater rims do not appear to rise more than 200–300 meters above the local land level anywhere in the two pictures. Large-scale slopes, i.e., of the order of 2–3 km in extent, rarely exceed about 10 deg anywhere in either picture. Most of the "fresh" appearing features on the photographs exhibit slopes of 5 deg or less.

One crater, P9 L127 E111 (Picture 9B), exhibits a peculiar sharp corner, and is shown in detail in Appendix H. This might be caused by the presence of a smaller crater near the edge of the larger one, by an unusual pattern of slumping along local planes of weakness, or possibly by a combination of these effects with the presence of electrical harmonic noise in the camera system.

### Lineations

Prominent linear features in this pair of pictures are defined by surface *texture* as well as by albedo. One lineation is visible in the "fluctuation plot," Picture 9G, as a northeast-bearing dark (i.e., smooth) streak about 5–10 km wide. It starts at L165 E200 and curves gently to L7 E85, passing quite close to three prominent craters. The terrain on the northerly side of this feature is slightly rougher than on the southerly side. At least two more such lineations, shorter and less distinct, can be seen crossing the major one. These bear northwesterly and northerly, respectively. Although the principal streak seems much too long and regular to be explained as merely a chance alignment of low-contrast elements, the reality of the remaining features is less certain.

Linear streaks bearing generally northeasterly with some curves and bends are seen in both pictures, and often connect deformed crater walls. Lineation in a northwesterly direction is more weakly expressed by broader, more poorly defined markings. Both lineations are parallel to sides of polygonal craters and create a subtle "herringbone" pattern in the northwest portion of Picture 10.

### Albedo

An irregular pattern of albedo contrast is present throughout both pictures, sometimes extending without interruption across some of the smooth-bottomed craters, e.g., P10 L72 E44.

REFERENCE COORDINATES

Line and element numbers, as recorded on the original television photographs, are depicted around the perimeter of the imagery for the purpose of identifying and referencing of features.

Element Number . . . . . North to South
Line Number . . . . . East to West

0 20 40 60 80 100 200
km

Orthographic Projection
at 25°11'26"S and 168°08'13"W

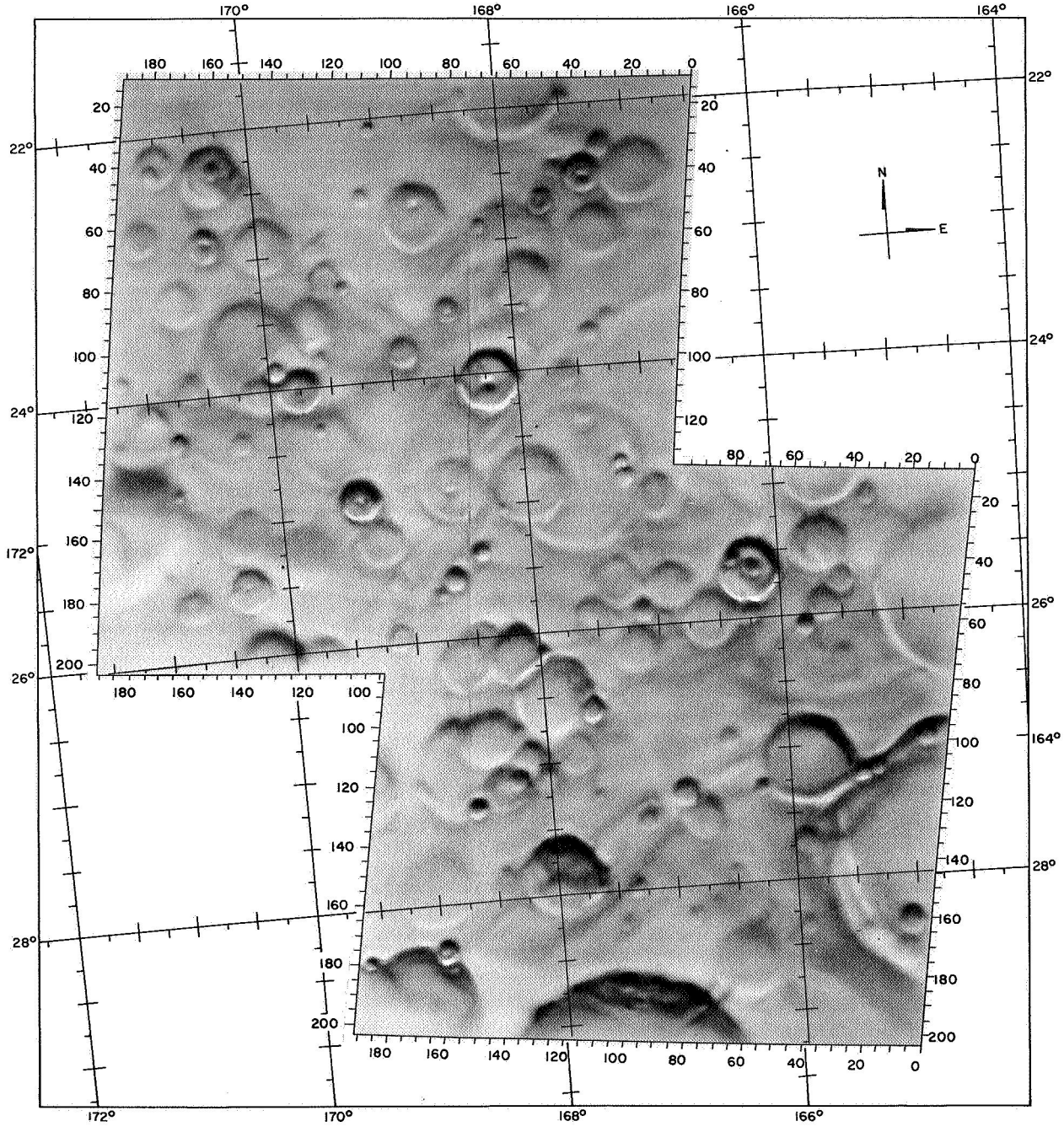


**9, 10A. ACIC version**



17- A

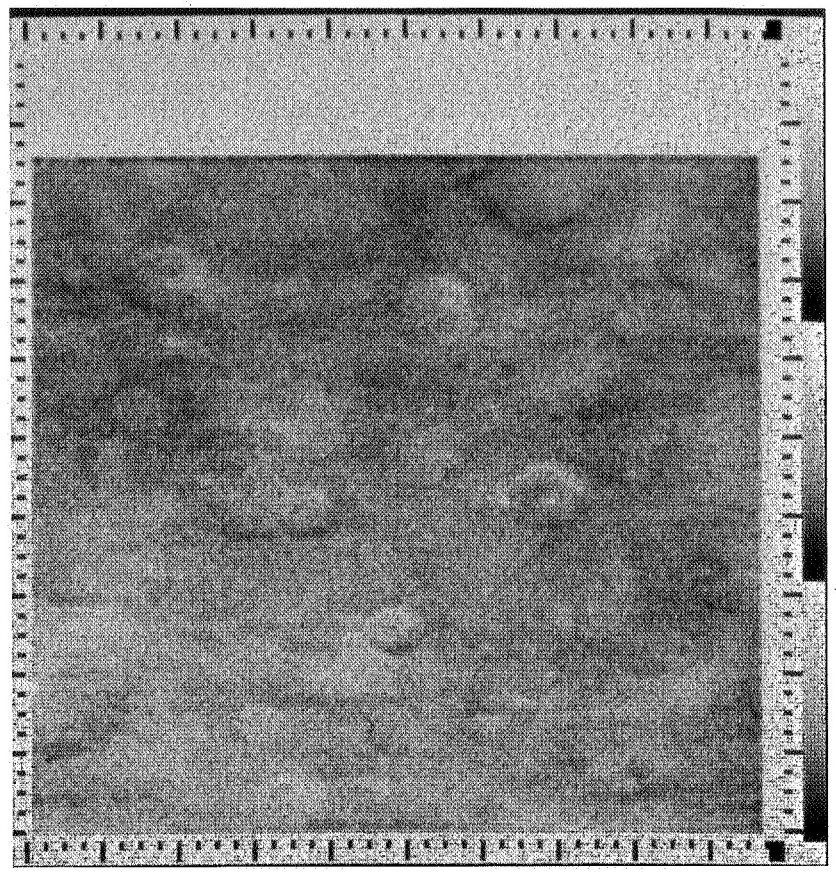

9D. Negative version, calibrated and unsharpened

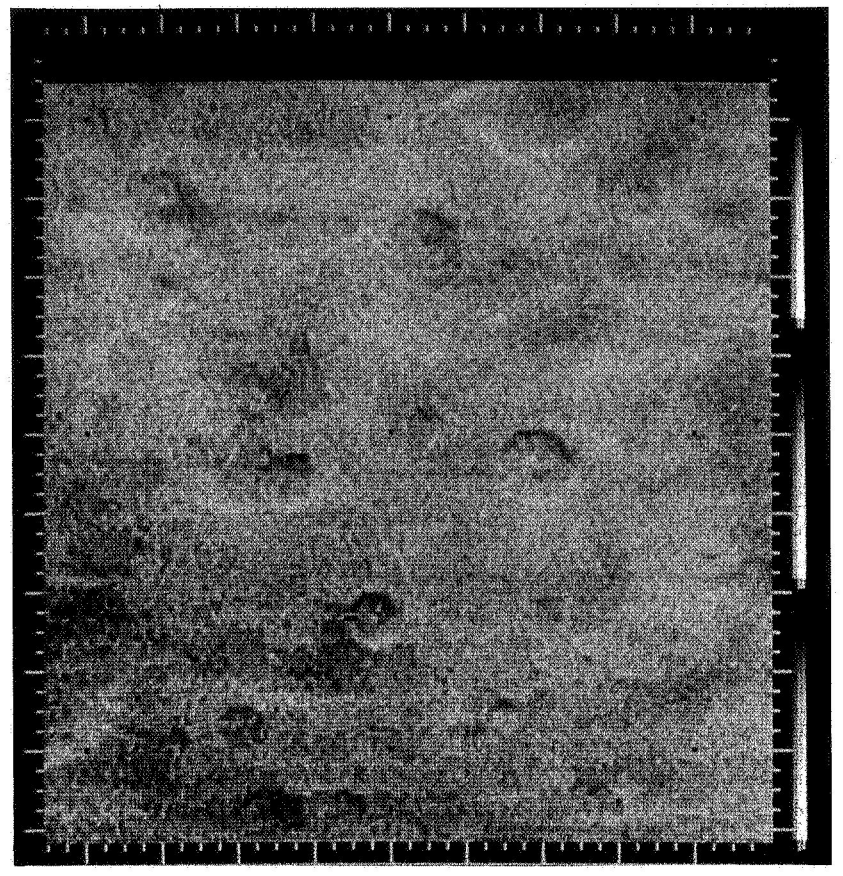

9C. Calibrated, rectified, and sharpened

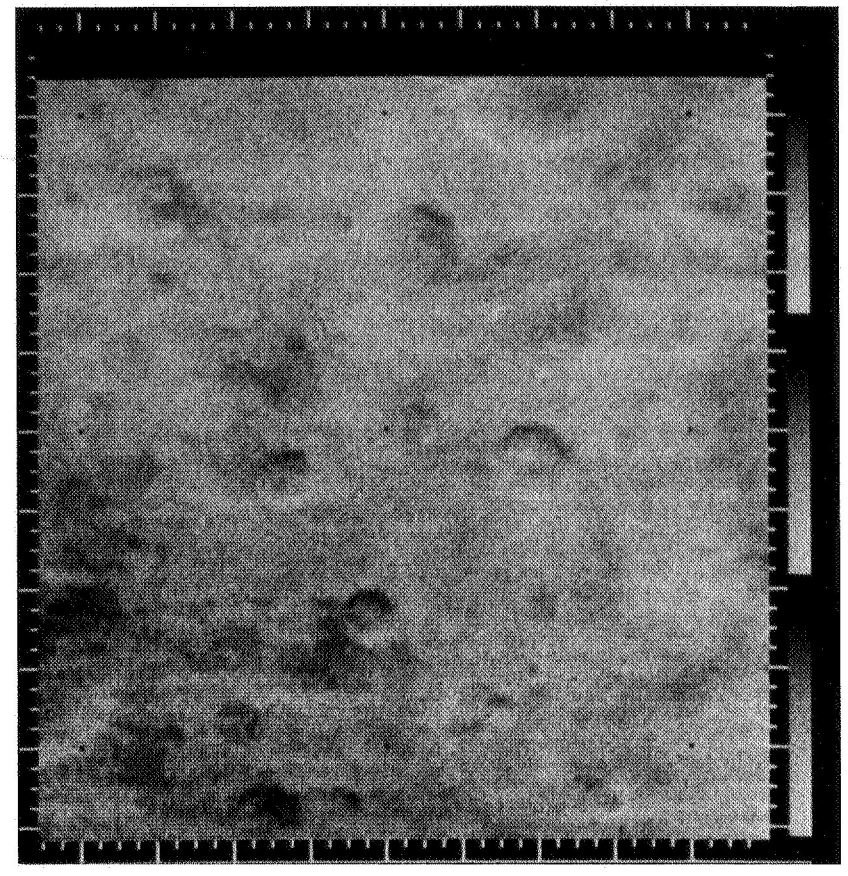

9B. Calibrated and rectified

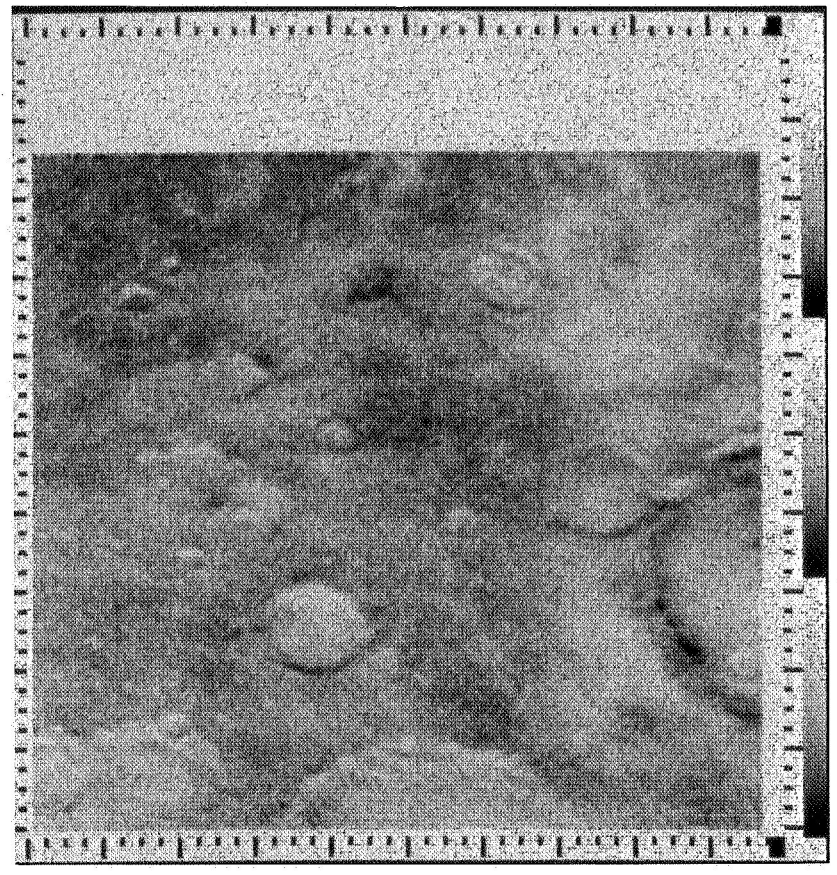

10D. Negative version, calibrated and unsharpened

17-B

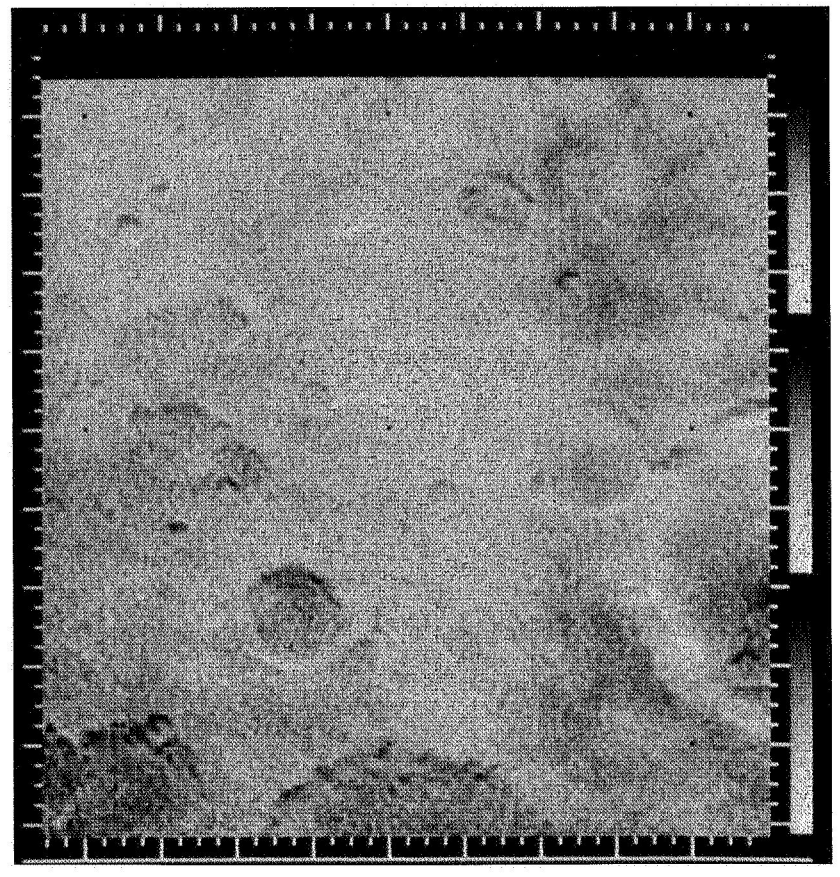

10C. Calibrated, rectified, and sharpened

17-C

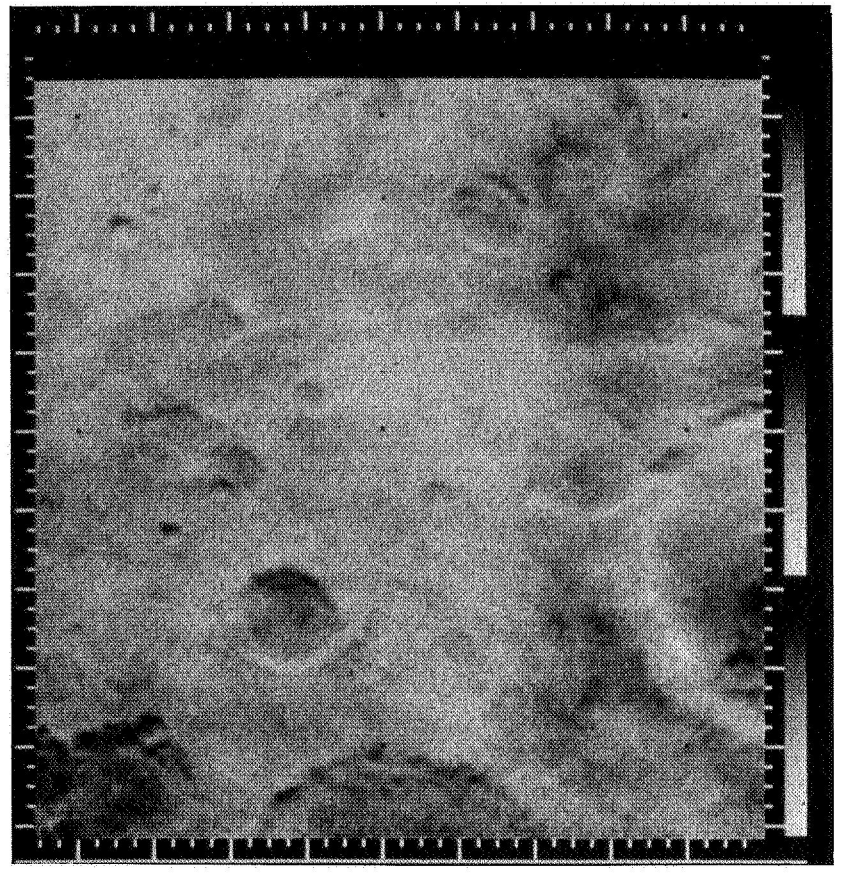

10B. Calibrated and rectified

17-D

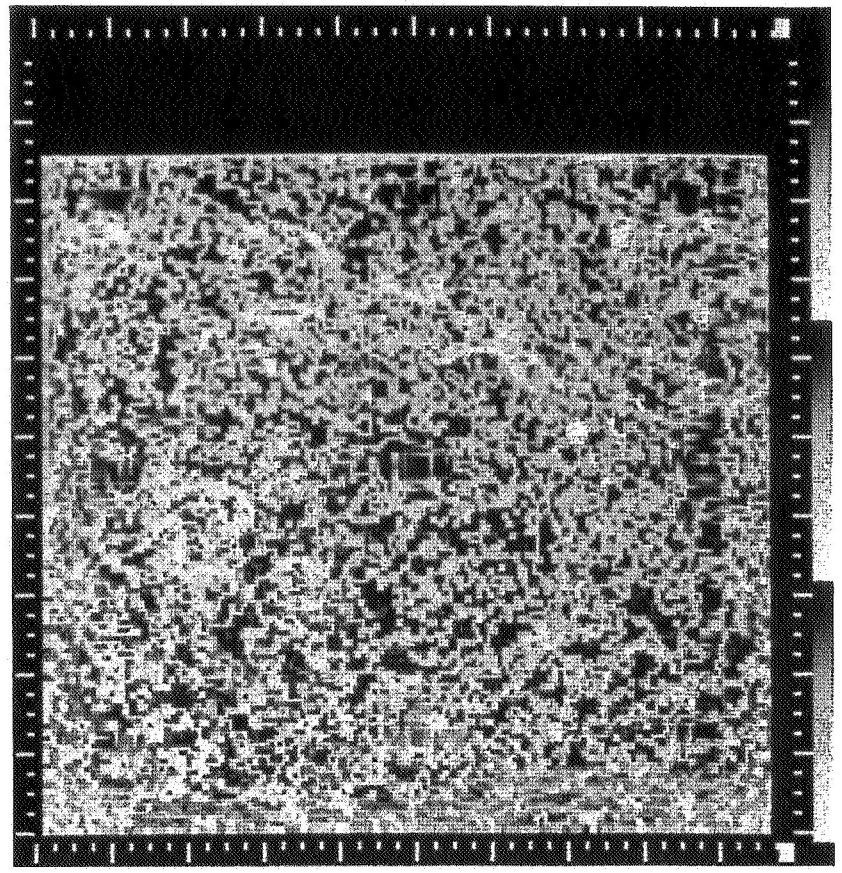

11G. Variance plot

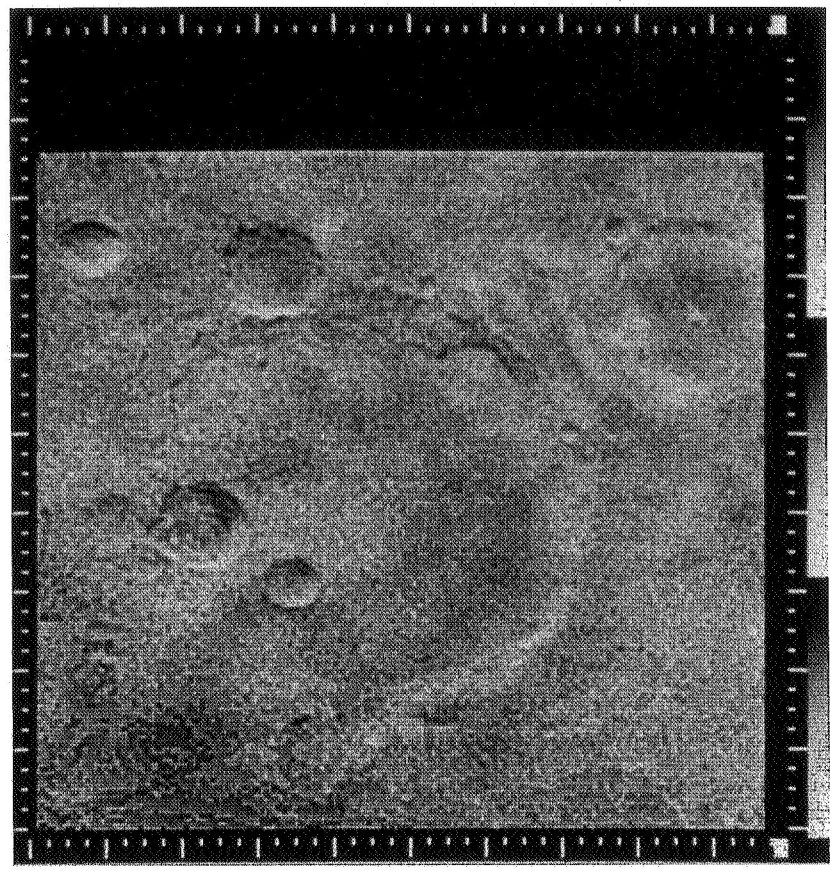

11F. Calibrated, sharpened, and enhanced

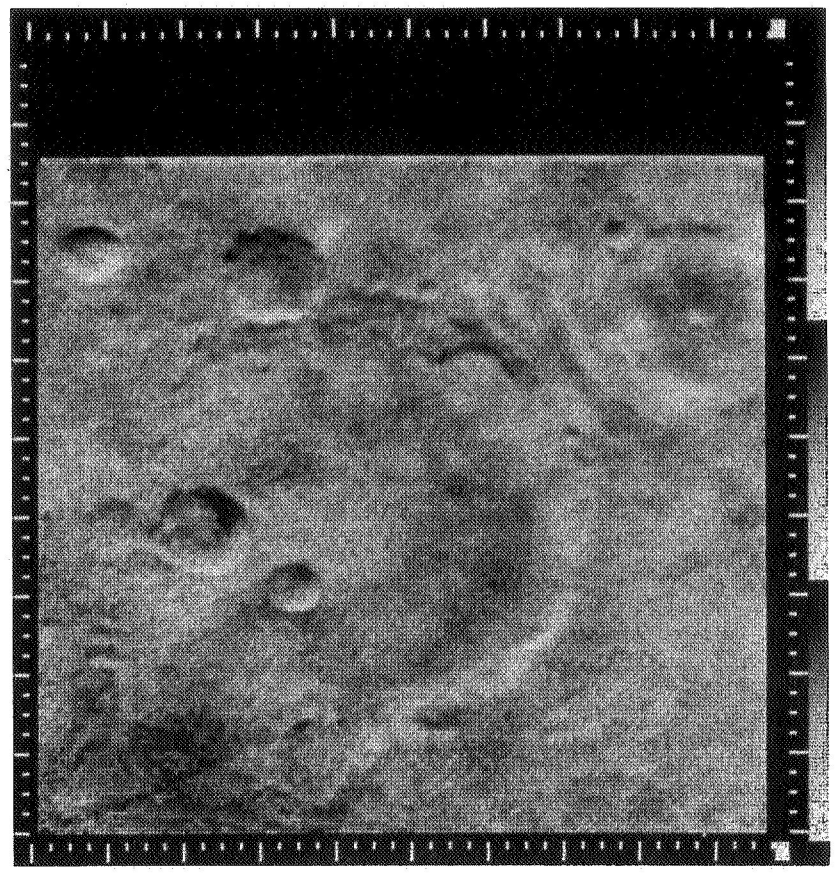

11E. Calibrated and enhanced

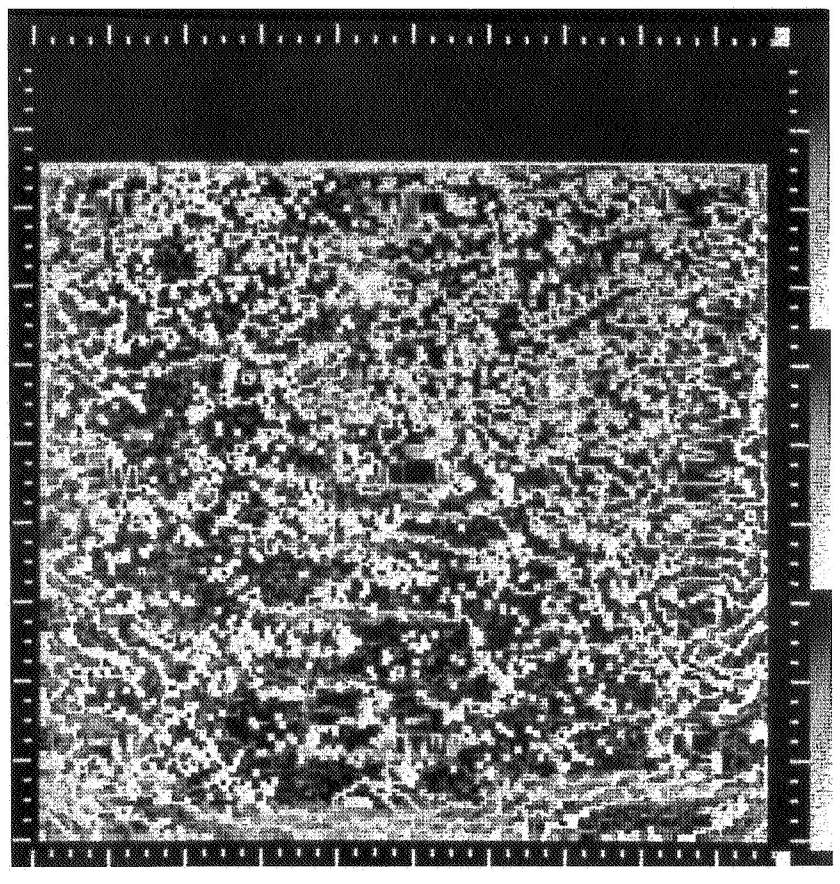

12G. Variance plot

18 – A

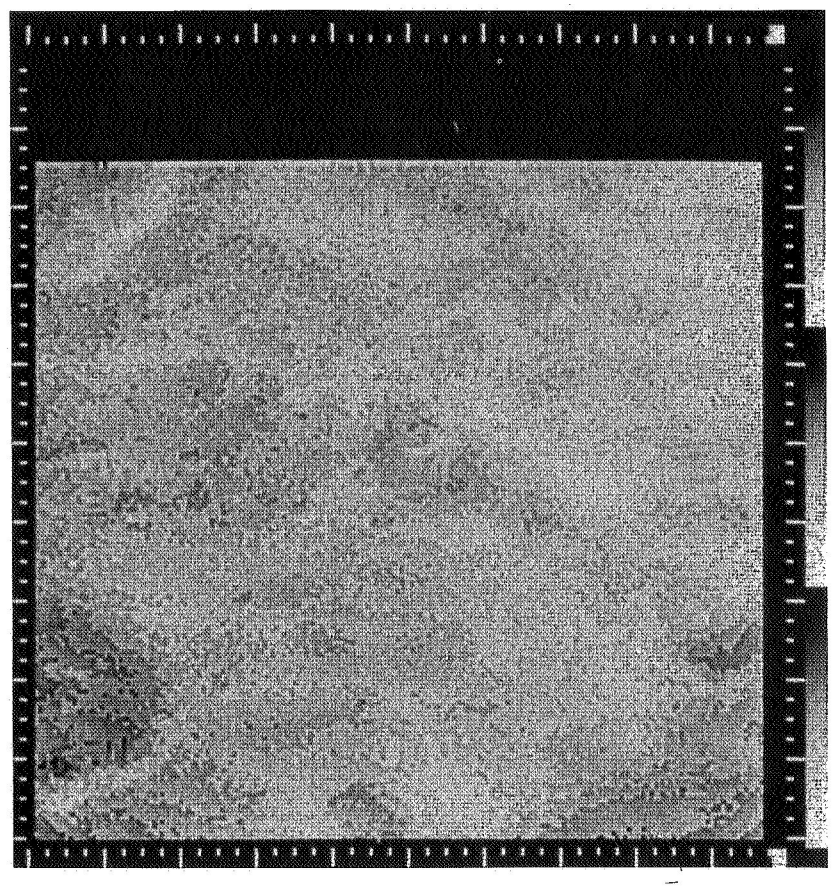

12F. Calibrated, sharpened, and enhanced

18 - B

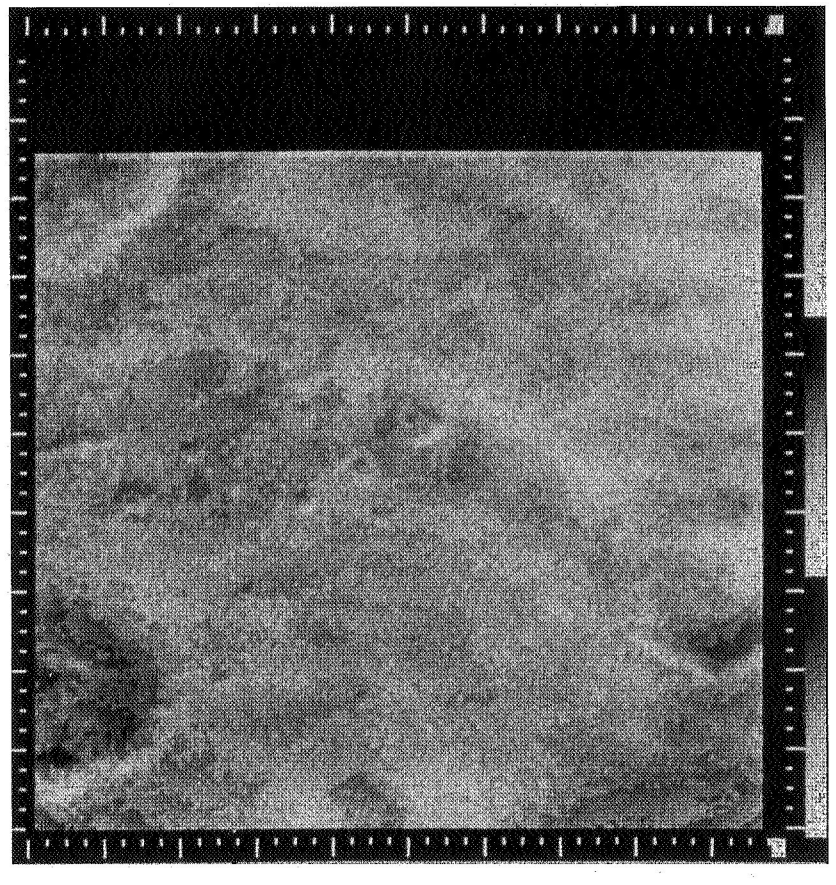

12E. Calibrated and enhanced

18 – C

## Pictures 11 and 12

### Filters

Picture 11—green  Picture 12—orange

### Location of Picture Center

Picture 11—33°S 197°E  Picture 12—35°S, 200°E

Picture 11 probably lies principally within the dark Mare Sirenum, but may be in or near the somewhat lighter area Atlantis between Mare Sirenum and Mare Cimmerium.

Picture 12 probably lies across the ill-defined border between Mare Sirenum and the light area Atlantis.

### Dimensions

Each picture covers an area roughly 275 km east-west and 240 km north-south.

### Time and Lighting

The local time is about 12:40.

The sun is 49° from the zenith in Picture 11 and 52° in Picture 12.

### Brightness Ranges

| Picture 11 | F | E | D | C | B |
|---|---|---|---|---|---|
| Min. | 50 | 57 | 57 | 53 | 57 |
| Max. | 94 | 85 | 85 | 93 | 85 |
| Picture 12 | F | E | D | C | B |
| Min. | 66 | 80 | 80 | 77 | 90 |
| Max. | 147 | 137 | 137 | 137 | 132 |

### Craters

One of the interesting aspects of this pair of photographs is the greater abundance of craters on Picture 11 compared to Picture 12. The difference is not considered to be real, but is probably the product of the decreasing light level, which adversely affects the discriminability. The use of orange and green filters has not produced a corresponding contrast in the instance of other photo pairs because of the higher light levels. One cannot exclude the possibility that the crater density actually is less in Picture 12, however. The general range of slopes and elevations measured on both pictures is similar to that of the previous two pictures.

A total of 97 possible craters have been counted on both pictures, ranging in diameter from 3 to 175 km. Of these, 8 clearly have central peaks, and 9 have well-defined polygonal shape. Twenty of the craters are classed as well preserved, 42 are of intermediate preservation, and 35 are poorly preserved. Outstanding is the large crater of 175-km diameter on Picture 11. This is one of the best preserved larger craters shown on the *Mariner IV* photos. In places its inner walls display features suggestive of slump blocks. This is rather common among the larger craters.

Contrasts in ages of craters are about as well shown on Picture 11 as on any photo of the *Mariner* sequence. The large, 175-km crater, although relatively well preserved, is obviously much older than the many craters pocking its floor, slopes, and rim. Some of the craters on its floor are faint, suggesting considerable modification and a relatively great age for the large crater. The relic crater centered at about P11 L82 E76 (Picture 11B) is reminiscent of Sinus Iridum on the moon, having been eroded away entirely on the side towards the center of the large crater and filled smoothly right to the edge of the other wall. As in the previous two pictures, albedo contrasts are sometimes localized within a crater (P11 L136 E41 and P12 L185 E170) and sometimes pass across the craters without apparent regard for the local relief (P11 L132 E135). The larger craters in Picture 11 show extensive modification by linear elements, particularly the interior of P11 L155 E114 and the rims of P11 L136 E41, P11 L155 E114, and P12 L20 E140.

The peculiar tendency for tonal variation to be brighter on the northern portion of crater floors and darker on the southern, noted previously in discussion of Pictures 7 and 8, and also 9 and 10, is conspicuously developed in P12 L20 E140, and less strongly in the large crater of Picture 11. In the former case, the effect is so strong that, if presumed to be solely topographic, the whole central area of the crater would be many hundreds of meters higher than the surrounding plain.

### Lineations

The most prominent lineation visible in these pictures is the long, straight, narrow rift visible in Picture 11. It runs northeast from the southwest corner of the picture toward L1 E125 (Picture 11B). At some points it is lighter than the surroundings, at other points darker. As it crosses the walls of a minor crater and the major crater, it seems to enhance the shading due to crater walls. Close inspection reveals that along much of its length it is double, consisting of two dark lines about 5 picture elements apart. There is no evidence of shear displacement of one side relative to the other.

Most of the other lineations in these pictures seem to be shorter, more diffuse, and to have a northwesterly trend, parallel to the prominent polygonal crater walls.

### Albedo and Surface Texture

There are few striking albedo variations in these pictures, although Picture 12 seems somewhat dark in the southwest and somewhat light in the northeast, a trend somewhat shared by Picture 11. This same area appears smoother on the fluctuation plot (Picture 11G).

18-D

REFERENCE COORDINATES

Line and element numbers, as recorded on the original television photographs, are depicted around the perimeter of the imagery for the purpose of identifying and referencing of features.

Element Number . . . . . North to South
Line Number . . . . . East to West

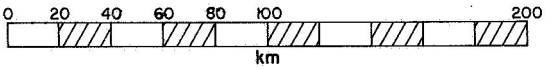


Orthographic Projection
at 33°58'40"S and 161°07'32"W

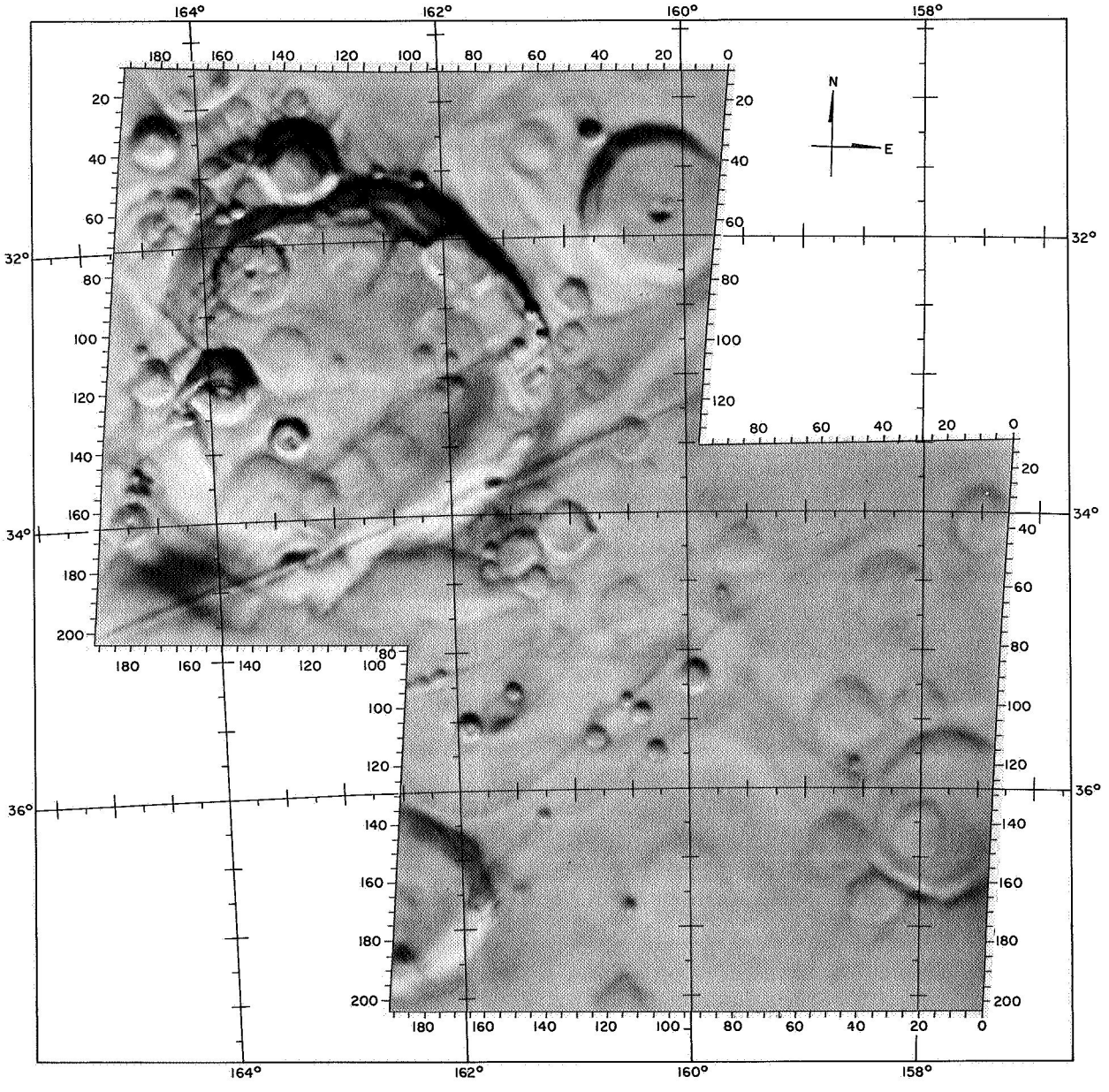


**11, 12A. ACIC version**

19 - A

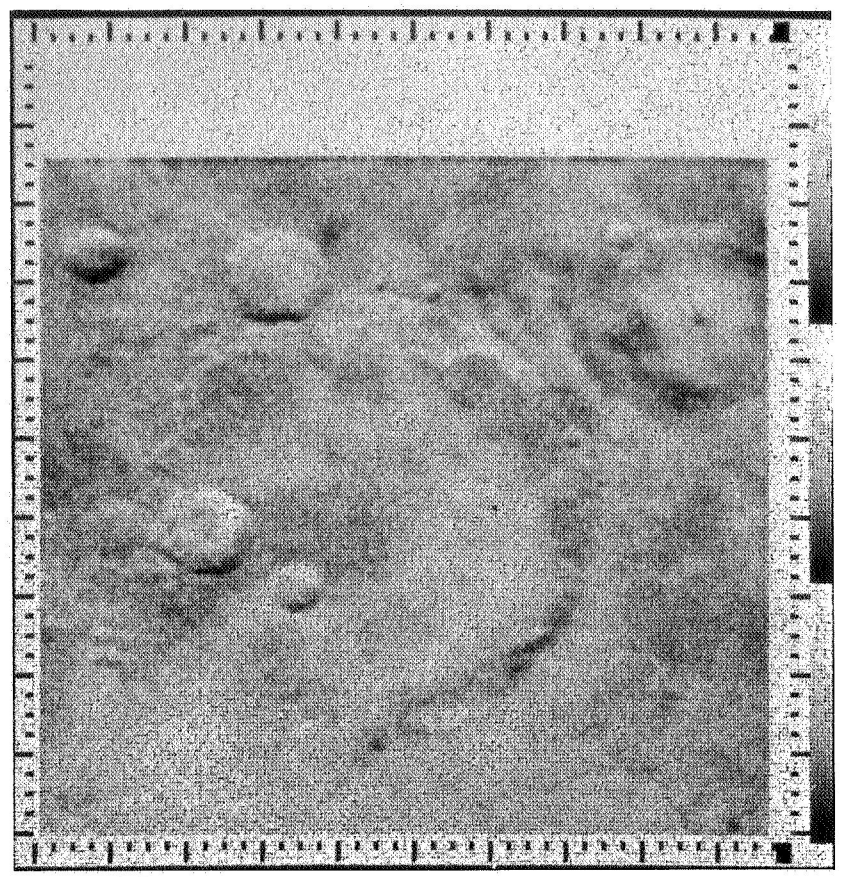

11D. Negative version, calibrated and unsharpened

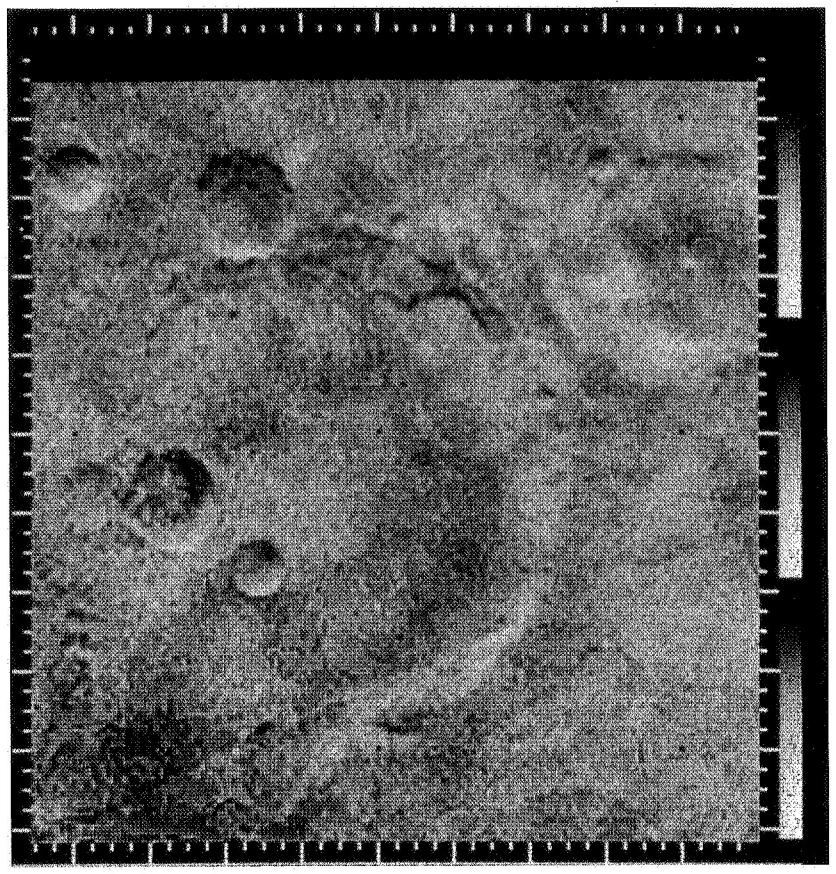

11C. Calibrated, rectified, and sharpened

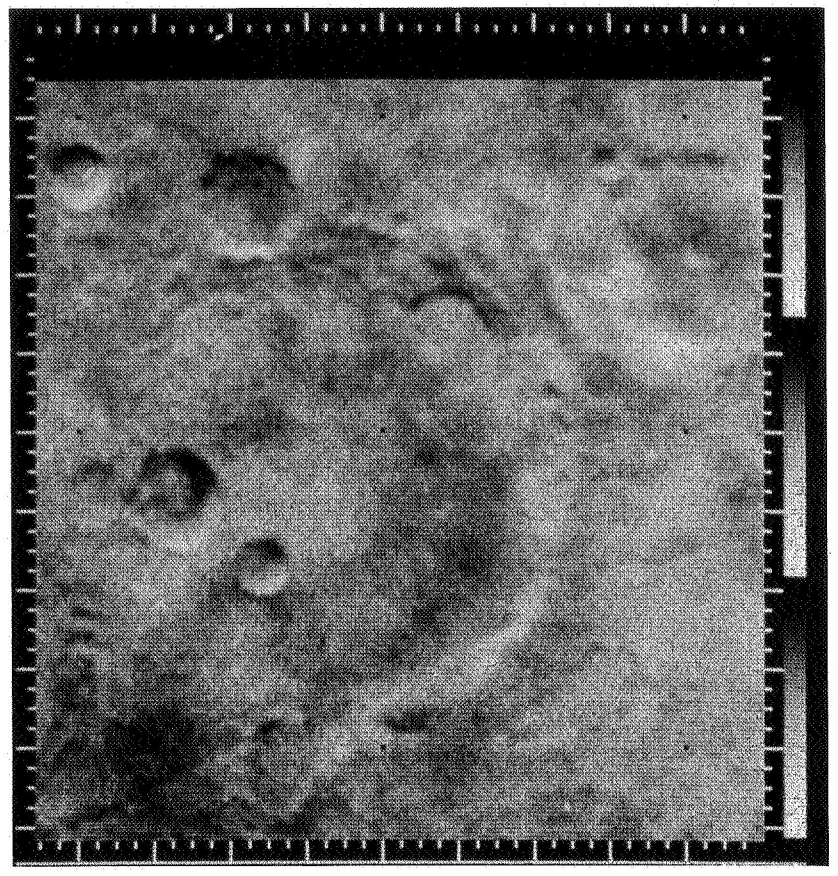

11B. Calibrated and rectified

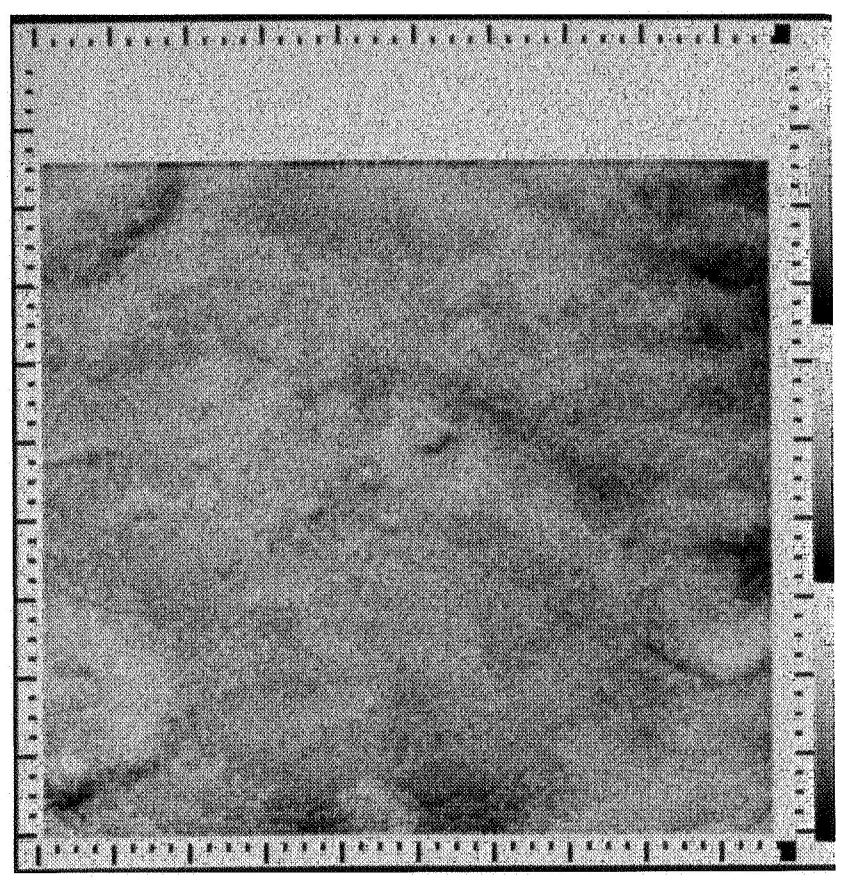

12D. Negative version, calibrated and unsharpened

19-B

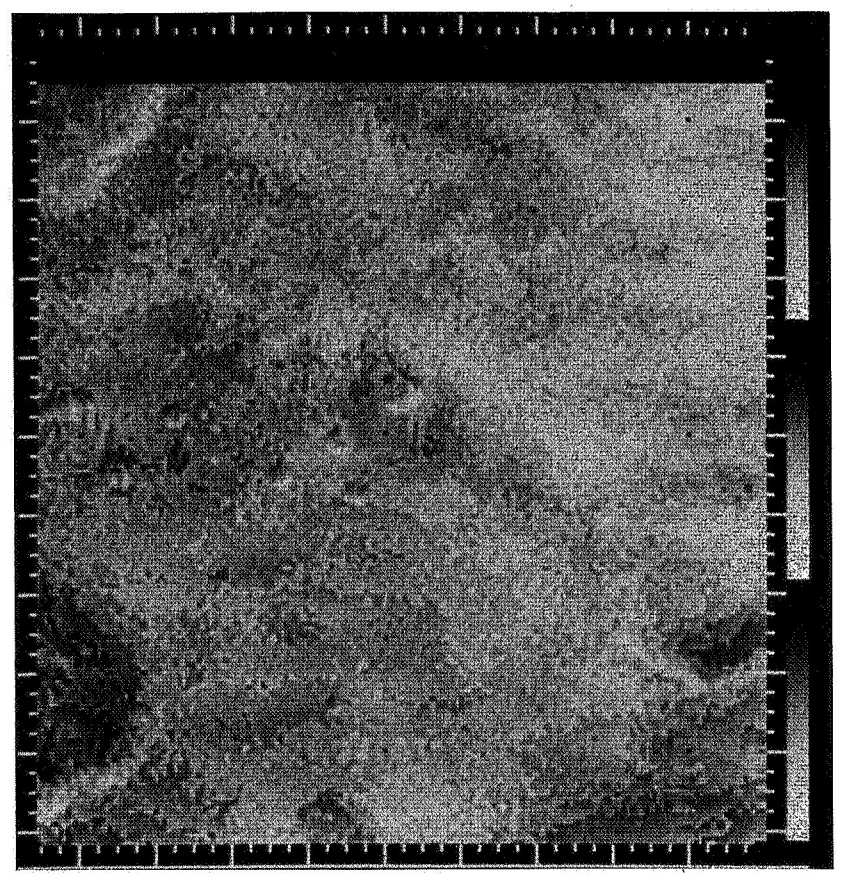

12C. Calibrated, rectified, and sharpened

19-C

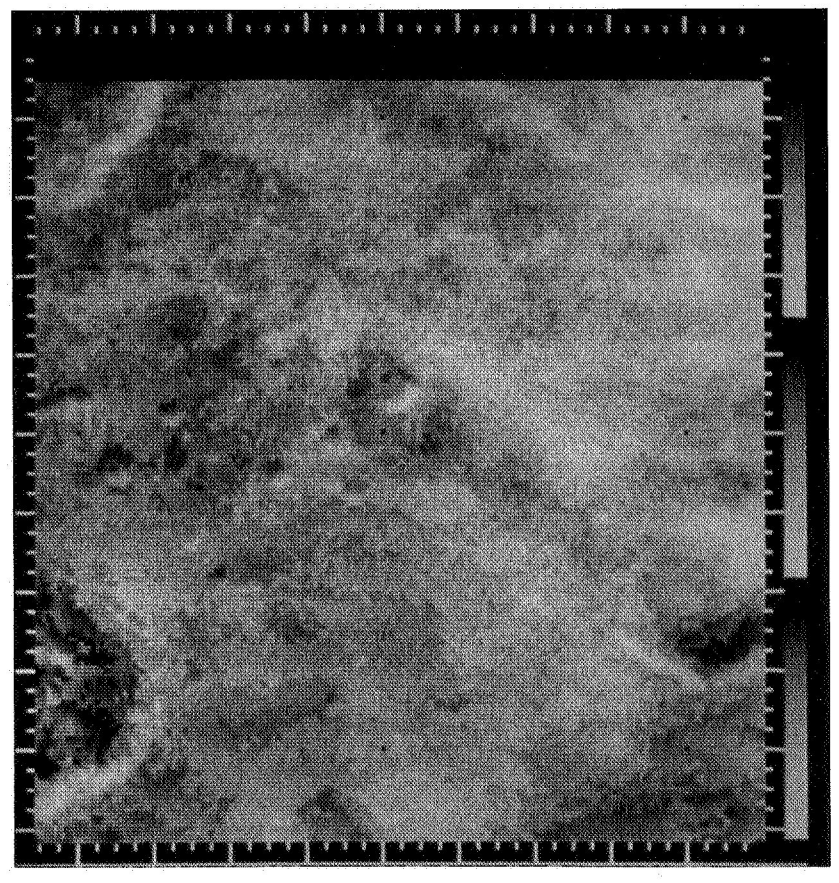

12B. Calibrated and rectified

19-D

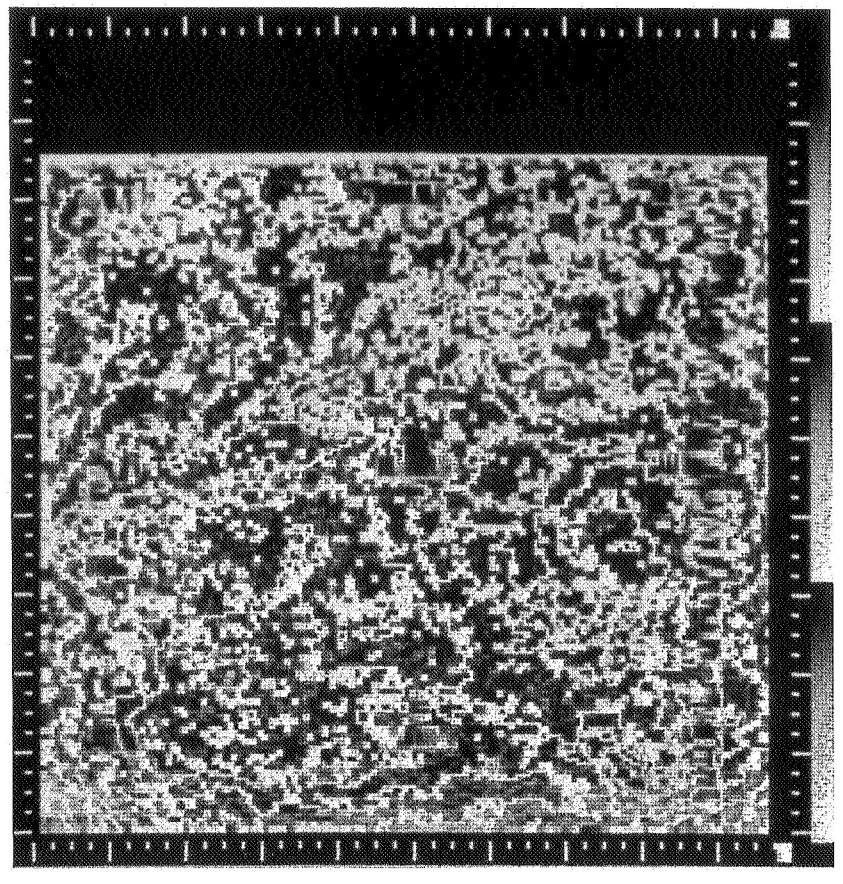

13G. Variance plot

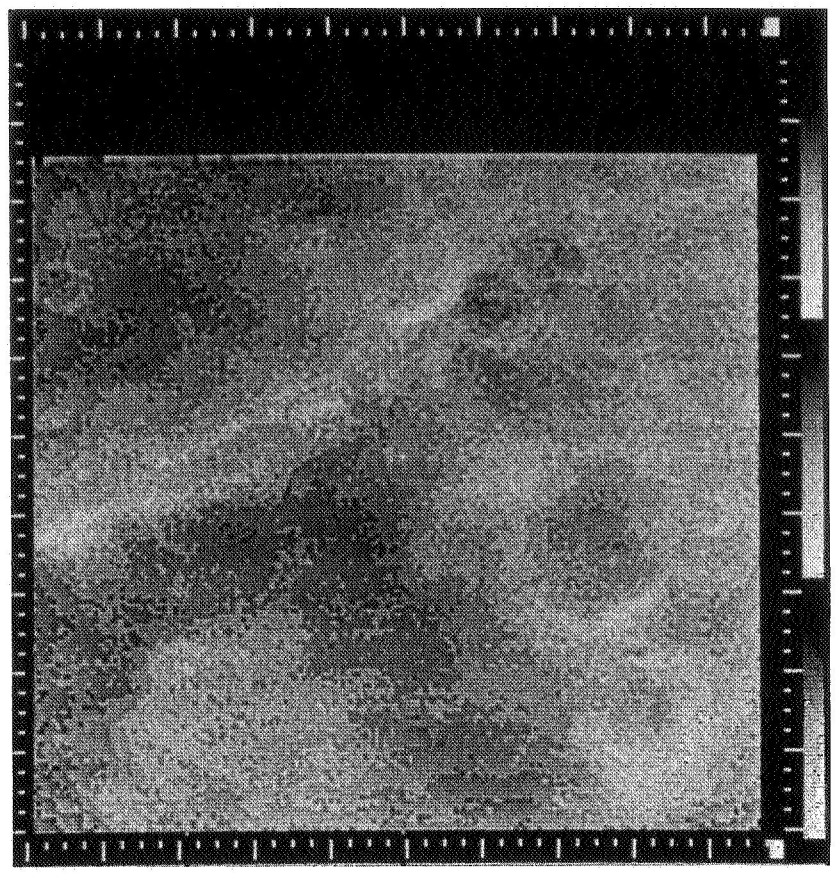

13F. Calibrated, sharpened, and enhanced

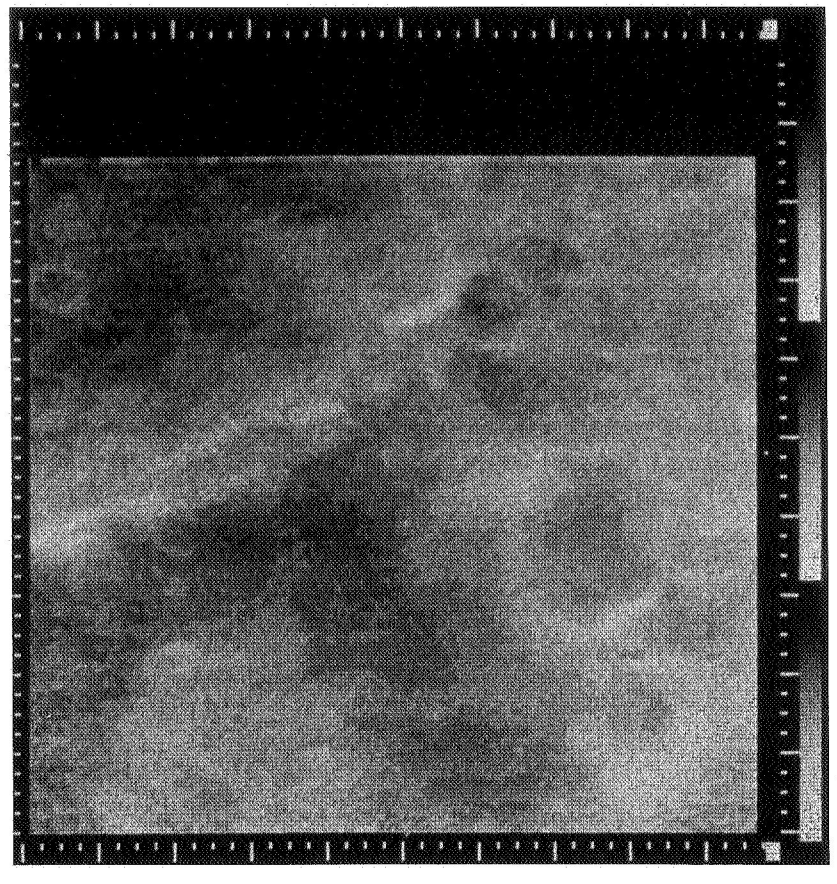

13E. Calibrated and enhanced

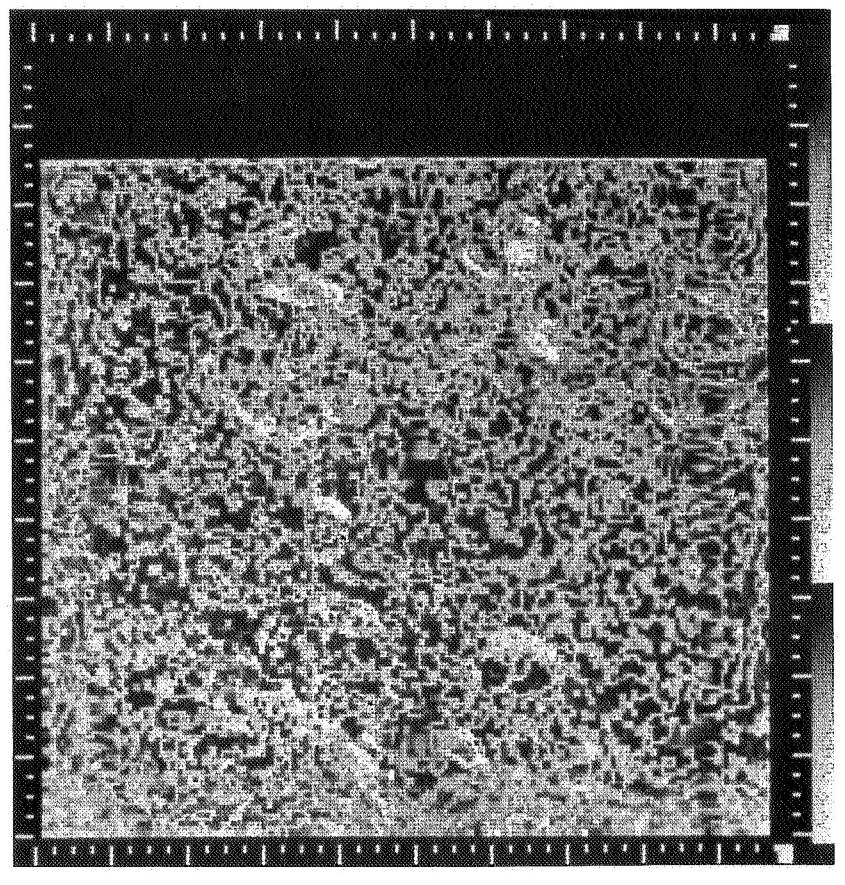

20 A

14G. Variance plot

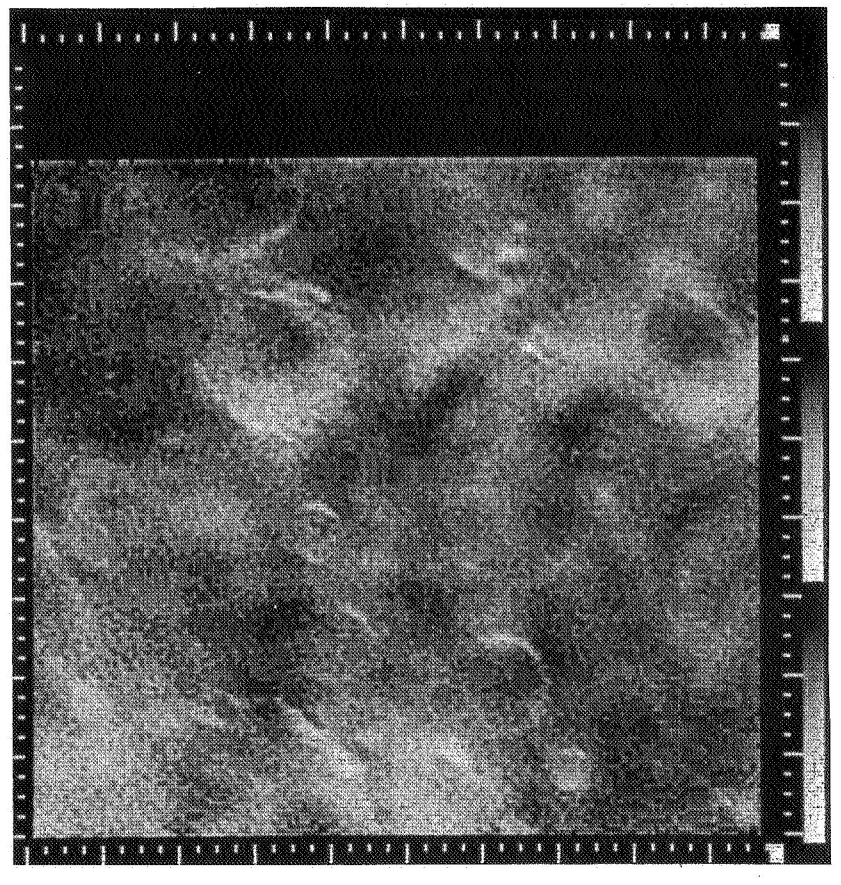

14F. Calibrated, sharpened, and enhanced

20 - B

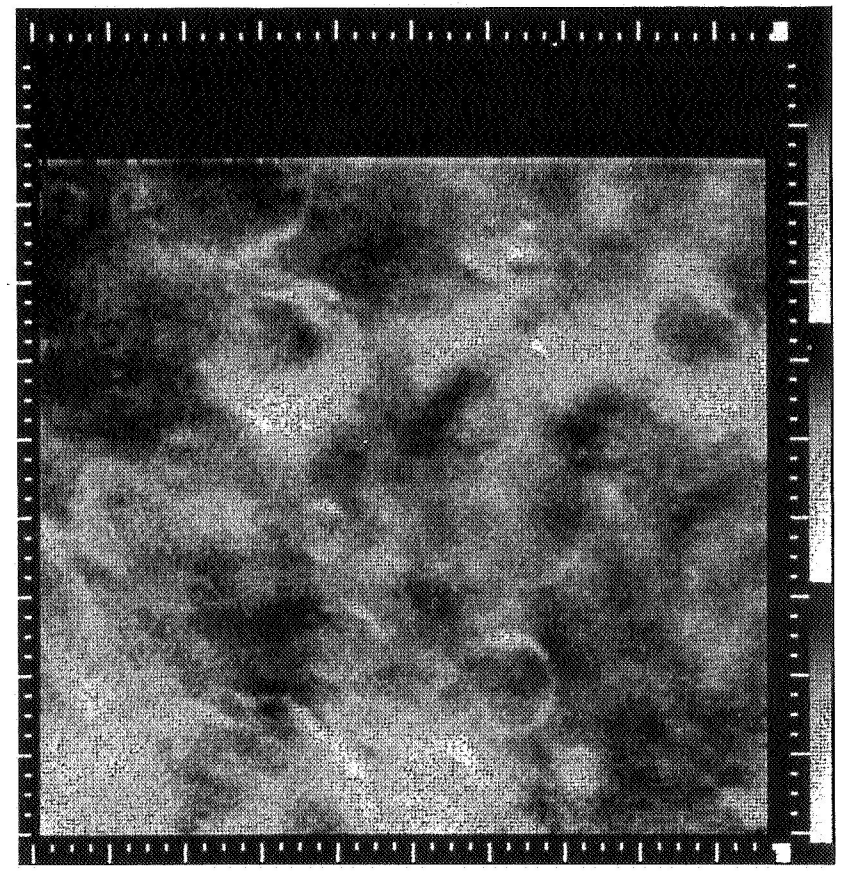

14E. Calibrated and enhanced

20 - C

## Pictures 13 and 14

### Filters

Picture 13—orange Picture 14—green

### Location of Picture Center

Picture 13—40°S, 206°E Picture 14—42°S, 209°E

The border between Mare Cimmerium on the north and the bright region Phaethontis probably passes through Picture 13. Picture 14 is wholly within the bright area Phaethontis.

### Dimensions

Each picture covers an area approximately 275 km east-west and 225 km north-south.

### Time and Lighting

The local time is about 13:00.

The sun is 58° from the zenith in Picture 13 and 61° in Picture 14.

### Brightness Ranges

| Picture 13 | F | E | D | C | B |
|---|---|---|---|---|---|
| Min. | 73 | 74 | 74 | 80 | 90 |
| Max. | 153 | 144 | 144 | 150 | 140 |
| Picture 14 | F | E | D | C | B |
| Min. | 56 | 61 | 61 | 60 | 63 |
| Max. | 106 | 98 | 98 | 102 | 97 |

### Craters

These two frames display a total of 67 possible craters, 4 with a central peak and 4 with good polygonal outline. The degree of preservation is judged to be good in 12, intermediate in 19, and poor in 36.

The smallest crater identified is 6 km across, and the largest, only a part of which is shown, is 350 km in diameter. Its opposite wall might appear as a dark patch in the extreme southeast corner of Picture 12. If this is a valid interpretation, this is by far the largest crater recognized on any of the *Mariner IV* photos. The next largest crater on these photos is 58 km.

### Lineations

A rather straight linear feature bears about N60°E through the northern part of Picture 13. It appears to cut the rim and floor of the large (350-km) crater but is in turn broken by smaller, seemingly younger craters to the northeast. Parallel to this line are the opposite walls of a polygonal crater at L 45 E 120 (Picture 13B). Suggestions of a less well defined set of lineations of shorter, more irregular character are seen in the southern part of Picture 14.

### Albedo and Surface Texture

Although Picture 13 lies near a mare-light area contact, no sign of this is seen here in terms of albedo or topographic features.

Visible in Picture 13, and even more in Picture 14, are several examples of a new phenomenon—circular features having a nearly continuous bright outline. These are interpreted as craters whose poleward inner slopes are illuminated by the sun, and whose equatorward inner walls are partially covered by "frost" or "snow" and which therefore appear brighter even though they are more obliquely illuminated. Many of the circular rings are incomplete in the northwest quadrant, as would be expected if the morning sun were able to evaporate a thin layer of overnight frost. The south polar cap edge is probably at about 60°–65°S latitude, or about 10°–15° south of Picture 14.

It is possible that some of the localized bright patches not associated with craters are also frost patches. The possibility that fog or low clouds exist in these latitudes must be considered also.

20-D

REFERENCE COORDINATES

Line and element numbers, as recorded on the original television photographs, are depicted around the perimeter of the imagery for the purpose of identifying and referencing of features.

Element Number . . . . . North to South
Line Number . . . . . East to West

0 20 40 60 80 100 200
km

Orthographic Projection
at 41°08'03"S and 152°32'20"W

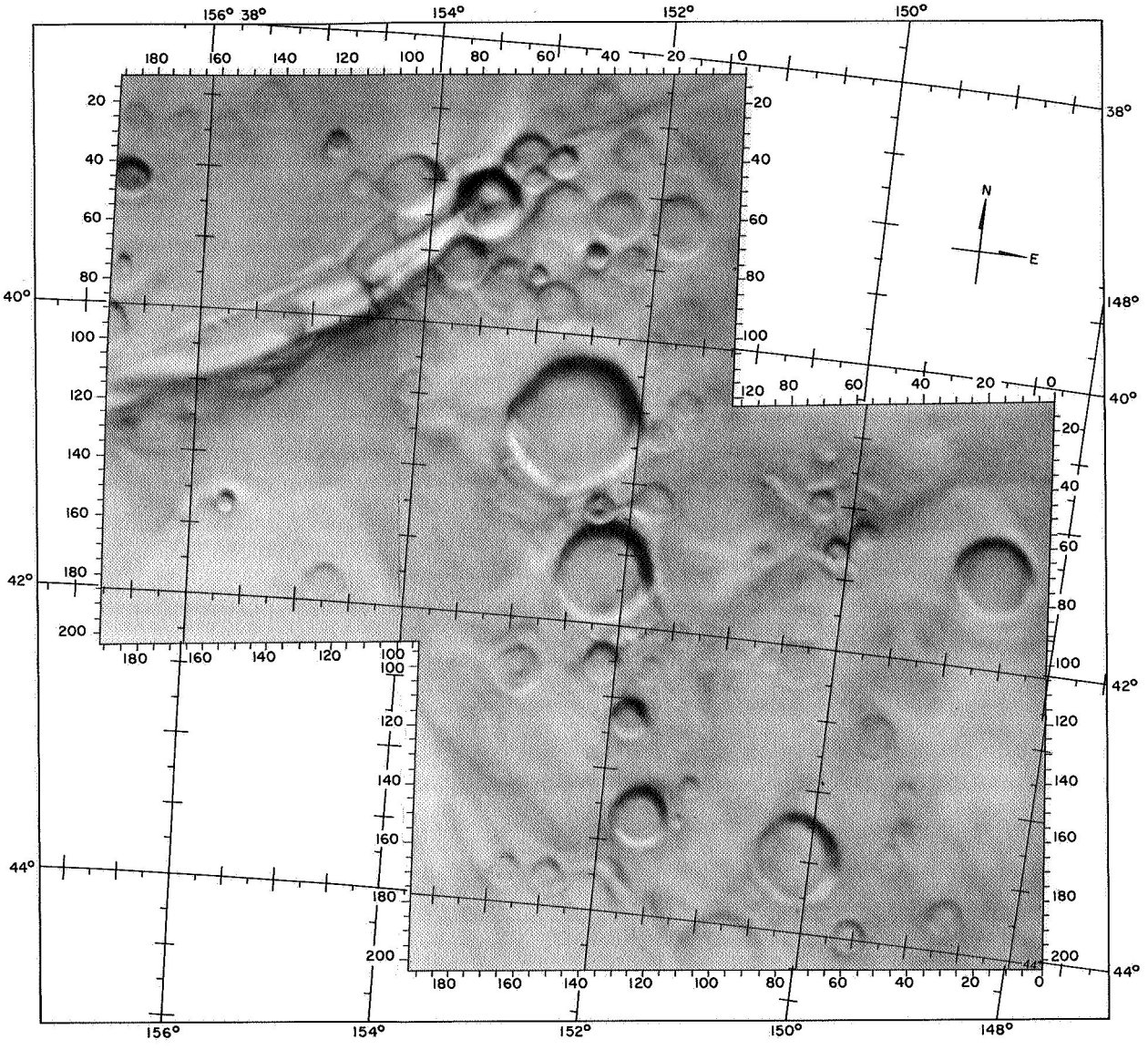


**13, 14A. ACIC version**



21 - A

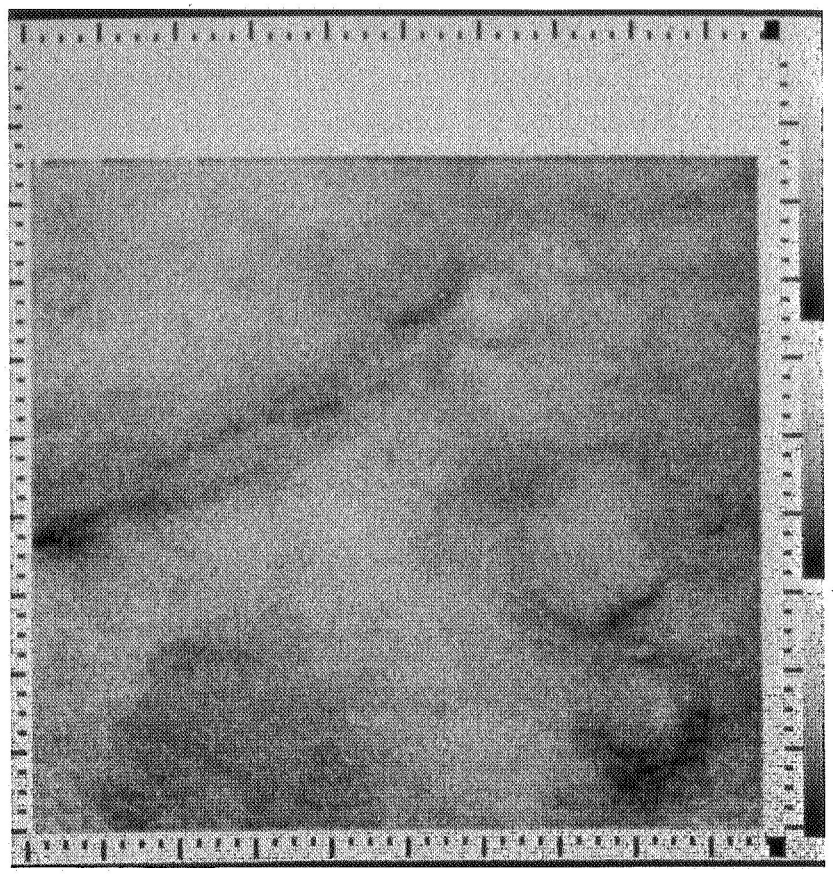

13D. Negative version, calibrated and unsharpened

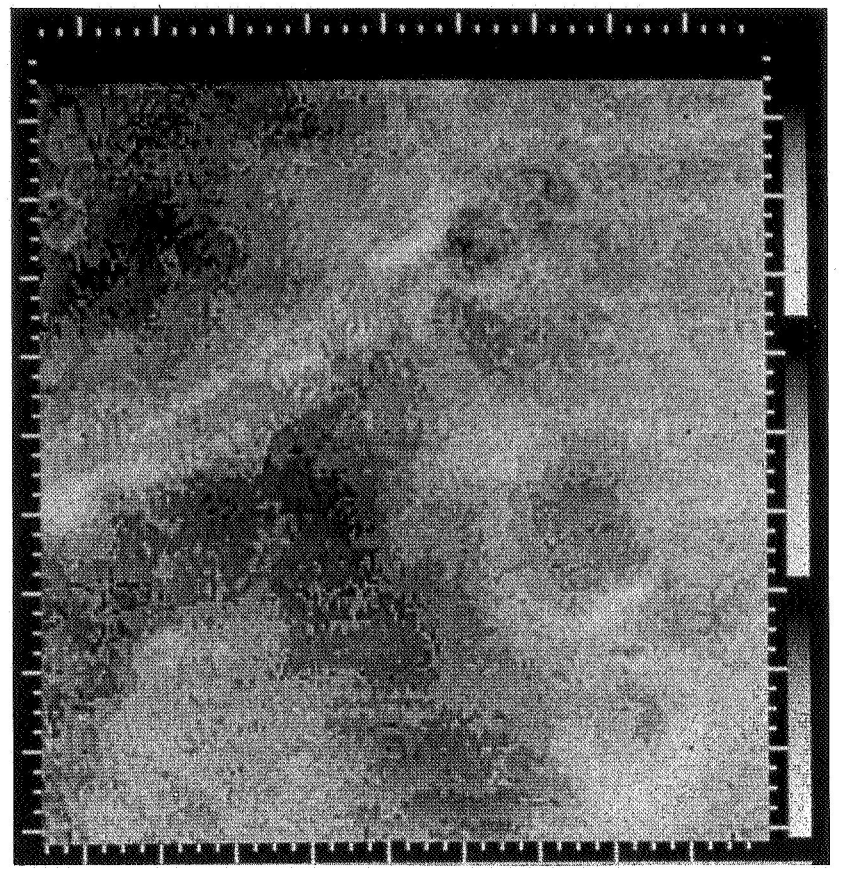

13C. Calibrated, rectified, and sharpened

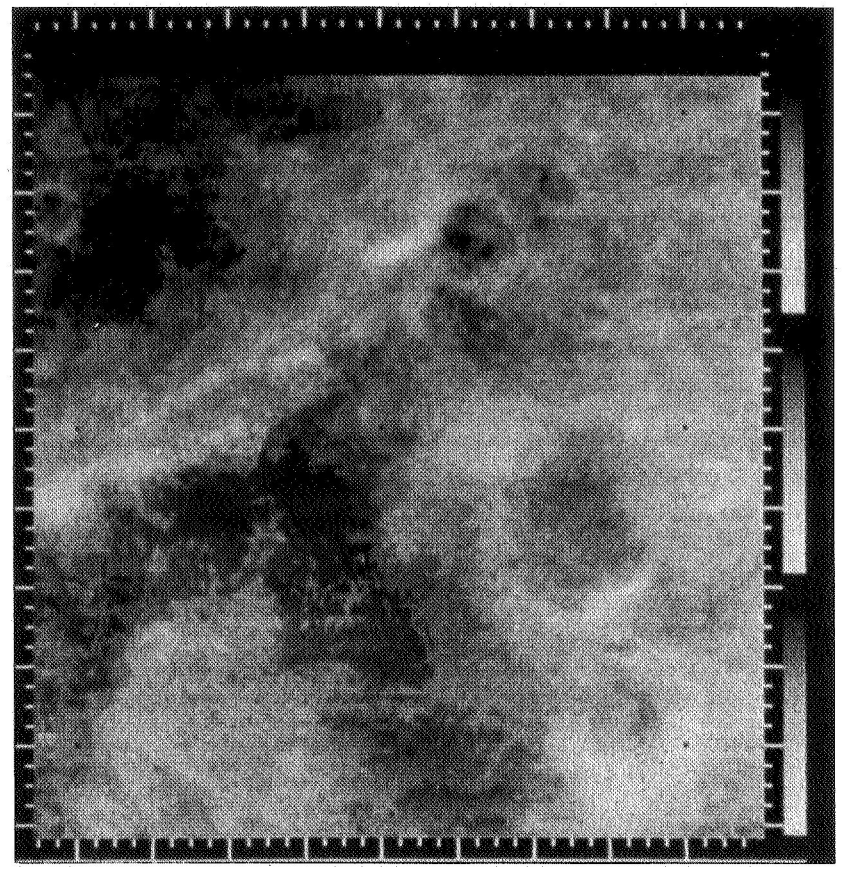

13B. Calibrated and rectified

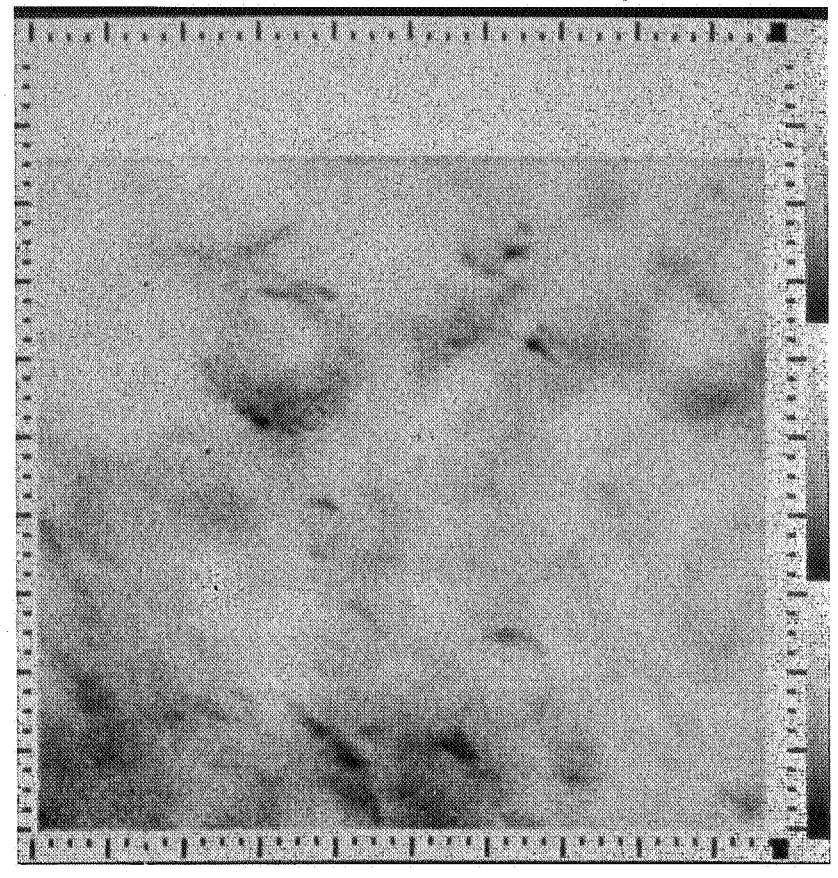

14D. Negative version, calibrated and unsharpened

21-B

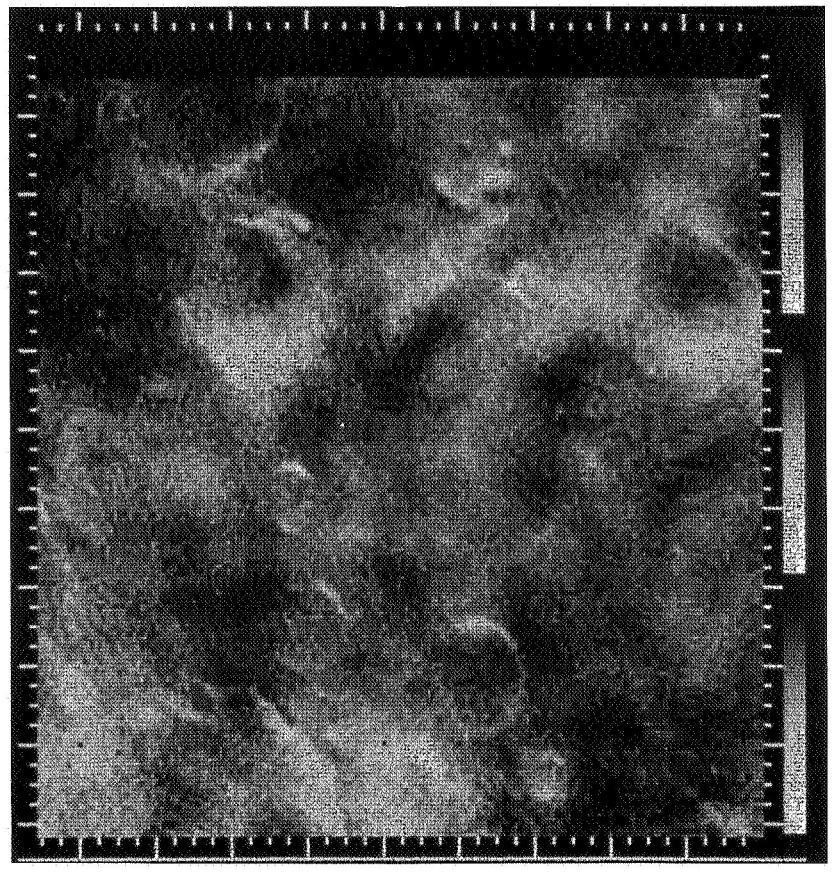

14C. Calibrated, rectified, and sharpened

21-C

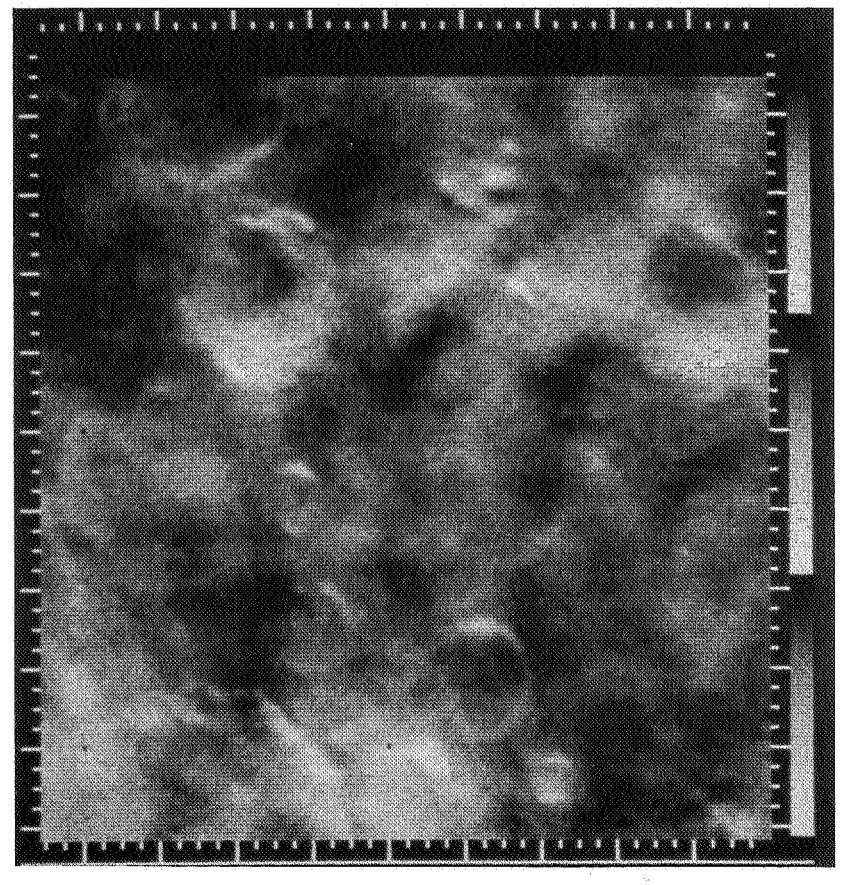

14B. Calibrated and rectified

21-D

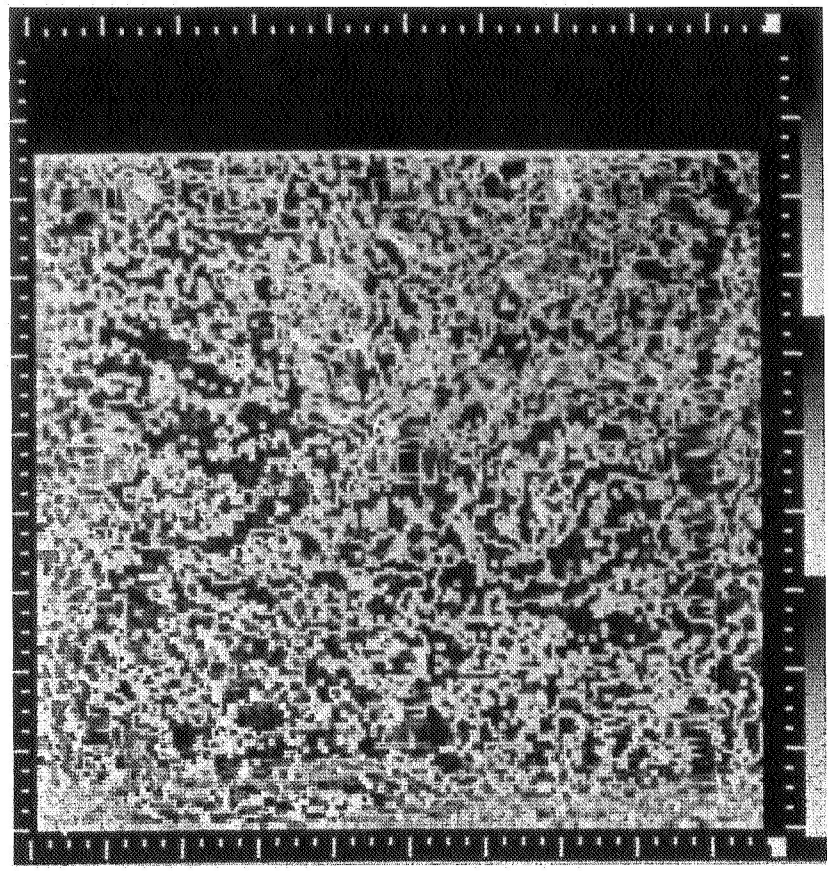

15G. Variance plot

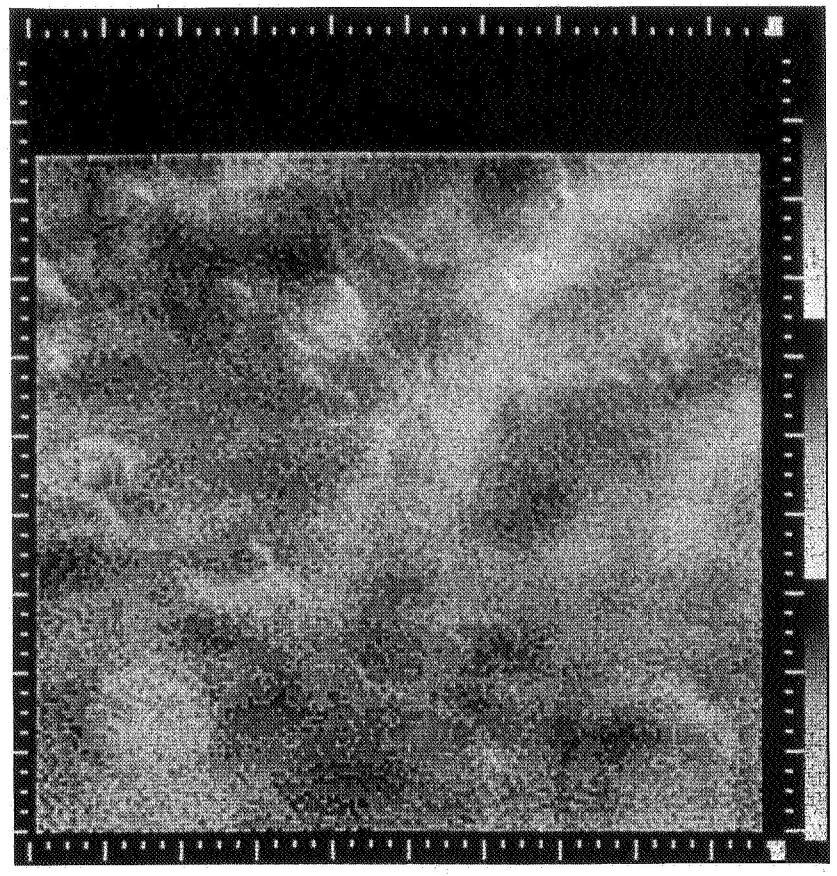

15F. Calibrated, sharpened, and enhanced

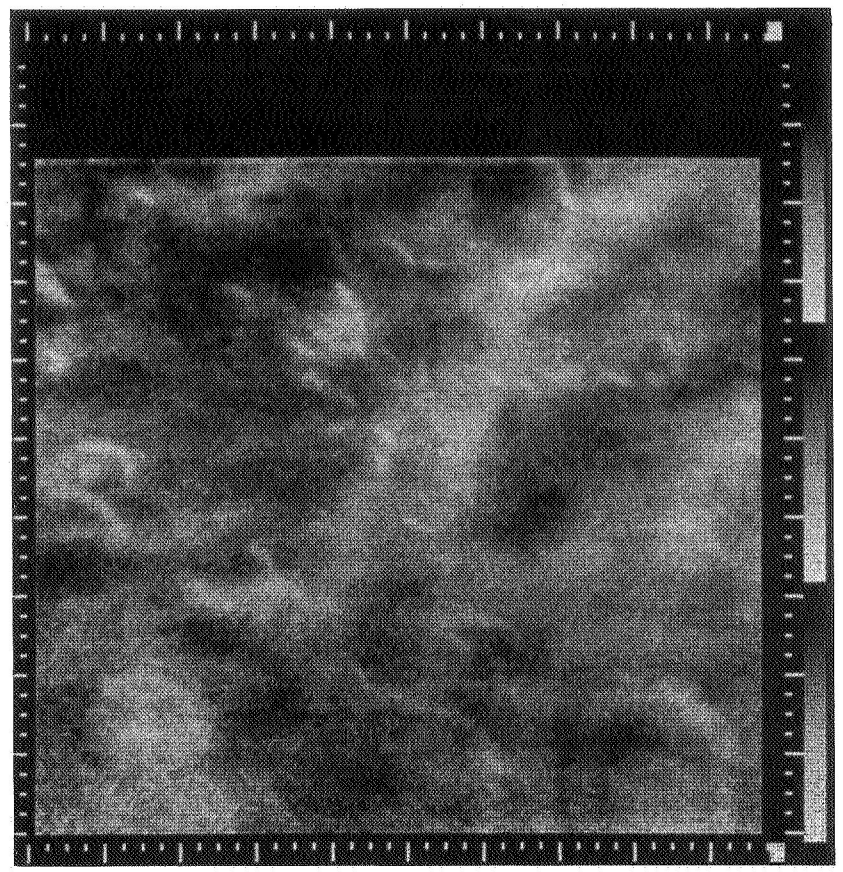

15E. Calibrated and enhanced

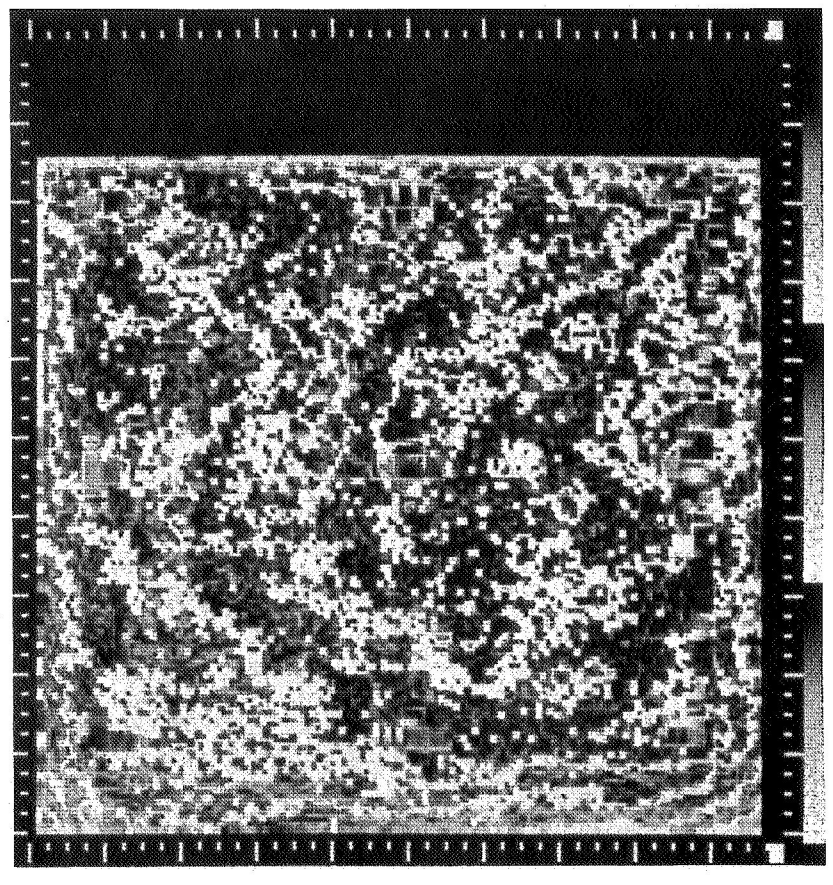

16G. Variance plot

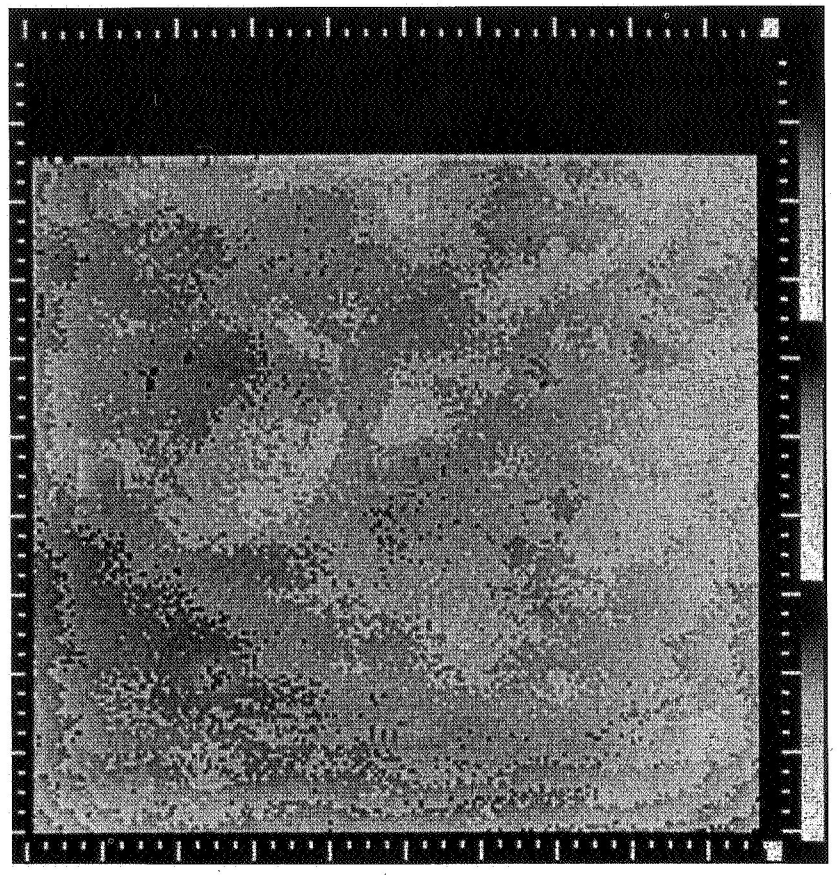

16F. Calibrated, sharpened, and enhanced

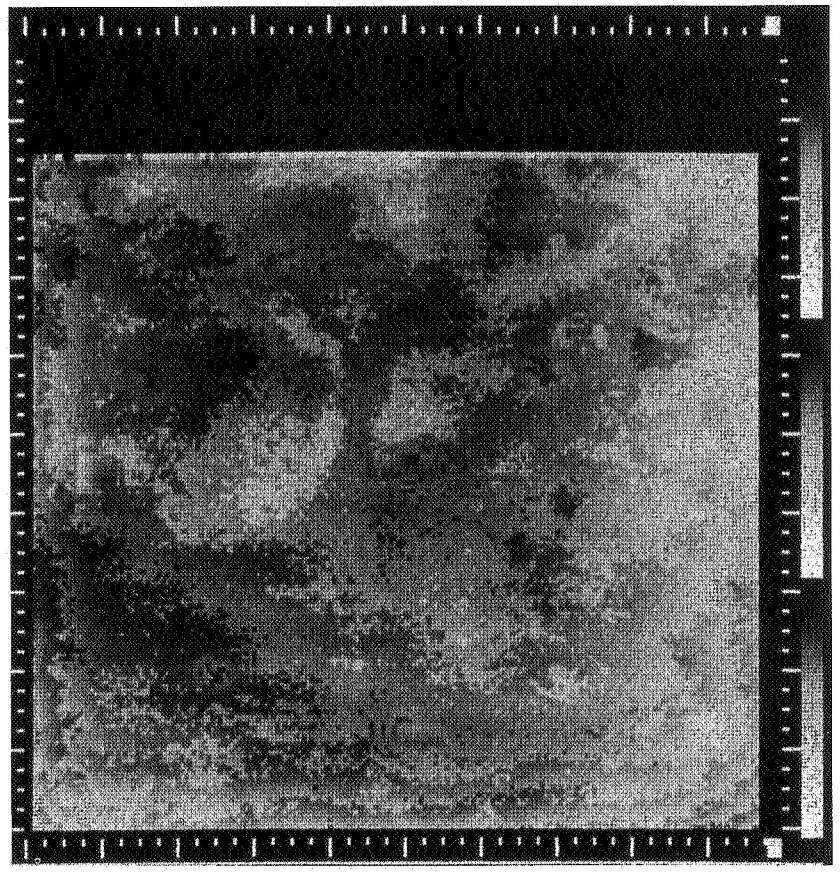

16E. Calibrated and enhanced

## Pictures 15 and 16

### Filters

Picture 15—green Picture 16—orange

### Location of Picture Center

Picture 15—46°S, 217°E Picture 16—48°S, 221°E

Both pictures are located wholly within the bright area Phaethontis.

### Dimensions

Picture 15 covers an area approximately 290 km east-west and 225 km north-south; Picture 16 covers an area 305 km east-west by 225 km north-south.

### Time and Lighting

The local time is 13:40 for Picture 15 and 14:00 for Picture 16.

The sun is 67° from the zenith in Picture 15 and 70° in Picture 16.

### Brightness Ranges

| Picture 15 | F | E | D | C | B |
|---|---|---|---|---|---|
| Min. | 52 | 57 | 57 | 55 | 57 |
| Max. | 93 | 87 | 87 | 90 | 86 |

| Picture 16 | F | E | D | C | B |
|---|---|---|---|---|---|
| Min. | 64 | 79 | 79 | 70 | 81 |
| Max. | 141 | 126 | 126 | 121 | 108 |

### Craters

A total of 45 possible craters are recognized on this pair of photos, 2 with a central peak and 3 with polygonal outline. Only 3 are judged to be well preserved; 22 are in an intermediate state and 20 a poor state of preservation. The largest crater identified is 114 km in diameter; the smallest is 7 km across.

The craters and other topographic features shown on these pictures appear relatively subdued, but this is due principally to the worsening discriminability of the camera system as the general light level diminishes. This effect is especially marked for the orange filter pictures 12, 13, 16, and 17.

### Lineations

No lineations comparable to those seen on other photos are displayed here.

### Albedo

Picture 15 strongly resembles Picture 14 with respect to the presence of bright-ringed craters as well as in other aspects of its general appearance. It presumably is to be interpreted in a similar way. Because of its relatively poor intensity discriminability, the camera reveals very little significant surface detail in Picture 16.

REFERENCE COORDINATES

Line and element numbers, as recorded on the original television photographs, are depicted around the perimeter of the imagery for the purpose of identifying and referencing of features.

Element Number . . . . . North to South
Line Number . . . . . East to West

0 20 40 60 80 100 200
km

Orthographic Projection
at 46°50'22"S and 140°59'10"W

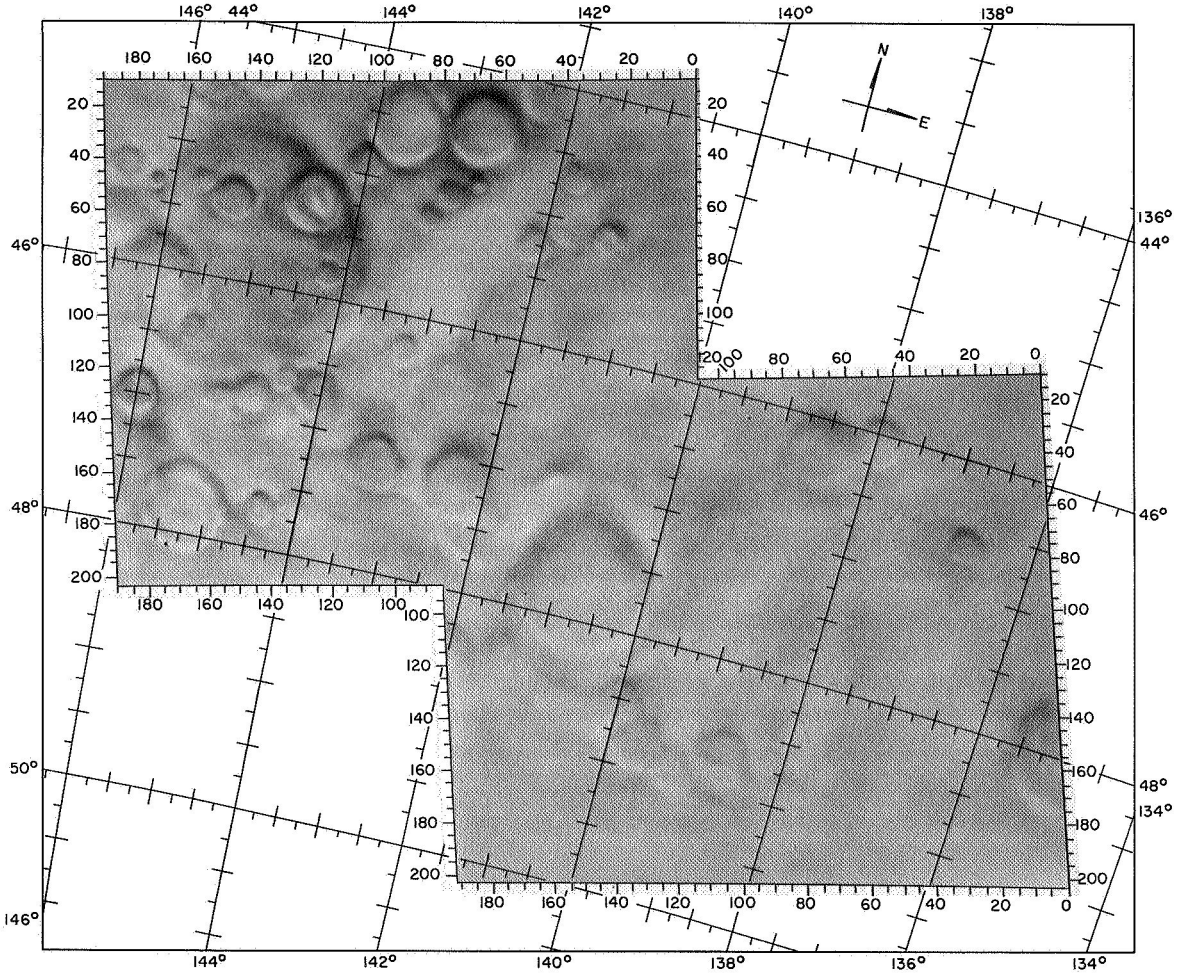


**15, 16A. ACIC version**



23-A

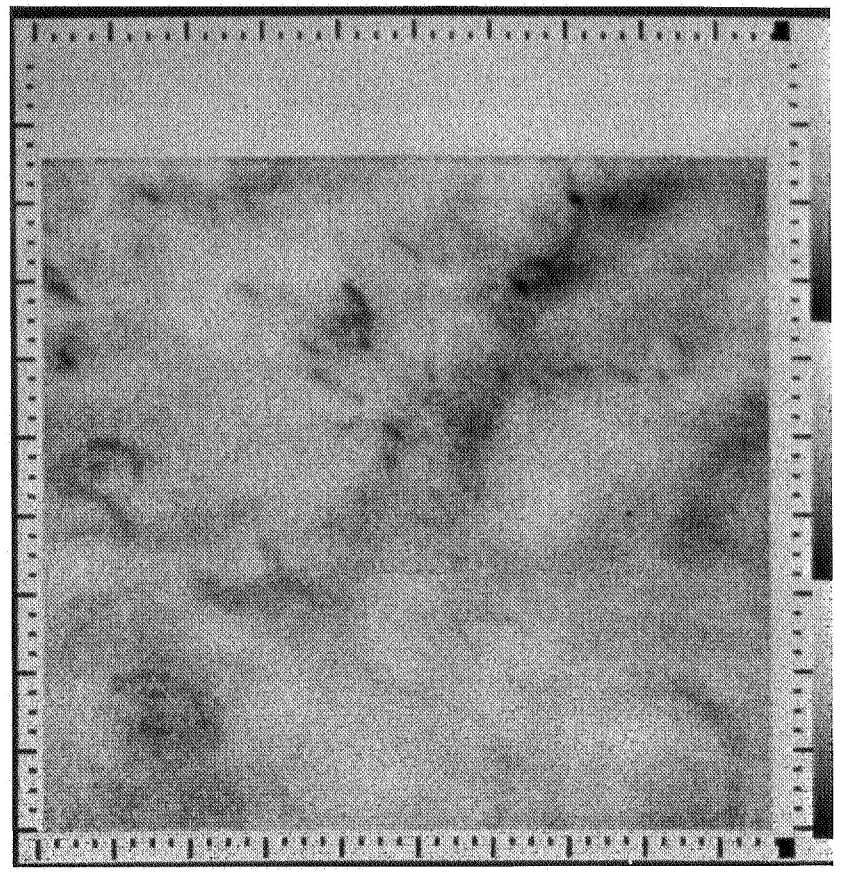

15D. Negative version, calibrated and unsharpened

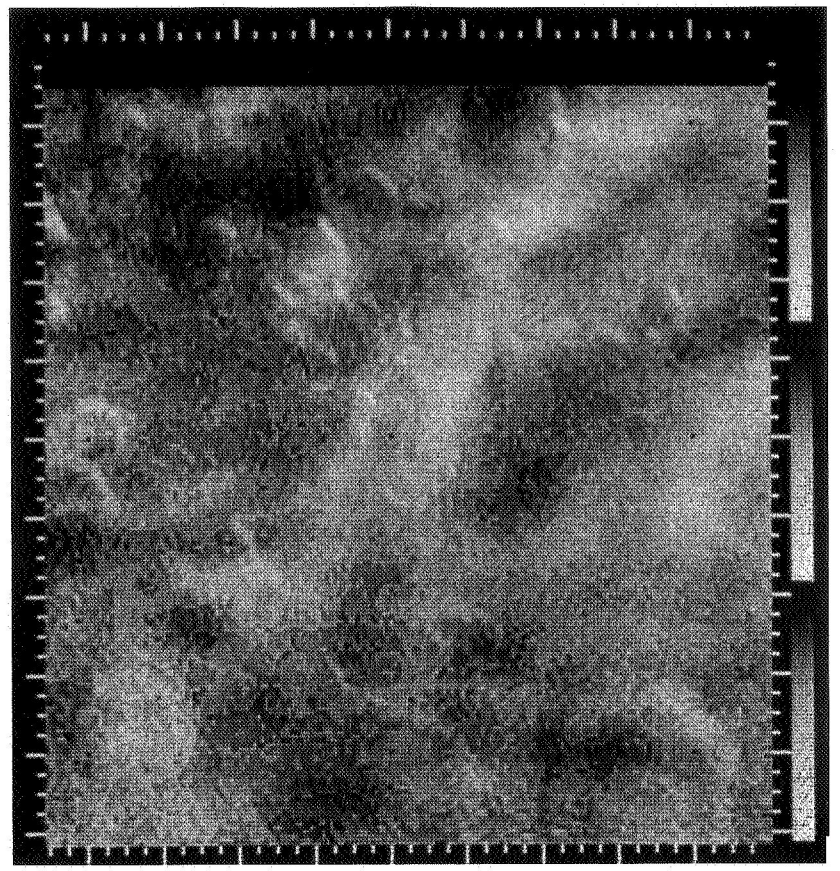

15C. Calibrated, rectified, and sharpened

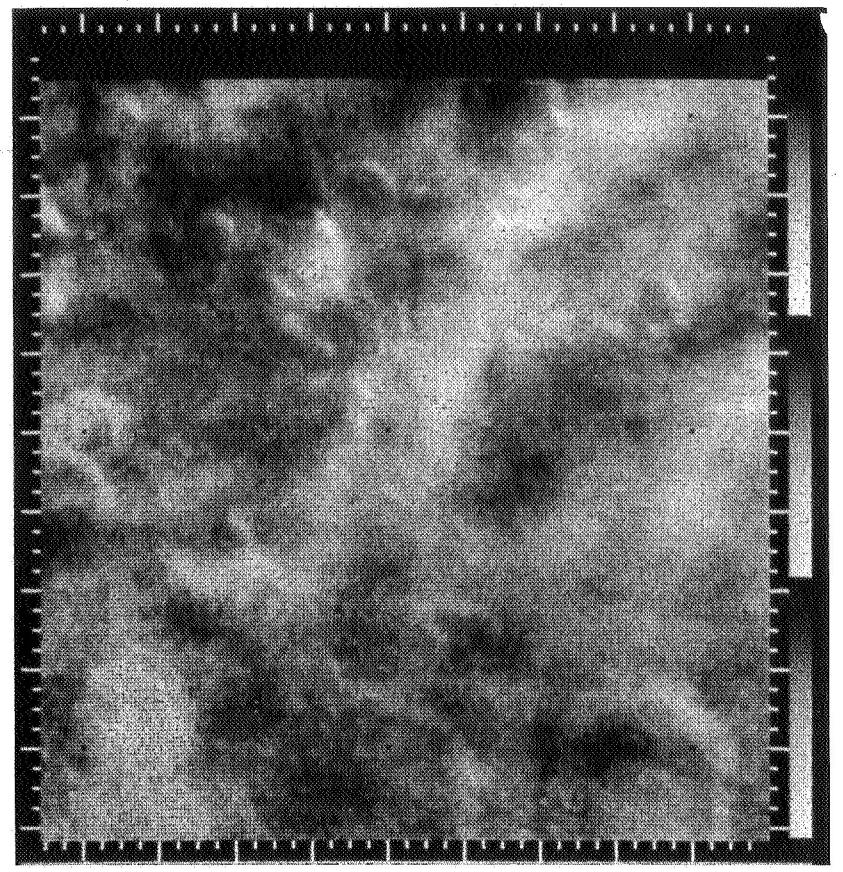

15B. Calibrated and rectified

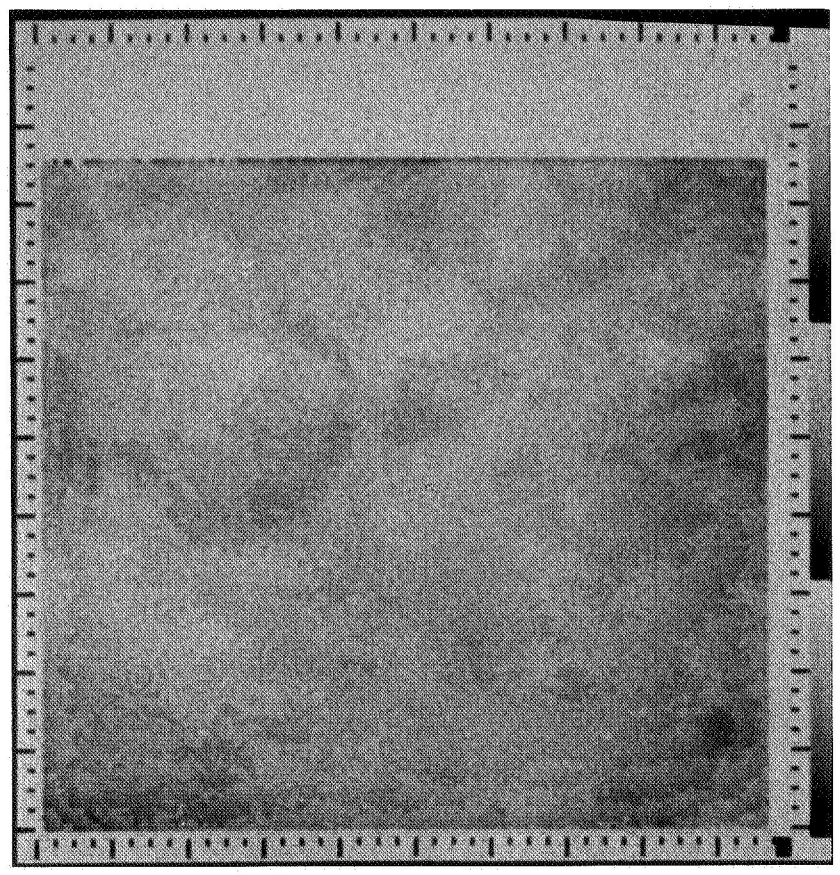

16D. Negative version, calibrated and unsharpened

23-B

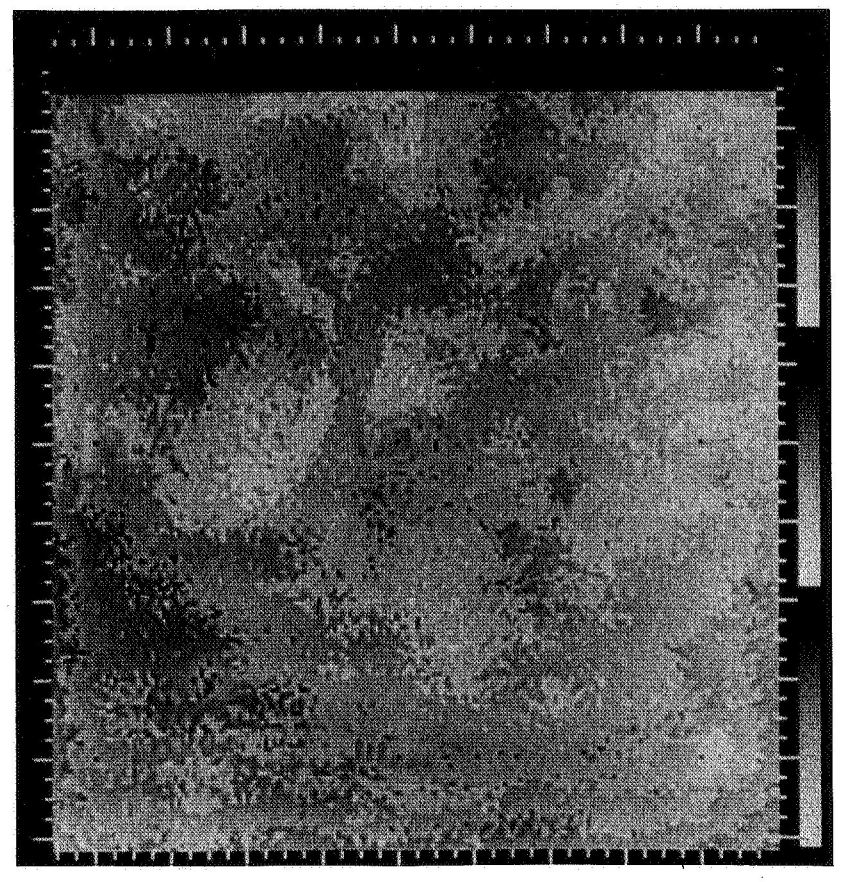

16C. Calibrated, rectified, and sharpened

23-C

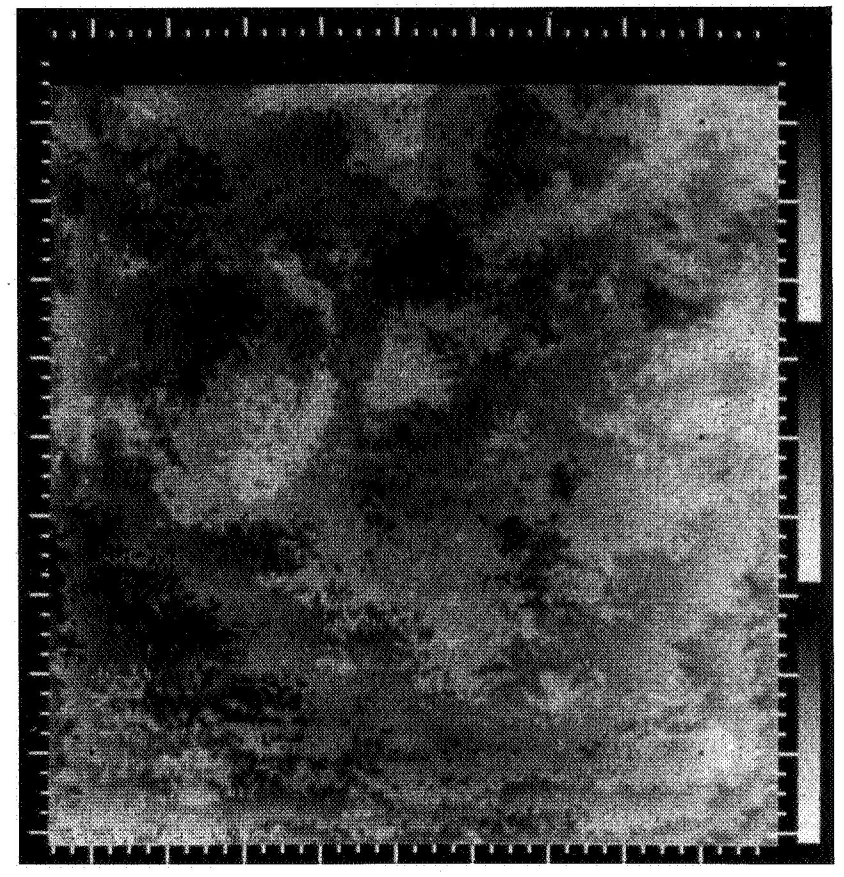

16B. Calibrated and rectified

23-D

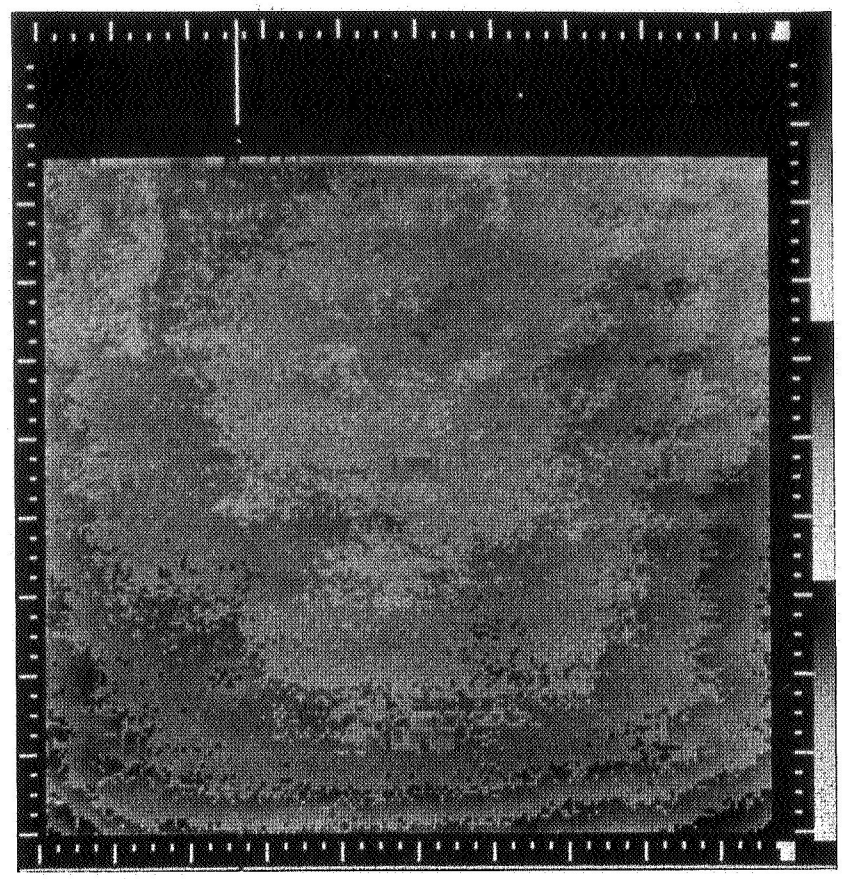

Picture 17

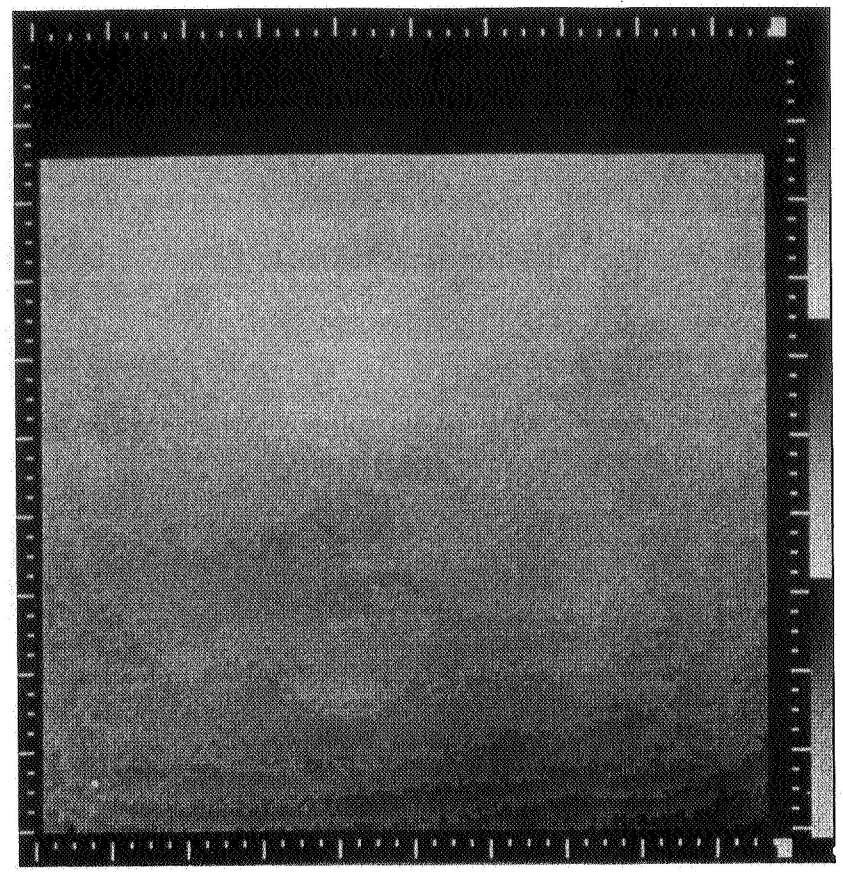

Picture 18

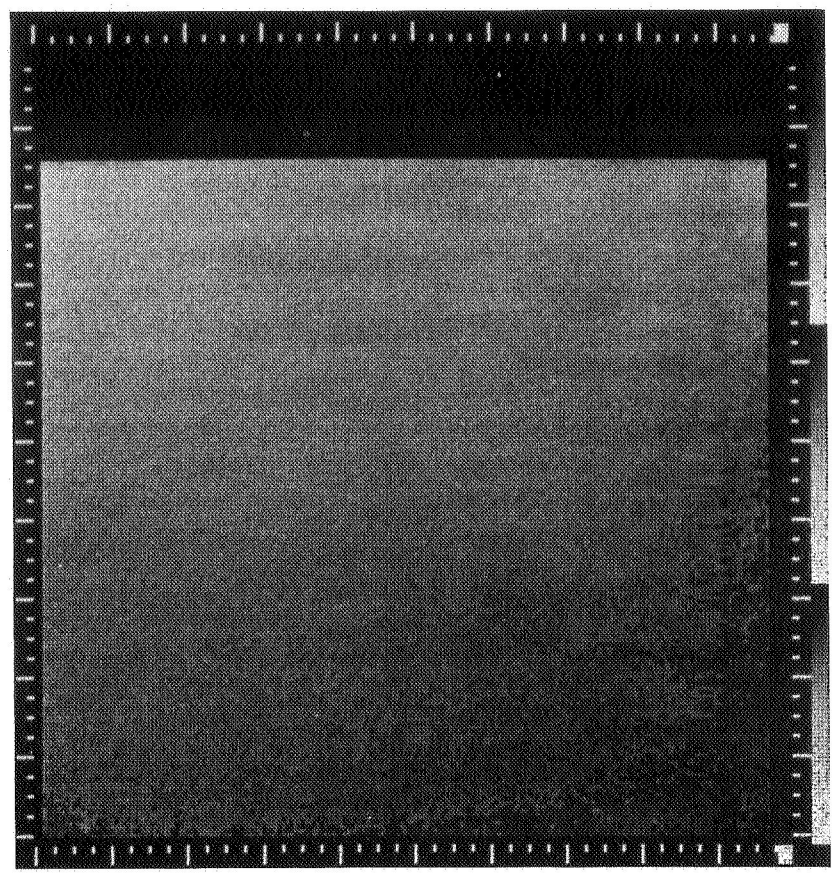

Picture 19

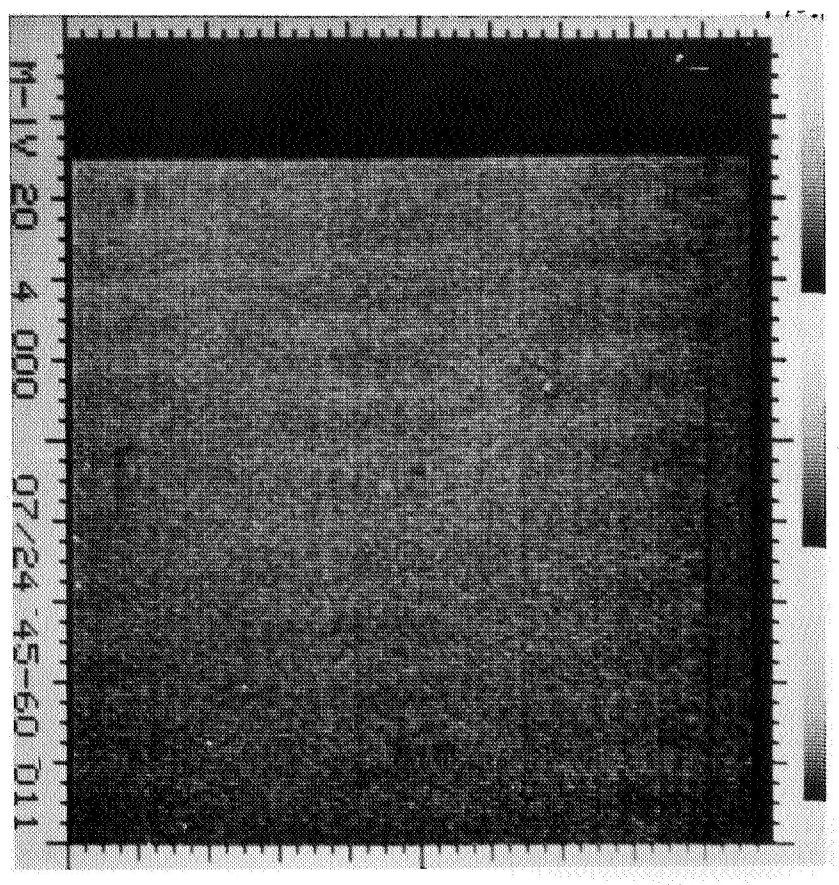


Picture 20

24 - A

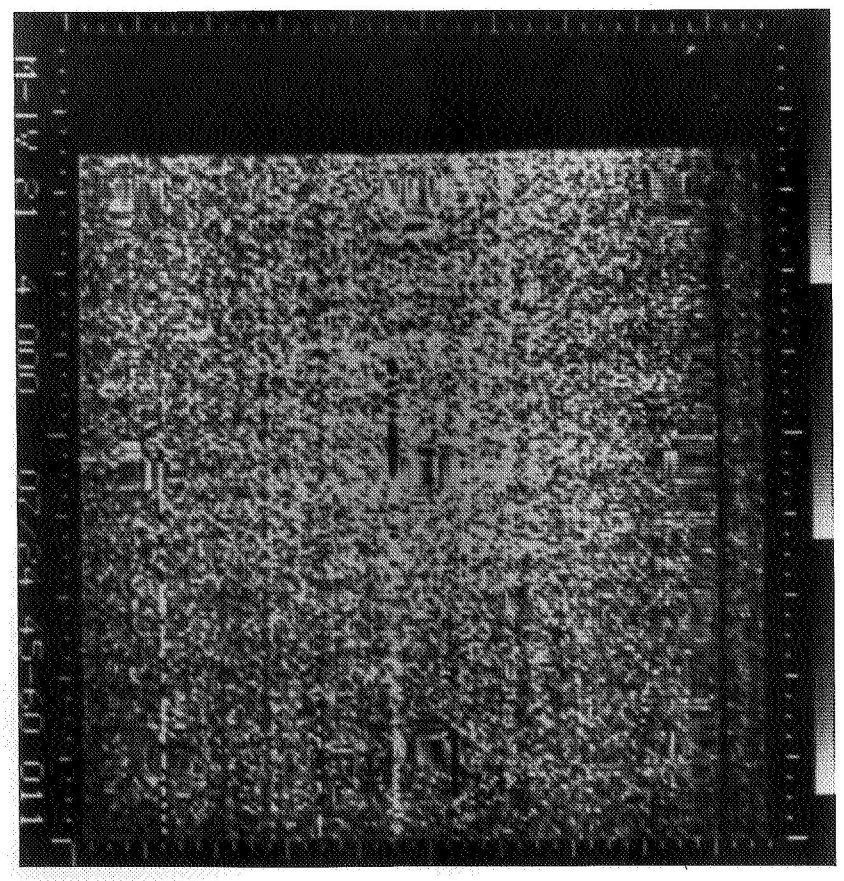


Picture 21

24 - B

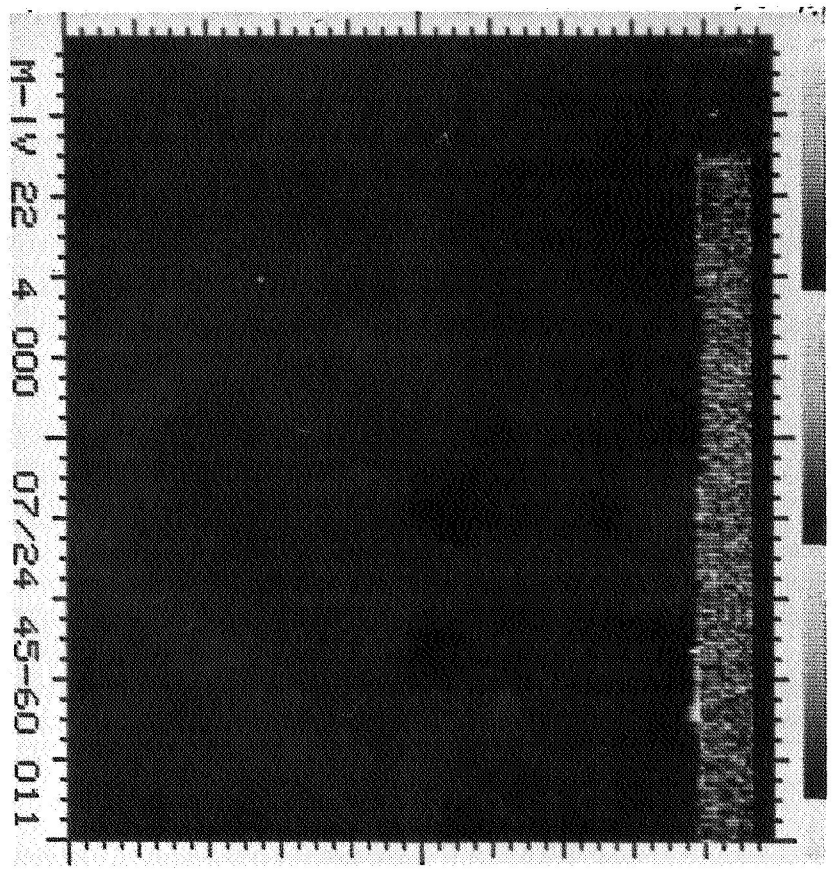


Picture 22

24 - C

## Pictures 17–22

### Filters

Picture 17—orange
Picture 18—green
Picture 19—green
Picture 20—orange
Picture 21—orange
Picture 22—green

### Location of Picture Center

Picture 17—50°S, 231°E
Picture 18—51°S, 237°E
Picture 19—51°S, 252°E
Picture 20—50°S, 260°E
Picture 21—44°S, 279°E
Picture 22—36°S, 291°E

Pictures 17 and 18 fall near Aonius Sinus. Picture 19 includes the sunset terminator, and falls near Aonius Sinus and the light area Thaumasia. Pictures 20, 21, and the small part of 22 that was recorded all fall on the nighttime side of the planet.

### Dimensions, km

| Picture | NE–SW | NW–SE |
|---|---|---|
| 17 | 320 | 225 |
| 18 | 330 | 225 |
| 19 | 380 | 235 |

### Time and Lighting

| Picture | Local time | Solar zenith angle, deg |
|---|---|---|
| 17 | 14:50 | 76 |
| 18 | 15:10 | 80 |
| 19 | 16:00 | 88 |

### Brightness Ranges

| Picture | Min | Max |
|---|---|---|
| 17 | 68 | 99 |
| 18 | 31 | 58 |
| 19 | 5 | 28 |

### Comments

These pictures show very little surface detail, for the reasons previously mentioned. A few craters and one or two lineations are faintly visible in Pictures 17 and 18.

## B. Summary Comments on *Mariner IV* Pictures

*Mariner IV* photos unquestionably record craters and linear markings. Other features possibly shown are subject to highly speculative interpretations. This is not surprising. Photos of Earth taken under similar conditions of slant distance (11,900 to 16,900 km), lighting (11 a.m. to evening), recording (200 scan line and 240,000 data bits), and transmission distance (215 to 240 million km) would probably yield even less certain interpretations owing to atmospheric complications and the more varied and detailed surface patterns. Regional comparisons across the Martian surface are hampered by these same considerations and are feasible only on overlapping photo pairs.

### 1. Craters

Without doubt the most significant fact revealed by *Mariner IV* pictures is that numerous craters exist on the surface of Mars. Even a casual inspection reveals more than a hundred of these structures in the set of pictures. It is not difficult to find twice or three times this number, and a careful search has yielded a total of over 600 craters and possible craters on frames 3 through 16.

The three-fold range in number of craters recognized per photo pair (Table II-1), 45 on Pictures 15–16 to 132 on 9–10, is probably more a function of illumination and photographic rendition than a representation of true variations on the Martian surface. Crater counts have not been attempted on Pictures 1 and 2 or beyond 16, although some, Picture 2 for example, display features suggesting that craters also exist on these other parts of the Martian surface.

It seems unlikely that *Mariner IV* recorded the largest crater on Mars, and the degree of resolution, 3 km, precluded detection of craters of smaller diameter. The largest crater confidently identified is 180 km across. Features displayed on Picture 13 suggest the possibility of a crater as large as 350 km. Craters smaller than 4 km in diameter are extremely difficult to recognize, and only 2 at 3 km diameter have been counted. However, within the 20–180 km range the size distribution of Martian craters is essentially the same as for lunar craters.

Crater shapes are predominantly circular, making allowances for distortion arising from obliquity of the photographs. However, 38 craters, just under 6% of the total, display definite polygonal outline, and a good many more show some hint of partial polygonalization. Polygonal craters are common on the moon. Polygonal outlines on Mars occur most abundantly in craters 15 to 45 km in diameter. On some photos it appears that the polygonal crater walls are conformable (parallel) with linear markings visible on the photos which presumably demarcate fracture systems in the Martian crust. The polygonal form may be developed by slumping on the crater walls controlled by pre-existing sets of fractures.

A number of craters, particularly the largest ones, have irregular circular outlines, and at the base of their inner slopes are features resembling slump blocks. It appears that on Mars slumping may have been an important process of crater modification, just as on the moon. It has enlarged and modified the shapes of these craters and created irregularities on their inner slopes and floors.

Central peaks are identified in 39 or slightly over 6% of the Martian craters. Little can be said about these peaks other than to mention their strong similarity to lunar central peaks. One or two broad domes have also been observed within Martian craters. Craters displaying

**Table II-1. Summary compilation of Martian crater data**

| Pictures | Total number | Central peaks | Polygonal outline | Smallest dia., km | Largest dia., km | Well preserved | Intermediate preservation | Poorly preserved |
|---|---|---|---|---|---|---|---|---|
| 3, 4 | 88 | 1 | 0 | 6 | 80 | 5 | 37 | 46 |
| 5, 6 | 92 | 6 | 2 | 5 | 64 | 9 | 40 | 43 |
| 7, 8 | 115 | 7 | 10 | 4 | 180 | 18 | 45 | 52 |
| 9, 10 | 132 | 11 | 10 | 4 | 123 | 19 | 64 | 49 |
| 11, 12 | 97 | 8 | 9 | 3 | 175 | 20 | 42 | 35 |
| 13, 14 | 67 | 4 | 4 | 5 | 350(?) | 12 | 19 | 36 |
| 15, 16 | 45 | 2 | 3 | 7 | 114 | 3 | 22 | 20 |
| | 636 | 39 | 38 | Smallest 3 km | Largest 350(?) km | 86 | 269 | 281 |

central peaks range from 7 to 68 km in diameter, with diameters of 15 to 20 km the most favored.

Central peaks and polygonal form are most commonly seen in craters with a relatively good degree of preservation, although only a modest number of craters display both central peaks and polygonal outline. The association of both characteristics with relatively well preserved craters suggests that central peaks and polygonal outlines are perhaps more common than indicated above and that perhaps 10% rather than 6% of the Martian craters have these characteristics.

Some of the larger craters show a peripheral belt of irregularly rough surface topography suggestive of rubble sheets or tongues blown out of the crater. Clustering of craters, particularly smaller ones, is recognizable in some instances, but it follows no consistent pattern. Linear strings of craters have not been seen. No consistent albedo differences between the floors of craters and the surrounding terrain have been noted. Some crater floors are lighter and some darker than the average albedo.

If Picture pair 9–10 is representative of the average Martian terrain, then the planet should display some 145,000 craters of greater than 4-km diameter over its entire surface. If an average of the craters found on Pictures 5–6, 7–8, 9–10, 11–12 is used, the planetary total falls to about 100,000. These represent only features well enough preserved to be recorded on *Mariner IV*-type photos. The true total number of Martian craters of all sizes must be much larger. As shown in Appendix J (Fig. J-3), the crater density on Pictures 7–12, normalized to unit area, falls only a little below the average for the heavily cratered lunar uplands.

Martian craters are clearly of many different ages, as shown by intersections, superimpositions, and degree of preservation. An arbitrary (subjective) classification of possible craters as to degree of preservation yields 86 well preserved, 269 intermediate, and 281 poorly preserved out of the total 636 craters counted. These numbers are undoubtedly biased in the poorly preserved direction by the photographic rendition within unfavorably lighted areas. The percentage of well preserved craters is much lower on Picture pair 3–4 than on 9–10.

A precise numerical comparison of crater densities on the moon and on Mars is rendered difficult or impossible by the radically different appearance of the lunar and Martian surfaces. Lunar craters appear relatively sharp and fresh, whereas Martian craters appear smooth and subdued. While some of this difference may be due to optical scattering from the Martian atmosphere, such effects are believed to be minor compared to processes which actually modify Martian topographic relief.

In spite of the difficulty of recognition, it is clear that the Martian surface shows vestiges of numerous craters, many of large diameter (20–50 km), but it shows relatively few sharp, fresh-appearing craters of any size. This relationship suggests the work of surface modifying processes, relatively more effective on Mars than on the moon, but relatively ineffective as compared with processes acting on earth. It seems likely that Martian surface material, to a depth of at least tens to hundreds of meters, is an impact breccia rich in fine grains because of the repeated disruptive effects of meteoroidal impacts. It is probably loose and incoherent because of the absence of any effective cementing action. The presence of a significant atmosphere, in distinction to the moon, means that the grains would be coated with adsorbed gas and other contaminants, and would have little tendency to stick together or "clod." Grains near the lunar surface exhibit a distinct tendency to cohere, probably because they exist in vacuum under the intense solar radiation and particle bombardment.

Granting a loose surface rubble and working within the limits of the present Martian surface environment of extreme dryness, cold temperatures, large temperature changes, and thin atmosphere, an analysis of possible erosive and depositional processes that might modify Martian craters leads to the following conclusions*: The two principal processes of crater modification likely to be more effective on Mars than on the moon are eolian deposition and thermal creep. If the yellow clouds of Mars are truly dust, then a mantle of dust might be expected to soften Martian topographic features, and wind-driven sand might help fill craters. Creep of loose rubble down slopes because of thermal fluctuations is known to occur on earth and could be perhaps something more than 20 times as effective on Mars than on the moon because of daily, compared to monthly, temperature changes. Insofar as Mars might be seismically more active than the moon or subject to a greater frequency of meteoroidal impacts, vibrations in its crust would aid downhill creep more effectively than on the moon.

Nothing shown on the *Mariner* photos unequivocally indicates the origin of the Martian craters. Most of the arguments advanced in support of an impact origin for lunar craters apply equally to Mars, and this is the working hypothesis favored herein.

*See Appendix I for a more complete development.

### 2. Lineations

Many linear markings are discernible on the Martian surface as represented by the *Mariner IV* photos. Some of these are straight over distances as great as 200–300 km. Others are gently curving and less sharply defined. Most lineations recognized have lengths approaching at least 100 km and widths of 3 to 5 km. In many instances they appear as dark streaks on the photos or as parallel light and dark bands. No consistent evidence of their elevation relative to the surrounding terrain or of differences in elevation on opposite sides of the lineations has been obtained. Some, expressed as parallel light and dark bands, look like linear depressions and others like ridges.

In general, the most consistent trends identified are northwestly and northeastly with divergences up to 20° on either side of these directions. We do not identify as many individual lineations as Binder (Ref. 1) but agree as to predominating trends.

In some instances the lineations are parallel to, if not coincident with, features earlier identified by optical observation as "canals." However, there are many instances of canals earlier seen and plotted for which no evidence is visible on the *Mariner IV* photographs. Location of the areas photographed by *Mariner IV*, and of the canals as earlier plotted, is uncertain enough so that exact coincidence of canals and individual lineations would be largely accidental, although one striking example has been observed on Picture 6.

The lineations look like fracture zones (tectonic features) in the Martian crust. They may represent a planet-wide system related in some way to deformation of the entire planet. Insofar as this is a true interpretation, it suggests that the canals are also of tectonic origin. Why many of the lineations appear as dark streaks is a question not resolved by the photographs. The possibility that dark volcanic material has been extruded along them or that the discoloration is in some way related to exhalations of primordial gases must be recognized for what it is, pure speculation.

### 3. Light and Dark Areas

The flight path of *Mariner IV* passed over the major bright areas Phlegra, Mesogaea, Zephyria, Atlantis, and Phaethontis and the prominent dark areas Mare Sirenum and Mare Cimmerium. The last few pictures were taken over the dark area Aonius Sinus, but the lighting was too low to give useful surface data. The differences displayed between picture pairs wholly within a light or a dark area are as great as, if not greater than, differences seen on pictures of dark compared to light areas. To date, no difference in crater density, topographic roughness, or other features seen on the pictures can consistently be related to dark as compared to light areas. Crossings made of the boundaries between light and dark areas suggest that these zones must be gradational rather than sharp, well-defined contacts.

Definite albedo variations on the Martian surface are recorded by the photographs. Dark areas of a few hundred to a few thousand km$^2$ and of highly irregular shape and arrangement are seen on some photographs. In a few instances, they also appear to be areas of unusually rough topography, but this is not a consistent relationship. Areas of unusually high albedo may represent deposits of frost.

### 4. Features Looked For but Not Recognized

Features postulated for the Martian surface by earlier speculations have been looked for but not recognized. Other workers with a more finely tuned sensitivity for particular features may be able to see them on the *Mariner IV* photographs.

Specifically, deposits of eolian sand in the form of sheets, dune fields or accumulations against the rims or inside the walls of craters have been searched for unsuccessfully. Considering the nature of the photographs and the unknown chemical and mineralogical state of materials on the Martian surface, such deposits might easily escape detection. The only tectonic features so far identified on the photographs are the lineations. Mountain ranges, fault blocks, and other evidences of orogenic deformation may well exist, but none has positively been identified. Granting an impact origin for the craters shown on the photos, we find no incontrovertible evidence for volcanism in the form of volcanic cones, chains, flows or other recognizable features or deposits. The photographs, on the other hand, certainly do not rule out the possibility of volcanism on Mars.

PRECEDING PAGE BLANK NOT FILMED.

# III. Intensity and Color Calibration of Flight Photographs

The intensity at each of the 200 × 200 elements of the TV picture was converted by the camera system into digital form for storage on magnetic tape and later transmission to earth. Each such intensity was represented by an integer in the range 0–63, 0 representing the brightest intensity and 63 the darkest. This digital number (DN) was linearly related to the output voltage of the video amplifier, but only roughly linearly related to the exposure level (intensity × time) of the picture element. Many factors entered into the problem of relating the DN at a given point of a given picture to the true surface brightness at the corresponding point on Mars. Some of these factors will be described in this section so as to provide a background for the later discussion of the actual procedures used and the results obtained.

The assignment of six binary bits per picture element was made at a very early stage in the design of the camera system, in the expectation that Mars would exhibit a rather low tonal contrast, in distinction to the case of the moon, for which five or even four bits would probably be adequate to record the significant detail. In spite of this seemingly conservative assignment, the resulting pictures were of such extraordinarily low contrast as to strain the ability of even a 64-level system to record the subtle shadings, and considerable contrast enhancement is necessary if the surface details are to be made visible to the eye. A certain amount of enhancement was incorporated into the photographs prior to their release in preliminary form on July 29, 1965. Direct enhancement of the digital information was accomplished simply by expanding the small range within which the majority of the DN's were distributed into a wider range. Thus if most of the DN's of a picture were in the range $A < DN < B$, the transformation $DN' = K(DN\text{-}A)$, where $K$ is the largest integer in $64/(B\text{-}A)$, would provide a new set of integral DN's which would more nearly span the 64-level range accepted by the photoconversion equipment.

Contrast enhancement by the above method is limited principally by the gross shading effects across the field of view due, for example, to variations in tube sensitivity and vignetting effects in the optical system. (Figure III-1 shows how the DN values vary across the picture for a number of flat-field* calibration pictures.) This limitation can be partially removed by the superposition in the data of empirically determined "smoothing functions" which

*That is, uniformly illuminated.

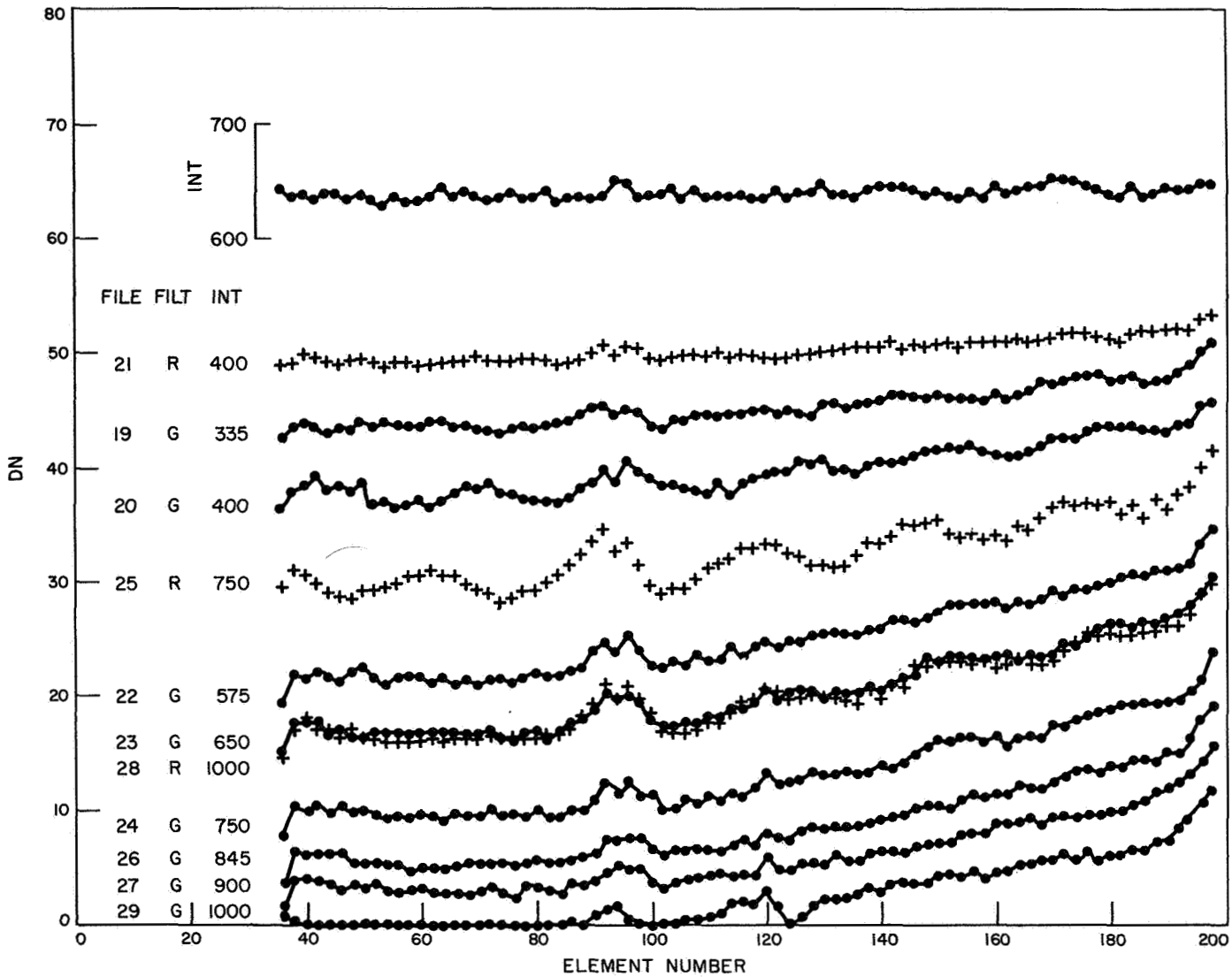


**Fig. III-1. Plot of 2 × 2 averages of DN's for lines 60 and 61 of flat-field calibration pictures (Tape K-67)**

**The averaging was done to minimize the effects of harmonic noise present in the pictures. At the top is plotted the corresponding average of lines 60 and 61 of calibration picture 23 after calibration.**

preserve local variations but remove the gross shading effects. John Morecroft of JPL has produced some remarkable improvements in the pictures by this method. However, photographs enhanced in this way cannot be used to compare intensities quantitatively from point to point within a given picture or from picture to picture. This capability is of course especially important in the study of color variations in overlapping parts of adjacent pictures.

Also evident in the enhanced pictures are a number of blemishes due to local variations in vidicon sensitivity, shadows due to dust particles on the tube face, etc. Some of these are obvious on the flight photographs, and others are visible on the flat-field calibration pictures (Fig. III-2). Some of these blemishes have a circular shape and could confuse the interpretation of strongly enhanced pictures. One of the objectives of the calibration procedures is to remove such blemishes in order to improve the appearance of the pictures, reduce the possibility of confusion in interpretation, and render the picture intensities photometrically more precise.

Before choosing a particular calibration procedure it is important to determine what degree of precision is needed. If the DN fluctuations from point to point are due in significant measure to intrinsic, incoherent noise in the system, then DN corrections finer than 1 unit would seem inappropriate. On the other hand, if little

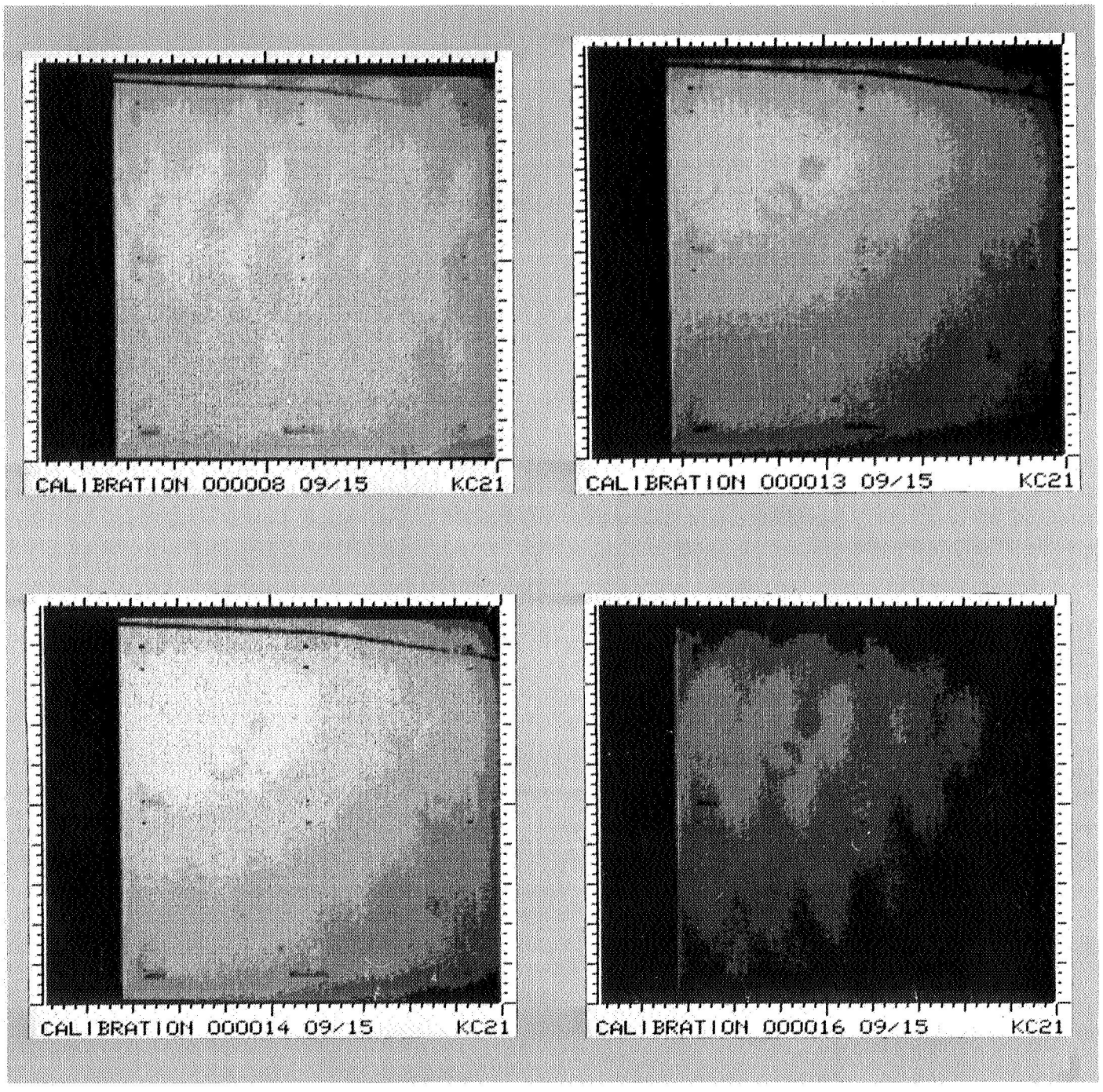


**Fig. III-2. Sample flat-field calibration pictures**

These are shown in a form which enhances the visibility of the DN fluctuations by reducing the number of gray levels from 64 to 16. The pictures shown are: Top (left), file 8; top (right), file 13; bottom (left), file 14; bottom (right), file 16. (All are from calibration tape K-67.)

or no such noise is present, calibration corrections limited in fineness to $\pm 1$ unit DN would add to the "quantization noise" already unavoidably present and might noticeably further degrade the picture quality.

To investigate this problem, DN contour maps of selected areas of the flight pictures were drawn. Several cases were found in which successive 1-unit contours were quite smooth and well separated, which suggests that (1) the vidicon tube is quite uniform in sensitivity from point to point, (2) the operation of the amplifier and the analog-to-digital conversion system of the camera is quite reliable in separating adjacent DN levels, and (3) the surface of Mars may be quite smooth in some areas. It even appeared that the system might have been capable of discriminating intensity fluctuations somewhat finer than the 64 levels actually used. Because of the importance of this rather unexpected result both for the interpretation of the present pictures and for planning future flight experiments, it was decided that the various relevant factors should be studied in greater detail. Therefore, considerable care was used to determine the true degree of uniformity and repeatability of the vidicon tube and the digitizing circuitry.

Further evidence of the reproducibility of the camera system was brought out by plotting the DN values (averaged over $2 \times 2$ picture element squares) vs element number, along Lines 60 and 61 for all flat-field calibration pictures taken under conditions of minimum amplifier gain (00). These curves, plotted in Fig. III-1, show a remarkable consistency in their detailed variation from point to point. One blemish is clearly present near Element 94, and another possible one at Element 120. These vary in magnitude with exposure level and may be due to different effects.

One source of noise in both the calibration and flight pictures was sinusoidal or harmonic noise due to electrical pickup in the amplification circuits. This noise, which appears as "waves" or "ripples," was sometimes approximately uniform in amplitude and phase throughout a given picture, and attained an amplitude of almost 1 unit DN in some pictures. The principal components appeared to have wavelengths along the scan line direction of 17.7, 8.8, and 4.4 elements, and about 80 elements in the perpendicular direction in the flight pictures (e.g., Pictures 12 and 20). In the calibration pictures the major pattern appeared as crossed plane-waves of wavelengths 27.2 and 29.1 elements along the scan line and 90 elements in the perpendicular direction (See Fig. III-2 and the File-25 curve in Fig. III-1). This harmonic noise entered through the amplifier system and therefore was presumably linear in its effects upon the DN's.

## A. Outline of Flight Picture Calibration Procedure*

The principal steps in the calibration procedure finally adopted will now be outlined. These steps are given in an idealized chronological order which approximates the actual order. In fact, two or more steps were sometimes in progress at the same time, or a given step might have been carried out only after a series of trials.

### 1. Selection of Calibration Pictures

A sample of 27 flat-field calibration pictures was chosen to establish the point-to-point sensitivity of the vidicon tube as a function of exposure level and filter combination. This sample comprised all those taken with amplifier gain in the lowest (00) and next lowest (10) states. The nominal surface brightness $I$ (in ft-lamberts of 3000°K color temperature light), filter, amplifier gain state, and shutter speed $T$ (msec) are given in Table III-1. Information found from this sample should be applicable to flight pictures 1–19, inclusive. Pictures 20, 21, and 22 were treated separately. As a first step, the integer DN values were converted to floating point form for further calculation.

### 2. Determination of Standard Calibration Curve

A "standard" calibration curve was obtained by plotting the average DN of a given picture vs the nominal exposure $E = IT$. (Fiducial marks and dark borders were of course omitted from the average.) Each gain state and filter combination gave a separate curve. From these curves, shown in Fig. III-3, it was deduced that the ratio of amplifier gains in the two states was 3.1 and that the response of the system through a red filter was equivalent to that through a green filter having about 0.68 as great an exposure, for these factors were found to bring all of the curves into agreement with a single curve. This curve (found by visually fitting to the combined data and displacing the resulting curve slightly so as to span all DN values $\geqq 0$) was adopted as a zero-order approximation to the response of the system. In the subsequent analysis, the (relatively small) departures from this standard curve were evaluated as a function of position, filter, and exposure level. The values read from this curve for integral DN values, adjusted to give smooth first differences, are tabulated in Table III-2. The fractional

*The able assistance of James K. Lo in carrying out the necessary computer processing of the data is gratefully acknowledged.

**Table III-1. Calibration picture exposure data[a]**

| File No. | Filter | Intensity $I$, ft-lambert | Amplifier gain state | Shutter $T$, msec |
|---|---|---|---|---|
| 5 | 1 | 0 | 11 | 201 |
| 6 | 1 | 13.5 | 11 | 201 |
| 7 | 1 | 26 | 11 | 201 |
| 8 | 0 | 45 | 11 | 201 |
| 9 | 1 | 45 | 11 | 201 |
| 10 | 1 | 60 | 11 | 201 |
| 11 | 1 | 87 | 11 | 201 |
| 12 | 1 | 87 | 01 | 201 |
| 13 | 0 | 110 | 01 | 201 |
| 14 | 1 | 110 | 01 | 201 |
| 15 | 1 | 196 | 10 | 201 |
| 16 | 1 | 180 | 10 | 201 |
| 17 | 1 | 204 | 10 | 201 |
| 18 | 0 | 204 | 10 | 201 |
| 19 | 1 | 335 | 00 | 201 |
| 20 | 1 | 400 | 00 | 201 |
| 21 | 0 | 400 | 00 | 201 |
| 22 | 1 | 575 | 00 | 201 |
| 23 | 1 | 650 | 00 | 201 |
| 24 | 1 | 750 | 00 | 201 |
| 25 | 0 | 750 | 00 | 201 |
| 26 | 1 | 845 | 00 | 201 |
| 27 | 1 | 900 | 00 | 201 |
| 28 | 0 | 1000 | 00 | 201 |
| 29 | 1 | 1000 | 00 | 201 |
| 30 | 0 | 900 | 00 | 132 |
| 31 | 1 | 1000 | 00 | 84 |
| 32 | 0 | 1000 | 00 | 84 |
| 33 | 1 | 900 | 00 | 84 |
| 34 | 1 | 845 | 00 | 84 |
| 35 | 1 | 750 | 00 | 84 |
| 36 | 1 | 650 | 00 | 84 |
| 37 | 0 | 650 | 10 | 84 |
| 38 | 1 | 650 | 10 | 84 |
| 39 | 1 | 575 | 10 | 84 |
| 40 | 1 | 400 | 10 | 84 |
| 41 | 1 | 335 | 10 | 84 |
| 42 | 0 | 335 | 01 | 84 |
| 43 | 1 | 335 | 01 | 84 |
| 44 | 1 | 204 | 01 | 84 |
| 45 | — | — | — | — |
| 46 | 1 | 110 | 01 | 84 |
| 47 | 0 | 110 | 11 | 84 |
| 48 | 1 | 110 | 11 | 148 |
| 49 | 0 | 110 | 01 | 201 |
| 50 | 1 | 110 | 01 | 201 |

Filter: 1 = green, 0 = red.

Intensity: ft-lamberts at ~3000°K color temperature.

Gain: 00 = minimum, 10 ≈ 3.1 × min, 01 ≈ 11 × min, 11 ≈ 27 × min.

Shutter: exposure times in msec.

[a]From Calibration Data Tape K-67.

sensitivity $\Delta I/I$, where $I$ is the intensity and $\Delta I$ is the intensity change corresponding to 1 unit change in DN,

**Table III-2. Tabulation of $I$ vs DN**

| DN | $I$ | $\Delta I/I$ | DN | $I$ | $\Delta I/I$ | DN | $I$ | $\Delta I/I$ |
|---|---|---|---|---|---|---|---|---|
| 0 | 1000 | | 22 | 611 | | 44 | 344 | |
| | | 0.027 | | | 0.0199 | | | 0.0386 |
| 1 | 973 | | 23 | 599 | | 45 | 331 | |
| | | 0.026 | | | 0.0203 | | | 0.0401 |
| 2 | 948 | | 24 | 587 | | 46 | 318 | |
| | | 0.026 | | | 0.0207 | | | 0.0417 |
| 3 | 924 | | 25 | 575 | | 47 | 305 | |
| | | 0.025 | | | 0.0210 | | | 0.047 |
| 4 | 901 | | 26 | 563 | | 48 | 291 | |
| | | 0.025 | | | 0.0215 | | | 0.049 |
| 5 | 879 | | 27 | 551 | | 49 | 277 | |
| | | 0.024 | | | 0.0220 | | | 0.052 |
| 6 | 858 | | 28 | 539 | | 50 | 263 | |
| | | 0.0236 | | | 0.0227 | | | 0.055 |
| 7 | 838 | | 29 | 527 | | 51 | 249 | |
| | | 0.023 | | | 0.0231 | | | 0.062 |
| 8 | 819 | | 30 | 515 | | 52 | 234 | |
| | | 0.023 | | | 0.0236 | | | 0.066 |
| 9 | 800 | | 31 | 503 | | 53 | 219 | |
| | | 0.0229 | | | 0.0241 | | | 0.071 |
| 10 | 782 | | 32 | 491 | | 54 | 204 | |
| | | 0.022 | | | 0.0247 | | | 0.082 |
| 11 | 765 | | 33 | 479 | | 55 | 188 | |
| | | 0.0212 | | | 0.0255 | | | 0.095 |
| 12 | 749 | | 34 | 467 | | 56 | 171 | |
| | | 0.0216 | | | 0.0261 | | | 0.111 |
| 13 | 733 | | 35 | 455 | | 57 | 153 | |
| | | 0.0207 | | | 0.0267 | | | 0.133 |
| 14 | 718 | | 36 | 443 | | 58 | 134 | |
| | | 0.0211 | | | 0.0274 | | | 0.161 |
| 15 | 703 | | 37 | 431 | | 59 | 114 | |
| | | 0.0201 | | | 0.0282 | | | 0.203 |
| 16 | 689 | | 38 | 419 | | 60 | 93 | |
| | | 0.0206 | | | 0.0291 | | | 0.282 |
| 17 | 675 | | 39 | 407 | | 61 | 70.0 | |
| | | 0.0194 | | | 0.0299 | | | 0.50 |
| 18 | 662 | | 40 | 395 | | 62 | 42.5 | |
| | | 0.0197 | | | 0.0308 | | | |
| 19 | 649 | | 41 | 383 | | 63 | 0 | |
| | | 0.0203 | | | 0.0345 | | | |
| 20 | 635 | | 42 | 370 | | | | |
| | | 0.0207 | | | 0.0358 | | | |
| 21 | 623 | | 43 | 357 | | | | |
| | | 0.0194 | | | 0.0372 | | | |

is plotted in Fig. III-4 for the data of Table III-2. This curve serves as an approximate guide to the minimum detectable intensity change for a given DN.

### 3. Removal of Harmonic "Noise"

The amplitude and phase of the harmonic noise in each calibration picture were evaluated and the resulting wave subtracted out. This resulted in nonintegral DN values. This step in the treatment of the calibration pictures was perhaps unnecessary because of the apparent randomness of phase of the harmonic noise from picture to picture, but a preliminary analysis showed that the statistical averaging of the noise in this particular sample would not adequately reduce the amplitude of the 27- or 29-element noise. The 5.8-element noise appeared to be adequately averaged out, and was therefore not removed from individual pictures.

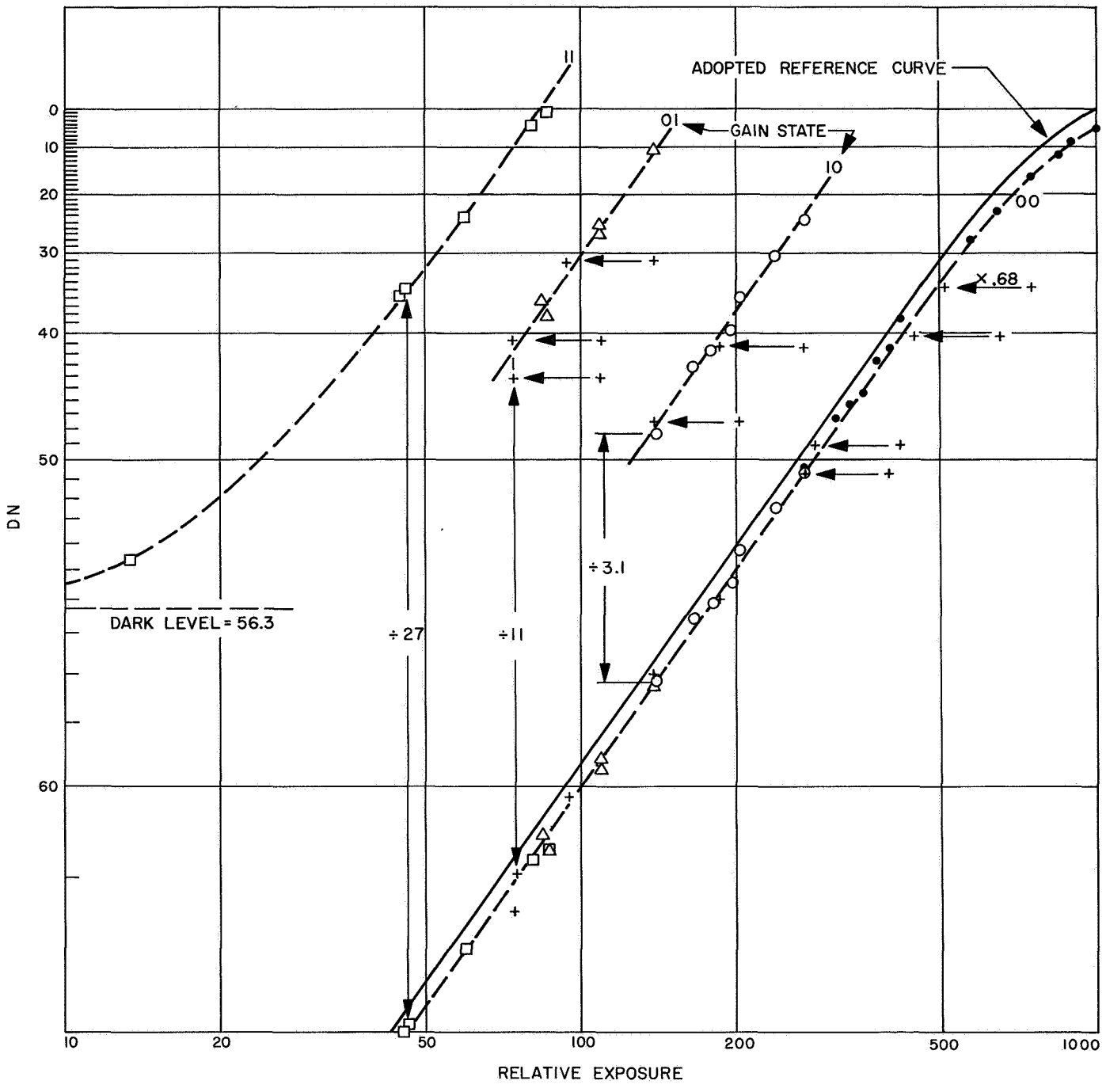


**Fig. III-3. Plot of average DN vs light intensity for 45 flat-field calibration pictures**

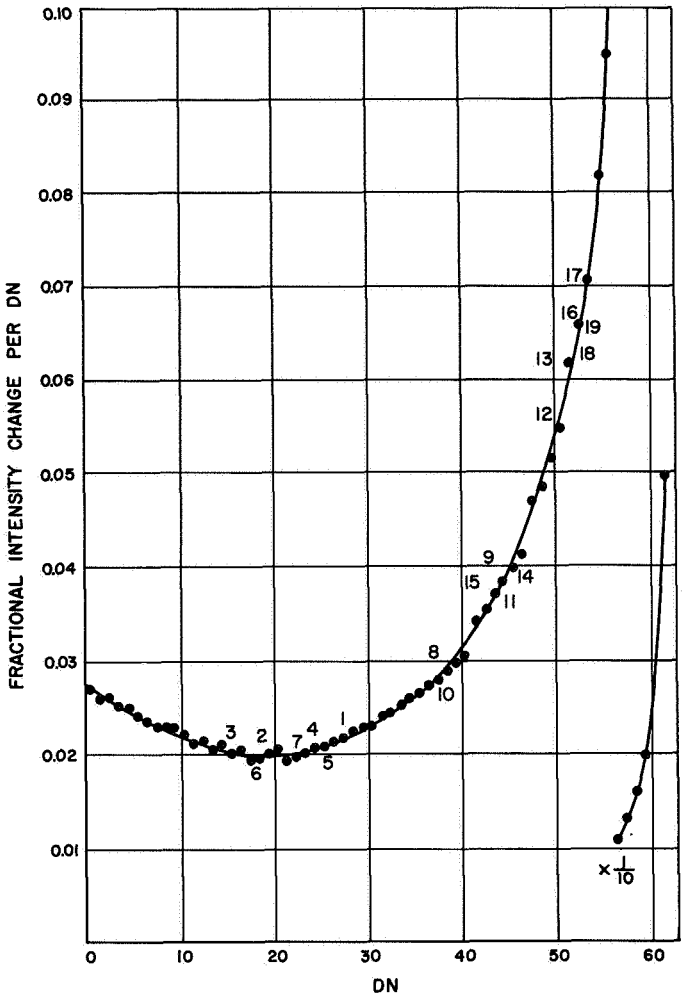


**Fig. III-4. Plot of fractional sensitivity $\Delta I/I$ per unit DN, as a function of DN; approximate locations of flight pictures on this curve are also indicated**

### 4. Apparent Exposure APP

The "apparent exposure" APP was evaluated for each picture element of each calibration picture by linear interpolation in Table III-2. The effective DN, DNE, for a picture taken in the (10) gain state was found from the formula $DNE = 63. - (63. - DN)/3.1$.

### 5. Ratio of Apparent to True Exposure

The ratio of this apparent exposure to the "true exposure" TRU was evaluated for each picture element of each calibration picture. The "true exposure" was found from the formula $TRU = ITF/201000$, where $I$ and $T$ are tabulated in Table III-1, and $F$ is a filter factor equal to unity for a green filter and approximately 0.68 for a red filter. The denominator serves to normalize TRU to unity for the brightest green picture. The subsequent analysis included a test for possible variation of $F$ with position and intensity, such as would be expected if, for example, the spectral responsivity of the vidicon tube were to vary from point to point. (A variation in $F$ from 0.65 to 0.72 across the picture area was found, as will be described below.)

### 6. Fitting of Observed Ratio vs True Intensity by Polynomials; Variable Filter Factor

We now focus our attention upon a given picture element and consider the 27 pairs of values of TRU and $R = APP/TRU$. Regarding these as rectangular coordinates $x_i = TRU_i$ and $y_i(x_i) = R_i, i = 1, 2, \cdots, 27$, we next investigate the functional dependence of $y$ upon $x$. If the "standard" calibration curve were valid for all points, we should find $y(x) = 1.00$, independent of $x$, for each picture element. If all picture elements had the same intrinsic sensitivity but were subject to a vignetting effect, we should find $y$ still to be independent of $x$ for a given element. Actually, even a rough inspection showed that $y(x)$ would depend upon $x$, so a power series expansion

$$y = C_0 + C_1 + C_2x^2 + \cdots \tag{1}$$

was investigated. Since it was not known *a priori* how many terms of such a series would be needed to adequately represent the data, and it was desired for computational efficiency to keep the number of terms to a minimum, a pilot investigation was carried out on a $32 \times 29$ matrix, each element of which was the average DN of a $6 \times 6$ square of picture elements of the actual picture field. A set of normalized orthogonal polynomials, orthogonal on the set $x_i$, was used to express the dependence $y(x)$. Thus if $P_n(x)$ is the orthogonal polynomial of order $n$, with

$$P_n(x) = \sum_{s=0}^{n} a_{ns}x^s \tag{2}$$

the orthonormality condition is

$$\sum_{i=1}^{27} P_n(x_i)\,P_m(x_i) = \delta_{nm} \tag{3}$$

The coefficients $a_{ns}$ found by solving Eq. (3) are shown in Table III-3 for $n \leq 5$.

**Table III-3. Coefficients $a_{ns}$ of orthogonal polynomials**

| Order $n$ | Degree $s$ | | | | | |
|---|---|---|---|---|---|---|
| | 0 | 1 | 2 | 3 | 4 | 5 |
| 0 | 0.19245 | 0 | 0 | 0 | 0 | 0 |
| 1 | −0.32568 | 0.79522 | 0 | 0 | 0 | 0 |
| 2 | 0.69618 | −3.55106 | 3.35023 | 0 | 0 | 0 |
| 3 | −1.33825 | 10.57390 | −22.74505 | 13.92416 | 0 | 0 |
| 4 | 2.85724 | −30.89345 | 106.61614 | −142.4243 | 64.08020 | 0 |
| 5 | −6.14718 | 82.79888 | −391.67340 | 827.17132 | −794.71194 | 282.59162 |

The coefficients $A_n$ in the expansion

$$y(x) = \sum_{n=0}^{N} A_n P_n(x) \tag{4}$$

were found by the formula

$$A_n = \sum_{i=1}^{27} y_i(x_i)\, P_n(x_i) \tag{5}$$

The utility of this approach is that the coefficients $A_n$ found in this way automatically minimize the mean square deviation $\sigma^2$ of $y(x)$ from the 27 given values $y_i(x_i)$ for a given $N$. By studying the decrease of this variance as a function of $N$, a suitable number of terms can be decided upon. On the basis of the curve shown in Fig. III-5 it was determined that three terms would suffice.

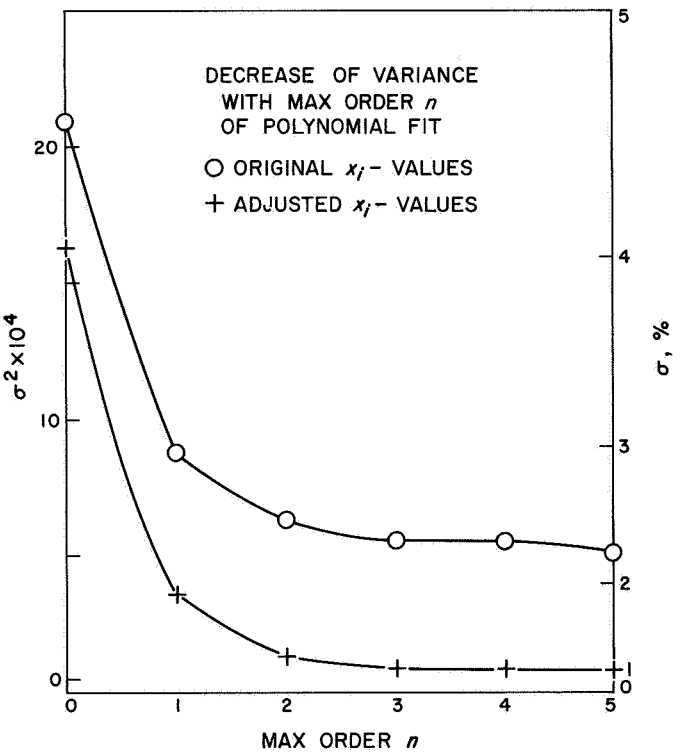


**Fig. III-5. Plots showing the residual errors when polynomials of various orders are fitted to the calibration data**

In the course of this study it was also found that the average $\sigma^2$ for the entire picture area could be reduced by a factor of 3 simply by adjusting the $x$–value–that is, the true illumination intensity–of each of a half dozen or so points by 1 to 4%. Such an adjustment is reasonable in view of the fact that the photometer used to standardize the illumination level could be read only to about 1%, and the neutral density filters used to attenuate the light were measured only to a similar accuracy. The necessary changes $\Delta x_i$ needed to minimize $\sigma^2$ for a three-term polynomial fit are plotted as a function of $x_i$ in Fig. III-6. New orthogonal polynomials corresponding to the new $x_i$'s were calculated and $\sigma^2$ again evaluated as a function of $n$. The resulting variation of $\sigma^2$ with $n$ is shown as the lower curve of Fig. III-5. The final set of $x_i$'s, the correcting $\Delta x_i$, and the values of the resulting orthogonal polynomials are shown in Table III-4.

In the preceding analysis, a red filter factor of 0.68 was used for the purpose of establishing the values $x_i$ of the independent variable, but was evaluated separately for each element of the $32 \times 29$ pilot matrix for red pictures when the coefficients $A_n$ were being evaluated. In the latter case the red filter factor was taken to be

$$F = 0.65 + \frac{L}{4800} + \frac{E}{18000} \tag{6}$$

where $(L, E)$ are the picture line and element numbers of the center of a $6 \times 6$ average matrix point. The basis for this choice of filter factor is shown in Fig. III-7, wherein the average numerical values of this factor for the seven red calibration pictures are presented in matrix form.

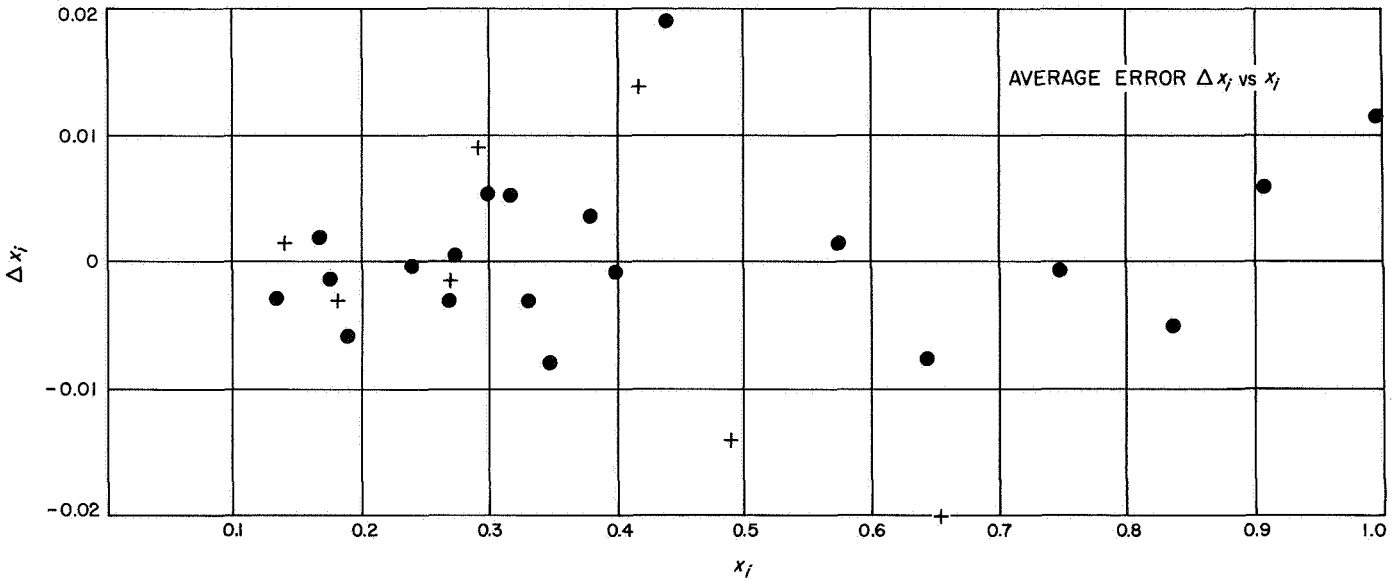


**Fig. III-6. Plot of the intensity corrections needed to improve the fitting of the calibration data by second-degree polynomials**

**Table III-4. Normalized exposures $x_i$ and orthogonal polynomials $P_n(x_i)$**

| $i$ | $x_i$ | $\Delta x_i$ | $P_1(x_i)$ | $P_2(x_i)$ | $P_3(x_i)$ | $P_4(x_i)$ | $P_5(x_i)$ |
|---|---|---|---|---|---|---|---|
| 1 | 0.19036 | −0.00564 | −0.17430 | 0.14161 | −0.05357 | −0.05850 | 0.15433 |
| 2 | 0.17870 | −0.00130 | −0.18358 | 0.16860 | −0.09559 | −0.00615 | 0.10275 |
| 3 | 0.20928 | 0.00528 | −0.15926 | 0.09975 | 0.00610 | −0.12111 | 0.19729 |
| 4R | 0.14034 | 0.00162 | −0.21408 | 0.26381 | −0.26380 | 0.25269 | −0.24788 |
| 5 | 0.33174 | −0.00326 | −0.06188 | −0.11315 | 0.17476 | −0.08170 | −0.07455 |
| 6 | 0.39933 | −0.00067 | −0.00813 | −0.18762 | 0.14388 | 0.08209 | −0.20676 |
| 7R | 0.27064 | −0.00136 | −0.11047 | −0.01948 | 0.13350 | −0.17409 | 0.11697 |
| 8 | 0.57678 | 0.00178 | 0.13299 | −0.23746 | −0.13439 | 0.27055 | 0.11346 |
| 9 | 0.64220 | −0.00780 | 0.18501 | −0.20260 | −0.24032 | 0.16561 | 0.26869 |
| 10 | 0.74938 | −0.00062 | 0.27024 | −0.08352 | −0.32763 | −0.14920 | 0.20884 |
| 11R | 0.49543 | −0.01457 | 0.06829 | −0.24081 | 0.01081 | 0.26198 | −0.11918 |
| 12 | 0.84032 | −0.00468 | 0.34256 | 0.07788 | −0.25158 | −0.37711 | −0.17585 |
| 13 | 0.90642 | 0.00642 | 0.39512 | 0.22997 | −0.07163 | −0.35925 | −0.43327 |
| 14R | 0.65976 | −0.02024 | 0.19897 | −0.18837 | −0.26378 | 0.12280 | 0.29075 |
| 15 | 1.01136 | 0.01136 | 0.47857 | 0.53157 | 0.49515 | 0.37361 | 0.22039 |
| 16R | 0.41594 | 0.01403 | 0.00508 | −0.20124 | 0.12681 | 0.12178 | −0.21479 |
| 17 | 0.43718 | 0.01927 | 0.02197 | −0.21596 | 0.10072 | 0.16871 | −0.20993 |
| 18R | 0.29288 | 0.00870 | −0.09278 | −0.05648 | 0.15741 | −0.15204 | 0.04812 |
| 19 | 0.37972 | 0.00360 | −0.02372 | −0.16917 | 0.15968 | 0.03345 | −0.18398 |
| 20 | 0.34447 | −0.00866 | −0.05175 | −0.12952 | 0.17437 | −0.05289 | −0.10990 |
| 21 | 0.31843 | 0.00500 | −0.07246 | −0.09488 | 0.17209 | −0.10930 | −0.03419 |
| 22 | 0.27128 | −0.00036 | −0.10995 | −0.02061 | 0.13436 | −0.17369 | 0.11510 |
| 23R | 0.18176 | −0.00296 | −0.18114 | 0.16142 | −0.08415 | −0.02099 | 0.11839 |
| 24 | 0.26823 | −0.00341 | −0.11238 | −0.01528 | 0.13025 | −0.17543 | 0.12382 |
| 25 | 0.24013 | −0.00017 | −0.13473 | 0.03665 | 0.08213 | −0.17247 | 0.18713 |
| 26 | 0.16913 | 0.00196 | −0.19119 | 0.19142 | −0.13315 | 0.04538 | 0.04344 |
| 27 | 0.13667 | −0.00333 | −0.21700 | 0.27344 | −0.28242 | 0.28526 | −0.29919 |

Note: (1) The tabulated $x_i$ are the corrected values; the $\Delta x_i$ are the corrections that were applied to the original $x_i$.
(2) $P_0(x_i) = 27^{-1/2} = 0.19245$.
(3) An R in column 1 signifies a red filter picture.

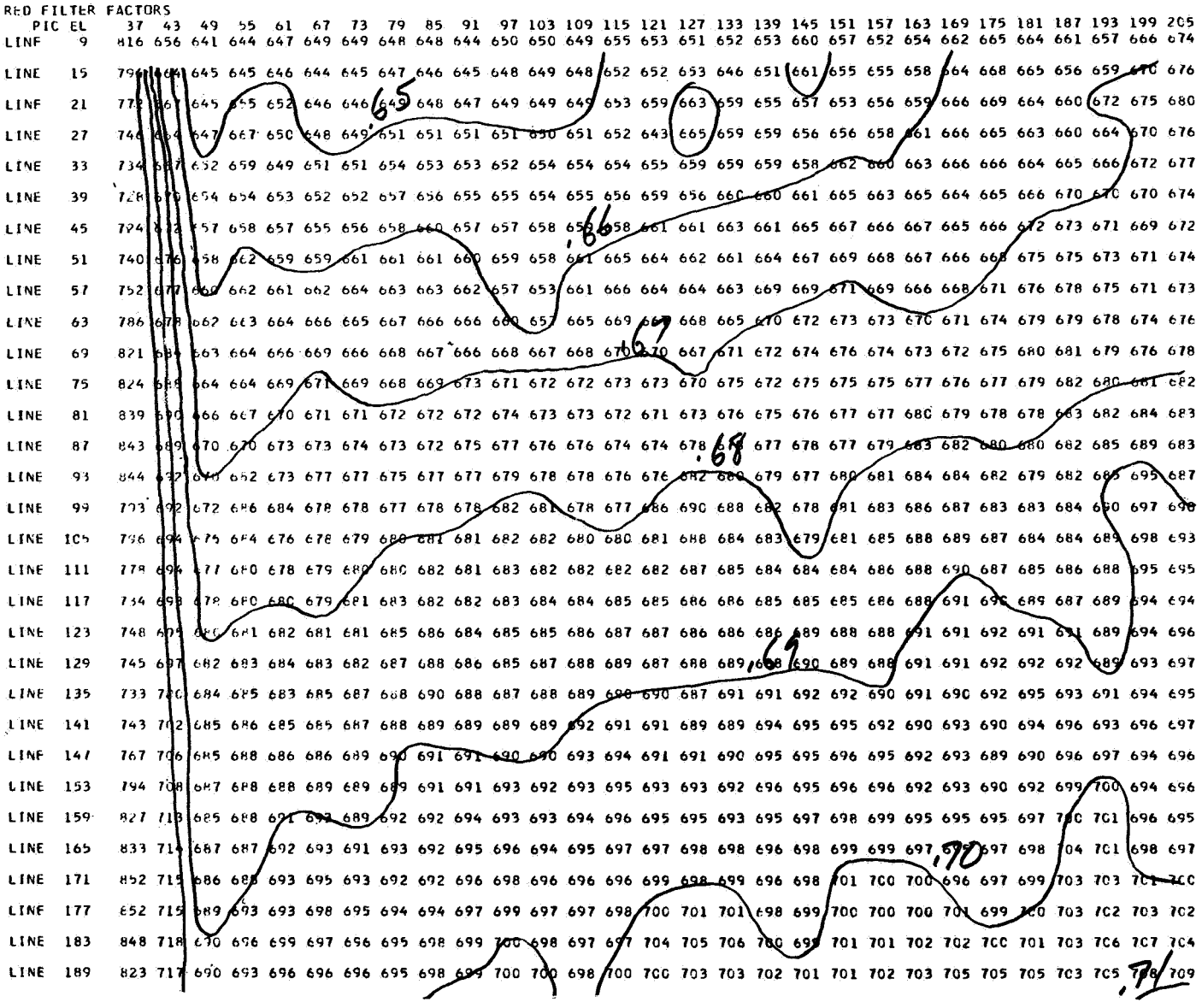


**Fig. III-7. Printout of red filter factor as a function of position**

Of course, it is not certain where this relative variation in green and red sensitivity of the system actually arises. It could be caused by variations in transmission of the filters over the picture area, although this seems unlikely in view of the close tolerances on parallelism of the faces of a filter that were achieved. Alternatively, it might be due to an actual variation in spectral responsivity over the target area. Again, attributing the variation to the red filter rather than the green is a matter of convenience, and an investigation was not made as to whether the actual uniformity of sensitivity was better for the red or the green pictures. The green response was taken as the reference simply because there were more green pictures in the calibration sequence. No tests could be made concerning possible differences between the two individual green filters or the two red filters used in the camera, since this distinction was not made during the calibration tests and the necessary data were not recorded. The internal consistency of the final results achieved suggests that any such differences must have been quite small.

### 7. Polynomial Coefficients for Individual Picture Elements

The coefficients $A_0$, $A_1$, and $A_2$ for each picture element were calculated by Eq. (5) and stored on magnetic tape, and the entire array was also printed in a picture-like form. At this stage it was possible to study the uniformity of sensitivity of the vidicon tube from element to element on the basis of the "smoothness" of the coefficients $A_i$. Typical samples of these printouts (each coefficient is multiplied by 100) are shown in Fig. III-8. All three coefficients show quite smooth variations from place to place, the numerical values being remarkably consistent along the rather clear-cut contour lines. The rms fluctuations of the coefficients were evaluated for samples of 10 to 50 points in various locations, and $\sigma$ values of about 0.2% were normally obtained, approximately consistent with the expected sample standard deviation based upon 27 independent measures, each having a maximum uncertainty of $\pm 0.012$ (Fig. III-3): $27^{-1/2} \times 0.012 \times 3^{-1/2} = 0.0014$. This result seems to indicate not only that the point-to-point "graininess" of the vidicon target surface is very small but also that the response of a given element is accurately reproducible in successive exposures under uniform lighting conditions.

### 8. Conversion from Orthogonal Polynomials to Power Series; Shutter Mark Removal

Preparatory to applying the calibration data to the flight pictures, the matrices $A_0$, $A_1$, and $A_2$ were combined with the coefficients $a_{ns}$ to form the three matrices $C_0$, $C_1$, and $C_2$ of Eq. (1). At this time the shutter mark (a dark streak running across the top of each picture) was eliminated by linearly interpolating across the seven elements spanning the mark in each column. The interpolation was applied to the $A$-matrices before they were converted into the $C$-matrices.

### 9. Check of Results for Sample Calibration Picture

As a test of the correctness of the calibration data, the $C$-matrices were used to correct one of the calibration pictures: that of File 23, a green picture taken under illumination conditions similar to Flight Pictures 2 and 3. Examination of a numerical printout of the corrected intensities showed quite satisfactory uniformity over the entire frame, even at points quite near the edges and the fiducial marks. In fact, about half of the picture elements normally comprising a fiducial mark were corrected up to within 10% or so of the appropriate value of 640 units; these elements had evidently shown enough response to the incident light in each of the 27 calibration pictures to permit a satisfactory evaluation of their reduced sensitivity!

A plot of the corrected intensities along Lines 60 and 61 of this calibration picture is shown as the top curve in Fig. III-1. Only a small vestige of the major blemish at Element Number 94 remains, and a slight upward trend of intensity with position along the line is evident. The latter could be due to small differences among the two green and two red filters used in the camera. The scatter seen in the points to the left of the blemish is consistent with that expected on the basis of a $\pm 0.5$ unit uncertainty in DN, combined with a $\pm 0.5$ unit uncertainty in rounding to a 2-digit integer for printing. A small amount of 27- or 29-element harmonic noise seems to be present, although it was supposedly removed prior to conversion of DN's into intensities. The 5.8-element harmonic noise was not removed and is prominent in the numerical printout. This harmonic reverses in sign from line to line and is easily removed simply by averaging two adjacent lines, as was done in Fig. III-1.

### 10. Shift from Calibration Format to Flight Picture Format; Extrapolation to Picture Edges

The matrices $C_0$, $C_1$, $C_2$ described above were judged satisfactory for application to the flight pictures. However, this application is not quite straightforward, because the picture coordinates (line and element numbers) of a given

physical point of the vidicon target were not the same for the flight pictures as for the calibration pictures. The principal effect was a lateral displacement due to the difference in external magnetic field conditions under which the two sets of pictures were taken. (The vidicon was magnetically shielded sufficiently to reduce the earth's field intensity to less than 100$\gamma$, but this small amount of leakage field was sufficient to deflect the electron beam through about 10 picture elements.)

In addition to a lateral displacement, the picture was also slightly expanded and rotated, perhaps due to small changes in the vidicon grid potentials and in the electron beam deflection voltages.

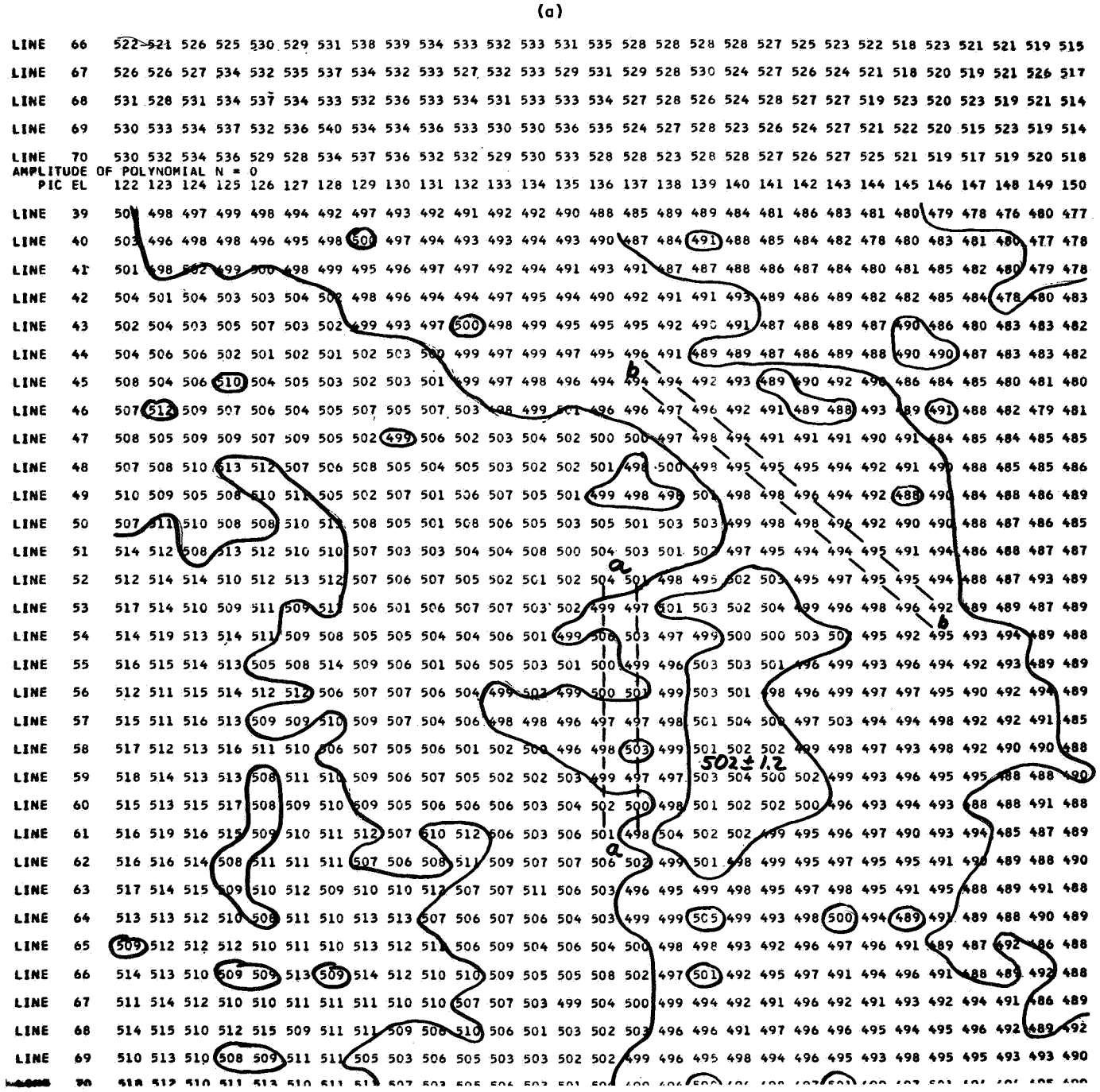


**Fig. III-8. Sample printouts of orthogonal polynomial coefficients $A_0$, $A_1$, $A_2$ (each is multiplied by 100)**

(b)

| | | | | | | | | | | | | | | | | | | | | | | | | | | | | | | | |
|---|---|---|---|---|---|---|---|---|---|---|---|---|---|---|---|---|---|---|---|---|---|---|---|---|---|---|---|---|---|---|---|
| LINE | 66 | 0 | 3 | 0 | 0 | -1 | 0 | 2 | -3 | -1 | -2 | -0 | -0 | -1 | -1 | -1 | -4 | -4 | -1 | -0 | -5 | -3 | -4 | -5 | -1 | -6 | -3 | -5 | -0 | -4 | |
| LINE | 67 | 0 | 3 | 0 | -2 | -2 | -2 | -1 | 1 | 0 | -2 | 1 | -3 | -2 | -1 | -1 | -5 | -7 | -2 | -3 | -3 | -3 | -2 | -5 | -4 | -5 | -4 | -1 | -11 | -2 | |
| LINE | 68 | 1 | 1 | -1 | -2 | -1 | 0 | 0 | -0 | -4 | -1 | -2 | -1 | -1 | -4 | -3 | -2 | -7 | -3 | -3 | -5 | -1 | -6 | -2 | -6 | -4 | -5 | -5 | -5 | -1 | |
| LINE | 69 | -3 | 0 | -0 | -1 | 1 | -0 | -3 | -3 | -1 | -3 | -2 | -0 | -3 | -6 | -5 | -0 | -7 | -3 | -4 | -3 | -2 | -1 | -4 | -3 | -5 | -4 | -6 | -4 | -2 | |
| LINE | 70 | -2 | -5 | -0 | 1 | 1 | 0 | -1 | -3 | -3 | -1 | -2 | -0 | -2 | -5 | -2 | -4 | -2 | -5 | -3 | -6 | -4 | -3 | -6 | -2 | -5 | -4 | -5 | -5 | -5 | |

AMPLITUDE OF POLYNOMIAL N = 1

| PIXEL | 122 | 123 | 124 | 125 | 126 | 127 | 128 | 129 | 130 | 131 | 132 | 133 | 134 | 135 | 136 | 137 | 138 | 139 | 140 | 141 | 142 | 143 | 144 | 145 | 146 | 147 | 148 | 149 | 150 |
|---|---|---|---|---|---|---|---|---|---|---|---|---|---|---|---|---|---|---|---|---|---|---|---|---|---|---|---|---|---|
| LINE 39 | 12 | 9 | 9 | 5 | 5 | 5 | 7 | 5 | 8 | 8 | 5 | 6 | 7 | 8 | 8 | 7 | 2 | 5 | 6 | 5 | 5 | 5 | 7 | 4 | 4 | 4 | 7 | 3 | 3 |
| LINE 40 | 10 | 11 | 7 | 6 | 6 | 8 | 7 | 4 | 5 | 8 | 9 | 4 | 7 | 6 | 6 | 8 | 8 | 4 | 4 | 8 | 7 | 8 | 6 | 3 | 3 | 4 | 5 | 4 | 5 |
| LINE 41 | 7 | 7 | 6 | 7 | 8 | 5 | 8 | 5 | 8 | 6 | 4 | 7 | 6 | 6 | 8 | 9 | 5 | 6 | 5 | 4 | 4 | 9 | 7 | 3 | 1 | 5 | 8 | 7 | 3 |
| LINE 42 | 11 | 8 | 4 | 5 | 6 | 6 | 10 | 7 | 2 | 6 | 4 | 3 | 4 | 4 | 7 | 3 | 5 | 6 | 3 | 2 | 5 | 6 | 7 | 5 | 5 | 4 | 5 | 3 | 3 |
| LINE 43 | 7 | 7 | 5 | 8 | 5 | 8 | 3 | 5 | 4 | 1 | 4 | 2 | 1 | 4 | 6 | 3 | 3 | 4 | 4 | 5 | 5 | 4 | 4 | 1 | 3 | 5 | 2 | 2 | 3 |
| LINE 44 | 6 | 4 | 6 | 6 | 8 | 4 | 3 | 2 | 2 | 5 | 4 | 5 | 6 | 3 | 5 | 3 | 5 | 3 | 5 | 2 | 3 | 3 | 4 | 2 | 3 | 4 | 3 | 1 | 1 |
| LINE 45 | 3 | 7 | 5 | 7 | 9 | 5 | 2 | 4 | 1 | 2 | 4 | 5 | 4 | 6 | 6 | 6 | 3 | 3 | 3 | 6 | 5 | 4 | 3 | 5 | 3 | 4 | 7 | 1 | 1 |
| LINE 46 | 3 | 2 | 5 | 5 | 5 | 4 | 4 | -0 | 1 | 1 | 5 | 5 | 1 | 1 | 4 | 3 | 0 | 4 | 5 | 2 | 4 | 3 | 1 | 3 | 0 | 0 | 0 | 2 | -0 |
| LINE 47 | 4 | 5 | 6 | 7 | 8 | 3 | 2 | 2 | 4 | 2 | 5 | 3 | -0 | 0 | 1 | 3 | 2 | 1 | 3 | 3 | 1 | 3 | 3 | 1 | 5 | 2 | 4 | -1 | -1 |
| LINE 48 | 7 | 3 | 0 | 0 | 3 | 6 | 7 | 0 | 3 | 0 | 0 | 0 | 2 | 1 | -0 | 2 | 2 | 2 | 3 | 1 | -0 | 2 | 3 | 2 | -0 | 0 | 1 | 0 | -1 |
| LINE 49 | 3 | 1 | 2 | 2 | 5 | 4 | 6 | 4 | -0 | 4 | -1 | 0 | 6 | 3 | 2 | 3 | 1 | 4 | 4 | 0 | 0 | 3 | 4 | 0 | 0 | 1 | 0 | -0 | 0 |
| LINE 50 | 4 | 2 | 0 | 2 | 2 | 5 | 1 | 4 | -0 | 0 | 0 | 0 | 3 | 5 | 2 | 3 | 2 | 2 | 3 | 0 | 0 | 1 | 2 | 3 | 2 | 2 | 2 | -0 | 0 |
| LINE 51 | 2 | 0 | 2 | -3 | 2 | 4 | 2 | 0 | 1 | 2 | 2 | 0 | -2 | 5 | -1 | 3 | 0 | 1 | 1 | 1 | 1 | 0 | 0 | 1 | -1 | 1 | 2 | -1 | -0 |
| LINE 52 | 3 | 4 | -1 | 2 | 0 | 1 | 2 | 4 | -2 | -0 | 2 | 3 | 5 | 3 | -1 | -0 | 0 | 4 | -1 | 0 | 1 | -2 | -1 | -1 | -0 | 2 | 0 | -2 | -0 |
| LINE 53 | 3 | 5 | 2 | 0 | 0 | -1 | 3 | 1 | 1 | -2 | 2 | 0 | 0 | 6 | 1 | 2 | -1 | 2 | -1 | -1 | 0 | -0 | -1 | 0 | -0 | -0 | 0 | -0 | -0 |
| LINE 54 | -0 | 1 | 6 | 2 | 1 | -2 | -1 | 0 | -1 | -2 | -1 | -1 | 2 | 1 | 2 | -0 | 3 | -0 | 1 | 1 | -2 | -0 | 1 | -2 | -0 | -3 | -2 | -0 | 0 |
| LINE 55 | 1 | -0 | 3 | 2 | 3 | -1 | -3 | -2 | -0 | 1 | -1 | -1 | 1 | 0 | 1 | 3 | 1 | -1 | -1 | 1 | -1 | -2 | -0 | -1 | -4 | -2 | -0 | 1 | -3 |
| LINE 56 | 0 | 3 | 1 | 1 | -1 | -1 | -0 | -2 | -2 | 0 | 1 | 0 | -2 | 0 | 0 | -1 | -0 | -0 | 0 | -0 | -1 | -4 | -2 | -2 | -1 | -1 | 0 | -4 | -1 |
| LINE 57 | 0 | 2 | 0 | -3 | 1 | 0 | -0 | -3 | -3 | 1 | 2 | 0 | 0 | 1 | -1 | 0 | 0 | -2 | -1 | 1 | -2 | -4 | -1 | -2 | -3 | -1 | -3 | -0 | 0 |
| LINE 58 | -1 | 2 | 3 | -2 | -0 | 0 | -0 | -0 | 0 | -0 | -0 | -2 | -0 | 0 | 0 | -3 | -1 | -4 | -1 | -2 | -3 | -5 | -3 | -2 | -4 | -0 | -1 | -1 | -1 |
| LINE 59 | 0 | 2 | 1 | 1 | -0 | -3 | -2 | -3 | -2 | -1 | -5 | -3 | -1 | -2 | -0 | 0 | -1 | -4 | -1 | -0 | -4 | -2 | -1 | -4 | -4 | -3 | -0 | -3 | -4 |
| LINE 60 | 2 | -0 | -2 | -2 | 2 | -1 | -3 | 0 | -0 | -0 | -1 | -1 | -1 | -2 | -0 | -0 | -2 | -3 | -2 | -1 | -2 | -0 | 2 | -3 | -3 | -2 | -0 | -6 | -1 |
| LINE 61 | 1 | 0 | 0 | -0 | 3 | -2 | -3 | -1 | -0 | -6 | -3 | -3 | -0 | -1 | 0 | -1 | -3 | -3 | -2 | -1 | -3 | -4 | -3 | -2 | -3 | -5 | -3 | -4 | -5 |
| LINE 62 | -0 | 1 | 2 | 0 | -0 | -3 | -2 | -2 | -4 | -2 | -5 | -1 | -3 | -2 | -3 | 0 | -2 | -2 | -3 | -4 | -4 | -4 | -0 | -5 | -4 | -5 | -0 | -3 | -6 |
| LINE 63 | -1 | 2 | 1 | -2 | -4 | -3 | -2 | -4 | -6 | -5 | -4 | -1 | -5 | -3 | 0 | -2 | -3 | -4 | -1 | -1 | -7 | -6 | -2 | -4 | -7 | -2 | -6 | -4 | -5 |
| LINE 64 | 0 | -1 | 1 | -1 | -2 | -4 | -4 | -4 | -4 | -0 | -1 | -4 | -4 | -4 | -2 | -0 | -6 | -6 | -6 | -2 | -7 | -3 | -1 | -3 | -8 | -7 | -4 | -3 | -4 |
| LINE 65 | -1 | -1 | -1 | -3 | -4 | -4 | -2 | -3 | -4 | -3 | -2 | -6 | -3 | -5 | -4 | -4 | -5 | -1 | -0 | -2 | -6 | -6 | -6 | -4 | -5 | -3 | -7 | -2 | -5 |
| LINE 66 | -4 | -3 | -0 | -4 | -4 | -6 | -3 | -8 | -3 | -2 | -4 | -3 | -7 | -4 | -6 | -3 | -4 | -6 | -1 | -4 | -6 | -2 | -5 | -7 | -7 | -5 | -3 | -5 | -4 |
| LINE 67 | -1 | -3 | -6 | -6 | -3 | -4 | -8 | -3 | -4 | -5 | -3 | -3 | -4 | -2 | -6 | -5 | -5 | -3 | -3 | -5 | -8 | -5 | -4 | -7 | -6 | -7 | -7 | -5 | -7 |
| LINE 68 | -2 | -5 | -1 | -3 | -3 | -1 | -7 | -5 | -4 | -4 | -5 | -3 | -6 | -7 | -7 | -5 | -1 | -5 | -3 | -7 | -7 | -4 | -7 | -7 | -9 | -10 | -7 | -6 | -8 |
| LINE 69 | -5 | -3 | -4 | -1 | -2 | -4 | -5 | -4 | -2 | -7 | -5 | -3 | -6 | -7 | -5 | -5 | -5 | -6 | -5 | -3 | -5 | -8 | -9 | -11 | -5 | -9 | -8 | -8 | -8 |
| LINE 70 | -5 | -4 | -5 | -8 | -6 | -4 | -3 | -7 | -5 | -4 | -4 | -4 | -6 | -7 | -5 | -6 | -7 | -8 | -6 | -9 | -5 | -8 | -8 | -6 | -10 | -7 | -9 | -7 | -5 |

Fig. III-8 (contd)

(c)

| LINE | 65 | -6 | -8 | -7 | -10 | -5 | -7 | -6 | -6 | -7 | -8 | -9 | -8 | -5 | -6 | -4 | -4 | -5 | -9 | -8 | -6 | -7 | -6 | -10 | -6 | -8 | -3 | -6 | -9 | -8 |
|---|---|---|---|---|---|---|---|---|---|---|---|---|---|---|---|---|---|---|---|---|---|---|---|---|---|---|---|---|---|---|
| LINE | 66 | -6 | -9 | -7 | -5 | -4 | -7 | -11 | -5 | -5 | -5 | -6 | -6 | -5 | -8 | -7 | -6 | -6 | -5 | -5 | -5 | -8 | -8 | -8 | -6 | -5 | -7 | -7 | -3 | -5 |
| LINE | 67 | -9 | -5 | -7 | -6 | -6 | -7 | -7 | -8 | -6 | -6 | -10 | -3 | -5 | -10 | -4 | -6 | -5 | -6 | -5 | -4 | -8 | -3 | -9 | -7 | -7 | -5 | -4 | -4 | -6 |
| LINE | 68 | -9 | -7 | -5 | -6 | -7 | -6 | -9 | -8 | -5 | -7 | -6 | -6 | -8 | -5 | -7 | -5 | -2 | -6 | -7 | -7 | -4 | -5 | -6 | -8 | -7 | -6 | -4 | -2 | -6 |
| LINE | 69 | -9 | -5 | -5 | -7 | -9 | -8 | -3 | -6 | -7 | -5 | -10 | -5 | -8 | -2 | -5 | -5 | -7 | -2 | -6 | -7 | -5 | -4 | -6 | -4 | -3 | -6 | -6 | -5 | -6 |
| LINE | 70 | -7 | -11 | -8 | -9 | -7 | -6 | -7 | -7 | -7 | -5 | -11 | -8 | -4 | -9 | -7 | -6 | -7 | -6 | -8 | -5 | -5 | -4 | -5 | -4 | -5 | -8 | -7 | -6 | -8 |

AMPLITUDE OF POLYNOMIAL N = 2

| PIC EL | | 122 | 123 | 124 | 125 | 126 | 127 | 128 | 129 | 130 | 131 | 132 | 133 | 134 | 135 | 136 | 137 | 138 | 139 | 140 | 141 | 142 | 143 | 144 | 145 | 146 | 147 | 148 | 149 | 150 |
|---|---|---|---|---|---|---|---|---|---|---|---|---|---|---|---|---|---|---|---|---|---|---|---|---|---|---|---|---|---|---|
| LINE | 39 | -7 | -7 | -9 | -6 | -11 | -8 | -10 | -10 | -9 | -11 | -12 | -11 | -12 | -12 | -9 | -11 | -7 | -10 | -10 | -11 | -9 | -7 | -10 | -9 | -9 | -6 | -10 | -9 | -6 |
| LINE | 40 | -6 | -7 | -10 | -6 | -10 | -10 | -11 | -8 | -7 | -11 | -13 | -10 | -9 | -10 | -11 | -7 | -8 | -9 | -8 | -10 | -11 | -10 | -9 | -7 | -7 | -10 | -9 | -9 | -8 |
| LINE | 41 | -11 | -9 | -10 | -10 | -5 | -10 | -11 | -9 | -10 | -9 | -8 | -10 | -7 | -9 | -9 | -7 | -8 | -1[illegible] | -10 | -9 | -8 | -12 | -9 | -6 | -8 | -11 | -7 | -9 | -8 |
| LINE | 42 | -8 | -4 | -8 | -9 | -11 | -5 | -9 | -6 | -9 | -10 | -9 | -10 | -7 | -10 | -10 | -7 | -9 | -1[illegible] | -8 | -8 | -8 | -11 | -10 | -11 | -8 | -8 | -10 | -8 | -6 |
| LINE | 43 | -10 | -6 | -11 | -8 | -8 | -7 | -6 | -9 | -9 | -8 | -9 | -10 | -8 | -9 | -10 | -7 | -9 | -11 | -8 | -9 | -7 | -8 | -10 | -8 | -10 | -7 | -7 | -4 | -6 |
| LINE | 44 | -9 | -10 | -9 | -11 | -5 | -8 | -5 | -7 | -9 | -10 | -9 | -8 | -8 | -8 | -10 | -6 | -10 | -8 | -9 | -7 | -9 | -8 | -10 | -6 | -5 | -6 | -6 | -7 | -6 |
| LINE | 45 | -6 | -13 | -11 | -8 | -5 | -4 | -8 | -9 | -8 | -7 | -9 | -9 | -9 | -9 | -10 | -8 | -7 | -8 | -8 | -8 | -8 | -8 | -7 | -7 | -6 | -5 | -7 | -2 | -6 |
| LINE | 46 | -9 | -8 | -7 | -5 | -8 | -10 | -11 | -7 | -7 | -7 | -8 | -8 | -8 | -6 | -10 | -8 | -8 | -8 | -9 | -8 | -10 | -10 | -10 | -6 | -4 | -3 | -5 | -7 | -4 |
| LINE | 47 | -8 | -10 | -10 | -8 | -8 | -7 | -9 | -8 | -11 | -6 | -8 | -8 | -8 | -6 | -10 | -10 | -8 | -9 | -9 | -7 | -7 | -10 | -7 | -9 | -7 | -8 | -8 | -3 | -7 |
| LINE | 48 | -9 | -8 | -6 | -2 | -10 | -5 | -7 | -7 | -6 | -7 | -6 | -9 | -8 | -8 | -6 | -9 | -7 | -8 | -8 | -6 | -8 | -8 | -9 | -7 | -6 | -2 | -6 | -7 | -5 |
| LINE | 49 | -8 | -7 | -10 | -10 | -7 | -5 | -6 | -10 | -6 | -8 | -4 | -5 | -4 | -7 | -9 | -8 | -7 | -7 | -8 | -9 | -9 | -8 | -5 | -6 | -8 | -7 | -8 | -4 | -5 |
| LINE | 50 | -12 | -10 | -8 | -10 | -10 | -5 | -4 | -4 | -7 | -7 | -10 | -6 | -8 | -5 | -9 | -7 | -5 | -7 | -9 | -6 | -6 | -9 | -8 | -9 | -6 | -5 | -7 | -6 | -6 |
| LINE | 51 | -9 | -8 | -7 | -6 | -7 | -5 | -8 | -8 | -7 | -11 | -7 | -6 | -4 | -8 | -7 | -9 | -6 | -4 | -6 | -8 | -8 | -8 | -7 | -6 | -4 | -8 | -6 | -3 | -4 |
| LINE | 52 | -9 | -5 | -5 | -8 | -7 | -3 | -8 | -8 | -6 | -7 | -10 | -9 | -8 | -8 | -7 | -5 | -3 | -11 | -4 | -6 | -7 | -6 | -8 | -4 | -7 | -6 | -7 | -7 | -8 |
| LINE | 53 | -7 | -8 | -9 | -9 | -8 | -4 | -6 | -5 | -5 | -8 | -8 | -4 | -5 | -7 | -7 | -8 | -5 | -11 | -5 | -4 | -8 | -8 | -3 | -7 | -5 | -7 | -10 | -6 | -6 |
| LINE | 54 | -8 | -7 | -8 | -6 | -8 | -6 | -5 | -5 | -5 | -6 | -6 | -6 | -9 | -9 | -5 | -6 | -10 | -1[illegible] | -7 | -4 | -5 | -7 | -5 | -4 | -4 | -4 | -7 | -7 | -8 |
| LINE | 55 | -6 | -9 | -6 | -8 | -8 | -6 | -5 | -8 | -8 | -7 | -7 | -9 | -6 | -5 | -9 | -9 | -8 | -7 | -7 | -7 | -4 | -6 | -5 | -5 | -4 | -6 | -7 | -6 | -2 |
| LINE | 56 | -7 | -10 | -4 | -7 | -7 | -8 | -13 | -6 | -7 | -7 | -3 | -7 | -6 | -6 | -7 | -6 | -7 | -7 | -6 | -5 | -5 | -6 | -5 | -4 | -5 | -6 | -5 | -2 | -6 |
| LINE | 57 | -8 | -11 | -4 | -6 | -10 | -7 | -7 | -6 | -5 | -8 | -5 | -5 | -8 | -6 | -5 | -10 | -7 | -7 | -8 | -7 | -5 | -7 | -6 | -4 | -2 | -6 | -6 | -5 | -7 |
| LINE | 58 | -7 | -9 | -10 | -10 | -9 | -8 | -8 | -8 | -7 | -4 | -5 | -7 | -6 | -6 | -9 | -5 | -6 | -6 | -5 | -2 | -6 | -5 | -4 | -1 | -5 | -3 | -3 | -5 | -6 |
| LINE | 59 | -8 | -7 | -7 | -8 | -6 | -6 | -8 | -6 | -5 | -4 | -4 | -7 | -8 | -5 | -8 | -7 | -6 | -6 | -7 | -6 | -4 | -7 | -5 | -4 | -5 | -6 | -4 | -3 | -6 |
| LINE | 60 | -5 | -8 | -6 | -10 | -3 | -6 | -6 | -9 | -4 | -7 | -8 | -9 | -7 | -6 | -5 | -6 | -9 | -8 | -4 | -6 | -4 | -7 | -6 | -5 | -5 | -4 | -6 | -4 | -7 |
| LINE | 61 | -5 | -4 | -4 | -5 | -5 | -6 | -6 | -5 | -4 | -4 | -8 | -7 | -7 | -5 | -9 | -5 | -7 | -3 | -5 | -2 | -5 | -5 | -4 | -6 | -3 | -4 | -5 | -7 | -4 |
| LINE | 62 | -8 | -6 | -5 | -7 | -8 | -7 | -4 | -4 | -4 | -6 | -7 | -4 | -4 | -5 | -4 | -9 | -4 | -6 | -3 | -5 | -2 | -7 | -4 | -2 | -2 | -2 | -5 | -5 | -4 |
| LINE | 63 | -6 | -9 | -6 | -5 | -5 | -7 | -4 | -4 | -6 | -5 | -8 | -8 | -6 | -7 | -5 | -5 | -7 | -5 | -5 | -3 | -2 | -3 | -6 | -3 | -2 | -5 | -4 | -4 | -5 |
| LINE | 64 | -5 | -6 | -4 | -6 | -6 | -6 | -7 | -9 | -4 | -7 | -8 | -2 | -5 | -4 | -7 | -5 | -1 | -4 | -5 | -4 | -1 | -4 | -4 | -3 | -1 | -4 | -4 | -6 | -3 |
| LINE | 65 | -6 | -8 | -7 | -4 | -6 | -6 | -6 | -6 | -5 | -6 | -7 | -6 | -6 | -5 | -5 | -4 | -3 | -7 | -6 | -0 | -3 | -5 | -2 | -2 | -2 | -4 | -2 | -6 | -5 |
| LINE | 66 | -9 | -7 | -3 | -6 | -7 | -2 | -5 | -6 | -4 | -6 | -5 | -7 | -4 | -4 | -4 | -6 | -4 | -5 | -5 | -1 | -2 | -4 | -6 | -2 | -3 | -3 | -6 | -3 | -4 |
| LINE | 67 | -8 | -7 | -3 | -6 | -5 | -6 | -6 | -7 | -4 | -5 | -7 | -7 | -4 | -6 | -4 | -5 | -6 | -4 | -5 | -1 | -2 | -2 | -3 | -6 | -3 | -2 | -1 | -3 | -4 |
| LINE | 68 | -5 | -5 | -10 | -4 | -5 | -4 | -6 | -7 | -7 | -5 | -6 | -7 | -3 | -5 | -4 | -3 | -3 | -4 | -4 | -2 | -1 | -5 | -1 | -4 | -4 | -2 | -4 | -4 | -3 |
| LINE | 69 | -8 | -9 | -4 | -10 | -5 | -5 | -7 | -6 | -6 | -5 | -5 | -5 | -5 | -5 | -5 | -2 | -2 | -3 | -5 | -4 | -1 | -1 | -5 | -2 | -3 | 0 | -3 | -3 | -5 |

Fig. III-8 (contd)

The coordinates of the fiducial marks and picture edges are compared in Table III-5. From these data a transformation relating the two sets of coordinates was derived. If $(L', E')$ are the calibration picture coordinates of a physical point whose flight picture coordinates are $(L, E)$, and if $L' = L + \Delta L$, $E' = E + \Delta E$, then the transformation

$$\Delta L = -1.7 + 0.030\,(L - 99.7) - 0.00365\,(E - 108.3) - 3 \times 10^{-5}\,(L - 99.7)^2 \quad (7)$$

$$\Delta E = +7.82 + 0.029\,(E - 108.3) + 0.00365\,(L - 99.7) - 1.05 \times 10^{-4}\,(E - 108.3)^2 \quad (8)$$

brings the nine fiducial marks into correspondence within an rms uncertainty of 0.2 picture element.

The coordinate transformation given above illustrates a further complicating feature, namely, that a certain part of the vidicon target area that appears in the flight pictures was not included in the calibration pictures, so that no calibration data for this area exist. In order to obtain approximate calibration information for this region, the $C$-matrices were extrapolated outward for as many picture elements as necessary at the top, right edge, and bottom of the picture. The greatest extrapolation, 10 elements, had to be made along the right edge. Here the extrapolation was accomplished using linear least-squares fitting to a running five-line average of the rightmost 8 elements of the calibration picture. A similar procedure was used on the remaining two edges.

**Table III-5. Picture coordinates (*L*, *E*) of fiducial mark corners[a] (C = Calibration, F = Flight, D = Difference, *L* = Line, *E* = Element)**

| | | |
|---|---|---|
| C (23.4, 43.4) | C (21.0, 115.1) | C (19, 185) |
| F (27.4, 38.3) | F (25.5, 107.4) | F (23.2, 176.0) |
| D (−4.1, +5.1) | D (−4.5, +7.7) | D (−4.2, +9.0) |
| C (99.5, 44.3) | C (98.0, 116.1) | C (96.3, 186.3) |
| F (101, 39.3) | F (99.7, 108.3) | F (98.5, 177.3) |
| D (−1.5, +5.0) | D (−1.7, +7.7) | D (−2.2, +9.0) |
| C (185.4, 46.0) | C (183.5, 117.2) | C (181.9, 188.0) |
| F (184.5, 40.3) | F (183.2, 109.2) | F (182.0, 178.3) |
| D (+0.9, +5.7) | D (+0.3, +8.0) | D (−0.1, +9.7) |
| Left picture edge: | | |
| C: $E = 34$ at $L = 5$; | $E = 35.5$ at $L = 198$ | |
| F: $E = 28.5$ at $L = 5$; | $E = 30.0$ at $L = 198$ | |

[a]The coordinates were estimated visually to 0.1 element by inspection of numerical printouts of several pictures.

Using the point transformation given above, together with the extrapolated values just described, a new set of $C$-matrices was calculated in the flight picture format. Where fractional line and element numbers appeared, the values of $C_0$, $C_1$, and $C_2$ were calculated by the interpolation formula

$$\begin{aligned} C_n(I + x, J + y) = {} & (1 - x)(1 - y)\,C_n(I, J) \\ & + (1 - x)\,y\,C_n(I, J + 1) \\ & + x(1 - y)\,C_n(I + 1, J) \\ & + xy\,C_n(I + 1, J + 1) \end{aligned} \quad (9)$$

where $I$ and $J$ refer to integral line and element numbers and $0 < (x, y) < 1$ are the fractional remainders:

$$L' = I + x \quad (10)$$

$$E' = J + y \quad (11)$$

### 11. Flight Pictures; DN Conversion

We now turn to the flight pictures themselves. The first operation preparatory to applying the calibration matrices was to convert the picture DN's from integer to floating point format.

### 12. Harmonic Noise Removal

Next, the Fourier amplitude and phase of the fundamental 17.7-element harmonic noise was evaluated and the resulting wave subtracted from each flight picture except the first. In this step, a complicating feature was the presence of a varying signal, due to the Martian topography, whose Fourier spectrum often included a significant 17.7-element term. This was particularly true of Picture 3, for which a considerable amount of 17.7-element coherent noise was still visible in the final picture. Harmonic removal at this stage was limited to the fundamental component, because (a) this component had the greatest amplitude and seemed to be present throughout a picture, and (b) the 8.8- and 4.4-element components, being of much smaller amplitude, were often present only in certain parts of a picture, making their evaluation and removal much more difficult and subject to greater error through spurious amplitude contributions from topographic features.

### 13. Evaluation of True Exposure TRU by Iteration

The true intensity TRU was evaluated at each point of a flight picture using an iterative approach, as follows:

(1) The apparent intensity $APP = I/1000$ (in units of 1000 ft-lamberts) was evaluated from the standard calibration curve by linear interpolation in Table III-2. No distinction was made between red and green pictures.

(2) The ratio $y = APP/TRU$ was evaluated from Eq. (1), substituting $x = APP$ (instead of the unknown value $TRU$). The coefficients $C_0$, $C_1$, $C_2$ for each particular picture element were taken from the $C$-matrices found in Step 10.

(3) A better approximation $T_1$ to $TRU$ was found by solving $y = APP/TRU$ for $TRU$, using the numerical value of $y$ just obtained:

$$T_1 = APP/y$$

(4) A new value of $y$ was calculated from Eq. (1), using $x = T_1$.

(5) Steps (3) and (4) were repeated six times, or until the change in $T_1$ was less than $10^{-3}$. Generally, two or three iterations were sufficient. Then $TRU$ was taken as the final value of $T_1$.

This procedure worked quite well for the vast majority of picture elements, but in a few instances the coefficients $C_0$, $C_1$, $C_2$ were such that this iterative approach diverged for the particular DN involved. This was particularly evident in the second column of the pictures, where the coefficients seemed to be especially unfavorable, probably as a result of the calibration scheme's attempt to correct for the overshoot of the video amplifier as the reading electron beam passed off the black mask area and onto the illuminated area of the picture.

### 14. Spectral Data

The intensities obtained above are measured in units of 1000 ft-lamberts of 3000°K quality light. However, such units are not an easily interpretable measure of the intensity of Mars, depending as they do upon the spectral distribution of the lamp used for calibration of the system, the spectral transmission of the TV camera filters, and the spectral responses of the vidicon and of the photometer used to measure the calibration lamp intensity. In terms of these factors, shown graphically in Fig. III-9, the output signals of the photometer and of the TV camera* when viewing a light source having a spectral distribution of intensity $I(\lambda)$ W cm$^{-2}$ sterad$^{-1}$ would be

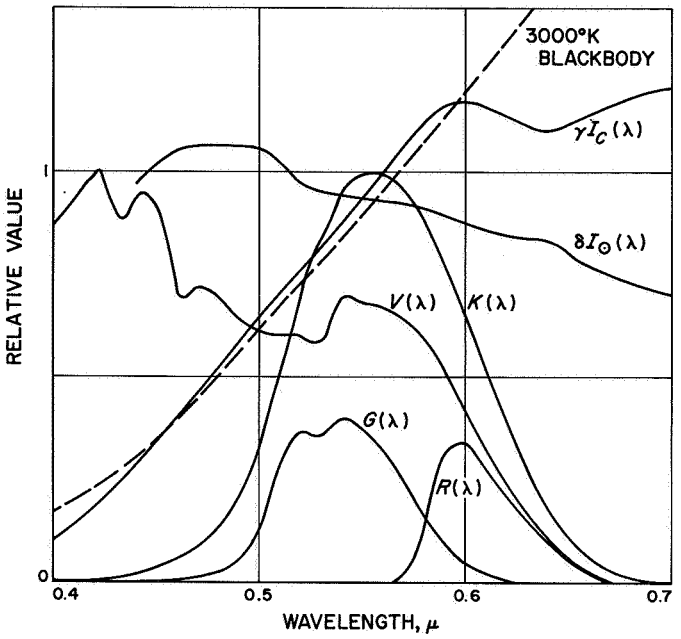


**Fig. III-9. Spectral responses of visual photometer (K), vidicon (V), vidicon with green filter (G), vidicon with orange-red filter (R); also shown are relative spectral distributions of the collimator light source (C) and of sunlight (⊙)**

$$\text{Photometer output} \qquad P = \alpha \int_0^\infty K(\lambda)\, I(\lambda)\, d\lambda \tag{12a}$$

$$\text{TV exposure (green filter)} \qquad G = \beta \int_0^\infty G(\lambda)\, I(\lambda)\, d\lambda \tag{12b}$$

$$\text{TV exposure (red filter)} \qquad R = \beta \int_0^\infty R(\lambda)\, I(\lambda)\, d\lambda \tag{12c}$$

where $\alpha$ and $\beta$ are fixed instrumental constants, and $K(\lambda)$, $G(\lambda)$, $R(\lambda)$ are, respectively, the spectral response function of the photometer and of the vidicon with the green and red filters. As special cases, if the source was

*For the TV camera, "signal" means the relative exposure effective in producing an electrical output, not the electrical output itself. The latter is a nonlinear function of the relative exposure (see Fig. III-3).

the calibration source $I_c(\lambda)$ or light having the spectral distribution $I_\odot(\lambda)$ of sunlight but diluted by a factor $E$, the outputs would be

$$P_c = \alpha \int_0^\infty K(\lambda)\, I_c(\lambda)\, d\lambda \tag{13a}$$

$$G_c = \beta \int_0^\infty G(\lambda)\, I_c(\lambda)\, d\lambda \tag{13b}$$

$$R_c = \beta \int_0^\infty R(\lambda)\, I_c(\lambda)\, d\lambda \tag{13c}$$

$$P_\odot = \alpha E \int_0^\infty K(\lambda)\, I_\odot(\lambda)\, d\lambda \tag{14a}$$

$$G_\odot = \beta E \int_0^\infty G(\lambda)\, I_\odot(\lambda)\, d\lambda \tag{14b}$$

$$R_\odot = \beta E \int_0^\infty R(\lambda)\, I_\odot(\lambda)\, d\lambda \tag{14c}$$

A more convenient measure of the intensity of Mars is the ratio of the observed signal $G$ or $R$ to the signals $G_\odot$ or $R_\odot$ that would be found if the camera was viewing a diffuse, perfectly reflecting ("white") screen oriented perpendicular to the sun's rays at Mars' orbit. Such a standard source would have the quality of sunlight, but it would be diluted by a factor $(r_\odot/r_M)^2 = 0.93 \times 10^{-5}$, where $r_M$ is the radius of Mars' orbit and $r_\odot$ is the radius of the sun. The ratios

$$\rho_G = G/G_\odot \qquad \text{and} \qquad \rho_R = R/R_\odot \tag{15a, b}$$

are thus closely related to the reflectivity of Mars at 60-deg phase angle in the wavelength bands used for the observations.

In order to evaluate these ratios, we must know $G_\odot$ and $R_\odot$ in units of 1000 ft-lamberts. We may calculate $G_\odot$ and $R_\odot$ from the graphs of Fig. III-9. Bearing in mind that only *relative* values of $I_c(\lambda)$ and $I_\odot(\lambda)$ are given in this graph, as signified by the arbitrary multiplying factors $\gamma$ and $\delta$, we may write

$$\rho_G = \frac{G}{G_\odot} = \frac{G}{G_c} \cdot \frac{G_c}{G_\odot} = \frac{G}{G_c} \frac{\int_0^\infty G(\lambda)\, I_c(\lambda)\, d\lambda}{E \int_0^\infty G(\lambda)\, I_\odot(\lambda)\, d\lambda}$$

$$= \frac{G}{G_c} \frac{\delta}{\gamma} \frac{\int_0^\infty G(\lambda)\, \gamma I_c(\lambda)\, d\lambda}{E \int_0^\infty G(\lambda)\, \delta I_\odot(\lambda)\, d\lambda} \tag{16}$$

But $\delta/\gamma$ is also equal to

$$\frac{\delta}{\gamma} = \frac{P_c}{P_\odot} \frac{E \int_0^\infty K(\lambda)\, \delta I_\odot(\lambda)\, d\lambda}{\int_0^\infty K(\lambda)\, \gamma I_c(\lambda)\, d\lambda} \tag{17}$$

The integrals appearing in these equations may be evaluated by numerical integration using the curves of Fig. III-9. The results are (in arbitrary units)

$$g_c = \int_0^\infty G(\lambda)\, \gamma I_c(\lambda)\, d\lambda = 130.6 \tag{18}$$

$$g_\odot = \int_0^\infty G(\lambda)\, \delta I_\odot(\lambda)\, d\lambda = 140 \tag{19}$$

$$p_c = \int_0^\infty K(\lambda)\, \gamma I_c(\lambda)\, d\lambda = 512 \tag{20}$$

$$p_\odot = \int_0^\infty K(\lambda)\, \delta I_\odot(\lambda)\, d\lambda = 500 \tag{21}$$

Further,

$$r_c = \int_0^\infty R(\lambda)\, \gamma I_c(\lambda)\, d\lambda = 95.2 \tag{22}$$

$$r_\odot = \int_0^\infty R(\lambda)\, \delta I_\odot(\lambda)\, d\lambda = 71.5 \tag{23}$$

Thus we have

$$\rho_G = \frac{G}{G_c} \frac{g_c}{g_\odot} \frac{P_c}{P_\odot} \frac{p_\odot}{p_c} = \frac{G}{G_c} \frac{P_c}{P_\odot} \frac{130.6}{140} \frac{500}{512} \tag{24}$$

But $P_c = G_c = R_c$ by calibration, and $P_\odot$, the visual intensity of a white screen at Mars' distance from the sun, is taken to be 5300 ft- lamberts (Ref. 2).

Thus the desired reflectivities are related to the direct TV outputs by the equations

$$\rho_G = \frac{G}{5.80} \tag{25}$$

and

$$\rho_R = \frac{R}{5.3}\,\frac{95.2}{71.5}\,\frac{500}{512} = \frac{R}{4.08} \tag{26}$$

### 15. Correction for Temperature

It is also necessary to correct the picture intensities for the effects of the difference of temperature of the camera between conditions of calibration (20°C) and at encounter (−7°C). During environmental testing of the camera systems, tests were made at +50, +25, and −30°C. When the relative response of the camera at these temperatures was plotted as a function of illumination level, it was found that the relative sensitivity at two temperatures is substantially independent of illumination level. Figure III-10 shows the sensitivity, relative to that at 25°C, as a function of temperature. The sensitivity at −7°C appears to be about 0.82 as great as at 25°C. It is assumed that this factor applies to both red and green pictures. Inclusion of this factor changes the expressions for $\rho_G$ and $\rho_R$ to

$$\rho_G = \frac{G}{4.75} \tag{27}$$

$$\rho_R = \frac{R}{3.36} \tag{28}$$

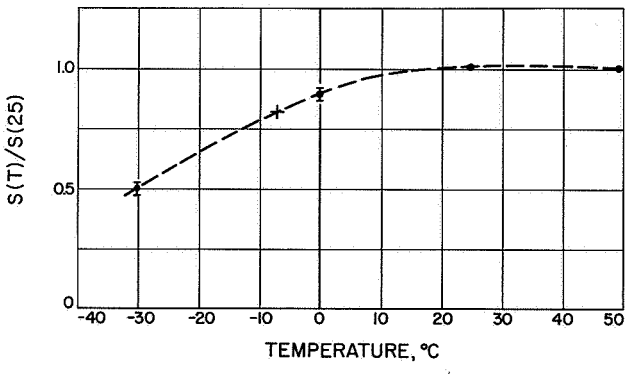


**Fig. III-10. Variation of camera sensitivity with temperature**

The operating temperature of the camera at the time of Mars encounter was −7°C.

### 16. Incorporation of Variable Red Filter Factor

Finally, the variable red filter factor was included. The expression for $\rho_R$ is thereby modified to

$$\rho_R = \frac{R}{2.18 + 0.00070\,L + 0.00018\,E} \tag{29}$$

The picture intensities were modified according to Eqs. (27) and (29).*

### 17. Proof Prints; Blemishes

Pictorial proof prints of the flight pictures were produced using as great a contrast enhancement as possible (approximately a factor of 3) to check the results to this point. The prints were generally quite satisfactory, being greatly improved over the enhanced prints originally released. The major blemishes and the fundamental component of harmonic noise were quite unnoticeable (except in Picture 3), and the intensity remained uniform up to the edge of the picture. Many new craters and other features were visible.

There were, however, a few minor blemishes and other imperfections still in evidence. The most prominent of these were small spots having coordinates near (43, 66), (115, 82), (156, 81) and (172, 97). Evidently these spots were so small that the various nonlinearities or "jitter" of the vidicon scan system caused them to appear at different picture positions from one exposure to the next, or perhaps the temperature dependence of the vidicon sensitivity for these points was different from that of the target at large.

Also rather prominent were the dozen or so individual picture elements for which the intensity calibration process did not converge. These were mainly found in the second column of the picture, corresponding to Element 30, and at line numbers greater than approximately 180.

The next most prominent imperfection was the residual harmonic noise, particularly the 8.8- and 4.4-element harmonics of the 17.6-element fundamental. Since these harmonics had not been evaluated or removed, their presence was not surprising. However, the possibility of removing them at all was made doubtful by the fact that a given picture would show such effects only in certain irregular areas. This is what would be expected if, for

*In the first such modification, slightly different numerical factors were used because of an uncertainty in the true value of the luminous intensity of the sun above the earth's atmosphere, an uncertainty that may even now not be fully resolved.

example, the amplitude of a given term were a small fraction of a DN, for then it could appear only in those places where the DN level lay close enough to the next higher or lower value that this small amplitude could affect the DN discrimination. In such a case the correct average amplitude would be measured, but correcting the picture by this amount would not only fail to remove the noise where it occurred but would introduce it where it was not already present. In view of this situation it was decided to postpone any attempt at removing the higher harmonics until a later time, when it might be considered further.

Less prominent than the imperfections so far described was one which was quite unobtrusive upon casual inspection but which could introduce significant problems in interpretation of some of the pictures. This was a faint ring-shaped blemish which nearly coincided with the prominent oblong feature in the NE quadrant of Picture 3. This blemish was quite prominent as a dark ring in the calibration pictures. Its appearance as a faint bright ring in the corrected flight pictures might raise some question as to the reliability of the calibration procedure, particularly the assumption that the system properties did not change significantly between calibration and encounter. In view of the high degree of uniformity of illumination over the entire picture yielded by the calibration procedure, including the satisfactory removal of most

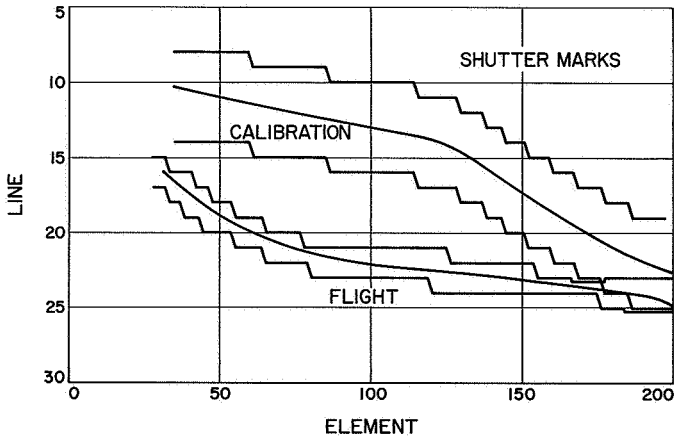


**Fig. III-11. Line and element coordinates of the shutter marks for the calibration pictures and the flight pictures**

The camera sensitivities (calibration pictures) or the intensities of the picture elements (flight pictures) on and within these boundaries were replaced by values obtained by linear interpolation across the mark. The width of the mark was taken to be greater for the calibration pictures because of the relative uniformity of vidicon response. The flight picture mark was held to as narrow a width as possible to retain as much independent picture information as possible without having the mark appear in the pictures.

blemishes and of the strong darkening around the edges of the picture, it does not seem reasonable to attribute much of this effect to a general change of sensitivity of the system. It is clear, however, that different kinds of blemishes might exist whose temperature or time dependence might differ. For example, an area having a high electrical leakage tending to discharge the target film locally would exhibit quite a different variation in strength of effect with light intensity and temperature than would another area which happened to lie behind a faint smudge on the front face of the vidicon. If a smudge were to involve a slightly volatile substance, this would further complicate the time behavior.

### 18. Removal of Shutter Mark, Fiducial Marks, Blemishes

The shutter mark, fiducial marks, and the localized blemishes noted in Step 17 were removed from the flight pictures by replacing the intensities of picture elements lying within a mark by linear interpolation across the narrow dimension of the mark. The number of picture elements so replaced in a given line or column was three or four. Most elements so replaced are indicated in Figs. III-11 and III-12.

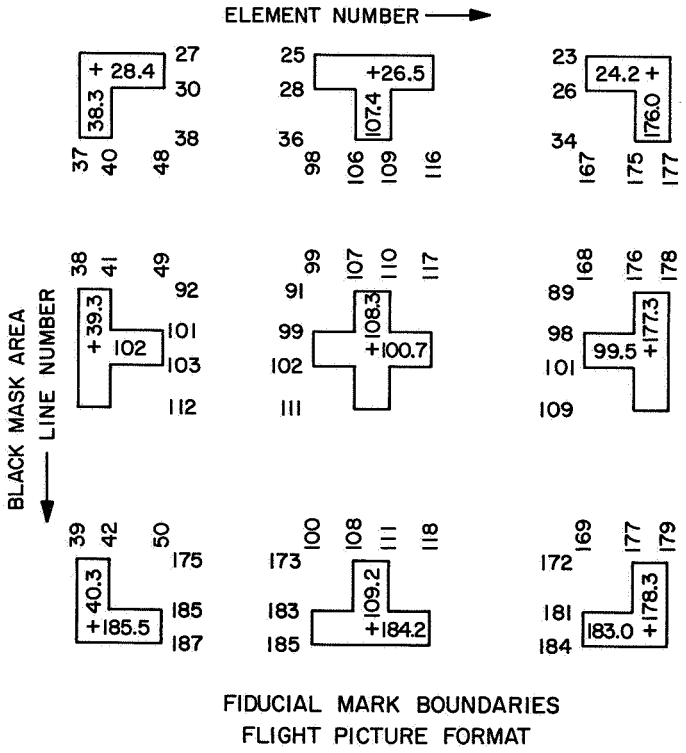


**Fig. III-12. Line and element coordinates of fiducial marks for flight pictures**

The elements lying within and on these boundaries were replaced by linear interpolation as in Fig. III-11.

### 19. Correction of Systematic Blemishes by Averaging

Considering the smallness of the residual effects described in 17 above, it seemed most reasonable to recognize that there might be small local departures from the sensitivity deduced from the calibration data and to adopt some procedure for removing any such effects that might be present without departing basically from the overall quantitative reliability of the results. To this end, the flight picture intensities were averaged over two independent samples consisting respectively of the eight green pictures 2, 3, 6, 7, 10, 11, 14, 15 and the six red pictures 4, 5, 8, 9, 12, 13. The result was an "average green picture" and an "average red picture." These were in turn enhanced and reproduced in pictorial form and were compared graphically as well (Figs. III-13 and III-14). As was expected, the effect of the averaging was to suppress the Martian topographic features, leaving the systematic blemishes relatively unaffected. It was clear by inspection that these average pictures strongly resembled one another and that a considerable improvement in picture quality might result if the individual pictures were appropriately corrected.

The flight picture intensities were accordingly multiplied by a correction function defined as follows. Let $GAV(I,J)$ and $RAV(I,J)$ be the average green and red picture intensities as described above, and let $S(I,J) = GAV(I,J) + 0.9\,RAV(I,J)$.* Also, let $SAV$ be the average value of $S(I,J)$ over the entire picture area. Then a correction function

$$COR(I,J) = \frac{SAV}{S(I,J)} \tag{30}$$

was evaluated and stored on magnetic tape. Subsequently, all 19 of the flight pictures were corrected by multiplying the intensity $P(I,J)$ by $COR(I,J)$.

### 20. Correction of Geometrical Distortions

The fiducial marks in the pictures were designed to provide a rectilinear reference grid with respect to which picture distortions introduced by nonlinearities in the

*The factor 0.9 was intended to allow for the smaller number of red pictures used in the averages. In view of the somewhat poorer discriminability of the system for the red pictures, and their higher average intensity, a relative weight as low as 0.5 could have been used. This weight factor has a negligible effect on the results, so that its precise value is unsure.

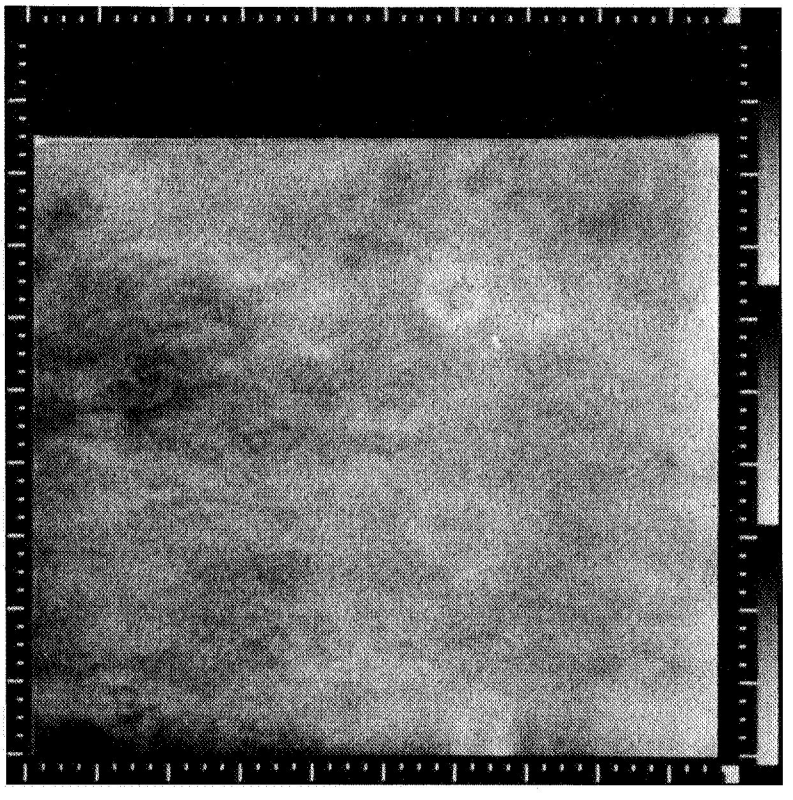

**Fig. III-13. Average of green pictures 2, 3, 6, 7, 10, 11, 14, and 15, enhanced such that the brightness range 100–130 spans the DN range 63–0**

vidicon electron beam deflection could be measured and corrected. A certain amount of such distortion was actually present, as indicated by the fact that the fiducial marks did not fall in a square pattern in the final pictures. The average spacing between fiducial marks in the horizontal direction* was 69 elements; in the vertical direction it was 79 elements. Furthermore, the vertical spacing was about 75 elements for the top part of the picture and 83 elements for the bottom part (see Table III-5 and Fig. III-12).

In order to rectify the pictures, a point transformation was developed which would render the picture square, expanding it slightly in the horizontal direction and introducing higher-order terms as necessary to bring the marks into a square pattern. For convenience, it was also decided to shift the central mark to the point (100,100) and to adopt 80 elements as the desired spacing of adjacent marks. The resulting transformation was as follows: Let $(L, E)$ be the picture coordinates of a given Martian feature in the final, rectified picture, and let $(L', E')$ be the coordinates of the corresponding point in the original flight picture format. Then, if $l = L - 100$ and $e = E - 100$, the transformation

$$L' = L - 0.3 - 0.01375\,l + 7.19 \times 10^{-4}\,l^2 - 0.0160\,e + 6.64 \times 10^{-5} el - 8.3 \times 10^{-7}\,el^2 \quad (31)$$

$$E' = E + 8.3 - 0.1375\,e + 0.0126\,l \quad (32)$$

brings the fiducial marks into the desired square pattern within a residual rms deviation of less than 0.2 element.

This transformation was applied to the flight pictures, using the same two-dimensional linear interpolation formula as in Step 10. Finally, the new locations of the fiducial mark corners were indicated by replacing the appropriate single-picture-element intensities by zeros (black).

*As viewed with the black mask at the left.

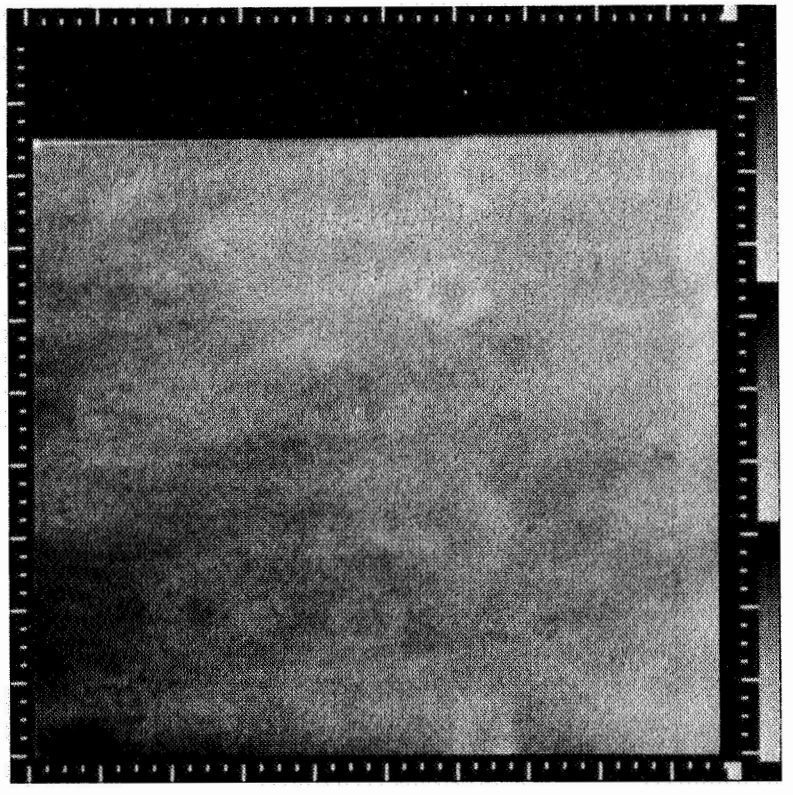

**Fig. III-14. Average of red pictures 4, 5, 8, 9, 12, and 13, enhanced so that the brightness range 160–220 spans the DN range 63–0**
Note the strong similarity of the two pictures.

#### 21. Calibration of Pictures 20–22

Pictures 20–22 were calibrated in a similar way as Pictures 1–19, except that a different sample of calibration pictures was used, and, since no fine detail was present in these pictures, there was no need to evaluate the sensitivity of each picture element. The calibration data sample consisted of all pictures taken with amplifier gain 01 and 11, and in order to enlarge the sample and provide a tie-in with the remaining pictures, gain state 10 was also included. This made it possible to recalibrate Picture 19 for comparison with the results found previously.

The calibration steps were carried out on $32 \times 29$ element matrices of $6 \times 6$ averaged DN's as described in Step 6, both for the calibration pictures and the flight pictures.

### B. Photometric Accuracy

The purpose of the rather extensive treatment of the digital picture data described in the preceding section was to convert the DN value of each element of a given picture into an equivalent intensity of illumination of the corresponding point on the Martian surface. Of the numerous systematic and random factors which affect the overall precision with which this intensity is finally known, most tend to be eliminated by the calibration procedures.

#### 1. Systematic Effects

The most important remaining systematic effects are the following:

(1) The absolute calibration of the photovisual photometer used to set the intensity of the collimator light source. The photometer was calibrated just before use by comparison with a National Bureau of Standards secondary standard light source. However, because of the fact that a scale change was required, the precision of this measurement was limited to about 3%.

(2) The shapes of the spectral intensity distributions of the collimator light source as compared with that of sunlight. The collimator lamp approximated a 3000°K black body, while the sun approximates a 5700°K black body. The relative precision with which these two distributions were known was about 5%.

(3) The relative shapes of the vidicon spectral sensitivity curves through the green and red filters, and the spectral sensitivity curve of the photometer. The errors introduced through uncertainties in these functions are proportional to the "skewness" of the spectral distribution of the collimator light source relative to that of sunlight, since the calibration procedure itself determined the proper "filter factor" needed to compare red picture intensities with green picture intensities for the collimator light source. A rough indication of this uncertainty is provided by a comparison of the experimentally determined filter factor of 0.68 (giving the sensitivity of the system through the red filter relative to that through the green filter) with the value 0.73 calculated from the spectral sensitivity curves. The overall error from this source is probably about 7%.

(4) Correction of the sensitivity of the system for the 27°C temperature difference between calibration and Mars encounter. On the basis of the internal consistency of the data leading to the curves of Fig. III-10, the uncertainty introduced from this source is probably less than 5%.

(5) Uncertainty in the luminous flux of sunlight at the top of the earth's atmosphere. This factor is probably known to within 3%.

(6) Long-term drifts in the sensitivity of the camera system during the 8-month cruising period. Unfortunately, it was not possible to include a standard light source along with the camera system; consequently, it is not known whether any significant drift took place. The great care that was taken in the design of the electronic system, the use of screened components, and experience with similar systems over long periods of shelf storage suggest that any such drift was probably much less than 10%. The two television camera voltages that were monitored during the encounter agreed within the reading error, approximately 0.5%, with the values measured during calibration.

The combined effect of the first five of the above factors is about 10%; inclusion of a nominal value of 10% for the sixth yields a total uncertainty of approximately 15% due to systematic errors.

#### 2. Random Effects

In contrast with the rather large systematic uncertainty, the *relative* precision with which the intensities of two

points in a given picture are known is quite good, although somewhat variable through the picture sequence. The principal random effects which limit this precision are:

(1) The basic discriminability of the system arising from the six-binary-bit encoding scheme, together with the small inherent "jitter" in the operation of the encoding circuitry. Figure III-4 shows that a 1-DN change corresponds to a fractional intensity change of from 2% at the best to 10% or so at the worst. The $\Delta I/I$ discrimination levels of seven of the pictures fell near the minimum, while those of another seven were less than 0.05. All of the first 19 pictures were below 0.07 in this factor.

(2) Statistical uncertainties in the calibration process. As was described in the preceding section, the statistical uncertainty was essentially negligible, being less than about 0.25%.

(3) Fiducial marks and blemishes. The regions of the vidicon target near fiducial marks, the shutter mark, and the several localized blemishes that were removed by linear interpolation across the affected areas all have an unknown statistical error because the intensities at those points are not independent of those at other points. However, studies of the local variations of intensity across a picture suggest that errors of more than 1% in these areas are unlikely.

(4) The method that was used to remove the numerous low-contrast blemishes. The use of an average of 14 pictures must itself have introduced some statistical uncertainty because of the lack of complete averaging out of the true intensity variations in the pictures. The magnitude of this effect is estimated to be less than 1%, since the rms intensity fluctuation over one-half-line intervals of individual pictures was measured and found to average 3.4%: $3.4/14^{1/2} = 0.9$.

(5) Incomplete erasure of the previous picture. Each picture contains a faint "ghost" of the previous one. This effect was noticeable only in Picture 2, which contained a very faint remanent image of the limb of the planet. The intensity ratio across the "ghost" limb was 1.04, whereas it was 1.40 in the first picture. Thus, a given picture will contain about 10% of the previous picture. The effect will therefore contribute only about 0.3% to the statistical uncertainty in those cases where the effect cannot be subtracted out. No attempt was made to correct for this small residue.

(6) Harmonic noise. Harmonic noise was present in nearly all pictures, but could only be partially removed. Pictures 3, 4, and 12 contain visible remnants of the "fundamental" wavelength, while Pictures 3, 4, 5, 6, 8, 9, and 13 exhibit the second and higher harmonics of this fundamental. The average amplitude of the fundamental term in Pictures 2 through 21 before it was subtracted out was 0.28 DN. The higher harmonics, which were not removed, seem to have considerably less amplitude, so that we would expect to have an average $\Delta I/I$ uncertainty of well under 1% from this source. We shall assume a value of 0.3% due to this factor.

(7) Printout uncertainty. The intensities that resulted from the calibration procedures were printed using a four-digit format in which one to four of the places may actually be used. The roundoff error is $\pm 0.5$ unit, which corresponds to 0.3% in Pictures 4 and 5, and 4% at the center of Picture 19. This error is present only in the printouts as presented in Part II of this report, and is not present in the data as it is stored on magnetic tape.

Before combining the various statistical uncertainties just described into a single value, we must consider in more detail how to treat the first item—the basic discriminability of the system. The effect of this encoding uncertainty is that the DN value of a given point will be within the range $T - 0.5 < DN < T + 0.5$, where $T$ is the "true" DN that would have been found by a perfect encoder of unlimited discriminability. (It might appear that the range should be $T < DN < T + 1$, but the calibration procedure has the effect of shifting this range to the one given above.) Further, the actual DN's will be uniformly distributed within this range. Thus the rms DN uncertainty is

$$\left(\int_{-0.5}^{+0.5} x^2\,dx\right) = 0.5/3^{1/2} \approx 0.3\,DN$$

corresponding to an intensity uncertainty of 0.6 to 2.1% over the series of pictures.

The various sources of statistical uncertainty combine to yield about 1.2% rms error in the most favorable case, 1.5% in an average case, and 2.4% for Picture 19. If printout errors are included, the corresponding numbers are 1.4, 1.6, and 4.6%.

The largest uncertainty, outside the printout error, is due to the effect of averaging the red and green pictures to remove the residual blemishes. This effect is probably

of greater importance for widely separated picture elements in a single picture than for nearby ones. This is of some significance in connection with the use of the data for the study of intensity variations in a local area, where we would expect the statistical uncertainties to be somewhat less than the average.

In summary, we believe that the photometric precision attained in the *Mariner IV* pictures is ±15% due to systematic effects, and from 1.5 to about 3% due to random effects, the latter varying from picture to picture. The random uncertainty as a function of picture number is shown in Table III-6.

**Table III-6. DN discrimination and random error**

| Picture No. | $I_{av} \times 1000$ | $DN_{av}$ | $\Delta I/I$ (per DN) | Random error[b] |
|---|---|---|---|---|
| 1 | 205[a] | 23 | 0.020 | 0.013 |
| 2 | 140 | 16.5 | 0.020 | 0.013 |
| 3 | 150 | 12.5 | 0.020 | 0.013 |
| 4 | 250 | 20 | 0.021 | 0.013 |
| 5 | 250 | 21 | 0.020 | 0.013 |
| 6 | 140 | 15 | 0.020 | 0.013 |
| 7 | 130 | 19.5 | 0.020 | 0.013 |
| 8 | 180 | 37 | 0.028 | 0.014 |
| 9 | 150 | 43 | 0.036 | 0.016 |
| 10 | 85 | 37 | 0.028 | 0.014 |
| 11 | 70 | 43.5 | 0.037 | 0.016 |
| 12 | 100 | 50 | 0.055 | 0.020 |
| 13 | 100 | 51 | 0.060 | 0.021 |
| 14 | 75 | 44 | 0.038 | 0.016 |
| 15 | 70 | 43 | 0.037 | 0.016 |
| 16 | 98 | 52 | 0.066 | 0.023 |
| 17 | 82 | 53 | 0.070 | 0.024 |
| 18 | 51 | 51.5 | 0.062 | 0.022 |
| 19 | 15 | 51 | 0.062 | 0.022 |

[a]Average of planet disc (sky excluded).
[b]The random errors, including printout errors, are the same, except for Pictures 18 (0.023) and 19 (0.027).

## C. Correction of Pictures for Haze or Glare

The procedures described in the foregoing sections yield rather precise values of the light intensity incident upon each element of the vidicon target surface for the 21 individual pictures recorded: The absolute photometric precision attained may approach 10 or 15%, and relative intensities are probably known within a percent or so. However, the true brightness of the Martian surface is less well known because of the suspected presence of haze or glare in the pictures. Definite evidence that such effects are present was found in Picture 1 and in Pictures 19–22, and is also suggested by the seemingly very low contrast of the surficial features seen in the intermediate photographs.

In the first picture, the sky above the bright limb of the planet does not fall off in brightness as rapidly with altitude as would be expected on the basis of the 9-km-scale height of the Martian atmosphere. The apparent brightness of the sky at a height of about 150 km above the planet is nearly 40% that of the planet itself (Fig. III-15), whereas the atmospheric density at this height should be less than a millionth that at the surface.

In Picture 19, which includes the evening terminator, the brightness does not fall to zero at the terminator. Similarly, Pictures 20, 21, and the small part of of 22 that was recorded all exhibit brightnesses definitely distinguishable from the true black-sky as it was recorded several days after the completion of picture playback.

The value of the *Mariner IV* pictures for quantitative purposes, such as the evaluation of the slopes of crater

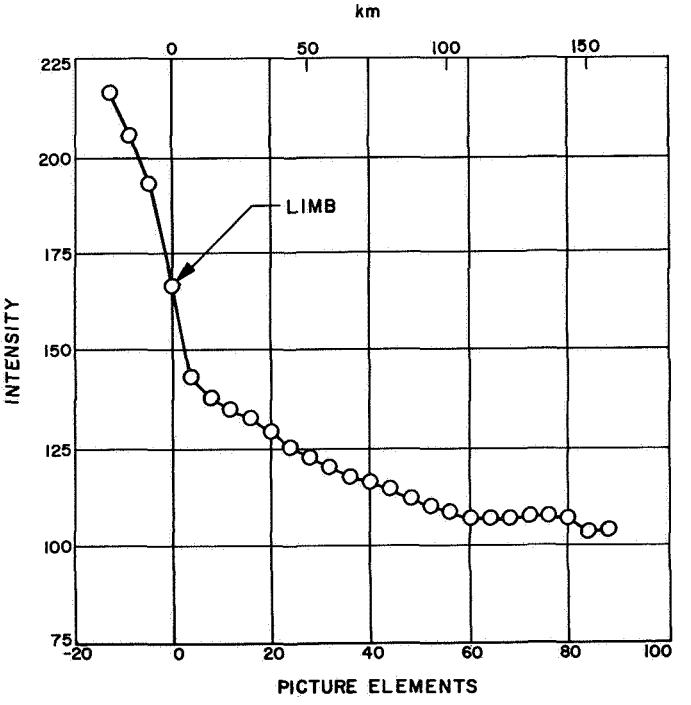


**Fig. III-15. Plot of intensity vs altitude above the planet for the sky area of Picture 1**

*The unit of intensity is that of a white Lambert surface situated normal to the sunlight at the orbit of Mars.*

walls, is of course dependent upon corrections for the haze or glare. However, the amount of scattered light present in the intermediate photographs cannot be determined unambiguously from the amounts seen in the limb and terminator pictures, because the physical origin of the light is not certain. If the scattered light is of instrumental origin, the large amount of glare in the first picture would indicate rather large amounts of glare in the intermediate pictures also. If, on the other hand, the light actually originates in the Martian atmosphere, the intermediate frames should then contain relatively small amounts of haze.

Arguments can be advanced both for and against each of these possibilities:

(1) Mars is known to have a very hazy (albeit low-density) atmosphere. Many observations from earth have indicated the presence of various kinds of clouds, some at heights of more than 25 km. Also, some current models of Mars' atmosphere suggest the presence of $CO_2$ crystals at even greater heights, up to perhaps 100 km. The observed glare showed inhomogeneities near the limb suggestive of thin clouds.

(2) The large amount of light present in the first picture at great heights above the limb, together with the small amount of residual atmosphere expected at such heights, argues against an atmospheric origin (Fig. III-15).

(3) The intensity distributions seen in Pictures 21 and 22 are relatively uniform whereas the height of the lowest illuminated portion of the atmosphere varies by about 100 km over each picture. If the scattered light originates in Mars' atmosphere, one would expect to see the scattered intensity in each picture fall off in a systematic way with increasing altitude above Mars at which the sunlight intercepts the line of vision, and to agree more or less from picture to picture. If the scattering is instrumental, the variation across a given picture might be quite small and could lead to the stepwise-changing function that is observed (Fig. III-16).

(4) Great care was used in the design and construction of the Cassegrain camera system to avoid scattered light. The design itself incorporated adequate shielding to hold the veiling glare below a few percent, even in the presence of extensive illumination outside the field of view. This property was tested, for each unit produced, under illumination conditions at least as severe as were encountered at

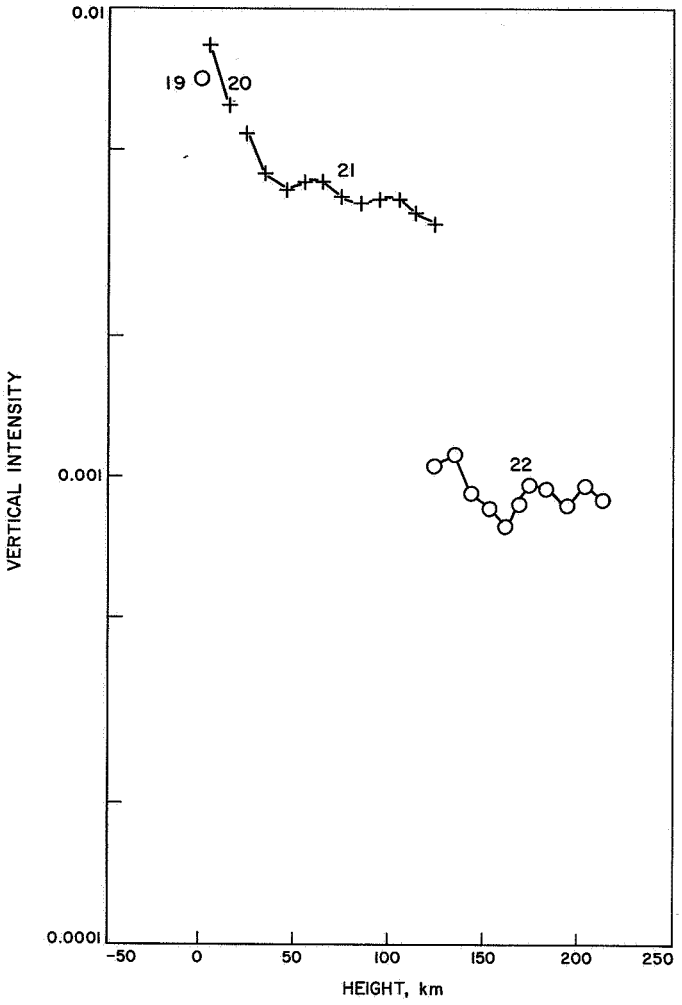


**Fig. III-16. Plot of scattered intensity from a vertical column of atmosphere vs the altitude of the bottom of the column above the planet**

Mars, and in no case was a veiling glare greater than 10% observed. The camera itself incorporated no paints or other volatiles that might evaporate and contaminate the optical surfaces. The vidicon tube was cushioned in polyurethane foam, but vapors from this unlikely source could have reached the filters or mirror surfaces only by leaking past a close-fitting, camera-mount-to-vidicon-face teflon gasket and through a rather tortuous path through the shutter mechanism. Attempts to simulate such contamination in a flight-type camera by rather extreme thermal-vacuum conditions were not successful.

(5) The mirrors were fabricated from pure beryllium, Kanigen-coated prior to polishing and figuring. This surface was aluminized and overcoated with $SiO_2$.

None of the *Mariner* camera units has exhibited any deterioration of the optical surfaces up to the time of writing, but other workers are said to have experienced some difficulty with blistering of such surfaces when exposed for long periods to high-vacuum conditions, and if so it is possible that blistering actually occurred in the flight unit. Studies of the effects of simulated blisters on the optical surfaces suggest that blisters, if present and of the right size and shape, could have produced considerable scattered light without serious loss in overall intensity. However, no quantitatively satisfactory agreement with the observed glare condition was obtained in these tests.

(6) Degradation of the primary mirror by micrometeorite bombardment is considered impossible in view of the very small micrometeorite flux registered by the cosmic dust experiment carried on the same spacecraft and the relatively well-protected location of the mirror.

(7) Contamination of the optical surfaces during handling and mounting is extremely unlikely. While on the launch pad the entire spacecraft shroud was held at a slight positive pressure by a flow of clean dry $N_2$ gas. During launch, stage separation, shroud ejection, spacecraft separation and *Agena* retro maneuver, the optics were protected by a close-fitting, teflon-gasketed, nearly-gas-tight cover. This cover was removed on February 11, 1965, 2½ months after launch. It is possible, but it seems unlikely, that contaminants from the launch environment could have leaked past the cover and into the optical system.

(8) Target leakage or other electronic effects were eliminated as possible origins of the haze by the dark-sky test carried out a few weeks after encounter.

None of the arguments outlined, nor any of the laboratory tests of optical systems, leads to a definite conclusion as to the actual nature of the observed effect. In order to study the matter further, and to deduce limiting values for the haze or glare in the individual photographs, the measured haze values in Pictures 1 and 19–22 were tested quantitatively for consistency with the two hypotheses of purely instrumental origin and purely atmospheric orgin.

A drawing was prepared which portrayed the disc of Mars as it was seen by the camera during the picture sequence, and the most prominent features were sketched in. The picture track was drawn and the picture centers approximately located. Isophotes were lightly sketched in, as they would appear if Mars were a uniform, Lambert sphere, and the normalized intensities seen in the pictures were plotted at the picture centers. The isophotes were then modified to accommodate these known intensity values and also to follow approximately the outlines of the dark areas and the polar cap. The result is shown in Fig. III-17. Relative intensities were then read from this drawing at points lying on a square grid at 1-deg spacings (as seen from the spacecraft).

A computer program was written which would evaluate the average intensity that would result in a given picture from any given axially symmetric scattering function specified at 0.5-deg intervals from 0.5 to 12.5 deg. Various scattering functions, mostly taken from the laboratory measurements on *Mariner*-type camera systems, were used with this program to estimate the relative amounts of glare to be expected in the photographs (Appendix F).

These calculations were in agreement in that any scattering function that gave approximately the observed intensities in Pictures 19–22 also gave far more scattered light in most of the intermediate pictures than could have been present. The glare in Picture 1 seemed to require mostly narrow-angle scattering, while Pictures 19–22 were better accounted for if the scattered light entered the system at an average angle of 6 or 7 deg from the axis. No wholly satisfactory fit was found.

In considering the possibility that the observed glare might be of atmospheric origin, an attempt was made to evaluate the approximate amount of light scattered by the atmosphere using Pictures 19–22 and, on the basis of this value, to calculate the expected glare for Picture 1. That such a procedure might prove successful can be seen by recalling that the scattering phase angle was a constant 60 deg throughout the encounter, and that the atmosphere at the terminator was illuminated obliquely but viewed approximately normally, while at the limb it was illuminated nearly normally but viewed obliquely. The scattering seen at the limb should therefore be much more intense than that at the terminator, as observed. Of course, only an approximate agreement is to be expected because of the quite different seasons and times of day at the two locations.

First, the actual scattered intensity in Pictures 19–22 was evaluated, using the $6 \times 6$ square averages described in the section on photometric calibration. Next, the altitude above the Martian surface at which the camera line

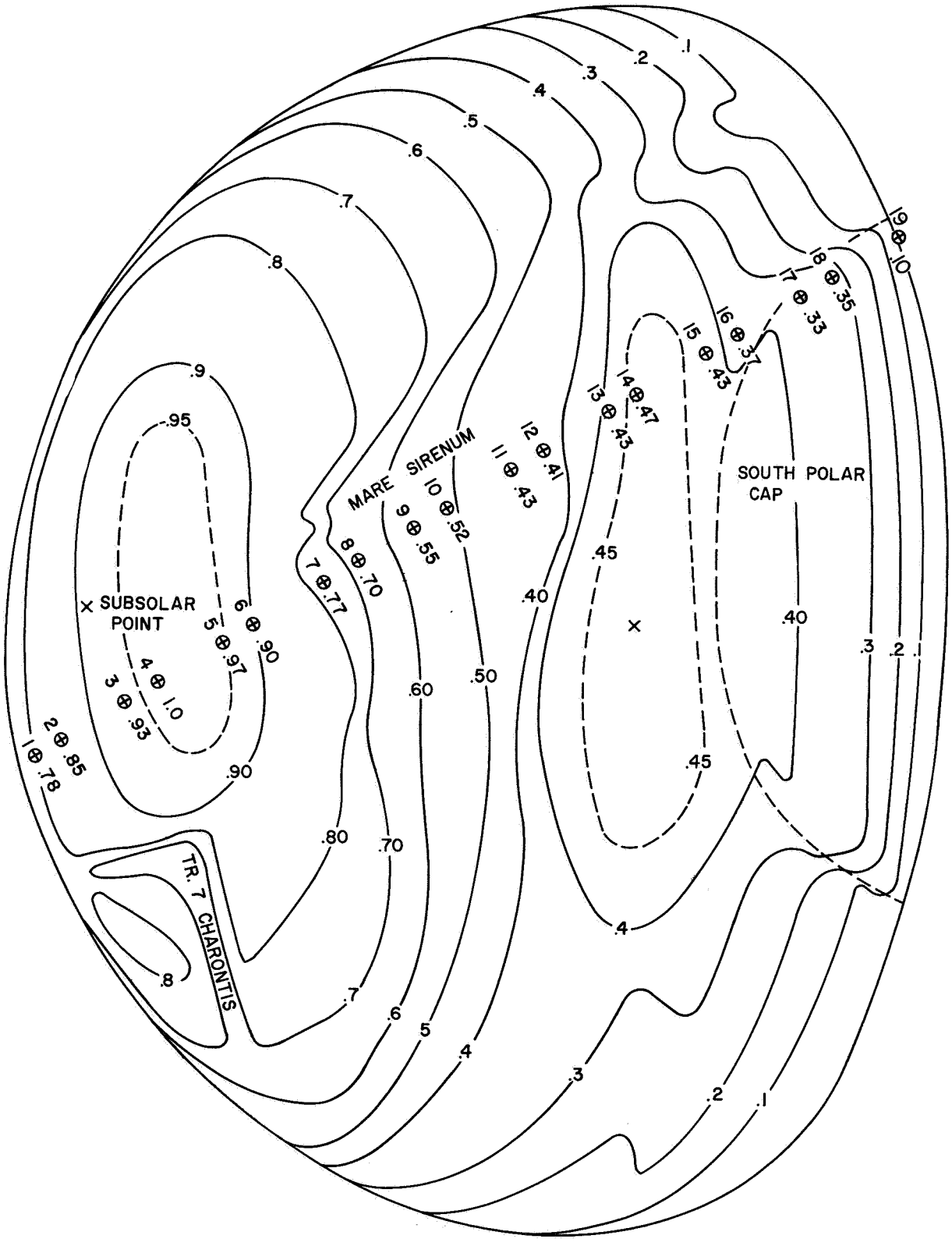


**Fig. III-17. Schematic intensity map of Mars as viewed by the spacecraft**

This chart was used to estimate the glare intensities seen by the vidicon for various assumed scattering functions.

of sight intersected the shadow edge of Mars was computed for each (averaged) picture point, and the corresponding zenith angle of the spacecraft as viewed from that intersection point was also found. Each picture intensity was then converted to an equivalent vertical view at the same phase angle, by multiplying by the cosine of the spacecraft zenith angle, and was correlated with the corresponding altitude. The various points associated with a given altitude were then averaged and the resulting curve plotted (Fig. III-16). This curve, for red pictures 20 and 21, indicated an average of approximately $3 \times 10^{-3}$ units of scattered intensity, in terms of the "reflectivity units" used to describe Mars intensities in this investigation. Further, the intensity seems to fall off on a height scale of about 50 km for low altitudes.

To estimate the amount of scattering to be expected near the limb in Picture 1, we neglect absorption of solar rays at slanting paths near the terminator and write the intensity seen in Picture 20 as

$$I_T \approx \sigma I_0 H$$

where $\sigma$ is an average scattering coefficient, $I_0$ is the intensity of incident sunlight (assumed to be at full vertical intensity at all points on the daylit hemisphere), and $H$ is the effective layer thickness (approx 50 km). Then, near the limb the scattered intensity should be

$$I_L \approx \sigma I_0 H'$$

where now $H' \approx 2(2RH)^{1/2}$ is the effective path length over which the scattered light is integrated, and $R = 3350$ km is the radius of Mars.

Thus we would expect an intensity ratio

$$\frac{I_L}{I_T} \approx \frac{H'}{H} \approx 2\left(\frac{2R}{H}\right)^{1/2} \approx 2\left(\frac{6700}{50}\right)^{1/2} \approx 23$$

between the limb and terminator. The observed ratio was about $140/10 = 14$.

We therefore conclude that the limb and terminator scattered light intensities might well be consistent with an atmospheric origin. Of course, a more thorough analysis would be required to establish the actual degree of compatibility of the two sets of data. We shall not pursue this rather complex problem here, but shall instead simply estimate the expected amount of haze in each picture if the scattering were atmospheric, on the assumptions outlined above. In this case, only the spacecraft zenith angle plays an important role. Taking $9 \times 10^{-3}$ units as the observed haze intensity in Picture 19 at the terminator,* we estimate the intensity in the $n$th picture as

$$I_n = 9 \times 10^{-3} \frac{\sec \varepsilon_n}{\sec \varepsilon_{19}}$$

where $\varepsilon_n$ is the average zenith angle of the spacecraft in the $n$th picture.

We now consider what actual amounts of haze or glare might be in each picture. Evidently the *minimum* amount of scattered light must be that due to clean optics plus the atmospheric haze just estimated, since any instrumental glare that would explain the light seen in Pictures 1 and 19–22 implies very high values in the intermediate pictures, as described previously.

In order to place a *maximum* value upon the glare, we make use of a test first called to our attention by Clyde Chadwick, a graduate student at Caltech. This test is based upon the idea that, in the absence of significant albedo variations, the brightest point in a given picture must be that place where the sun is most nearly normally incident upon the surface and, for a Lambert surface, the ratio of the average intensity for a horizontal surface to this maximum intensity must be greater than $\cos i$, where $i$ is the solar zenith angle. Thus

$$I_{av}/I_{max} \geqq \cos i$$

The equality would hold, in the absence of haze, if the Lambert surface were actually tilted so as to be perpendicular to the sun's rays.

If haze is present, it contributes equally to $I_{av}$ and $I_{max}$. Thus we have also

$$\frac{I_{av} - I_h}{I_{max} - I_h} \geqq \cos i$$

where, again, the equality implies actual normal incidence.

To apply this test, we may use the *Martian craters* as examples of topographic relief whose intensity variations are certainly indicative of slope illumination effects,

*The glare contribution of a clean optical system was estimated to be $3 \times 10^{-3}$ units; the total intensity at the terminator was $12 \times 10^{-3}$ units.

albeit possibly somewhat modified by local albedo variations. Suitable examples were found in Pictures 7, 9, and 11, and these gave quite consistent haze values

$$I_h \leq \frac{I_{av} - I_{max} \cos i}{1 - \cos i}$$

which ranged from 0.3 $I_{av}$ to 0.5 $I_{av}$.

The haze estimates are summarized in Fig. III-18, which indicates the maximum and minimum intensities seen in each picture, together with limits and estimates of the haze contribution to each picture.

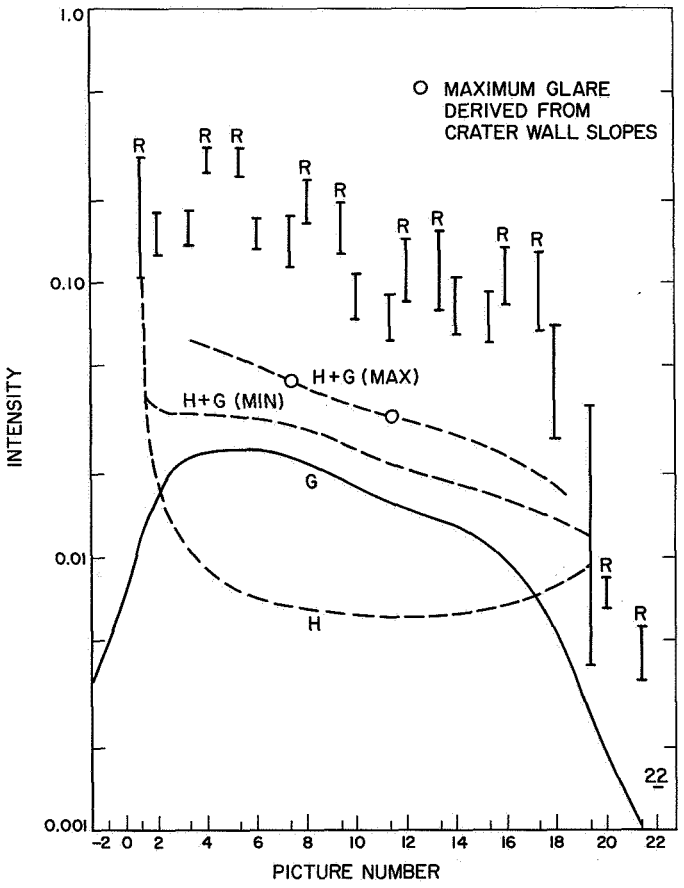


**Fig. III-18. Plot of maximum and minimum intensities observed in each picture, the glare contribution from a clean camera (curve *G*), the estimated atmospheric scattering (curve *H*), and total haze and glare effects (curve *H* and *G MIN*), vs picture number**

The maximum background haze and glare are also shown, as estimated from crater wall intensities according to a procedure described in the text (curve *H* plus *G MAX*).

Our tentative conclusion is that the observed scattered light in the *Mariner IV* pictures is probably accounted for by a combination of scattering by the clean optics, plus a significant scattering by the Martian atmosphere.

## D. Sine-Wave Response Function of the Camera System

As part of the comprehensive preflight calibration tests, the sine-wave response function of the camera system was measured by photographing sinusoidal intensity patterns of various wavelengths and contrasts, the waves being aligned approximately horizontally or vertically in the camera field (see Appendix B). As with the other calibration tests, the digital data numbers were tape recorded for convenient analysis by computer. Both high-contrast (12:1) and low-contrast (3:1) patterns were photographed. Only the high-contrast data were analyzed.

The data were first converted to pictorial form in the VFC, and the photographs were measured to find the wavelengths of the various sine waves in terms of picture elements. Appropriate rectangular domains in each picture over which the Fourier amplitudes of the sine waves could be determined were also found.

The digital DN's were converted to true intensities using the flat-field calibration data as described previously in this section. The Fourier amplitude $A_n$ of each sine wave was determined by integrating over its domain described above, and the normalized amplitude $A_n/I_{av}$ was evaluated, where $I_{av}$ is the average intensity. This quantity was in turn divided by the corresponding normalized amplitude of the original transparency, measured with a scanning microphotometer.

The essential data concerning the wavelengths, domains, and Fourier amplitudes are presented in Table III-7. A graph of the results is shown in Fig. III-19.

The shape of the sine-wave response of the system is rather well described by a two-dimensional gaussian function having slightly different widths in the horizontal and vertical directions. The point spread function

$$S(x, y) = (2\pi\sigma_x \sigma_y)^{-1/2} \exp\left(-x^2/2\sigma_x^2 - y^2/2\sigma_y^2\right)$$

where $x$ and $y$ are measured in units equal to the TV line spacing and

$$\sigma_x = 0.65, \qquad \sigma_y = 0.85$$

was found to agree quite satisfactorily with the sine-wave response data.

**Table III-7. Sine-wave response data[a]**

| File No. | Line direction | λ (elements) | Domain | | | | $A_n/I_{av}$ | | Response | $4\pi^2/\lambda^2$ |
|---|---|---|---|---|---|---|---|---|---|---|
| | | | ≤ L ≤ | | ≤ E ≤ | | observed | nominal[b] | | |
| 10 | V | 22.75 | 65 | 150 | 69 | 159 | 0.73 | 0.82 | 0.89 | 0.076 |
| 12 | V | 11.667 | 55 | 145 | 124 | 158 | 0.69 | 0.80 | 0.86 | 0.292 |
| 12 | V | 7.80 | 55 | 145 | 65 | 103 | 0.615 | 0.82 | 0.75 | 0.650 |
| 14 | V | 5.778 | 60 | 150 | 119 | 170 | 0.595 | 0.82 | 0.725 | 1.19 |
| 14 | V | 3.83 | 60 | 150 | 67 | 112 | 0.428 | 0.84 | 0.51 | 2.70 |
| 16 | V | 2.88 | 50 | 140 | 62 | 110 | 0.250 | 0.86 | 0.29 | 4.75 |
| 16 | V | 2.33 | 50 | 140 | 131 | 165 | 0.168 | 0.85 | 0.198 | 7.30 |
| 18 | V | 1.937 | 56 | 146 | 63 | 93 | 0.070 | 0.85 | 0.082 | 10.5 |
| 18 | V | 1.45 | 56 | 146 | 128 | 156 | 0.019 | 0.88 | 0.022 | 18.7 |
| 11 | H | 26.25 | 53 | 157 | 86 | 160 | 0.725 | 0.82 | 0.885 | 0.057 |
| 13 | H | 12.667 | 56 | 93 | 75 | 150 | 0.615 | 0.80 | 0.77 | 0.246 |
| 13 | H | 9.40 | 118 | 164 | 75 | 150 | 0.575 | 0.82 | 0.70 | 0.450 |
| 15 | H | 6.28 | 48 | 91 | 87 | 162 | 0.460 | 0.82 | 0.56 | 1.00 |
| 15 | H | 4.583 | 100 | 154 | 87 | 162 | 0.357 | 0.84 | 0.425 | 1.88 |
| 17 | H | 3.500 | 109 | 164 | 85 | 150 | 0.238 | 0.86 | 0.28 | 3.24 |
| 17 | H | 2.526 | 47 | 94 | 85 | 150 | 0.122 | 0.85 | 0.145 | 6.20 |
| 19 | H | 2.32 | 103 | 160 | 70 | 150 | 0.088 | 0.85 | 0.104 | 7.35 |
| 19 | H | 1.587 | 45 | 90 | 70 | 150 | 0.014 | 0.88 | 0.016 | 15.8 |

[a]From Calibration Data Tape K-76, Files 10–19.

[b]Ratio determined by microphotometer measurement of original film.

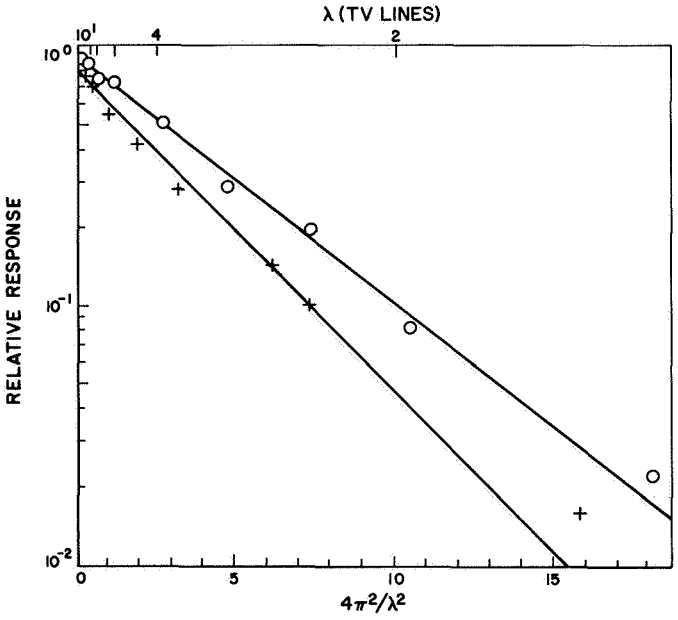


**Fig. III-19. Plot of modulation transfer function (relative response vs sine-wave wavelength)**

The plot is such that a Gaussian point-spread function would give a straight line.

Having determined a suitable point-spread function for the overall optical system, it is possible to correct the pictures for the effects of this function. Let $R(k, l)$ be the Fourier transform (FT) of the point-spread function, and let $M(x', y')$ be the inverse FT of $1/R$. Then the corrected intensity $I_c(x, y)$ is given by the convolution integral

$$I_c(x, y) = \iint I(x - x', y - y')\, M(x', y')\, dx'\, dy'$$

In practice, the correction for falloff of the sine-wave response must be carried out with care to avoid spurious effects due to the finite accuracy of the digital intensity field and of the point-spread function itself. If carried too far, the correction process may result in a grainy picture dominated by the point-to-point DN fluctuations. It was found that if the short-wavelength Fourier terms were multiplied by a factor as great as 5, the corrected picture contained an objectionable amount of graininess. A maximum correction of a factor of 3 was adopted, since this led to a significant sharpening of fine detail without undue graininess.

The function $M(x', y')$ was accordingly taken as the inverse FT of a truncated inverse gaussian, being equal to $1/R$ for $|R| \geq 1/3$ and equal to 3 for $|R| < 1/3$. This inverse transform was presented in the form of a $15 \times 15$ element matrix* (Table III-8), and the convolution integral was evaluated as a summation over the 225 elements in a $15 \times 15$ square centered on the element of interest:

$$I_c(L, E) = \sum_{-7}^{+7} \sum_{-7}^{+7} I(L - L', E - E') M(L', E')$$

Near the boundaries, the picture was continued as necessary by reflecting across the boundary.

The effect of this sharpening process is to increase the sharpness and contrast of fine detail while leaving large-scale features unaffected. Although at first sight the sharpened pictures appear noticeably grainier than the originals, a little study reveals a great deal of detail that is only marginally visible in the unsharpened pictures. Sharpened versions of all pictures are included in the section on analysis and interpretation of the photographs.

## E. Treatment of Color Overlap Areas

One reason for incorporating two different types of color filter in the *Mariner IV* camera system was to study color variations across those areas of the Martian surface where successive pictures overlapped. Although the data obtained are roughly equivalent to a two-color photograph,** it was not intended that the two pictures should be combined to form a color picture, and many factors combine to prevent the direct interpretation of the digital data as indicative of any specific color. Indeed, even after transformation into true intensities the problem is not straightforward, even with respect to the more limited goal of ascertaining whether real color differences exist from place to place. Among these factors are the following:

(1) Electronic shading and optical vignetting effects in the camera and vidicon system introduce gradients into the picture which are accentuated by the fact that the overlap area between two pictures lies in extreme opposite corners of the two frames.

(2) Geometrical distortions introduced by nonlinearities in the electron beam deflection pattern cause the overlapping area to be of slightly different shape in the two pictures, so that exact registration of the pictures is impossible.

(3) Systematic variations in the transmission curves of the red and green filters over the focal plane may introduce a few percent of systematic shading that cannot be removed by calibration.

(4) The "ghost" of the previous picture may contribute significantly to the difference between two pictures. This was especially marked in Pictures 1 and 2, but must have been present in other pictures to a lesser extent, and could mask or alter the true color effects.

(5) The color filters were chosen so as to maximize the spectral separation of the two color bands without undue loss of light, and to equalize the two signal amplitudes. The resulting spectral sensitivity curves are not standard ones for color separation work.

(6) Because the pictures were of such low contrast, a true color reproduction would be essentially featureless; any color differences that were present would tend to be very subtle. Enhancement of the contrast of the original pictures before color printing would accentuate any color differences that might be present, but would also alter the colors themselves.

(7) The original data contained periodic fluctuations due to unidentified electrical pickup, probably in the preamplifier electronics. Only a part of this signal, the fundamental frequency, could be removed from the pictures, and even this could be removed only approximately. The combination of two such patterns with random phase leaves significant periodic signal present in some of the color overlap areas.

Considerable care was used to avoid or at least minimize the problems just discussed. The picture intensities were carefully calibrated, and the geometrical distortions were corrected, as described in the section on intensity and color calibration. The overlap areas themselves were found by superimposing large transparencies of the geometrically corrected pictures, placing corresponding surface features in register. Table III-9 shows the required picture offsets. New pictures were then produced, in which the overlapping areas corresponded to the same

*We are indebted to Robert H. Selzer of the Jet Propulsion Laboratory for computing the sharpening matrices used in this work.

**The fact that only two successive pictures could overlap precluded the use of a full three-color separation filter system. However, the expected character of a "blue" picture, had it been obtained, would be that of a uniform, featureless field because of the strong atmospheric contribution to the light reflected by Mars in the blue. Thus one might hope to reconstruct an approximation to the true three-color scene by simply adding a small amount of unfocussed blue light to the red and green pictures that were obtained.

**Table III-8. Picture sharpening matrix**

| | | | | | | | | | | | | | | |
|---|---|---|---|---|---|---|---|---|---|---|---|---|---|---|
| 0.0014 | 0.0011 | −0.0026 | −0.0019 | 0.0026 | 0.0052 | 0.0048 | 0.0042 | 0.0048 | 0.0052 | 0.0026 | −0.0019 | −0.0026 | 0.0011 | 0.0014 |
| 0.0019 | −0.0015 | −0.0025 | 0.0031 | 0.0050 | −0.0002 | −0.0055 | −0.0072 | −0.0055 | −0.0002 | 0.0050 | 0.0031 | −0.0025 | −0.0015 | 0.0019 |
| 0.0008 | −0.0031 | 0.0012 | 0.0052 | −0.0026 | −0.0103 | −0.0091 | −0.0068 | −0.0091 | −0.0103 | −0.0026 | 0.0052 | 0.0012 | −0.0031 | 0.0008 |
| −0.0010 | −0.0022 | 0.0047 | 0.0003 | −0.0104 | −0.0023 | 0.0146 | 0.0209 | 0.0146 | −0.0023 | −0.0104 | 0.0003 | 0.0047 | −0.0022 | −0.0010 |
| −0.0024 | 0.0000 | 0.0050 | −0.0068 | −0.0057 | 0.0215 | 0.0270 | 0.0173 | 0.0270 | 0.0215 | −0.0057 | −0.0068 | 0.0050 | 0.0000 | −0.0024 |
| −0.0030 | 0.0021 | 0.0029 | −0.0105 | 0.0084 | 0.0274 | −0.0378 | −0.0965 | −0.0378 | 0.0274 | 0.0084 | −0.0105 | 0.0029 | 0.0021 | −0.0030 |
| −0.0031 | 0.0034 | 0.0007 | −0.0103 | 0.0195 | 0.0045 | −0.1606 | −0.2804 | −0.1606 | 0.0045 | 0.0195 | −0.0103 | 0.0007 | 0.0034 | −0.0031 |
| −0.0031 | 0.0038 | −0.0003 | −0.0097 | 0.0230 | −0.0118 | −0.2252 | 2.6267 | −0.2252 | −0.0118 | 0.0230 | −0.0097 | −0.0003 | 0.0038 | −0.0031 |
| −0.0031 | 0.0034 | 0.0007 | −0.0103 | 0.0195 | 0.0045 | −0.1606 | −0.2804 | −0.1606 | 0.0045 | 0.0195 | −0.0103 | 0.0007 | 0.0034 | −0.0031 |
| −0.0030 | 0.0021 | 0.0029 | −0.0105 | 0.0084 | 0.0274 | −0.0378 | −0.0965 | −0.0378 | 0.0274 | 0.0084 | −0.0105 | 0.0029 | 0.0021 | −0.0030 |
| −0.0024 | 0.0000 | 0.0050 | −0.0068 | −0.0057 | 0.0215 | 0.0270 | 0.0173 | 0.0270 | 0.0215 | −0.0057 | −0.0068 | 0.0050 | 0.0000 | −0.0024 |
| −0.0010 | −0.0022 | 0.0047 | 0.0003 | −0.0104 | −0.0023 | 0.0146 | 0.0209 | 0.0146 | −0.0023 | −0.0104 | 0.0003 | 0.0047 | −0.0022 | −0.0010 |
| 0.0008 | −0.0031 | 0.0012 | 0.0052 | −0.0026 | −0.0103 | −0.0091 | −0.0068 | −0.0091 | −0.0103 | −0.0026 | 0.0052 | 0.0012 | −0.0031 | 0.0008 |
| 0.0019 | −0.0015 | −0.0025 | 0.0031 | 0.0050 | −0.0002 | −0.0055 | −0.0072 | −0.0055 | −0.0002 | 0.0050 | 0.0031 | −0.0025 | −0.0015 | 0.0010 |
| 0.0014 | 0.0011 | −0.0026 | −0.0019 | 0.0026 | 0.0052 | 0.0048 | 0.0042 | 0.0048 | 0.0052 | 0.0026 | −0.0019 | −0.0026 | 0.0011 | 0.0014 |

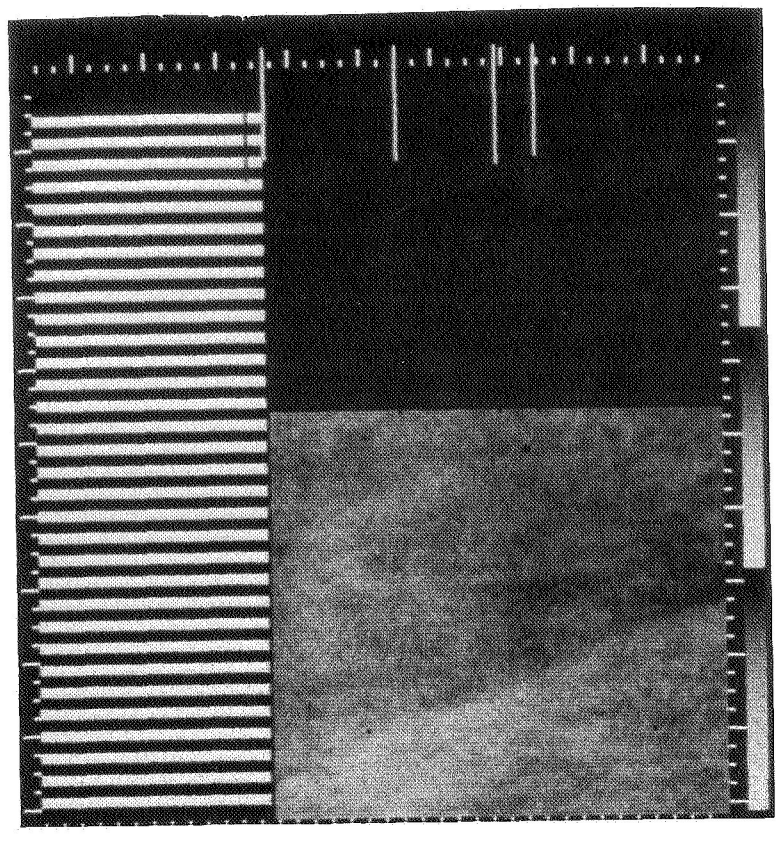

(a) PICTURES 1 AND 2

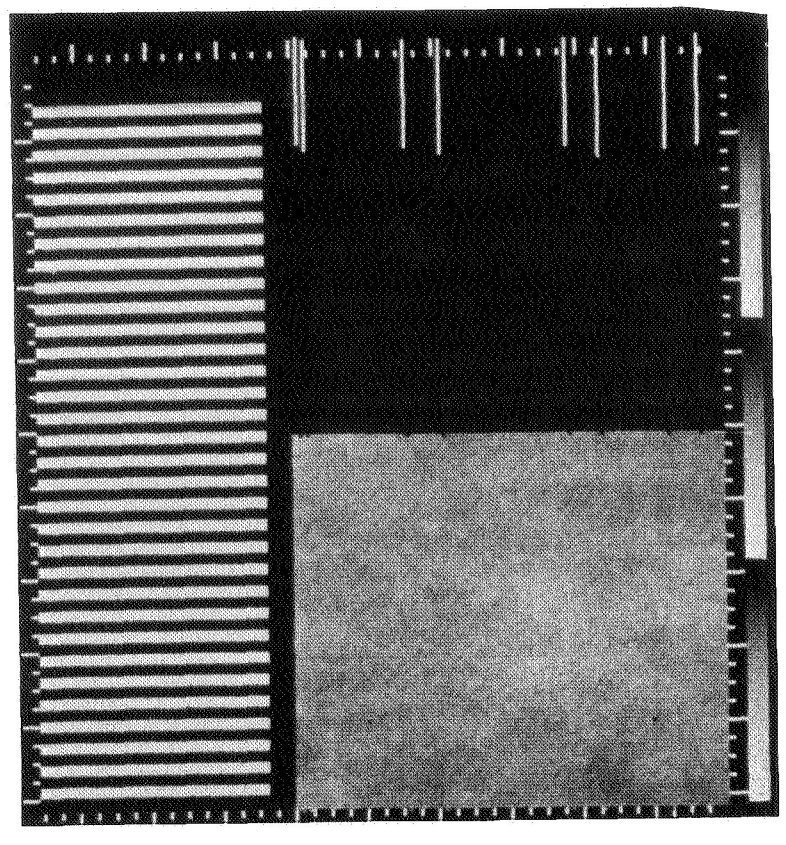

(b) PICTURES 3 AND 4

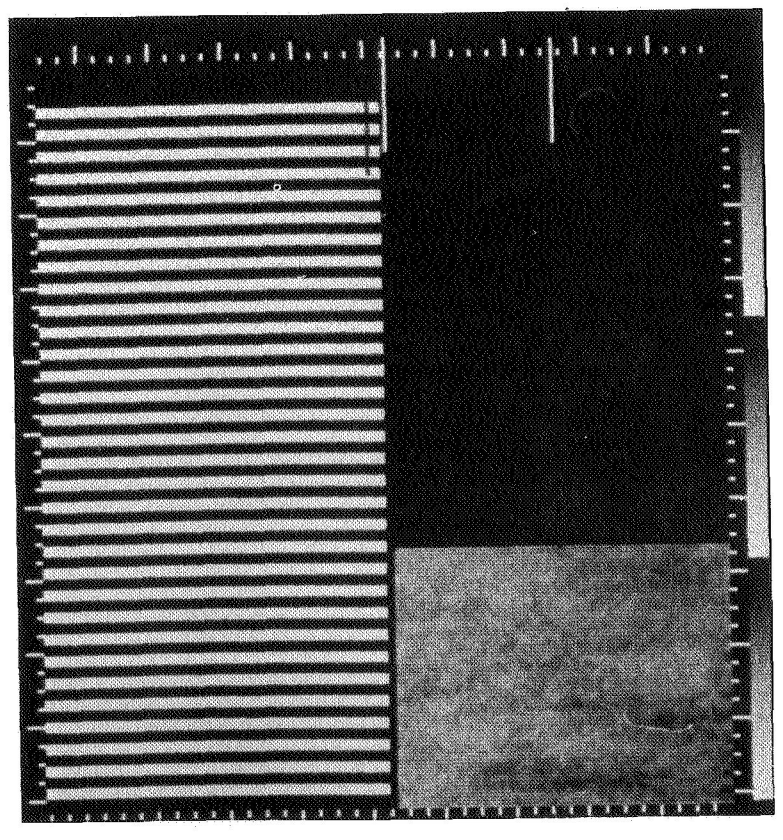

(e) PICTURES 9 AND 10

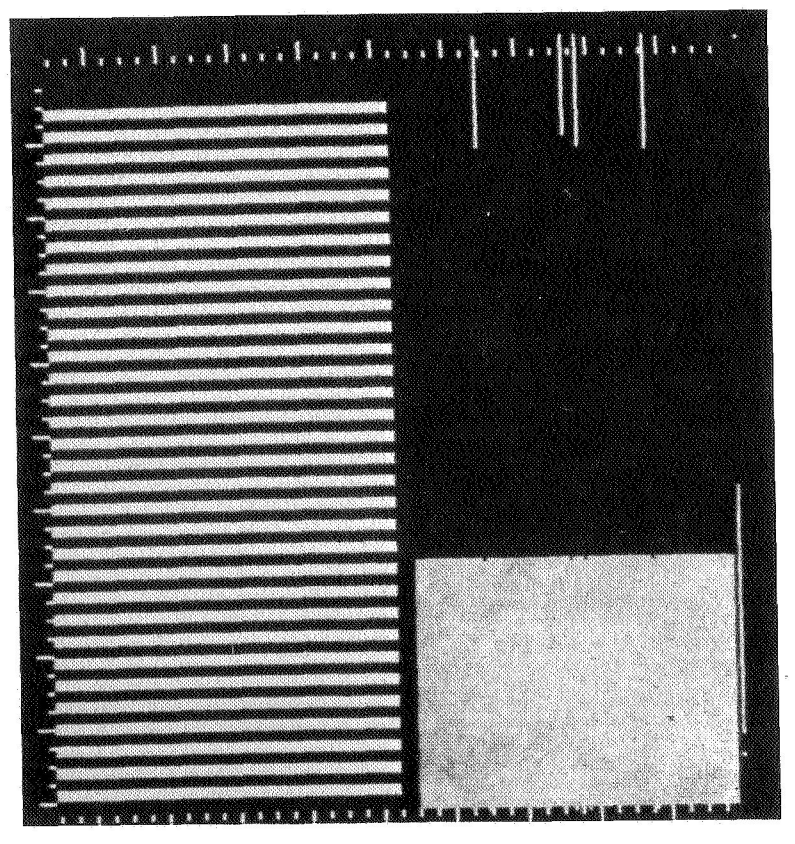

(f) PICTURES 11 AND 12



61-A

61-B

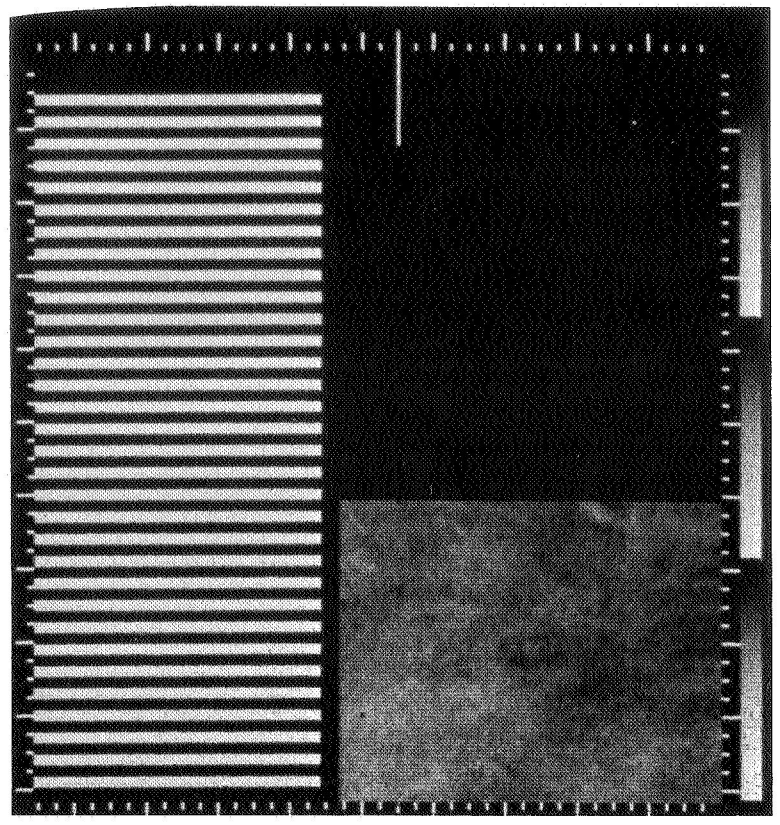

(c) PICTURES 5 AND 6

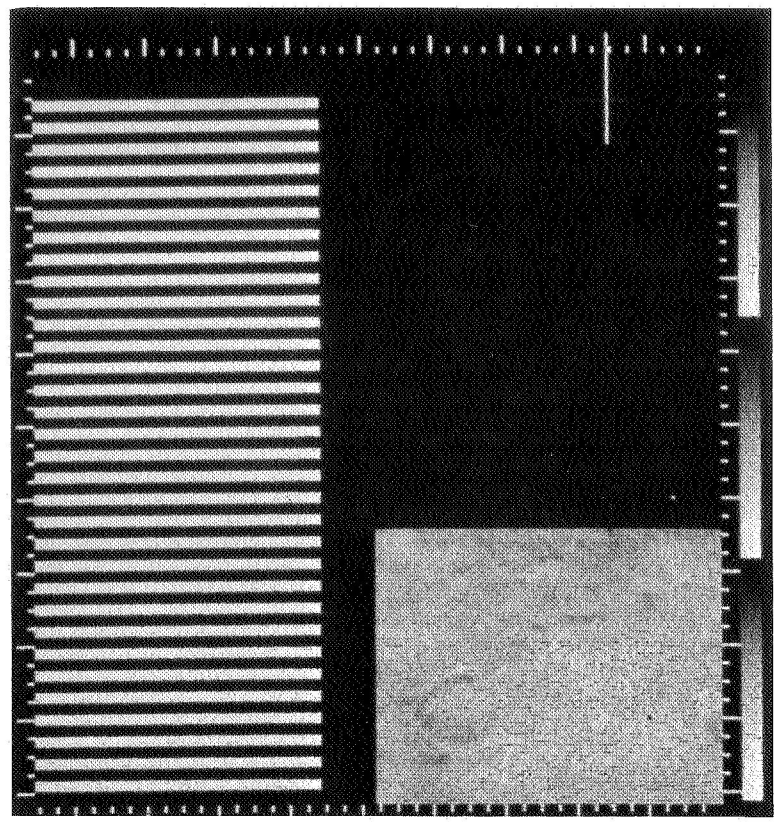

(d) PICTURES 7 AND 8

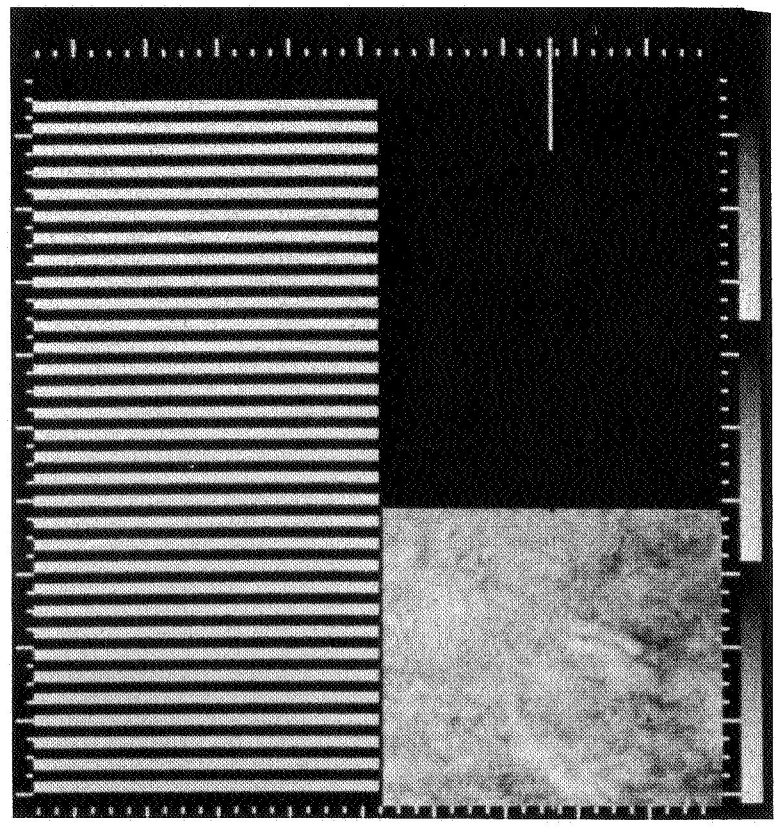

(g) PICTURES 13 AND 14

**Fig. III-20. Color intensity ratio pictures of overlap areas of Pictures 1–14**

**The intensity ratio $\rho_G/\rho_R$ was evaluated at each picture point and converted into an integer in the range 0–63. The "polarity" is such that greener areas appear lighter in tone.**

**Table III-9. Relative displacements of overlapping pictures**

| Fixed picture / Displaced picture | Displacement ΔL | ΔE |
|---|---|---|
| 1/2 | −64 | 82 |
| 3/4 | −70 | 91 |
| 5/6 | −84 | 111 |
| 7/8 | −95 | 118 |
| 9/10 | −98 | 122 |
| 11/12 | −100 | 125 |
| 13/14 | −96 | 112 |

coordinate ranges in a given pair of pictures. (In this operation the small amounts of rotation about the camera axis from frame to frame that resulted from attitude drift of the spacecraft were found to be negligible, so that the picture elements in the overlap area were in one-to-one correspondence.)

From this point, two approaches were used to study colors and color differences. One method, carried out at the JPL Photography Section laboratory by Ronald J. Wichelman, was to treat the red and green overlap pictures as color separation negatives, combining them into color prints using the standard color filters. Relative exposures for the red and green negatives and an appropriate amount of yellow (minus blue) were determined so that a 64-step intensity wedge included in the overlap pictures appeared neutral gray in the color print. The pictures showed some color variation from picture to picture, but relatively little variation within a given picture. The results of this approach were, as expected, rather uninteresting.

The second method used to reveal color differences was to compute the ratio $\rho_G/\rho_R$ of the green and red intensities at each picture point and convert this ratio, suitably enhanced in contrast, into a black and white picture. A gray color (equal spectral reflectance at all wavelengths) would give a ratio $\rho_G/\rho_R = 1.00$; a reddish color would correspond to a ratio less than unity, and a greenish one to a ratio greater than unity. This approach has certain advantages over an actual color picture. First, it avoids many of the subjective effects which unavoidably enter into color photography, while still presenting the results in pictorial form. Second, the procedures are simpler to carry out and the pictures are easier to reproduce. Third, and most important, an intensity ratio expresses the "color" of a picture point in a way that is independent of the *brightness* of that point.

The results of the second approach are shown in Fig. III-20. These pictures were printed in such a way that "black" corresponds to a ratio $\rho_G/\rho_R = 0.710$, and "white" corresponds to a ratio $\rho_G/\rho_R = 0.510$. The advantage of this method is immediately evident in the ratio map of Pictures 1, 2. What appears in the corresponding color print as a trend from a reddish tone near the limb to a greenish one farther onto the planet is now seen as a sharp line of demarcation parallel to the limb. The position of this line in the green picture, No. 2, agrees precisely with the limb position in the red picture No. 1. In fact, this ratio map provides the only quantitative evidence available concerning the erasure efficiency during the operation of the camera system at the time of encounter. From it, one finds that approximately 10% of the intensity of a given exposure appears as a "ghost" in the following exposure. This will have the effect both of distorting the average color ratio and of introducing spurious "color" fine structure, just as is seen in Pictures 1, 2. Thus care must be used in interpreting the apparent colors that appear in the overlap areas.

Pictures 3, 4 show very little color variation. Pictures 5, 6 show some variation, particularly in the eastern portion. Pictures 7, 8 seem lighter (greener) and show some interesting apparent color detail around the rim of the prominent crater at P7 L74 E177. The effect, although small, is well outside the rms error limits discussed elsewhere in this chapter. Such an appearance could result from incorrect registration of the two pictures, and upon carefully checking the detailed intensity profiles across this area, it was found that the adopted average displacement for this picture pair was in error by one picture element in this region, an amount sufficient to produce the observed effect.

Pictures 9, 10 seem to show some color variation, but close inspection of the pictures themselves reveals that this is at least partly due to residual harmonic noise present in Picture 9. Some of the shading may be due to real color variations, however.

Pictures 11, 12 reveal little detailed color variation, but the lighter appearance of this picture indicates an overall greener color for this area.

Pictures 13, 14 show a "greenish" ring associated with a crater that appears to be ringed by frost. The color ratio is near unity (gray) in the "greener" parts of this picture, while other nearby areas show a relatively red

color corresponding to a ratio $\rho_G/\rho_R$ of approximately 0.55. The average value of $\rho_G/\rho_R$ is about 0.60.

To summarize, the color of Mars, as indicated by the green-to-red intensity ratios, is generally reddish, but attains a less red color in a few places. There is little detailed color variation to be seen, but a few small but significant color variations may be present. The color trends observed in the pictures agree generally with those expected on the basis of the kinds of terrain covered in the pictures: light areas ("desert") tend to be redder than dark areas ("mare").

# Appendix A

# The Spacecraft*

## I. Introduction

The *Mariner* Mars 1964 spacecraft weighed 261 kg, stood 2.9 meters high, and had a span of 6.85 meters, including solar panels and pressure vanes. Designed primarily for scientific and television experiments near Mars, the spacecraft was built to operate in space for at least 6,000 hr. Photovoltaic cells were mounted on solar panels which (during flight) had a fixed orientation with respect to the spacecraft body structure. The sun and Canopus provided the references for stabilizing the attitude of the spacecraft. The sensors, instruments, and electromechanical devices that made up the visible configuration are illustrated in Figs. A-1 and A-2.

A telecommunication system (consisting of the radio, command, and data encoder subsystems) not only provided telemetering capability to ground stations and command capability to the spacecraft, but also furnished extremely precise measurements of the spacecraft's radial velocity and range, which were used for determining its orbit. A central computer and sequencer (CC&S) provided the timing for events such as solar-panel deployment, control and sequencing of the attitude control system, events related to planetary encounter, changes in spacecraft data rate, and antenna switching. The command subsystem decoded and routed 30 possible commands that could be transmitted to the spacecraft. The data encoder, operating in four data modes, sampled 100 engineering measurements while operating at either of two rates, 8⅓ or 33⅓ bps.

## II. Structure

The *Mariner* spacecraft structure consisted of a basic octagonal frame, the superstructure, solar panel mounting, boost dampers, panel deployment area, and the science platform. In its eight "bays," the octagonal frame housed six electronic assemblies, a battery and power subsystem, and supported the postinjection propulsion system. The base of the octagon provided the structural portion of the spacecraft, including the launch vehicle interface.

### A. Superstructure

The superstructure supported the high-gain antenna, the solar panels (through their boost dampers), one low-gain antenna damper, the cosmic dust detector and the upper thermal shield. The superstructure was an eight-member aluminum truss at the top of which a ring was formed to mount the high-gain antenna. At the base of this welded superstructure were four feet for attaching it to the octagonal frame (Fig. A-3).

### B. Solar Panels

Electrical power was provided by four solar panels, each of which consisted of a corrugated substrate on which photovoltaic cells were bonded. Intercostals, diagonal cross braces and an outboard end beam were installed between spars to provide rigidity to the structure. The end beam also provided mounting surfaces for attitude control plumbing, gas jets, and solar pressure vane assemblies. A pair of elastically supported guide rails was installed to protect the solar panels from impact and possible damage by the shroud as it was ejected from the launch vehicle. The panels were hinged so that they could be stowed relatively compactly during launch, and were deployed into a fixed position during the cruise phase (Fig. A-4).

### C. Boost Dampers

Solar panel boost dampers were provided to position the solar panel during ground operations and during the boost phase of the mission, and to reduce the vibrational environment seen by the solar panel. The low-gain antenna dampers were provided to position the low-gain antenna at all times and to reduce the antenna's vibrational environment during the boost phase.

### D. Panel Deployment Area

The solar panels were held in their stowed (vertical) position by two boost dampers per panel. Explosive-squib pinpullers were actuated after separation of the spacecraft from the *Agena* to deploy the panels to their cruise position. Deployment was motivated by clock-type coil springs. To reduce panel flapping during midcourse motor burn, panel cruise dampers were provided. To maintain contact between the panel and the cruise damper during midcourse vibration, latches were used. Cruise dampers arrested the deployment motion of the solar panels, positioned the panels during flight, and coupled the spacecraft bus and solar panels dynamically (Fig. A-5).

*A complete description of the *Mariner IV* spacecraft can be found in JPL Technical Report 32-740 (*Mariner Mars 1964 Project Report: Mission and Spacecraft Development*), March 1, 1965.

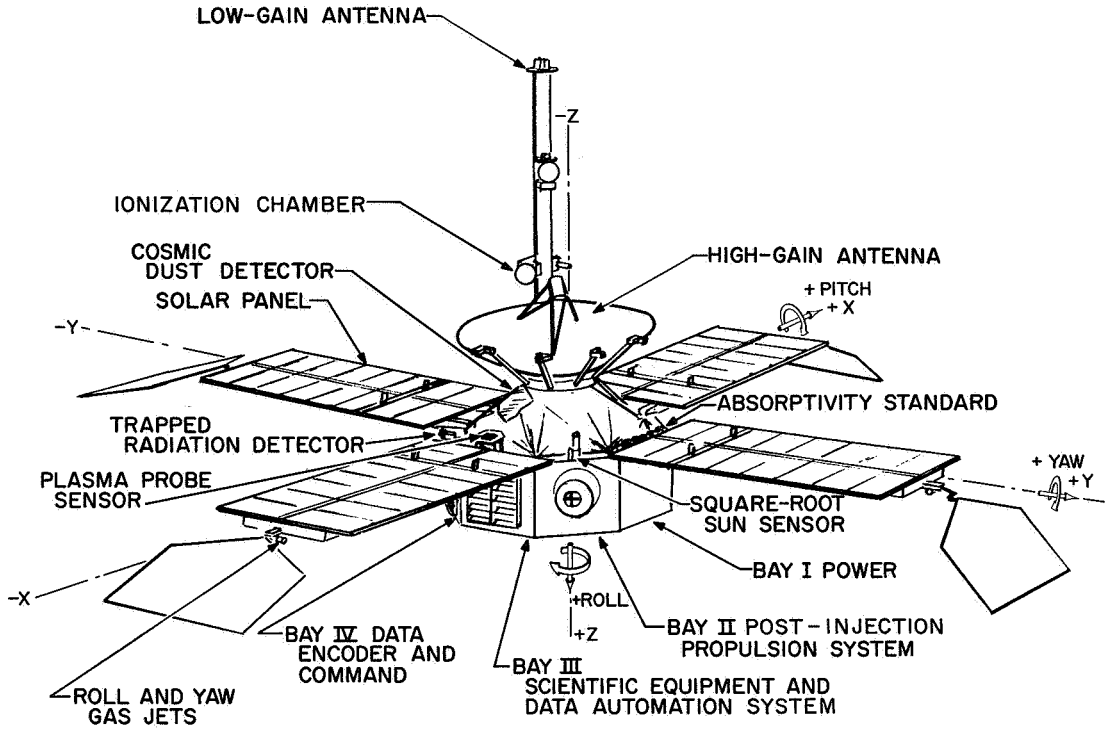


**Fig. A-1. *Mariner* Mars 1964 spacecraft: top view**

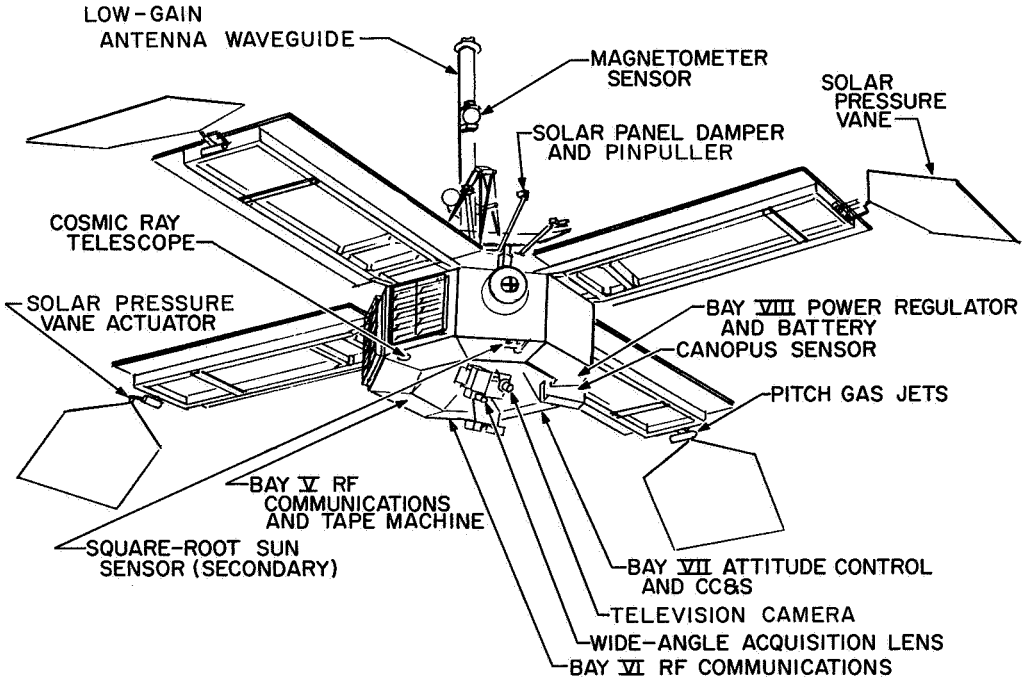


**Fig. A-2. *Mariner* Mars 1964 spacecraft: bottom view**

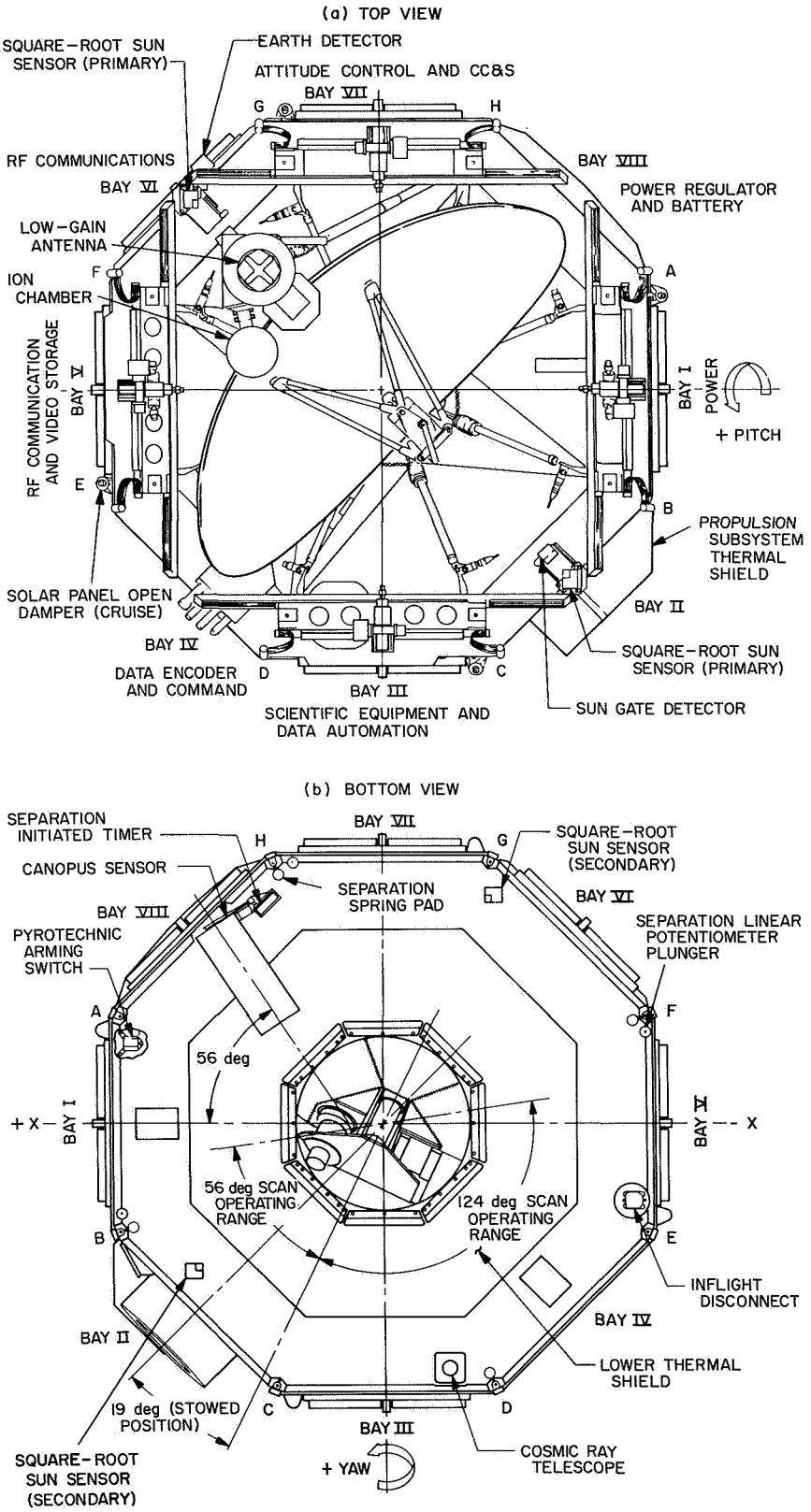


**Fig. A-3. Spacecraft mechanical configuration: top and bottom views**

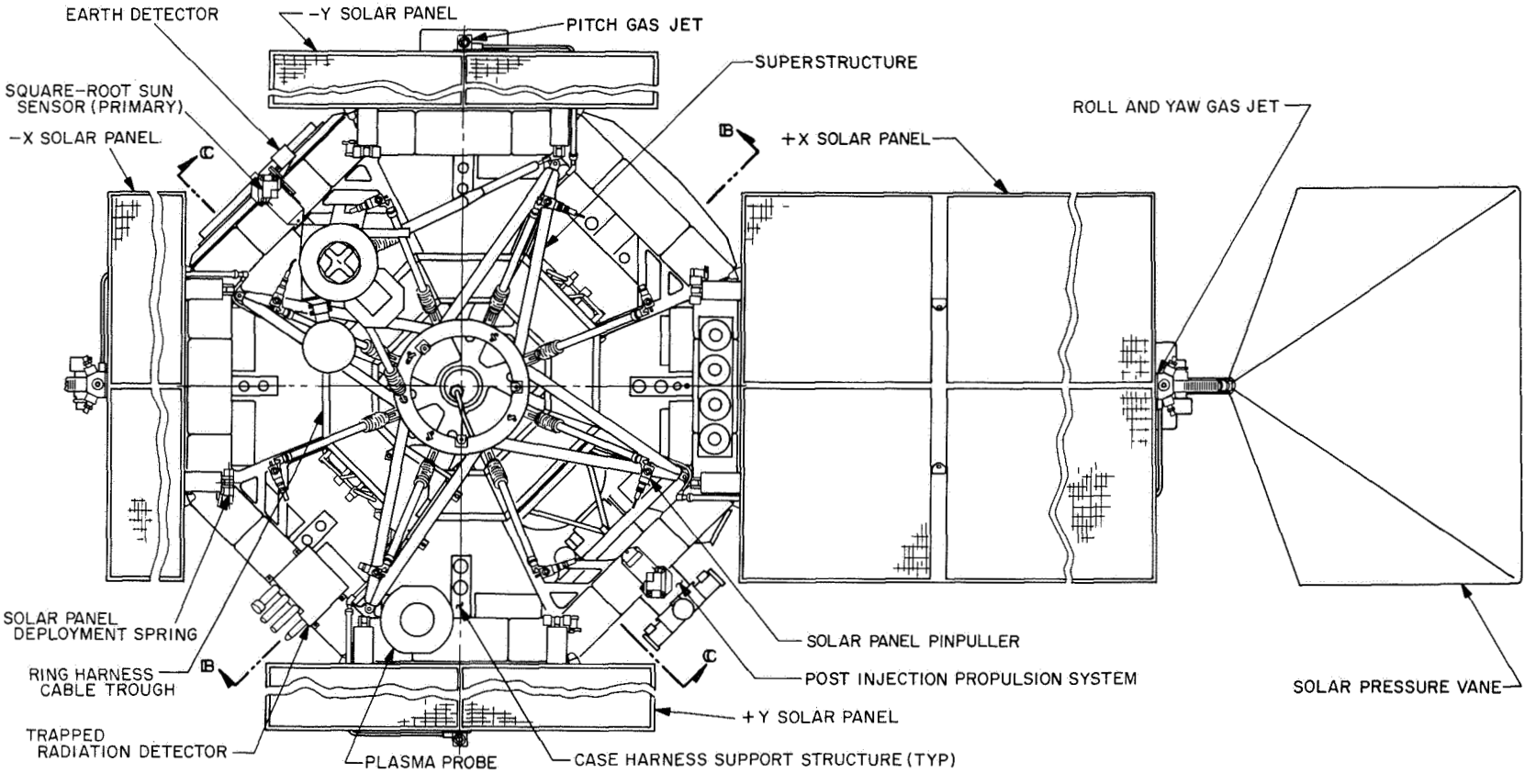


**Fig. A-4. Spacecraft mechanical configuration: top view, solar panels extended**

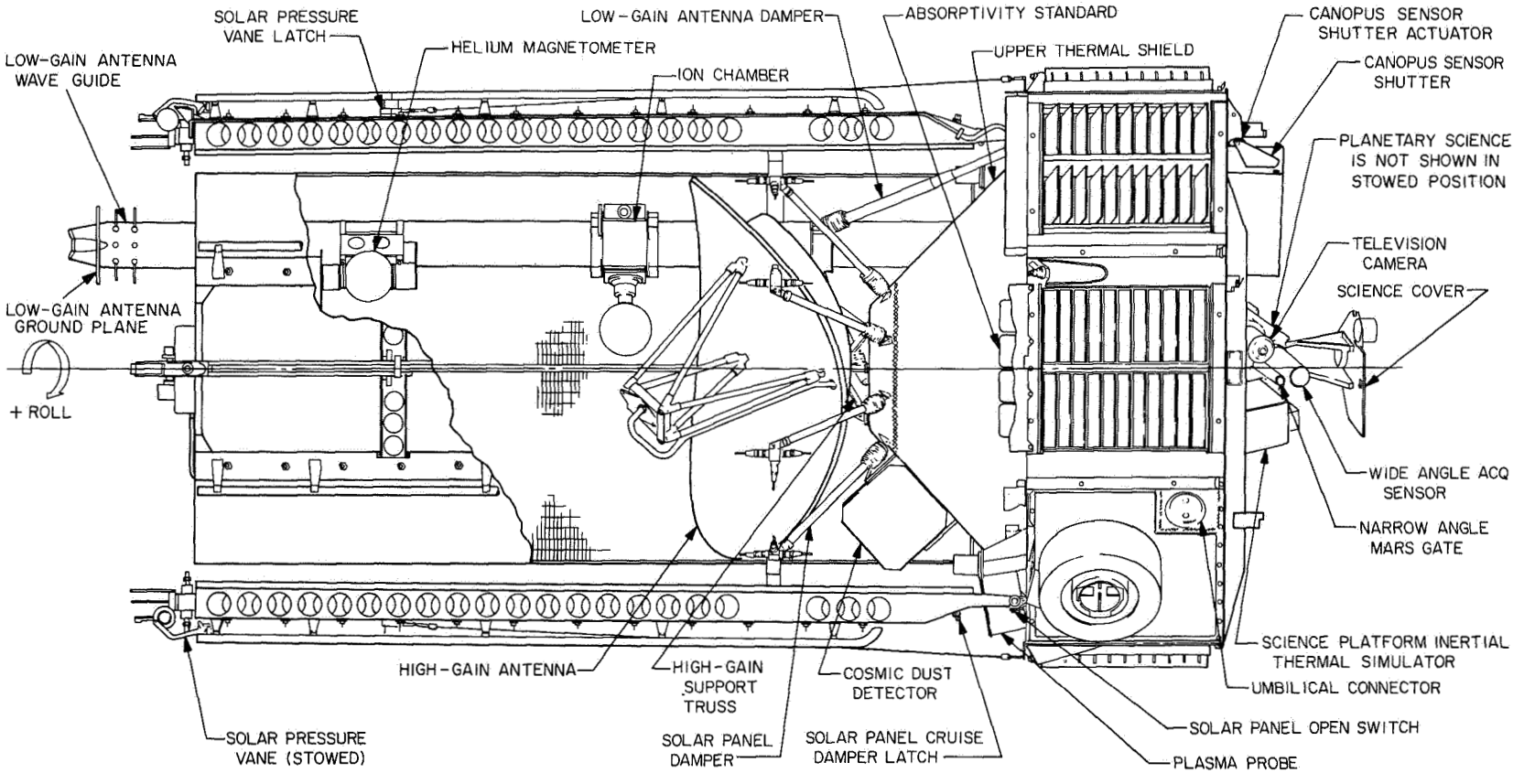


**Fig. A-5. Spacecraft mechanical configuration: side view, solar panels folded**

### E. Science Platform and Actuator

The science platform provided a gimbaled support structure for the planet-oriented science instruments capable of satisfying the pointing requirements of these instruments. In addition to providing structural support and articulation, a deployable cover was integrated with the platform to protect sensor optics from stray sunlight, micrometeorities, and contaminants from the launch and midcourse environments. The cover also provided a light-source array powered from ground umbilical for checking the operation of science and acquisition sensors during tests. The scan actuator was located on top of the primary structure, separate from the scan platform. The scan actuator consisted of a 400-Hz, 26-V, 8000-rpm synchronous motor and reduction gearing to provide an output of 0.5 deg/sec. A set of cam-operated mircoswitches pulsed the scan logic system at each limit to reverse the direction of the scan. A potentiometer coupled to the output shaft through a stage of antibacklash gearing indicated angular position.

## III. System Configuration

The spacecraft consisted of the following ten subsystems:

### A. Attitude Control

The attitude control subsystem operated in three distinct, but related, modes: acquisition and cruise, maneuver, and inertial roll. In the acquisition and cruise modes, the subsystem used the sun and Canopus to establish and maintain, by nitrogen gas reaction jets, three-axis stabilization to a nominal accuracy of $\pm 0.5$ deg with respect to each axis. In the event that the sun was lost from view for any noncatastrophic reason, reacquisition was automatic. In the maneuver mode, the attitude control subsystem, responding to commands from the CC&S, was able to point the thrust axis of the propulsion subsystem to any desired new orientation with a $1\sigma$ accuracy of $\pm 0.5$ deg from the nominal reference attitude and with a drift rate of less than 0.5 deg/hr. This stability was maintained during motor burn by using an autopilot jet vane actuation system. In the inertial roll mode, similar to the acquisition and cruise mode with respect to the pitch and yaw axes, the attitude control subsystem accepted an inertial position error signal in the roll channel, rather than the position error of the Canopus sensor. In the inertial mode, the roll-turn increment commands could also be accomplished by ground command (Figs. A-6 and A-7).

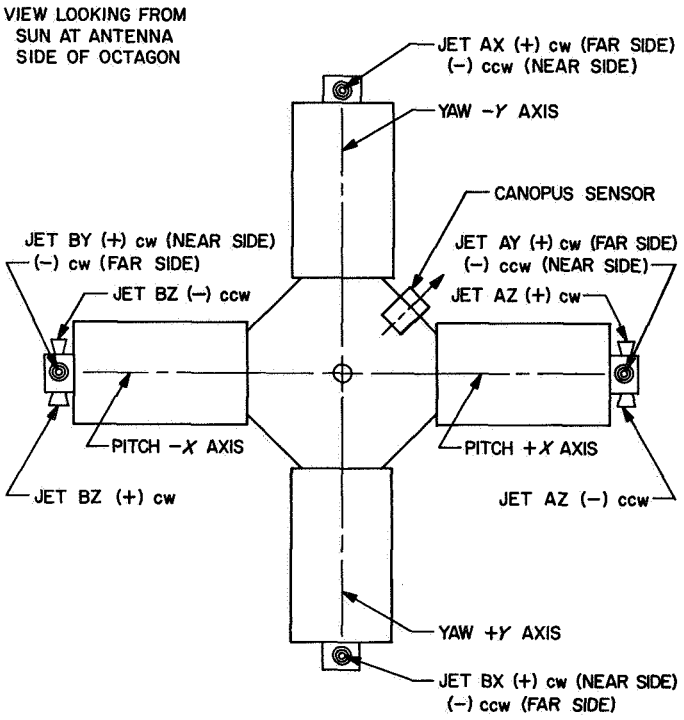


**Fig. A-6. Attitude control gas jet configuration**

### B. Propulsion

The propulsion subsystem provided the capability of two maneuvers for correcting the spacecraft trajectory. The vacuum-thrust capability of 23 kgf provided by the motor was used once to place the spacecraft in a near-perfect trajectory. The fuel supply was sufficient to give a maximum velocity increment of 80 m/sec to a 270 kg payload and velocity increments as small as 0.2 m/sec were possible for a spacecraft weighing 270 kg. Jet vanes capable of deflecting the midcourse motor jet stream provided thrust-vector control through $\pm 5$ deg. The ignition and thrust termination signals were generated by the CC&S.

### C. Central Computer and Sequencer (CC&S)

The CC&S provided timing, sequencing, and control of the power, radio, and attitude-control subsystems. It also initiated timed events and sequences for other subsystems. From the CC&S, the power subsystem received a timing pulse every 66⅔ hr. The CC&S controlled the burn time of the midcourse propulsion motor to an accuracy of $\pm 0.08$ sec. The Canopus sensor cone angle was changed before and after encounter by commands from the CC&S. The sequence of science experiments was not included in the CC&S operations. However, it kept track of spacecraft

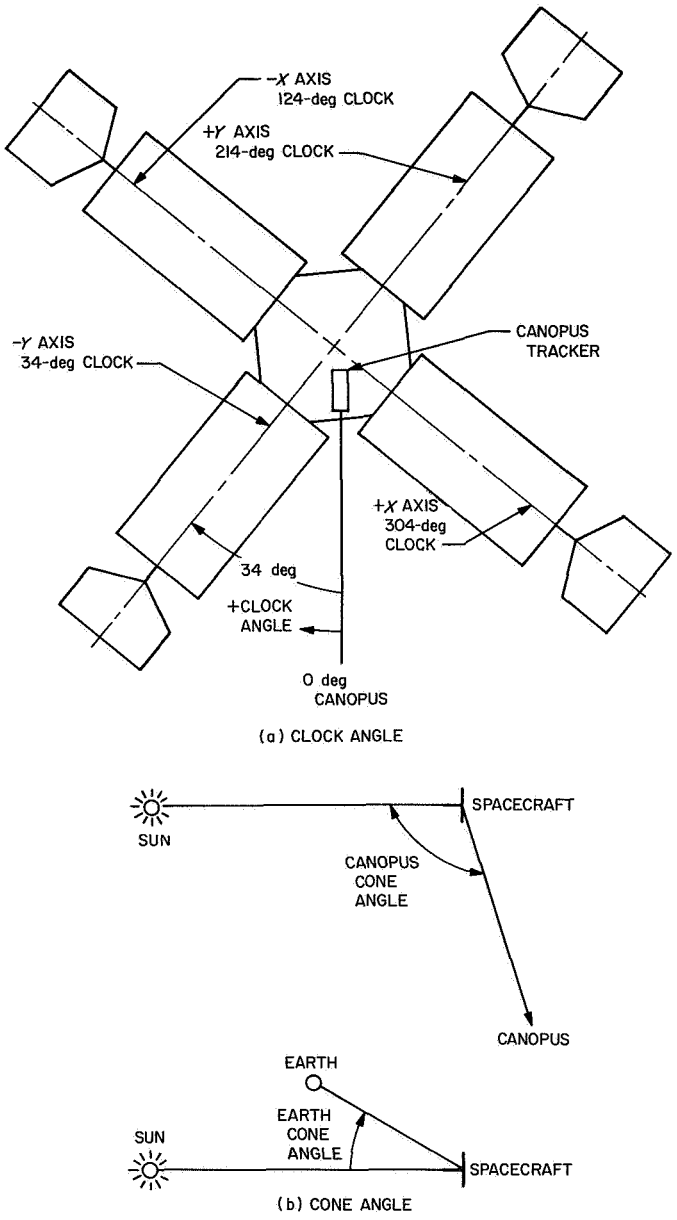


**Fig. A-7. Clock- and cone-angle descriptive diagram: (a) clock angle, (b) cone angle**

times after launch and executed commands at predetermined intervals during the mission.

### D. Radio

The radio subsystem, encompassing tracking, command, and telemetry, consisted of a transmitter and receiver (transponder) operating in conjunction with a high-gain and a low-gain antenna. The radio subsystem was designed to receive a modulated RF signal transmitted from earth, coherently translate its frequency and phase by a fixed ratio, and demodulate it. If the signal included a command, a composite command signal was sent to the command subsystem. The signal from earth was always modulated with a range code.* The receiver demodulated the range code sent from the DSIF, and the radio subsystem modulated the returned signal with the demodulated ranging signal and a composite telemetry signal.

The primary antenna linking the earth to the spacecraft was the low-gain antenna. This omnidirectional antenna was able to receive commands from earth during the entire flight and transmit telemetry to and receive commands from ground stations during midcourse maneuvers. The switch-over between the low- and high-gain antennas was accomplished by ground command. The fixed elliptical paraboloid was mounted so that, during the last half of the flight to Mars (after midcourse maneuver), earth fell within the main lobe of the antenna radiation pattern. The purpose of the high-gain antenna was to transmit telemetry to earth during the last half of the transfer orbit and for 20 days after planetary encounter, during the video playback period.

### E. Command

Signals from ground stations could be modulated by "commands" in such a way as to control various functions in the spacecraft. The spacecraft receiver demodulated the composite received signal and routed the command subcarriers to the command subsystem. Operating at a rate of 1 bps, the subsystem had a capacity for 29 direct commands and three quantitative commands. The command subsystem detected the command wave train, decoded its binary information content, and issued the necessary command signals to the appropriate spacecraft subsystems.

### F. Pyrotechnic

The pyrotechnic subsystem accepted commands from various spacecraft subsystems and provided the energy (via squib-initiated explosions) necessary to retract pins or start and stop the midcourse motor. It also provided an electric trigger signal to release the solenoid for the science cover.

*A range code is an extended sequence of 0 and 1 bits, statistically similar to a random sequence but actually precisely defined. The signal sent to earth by the spacecraft is again modulated with this same sequence. The return of this code to earth is detected by cross-correlation measurements, and the elapsed time from transmission to return gives the range of the spacecraft in light-seconds.

### G. Data Encoder

The data encoder subsystem accepted analog voltages and digital information, converted the data into 7-bit words, modulated a subcarrier with the binary data, and synchronized it to form a signal for the radio transmitter. The data encoder operated at 8⅓ and 33⅓ bps and four data modes. Each of the four modes of operation utilized a different data format. Engineering and science measurements were alternately sequenced by the data encoder subsystem. The data modes and their operations were:

| Data Mode | Function |
|---|---|
| 1 | Maneuvers—engineering data only. |
| 2 | Launch and cruise—normal mode with ⅓ engineering (140 bits). |
| 3 | Encounter—science data only. |
| 4 | Video playback – data from tape recorder played back with Mode 1 data inserted between television pictures. |

### H. Power

Four solar panels, containing a total of 28,224 individual photovoltaic solar cells and covering an area of 6.5 $m^2$, comprised the primary power source. As a secondary source, a rechargeable 1200-W-hr silver-zinc battery provided power to the spacecraft during launch, trajectory correction, and other maneuvers which required more power than could be supplied by the solar panel. Two power regulators, the main booster and the maneuver booster, each capable of operating at power levels up to 150 W, provided a redundant capability in case of a failure in either regulator.

### I. Science

The scientific payload consisted of instruments necessary to perform cruise and encounter experiments, the television experiment, and ancillary subsystems designed to support the experiments. The scientific payload comprised the following:

(1) *Cosmic ray telescope*—used solid-state detectors and electronic logic to detect and measure charged particles trapped in the vicinity of Mars, solar flare particles in space, and cosmic ray intensity in the inner solar system between 1 and 1.5 au from the sun.

(2) *Cosmic dust detector*—used a sensor, transducer, an amplifier, and a memory to detect and measure directly the momentum and mass distribution of cosmic dust particles in the earth–moon, Mars–Deimos–Phobos, and interplanetary regions.

(3) *Trapped radiation detector*—used three Geiger-Mueller counters and one 35-$\mu$ surface barrier detector, amplifiers, and discriminators to provide measurements of magnetically trapped charged particles in the vicinity of Mars. The experiment was also designed to monitor the occurrence of solar cosmic rays and energetic electrons in interplanetary space.

(4) *Ionization chamber*—used an argon-filled ionization chamber to measure total ionization current collected from the gas and a Geiger-Mueller counter to measure the total flux of charged particles which passed through any portion of the sensitive volume, in the regions between earth and Mars.

(5) *Solar plasma probe*—used a sensor and electronics to measure the flux density, spectral distribution, and time history of the positively charged solar plasma and to correlate these measurements with those of the magnetic field, as made by the magnetometer.

(6) *Helium magnetometer*—used a sensor and electronics to furnish 3-axis outputs which represented measurements of Martian and interplanetary magnetic fields to determine their magnitude, direction, multipolarity, and orientation relative to the planetary rotational axis.

(7) *Television camera*—used to take television pictures of Mars during a 20-min period near closest approach when the planet was in the camera's field of view. These pictures were recorded on video tape, and stored data was telemetered to earth after occultation.

(8) *Occultation*—used the radio tracking and changes in frequency, phase, and amplitude of the spacecraft signal to measure the refractive effect of Mars atmosphere and ionosphere. For its operation, this experiment required only a slight change in the planned spacecraft trajectory and modification of the ground station transmitter and receiver.

(9) *Data Automation System (DAS)*—consisted of the real-time (RT) and non-real-time (NRT) subsystems; provided the processing interface between the science and data encoder subsystems. The RT DAS processed formed data samples from the scientific

instruments for real-time transmission. The NRT DAS controlled the encounter sequence, the video storage subsystem, TV data processing, and RT data transferred to the tape recorder (Figs. A-8 and A-9).

(10) *Planetary scan subsystem*—consisted of a sensor, electronics, and a drive motor to provide a 180-deg scan motion of the science platform to search for Mars. The scan was cyclic until the planet came into the sensor's 25-deg field of view (acquisition), whereupon a 2.4-kHz signal was routed to the DAS for processing. A scan-inhibit command from the DAS could stop the cyclic scan and the tracking motion guided by the optical sensor (Fig. A-10).

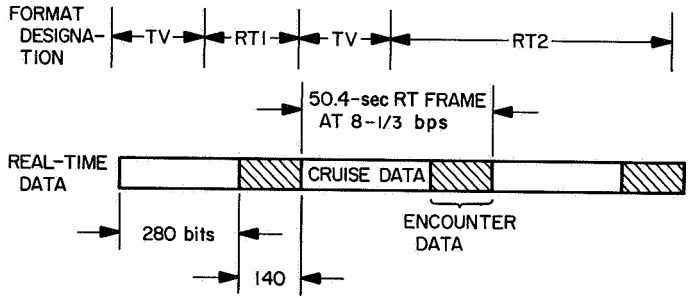


**Fig. A-8. Data automation system encounter timing**

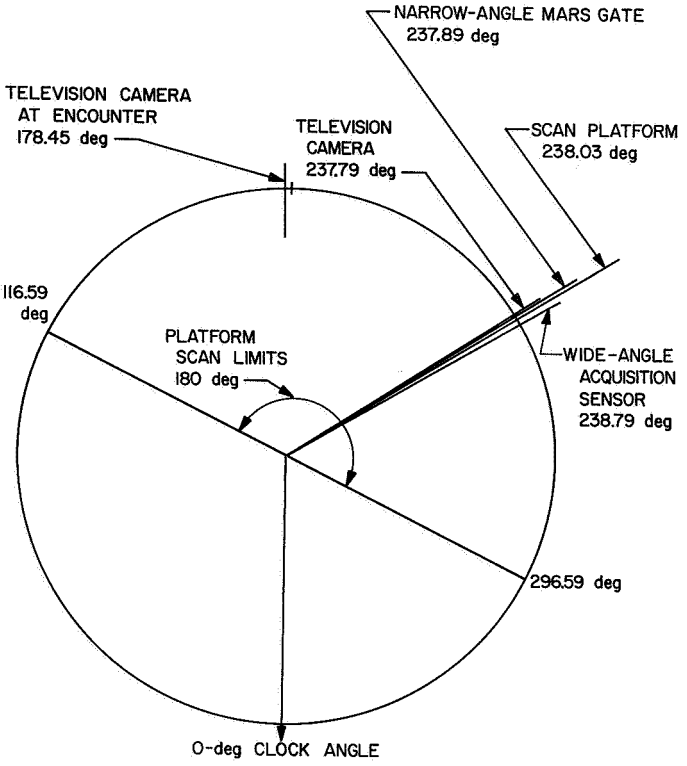


**Fig. A-10. Planetary scan platform relative look angles, shown with platform in pinned position**

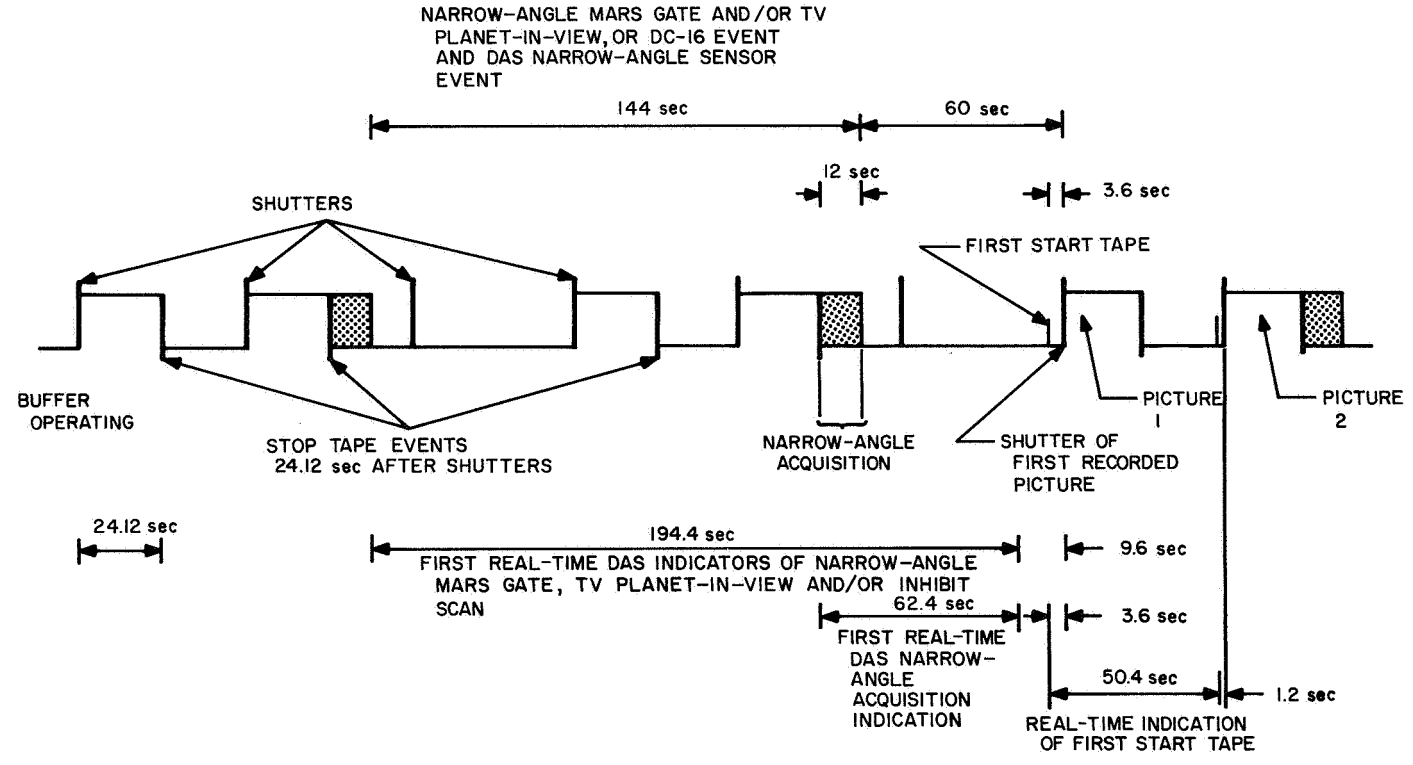


**Fig. A-9. Data automation system non-real-time sequencing at narrow-angle acquisition**

(11) *Narrow angle Mars gate*—located on the planetary scan platform, the NAMG supplied an acquisition signal to the DAS when Mars entered its field of view. The signal initiated the planetary encounter sequence for the science experiments. The NAMG consisted of a lens, a photoconductive cell, and electronics in an integrated module.

### J. Tape Recorder

The tape recorder subsystem stored digitized television data during encounter with Mars and reproduced these data for coding by the data encoder subsystem and transmission to earth. The recorder accepted serialized NRZ data from the NRT DAS at a rate of 10,700 bps and delivered the binary data at a rate of 8⅓ bps. The storage capacity of $5.24 \times 10^6$ bits of video data was equivalent to more than 20 television pictures (Fig. A-11).

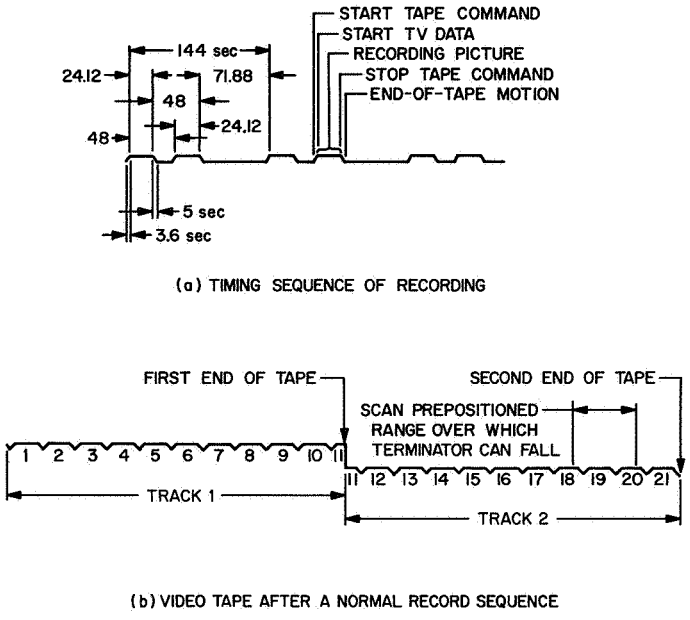


**Fig. A-11. Video recording timing sequence**

During launch the tape transport was operated at the record mode tape speed (32.5 cm/sec) to reduce the possibility of spilling tape. No recording was done during launch. The record motor was started before launch and ran until the spacecraft had separated from the *Agena D*. After separation, the tape was positioned to its starting point in preparation for encounter.

In the record mode all sections of the subsystem except launch mode signals were energized by application of 2.4-kHz power. The tape subsystem recorded the television picture sequences as it made two complete passes. After making the first pass on the tape, the recorder changed tracks, and returned to the initial track after the second pass. When the end-of-tape foil passed the sensor contacts the second time, response to record commands was inhibited. Whenever the recorder subsystem was not actually operating in the reproduce mode, it was set in the record mode.

A command from the data encoder switched the tape recorder subsystem into the reproduce mode after planetary encounter and data recording. The tape speed in this mode was 0.025 cm/sec. The playback signals were amplified and processed to reproduce the recorded frequency-doubled code waveform. Signals from both tracks were applied simultaneously to the playback track switch, which selected one signal at a time. A temperature transducer attached to the transport mounting plate provided temperature measurement which the data encoder monitored for telemetry.

The record motor used a special 400-Hz power source while recording during planetary encounter. During launch mode, spacecraft gyro power was used to run the record motor. The 2.4-kHz power supply furnished the electrical power for the video storage subsystem.

The encounter trajectories, aiming zones, and near-Mars trajectory parameters are illustrated for reference in Figs. A-12, -13, and -14.

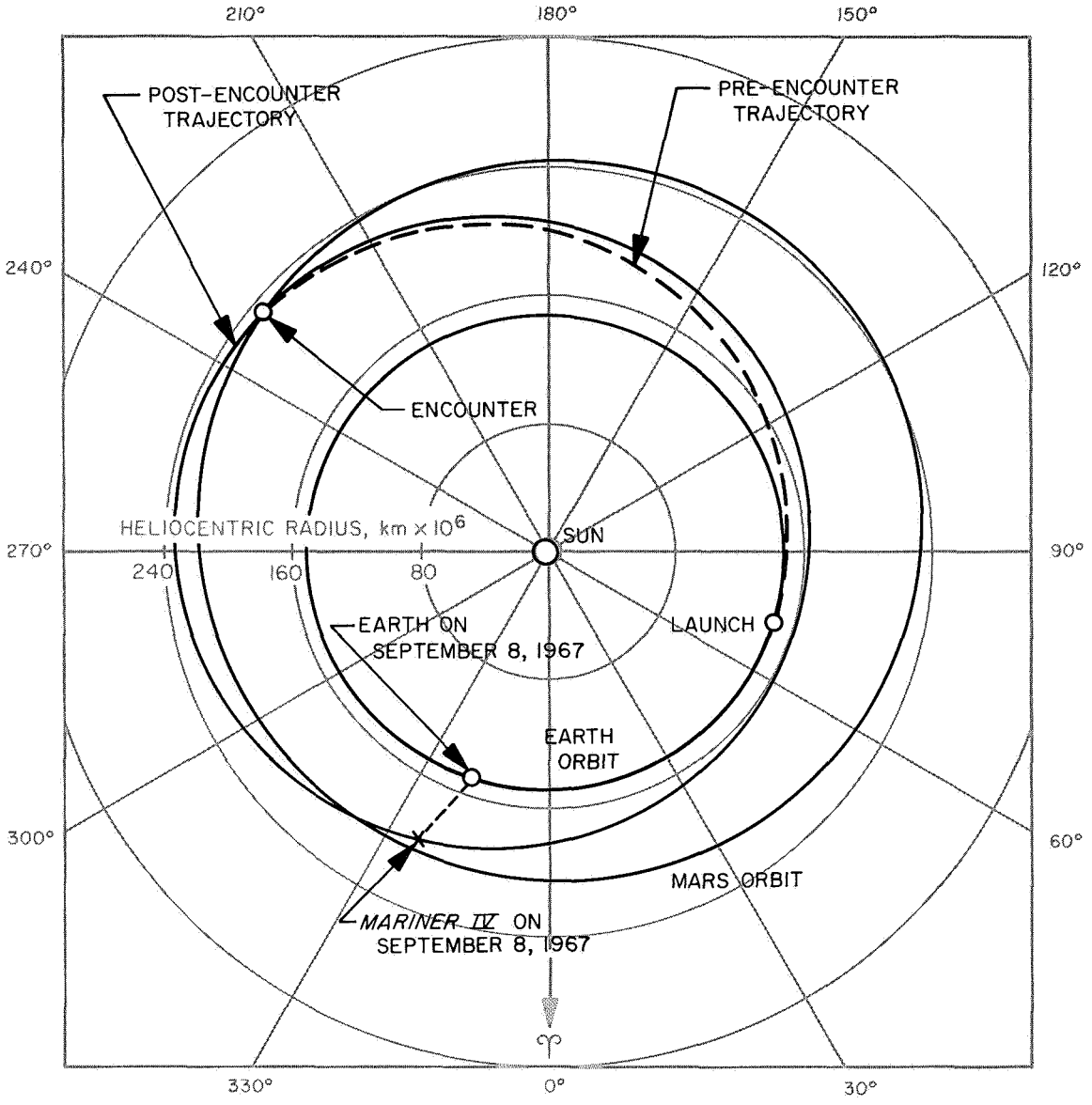


**Fig. A-12. Pre- and postencounter trajectory, ecliptic view**

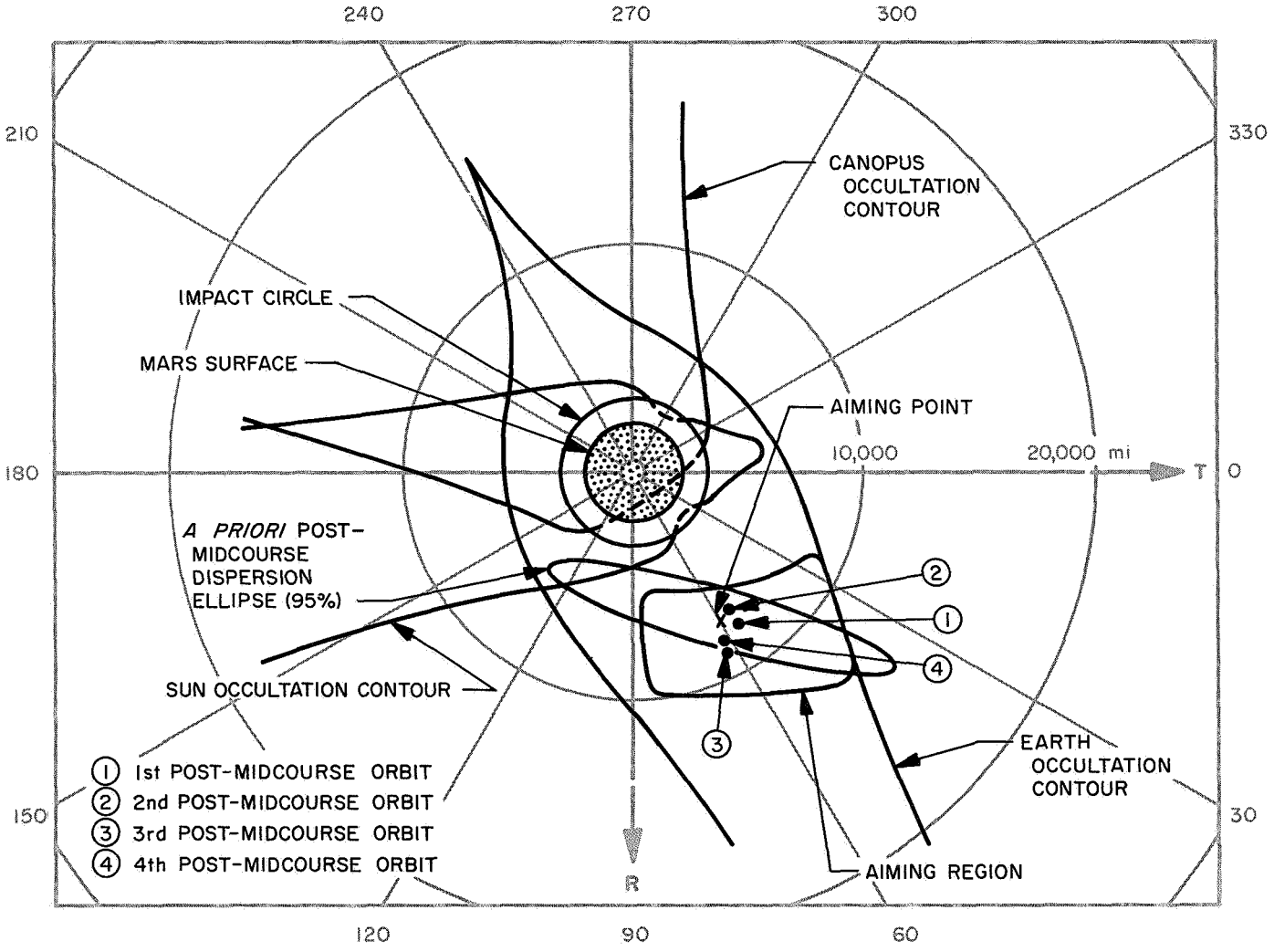


**Fig. A-13. Aiming zones: (a) aiming point diagram,(b) trajectories at Mars**

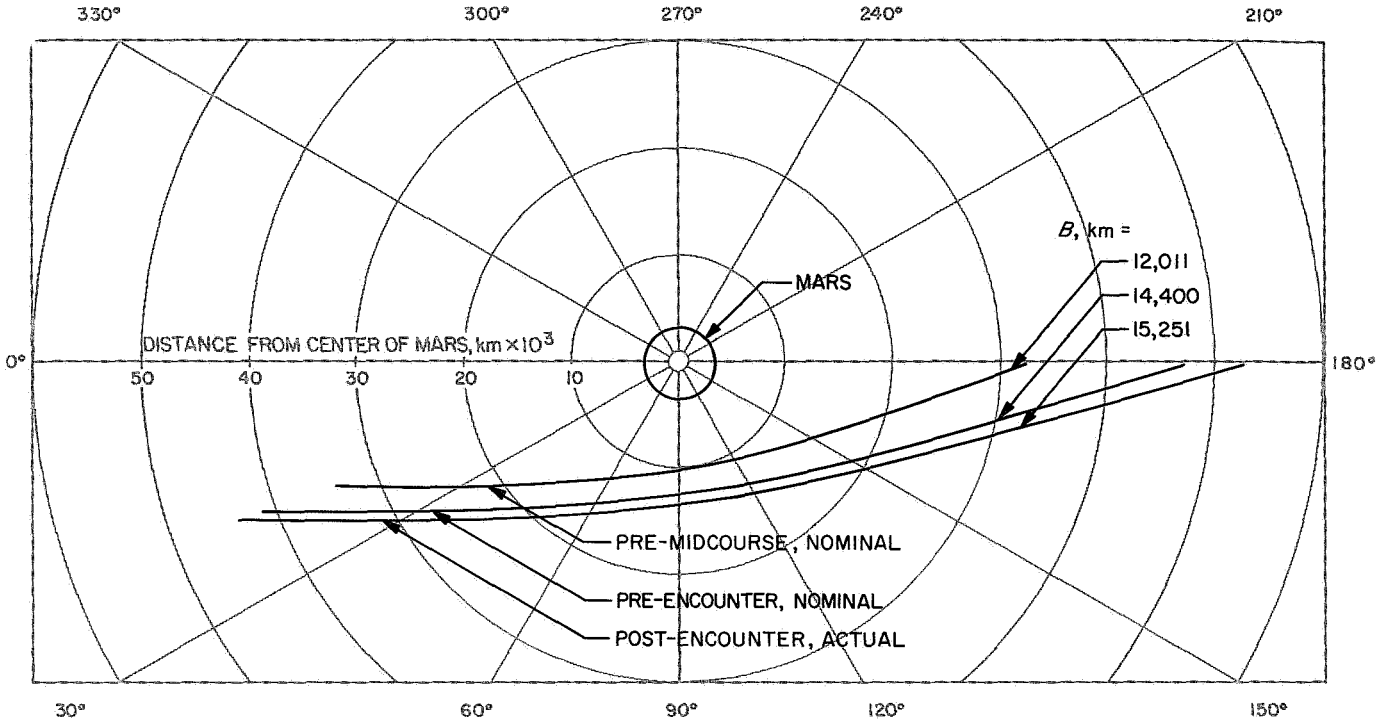


**Fig. A-14. Near-Mars trajectory parameters**

PRECEDING PAGE BLANK NOT FILMED.

# Appendix B

# Television Camera Subsystem

## I. Introduction

The television camera subsystem consisted of a narrow-angle reflecting telescope, a shutter and filter assembly, a "slow scan" vidicon tube, and related electronics. The subsystem was designed to take and encode a sequence of TV pictures upon receipt of appropriate electrical signals from the data automation system.

The television camera subsystem was composed of six physical subassemblies. Two of these, the optics and camera head, were joined together and were located on the scan platform of the spacecraft. The other four subassemblies, comprising the bulk of the electronics, were contained in standard *Mariner* subchassis and located in spacecraft Bay III. Figure B-1 is a photograph of the television camera head. The total weight of the camera subsystem was 5.1 kg, and the total power consumed varied between 7.8 and 8.3 W.

The television subsystem (Fig. B-2) evolved from the design of a two-camera subsystem based on the *Mariner B* spacecraft. This design had reached the breadboard stage and the fabrication of a prototype was underway in 1962, when the *Mariner B* project was cancelled. Most of the circuits used in the *Mariner Mars 1964* subsystem are virtually identical to the *Mariner B* design. Timing differences brought about some changes in the logic, but this primarily involved changing interconnections between counting units and gates.

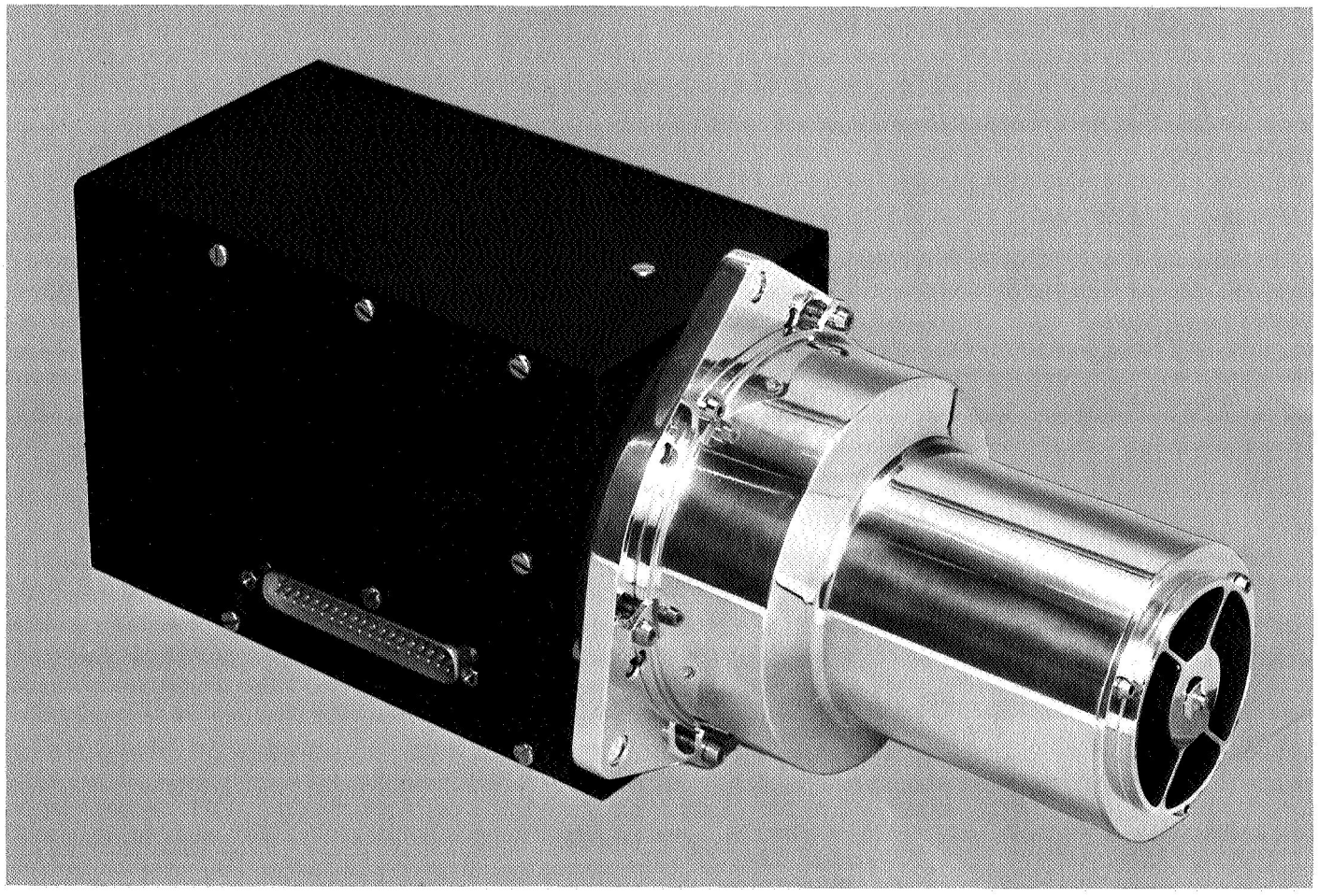

**Fig. B-1. Television camera head**

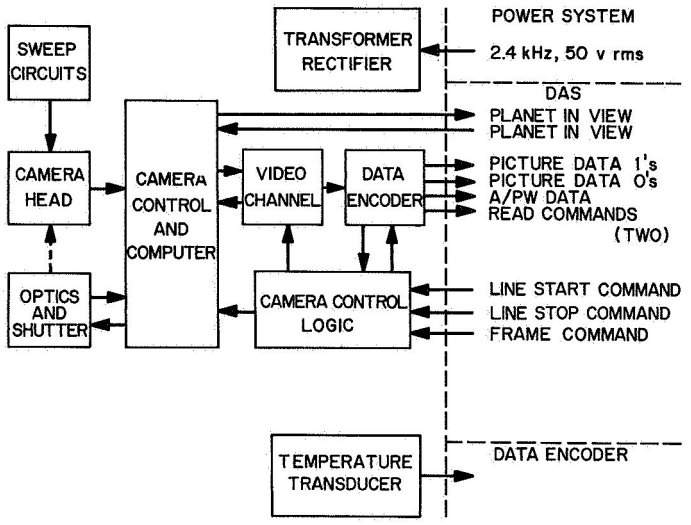


**Fig. B-2. Television subsystem, functional block diagram**

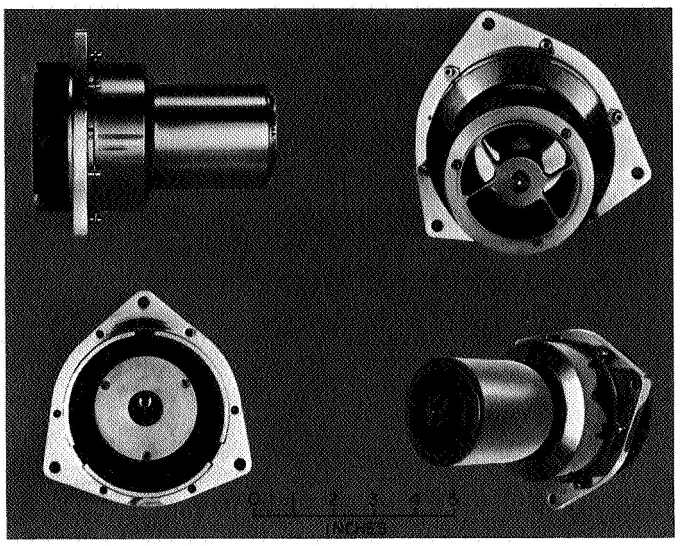

**Fig. B-4. Components of camera head**

## II. Camera Optics, Shutter, and Filters

The telescope is an $f/8$ (Cassegrain) reflecting telescope with a 30.5-cm effective focal length and $1.05 \times 1.05$ deg field of view. It is pictured in Fig. B-3. Although the shutter and stray light shield are part of the optics subassembly (see Fig. B-4), they are shown mounted on the camera head.

### A. Telescope

The telescope design utilized beryllium mirrors and a beryllium–copper supporting structure. The beryllium mirrors were coated with nickel–nickel phosphorous (Kanigen) before final polishing. The use of materials having similar thermal expansion coefficients in the mirrors and optical supporting structure makes the optical system self-compensating with respect to focus over a large temperature range, and the high thermal conductivity of beryllium and beryllium–copper tends to prevent temperature gradients within the optical system, thus avoiding image degradation.

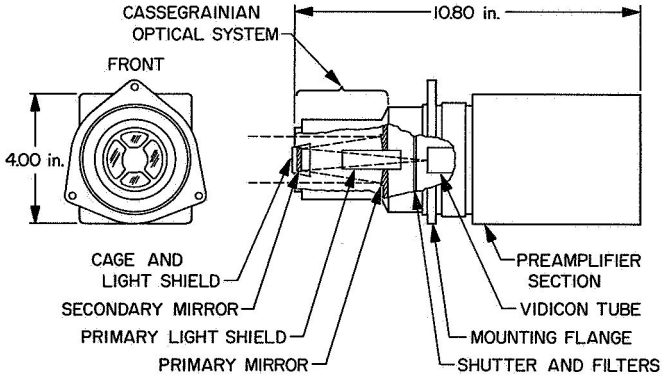


**Fig. B-3. Cassegrain reflecting telescope**

### B. Shutter

The *Mariner IV* shutter is of the intermittent, rotary type. It consists of a disc containing four cutouts, two of which contain red filters and two green. The filters consisted, respectively, of a 4-mm thickness of Schott OG-3 (orange-red) filter glass, and a two-layer filter composed of 3 mm of BG-18 and 1 mm of OG-4 filter glass. These filters were chosen to exclude deep blue light and to divide the spectral range from about 5000 Å to about 7000 Å into two distinct bands in an efficient manner. These filters are successively introduced into the light path by a rotary solenoid energized by a momentary current pulse and remain until a second current pulse energizes the solenoid. Four such pairs of pulses cause one complete rotation of the shutter filter wheel, each pulse advancing the disc 45 deg. A ratchet-type linkage coupled the solenoid to the disc and also unlocked the disc-locking mechanism which secured the disc between shutter pulses. Figure B-5 is a view of the prototype filter and shutter. Some shutter failures were experienced during thermal-vacuum lifetime tests because of thermally induced binding between a teflon sleeve bearing and a steel shaft, and excessive wear was observed in some parts of the shutter mechanism. These defects were remedied by the use of a "nylatron" spool bushing and replacing the shutter just before final systems test of the spacecraft so that a shutter having only a small amount of preflight wear would be flown.

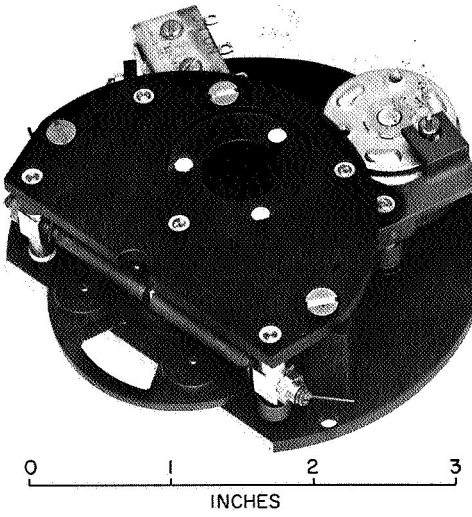


**Fig. B-5. Camera filter and shutter**

### C. Shutter Control

As previously discussed, a two-pulse shutter control was adopted. It was also desired to have two different shutter "speeds," corresponding to 0.08- and 0.2-sec exposure time. A circuit to control the timing between shutter pulses (exposure time) was therefore provided. This circuit was capable of switching to either the 0.08- or the 0.2-sec interval upon command. Closure of a microswitch located on the shutter provided synchronizing information to the control circuitry when the shutter filter wheel was in the closed-shutter, red-filter position.

## III. Camera Head

The camera head contained the vidicon tube, preamplifier circuits, a 110-kHz oscillator, and the electronic filtering and distribution circuits (Fig. B-6). The vidicon tube translated the optical image into an electrical video signal. The 110-kHz oscillator was provided to modulate the vidicon "reading" beam. This frequency then served as a carrier frequency for amplitude-modulated video information. The 110-kHz video signal was amplified by a tuned preamplifier. The filtering and distribution circuits provided specified voltages required to operate the vidicon tube. Fig. B-7 shows six different views of the camera head subassembly. The camera head chassis had five separate compartments. The vidicon tube was located in the center compartment, while the tuned preamplifier, the 110-kHz oscillator, and the filtering and distribution circuits were each located in the remaining compartments, electrostatically shielded from each other.

### A. Vidicon Tube

A vidicon tube was selected as the camera sensing device because of the ruggedness, light weight, small size, and simplicity of this type of tube. An all-electrostatic type offered a saving of 1 kg over a magnetic deflection and focus system. The vidicon tube potentials are compatible with solid-state circuit capabilities.

The operation of a vidicon is based on the phenomenon of photoconductivity, the change in electrical conductivity of certain materials with variations in incident light intensity. The inside surface of the vidicon end window is coated with a transparent conductive coating as indicated in Fig. B-8. A photoconductive layer is deposited over this coating. This material, when in the dark, is an insulator, but becomes conductive when exposed to light. To "prime" the vidicon, an electron beam is made to scan the back (photoconductive) surface in the absence of light, while the conducting front surface of the photoconductor is held at a positive potential with respect to the cathode. The scanning electron beam thus deposits a uniform negative charge on the photoconductor back surface, the charge accumulating until the back surface reaches cathode potential. In this state the photoconductive film is charged like a capacitor, with a uniform charge in each unit area.

Where light from the scene falls on the photoconductor, the conductivity increases, reducing the negative charge at the illuminated point by allowing it to leak through the photoconductive film to the transparent conducting film. The photoconductor therefore becomes partially discharged in a pattern corresponding to the scene image. This stored charge pattern is "read" by scanning the vidicon target surface with a sharply focused electron beam in a series of linear sweeps in the manner of the picture tube of a TV receiver. As the "reading" electron beam scans across the back surface, it will supply electrons preferentially to the less negatively charged areas; the resultant varying electron flow, which induces an opposite charge flow to the transparent electrode, constitutes the video signal current.

In view of the proposed 24-sec frame time, the camera tube selected for the television subsystem had to be capable of a slow-scan readout and storage of an image with negligible degradation for the 24 sec. The photoconductor target material of the vidicon was a new target material based on a selenium compound, developed by the General Electrodynamics Corporation (GEC).

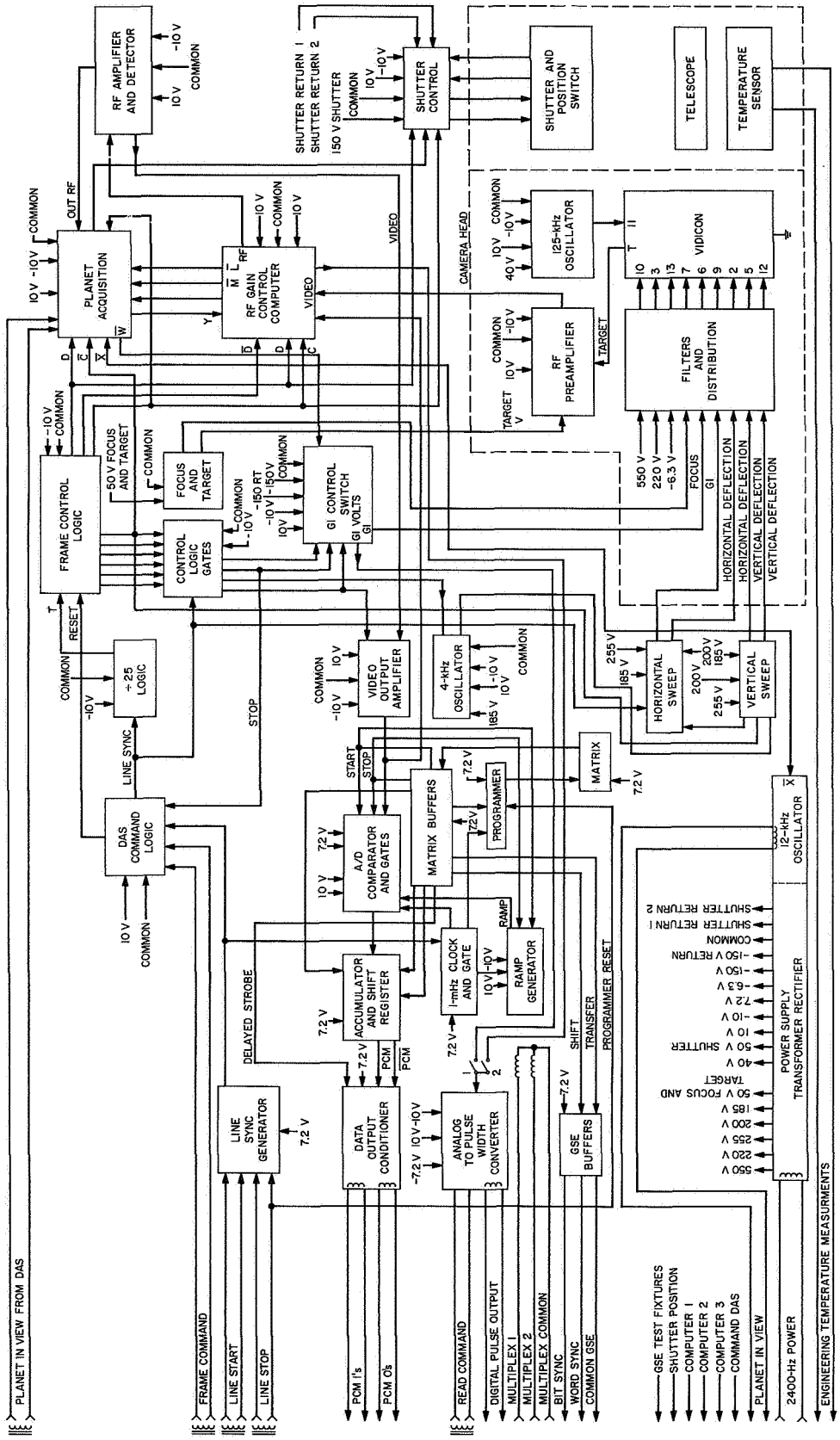


**Fig. B-6. *Mariner IV* television system, block diagram**

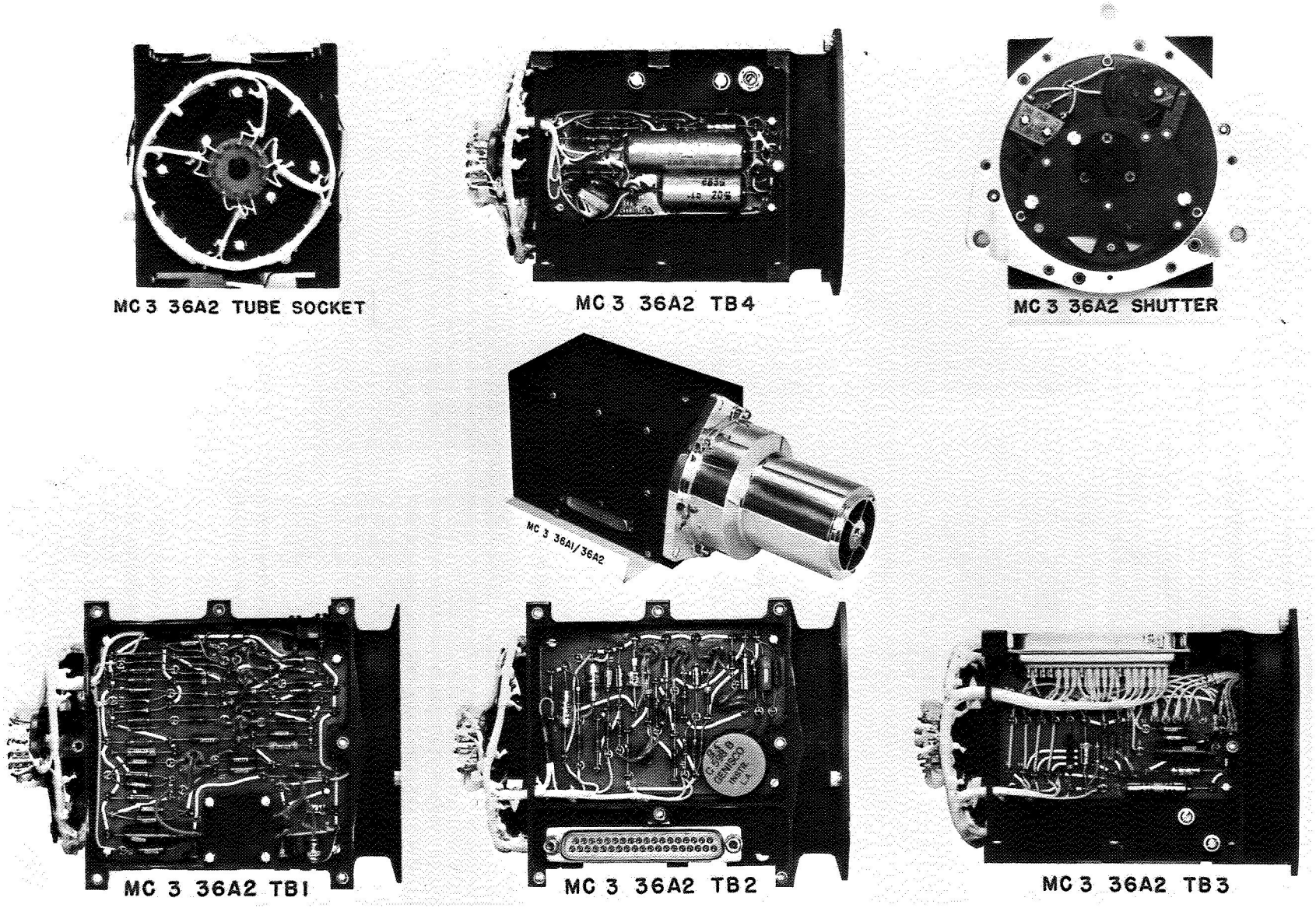


Fig. B-7. Six views of TV camera head subassembly

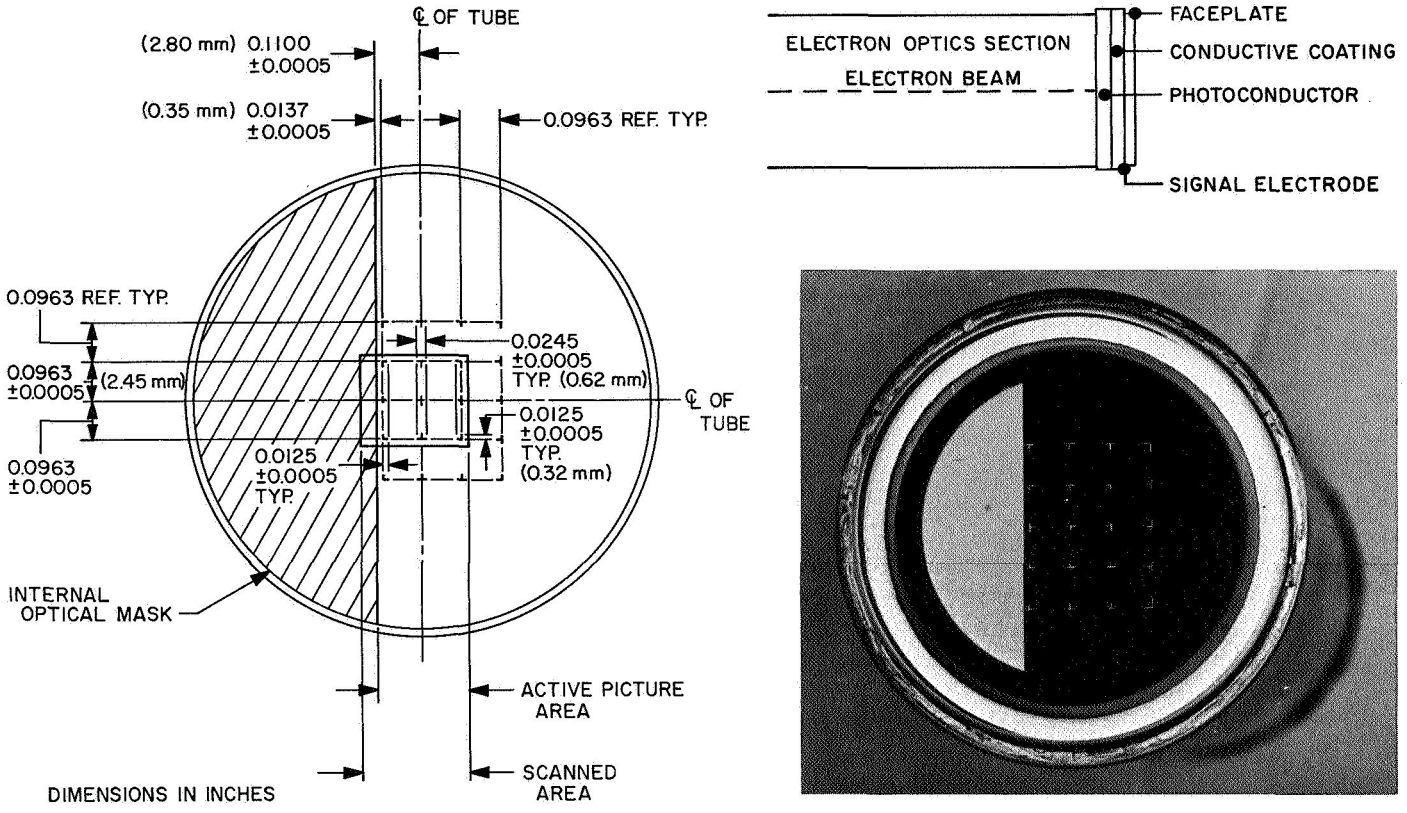


**Fig. B-8. Vidicon faceplate**

Apart from the new target material, the GEC vidicon had electrical characteristics generally similar to previous tubes supplied for the *Mariner* program. However, some desirable improvements dictated by experience with the earlier *Mariner B* TV subsystem were incorporated. Probably the most significant characteristic of this new tube and its target material was its ability to erase stored signals without the use of erase lamps as were required for the earlier tubes having an antimony sulphide oxygen sulphide (ASOS) target material. This characteristic eliminated an entire circuit, reduced the power requirement, and simplified the operation. The new target material also had improved sensitivity and good operating characteristics over a wider range of temperatures than the ASOS surface. This temperature characteristic eliminated the need of a temperature stabilization circuit that had been designed for the *Mariner B* TV subsystem.

The mechanical construction of the electrostatic vidicon is illustrated in Fig. B-9. The original ruggedized 1351 vidicon, type 1351-13 is shown in Fig. B-9a, and the structurally modified unit (type 1343-010) developed to meet the more stringent type-approval specifications is shown in Fig. B-9b. Note that the tube electrodes are strap-welded to ceramic rods in order to provide a single

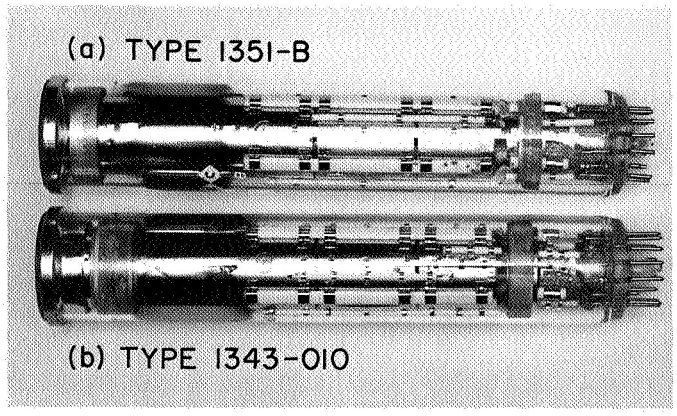


**Fig. B-9. Vidicon, mechanical construction**

integrated mechanical structure within the glass envelope. Connections to the various electrodes are made through hollow ceramic support members. Strap-welds to the 13-pin base anchor the structure in the axial direction. The 130 individual pieces in the tube assembly weigh 80 g.

The combination of the new target material and the improved ruggedized tube construction resulted in the final flight vidicon tubes that met all specifications.

### B. Vidicon Tube Mechanical Mounting

In the mounting of the vidicon tube in the camera head chassis, the face plate of the vidicon had to be maintained at a specific distance from the optics for good optical focus. The vidicon also had to be centered so that the optical image was focused on the small electrically scanned area of the vidicon face plate. The vidicon had to survive vibration environment during launch.

A number of different mounting schemes were tested. In the one finally adopted, the tube suspension in the camera head was a radially flexing mount (soft mount) rather than a rigid, hard mount. This mounting scheme is illustrated in Fig. B-10. Two cylindrical polyurethane foam dampers support the tube radially. A spring-loaded centering device assists the foam in centering the tube optically. The tube is constrained axially by the flat spring-loaded tube socket, while teflon bearing surfaces permit the tube to slide freely in the radial direction. The axial socket pressure and the mechanical centering device provide additional assurance of correct tube alignment should there be any deterioration of the foam in space. With the tube mounted in the camera head, triaxial accelerometers have indicated that the gain is less than 2 over the range 25 to 2000 Hz. With this arrangement, no problems were experienced in passing full type-approval specifications for the camera head subassembly. Optical centering was well within the specified tolerances after vibration test.

## IV. Sweep Circuits

The sweep circuits provide the voltages necessary for horizontal and vertical deflection of the vidicon beam both during picture readout and when the vidicon target is being erased and primed for the next picture. The sweep circuits consist essentially of constant-current integrators providing push-pull sweep voltages to the vidicon deflectrons. The sweep voltages are adjusted to scan a $5.5 \times 5.5$ mm square area of the vidicon target. A 4-kHz oscillator, turned on during the interval between pictures, causes the vertical sweep voltage to vary at that rate. This provides erasure of the image on the vidicon target.

## V. Camera Control and Computer

### A. Gain Control Computer

When the scientific requirements of the mission became established, it was apparent that the television sub-

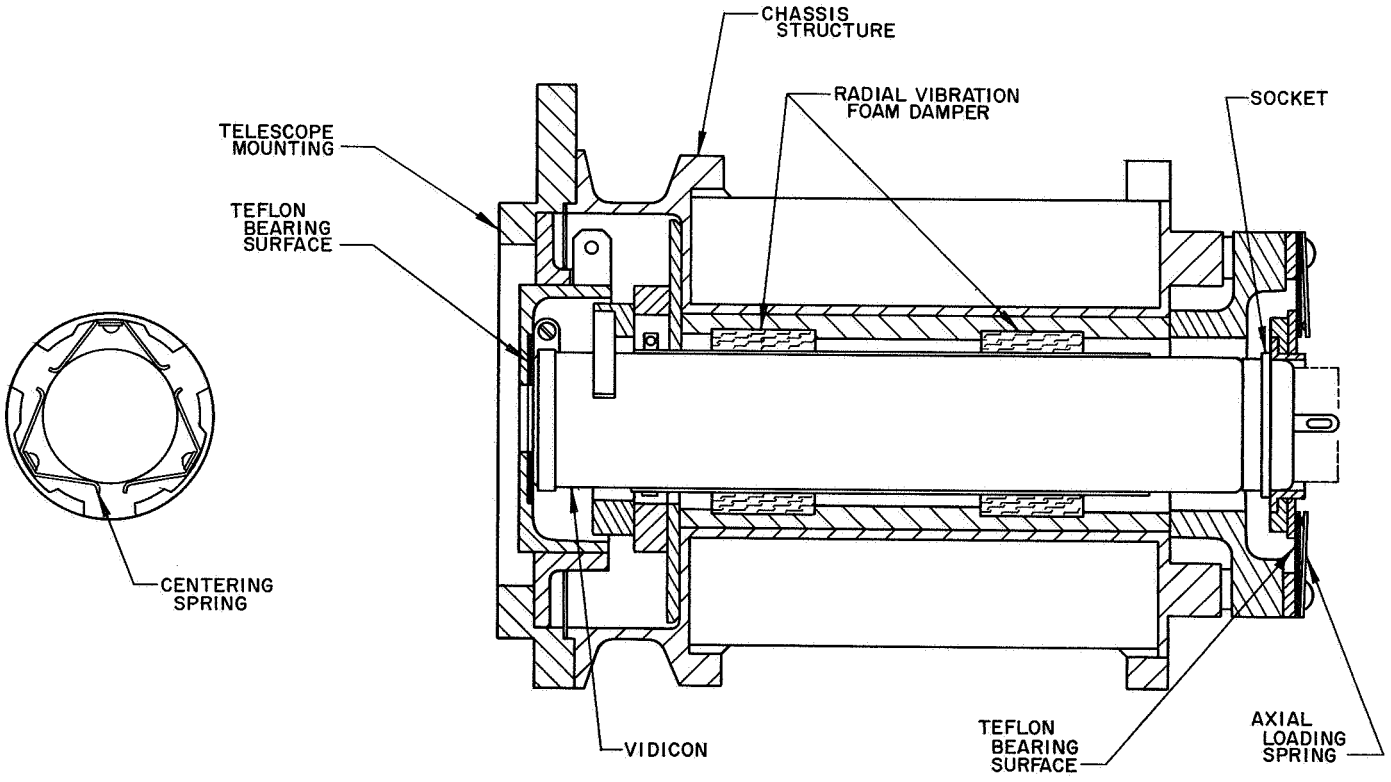


**Fig. B-10. Flexible mounting of vidicon in camera head**

system would have to cover virtually the entire range of illumination, from the noon day subsolar region of Mars, to darkness at the terminator. To cover this wide light range, it was necessary to utilize a high-gain system for dark areas which could be reduced in gain for photographing the bright areas.

A simple computer was designed to control four levels of video gain by switching any one of four different attenuation circuits into the video signal chain. The video signal level is sampled. If the level is greater than 6 V (out of a maximum of 8 V) then the next higher attenuation is used. The computer is designed to raise the gain after a "red" exposure, but it can reduce the gain after any exposure.

Owing to uncertainties in the expected value of Mars illumination, an additional safety factor was incorporated into the subsystem. Prior to planetary encounter, the camera was in what is known as the "photometer" mode. In this mode, the vidicon beam current was higher than required for a normal picture. This high-beam current creates sufficient charge at the target surface to prevent distortion by excessive illumination. When the scene brightness is greater than 1 lambert, the video signal is large enough to cause the computer to issue a logic command to the shutter control circuit to switch to the faster shutter exposure time. The shutter control circuit switches to slow exposure time when the scene brightness decreases sufficiently. The vidicon beam current is reduced to the normal value after planet acquisition has been achieved. This computer greatly extended the dynamic range of the TV subsystem in providing the capability to take both good highlight pictures and good lowlight pictures.

### B. Planet-In-View Circuit

Another requirement was for the television subsystem to indicate planet acquisition as an alternate to the narrow-angle planet sensor. To meet this requirement, a planet-in-view circuit was designed. This circuit samples the video signal level and provides commands when the signal level exceeds a certain reference voltage for a specified period of time. One of these commands unlocks the computer and causes the beam current control to switch the vidicon beam current to normal. The other command gates "on" an oscillator which sends a continuous signal to the DAS. A planet-in-view signal can be received from the DAS that bypasses the signal-level sensing circuit and causes the commands to be issued.

## VI. Camera Control Logic

The camera control logic comprises the external DAS command logic, divide-by-25 logic control, frame control logic, and control logic gates circuitry. These circuits control all camera timing functions, such as shutter pulses, picture readout, target erase and prime, and various necessary switching functions. The control logic operates synchronously from external frame-and-line-timing information received from the DAS. The block diagram of the television system (Fig. B-6) illustrates the logical interconnections, the input signals, and the outputs generated. Section B-X includes a discussion of the camera control logic operation sequence.

## VII. Video Channel

The video channel consists of an rf amplifier and detector, and a video output amplifier, which provide amplification, demodulation, and dc clamping for the video signal. A feedback channel is provided for video gain control. The output from the video output amplifier is sent to the television data encoder. As shown in Fig. B-11, all of the video channel functions, the gain control computer, and planet acquisition circuits of the camera control and computer functions are contained in the standard subassembly designed for *Mariner*. This subchassis also contains the frame control logic and control logic gate circuits of the camera control logic functions. Also illustrated in Fig. B-11 are two views of the deflection and control subassembly which contains all the sweep functions, the vidicon beam current control, shutter control circuit, the DAS command logic, and the divide-by-25 logic control circuits.

## VIII. TV Data Encoder

The TV data encoder provided analog-to-digital conversion of the TV picture data using six binary bits per picture element. The digital signal was transferred to the DAS at a rate of 83,333 bps. The data output conditioner, accumulator and shift register, analog-to-digital comparator and gates, 1-MHz clock and gate, ramp generator, matrix, matrix buffers, programmer and GSE buffers circuitry performed this encoding function. In addition, analog-to-pulse-width (A/PW) conversions were performed on certain critical TV performance data and were coupled to the DAS by the A/PW converter circuit. The line sync generator circuit reconstructed line synchronization information and coupled it to the camera control logic. The TV encoder subassembly contains all the TV encoder functions.

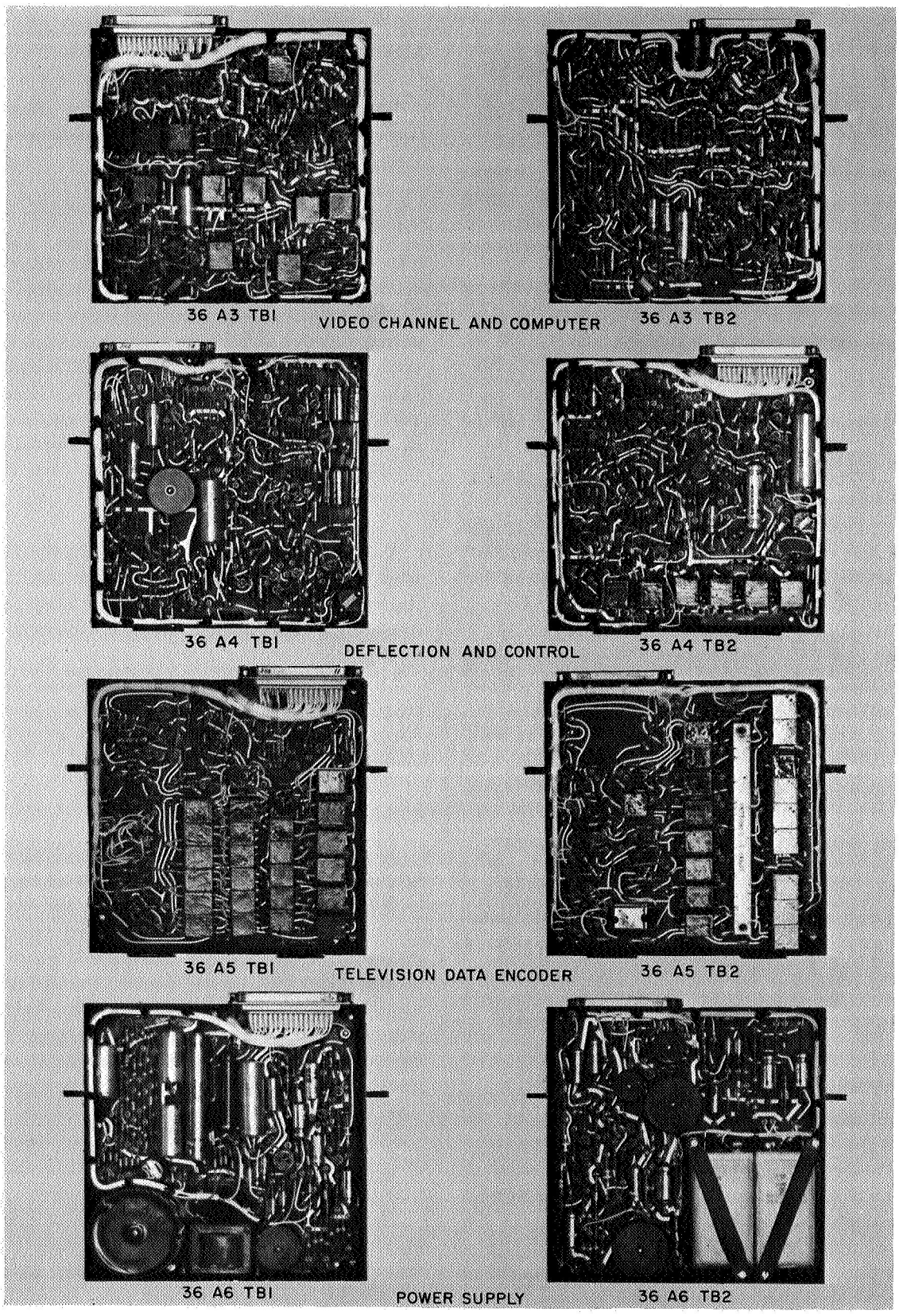


**Fig. B-11. Television camera electronics**

## IX. Power Supply

The power supply transforms the 2400-Hz square wave power into voltages, with appropriate regulation, necessary to operate the television subsystem. The logic, sweep, control, and vidicon circuits use 13 separate voltages generated by the power supply. A current-limiting circuit located in the input to the power supply was designed to limit the current dissipation to 160% of nominal in the event of a failure in the circuits of the camera system.

## X. Sequence of Operations

### A. Timing

The basic timing information for the operation of the television subsystem was received from the DAS. "Line start" and "line stop" commands were used for the generation of the line synchronization function. The "line start" pulses were received every 120 msec and a "line stop" pulse was received 14.4 msec after each line start pulse. Figure B-7 shows the logical relationships of the inputs and outputs.

The "line sync" pulses are counted down by combinations of bistable multivibrators in the divide-by-25 and frame control circuits. Thus timing cycles of 48, 24, 12 sec, etc., are achieved. The various timing pulses are combined and gated together in the control logic gates to generate commands such as vertical blanking and prime.

The entire counting sequence is inhibited by a gate in the command logic circuit until a frame command is received from the DAS. The frame command switches the gate, allowing the counting sequence to begin. After 45 sec, the gate is reset by the logic command, *vertical blanking*. The frame commands are received every 48 sec. The subsystem will not respond to any frame command received less than 45 sec from the previous command.

### B. Vidicon Operation

The beam current of the vidicon is controlled by the potential on the first control grid (G1). The G1 potential is regulated and switched by the G1 control switch circuit. A G1 potential of approximately 40 V allows a normal beam current to flow. In the photometer mode, the G1 potential is changed by +4 V from normal, which allows a slightly higher beam current to flow. A G1 potential of −10 V allows a higher beam current to flow during "erase" or "prime" operations. A G1 potential of approximately −60 V cuts off the beam current flow. This cut-off potential is used during horizontal and vertical blanking time.

Beam deflection is accomplished by changing electrostatic fields produced by an electrode assembly to which deflection voltages generated by the horizontal and vertical sweep circuits are applied. The vertical sweep circuit provides a linearly varying voltage for the 24-sec scan readout time. During the 18-sec erasure or prime time, the 4-kHz oscillator is gated on and coupled to the vertical deflection, producing a "fire-hosing" type of scan. The horizontal sweep circuit provides a sawtooth voltage with a duration of 14.4 msec. The timing of the horizontal sweep voltage is provided by the line sync logic. The vidicon beam current is cut off by the G1 control switch during the 105.6-msec interval between each horizontal scan. The sweep voltage limits for a normal scan size are extended during the erase or prime time to provide an overscan of the vidicon target.

A 110-kHz square wave signal from the 110-kHz oscillator is supplied to the vidicon cathode. This 110-kHz signal chops the beam current, providing an amplitude-modulated signal output from the vidicon target.

Other potentials required for vidicon operation are supplied by the power supply. The focus and target voltages are adjustable and are set by voltage divider circuits.

### C. Power Turn-on

At power turn-on, the counting multivibrators are inhibited for three frames by the slow-charging action of an RC circuit. The camera is held in the "erase" mode to provide time for the control sequencing circuits to become properly "aligned" and to adequately prime the vidicon target. After this initial period, the subsystem begins cycling through normal sequences. The shutter is aligned with the vidicon operation commands by the action of the position switch and control circuit. The subsystem is now in the photometer mode prior to a planet acquisition signal. The vidicon target is being scanned and the amplitude-modulated video signal amplified by the preamplifier.

The RF signal passes through a video blanking circuit in which the signal is shorted out during the prime time and during the time needed for the first six lines of scan. This video blanking prevents any erroneous pulses or spikes, which might occur during these times, from energizing sensitive sampling circuits farther along the video

chain. The amplitude of the RF signal is then sampled by the exposure control circuit of the computer. The RF signal passes through the attenuation circuits of the computer. Prior to planet acquisition the attenuation circuits are held in the maximum attenuation state, since the bright limb of the planet would be first to enter the field of view.

From the gain control computer, the RF signal passes to the RF amplifier and detector. Here, the RF signal is amplified and detected. The output of the circuit is the video signal with a bandwidth of 6.9 kHz.

When the vidicon target is scanned, the first 2 msec of each 14.4-msec line scan is spent on a portion of the target permanently shielded from exposure to light and known as the *black mask*. This provides a "black" reference or base for the video signal at the start of each scan line. In the "black clamp" circuit of the output amplifier, the first 1.1 msec of each scan line of video is clamped to a reference dc voltage corresponding to an optical black signal.

The video signal is then amplified a final time by the output amplifier so as to span the range +8 V for "black" to approximately +0.5 V for "white." By a feedback loop, the output video signal is sampled by both the gain control computer and the planet acquisition circuit.

### D. Planet Acquisition

When the output video signal differs by more than 2 V from the +8 V "black" level, the planet acquisition circuit is energized. A logic command is coupled to the 12-kHz oscillator, gating it "on," thereby sending a planet-in-view signal to the DAS. A logic command is also coupled to the gain control computer, releasing it for gain switching as required. A third logic command, coupled to the G1 control switch, switches the G1 readout potential from "photometer" to "normal" mode. A "planet-in-view" signal can be received from the DAS causing the video sampling circuit to be bypassed and the logic commands issued.

After inhibit is released, the gain control computer, with its four levels of attenuation, will attempt to maintain an output video signal level between 2 and 6 V. If the RF signal sampled by the exposure control circuit of the computer indicates that the light level is too bright, a logic command is issued to the shutter control to change the shutter exposure time from 200 to 80 msec. The fast shutter condition will remain until the light level becomes so dim as to cause the computer to switch to the maximum gain state.

### E. Encoding

The output video signal is sampled at twice the maximum video frequency or 13.9 kHz for digital encoding. To minimize quantization "noise," approximately 64 distinct video levels must be recognized by the encoder. A six-bit word length is sufficient to encode the video amplitude to this degree of accuracy. The bit rate at the output of the encoder is thus 6 by 13.9 kHz or 83.3 kilobits per sec.

A 1-MHz crystal oscillator provides the basic timing for the encoder. Sixty-four pulses are required during each sampling interval of 1/13.9 kHz or 72 msec. The programmer, matrix, and matrix buffers provide the various timing and logic commands necessary for the encoding operation.

The ramp generator generates a linear sawtooth voltage of 64-msec duration every 72 msec. This linear ramp voltage is compared with the video output voltage in the A/D comparator. Clock pulses (at a 1-MHz rate) sequence a binary counter in the accumulator until the ramp voltage reaches the video level, at which time the counter is stopped. The counter now contains a binary number which is related to the magnitude of the video voltage present during the sampling interval. Because of the inverted "polarity" of the video signal, the smallest binary word 000000 corresponds to "white," while the largest word 111111 corresponds to "black." The six-bit binary word is then transferred in parallel to the shift register.

The action of transfer starts the first bit of the pulse-code-modulated (PCM) word at the output of the shift register and, also, at the input to the data conditioner. The PCM data at this point are non-return-to-zero data such that a long sequence of digital 1's would appear as a dc voltage. To provide isolation between the TV subsystem and the DAS, pulse transformers are used. The digital data must, therefore, be converted to pulse or return-to-zero data. This is accomplished by gating the PCM data with a pulse that occurs one clock-pulse time after each binary bit is shifted or transferred. Since both digital 1's and 0's are required, the same logical operation is performed with the inverse of PCM data or $\overline{\text{PCM}}$. The output of the encoder is thus a series of 1-$\mu$sec pulses from each of two pulse transformers—one for digital 1's and one for digital 0's.

### F. Performance Data Output

The G1-regulated readout potential is monitored and converted to a pulse width value in the A/PW converter. This measurement was chosen for monitoring because it gave an indication of the expected vidicon performance. The subsystem +10 V is also monitored through the A/PW converter. The +10 V is the voltage used in the video output amplifier and encoder. Variations in the +10 V affect the illumination transfer characteristic of the system.

The AAC-1 and AAC-2 status bits indicate the gain state of the gain control computer. Digital 1's at both outputs indicate the maximum gain state, while 0's at both outputs indicate minimum gain. The relative gains for the various gain states were:

| State | Gain* |
|---|---|
| 00 | 1.00 |
| 10 | 3.1 |
| 01 | 11 |
| 11 | 27 |

The AAC-3 status bit indicates roughly the video level in any gain state. A digital 1 indicates greater than 2 V of video, while a 0 indicates less than 2 V of video.

A digital 1 in the shutter time status bit indicates a slow shutter condition. A digital 1 in the filter position status bit indicates the present picture was taken through a green filter, while a 0 indicates a red filter.

## XI. Calibration and Test of TV System

During the breadboard stage of camera development, the goal of the design team was primarily to obtain a satisfactory picture. When this had been accomplished and the prototype instrument was being built, attention was focused upon obtaining quantitative photometric data from the television system.

The Mars spectral illuminance data of Dollfus and Guerin (Ref. 3) established a brightness model that could be approximated by a 3000°K illumination source (Table B-1). Using the formula for illuminance of scene, $I_s$:

$$I_s = \rho E (r_e/r_m)^2 \cos\theta$$

*Determined empirically from the calibration data.

**Table B-1. Mars spectral illuminance data**

| Wavelength, nm | f (λ)/f (550) |
|---|---|
| 430 | 0.570 |
| 40 | 0.575 |
| 50 | 0.580 |
| 60 | 0.585 |
| 70 | 0.595 |
| 80 | 0.615 |
| 90 | 0.640 |
| 500 | 0.685 |
| 10 | 0.745 |
| 20 | 0.800 |
| 30 | 0.865 |
| 40 | 0.930 |
| 50 | 1.000 |
| 60 | 1.080 |
| 70 | 1.155 |
| 80 | 1.230 |
| 90 | 1.310 |
| 600 | 1.390 |
| 10 | 1.465 |
| 20 | 1.525 |
| 30 | 1.565 |
| 40 | 1.590 |
| 50 | 1.610 |
| 60 | 1.620 |

where

$\rho$ = albedo (0.07 maria; 0.18 desert)

$E$ = solar constant (14.1 lumen cm$^{-2}$)

$r_e/r_m$ = ratio of earth-Mars orbital radii

$\theta$ = incidence angle (from normal to surface)

the highlight levels at the subsolar point were calculated to be 0.4 lambert for maria and 1.0 lambert for desert regions. A camera responsivity covering the range from 0.01 to 2.0 lambert was judged to be adequate to provide for local brightness variations, low illumination angles, and a comfortable margin of safety at high light levels.

Prior to the assembly and adjustment of each camera, the vidicon tube spectral response was determined by measuring the monochromatic energy required to maintain constant vidicon signal current at a number of wavelengths throughout the visible spectrum (see Fig. B-12). Monochromator output was measured with a thermopile. Using these data and the Mars illumination model (see Fig. B-13), filters were selected to give equal signal currents at 542 and 610 nm (see Fig. B-14).

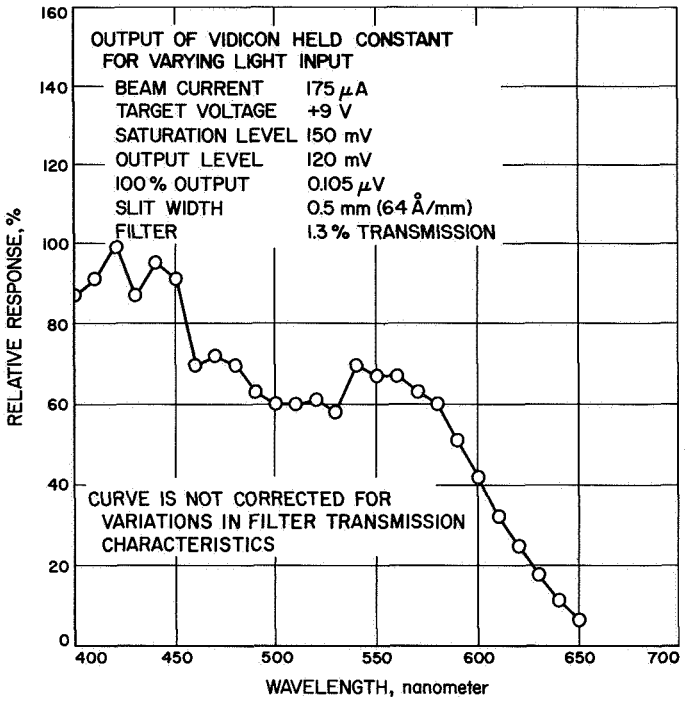


**Fig. B-12. *Mariner IV* vidicon spectral response**

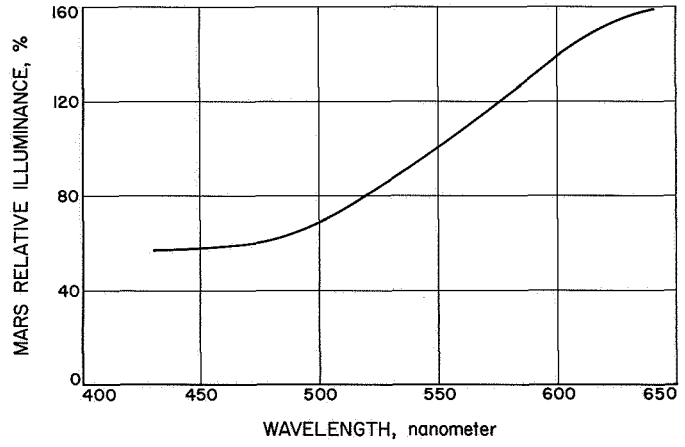


**Fig. B-13. Mars illuminance curve**

The assembled camera system was adjusted for maximum output with 1.0 lambert illumination at 200 msec exposure time (2.4 lambert with 84 msec exposure), corresponding to a binary digital data number of 000000.

System responsivity was determined by taking pictures of a 1.075 lumen, 3000°K collimated light source of

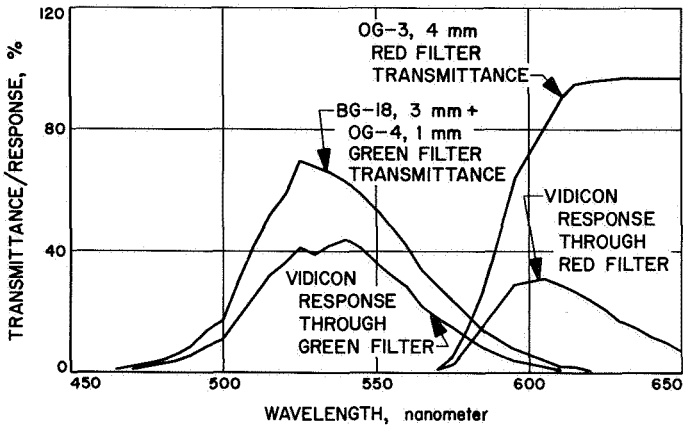


**Fig. B-14. Vidicon response through red and green filters**

22.8 cm effective focal length. Levels between 0.01 and 1.075 lumen were obtained by the use of neutral density filters. The output, in digital form, was recorded on magnetic tape in a format suitable for reduction by an IBM 7094 computer. The data for each illumination level were printed out in decimal form and in picture form for visual examination.

To determine the temperature coefficient of vidicon response and circuit linearity, abbreviated flat-field illumination tests were repeated at −30, 0, and +50°C. The relative response as a function of temperature is shown in Fig. B-15.

The resolution and modulation transfer function (MTF) characteristics were measured from picture data of high (10:1) and low (3:1) contrast sine-wave slides in the collimator (see Fig. B-16). To check geometric fidelity, a RETMA television ball slide picture was used by comparing the ball pattern with the fiducial marks on the vidicon faceplate. A rough plot of the MTF data is shown in Fig. B-17.

To confirm stability of operation and adjustments, the camera systems were removed from their spacecraft and all calibration tests except temperature variation rerun just prior to launch. No changes of sensitivity or variations in performance with respect to the values obtained during the earlier calibrations were noted.

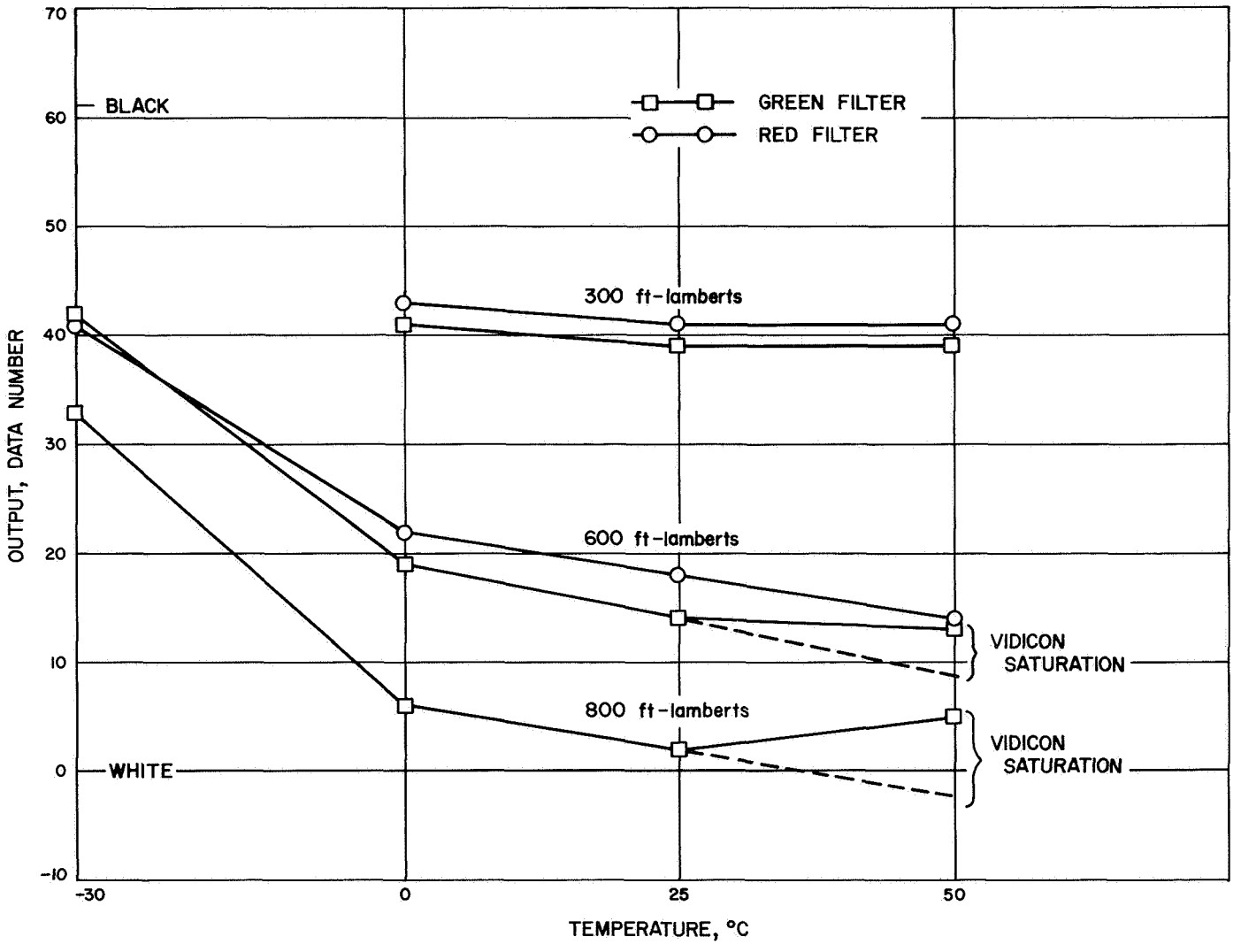


**Fig. B-15. System responsivity vs temperature**

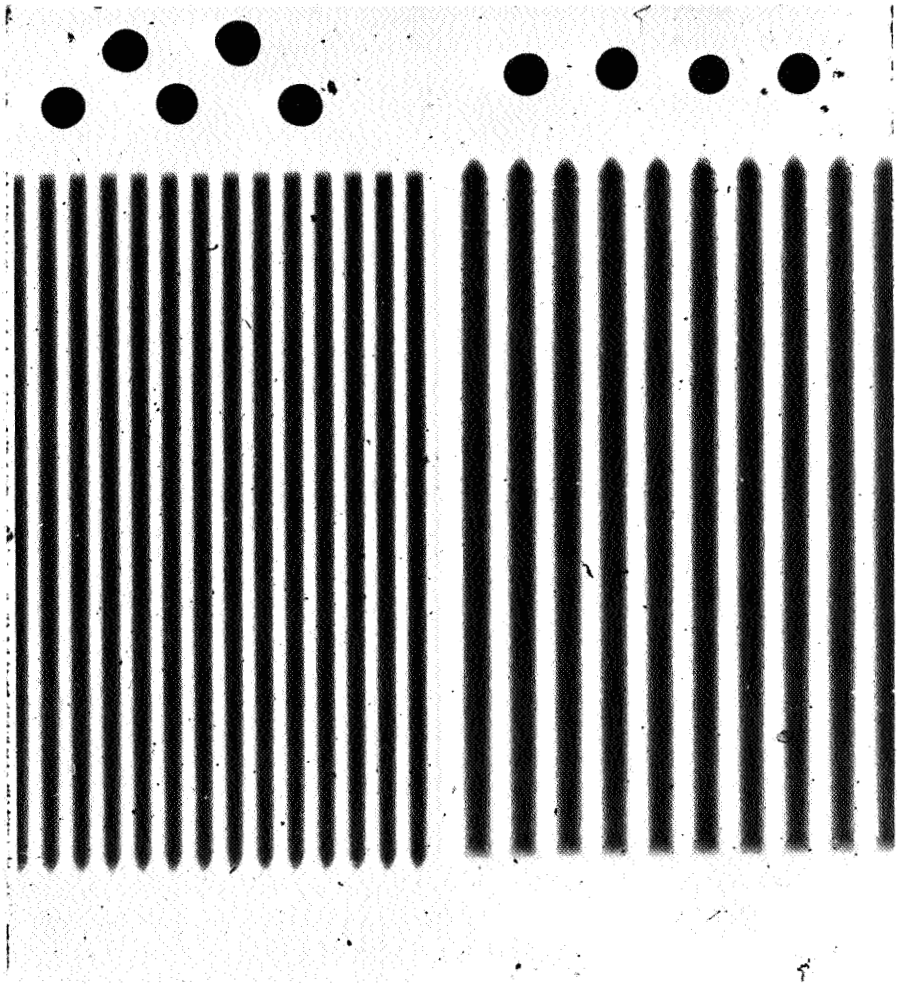

**Fig. B-16. High contrast sine-wave test slides**

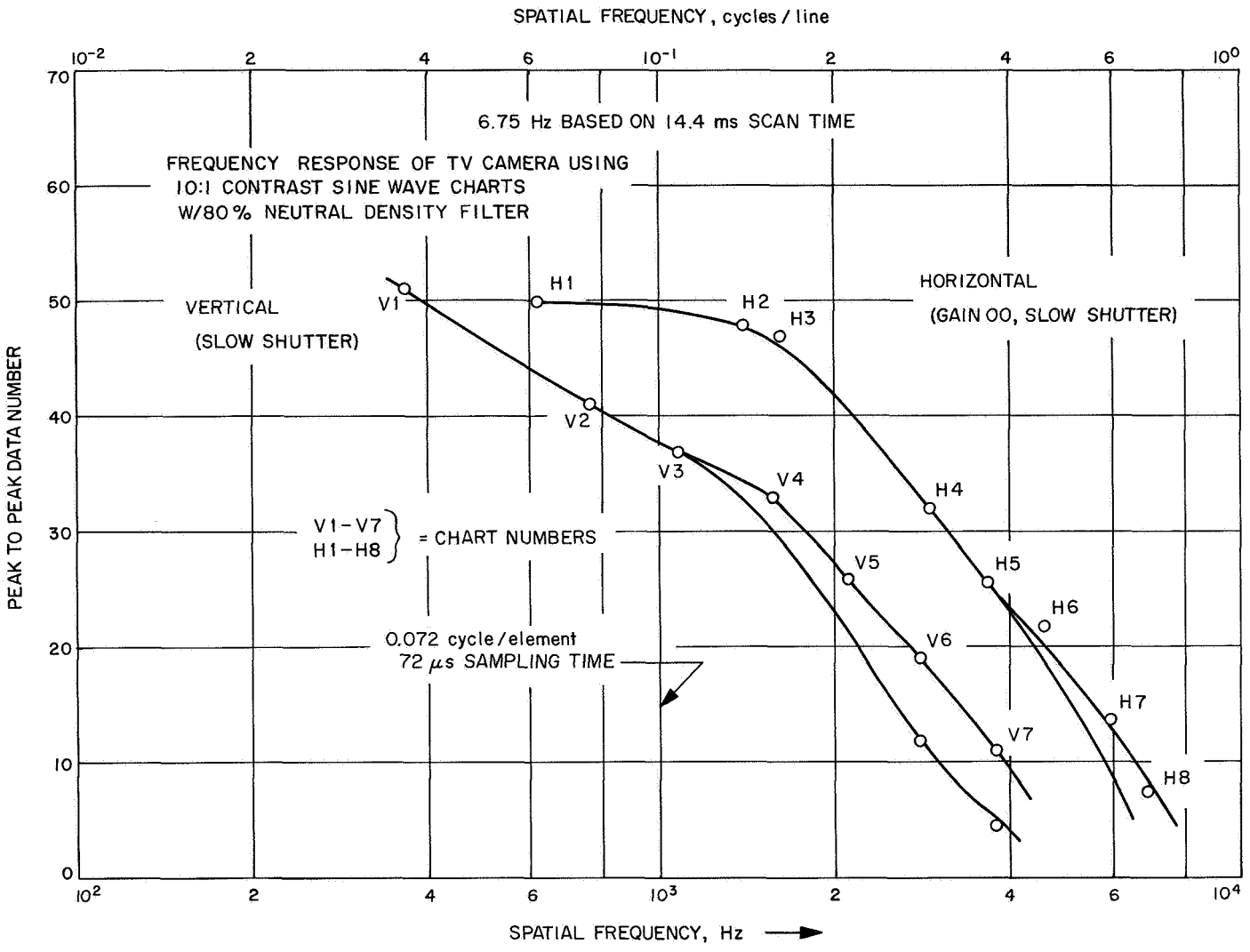


**Fig. B-17. Horizontal and vertical frequency response curves**

# Appendix C

# Flight Sequence and Performance

## I. Spacecraft Performance

A complete account of the performance of the *Mariner IV* spacecraft throughout its flight is available in JPL Technical Report 32-882.* Those aspects of the mission that relate to the television experiment have been digested from that document and are presented below.

### A. Science Cover Deployment Exercise

One of the principal spacecraft activities during the period preceding February 18, 1965 was the ground-command-initiated science cover deployment exercise performed on February 10, 1965. The objectives of this exercise were threefold: (1) to deploy the science cover, (2) to preposition the scan platform to the optimum encounter position, and (3) to turn off the battery charger and enable the boost mode. The exercise was carried out from DSS 11 (the Goldstone, California, tracking station). A total of 12 ground commands were transmitted to the spacecraft. All were received and executed normally. All objectives of the exercise were fully achieved, and the spacecraft was returned to the cruise state without difficulty.

### B. Planetary Encounter

The basic design of the *Mariner* Mars 1964 spacecraft provided for a completely automatic planetary encounter sequence with no ground action required. If the ground command option was available, however, there were a number of possible backups to the on-board functions, and, in addition, a number of alternate modes which could be superior in any given situation to the normal mode of operation.

The major problem in encounter operations was the transmission delay between the earth and the spacecraft. Approximately 13 min was required from data transmission at the spacecraft until data presentation in SPAC; over 12.5 min was required from command initiation at the DSIF station until command execution at the spacecraft. Thus, even immediate response to anomalous indications in the data could only reduce the effective reaction time in an emergency to something over 25 min. Conversely, normal command action as a part of the sequence of events could be taken only if it was assumed that nothing abnormal had occurred in the 13 min prior to command initiation, and that nothing abnormal would occur during the 12.5 min before command execution. Since most of the commands to be transmitted during the planetary encounter were critical with respect to time or function, it was important to prevent accidental losses of command lock and, in the event that such occurred, to provide for minimum-time reacquisition of the command loop.

The encounter sequence was initiated with the transmission of DC-25 from DSS 51 (Johannesburg, South Africa) on July 14, 1965, 14:27:55 GMT. This time was selected to initiate scan search at such a time that, given nominal performance, the scan platform would be pointing at the planet at nominal narrow-angle acquisition time in the event that the scan platform failed to inhibit either via ground command or internal logic. The command was verified in the data at 14:52:32.3 GMT. Spacecraft response to the command was normal: non-real-time power went on, video storage subsystem 2.4-kHz power went on, the scan platform went into a normal search, and power levels and temperatures increased as predicted.

The CC&S MT-7 Event was observed in the telemetry data at 15:43:48.6 GMT, but inasmuch as it had been preempted by DC-25, it had no effect upon spacecraft performance.

Prior to the planetary encounter it had been determined that a scan position of 180 deg would yield the best television data. This position was selected as the nominal position at which to inhibit the scan platform. An inhibit command (DC-24) was initiated at DSS 51 at 17:10:18 GMT for a predicted scan platform position of 179.9 deg. Command execution was verified in the data at 17:34:55 GMT with the scan platform positioned to 178.45 deg, well within the tolerances. Based upon this position, wide-angle acquisition was predicted for 23:55 GMT, with less than 0.01 probability of occurrence prior to 23:24 GMT.

Beginning just prior to 20:00 GMT and continuing through the encounter, anomalous indications were noted in the magnetometer X-axis data which appeared to be cyclic with a period of approximately 16 min. Although unexplained to date, the period corresponds to coincidences between the real-time and non-real-time portions

**Mariner Mars 1964 Project Report: Spacecraft Performance and Analysis*, Technical Report 32-882, Jet Propulsion Laboratory, Pasadena, February 15, 1967.

of the DAS which count at different rates. The anomaly had no effect upon the quality of planetary data gathered.

Had the scan platform been allowed to search for and track the planet automatically, acquisition of the planet by the scan sensor would have initiated a switch to Mode 3 data (all science data) several hours before the recording sequence. With the scan platform prepositioned, however, the expected time of wide-angle acquisition was so near the beginning of the television record sequence that insufficient time was available for television performance analysis prior to the latest time to transmit commands. For this reason, a commanded switch to all science data (DC-3) was included in the encounter sequence. DC-3 was transmitted from DSS 11 at 22:10:29, was received by the spacecraft at 22:23:07, and was observed in the data at 22:35:08 GMT. Subsequent analysis indicated that television sequencing was normal.

Wide-angle acquisition occurred at the spacecraft at 23:42:00 GMT on July 14, 1965. No effect was noted other than the indication in the science telemetry data because the scan platform had been inhibited by DC-24 and the switch to Mode 3 data had been accomplished by DC-3. The backup command (DC-16) for the initiation of the recording sequence was transmitted on July 15, 1965, 00:11:57 GMT. It was anticipated that this command would arrive at the spacecraft after two pictures had been recorded by the video storage subsystem if normal narrow-angle acquisition by the on-board sensors had initiated the sequence.

On the basis of the latest trajectory information and the DC-16 transmission time, the latest time for transmission of a DC-26 command to assure the termination of the recording sequence was found to be 00:36:30 GMT. The actual time for DC-26 transmission was to be determined from the narrow-angle acquisition indication in the data, if narrow-angle acquisition was observed earlier than 00:34:40 GMT. Narrow-angle acquisition was indicated in the data at 00:29:59 GMT and confirmed on the next data frame. The DC-26 was initiated at 00:31:42 GMT. A DC-2 command to turn on cruise science followed at 00:32.40 GMT and was followed by several more DC-2 transmissions, beginning at 00:37:00 GMT and continuing every 5 min until a total of 6 DC-2 commands had been transmitted to the spacecraft.

Although the recording sequence appeared to start normally, anomalous indications of status were observed in the science data which could not be interpreted until after the video data playback was completed. The first of these was observed at 00:34:57 GMT and appeared to be an end-of-tape event, although none was expected until approximately 00:42:30 GMT. One of the postulated failure modes for the record sequence involved the failure of the DAS to send, or the video storage subsystem to receive, tape stop commands, with the result that the video storage subsystem recorded continuously. Given this failure mode, the first end-of-tape event would have been expected at about 00:35:30 GMT. If it were assumed that the tape was improperly positioned past the end-of-tape foil, then the observed event would correlate with expected telemetry indications for this failure mode, and a second event would be expected at approximately 00:40:08 GMT. A second end-of-tape event was observed in the data at 00:40:50 GMT. Since the uncertainty in time of occurrence of an event based upon the time of first observation in the data is $\pm 0.0$ and $-50.4$ sec, this time also correlated with the postulated failure mode. With the possibility clearly established that the failure mode existed, it was expected that either no further end-of-tape events would occur, or that they would occur at 309-sec intervals. This was not the case, because a third end-of-tape event was observed in the data at 00:43:20 GMT, the proper time for track change in a nominal sequence. In the next data frame the false shutter event (distinguishable from end-of-tape events only by its timing) was observed. This also would be expected in a nominal sequence. No further events were observed in the science data. Table C-1 lists the encounter event times as determined from DAS data to the best available accuracy. These times are all referenced to teletype print times (except command initiate times), so that 0.3 sec of fixed teletype delay should be subtracted from each time to make the times absolute.

The contradictory indications in the data made it impossible to determine what had taken place until it was determined during video playback what data, if any, was stored upon the tape. It was expected, however, that if the sequence were in fact normal, the second true end-of-tape would occur during the recorder runup prior to Picture 22 and would immediately switch the data encoder to Mode 2 data. The mode switch would be observed in the data at about 00:55:24 GMT. The actual switch to Mode 2 data was not observed until 00:55:46.6 GMT, coincident with the end of Picture 22, indicating that the data mode switch was initiated by the DAS rather than the video storage subsystem. This tended to lend support to the hypothesis that the video storage subsystem was not running during the latter portion of the recording sequence. However, the engineering data upon

**Table C-1. Encounter events from DAS time (GMT)**

| Event | Initiate | Spacecraft | Verify | Uncertainty, sec |
|---|---|---|---|---|
| July 14, 1965 | | | | |
| DC-25 (turn on planet science) | 14:27:55 | 14:40:32.8 | 14:52:32.3 | −0.1 +1.0 |
| MT-7 (encounter power turn-on) | | 15:41:48.9 | 15:53:48.6 | ±0.3 |
| DC-24 (inhibit scan search) | 17:10:18 | 17:22:55 | 17:34:55 | −0.1 +1.0 |
| DC-3 (Data Mode 3) | 22:10:29 | 22:23:07 | 22:35:08 | −0.1 +1.0 |
| Wide-angle acquisition | | 23:42:00.3 | 23:54:01.6 | ±10.8 |
| July 15, 1965 | | | | |
| Narrow-angle scan | | 00:16:50.1 | 00:28:51.5 | ±12.6 |
| Narrow-angle acquisition | | 00:17:21.1 | 00:29:22.5 | ±0.1 |
| First start tape | | 00:18:29.6 | 00:30:31 | ±0.1 |
| Shutter 1 | | 00:18:33.1 | 00:30:34.5 | ±0.1 |
| Shutter 2 | | 00:19:21.1 | 00:31:22.5 | ±0.1 |
| Shutter 3 | | 00:20:57.1 | 00:32:58.5 | ±0.1 |
| Shutter 4 | | 00:21:45.1 | 00:33:46.5 | ±0.1 |
| First EOT[a] Event | | 00:22:30.3 | 00:34:31.7 | ±25.2 |
| Shutter 5 | | 00:23:21.1 | 00:35:22.5 | ±0.1 |
| Shutter 6 | | 00:24:09.1 | 00:36:10.5 | ±0.1 |
| DC-16 (narrow-angle acquisition) | 00:11:57 | 00:24:36 | 00:36:37 | −0.1 +1.0 |
| Shutter 7 | | 00:25:45.1 | 00:37:46.5 | ±0.1 |
| Shutter 8 | | 00:26:33.1 | 00:38:34.5 | ±0.1 |
| Shutter 9 | | 00:28:09.1 | 00:40:10.5 | ±0.1 |
| Second EOT[a] Event | | 00:28:23.1 | 00:40:24.5 | ±25.2 |
| Shutter 10 | | 00:28:57.1 | 00:40:58.5 | ±0.1 |
| Shutter 11 | | 00:30:33.1 | 00:42:34.5 | ±0.1 |
| Third EOT[a] Event | | 00:30:54.3 | 00:42:55.7 | ±25.2 |
| Shutter 12 | | 00:31:21.1 | 00:43:22.5 | ±0.1 |
| Shutter 13 | | 00:32:57.1 | 00:44:58.6 | ±0.1 |
| Shutter 14 | | 00:33:45.1 | 00:45:46.6 | ±0.1 |
| Shutter 15 | | 00:35:21.1 | 00:47:22.6 | ±0.1 |
| Shutter 16 | | 00:36:09.1 | 00:48:10.6 | ±0.1 |
| Shutter 17 | | 00:37:45.1 | 00:49:46.6 | ±0.1 |
| Shutter 18 | | 00:38:33.1 | 00:50:34.6 | ±0.1 |
| Shutter 19 | | 00:40:09.1 | 00:52:10.6 | ±0.1 |
| Shutter 20 | | 00:40:57.1 | 00:52:58.6 | ±0.1 |
| End NAMGA[b] | | 00:42:14.7 | 00:54:15.2 | ±25.2 |
| Shutter 21 | | 00:42:33.1 | 00:54:34.6 | ±0.1 |
| Shutter 22 | | 00:43:21.1 | 00:55:22.6 | ±0.1 |
| Last stop tape | | 00:43:45.1 | 00:55:46.6 | ±0.1 |
| Switch to Mode 2 | | 00:43:45.1 | 00:55:46.6 | ±0.2 |
| DC-26 (turn off planet science) | 00:31:42 | 00:44:21.5 | 00:56:23.0 | −0.1 +0.2 |
| DC-2 (No. 1) | 00:32:40 | 00:45:19.6 | 00:57:21.1 | ±0.3 |
| Telemetry lost | | 02:18:44 | 02:30:45.8 | ±1.0 |
| Enter occultation | | 02:19:11 | 02:31:12 | |
| Exit occultation | | 03:13:04 | 03:25:06 | |
| MT-8 (encounter power turn-off) | | 05:01:49 | 05:13:52 | ±0.3 |
| MT-9 (start playback sequence) | | 11:41:49.8 | 11:53:53.3 | ±0.2 |

[a] End-of-tape.

[b] Narrow-angle Mars gate acquisition.

return to Mode 2 indicated the correct number of event register changes for a nominal recording sequence.

After the planetary encounter, investigation showed that the *Mariner IV* spacecraft (MC-3) had shown a tendency toward spurious end-of-tape events in the Mode 3 science data although the previous occurrences had been associated with some ground action such as *boost mode inhibit off* or *narrow-angle Mars gate stimulus on/off*. Thus the two anomalous end-of-tape events could have been triggered by noise in the system, or by some normal transient in the television sequencing.

That the recording sequence was, in fact, normal throughout was verified during the playback of the stored data. All of the postulated failures would have resulted in less than 21 pictures, while only the normal sequence would have yielded the 21 pictures plus 21 lines of the 22nd picture which were found to be present on the tape.

The DC-26 command (*all science off*) was observed in the telemetry data on July 15, 1965, 00:56:23.0 GMT, and SPAC confirmed all zeros science data. The first DC-2 command (*cruise science on*) followed at 00:57:20 GMT. After confirming that cruise science was on and appeared normal, the DSIF was requested to cease the transmission of DC-2 commands. Event register changes confirming the reception of the remaining five DC-2 commands by the spacecraft were subsequently received at the expected times. Further analysis of the telemetry indicated that all engineering and science subsystems were performing as before encounter, and that the spacecraft had been returned to a normal cruise state. The remaining encounter event, MT-8, occurred several hours later, appearing in

the data at 05:14:39 GMT. This event, a CC&S command to turn off encounter science, had been preempted by ground command and did not affect the state of the spacecraft.

### C. Playback of Pictures

Postencounter cruise was terminated and video data playback initiated by the CC&S MT-9 Event* on July 15, 1965, 11:41:49.8 GMT. The event was observed on earth at 11:53:53.3 GMT, and the expected switch to Mode 4/1 data was confirmed.

After approximately 68 min of engineering data, the first Mode 4 (picture) data were observed in telemetry at 13:01:58 GMT. From this point the playback proceeded in an entirely normal manner through the termination of the record playback on August 3, 1965. During this period, the data from each of the pictures were transmitted to earth twice, with the exception of the last few lines of Picture 22. The data recovery rate was quite high, and the performance of the spacecraft was normal throughout.

In view of the uncertainty associated with the recording sequence because of the unexplained end-of-tape events, it was decided that command alerts should be called for each of the suspect periods during playback. After the end of Picture 4, DSS 42 locked up with the spacecraft command detector and maintained lock until after Picture 5 had been identified in the data and it was verified that the video data had been recorded on the day of encounter. Similarly, DSS 11 locked up with the command detector after the end of Picture 8, and maintained lock until Picture 9 could be verified. DSS 51 locked up with the command detector and maintained lock until after the time required to reach the point on the tape where the tape rundown after Picture 9 had stopped. Thus, during all of the periods which could have coincided with the spurious events received on July 15 (229th day of mission), a minimum reaction time command capability was provided to ensure that corrective action could be taken, if necessary, to obtain the most useful data from the playback. During all three command alerts, all of the spacecraft data indicated that the performance both in playback and at the encounter was normal.

An additional alert was called at the expected video storage subsystem track change, although the command detector was not locked up. The alert was called because it was possible, due to the low speed with which the end-of-tape foil passes the end-of-tape sensor during playback, to obtain multiple track changes. The track change occurred without incident.

The first complete transmission of the stored data ended on July 24, 1965, 19:26:33 GMT, and a second transmission began automatically. This second playback was necessary to ensure that any data missing from the first transmission of the pictures might be recovered and to provide duplication of the remainder of the data for comparison purposes. Spot checks of the data from both transmissions confirmed that the data were essentially identical, so it was planned to return the spacecraft to the cruise mode at the end of the second playback.

Shortly before the playback phase of the mission was terminated, SSAC (Space Science Analysis and Command group) and the television experimenters recommended that a second recording sequence be considered to provide information on the behavior of the television electronics for uniformly black pictures at each of the various gain settings. With this possibility in mind, the playback was terminated in such a manner that some portion of the Mars data would not be erased in the event that another recording sequence was performed. By stopping the tape at some position other than the end-of-tape foil, from 1 to 10½ pictures could be protected, since in a recording sequence the tape would run only until the end-of-tape foil had been crossed twice. Accordingly, the second playback was terminated in the 18th line of Picture 22, thus protecting all of the complete pictures on the second track.

### D. Television Haze Calibration Sequence

A television haze calibration sequence designed to test the performance of the television subsystem in the absence of incident light was initiated with DC-25 command (*encounter science on*) at 20:30:00 GMT on August 30. The sequence proceeded without incident as each command was received and executed in a normal manner.

A series of pictures was taken, starting with the gain setting at the least sensitive value and stepping through the more sensitive settings in the automatic sequence as designed. The stored data was played back until the first five pictures, which included all of the television gain settings, had been completed (September 2, 04:39:23 GMT).

*Start playback sequence.

## II. Television Subsystem Performance

### A. Planetary Scan

The planetary scan subsystem operated properly throughout the early science cover deployment operation on February 10, 1965. The correct initial search direction was obtained after the receipt of non-real-time power by the subsystem. Neither wide-angle nor narrow-angle acquisition events occurred throughout the sequence.

The scan subsystem completed a total of 10 search cycles. Calculation of the initiation time of DC-24 (*inhibit scan*) was based on the desired television pointing direction in terms of spacecraft clock angle and the scanning speed calculated from the data received for the first 6 scan cycles. The DC-24 transmitted stopped the scan platform 0.72 $\pm$0.36 deg from the desired position. The accuracy of positioning was well within the preestablished tolerance of $\pm$3.0 deg.

On July 14, 1965, the scan subsystem responded to the encounter science power-on command (DC-25) by initiating a planet searching operation at 14:40:33 GMT at the spacecraft. The subsystem began its search in the correct direction. To evaluate the planet searching performance, a graph of the platform position as a function of search time was generated based on the received real-time flight data. Analysis of the graph indicated that the subsystem was operating properly.

The original encounter operating plan was revised such that, operational and scan subsystem conditions permitting, the scan platform inhibit command (DC-24) would be used to preposition the platform. The command initiation time was to be calculated to stop the platform at a position for optimum pictures. The automatic planet tracking sequence was to be used as the backup operation in the event the prepositioning could not be exercised or failed to produce the intended results. Because of the occultation experiment, the final prelaunch trajectory change was such that the expected value of television pictures that would be attained with automatic planet tracking was not optimum.

Accordingly, a command initiation time was calculated based on the desired television pointing direction, the calculated scan search speed averaged over the first 7 search cycles, the communication transmission delay, and command processing time. The initiation time of DC-24, projected 7 scan cycles ahead, was calculated to be 17:10:18 GMT for the desired inhibit position of a 179.19-deg clock angle. Upon receipt of DC-24, the scan platform motion was inhibited at a clock angle of 178.45 deg, or 0.72 deg away from the desired position. This positioning was considered acceptable.

At 23:42:00.3 GMT at the spacecraft, the wide-angle sensor detected the edge of the planet and generated a wide-angle planet-in-view signal. The planet came into the TV camera field of view 23 min later. As the planet entered and swept across the sensor field of view the Y-axis output varied in accordance with the relative planet–spacecraft position and the amount of radiant energy received. Figure C-1 shows the actual Y-axis output as a function of GMT (Curve A) along with the calculated Y-axis output based on the pre-encounter trajectory data (Curve B). It is seen in Fig. C-1 that Curve A is located to the left of Curve B, indicating that the planet entered the wide-angle sensor field of view about 5 min earlier than expected. This deviation is due partially to an error in the prediction of the spacecraft arrival time and partially to error in the Y-axis output prediction calculation.

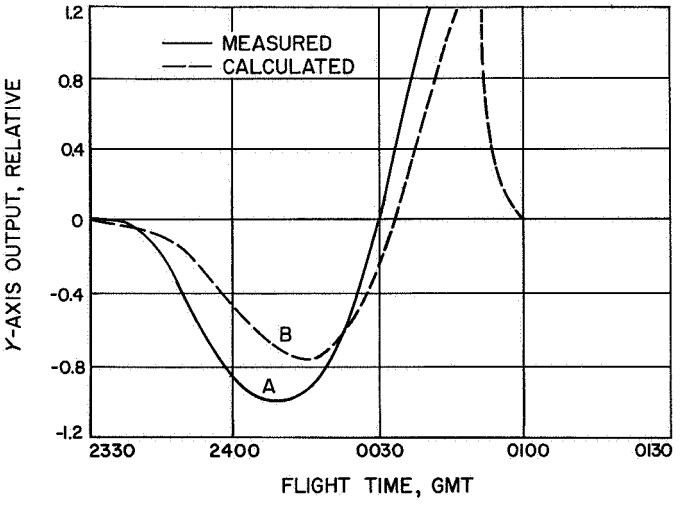


**Fig. C-1. Measured and calculated scan subsystem Y-axis output**

The performance of the scan subsystem during the planet encounter period is summarized in Table C-2. The data received during the science cover deployment sequence are shown for comparison.

The scan subsystem was energized during the television dark encounter sequence on August 30, 1965. The subsystem operated properly throughout the sequence. Upon the receipt of encounter science power resulting from DC-25, the subsystem responded by initiating a planet searching operation in the correct search direction.

**Table C-2. Scan subsystem performance**

| Function | Prelaunch or predicted value | Data readout during science cover deployment | Data readout during Mars encounter |
|---|---|---|---|
| 1. Average scan time per cycle, sec | 717.0 | 712.0 | 713.4 |
| 2. Desired platform inhibit position, deg | | 177.19 | 179.19 |
| 3. Actual platform inhibit position, deg | | 177.94 | 178.45 |
| 4. Calibration signal, V | 0.998 | 0.998 | 0.998 |
| 5. Transformer-rectifier, V | 4.896 | 4.896 | 4.896 |
| 6. Sensor temperature, °C | −10°C for encounter operation | −3.0 | −8.5 |
| 7. Actuator pressure, psia | 30 | 30 | 26 |
| 8. Y-axis output with no input, V | 3.064 | 3.064 | 3.076 |
| 9. Number of search cycles performed | | 10 | 14 |

A total of eleven search cycles was performed with each reversal actuated by the primary limit switches. During this time, the subsystem sensor and optics assembly was operating at a temperature of −11.0°C as compared to −8.5°C at planet encounter. The Y-axis output remained constant at a numerical value corresponding to no significant input; i.e., the Y-axis output indicated that no objects having radiation energy of 1.0 $\mu$W or greater in the integrated spectral range of 0.5 to 1.1 $\mu$ were observed by the wide-angle sensor. All other signals were well within the specified and predicted limits.

### B. Television Electronics

The television subsystem was turned on by ground command DC-25 at 14:40:32.8 GMT spacecraft time on July 14, 1965. The subsystem operated for about 7 hr 45 min before transfer to Mode 3 (*encounter science data*) by ground command DC-3. Reduction of the TV voltage data received before narrow-angle acquisition agrees exactly with the data obtained during the science cover deployment operation on February 11, 1965. It was known from tests performed before launch that the voltage-measuring device varied about one order of magnitude more than the voltage being measured and that the measuring device was also more temperature-sensitive. Shutter and filter data indicated that the red and green filters were alternating as designed, that the shutter speed was 200 msec, that there was less than 2 V of video signal, that there was no planet-in-view signal, and that the gain control computer was in its minimum gain state.

In DAS Frame 41 (the DAS frame counter was reset to zero at wide-angle acquisition), telemetry indicated a television planet-in-view signal; all other television data remained unchanged. During prelaunch testing and calibration the video level always indicated over 2 V before the light intensity was sufficient to cause a television planet-in-view signal to be initiated. Therefore, it is believed that the television subsystem received the planet-in-view signal from the narrow-angle Mars gate via the DAS, rather than from the video level indicator.

Frame 42 data indicated a video level over 2 V. Frame 43 data (start of Picture 1) showed that the television G1 voltage had changed abruptly, indicating that the television subsystem had switched out of the photometer mode and that the inhibit was released from the gain control computer. The gain computer remained in the minimum state because the video level was sufficiently great. However, the video signal was not sufficient to cause a switch to the fast shutter speed of 80 msec. For the remainder of the recording sequence the G1 voltage in the normal mode was 46.4 ±0.2 Vdc, identical to the prelaunch value.

Television data remained unchanged, except for filter color alternation, until Frame 59 (green filter), when a video signal level less than 2 V was indicated. The television subsystem was designed so that the gain would change after a green filter picture having less than 2 V of video signal. Frame 60 showed more than 2 V of video signal, but the gain was unchanged. Analysis showed that the sampling had occurred during the blanked out first 6 lines of the television picture. This condition occurred several times during system testing and was not considered a problem or anomaly.

The video signal decreased below 2 V in Frame 67. The gain remained at its minimum setting (00) until Frame 68, when it increased one level (to 01). The gain increased again in Frame 70 (to 10) and switched to maximum (11). The spacecraft switched to Mode 2 data before Frame 73 data was received.

The pictures received during playback and telemetry during encounter both indicated that the television subsystem operation was excellent. The electronic focus, resolution, gray-scale rendition, and sensitivity seemed as good as before launch.

The "dark encounter" exercise was undertaken in an attempt to learn more about the "haze" seen in the pictures of Mars. Secondarily, it was hoped that some explanation of the periodic interference seen in pictures taken through the red No. 2 filter might be found.

Although the aborted "Altair encounter" moved in the shutter disc, analysis of the timing indicated a 0.8 probability that the first red picture recorded would be Filter No. 1 if the proper sequence of turn-on commands was used.

The predetermined procedure was followed, and the encounter sequence was initiated at 20:30 GMT, August 30, 1965. The Mode 3 telemetry was carefully analyzed to determine whether the AAC-3 function ($>$ 2-V pk video) tripped. Additionally, the frame start/end of tape (bit 408) and the television filter (bit 406) functions were monitored for a repeat of the anomalous events seen during the Mars encounter.

The results of the exercise were essentially negative. No video was detected, and the played-back pictures showed no excessive noise indicative of the increased dark current in the vidicon. At the maximum gain state, the average video level DN was 61.5 compared with 59.0 as the quietest "capped optics" picture taken during calibration. Space would appear to be quieter and/or darker than a test lab.

All telemetry data were nominal, including bias voltages and temperature, and the conclusion can be drawn that the "haze" is either on Mars or, if it is an instrumental effect, a result of peculiarities of the encounter lighting conditions.

PRECEDING PAGE BLANK NOT FILMED.

# Appendix D

# Design of the Television Experiment

## I. Requirements and Constraints

The design of the television experiment was influenced by a variety of factors. The stated scientific objectives had to be translated into specific instrumental requirements, thereby affecting the gross design of the spacecraft and the operational plan for the flight itself. As time went on, the spacecraft design became more definite, and certain constraints upon the TV experiment were imposed, thus limiting the range of selection of camera parameters and flight trajectories. These constraints can be categorized as (1) by-products of the TV and other science experiments, (2) spacecraft design constraints, and (3) operational constraints including arrival date, visibility of the spacecraft at Goldstone at the time of encounter, and sterilization.

### A. Resolution and Area Coverage Requirements

In order to make a significant improvement over earth-based observations, much higher ground resolution was required. The best earth-based photographs are of the order of 100 km in resolution, and the best visual observations improve on this by perhaps a factor or two. It was expected that at least an order of magnitude improvement should be achievable by *Mariner*.

It was of course desirable to cover the greatest possible area at the highest possible resolution. However, the spacecraft was capable of storing and returning to earth only a relatively modest amount of data. At a minimum, it was desired that the area coverage per picture should be great enough to permit correlation of picture information with surface features observed from earth. Further, to maximize the possibility of interpreting the observed features, it was desired that adjacent frames should be contiguous. Finally, if color filters could be used, it was desirable that adjacent frames actually overlap so as to permit color comparisons.

To maximize the probability of observing surface topography by means of shading and shadows, it was strongly desired that at least part of the picture coverage be in the near-terminator region. In addition to terminator region coverage, it was desired that some pictures be taken under conditions of near-vertical solar illumination in order to study albedo variations independent of shading due to surface slopes. It was felt that this information would be useful in characterizing the differences between light and dark regions as well as in the design of future photographic missions.

Except for the polar caps, the most distinctive Martian features are the more or less permanent light and dark areas. It has long been thought that these distinctive markings represent essentially different surface characteristics. Some of the dark areas have been observed to change in size and in depth of shading, leading a few astronomers and others to speculate that they might be areas of vegetation. Whatever the essential differences, it was desired that areas of both types be sampled.

The Martian polar caps are the most predictably changing features on the planet, yet the polar cap phenomena are not entirely understood. It was thought that observations of the edge of the cap might yield useful information. Also, it was thought that near-terminator pictures within the cap might show surface relief particularly well since the bright surface would give good exposure levels even near the terminator. Coverage of one of the polar caps, particularly near its edge, was therefore considered desirable.

Prior to flight, there was no way of knowing how finely detailed the surface would appear. There was some possibility that the surface might be very regular without much brightness variation, or some failure of the camera might seriously degrade the resolution in the pictures. To guard against these possibilities, it was desired that the picture coverage should include a maximum number of known light–dark boundaries, so that some information would be returned even if no finer detail was to be seen.

Over the years, certain Martian features have received special attention from astronomers either because of their prominence or because of changes in appearance. Examples of the former are Syrtis Major, the most prominent dark marking, Sabaeus Sinus, another dark area, and "deserts" such as Hellas in the south and Elysium in the north. Among those features that exhibit seasonal or secular changes are Solis Lacus, Trivium Charontis, and the "oases" in the "desert" Aethiopis. These were among the areas considered to be of special interest; it was felt that one or more of them should be observed during the *Mariner* experiment in order to try to determine the reasons for their peculiarities.

### B. Phase Angle

To obtain new information about surface reflectivity, it was desired that the phase angle, which was restricted to a constant value by the scan platform mechanization, be greater than 47 deg, the maximum Martian phase angle observable from earth. It was felt, however, that the phase angle should not be so large as to render unreliable the prediction of the disc brightness for purposes of camera design or to limit the view to only a thin Martian crescent.

### C. Limb

It was thought that the atmospheric blanket might be visible above the limb. Therefore, photography of the bright limb was desired, since near-limb photographs of the subsolar region were to be made in any case. This requirement was considered to be far less important than the requirement for terminator coverage, but turned out to be quite important in the interpretation of the pictures that were obtained.

### D. Other Science Requirements

Requirements imposed by the other scientific experiments joined with those of the television experiment in influencing selection of certain mission parameters. In general, experiments on fields and particles were considered to increase in value as the periapsis altitude decreased. In addition, some preference was given trajectories near Mars' equator because of the possibility that there might be a radiation belt like earth's Van Allen belt. The occultation experiment required that the spacecraft pass behind Mars as viewed from earth, so that the telemetry signal would pass through the Martian atmosphere just before and just after occultation. The requirement severely limited the choice of trajectories.

### E. Spacecraft Constraints

The spacecraft configuration strongly affected the scientific experiments that could be performed. A few of the spacecraft constraints, particularly those which directly influenced the design of the television experiment, are mentioned here.

*1. Payload weight.* The actual scientific payload weight was determined by the *Atlas/Agena* launch vehicle and the minimum spacecraft configuration required to provide a stable instrument platform. The allowable payload weight severely limited the magnitude of the television experiment, both in terms of total data returned and maximum resolution attainable. A two-camera system was originally proposed, but the limited weight allocation ruled out such a system.

*2. Data storage capacity.* Largely because of the weight limitation, the total data capacity of the video storage subsystem tape recorder was limited to five million bits.

*3. Scan platform.* In order to point the camera at the desired regions on the planet, the spacecraft was provided with a scan platform and a planet tracker to aim the camera. Again because of the weight limitation and also because of reliability considerations, the platform was permitted to have only one degree of freedom, rotation about the spacecraft roll axis.

*4. Attitude sensors.* The *Mariner* spacecraft used the sun and Canopus as references for attitude control. To prevent loss of control during the crucial period of Mars encounter, trajectories on which the planet itself would occult the sun and cause loss of sun lock and loss of solar panel power were avoided, as were trajectories which would allow reflected light from Mars to enter the Canopus sensor and cause the Canopus tracker to attempt to follow Mars. These constraints thus limited the attainable television coverage, although not seriously.

### F. Operational Constraints

In addition to the above constraints, which were imposed directly by the spacecraft configuration, there were three others that directly affected the trajectory selection and therefore the television experiment. Two of these constraints related to date and time of day of encounter. The third was a sterilization-related requirement.

Of all possible planetary transfer trajectories, the least launch vehicle impulse is required for those lying very nearly in the ecliptic plane. In 1965, Mars crossed the ecliptic on July 18, so the minimum-energy trajectories required an arrival on or near that date. The arrival "window" extended from July 15 to July 21.

In order to increase reliability of control of the spacecraft during the encounter period, it was required that the spacecraft be "visible" from the Goldstone tracking station during the crucial parts of the encounter phase. In this way, telemetry could be received at the SFOF at JPL via telephone and radio link through Goldstone rather than the relatively remote Johannesburg or Woomera stations, and use could be made of the 100-kW transmitter at Goldstone. Together with the arrival date constraint, this "Goldstone constraint" permitted television coverage only in a limited longitude range on Mars, because Mars' rotation period nearly matches that of the earth.

The sterilization constraint, deriving from the biological quarantine of the moon and planets, requires that all reasonable steps be taken to prevent contamination due to organisms or organic substances carried by spacecraft. In the case of flyby vehicles, it has been ruled that trajectories must be chosen having very low probabilities of impacting the body, less than $10^{-4}$ in the case of *Mariner IV*.

### G. Selection of Camera Parameters

The basic parameters of picture format, camera focal length, pointing direction, and operating sequence were chosen to best carry out the experiment objectives within the constraints outlined above.

*1. Format.* The final scan platform configuration did not permit motion of the camera pointing direction during encounter, but in the early design period it had been planned to reposition the scan platform after every picture pair in a zigzag pattern across the planetary disc. With such a scheme, contiguous surface coverage called for a large number of pictures. For this reason it was planned to take twenty pictures having a relatively small number of picture elements per picture, rather than four or five separated pictures having a larger format. The actual dimensions of the pictures were then determined by the number of quantization levels and the tape recorder bit capacity. Since the brightness contrast of the pictures could not be predicted in advance because of the unknown character of the Martian topography—and even the average brightness levels the camera would see as it traversed the planet were not well known—it was decided that each picture element should be represented by 6 binary bits, or 64 quantization levels.

Twenty pictures divided into the total capacity of $5 \times 10^6$ bits, gives $2.5 \times 10^5$ bits per picture. Dividing this by 6 bits per picture element gives $4 \times 10^4$ elements per picture. Thus a square format with 200 elements/line and 200 lines/picture format was chosen. This format was fit into a 5.6-mm square on the vidicon faceplate.

*2. Focal length.* Given the picture format, the surface resolution and area coverage depended on the distance to the surface and the camera focal length. Preliminary trajectory analysis showed that to satisfy the sterilization constraint, the minimum altitude reached on a standard trajectory should be 25,000 km. Closer trajectories later became possible, but the focal length was chosen on the basis of this preliminary altitude estimate. It was decided that resolution should be emphasized over broad area coverage in order to obtain a significant increase in knowledge of surface detail over that obtainable using earth-based telescopes. A focal length of 30.5 cm was chosen, giving a nominal resolution better than 2.5 km/TV line and an area coverage of nearly $500 \times 500$ km per frame. It was felt that this coverage would be adequate for correlation of picture information with known surface markings.

*3. Phase angle.* The scan platform was to have only one degree of freedom, rotation about the roll axis, i.e., the spacecraft–sun line. The phase angle (the angle between an incident ray of sunlight and the reflected ray from the observed surface into the camera) at which the planet would be viewed by the camera was fixed. It was therefore necessary to select this phase angle during initial design. A value of 60 deg was chosen. This was somewhat larger than the maximum Mars phase angle observable from earth, consistent with the exploratory nature of the experiment and the desire to obtain new information about Mars. It would also give a nearly vertical view of the surface near the time of closest approach.

*4. Operating sequence.* Once the phase angle was chosen, it was possible to determine the interval of time during which the camera could view the illuminated part of the planet. On the basis of this determination, it was decided that an interval between exposures of 48 sec would locate all the pictures within the illuminated part of the apparent disc. After the circuits had been designed for this 48-sec exposure interval, it was decided that the picture track should somewhat overlap both the bright limb and the terminator. This required an extension of the picture-taking sequence, which was most easily accomplished by omitting every third picture from the data recording sequence. The camera was thus operated each 48 sec, but only two out of every three pictures taken during encounter were recorded on tape. Since the filter color was alternated at each camera operation, this resulted in a color sequence R, G; G, R; R, G; etc . . . for the recorded pictures.

### H. Prelaunch Trajectory Selection

In the analysis of flyby trajectories, considerable use was made of the aiming point coordinate system shown in Fig. D-1. The R-T plane, or aiming point plane, is perpendicular to the incoming asymptote of the spacecraft trajectory relative to the planet. This asymptote is described by an S-vector which, with the vectors **R** and **T** shown in the figure, forms a right-handed orthogonal coordinate system. The **T**-vector is perpendicular to the incoming asymptote and parallel to the plane of the ecliptic. The vector **R** is defined by $\mathbf{S} \times \mathbf{T}$. The vectors **R** and **T** are then used to define the "aiming point plane," shown in the

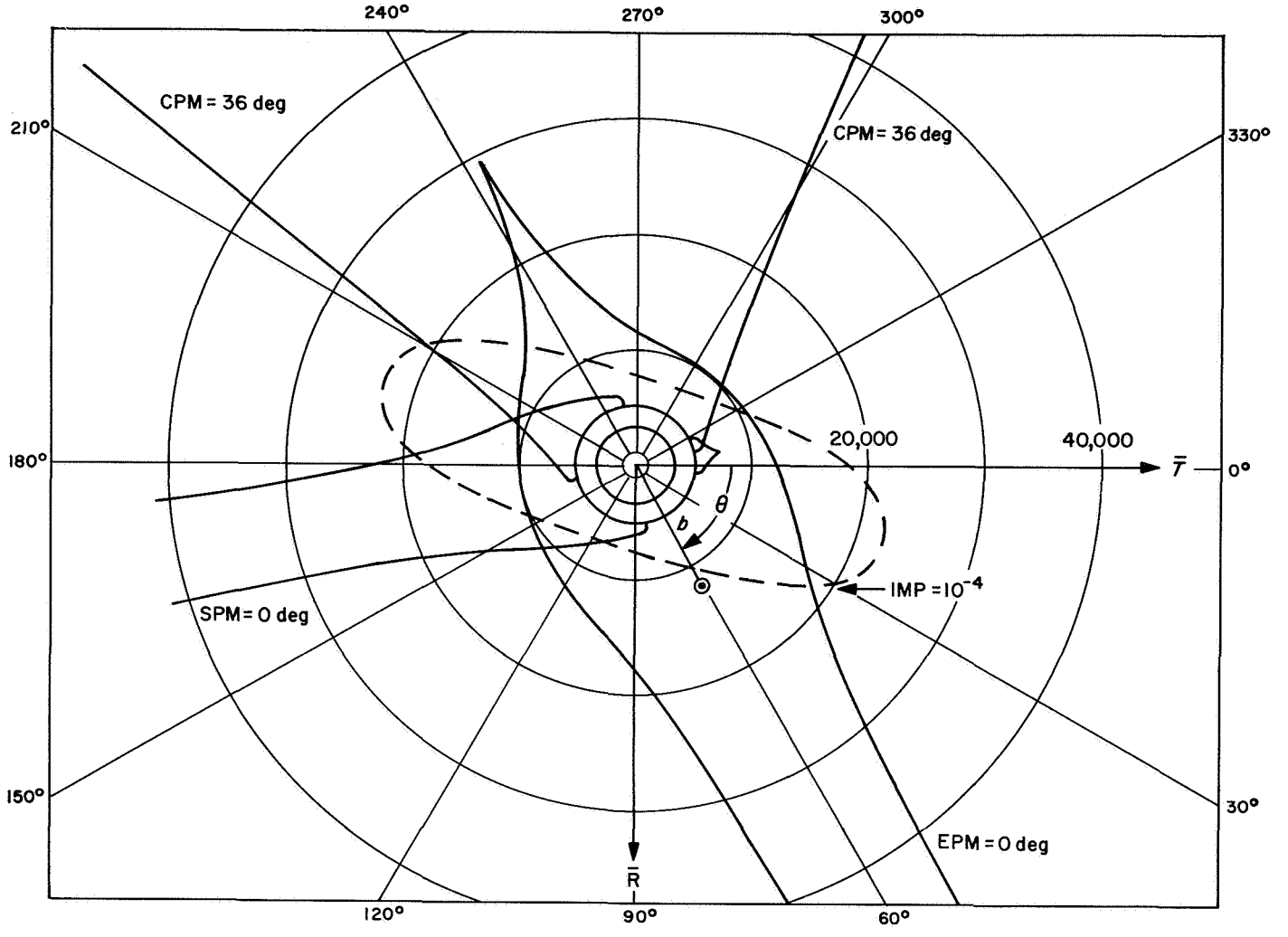


**Fig. D-1. Engineering constraints for July 15 arrival; aiming point defined by vector b and angle $\theta$**

figure. "Aiming points" are specified by $b$ and $\theta$, the length and angle respectively of the impact parameter. As an example, the final ("standard") aiming point for *Mariner IV* with $b = 12{,}000$ km and $\theta = 60$ deg is indicated. The small circle at the center of the coordinate system represents the size of Mars, while the larger circle represents its capture radius for a typical *Mariner IV* flyby velocity.

*1. Initial aiming point.* Figure D-1 also shows some of the engineering constraints. Aiming points within the boundary marked CPM = 36 deg would result in probable loss of Canopus lock. Aiming points within the boundaries labelled SPM = 0 deg or the EPM = 0 deg would result in sun occultation or earth occultation, respectively. The IMP = $10^{-4}$ curve encloses the aiming point region in which the probability of Mars impact by the spacecraft would be greater than one part in $10^4$, thereby violating the sterilization constraint. The curves shown apply only to a specific launch date and arrival date combination. On the basis of combined analyses of several launch date/arrival date situations, an initial aiming point at $b = 25{,}000$ km and $\theta = -15$ deg was chosen. The earth occultation experiment was not at that time being considered, and the aiming point was chosen to avoid all the engineering constraint contours. It was on the basis of this aiming point that the television camera parameters were chosen.

*2. Second aiming point.* Because of the "Goldstone constraint," the 1965 arrival date window permitted photography only in the longitude range from about 140 to 280 deg east longitude. Furthermore, the initial aiming point located the trajectory very near the equator. These circumstances would have permitted television coverage only of the Martian deserts in the Amazonis–Tharsis region. In

order to obtain dark-area coverage as well, a more southerly aiming point, at $\theta = +30$ deg, was therefore chosen.

The second aiming point required a circuit change in the wide-angle sensor (WAS) tracking subsystem, whose purpose was to track the planet until initiation of the picture-taking and recording sequence. With the initial aiming point, the trajectory would have been nearly parallel to the sun–Mars line, and center-of-brightness tracking would have resulted in a picture track along a great circle. This condition no longer held for the $\theta = 30$ deg aiming point, and center-of-brightness tracking would have resulted in a picture track along a small circle about 20 deg in latitude to the north of the subspacecraft trace. This circumstance was caused by the fact that WAS tracking was to cease as soon as the picture sequence began. The small-circle track was undesirable in that it would prevent near-vertical viewing of the surface near the center of the picture-taking sequence. This condition was corrected by introducing a signal bias in the WAS to cause it to track to the south of the center of brightness. With the $\theta = 30$ deg aiming point, the WAS bias, and a typical arrival date and time within the "Goldstone constraint" window, parts of the Amazonis desert and Mare Sirenum would be viewed.

The requirement to photograph the bright limb at the start of the picture sequence necessitated a biased pointing direction for the narrow-angle Mars gate (NAMG). It was originally planned to boresight the NAMG with the television camera line of sight. However, the encounter timing sequences permitted a variable, random delay of from 60 to 204 sec after acquisition of the planet and before exposure of the first recorded television picture. To compensate for this delay, it was planned to bias the NAMG pointing direction ahead of the television camera by an angle of 1 deg. For the second aiming point, this angular bias guaranteed that pictures of both the bright limb and the terminator would be obtained.

*3. Final aiming points.* During early 1964, it was decided to carry out an earth-occultation experiment to study the effects of the Martian atmosphere upon the telemetry signal. This required aiming points lying within the earth occultation contours, designated by the EPM = 0 deg envelope in Fig. D-1. To assure occultation, the aiming point was placed in the center of the EPM = 0 deg contour. Since the location of the contour varied with both launch and arrival dates, $\theta$ values between 60 and 80 deg had to be used, depending on the launch/arrival date combination. At the same time, it was found that the scientific value of the occultation experiment would increase with decreasing altitude, as was the case for the particles and fields experiments. A value of $b$ near the minimum permitted by the sterilization constraint was thus requested for optimization of these experiments.

Fortunately, this recommended change in aiming point was in many aspects also favorable to the television experiment. It had been argued that greater emphasis should be placed on obtaining higher resolution, which would result from the new aiming point. While fully contiguous coverage would be lost and correlation of observed objects with features observed from earth would be made more difficult, overlap of frame-pairs would still occur, providing some data on spectral reflectivities. It was decided that no NAMG forward bias would be required (although this would result in a small probability, less than 0.1, of not photographing the planet limb) because the pictures would be taken somewhat earlier on the trajectory, when the apparent angular velocity of the limb in the camera field would be lower. In the case of the WAS signal bias, the circuitry changes had already been incorporated and would still have the effect of making the picture track tend toward a great circle, although not as effectively as for the $\theta = 30$ deg aiming point. The resulting picture coverage for the new aiming points would extend over a wider latitude range, providing a better balance between desert and dark-area coverage as well as coverage near the south polar cap. For the $\theta = 80$ deg case, the picture track would have extended into the south polar cap but would not have extended past the terminator.

One of the final aiming points is indicated in Fig. D-1 at $b = 12{,}000$ km and $\theta = 60$ deg. Other aiming points for different launch date/arrival date combinations required theta values of 70 and 80 deg.

### I. Premaneuver Trajectory Selection

Prior to the time of midcourse maneuver execution, quantitative techniques were developed to evaluate the effects on the science experiments of dispersed trajectories. Each spacecraft had the capability of two midcourse maneuvers to place it on the desired Mars flyby trajectory. Optimum use of both the prime and the backup maneuvers in operational situations was dependent on these trajectory evaluation tools.

*1. Television value contours.* The value contours shown in Fig. D-2 are typical of several such plots developed for evaluating the effects of various trajectories on the television experiment. This plot applies to a spacecraft arriving at Mars in the center of the "Goldstone constraint"

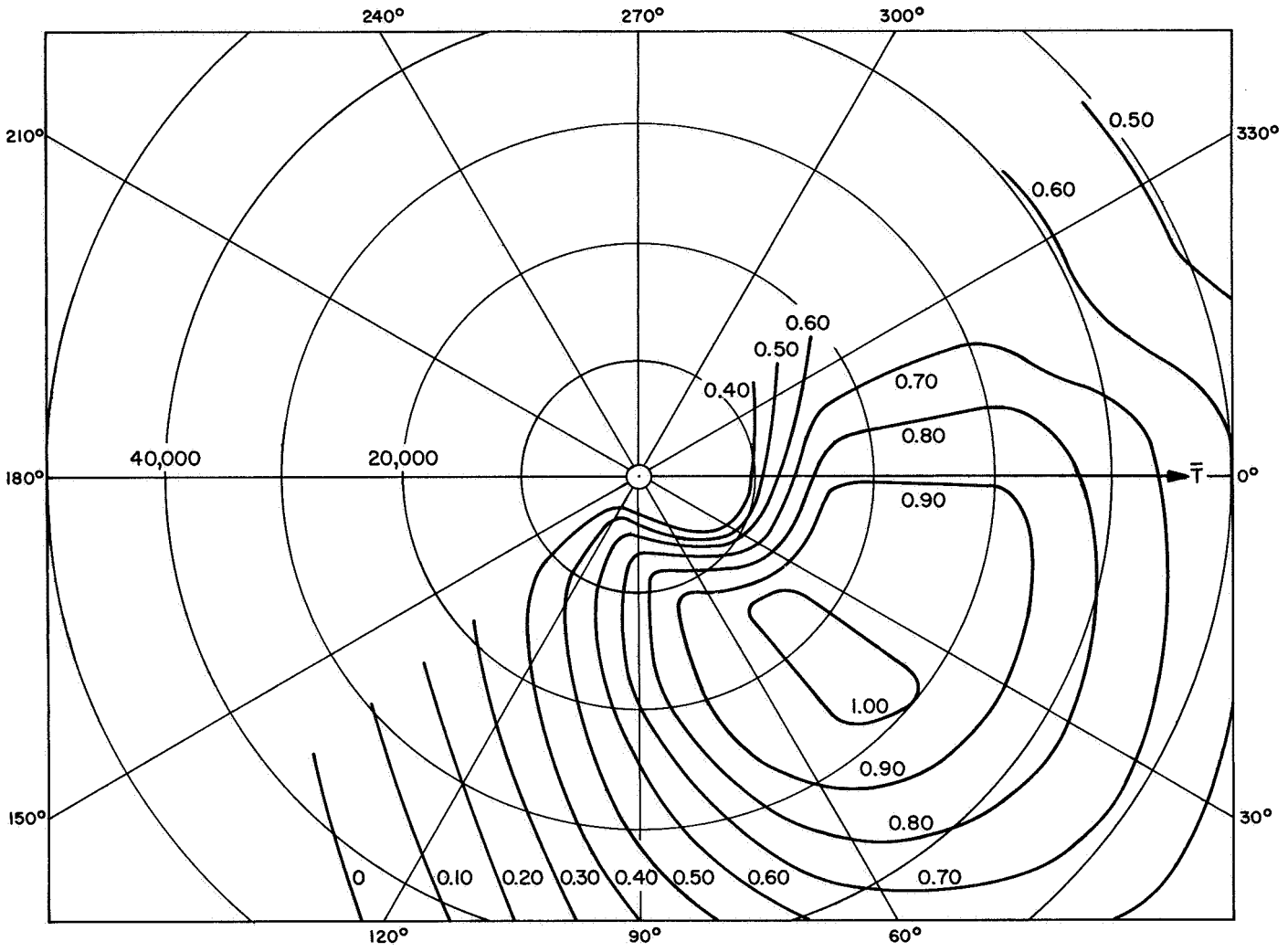


**Fig. D-2. Typical television value contours for July 15 arrival**

arrival-time window on July 15. The half-plane in which no contours appear represents trajectories on which the scan platform rotation limits would not have permitted viewing of the planet, necessitating rolling the entire spacecraft if pictures were to be taken. Decreasing relative value toward near-zero and negative theta values was caused by loss of dark-area coverage and by an increasing percentage of the pictures being taken beyond the terminator. Trajectories with high theta values, greater than 80 deg, would result in pictures taken earlier along the trajectory. This would have had two effects: (1) increased distance and poorer resolution, and (2) loss of coverage of the near-terminator region because of shortening of the picture track. Trajectories too near the planet would have caused severely decreased area coverage without an increase in resolution since the resolution would have been limited by image smear. Too distant trajectories would have resulted in poorer surface resolution.

The value contours were also checked with a set of maps made from photographs of a Mars globe showing the locations of picture tracks resulting from typical trajectories.

From Fig. D-2 it can be seen that the final aiming points were not judged to be optimum for the television experiment. The decrease in estimated value was offset by increased probabilities of success for the other planetary experiments.

*2. Mariner III aiming point.* The *Mariner III* trajectory would have been characterized by a theta value of 80 deg and an encounter time of 01:44 GMT. Had it achieved this trajectory and completed its mission successfully, its picture track would have crossed the equator at approximately 190 deg east longitude and extended southward into the south polar cap.

3. *Mariner IV trajectory.* *Mariner IV* very nearly achieved its planned trajectory following the first midcourse maneuver. Predictions from early tracking data indicated an arrival time about 36 min earlier than desired and a parameter $b$ about 1500 km greater than standard. These were well within tolerance and a second maneuver was not required.

### J. Pointing Direction Selection

The *Mariner IV* spacecraft was designed to carry out an automatic encounter sequence without control by ground command, although the capability of such control was provided. In the nominal automatic sequence of events, the camera pointing direction would be set by active tracking of the planet by the WAS-scan subsystem. The switch-on of encounter science power by CC&S command at about eight hours before the time of closest approach was to start the scan search mode. Later, at about 90 min before closest approach, the WAS would have detected and "locked on" the planet, beginning the tracking mode. The WAS-scan subsystem would have then actively tracked the planet until an acquisition signal from either the NAMG or the television camera initiated picture recording. This sequence of events would have resulted in a picture track about 10 deg farther to the northeast than the track actually obtained by *Mariner IV*. The actual track was achieved by presetting the scan platform position by ground command.

1. *Preset pointing direction.* During the period between the *Mariner IV* launch and encounter, the various encounter sequences made possible by the capability of the spacecraft to respond to various ground commands were carefully analyzed. One of the commands could be used to stop the scan at any time during its search mode. It was concluded that the use of this capability sufficiently early in the search mode would yield a higher probability of success. If the first attempt to preset the pointing direction failed to achieve a satisfactory result, there would be time for a second attempt or a return to the automatic sequence. On the other hand, if a fully automatic sequence alone was used, failure of the WAS to lock on the planet at its anticipated time (less than an hour before start of picture recording) would allow very little time for corrective action from earth because of the 24-min round-trip signal transmission time.

2. *Optimum camera pointing.* The capability to preset the camera pointing direction also widened the choice of picture coverage. It will be recalled from the previous discussion that the electronic bias of the WAS signal was designed for the $\theta = 30$ deg aiming point; this bias was not optimum for the final aiming point of $\theta = 60$ deg. Presetting of the pointing direction would permit more nearly vertical viewing of the surface near the middle of the picture track and would also maximize the percentage of pictures taken on the illuminated part of the planet (these conditions happened to be mutually compatible). In addition, presetting would to some extent permit selection of particular surface features to be viewed. It was decided to try to achieve a picture track that would include the interesting area Trivium Charontis. This track would also provide a viewing direction within a few degrees of vertical at the middle of the pass and a near-minimum coverage beyond the terminator.

3. *Camera aiming.* The final scan platform clock angle (angle about the spacecraft roll axis, referenced to the pointing direction of the Canopus tracker) was chosen on the basis of the latest possible tracking data, obtained about 12 hr before closest approach. These data were used to predict a flight path with $b = 14{,}430$ km, $\theta = 59.92$ deg, and time of closest approach = 01:01:12 GMT, July 15, 1965. Analysis of this trajectory showed that a camera clock angle of 179.2 deg would give the desired track. Scan platform position data were received and analyzed after initiation of the search mode, and a time for sending the command to stop the scan motion was computed. The command was sent at the computed time, and the platform stopped within 1 deg of the correct angle.

4. *Picture coverage obtained.* The actual trajectory achieved differed significantly from that predicted at 12 hr before encounter: $b$ was 820 km greater and $\theta$ was 2.2 deg smaller than predicted. These differences, added to the small difference (¾ deg) in clock angle from the desired value, combined to place the actual picture track about 15 Martian degrees northeast of the predicted location. The *Mariner IV* picture locations are shown in Fig. D-3 against a section of the ACIC Mars map.

## II. Picture Locations

Latitudes and longitudes of the pictures were deduced from trajectory data, known camera and spacecraft geometry, extrapolated spacecraft attitude control data, the location of the limb in Picture 1, and, finally, use of the picture information itself in the overlap areas between pictures. Very few features were seen in the *Mariner IV* photographs which could be precisely correlated with existing photographs or drawings of Mars.

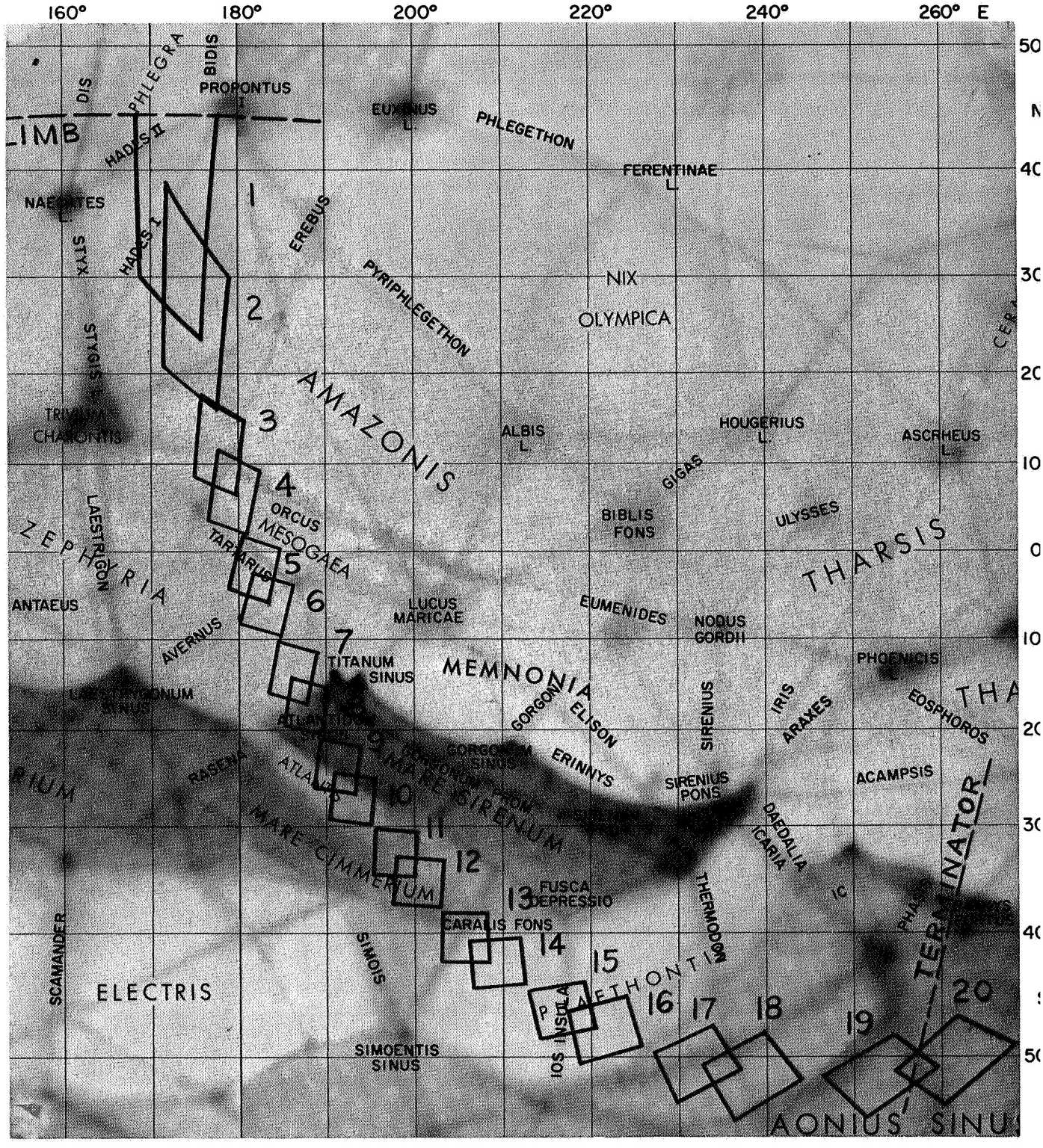


**Fig. D-3. Picture locations**

### A. Determining Factors

The coordinate system against which the picture data have been mapped was derived from elements given in the *American Ephemeris and Nautical Almanac*. The parameters which influenced the picture locations are given in Table D-1, along with $1\sigma$ uncertainty estimates. The first three are the impact parameter $b$, the angle $\theta$, and the closest approach $T_{CA}$. Values of these quantities were computed from tracking data received through and beyond encounter. Dispersions can be considered to be gaussian, and the errors indicated are standard deviations. The value for the equatorial radius of Mars, $R_M$, is a compromise between de Vaucouleurs' value, 3375 km (Ref. 4), and the higher value indicated by the *Mariner IV* occultation experiment.

**Table D-1. Preliminary values of parameters influencing picture locations**

| Parameter | Standard value | Error ($1\sigma$) |
|---|---|---|
| $b$ | 15,251 km | 17 km |
| $\theta$ | 57.74 deg | 0.08 deg |
| $T_{CA}$ | 01:00:57 | 10 sec |
| $R_M$ | 3380 km | 30 km |
| $C_A$ | 120.1 deg | 0.1 deg |
| $K_A$ | 178.45 deg | 0.7 deg |
| $F$ | 30.85 cm | 0.2 cm |
| $d$ | 2.45 mm | 0.01 mm |
| $r$ | 0 deg | 2 deg |
| $pn$ | 0 | 0.002 rad |
| $yn$ | 0 | 0.002 rad |
| $rn$ | 0 | 0.002 rad |
| $p$ | ±8.3 millirad | |
| $y$ | ±8.3 millirad | |
| $r$ | ±4.4 millirad | |

The cone and clock angles, $C_A$ and $K_A$, define the TV pointing direction relative to the spacecraft axes. The pointing direction is the projected direction of the central fiducial mark of each picture. Indicated errors are based on mechanical tolerances in the spacecraft assembly. The clock angle error also includes the uncertainty in readout of the position indicator.

The camera focal length, the fiducial mark spacing, and the frame rotation are given by $F$, $d$, and $r$, respectively. The vidicon faceplate pattern was aligned by rotating the vidicon and its pin connector until an output picture showed the fiducial marks to be aligned with respect to the camera mounting bracket. The error in rotation alignment was not actually measured, but was estimated to be about 2 deg. It was later found in correcting the map data to fit the observed limb contour that the frame rotation error may actually have been 3 deg.

The sun tracker optical axes were aligned with the spacecraft Z-axis within a ±2 millirad uncertainty, resulting in a $1\sigma$ error of 2 millirad in spacecraft attitude in pitch null position ($pn$) and yaw null position ($yn$). Uncertainty of Canopus tracker pointing with respect to nominal is of the same order, resulting in a 2-millirad probable error in the roll null position ($rn$). The attitude control system "deadbands" permitted free motion between fixed limits of ±8.3 millirad in pitch and yaw and ±4.4 millirad in roll about the null positions. Unfortunately, no attitude information was transmitted during the picture taking sequence. In initial estimates of the picture locations, therefore, the attitude was uncertain within the ranges given.

### B. Computation of Picture Locations

To find the picture locations, use was made of a computer program developed for mapping the *Ranger* photographs of the lunar surface. This program uses a hyperbolic approximation to the spacecraft trajectory near the planet. The program accepts trajectory data, camera pointing direction, exposure times, and camera geometry, and uses these parameters to compute the picture latitudes and longitudes as well as other picture geometry information. An option exists to perturb the camera pointing direction according to the spacecraft pitch, yaw, and roll excursions, if known, about the nominal spacecraft orientation. Some minor changes in the program and in the form of some of the inputs were made to adapt the program to the *Mariner* spacecraft configuration.

An initial computation of the picture locations was made using the nominal values of all the input parameters, assuming no attitude control motion. The computed location of the limb in Picture 1 was found to differ from the actual observed location by an appreciable fraction of the frame size. It was found that a small change in the camera pointing direction in both clock and cone angles, within the uncertainties in these angles, would suffice to make the computed limb location match the observed location. However, the effects of other error sources—in particular, the pitch, yaw, and roll uncertainties—were of the same order of magnitude as those of the clock and cone angle uncertainties. The precision of the picture locations would be somewhat improved if the attitude motion of the spacecraft could be deduced from picture information in the

overlap regions of the pictures and appropriate corrections then applied.

Using the *Ranger* program, it was possible to compute the location of the center of a given picture in terms of the set of rectangular coordinates centered in any other picture (Fig. D-4). This was done for each overlapping picture pair. Transparencies of each picture pair were overlaid and shifted to the position of best matching of the Martian topography. The center position of each picture was then measured in terms of the $I$ and $J$ (line and element) coordinates of its mate. Finally, the shifts due to attitude drifts were determined by calculating the differences, in terms of $I$ and $J$, between the computed center locations and the observed center locations. The resulting shifts are shown as vectors in Fig. D-5, along with unit vectors, on the same scale, showing the shifts that would result from a 1-millirad rotation about each of the spacecraft axes. The unit vectors are designated as $\hat{p}$ (pitch), $\hat{y}$(yaw), and $\hat{r}$(roll), and the actual position change vectors are labelled with number-pairs indicating the picture pair to which each vector corresponds. In each case, the vector represents the shift of the center of the even-numbered picture away from its computer-predicted position with

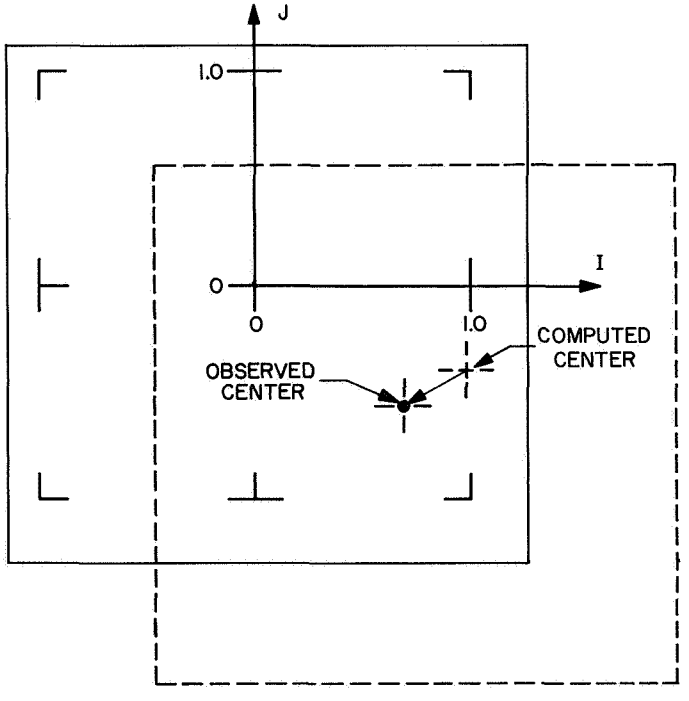


**Fig. D-4. Overlapping frames showing the shift of the center of the later picture away from its computed (predicted) location because of spacecraft rotation within the attitude control limits (see Fig. D-9 for scale)**

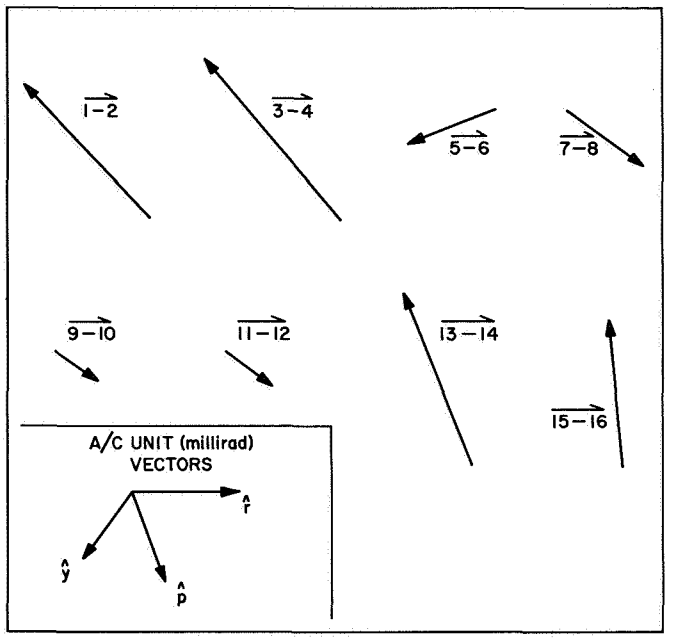


**Fig. D-5. Vectors showing the shifts between overlapping pictures due to spacecraft rotation, compared with the shifts that would result from 1 millirad rotation about each axis**

respect to the coordinates of the corresponding odd-numbered picture. Each vector is therefore a measure of the rotation rate of the spacecraft during the 48-sec interval between exposures. Alternate frame-pairs (e.g., Frames 8 and 9) did not overlap because of the 48- 96- 48- 96-sec picture-recording scheme. Consequently, it was not possible to plot a continuous history of spacecraft rotation during encounter from picture information alone.

The problem at this point was to resolve the rotation rate vectors into pitch, yaw, and roll components. Since there were three components of spacecraft rotation to be found from only one picture-translation vector in each case, unique solutions were not possible without additional information. The needed information might have been derived if picture rotations, as well as translations, could have been measured. However, at the time the overlap study was made, the only pictures available were not geometrically corrected, and the errors were large even for the more easily measured translations. The additional information needed was sought in existing attitude control data.

Attitude control information was transmitted from the spacecraft during most of the mission, but not during encounter when all the data channels were allocated to

science information. Transmission of engineering data ceased about 105 min before the exposure of Picture 1 and resumed about 16 min after the exposure of Picture 22. Plots of pitch, yaw, and roll positions within the attitude-control deadbands were made for the time period following encounter, and these curves were extrapolated backward through the television encounter period (00:18:33 to 00:43:12 GMT). However, uncertainties in the magnitudes of the attitude-control gas jet impulses (and also in the accelerations due to slow gas leakage) prevented unambiguous extrapolation.

Pitch, yaw, and roll plots, indicating the attitude motion for several days prior to encounter, were then examined. It was observed that the pitch motion was the most regular of the three. The acceleration in pitch due to solar pressure and gas jet leakage was much greater than for yaw and roll, so that the pitch sensor axis seldom crossed the deadband. Instead, the accelerating forces tended to drive the spacecraft toward the negative side of the pitch dead band, where it would "bounce" off as the gas jet was activated (see Fig. D-6); it would then return to the same side without ever reaching the positive side. The pitch "loops" typically alternated from large to small, as shown in Fig. D-6, but the ratio of the size of the large loop to that of the ensuing small loop varied considerably. One problem with the attempt to extrapolate the post-encounter pitch curve backward was that the loop size (amplitude) changed drastically just after the resumption of attitude data transmission. However, it was discovered

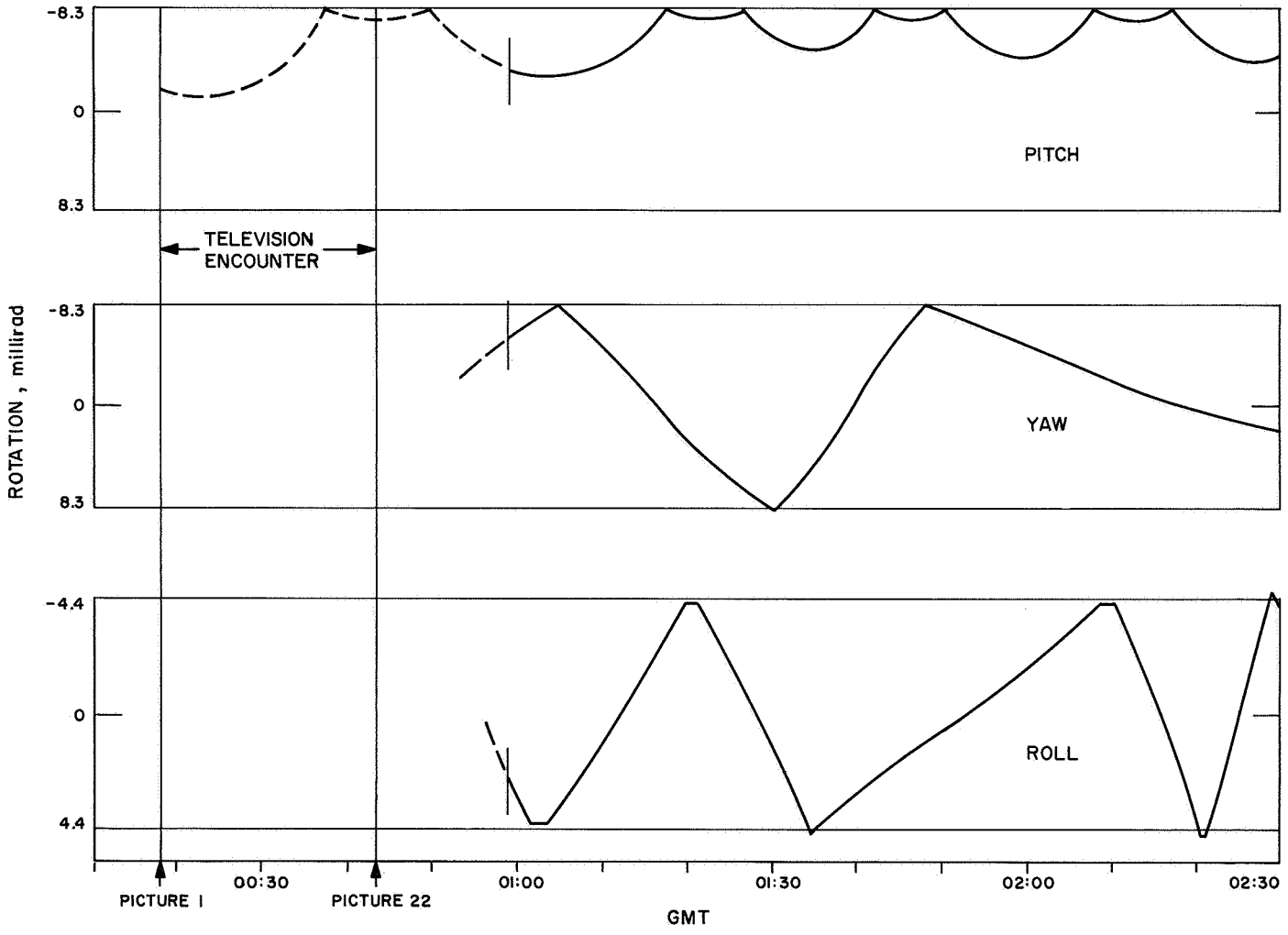


**Fig. D-6. Postencounter attitude control data showing spacecraft motion within pitch, yaw, and roll deadbands after resumption of attitude information transmission at about 00:59**

The broken-line curve represents interpolated pitch data through the television encounter period.

that the *duration* of one full pitch cycle, composed of one large and one small loop, remained fairly constant at about 40 min, independent of the varying amplitudes and durations of the individual loops. Using this information, it was possible to interpolate pitch cycles between 22:34 GMT on July 14 and 00:59 GMT on July 15, during which time the attitude data were missing. The broken-line curve in the pitch band in Fig. D-6 indicates the interpolated data. At this point, the yaw and roll curves remained to be extrapolated.

The pitch rates between the exposures of overlapping frames were derived from the interpolated pitch curves, and the rate information was applied to the resolution of the picture translation vectors. The resulting yaw and roll vectors are indicated in Fig. D-7 as the components $y$ and $r$. The solutions were not considered accurate enough for quantitative yaw and roll rate determinations because of the use of uncorrected pictures to find the frame translations and because of the scarcity of picture information in some of the overlap regions. However, significant trends are apparent in the rotation vector solutions in Fig. D-7. Apparently the yaw rate changed from negative to positive some time between Pictures 4 and 5, then back to negative between Pictures 12 and 13. The roll rate apparently changed from negative to positive between the exposures of Pictures 4 and 7, probably between Pictures 5 and 6. The roll rate then again became negative between Pictures 12 and 13. Hence the approximate times of attitude-gas-jet firings were determined with some degree of confidence, and the yaw and roll curves were plotted back to about the time of Picture 4 (see Fig. D-8). The curves were further extended back to the time of Picture 1 in such a way as to locate the

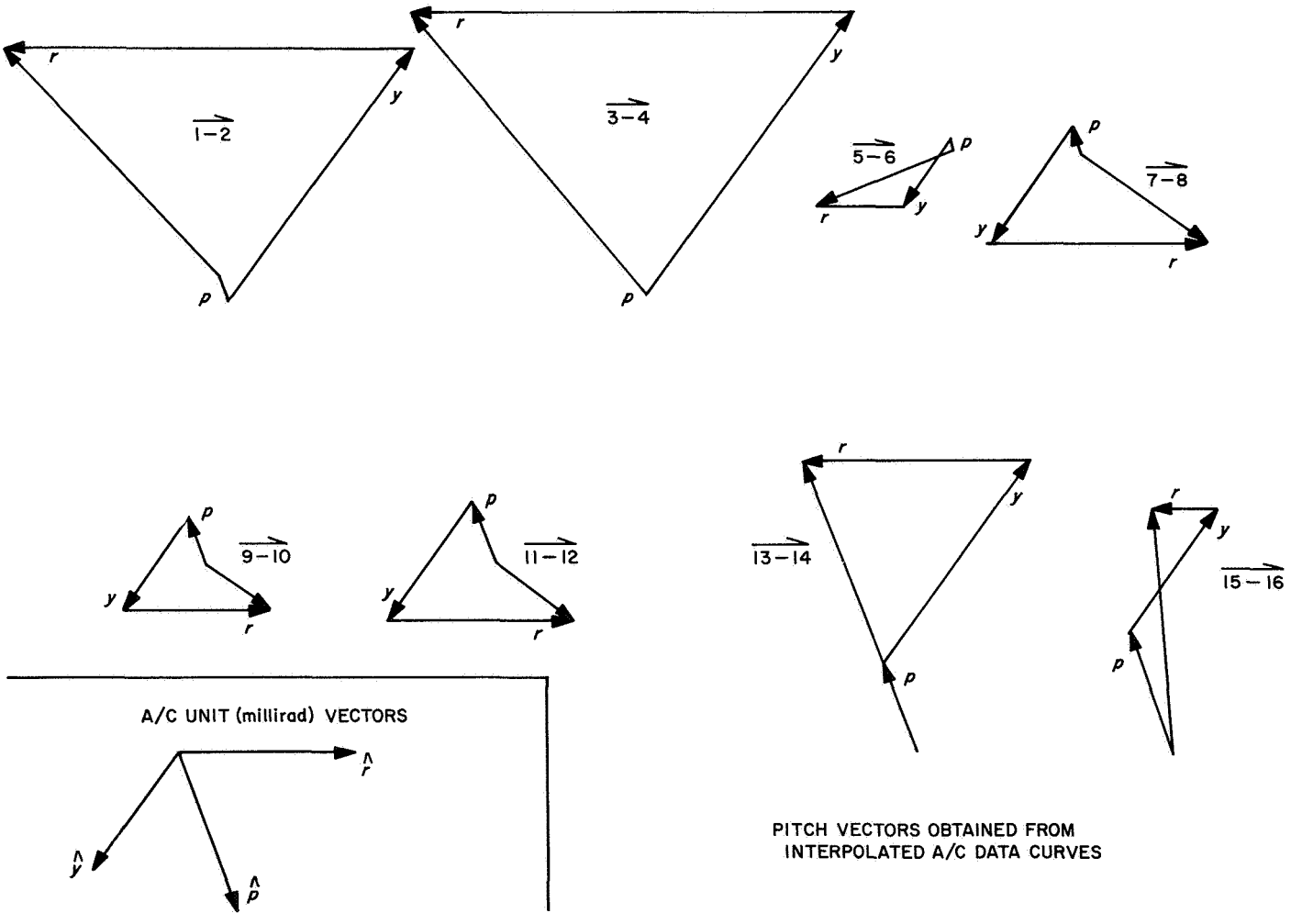


**Fig. D-7. Resolution of picture translations into vector components representing spacecraft rotation rates in pitch, yaw, and roll**

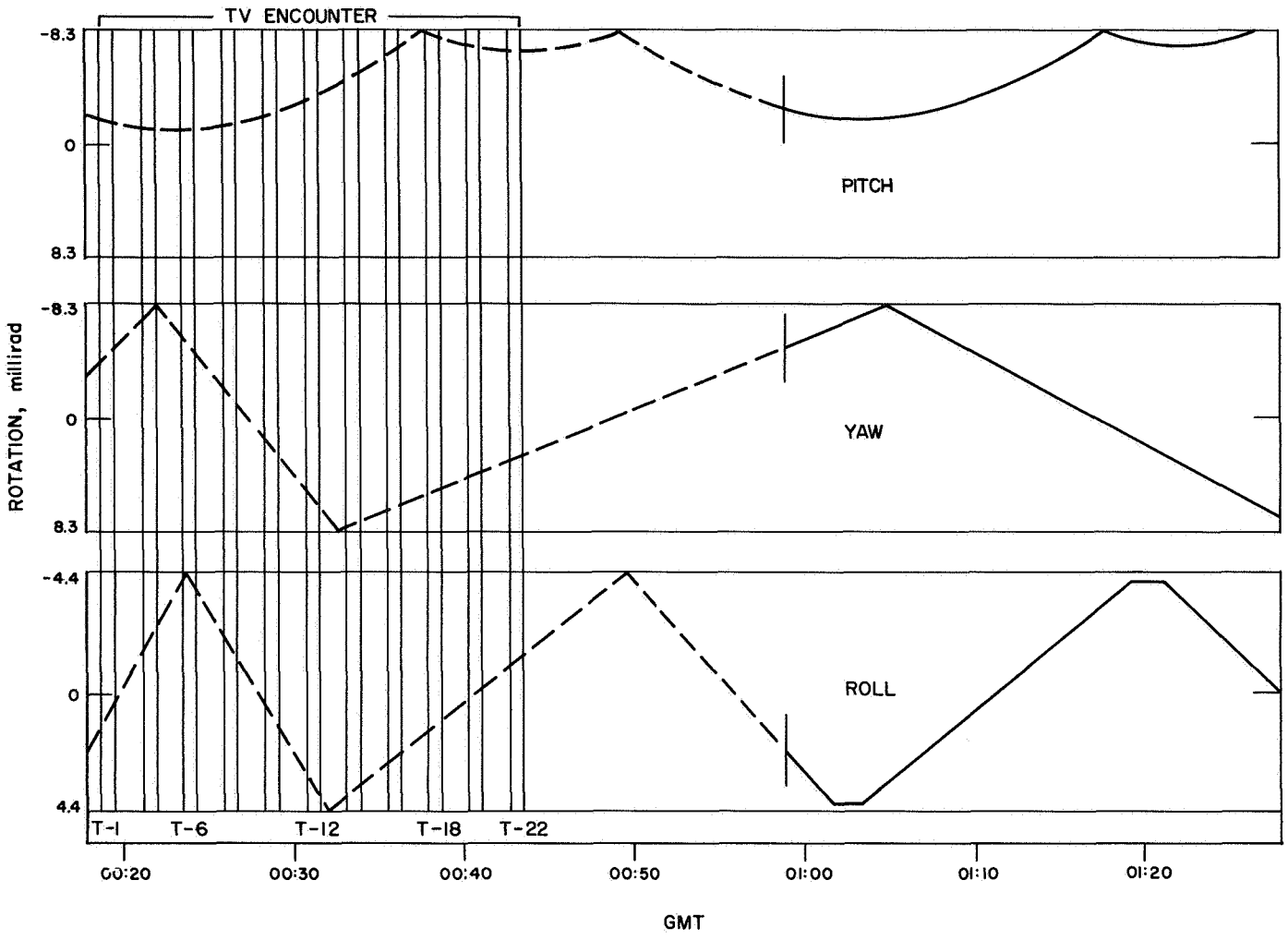


**Fig. D-8. Interpolated pitch curve and extrapolated yaw and roll curves through the television encounter period**
The vertical lines represent the times of television exposures.

computed limb position in the right place in that picture. The pitch, yaw, and roll data thus derived were used to compute all the picture locations.

It was observed at this point that the computed limb position was still slightly in error, requiring rotation of the picture about the camera axis. A clockwise rotation of 3 deg in the input frame orientation was made, and the input clock and cone angles were changed slightly, resulting in the correct positioning of the limb. The program was then rerun with these new inputs and the derived pitch, yaw, and roll motions to compute final values of the picture locations and data on the picture geometry. The parameter values listed in Table D-2 are those used in this computation, along with the attitude data given in Table D-3.

**Table D-2. Final parameter values**

| | |
|---|---|
| $b$ | 15,251 km |
| $\theta$ | 57.74 deg |
| $T_{CA}$ | 01:00:57 |
| $R_M$ | 3380 km |
| $C_A$ | 120.13 deg |
| $K_A$ | 178.32 deg |
| $F$ | 30.85 cm |
| $d$ | 2.45 mm |
| $R$ | 3.1 deg clockwise |
| Pitch null offset | 0 |
| Yaw null offset | 0 |
| Roll null offset | 0 |

**Table D-3. Attitude control data, interpolated pitch and extrapolated yaw and roll values**

| Picture | Pitch, millirad | Yaw, millirad | Roll, millirad |
|---|---|---|---|
| 1 | −1.33 | −5.90 | 0.35 |
| 2 | −1.20 | −6.25 | −0.35 |
| 3 | −1.00 | −7.00 | −1.75 |
| 4 | −0.95 | −7.40 | −2.50 |
| 5 | −0.95 | −8.10 | −3.95 |
| 6 | −1.00 | −7.40 | −3.85 |
| 7 | −1.20 | −3.95 | −2.05 |
| 8 | −1.35 | −2.25 | −1.15 |
| 9 | −1.75 | 1.25 | 0.60 |
| 10 | −2.00 | 3.00 | 1.45 |
| 11 | −2.75 | 6.45 | 3.25 |
| 12 | −3.15 | 8.20 | 4.20 |
| 13 | −4.15 | 7.60 | 3.30 |
| 14 | −4.70 | 7.25 | 2.75 |
| 15 | −6.05 | 6.55 | 1.60 |
| 16 | −6.90 | 6.20 | 1.00 |
| 17 | −8.40 | 5.50 | −0.15 |
| 18 | −8.05 | 5.10 | −0.70 |
| 19 | −7.50 | 4.40 | −1.85 |
| 20 | −7.30 | 4.05 | −2.45 |
| 21 | −7.05 | 3.35 | −3.60 |
| 22 | −7.00 | 3.30 | −4.20 |

### C. Picture Locations and Geometric Data

Latitudes, longitudes, and other pertinent data were computed for each fiducial mark location in each of the 22 pictures. The format in Fig. D-9 represents the projections of the fiducial marks on the object field, i.e., the surface of the planet. The shaded area represents the black mask, generally along the northern border of each picture. The parameters defined in the following list have been computed for each fiducial mark and presented in Table D-4.

Pt number of the point indicated in Fig. D-4

Lt north latitude, in deg, in areocentric coordinates of point on Martian surface intersected by fiducial mark projection (minus sign indicates south latitude)

Ln east longitude, in deg, in areocentric coordinates of point on Martian surface intersected by fiducial mark projection (minus sign indicates west longitude)

Range slant range from spacecraft to numbered point on the Martian surface, in km

Sur dist surface distance to numbered point from previous numbered point, assuming a smooth spherical surface, in km

Phase angle between incoming sunlight and line from spacecraft to Martian surface at numbered point, in deg

Zenith angle of sun angle between incoming sunlight and the local vertical at indicated point, in deg

Zenith angle of spacecraft angle between the local vertical and the direction to spacecraft at indicated point, in deg

The following information is also supplied in Table D-4:

GMT time of exposure (Greenwich mean time)

Lat areocentric north latitude of subspacecraft point, in deg

Lon areocentric east longitude of subspacecraft point, in deg

Alt altitude of spacecraft, in km

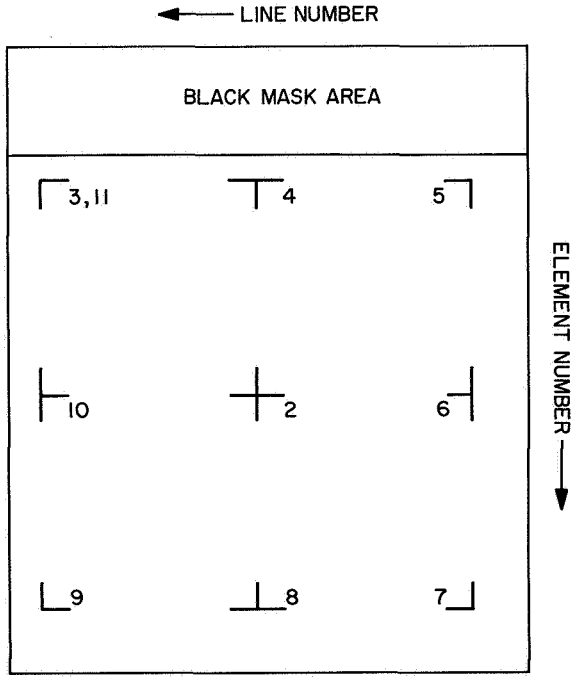


**Fig. D-9. Picture format, as seen projected toward the planet, with numbers designating the fiducial mark locations for which photographic data have been computed**

## Table D-4. Picture locations and related data

Picture 1

| GMT, 0:18:33; Filter, orange; Lat, −32.96 deg; Lon, 177.79 deg; Alt, 14,496 km | | | | | | | |
|---|---|---|---|---|---|---|---|
| Pt | Lt, deg | Ln, deg | Range, km | Sur dist, km | Phase, deg | Zenith angle of | |
| | | | | | | Sun, deg | Spacecraft, deg |
| 2 | 37.00 | 172.97 | 17,026 | — | 60.1 | 27.1 | 80.9 |
| 3 | — | — | — | — | — | — | — |
| 4 | — | — | — | — | — | — | — |
| 5 | — | — | — | — | — | — | — |
| 6 | 33.06 | 175.84 | 16,791 | — | 60.1 | 22.6 | 76.7 |
| 7 | 25.90 | 175.28 | 16,386 | 423.6 | 59.7 | 18.4 | 69.1 |
| 8 | 28.15 | 172.80 | 16,521 | 186.0 | 59.7 | 21.4 | 71.6 |
| 9 | 31.02 | 170.08 | 16,696 | 219.2 | 59.1 | 25.8 | 74.9 |
| 10 | — | — | — | — | — | — | — |
| 11 | — | — | — | — | — | — | — |

Picture 2

| GMT, 0:19:21; Filter, green; Lat, −33.47 deg; Lon, 177.93 deg; Alt, 14,345 km | | | | | | | |
|---|---|---|---|---|---|---|---|
| Pt | Lt, deg | Ln, deg | Range, km | Sur dist, km | Phase, deg | Zenith angle of | |
| | | | | | | Sun, deg | Spacecraft, deg |
| 2 | 25.08 | 175.04 | 16,223 | — | 60.1 | 18.0 | 68.9 |
| 3 | 35.77 | 172.73 | 16,836 | 641.6 | 60.6 | 26.2 | 80.3 |
| 4 | 32.04 | 175.54 | 16,613 | 259.8 | 60.6 | 21.9 | 76.2 |
| 5 | 29.42 | 178.06 | 16,462 | 200.4 | 60.6 | 18.5 | 73.4 |
| 6 | 23.26 | 177.35 | 16,120 | 365.2 | 60.1 | 15.2 | 66.8 |
| 7 | 18.54 | 176.71 | 15,870 | 280.6 | 59.7 | 14.2 | 61.7 |
| 8 | 20.04 | 174.51 | 15,953 | 151.0 | 59.7 | 16.5 | 63.4 |
| 9 | 21.77 | 172.22 | 16,054 | 162.3 | 59.7 | 19.1 | 65.5 |
| 10 | 27.28 | 172.59 | 16,354 | 326.1 | 60.2 | 21.0 | 71.4 |
| 11 | 35.77 | 172.73 | 16,836 | 501.0 | 60.6 | 26.2 | 80.3 |

Picture 3

| GMT, 0:20:57; Filter, green; Lat, −34.52 deg; Lon, 178.24 deg; Alt, 14,046 km | | | | | | | |
|---|---|---|---|---|---|---|---|
| Pt | Lt, deg | Ln, deg | Range, km | Sur dist, km | Phase, deg | Zenith angle of | |
| | | | | | | Sun, deg | Spacecraft, deg |
| 2 | 11.89 | 177.82 | 15,293 | — | 60.2 | 13.0 | 55.6 |
| 3 | 16.85 | 176.34 | 15,544 | 304.8 | 60.6 | 13.9 | 61.2 |
| 4 | 15.60 | 178.43 | 15,478 | 139.7 | 60.6 | 11.9 | 59.8 |
| 5 | 14.49 | −179.51 | 15,424 | 133.8 | 60.6 | 10.0 | 58.6 |
| 6 | 10.88 | 179.83 | 15,245 | 216.2 | 60.1 | 11.6 | 54.5 |
| 7 | 7.64 | 179.21 | 15,093 | 194.4 | 59.7 | 13.7 | 50.8 |
| 8 | 8.58 | 177.24 | 15,136 | 127.4 | 59.7 | 14.9 | 51.9 |
| 9 | 9.61 | 175.25 | 15,188 | 131.2 | 59.7 | 16.2 | 53.2 |
| 10 | 13.01 | 175.79 | 15,351 | 202.8 | 60.2 | 14.7 | 56.9 |
| 11 | 16.85 | 176.34 | 15,544 | 228.7 | 60.6 | 13.9 | 61.2 |

## Table D-4 (contd)

Picture 4

| GMT, 0:21:45, Filter, orange; Lat, −35.05 deg; Lon, 178.41 deg; Alt, 13,900 km | | | | | | | |
|---|---|---|---|---|---|---|---|
| Pt | Lt, deg | Ln, deg | Range, km | Sur dist, km | Phase, deg | Zenith angle of | |
| | | | | | | Sun, deg | Spacecraft, deg |
| 2 | 6.86 | 179.07 | 14,936 | — | 60.2 | 14.1 | 50.6 |
| 3 | 11.03 | 177.68 | 15,132 | 259.0 | 60.6 | 13.3 | 55.3 |
| 4 | 10.05 | 179.66 | 15,086 | 128.7 | 60.6 | 11.9 | 54.3 |
| 5 | 9.17 | −178.38 | 15,048 | 125.3 | 60.6 | 10.7 | 53.4 |
| 6 | 3.15 | −179.00 | 14,902 | 173.9 | 60.1 | 13.2 | 49.7 |
| 7 | 6.04 | 179.59 | 14,774 | 188.6 | 59.7 | 15.8 | 46.4 |
| 8 | 3.93 | 178.50 | 14,806 | 121.6 | 59.7 | 16.5 | 47.2 |
| 9 | 4.80 | 176.57 | 14,845 | 124.1 | 59.7 | 17.3 | 48.3 |
| 10 | 7.77 | 177.12 | 14,979 | 178.5 | 60.2 | 15.2 | 51.7 |
| 11 | 11.03 | 177.68 | 15,132 | 194.8 | 60.6 | 13.3 | 55.3 |

Picture 5

| GMT, 0:23:21; Filter, orange; Lat, −36.14 deg; Lon, 178.78 deg; Alt, 13,611 km | | | | | | | |
|---|---|---|---|---|---|---|---|
| Pt | Lt, deg | Ln, deg | Range, km | Sur dist, km | Phase, deg | Zenith angle of | |
| | | | | | | Sun, deg | Spacecraft, deg |
| 2 | −1.79 | −178.47 | 14,332 | — | 60.2 | 19.2 | 42.1 |
| 3 | 1.48 | −179.79 | 14,463 | 208.2 | 60.7 | 17.0 | 45.9 |
| 4 | 0.81 | −177.92 | 14,439 | 117.2 | 60.6 | 16.6 | 45.2 |
| 5 | 0.20 | −176.06 | 14,422 | 115.9 | 60.6 | 16.4 | 44.7 |
| 6 | −2.38 | −176.61 | 14,316 | 155.8 | 60.2 | 19.0 | 41.6 |
| 7 | −4.82 | −177.15 | 14,221 | 147.6 | 59.7 | 21.4 | 38.7 |
| 8 | −4.24 | −179.00 | 14,237 | 114.0 | 59.7 | 21.6 | 39.2 |
| 9 | −3.61 | 179.15 | 14,258 | 115.1 | 59.8 | 21.9 | 39.9 |
| 10 | −1.13 | 179.67 | 14,355 | 149.1 | 60.2 | 19.5 | 42.8 |
| 11 | 1.48 | −179.79 | 14,463 | 157.7 | 60.7 | 17.0 | 45.9 |

Picture 6

| GMT, 0:24:9; Filter, green; Lat, −36.70 deg; Lon, 178.99 deg; Alt, 13,470 km | | | | | | | |
|---|---|---|---|---|---|---|---|
| Pt | Lt, deg | Ln, deg | Range, km | Sur dist, km | Phase, deg | Zenith angle of | |
| | | | | | | Sun, deg | Spacecraft, deg |
| 2 | −5.83 | −177.14 | 14,063 | — | 60.2 | 22.3 | 38.2 |
| 3 | −2.86 | −178.46 | 14,171 | 191.75 | 60.6 | 20.0 | 41.6 |
| 4 | −3.43 | −176.62 | 14,155 | 113.57 | 60.6 | 19.9 | 41.1 |
| 5 | −3.95 | −174.78 | 14,145 | 112.78 | 60.6 | 19.9 | 40.8 |
| 6 | −6.34 | −175.30 | 14,054 | 144.56 | 60.1 | 22.3 | 37.9 |
| 7 | −8.63 | −175.82 | 13,972 | 138.21 | 59.7 | 24.7 | 35.1 |
| 8 | −8.13 | −177.66 | 13,981 | 111.33 | 59.7 | 24.7 | 35.4 |
| 9 | −7.57 | −179.49 | 13,995 | 112.00 | 59.7 | 24.8 | 35.9 |
| 10 | −5.27 | −178.98 | 14,078 | 138.98 | 60.2 | 22.5 | 38.7 |
| 11 | −2.86 | −178.46 | 14,171 | 145.49 | 60.6 | 20.0 | 41.6 |

## Table D-4 (contd)

Picture 7

| GMT, 0:25:45; Filter, green; Lat, −37.84 deg; Lon, 179.44 deg; Alt, 13,192 km | | | | | | | |
|---|---|---|---|---|---|---|---|
| Pt | Lt, deg | Ln, deg | Range, km | Sur dist, km | Phase, deg | Zenith angle of | |
| | | | | | | Sun, deg | Spacecraft, deg |
| 2 | −13.54 | −174.21 | 13,582 | — | 60.1 | 29.1 | 31.0 |
| 3 | −11.01 | −175.56 | 13,654 | 168.7 | 60.5 | 26.8 | 33.7 |
| 4 | −11.43 | −173.74 | 13,651 | 108.4 | 60.5 | 27.0 | 33.6 |
| 5 | −11.79 | −171.90 | 13,653 | 108.4 | 60.5 | 27.2 | 33.7 |
| 6 | −13.91 | −172.37 | 13,584 | 127.9 | 60.0 | 29.3 | 31.1 |
| 7 | −15.97 | −172.82 | 13,523 | 123.9 | 59.6 | 31.4 | 28.5 |
| 8 | −15.60 | −174.67 | 13,521 | 107.4 | 59.6 | 31.2 | 28.4 |
| 9 | −15.18 | −176.51 | 13,524 | 107.4 | 59.6 | 31.1 | 28.5 |
| 10 | −13.13 | −176.04 | 13,585 | 123.9 | 60.1 | 29.0 | 31.1 |
| 11 | −11.01 | −175.56 | 13,654 | 127.9 | 60.5 | 26.8 | 33.7 |

Picture 8

| GMT, 0:26:33; Filter, orange; Lat, −38.43 deg; Lon, 179.69 deg; Alt, 13,056 km | | | | | | | |
|---|---|---|---|---|---|---|---|
| Pt | Lt, deg | Ln, deg | Range, km | Sur dist, km | Phase, deg | Zenith angle of | |
| | | | | | | Sun, deg | Spacecraft, deg |
| 2 | −17.09 | −172.62 | 13,373 | — | 60.0 | 32.5 | 27.9 |
| 3 | −14.71 | −174.01 | 13,430 | 160.9 | 60.5 | 30.2 | 30.3 |
| 4 | −15.07 | −172.17 | 13,432 | 106.7 | 60.5 | 30.5 | 30.4 |
| 5 | −15.38 | −170.32 | 13,439 | 106.9 | 60.4 | 30.7 | 30.7 |
| 6 | −17.40 | −170.76 | 13,380 | 121.9 | 60.0 | 32.7 | 28.2 |
| 7 | −19.37 | −171.18 | 13,326 | 118.6 | 59.5 | 34.7 | 25.8 |
| 8 | −19.05 | −173.05 | 13,320 | 106.0 | 59.6 | 34.5 | 25.5 |
| 9 | −18.69 | −174.91 | 13,318 | 105.8 | 59.6 | 34.3 | 25.3 |
| 10 | −16.73 | −174.46 | 13,371 | 118.4 | 60.0 | 32.3 | 27.8 |
| 11 | −14.71 | −174.01 | 13,430 | 121.7 | 60.5 | 30.2 | 30.3 |

Picture 9

| GMT, 0:28:9; Filter, orange; Lat, −39.62 deg; Lon, −179.78 deg; Alt, 12,790 km | | | | | | | |
|---|---|---|---|---|---|---|---|
| Pt | Lt, deg | Ln, deg | Range, km | Sur dist, km | Phase, deg | Zenith angle of | |
| | | | | | | Sun, deg | Spacecraft, deg |
| 2 | −23.72 | −169.11 | 13,004 | — | 59.9 | 39.1 | 23.0 |
| 3 | −21.60 | −170.62 | 13,036 | 149.7 | 60.4 | 36.9 | 24.6 |
| 4 | −21.84 | −168.74 | 13,048 | 104.2 | 60.4 | 37.3 | 25.2 |
| 5 | −22.04 | −166.83 | 13,064 | 104.9 | 60.3 | 37.6 | 26.0 |
| 6 | −23.92 | −167.19 | 13,020 | 112.7 | 59.9 | 39.4 | 23.8 |
| 7 | −25.77 | −167.53 | 12,980 | 110.5 | 59.4 | 41.3 | 21.7 |
| 8 | −25.56 | −169.47 | 12,965 | 104.1 | 59.5 | 40.9 | 20.7 |
| 9 | −25.30 | −171.40 | 12,954 | 103.5 | 59.5 | 40.6 | 20.1 |
| 10 | −23.46 | −171.01 | 12,993 | 110.1 | 59.9 | 38.8 | 22.3 |
| 11 | −21.60 | −170.62 | 13,036 | 112.3 | 60.4 | 36.9 | 24.6 |

## Table D-4 (contd)

Picture 10

| GMT, 0:28:57; Filter, green; Lat, −40.22 deg; Lon, −179.49 deg; Alt, 12,660 km | | | | | | | |
|---|---|---|---|---|---|---|---|
| Pt | Lt, deg | Ln, deg | Range, km | Sur dist, km | Phase, deg | Zenith angle of | |
| | | | | | | Sun, deg | Spacecraft, deg |
| 2 | −26.83 | −167.15 | 12,843 | — | 59.9 | 42.4 | 21.2 |
| 3 | −24.81 | −168.75 | 12,865 | 145.9 | 60.3 | 40.2 | 22.5 |
| 4 | −25.01 | −166.82 | 12,881 | 103.4 | 60.3 | 40.6 | 23.3 |
| 5 | −25.16 | −164.88 | 12,901 | 104.3 | 60.3 | 41.0 | 24.4 |
| 6 | −26.99 | −165.18 | 12,863 | 109.1 | 59.8 | 42.7 | 22.4 |
| 7 | −28.79 | −165.48 | 12,830 | 107.3 | 59.4 | 44.5 | 20.4 |
| 8 | −28.62 | −167.47 | 12,810 | 103.7 | 59.4 | 44.1 | 19.2 |
| 9 | −28.41 | −169.44 | 12,794 | 102.8 | 59.4 | 43.8 | 18.2 |
| 10 | −26.63 | −169.09 | 12,827 | 106.9 | 59.9 | 42.0 | 20.3 |
| 11 | −24.81 | −168.75 | 12,865 | 108.6 | 60.3 | 40.2 | 22.5 |

Picture 11

| GMT, 0:30:33; Filter, green; Lat, −41.46 deg; Lon, −178.85 deg; Alt, 12,407 km | | | | | | | |
|---|---|---|---|---|---|---|---|
| Pt | Lt, deg | Ln, deg | Range, km | Sur dist, km | Phase, deg | Zenith angle of | |
| | | | | | | Sun, deg | Spacecraft, deg |
| 2 | −32.67 | −162.65 | 12,564 | — | 59.8 | 48.8 | 19.7 |
| 3 | −30.84 | −164.47 | 12,566 | 141.1 | 60.3 | 46.7 | 19.9 |
| 4 | −30.93 | −162.44 | 12,591 | 102.8 | 60.2 | 47.1 | 21.3 |
| 5 | −30.96 | −160.38 | 12,620 | 104.1 | 60.2 | 47.5 | 23.0 |
| 6 | −32.71 | −160.56 | 12,593 | 103.6 | 59.8 | 49.2 | 21.5 |
| 7 | −34.45 | −160.73 | 12,570 | 102.4 | 59.3 | 50.9 | 20.1 |
| 8 | −34.39 | −162.85 | 12,542 | 103.5 | 59.3 | 50.4 | 18.3 |
| 9 | −34.29 | −164.95 | 12,518 | 102.3 | 59.4 | 50.0 | 16.6 |
| 10 | −32.57 | −164.71 | 12,540 | 101.9 | 59.8 | 48.4 | 18.2 |
| 11 | −30.84 | −164.47 | 12,566 | 103.0 | 60.3 | 46.7 | 19.9 |

Picture 12

| GMT, 0:31:21; Filter, orange; Lat, −42.09 deg; Lon, −178.51 deg; Alt, 12,284 km | | | | | | | |
|---|---|---|---|---|---|---|---|
| Pt | Lt, deg | Ln, deg | Range, km | Sur dist, km | Phase, deg | Zenith angle of | |
| | | | | | | Sun, deg | Spacecraft, deg |
| 2 | −35.42 | −160.05 | 12,446 | — | 59.7 | 52.0 | 20.1 |
| 3 | −33.68 | −162.01 | 12,439 | 139.9 | 60.2 | 49.9 | 19.6 |
| 4 | −33.71 | −159.91 | 12,467 | 102.9 | 60.2 | 50.3 | 21.4 |
| 5 | −33.69 | −157.78 | 12,500 | 104.5 | 60.2 | 50.8 | 23.2 |
| 6 | −35.41 | −157.88 | 12,479 | 101.5 | 59.7 | 52.4 | 22.0 |
| 7 | −37.11 | −157.97 | 12,461 | 100.6 | 59.3 | 54.0 | 21.0 |
| 8 | −37.12 | −160.18 | 12,429 | 104.0 | 59.3 | 53.6 | 19.0 |
| 9 | −37.07 | −162.35 | 12,401 | 102.5 | 59.3 | 53.2 | 17.0 |
| 10 | −35.38 | −162.19 | 12,418 | 100.0 | 59.8 | 51.5 | 18.2 |
| 11 | −33.68 | −162.01 | 12,439 | 100.9 | 60.2 | 49.9 | 19.6 |

## Table D-4 (contd)

Picture 13

| GMT, 0:32:57; Filter, orange; Lat, −43.37 deg; Lon, −177.76 deg; Alt, 12,044 km | | | | | | | |
|---|---|---|---|---|---|---|---|
| Pt | Lt, deg | Ln, deg | Range, km | Sur dist, km | Phase, deg | Zenith angle of | |
| | | | | | | Sun, deg | Spacecraft, deg |
| 2 | −40.07 | −154.37 | 12,247 | — | 59.8 | 57.8 | 22.5 |
| 3 | −38.51 | −156.67 | 12,223 | 139.5 | 60.3 | 55.8 | 21.1 |
| 4 | −38.41 | −154.43 | 12,260 | 103.9 | 60.3 | 56.3 | 23.2 |
| 5 | −38.25 | −152.15 | 12,301 | 105.9 | 60.2 | 56.8 | 25.3 |
| 6 | −39.92 | −152.04 | 12,289 | 98.5 | 59.8 | 58.4 | 24.7 |
| 7 | −41.57 | −151.91 | 12,280 | 97.9 | 59.3 | 59.9 | 24.2 |
| 8 | −41.72 | −154.29 | 12,239 | 105.6 | 59.4 | 59.4 | 22.0 |
| 9 | −41.82 | −156.65 | 12,202 | 103.6 | 59.4 | 58.9 | 19.8 |
| 10 | −40.17 | −156.67 | 12,211 | 97.3 | 59.8 | 57.4 | 20.4 |
| 11 | −38.51 | −156.67 | 12,223 | 97.8 | 60.3 | 55.8 | 21.1 |

Picture 14

| GMT, 0:33:45; Filter, green; Lat, −44.02 deg; Lon, −177.35 deg; Alt, 11,928 km | | | | | | | |
|---|---|---|---|---|---|---|---|
| Pt | Lt, deg | Ln, deg | Range, km | Sur dist, km | Phase, deg | Zenith angle of | |
| | | | | | | Sun, deg | Spacecraft, deg |
| 2 | −42.21 | −151.11 | 12,166 | — | 59.9 | 60.8 | 24.4 |
| 3 | −40.75 | −153.61 | 12,133 | 140.3 | 60.3 | 58.7 | 22.7 |
| 4 | −40.57 | −151.28 | 12,174 | 104.9 | 60.3 | 59.2 | 24.8 |
| 5 | −40.34 | −148.91 | 12,220 | 107.2 | 60.3 | 59.8 | 27.1 |
| 6 | −41.98 | −148.68 | 12,212 | 97.4 | 59.8 | 61.3 | 26.7 |
| 7 | −43.61 | −148.40 | 12,207 | 97.0 | 59.4 | 62.9 | 26.4 |
| 8 | −43.84 | −150.89 | 12,161 | 106.9 | 59.4 | 62.4 | 24.2 |
| 9 | −44.02 | −153.35 | 12,120 | 104.7 | 59.4 | 61.9 | 21.9 |
| 10 | −42.39 | −153.49 | 12,125 | 96.3 | 59.9 | 60.3 | 22.2 |
| 11 | −40.75 | −153.61 | 12,133 | 96.6 | 60.3 | 58.7 | 22.7 |

Picture 15

| GMT, 0:35:21; Filter, green; Lat, −45.34 deg; Lon, −176.47 deg; Alt, 11,703 km | | | | | | | |
|---|---|---|---|---|---|---|---|
| Pt | Lt, deg | Ln, deg | Range, km | Sur dist, km | Phase, deg | Zenith angle of | |
| | | | | | | Sun, deg | Spacecraft, deg |
| 2 | −46.03 | −143.49 | 12,041 | — | 59.9 | 66.8 | 29.2 |
| 3 | −44.80 | −146.50 | 11,990 | 144.2 | 60.4 | 64.7 | 26.9 |
| 4 | −44.44 | −143.98 | 12,041 | 108.0 | 60.4 | 65.3 | 29.2 |
| 5 | −44.02 | −141.42 | 12,097 | 111.0 | 60.4 | 65.9 | 31.5 |
| 6 | −45.60 | −140.86 | 12,097 | 96.0 | 59.9 | 67.4 | 31.5 |
| 7 | −47.17 | −140.22 | 12,101 | 96.1 | 59.5 | 69.0 | 31.7 |
| 8 | −47.60 | −142.93 | 12,045 | 111.1 | 59.5 | 68.4 | 29.3 |
| 9 | −47.97 | −145.60 | 11,994 | 108.1 | 59.5 | 67.8 | 27.1 |
| 10 | −46.39 | −146.08 | 11,990 | 95.3 | 60.0 | 66.2 | 26.9 |
| 11 | −44.80 | −146.50 | 11,990 | 95.2 | 60.4 | 64.7 | 26.9 |

## Table D-4 (contd)

Picture 16

| GMT, 0:36:9; Filter, orange; Lat, −46.01 deg; Lon, −175.99 deg; Alt, 11,594 km | | | | | | | |
|---|---|---|---|---|---|---|---|
| Pt | Lt, deg | Ln, deg | Range, km | Sur dist, km | Phase, deg | Zenith angle of | |
| | | | | | | Sun, deg | Spacecraft, deg |
| 2 | −47.64 | −139.06 | 11,999 | — | 60.0 | 69.9 | 31.9 |
| 3 | −46.56 | −142.37 | 11,938 | 147.5 | 60.5 | 67.7 | 29.4 |
| 4 | −46.09 | −139.75 | 11,994 | 110.3 | 60.4 | 68.3 | 31.8 |
| 5 | −45.55 | −137.10 | 12,056 | 113.7 | 60.4 | 69.0 | 34.1 |
| 6 | −47.09 | −136.33 | 12,061 | 95.9 | 60.0 | 70.5 | 34.3 |
| 7 | −48.61 | −135.47 | 12,070 | 96.2 | 59.5 | 72.1 | 34.6 |
| 8 | −49.18 | −138.29 | 12,008 | 114.1 | 59.5 | 71.4 | 32.3 |
| 9 | −49.66 | −141.07 | 11,951 | 110.6 | 59.6 | 70.8 | 30.0 |
| 10 | −48.11 | −141.76 | 11,943 | 95.2 | 60.0 | 69.3 | 29.6 |
| 11 | −46.56 | −142.37 | 11,938 | 94.9 | 60.5 | 67.7 | 29.4 |

Picture 17

| GMT, 0:37:45; Filter, orange; Lat, −47.36 deg; Lon, −174.95 deg; Alt, 11,385 km | | | | | | | |
|---|---|---|---|---|---|---|---|
| Pt | Lt, deg | Ln, deg | Range, km | Sur dist, km | Phase, deg | Zenith angle of | |
| | | | | | | Sun, deg | Spacecraft, deg |
| 2 | −50.14 | −128.66 | 11,964 | — | 60.1 | 76.3 | 38.3 |
| 3 | −49.44 | −132.66 | 11,880 | 158.0 | 60.6 | 74.1 | 35.4 |
| 4 | −48.71 | −129.85 | 11,949 | 117.2 | 60.5 | 74.8 | 37.8 |
| 5 | −47.88 | −127.00 | 12,025 | 121.9 | 60.5 | 75.5 | 40.3 |
| 6 | −49.29 | −125.73 | 12,041 | 96.8 | 60.1 | 77.1 | 40.8 |
| 7 | −50.68 | −124.32 | 12,061 | 97.7 | 59.6 | 78.7 | 41.4 |
| 8 | −51.56 | −127.34 | 11,983 | 123.0 | 59.6 | 77.9 | 39.0 |
| 9 | −52.34 | −130.33 | 11,913 | 118.1 | 59.7 | 77.2 | 36.6 |
| 10 | −50.90 | −131.56 | 11,894 | 96.3 | 60.1 | 75.6 | 35.9 |
| 11 | −49.44 | −132.66 | 11,880 | 95.4 | 60.6 | 74.1 | 35.4 |

Picture 18

| GMT, 0:38:33; Filter, green; Lat, −48.04 deg; Lon, −174.39 deg; Alt, 11,285 km | | | | | | | |
|---|---|---|---|---|---|---|---|
| Pt | Lt, deg | Ln, deg | Range, km | Sur dist, km | Phase, deg | Zenith angle of | |
| | | | | | | Sun, deg | Spacecraft, deg |
| 2 | −51.00 | −122.35 | 11,981 | — | 60.1 | 79.9 | 42.1 |
| 3 | −50.57 | −126.76 | 11,881 | 166.6 | 60.6 | 77.6 | 39.0 |
| 4 | −49.66 | −123.85 | 11,959 | 122.5 | 60.5 | 78.3 | 41.4 |
| 5 | −48.64 | −120.91 | 12,045 | 128.2 | 60.5 | 79.1 | 44.0 |
| 6 | −49.95 | −119.33 | 12,067 | 98.3 | 60.1 | 80.8 | 44.7 |
| 7 | −51.23 | −117.58 | 12,095 | 99.7 | 59.6 | 82.4 | 45.5 |
| 8 | −52.32 | −120.68 | 12,007 | 130.2 | 59.6 | 81.6 | 42.9 |
| 9 | −53.29 | −123.76 | 11,927 | 124.1 | 59.7 | 80.8 | 40.4 |
| 10 | −51.94 | −125.34 | 11,902 | 97.8 | 60.1 | 79.2 | 39.6 |
| 11 | −50.57 | −126.76 | 11,881 | 96.6 | 60.6 | 77.6 | 39.0 |

## Table D-4 (contd)

Picture 19

| GMT, 0:40:9; Filter, green; Lat, −49.42 deg; Lon, −173.17 deg; Alt, 11,092 km | | | | | | | |
|---|---|---|---|---|---|---|---|
| Pt | Lt, deg | Ln, deg | Range, km | Sur dist, km | Phase, deg | Zenith angle of | |
| | | | | | | Sun, deg | Spacecraft, deg |
| 2 | −51.17 | −107.88 | 12,096 | — | 60.1 | 87.7 | 50.8 |
| 3 | −51.48 | −113.14 | 11,956 | 194.7 | 60.6 | 85.1 | 47.0 |
| 4 | −50.12 | −110.09 | 12,057 | 139.4 | 60.5 | 86.0 | 49.8 |
| 5 | −48.59 | −107.00 | 12,171 | 149.1 | 60.5 | 87.0 | 52.7 |
| 6 | −49.57 | −104.73 | 12,213 | 105.3 | 60.1 | 88.8 | 53.7 |
| 7 | −50.47 | −102.23 | 12,261 | 108.5 | 59.6 | 90.6 | 54.9 |
| 8 | −52.15 | −105.45 | 12,141 | 154.6 | 59.6 | 89.5 | 51.9 |
| 9 | −53.65 | −108.63 | 12,034 | 143.6 | 59.7 | 88.5 | 49.1 |
| 10 | −52.60 | −110.99 | 11,992 | 104.1 | 60.1 | 86.8 | 48.0 |
| 11 | −51.48 | −113.14 | 11,956 | 101.7 | 60.6 | 85.1 | 47.0 |

Picture 20

| GMT, 0:40:57; Filter, orange; Lat, −50.12 deg; Lon, −172.51 deg; Alt, 11,001 km | | | | | | | |
|---|---|---|---|---|---|---|---|
| Pt | Lt, deg | Ln, deg | Range, km | Sur dist, km | Phase, deg | Zenith angle of | |
| | | | | | | Sun, deg | Spacecraft, deg |
| 2 | −50.17 | −99.78 | 12,210 | — | 60.1 | 92.1 | 55.9 |
| 3 | −51.04 | −105.46 | 12,039 | 218.7 | 60.6 | 89.1 | 51.7 |
| 4 | −49.35 | −102.36 | 12,159 | 153.7 | 60.5 | 90.2 | 54.7 |
| 5 | −47.45 | −99.17 | 12,296 | 167.6 | 60.5 | 91.5 | 57.9 |
| 6 | −48.17 | −96.53 | 12,352 | 113.0 | 60.1 | 93.4 | 59.2 |
| 7 | −48.76 | −93.64 | 12,418 | 118.2 | 59.6 | 95.4 | 60.6 |
| 8 | −50.88 | −96.96 | 12,269 | 177.9 | 59.6 | 94.0 | 57.3 |
| 9 | −52.76 | −100.18 | 12,140 | 161.2 | 59.7 | 92.8 | 54.2 |
| 10 | −51.94 | −102.94 | 12,086 | 110.4 | 60.1 | 90.9 | 52.9 |
| 11 | −51.04 | −105.46 | 12,039 | 106.7 | 60.6 | 89.1 | 51.7 |

Picture 21

| GMT, 0:42:33; Filter, orange; Lat, −51.51 deg; Lon, −171.08 deg; Alt, 10,826 km | | | | | | | |
|---|---|---|---|---|---|---|---|
| Pt | Lt, deg | Ln, deg | Range, km | Sur dist, km | Phase, deg | Zenith angle of | |
| | | | | | | Sun, deg | Spacecraft, deg |
| 2 | −44.34 | −81.47 | 12,665 | — | 60.1 | 102.8 | 69.5 |
| 3 | −47.29 | −88.40 | 12,363 | 333.7 | 60.6 | 98.6 | 63.3 |
| 4 | −44.45 | −84.93 | 12,559 | 219.9 | 60.5 | 100.4 | 67.4 |
| 5 | −40.90 | −80.96 | 12,811 | 271.3 | 60.5 | 102.6 | 72.3 |
| 6 | −40.28 | −77.14 | 12,953 | 174.9 | 60.1 | 105.4 | 75.0 |
| 7 | −38.97 | −72.66 | 13,144 | 217.7 | 59.6 | 108.7 | 78.6 |
| 8 | −43.89 | −77.64 | 12,795 | 364.6 | 59.6 | 105.4 | 72.0 |
| 9 | −47.39 | −81.50 | 12,555 | 260.2 | 59.7 | 103.2 | 67.3 |
| 10 | −47.46 | −85.10 | 12,451 | 143.7 | 60.1 | 100.8 | 65.2 |
| 11 | −47.29 | −88.40 | 12,363 | 132.2 | 60.6 | 98.6 | 63.3 |

**Table D-4 (contd)**

Picture 22

| GMT, 0:43:21; Filter, green; Lat, −52.21; Lon, −170.31; Alt, 10,743 km | | | | | | | |
|---|---|---|---|---|---|---|---|
| Pt | Lt, deg | Ln, deg | Range, km | Sur dist, km | Phase, deg | Zenith angle of | |
| | | | | | | Sun, deg | Spacecraft, deg |
| 2 | −35.78 | −68.58 | 13,283 | — | 60.1 | 111.8 | 82.6 |
| 3 | −42.91 | −78.55 | 12,682 | 618.8 | 60.6 | 104.8 | 71.5 |
| 4 | −38.17 | −73.85 | 13,017 | 350.0 | 60.5 | 107.8 | 77.8 |
| 5 | — | — | — | — | — | — | — |
| 6 | — | — | — | — | — | — | — |
| 7 | — | — | — | — | — | — | — |
| 8 | — | — | — | — | — | — | — |
| 9 | −40.59 | −69.85 | 13,033 | — | 59.7 | 111.1 | 78.1 |
| 10 | −42.12 | −74.53 | 12,832 | 225.8 | 60.1 | 107.7 | 74.4 |
| 11 | −42.91 | −78.55 | 12,682 | 180.8 | 60.6 | 104.8 | 71.5 |

The latitude and longitude data given in Table D-4 were used by ACIC (Air Force Aeronautical Chart and Information Center) to make relief renditions from the pictures. Since it was found necessary to introduce additional shifts in picture locations to make the overlap picture information match, ACIC shifted the odd-numbered picture locations accordingly. The latitudes and longitudes of objects in the relief renditions will therefore differ slightly from those indicated by the picture data given in Table D-4 for odd-numbered pictures.

## III. Picture 11 Mapping Error Estimates

Estimates have been made of the uncertainty of the computed map location of Picture 11, based on individual uncertainties in the more significant parameters. The rss ($1\sigma$) latitude uncertainty was computed according to the following equation:

$$\Delta\psi\,(1\sigma) = \left[\sum_n \left(\frac{\partial\psi}{\partial X_n}\Delta X_n\right)^2\right]^{1/2}$$

where $\psi$ represents latitude, $X_n$ the $n$th parameter, and $\Delta X_n$ the $1\sigma$ uncertainty in the value of the nth parameter. Symmetrical probability densities about the input parameter values given in Tables D-2 and D-3 were assumed, and it may be assumed that the latitude probability distribution is gaussian and symmetrical about the computed value in Table D-4. The latter assumption is not strictly valid and would not hold for other pictures near the limb. Computation of the longitude uncertainty $\Delta\lambda$ was carried out in the same way, and the results are given in Table D-5.

**Table D-5. Latitude ($\phi$) and longitude ($\lambda$) uncertainties for Picture 11**

| Parameter | $\Delta X_n$ | $\lvert\partial\phi/\partial X_n\rvert$ | $(\Delta X_n\lvert\partial\phi/\partial X_n\rvert)^2$ | $\lvert\partial\lambda/\partial X_n\rvert$ | $(\Delta X_n\lvert\partial\lambda/\partial X_n\rvert)^2$ |
|---|---|---|---|---|---|
| $b$, km | 17 | 0.0058 | 0.0098 | 0.0079 | 0.018 |
| $\theta$, deg | 0.08 | 2.93 | 0.0547 | 3.88 | 0.096 |
| $T_{CA}$, sec | 10 | 0.056 | 0.3140 | 0.050 | 0.250 |
| $R_M$, km | 30 | 0.0040 | 0.0144 | 0.0054 | 0.026 |
| $C_A$, deg | 0.10 | 3.83 | 0.1468 | 0.203 | 0.000 |
| $K_A$, deg | 0.70 | 0.021 | 0.0002 | 3.92 | 7.530 |
| pn, millirad | 2 | 0.174 | 0.1211 | 0.056 | 0.012 |
| yn, millirad | 2 | 0.120 | 0.0576 | 0.124 | 0.062 |
| rn, millirad | 2 | 0.052 | 0.0108 | 0.225 | 0.213 |
| p, millirad | 2 | 0.174 | 0.1211 | 0.056 | 0.012 |
| y, millirad | 1 | 0.120 | 0.0144 | 0.124 | 0.015 |
| r, millirad | 2 | 0.052 | 0.0108 | 0.225 | 0.213 |
| | | | $\Sigma = 0.8757$<br>$\Delta\phi\,(1\sigma) = 0.94$ deg | | $\Sigma = 8.447$<br>$\Delta\lambda\,(1\sigma) = 2.91$ deg |

# Appendix E

# Data Acquisition and Handling

## I. Outline of Communication and Data Stream

The data encoder on the spacecraft determines which parameters are to be sampled, the sampling frequency, and the sampling order. The commutation scheme determines the order in which the samples are taken and which samples are selected. The Data Automation System in the science subsystem presents to the data encoder a complete package of science information regularly at the proper time. This package is combined with the engineering measurements by the data encoder (in Mode 2) and sent to the modulator, which impresses the data on the carrier for transmission to earth.

In addition to transmitting data from spacecraft to earth (down-link), communications capability from the earth to spacecraft (up-link) is also provided in order to obtain accurate doppler ranging information and to send commands from ground stations. In the "one-way-lock" condition, the spacecraft carrier frequency is determined by a crystal oscillator which drifts slightly about a nominal center frequency. Commands can only be sent from earth to spacecraft when a "two-way-lock" condition is established. In this condition the spacecraft receives the signal from earth and the carrier frequency is synchronized to the signal received by the spacecraft. Commands from earth are identified and separated by the command subsystem.

The data flow through the spacecraft to printout and plotting at the Space Flight Operations Facility is shown in generalized block diagram form in Fig. E-1. Data from the science instruments are combined in the DAS and presented to the data encoder. The television data rate is reduced by the video storage subsystem, where it is temporarily stored on tape, so that it is slow enough for transmission (8⅓ bps). As shown in Fig. E-2, these data are combined with engineering data, if appropriate, and sent to the modulator (see Fig. E-1), which modulates the rf carrier in the transmitter. The high-gain antenna directs the modulated carrier energy to earth. The CC&S furnishes synchronization signals for various commands, events, subsystems, and devices.

The weak radio signal from the spacecraft is tracked by the ground station antenna so that its associated receiver can detect and amplify the data to a useful level. In the event that the demodulator did not function properly, the data would be lost. For this reason, the data are recorded on magnetic tape for subsequent playback and recovery. The tape is also a check on the accuracy and reliability of data transmitted through the huge complex of teletype and communications networks. The demodulator separates the data from the carrier. At this point the ouput is again saved for possible future uses. The decommutator has exactly the opposite function of the commutator in the on-board data encoder. It separates the various measurements and prints out the data on a roll of paper. By reading this printout, the operators at the station can rapidly determine any abnormal operation of the spacecraft, subsystems, and instruments.

The teletype encoder puts the data stream in a form suitable for transmission to the SFOF by teletype lines. Every 5 min the Time Code Generator inserts a "time" word into the data stream. This time is part of an identifying message that inserts in the data stream the station number, the spacecraft number, and the time at which the data were received. The data and the associated time word go to a tape punch which punches holes representing paper tape data. The tape is then fed into a paper tape reader which reconverts the information on the tape to pulse form. These data are then transmitted by commercial teletype circuits to the SFOF.

At the SFOF a teletype printer prints out the incoming data but does not identify each measurement. At the same time, the data are fed through a data communications channel to an IBM "string" of processors for conversion to a form suitable for analysis. Shortly after reception, the data are subjected to near-real-time analysis, which is not detailed and serves as an approximate checkout of spacecraft performance. For NRT analysis, the data are displayed (printout) on an SC 3070 printer, which prints out each measurement as it identifies it. Those selected measurements that can be interpreted more readily as line graphs are plotted on the 30- × 30-in. plotter.

At the SFOF a tape record is also made of data coming in by teletype. This magnetic tape (No. 3) is stored with the two magnetic tapes and paper tape from the ground stations. These four sources are processed for comparison, and the best data are selected and used to compile the Master Data Library. From the MDL the data are printed out in final form for subsequent detailed analysis.

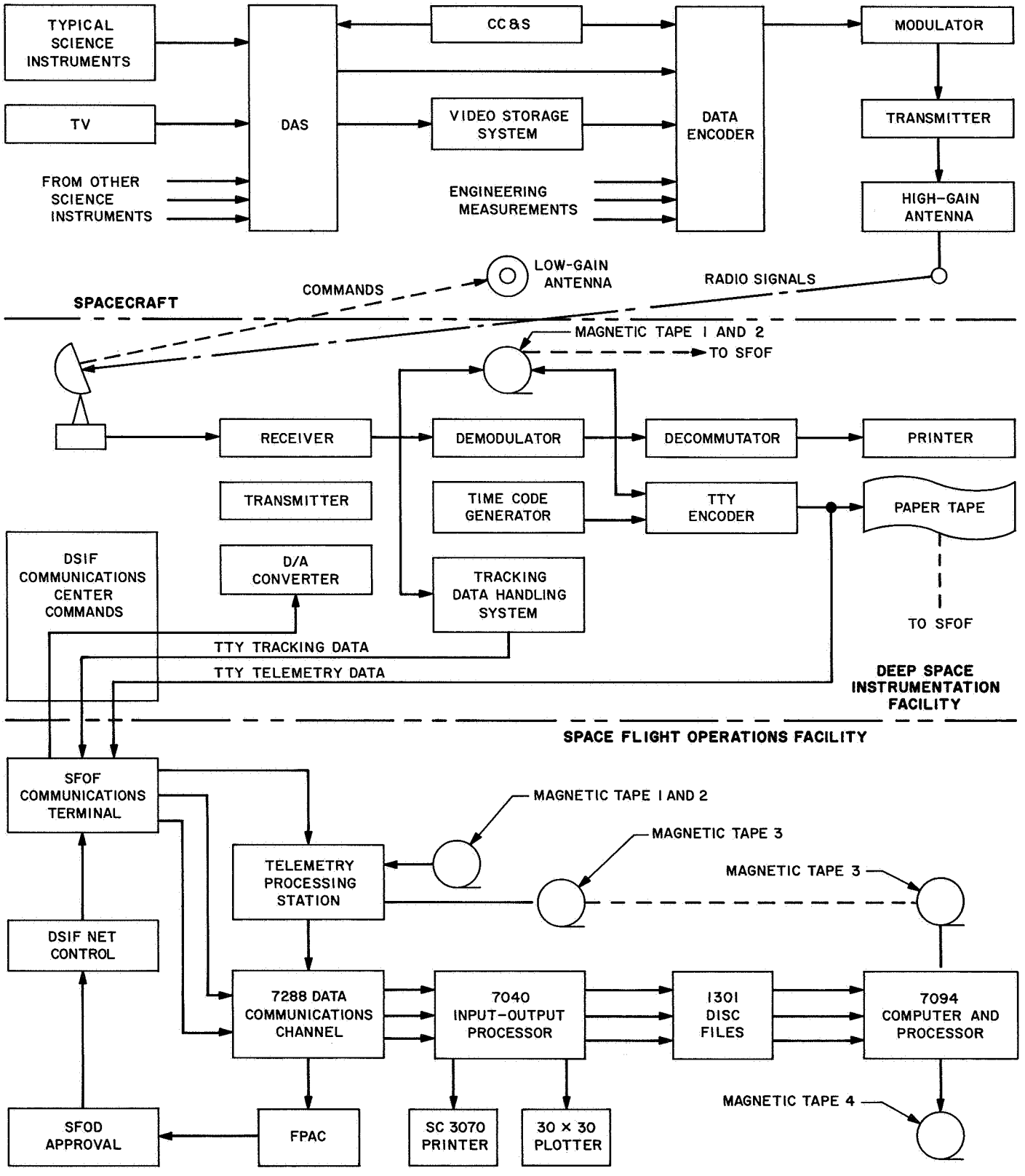


**Fig. E-1. Mariner Mars 1964 data stream**

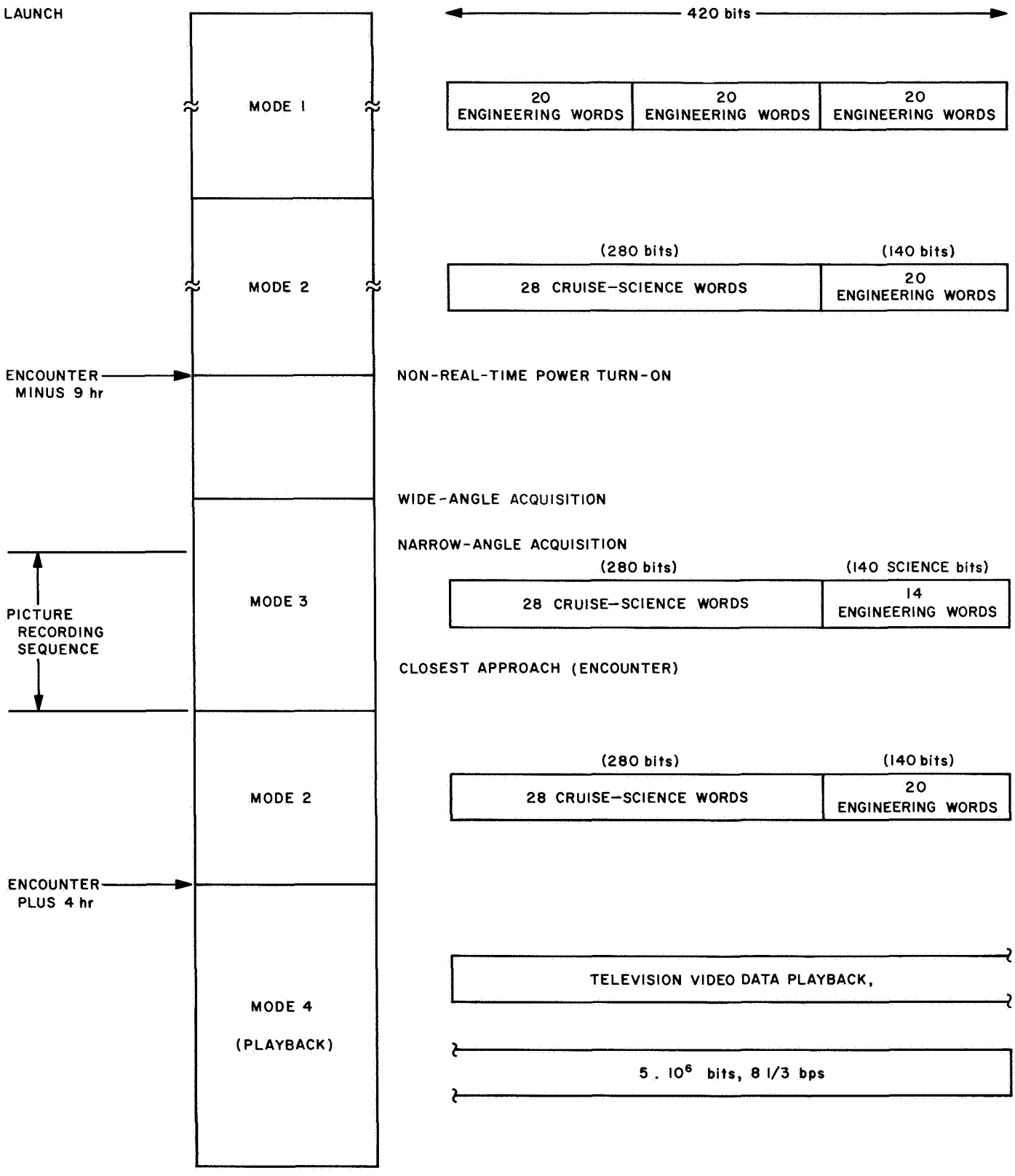


**Fig. E-2. Data modes during the nominal flight sequence**

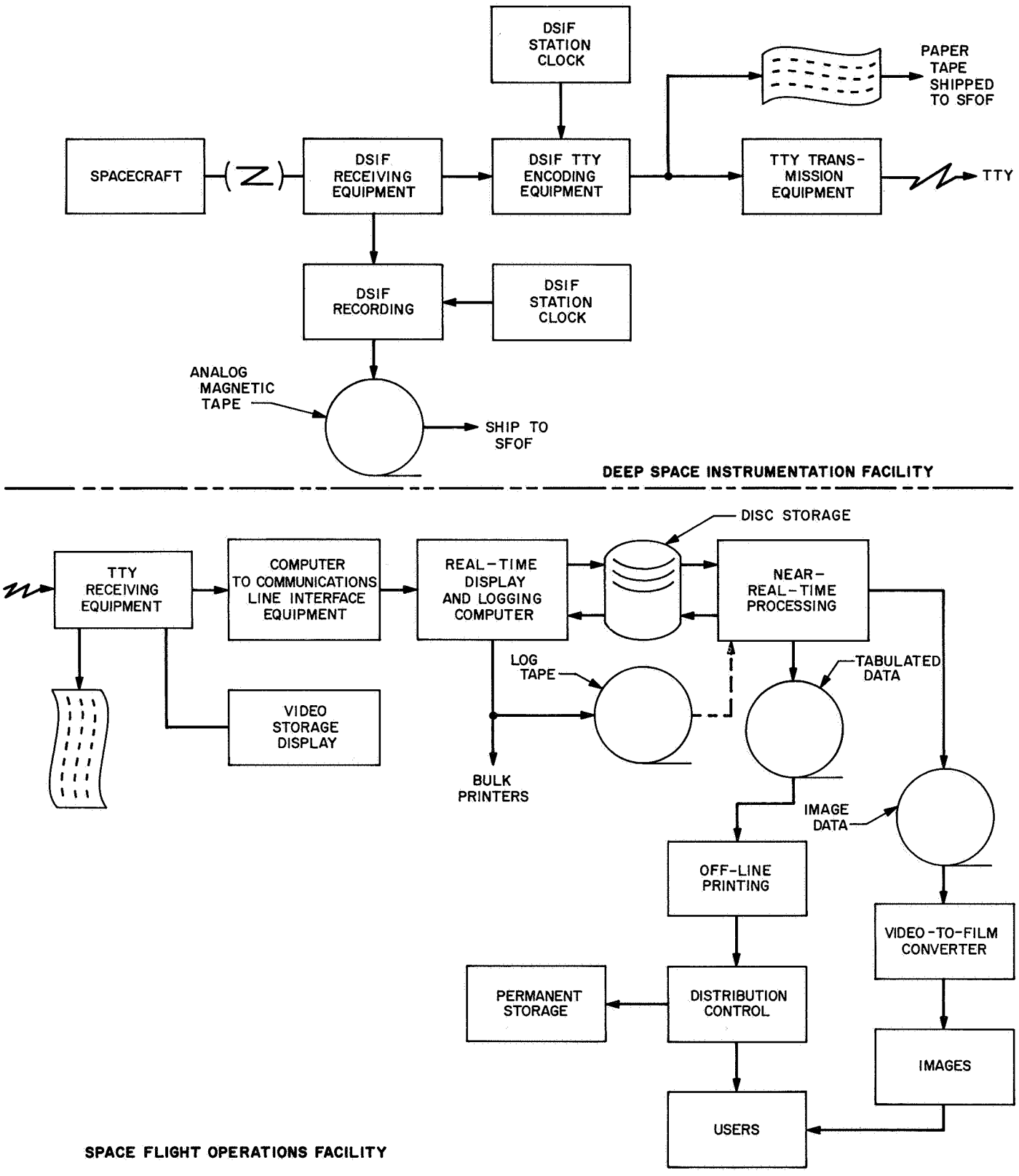


**Fig. E-3. Television ground data processing system**

## II. Television Data Processing

The *Mariner IV* television data were processed in two phases. The first of these was the establishment of a complete and correct data stream to provide pictures suitable for preliminary analysis and release to the scientific community and the public. The second phase was the more comprehensive treatment required to remove obscuring noise, correct geometric distortions, and restore the photometric fidelity of the data (see Section III). Since the second phase involved scientific processing analogous to that performed by the non-television experimenters on their respective data, the discussion is limited to the first phase.

Figure E-3 represents the *Mariner IV* TV Ground Data Processing System. The system is identical in configuration to the non-television ground data processing system, since the non-TV and TV data are fundamentally of the same form. Because of the special importance of the television data, extraordinary quality control measures were adopted to maximize the data return. These measures emphasized redundancy of functions and included:

(1) Two complete playbacks from the spacecraft tape recorder.

(2) Horizon-to-horizon tracking by all DSIF stations, providing dual tracking at each of the three DSIF tracking longitudes for the first playback period.

(3) Redundant reception and recording by those stations equipped with dual S-band receivers.

(4) Special coverage for the ground communication circuits for the first picture period.

(5) 24-hr monitoring of the data stream by telecommunications personnel and associated spacecraft engineering personnel.

(6) Near-real-time computer processing of each received picture during the first playback period.

(7) Redundant video-to-film conversion; calibrated and controlled film processing of the image displayed data.

An understanding of the spacecraft television data system helps simplify the description of the TV Ground Data Processing System. The general elements of the spacecraft TV data system are shown in Fig. E-4.

Digital data were buffered by the non-real-time Data Automation System at a rate of 83.3 kbps. The data from each picture were recorded on the spacecraft tape recorder from the DAS at a rate of 10.7 kbps. To guard against possible loss, the near-planet non-television instrument data, which were transmitted in real-time, were merged with the TV data and recorded during the picture-taking period. After the spacecraft had emerged from

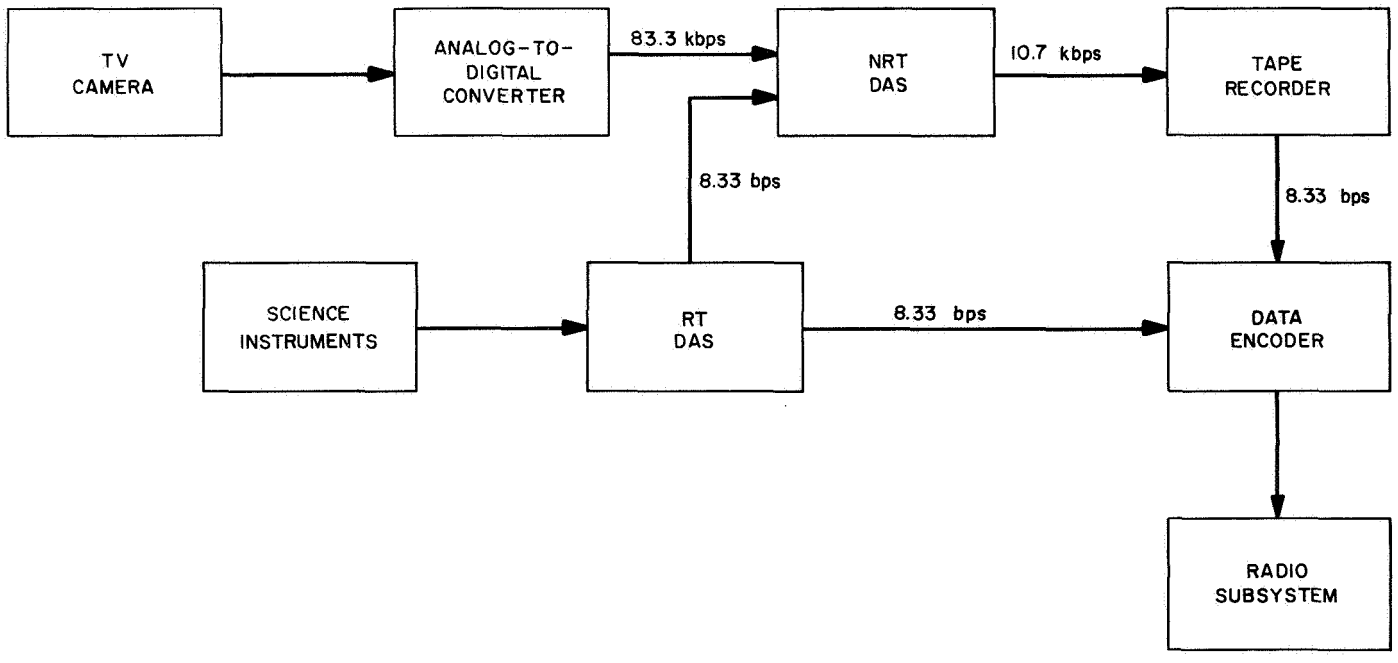


**Fig. E-4. Spacecraft TV data system, block diagram**

the near-planet region and returned to interplanetary space, the spacecraft tape recorder played back the recorded data and transmitted the data stream to earth at 8.33 bps. During encounter, the operation of the spacecraft tape recorder was stop-start; that is, there was tape motion only during each 24-sec picture-recording interval. On the other hand, the playback sequence was characterized by continuous tape motion. The interval of blank tape corresponding to the stop-start transient of the recorder was expanded by the reduced tape speed to approximately 1.5 hr. This time was used to transmit real-time spacecraft engineering information. The playback period for each picture was 8 hr 35 min.

The format of the TV data is shown in Fig. E-5. The TV data stream (Fig. E-5a) transmitted by the spacecraft consisted of two distinct subformats within the basic structure. Type A formats consisted of 200 lines of essentially TV data; Type B and C formats consisted primarily of non-television data. Figure E-5b shows the format of each of the lines for each subformat.

The length of each line was 1281 $\pm$1 bit. Type A blocks began with a 31-bit pseudonoise (PN) or synchronization pattern followed by 7 bits binary-coded to identify the block type. (The PN sequence is a unique pattern of sequential bits specially chosen to identify the beginning of a TV block.) The subsequent 9 bits were binary coded decimal to identify the line within the block. Three exposure status bits followed, alternating in meaning from even to odd line.

Since a single television line corresponded in time to the generation of one real-time bit, a real-time bit could be included in each line. Although the encounter sequence provided that the real-time or non-TV science data be transmitted to earth as generated, the spacecraft designers also inserted these real-time bits in the recording to preclude loss of the planetary information due to possible spacecraft antenna/earth disorientation during the critical moments of encounter. If the encounter phase transmission had been lost, some portion of the data would have been recovered from the on-board recording.

The 10 bits up to bit 61 were the analog-to-digital converted values of TV camera voltages alternating in source between even and odd lines. The next 1200 bits were the image information, with each group of 6 bits constituting the photometric value of each of the 200 elements in a line. The remaining 20 bits provided a tolerance before the beginning of the next line.

Since the spacecraft recorder was recording only during the 24 sec of camera readout of each desired picture, the non-TV data that accumulated between pictures were stored in the DAS as B and C blocks, and then recorded. Type B and C blocks were similar to A blocks, but began with 80 zeros. When the spacecraft recorder started, B

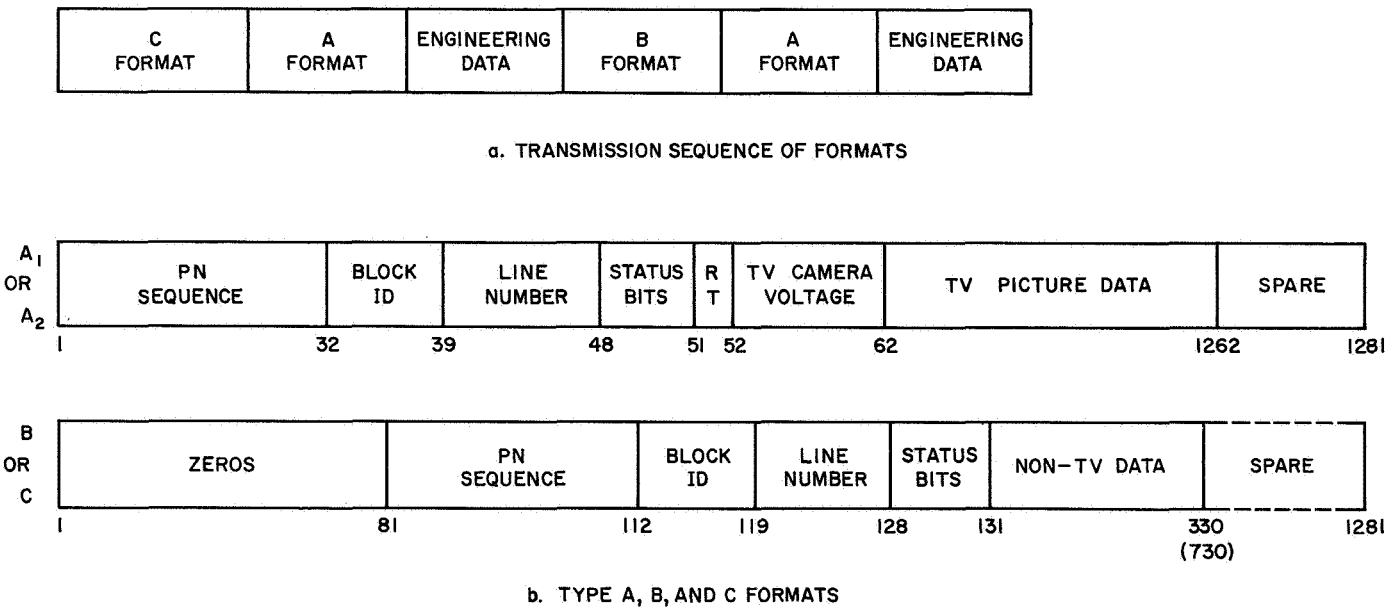


**Fig. E-5. Television data formats: (a) transmission sequence of events, (b) Types A, B, C formats**

and C blocks were the first to be recorded for each picture, and the zeros were used to establish bit synchronization within the recorder electronics. Following the 80 zeros were the 31-bit PN sequence, block type identifiers, and TV engineering information. The data bits for a B block were 200 non-TV bits; for a C block they were 600 non-TV bits. The remaining bits up to 1281 were tolerance bits to keep the B and C blocks equal in length to A blocks. The data stream telemetered by the spacecraft was a sequence of C block, A block, engineering data, B block, A block, engineering data, etc.

The processing required real-time display of received data to monitor playback performance in near-real-time and to accomplish the following:

(1) Recognize television data and decommutate the TV, engineering, and image data for tabular display. (Decommutation is the identification, selection, and extraction of groups of bits to form the value of a desired parameter. Decommutation may be accomplished by computer or by special equipment.)

(2) Format magnetic tapes of the image data for processing by the *Ranger* TV programs and for conversion to a film record.

(3) Extract the non-TV data from the data stream and format a magnetic tape for processing by the non-TV Science Summary Listing Program.

(4) Correct garbled image data, including the correction of individual bit errors.

### A. Processing Method Used and Problems Encountered

In the real-time 7044 computer processing of TV data,* the processor searched the data stream for the 31-bit television PN sequence and partially decommutated the TV data. In real-time, the 7044 displayed a tabular listing for each line, which included the picture number identification, the line number, the TV status and engineering parameters, and a count of the number of bits between PN sequences. Figure E-6, a sample of one portion of the tabular display, shows the decimal listing of the decommutated nonimage and image data. Twenty-eight pages of this format type were required for each picture. The column headings in Fig. E-6 are identified from left to right as follows:

Time of receipt of the PN sequence for the line (GMT).

Bit number referenced to the special binary printout.

Data frame and subframe to calculate picture number.

Line number.

The non-TV bit on each line.

The camera gain state.

The filter position bit.

The shutter or exposure indication bit.

Two camera voltages.

The intensity for each element.

As a result of the experience gained from processing the cruise data, a sorting capability based on the picture number, line number, and data type was included in the TV data processing scheme, as was the capability to extract the inserted non-TV data and format it for processing by the Science Summary Data Listing Program. This processing prepared a tape in the proper format for conversion of the image data to a film record. The 7094 processing also prepared tape in a format suitable for further computer processing by the *Ranger* Television Processing Programs.

The actual implementation included the TV data recognition, decommutation, sorting, and tabular display as part of the computer program (titled "Mission-Dependent Editor") and a separate program that accepted the image data and reformatted it for further processing. The sorting capability was extremely useful. The ordering sequence and validity checking of the data could accommodate correlation among 50 lines at one time. From an operational standpoint, this permitted overlap to be purposely included in the data when switching between DSIF stations as well as recovery of data by retransmission when ground commutation outages lost or garbled data. For the overlapped data, the sorting routine ordered the data and included the most complete and error-free data in the delivered stream. In order to maintain the geometrical relationship between the lines, if data were missing or nonrecognizable for a given line, an all-black filler line was inserted (labeled "Foney" in Fig. E-6). In both the tabular listings and the film records, the all-black line was immediately evident, thus facilitating correction.

The errors in the data stream were of two types: individual bit errors, caused by either the spacecraft or DSIF electronics, and garbled lines, caused by the loss or insertion of teletype characters in the ground communication data stream. Teletype communications were the prime method of data transmission from the DSIF to the SFOF.

*See JPL Technical Report 32-883, Appendix C.

ELEMENT MATRIX A, GENERAL DATA AND ELEMENTS 1 THRU 20

| HHMMSS | BITNO | D | S | LNO | R. | APER | AAC | FS | SIGL | VLTG | 1 | 2 | 3 | 4 | 5 | 6 | 7 | 8 | 9 | 10 | 11 | 12 | 13 | 14 | 15 | 16 | 17 | 18 | 19 | 20 |
|---|---|---|---|---|---|---|---|---|---|---|---|---|---|---|---|---|---|---|---|---|---|---|---|---|---|---|---|---|---|---|
| 005401 | 164983 | 2 | 2 | 100 | 0 | 0 | 001 | --- | 0269.00 | -.00 | 40 | 61 | 62 | 63 | 62 | 62 | 62 | 62 | 62 | 62 | 62 | 62 | 62 | 62 | 62 | 62 | 62 | 62 | 63 | 63 |
| FONEY | -0-0-0 | | | 101-0 | | -0 | --- | 0 | --- | -.00 | 63 | 63 | 63 | 63 | 63 | 63 | 63 | 63 | 63 | 63 | 63 | 63 | 63 | 63 | 63 | 63 | 63 | 63 | 63 | 63 |
| FONEY | -0-0-0 | | | 102-0 | | -0 | --- | 0 | --- | -.00 | 63 | 63 | 63 | 63 | 63 | 63 | 63 | 63 | 63 | 63 | 63 | 63 | 63 | 63 | 63 | 63 | 63 | 63 | 63 | 63 |
| FONEY | -0-0-0 | | | 103-0 | | 0 | --- | 0 | --- | -.00 | 63 | 63 | 63 | 63 | 63 | 63 | 63 | 63 | 63 | 63 | 63 | 63 | 63 | 63 | 63 | 63 | 63 | 63 | 63 | 63 |
| 010410 | 169693 | 2 | 2 | 104 | 0 | 0 | 001 | --- | 0269.00 | -.00 | 40 | 61 | 62 | 63 | 62 | 62 | 62 | 62 | 62 | 62 | 62 | 62 | 62 | 62 | 62 | 62 | 62 | 62 | 63 | 63 |
| 010705 | 170976 | 2 | 2 | 105 | 1 | 0 | --- | 0 | 01 | .00 289.00 | 40 | 61 | 62 | 63 | 62 | 62 | 62 | 62 | 62 | 62 | 62 | 62 | 62 | 62 | 62 | 62 | 62 | 62 | 63 | 63 |
| 010940 | 172258 | 2 | 2 | 106 | 0 | 0 | 001 | --- | 0269.00 | -.00 | 40 | 61 | 62 | 63 | 62 | 62 | 62 | 62 | 62 | 62 | 62 | 62 | 62 | 62 | 62 | 62 | 62 | 62 | 63 | 63 |
| 011207 | 173541 | 2 | 2 | 107 | 0 | 0 | --- | 0 | 01 | .00 289.00 | 41 | 61 | 62 | 63 | 62 | 62 | 62 | 62 | 62 | 62 | 62 | 62 | 62 | 62 | 62 | 62 | 62 | 62 | 63 | 63 |
| 011502 | 174823 | 2 | 2 | 108 | 0 | 0 | 001 | --- | 0269.00 | -.00 | 40 | 61 | 62 | 63 | 62 | 62 | 62 | 62 | 62 | 62 | 62 | 62 | 62 | 62 | 62 | 62 | 62 | 62 | 63 | 63 |
| 011714 | 176106 | 2 | 2 | 109 | 0 | 0 | --- | 0 | 01 | .00 289.00 | 41 | 61 | 62 | 63 | 62 | 62 | 62 | 62 | 62 | 62 | 62 | 62 | 62 | 62 | 62 | 62 | 62 | 62 | 63 | 63 |
| 012000 | 177388 | 2 | 2 | 110 | 0 | 0 | 001 | --- | 0269.00 | -.00 | 41 | 61 | 62 | 63 | 62 | 62 | 62 | 62 | 62 | 62 | 62 | 62 | 62 | 62 | 62 | 62 | 62 | 62 | 63 | 63 |
| 012223 | 178671 | 2 | 2 | 111 | 0 | 0 | --- | 0 | 01 | .00 289.00 | 41 | 61 | 62 | 63 | 62 | 62 | 62 | 62 | 62 | 62 | 62 | 62 | 62 | 62 | 62 | 62 | 62 | 62 | 63 | 63 |
| 012459 | 179954 | 2 | 2 | 112 | 0 | 0 | 001 | --- | 0269.00 | -.00 | 41 | 61 | 62 | 63 | 62 | 62 | 62 | 62 | 62 | 62 | 62 | 62 | 62 | 62 | 62 | 62 | 62 | 62 | 63 | 63 |
| 012737 | 181236 | 2 | 2 | 113 | 0 | 0 | --- | 0 | 01 | .00 289.00 | 41 | 61 | 62 | 63 | 62 | 62 | 62 | 62 | 62 | 62 | 62 | 62 | 62 | 62 | 62 | 62 | 62 | 62 | 63 | 63 |
| 013004 | 182519 | 2 | 2 | 114 | 0 | 0 | 001 | --- | 0269.00 | -.00 | 41 | 61 | 62 | 63 | 62 | 62 | 62 | 62 | 62 | 62 | 62 | 62 | 62 | 62 | 62 | 62 | 62 | 62 | 63 | 63 |
| 013239 | 183801 | 2 | 2 | 115 | 0 | 0 | --- | 0 | 01 | .00 289.00 | 41 | 61 | 62 | 63 | 62 | 62 | 62 | 62 | 62 | 62 | 62 | 62 | 62 | 62 | 62 | 62 | 62 | 62 | 63 | 63 |
| 013513 | 185084 | 2 | 2 | 116 | 0 | 0 | 001 | --- | 0269.00 | -.00 | 41 | 60 | 62 | 63 | 62 | 62 | 62 | 62 | 62 | 62 | 62 | 62 | 62 | 62 | 62 | 62 | 62 | 62 | 63 | 63 |
| 013748 | 186367 | 2 | 2 | 117 | 0 | 0 | --- | 0 | 01 | .00 289.00 | 42 | 61 | 62 | 63 | 62 | 62 | 62 | 62 | 62 | 62 | 62 | 62 | 62 | 62 | 62 | 62 | 62 | 62 | 63 | 63 |
| 014019 | 187649 | 2 | 2 | 118 | 0 | 0 | 001 | --- | 0269.00 | -.00 | 42 | 61 | 62 | 63 | 62 | 62 | 62 | 62 | 62 | 62 | 62 | 62 | 62 | 62 | 62 | 62 | 62 | 62 | 63 | 63 |
| 014255 | 188932 | 2 | 2 | 119 | 0 | 0 | --- | 0 | 01 | .00 289.00 | 42 | 61 | 62 | 63 | 62 | 62 | 62 | 62 | 62 | 62 | 62 | 62 | 62 | 62 | 62 | 62 | 62 | 62 | 63 | 63 |
| 014528 | 190214 | 2 | 2 | 120 | 1 | 0 | 001 | --- | 0269.00 | -.00 | 42 | 61 | 62 | 63 | 62 | 62 | 62 | 62 | 62 | 62 | 62 | 62 | 62 | 62 | 62 | 62 | 62 | 62 | 63 | 63 |
| 014809 | 191497 | 2 | 2 | 121 | 0 | 0 | --- | 0 | 01 | .00 289.00 | 42 | 61 | 62 | 63 | 62 | 62 | 62 | 62 | 62 | 62 | 62 | 62 | 62 | 62 | 62 | 62 | 62 | 62 | 63 | 63 |
| 015035 | 192780 | 2 | 2 | 122 | 1 | 0 | 001 | --- | 0268.00 | -.00 | 42 | 61 | 62 | 63 | 62 | 62 | 62 | 62 | 62 | 62 | 62 | 62 | 62 | 62 | 62 | 62 | 62 | 62 | 63 | 63 |
| 015311 | 194062 | 2 | 2 | 123 | 0 | 0 | --- | 0 | 01 | .00 289.00 | 42 | 61 | 62 | 63 | 62 | 62 | 62 | 62 | 62 | 62 | 62 | 62 | 62 | 62 | 62 | 62 | 62 | 62 | 63 | 63 |
| 015544 | 195345 | 2 | 2 | 124 | 1 | 0 | 001 | --- | 0269.00 | -.00 | 42 | 61 | 62 | 63 | 62 | 62 | 62 | 62 | 62 | 62 | 62 | 62 | 62 | 62 | 62 | 62 | 62 | 62 | 63 | 63 |
| 015820 | 196627 | 2 | 2 | 125 | 0 | 0 | --- | 0 | 01 | .00 289.00 | 42 | 61 | 62 | 63 | 62 | 62 | 62 | 62 | 62 | 62 | 62 | 62 | 62 | 62 | 62 | 62 | 62 | 62 | 63 | 63 |
| 020056 | 197910 | 2 | 2 | 126 | 1 | 0 | 001 | --- | 0269.00 | -.00 | 42 | 61 | 62 | 63 | 62 | 62 | 62 | 62 | 62 | 62 | 62 | 62 | 62 | 62 | 62 | 62 | 62 | 62 | 63 | 63 |
| 020331 | 199192 | 2 | 2 | 127 | 0 | 0 | --- | 0 | 01 | .00 290.00 | 43 | 61 | 62 | 63 | 62 | 62 | 62 | 62 | 62 | 62 | 62 | 62 | 62 | 62 | 62 | 62 | 62 | 62 | 63 | 63 |
| 020600 | 200475 | 2 | 2 | 128 | 0 | 0 | 001 | --- | 0269.00 | -.00 | 42 | 61 | 62 | 63 | 62 | 62 | 62 | 62 | 62 | 62 | 62 | 62 | 62 | 62 | 62 | 62 | 62 | 62 | 63 | 63 |
| 020845 | 201758 | 2 | 2 | 129 | 1 | 0 | --- | 0 | 01 | .00 289.00 | 43 | 61 | 62 | 63 | 62 | 62 | 62 | 62 | 62 | 62 | 62 | 62 | 62 | 62 | 62 | 62 | 62 | 62 | 63 | 63 |
| 021107 | 203040 | 2 | 2 | 130 | 0 | 0 | 001 | --- | 0269.00 | -.00 | 43 | 61 | 62 | 63 | 62 | 62 | 62 | 62 | 62 | 62 | 62 | 62 | 62 | 62 | 62 | 62 | 62 | 62 | 63 | 63 |
| 021342 | 204323 | 2 | 2 | 131 | 1 | 0 | --- | 0 | 01 | .00 289.00 | 43 | 60 | 62 | 63 | 62 | 62 | 62 | 62 | 62 | 62 | 62 | 62 | 62 | 62 | 62 | 62 | 62 | 62 | 63 | 63 |
| 021615 | 205605 | 2 | 2 | 132 | 1 | 0 | 001 | --- | 0269.00 | -.00 | 42 | 61 | 62 | 63 | 62 | 62 | 62 | 62 | 62 | 62 | 62 | 62 | 62 | 62 | 62 | 62 | 62 | 62 | 63 | 63 |
| 021850 | 206888 | 2 | 2 | 133 | 1 | 0 | --- | 0 | 01 | .00 289.00 | 43 | 60 | 62 | 63 | 62 | 62 | 62 | 62 | 62 | 62 | 62 | 62 | 62 | 62 | 62 | 62 | 62 | 62 | 63 | 63 |
| 022128 | 208171 | 2 | 2 | 134 | 0 | 0 | 001 | --- | 0269.00 | -.00 | 43 | 61 | 62 | 63 | 62 | 62 | 62 | 62 | 62 | 62 | 62 | 62 | 62 | 62 | 62 | 62 | 62 | 62 | 63 | 63 |
| 022403 | 209453 | 2 | 2 | 135 | 1 | 0 | --- | 0 | 01 | .00 289.00 | 43 | 61 | 62 | 63 | 62 | 62 | 62 | 62 | 62 | 62 | 62 | 62 | 62 | 62 | 62 | 62 | 62 | 62 | 63 | 63 |
| 022631 | 210736 | 2 | 2 | 136 | 0 | 0 | 001 | --- | 0269.00 | -.00 | 42 | 61 | 62 | 63 | 62 | 62 | 62 | 62 | 62 | 62 | 62 | 62 | 62 | 62 | 62 | 62 | 62 | 62 | 63 | 63 |
| 022916 | 212018 | 2 | 2 | 137 | 1 | 0 | --- | 0 | 01 | .00 289.00 | 42 | 61 | 62 | 63 | 62 | 62 | 62 | 62 | 62 | 62 | 62 | 62 | 62 | 62 | 62 | 62 | 62 | 62 | 63 | 63 |
| 023139 | 213301 | 2 | 2 | 138 | 0 | 0 | 001 | --- | 0269.00 | -.00 | 42 | 61 | 62 | 63 | 62 | 62 | 62 | 62 | 62 | 62 | 62 | 62 | 62 | 62 | 62 | 62 | 62 | 62 | 63 | 63 |
| 023414 | 214584 | 2 | 2 | 139 | 0 | 0 | --- | 0 | 01 | .00 289.00 | 42 | 61 | 62 | 63 | 62 | 62 | 62 | 62 | 62 | 62 | 62 | 62 | 62 | 62 | 62 | 62 | 62 | 62 | 63 | 63 |
| 023646 | 215866 | 2 | 2 | 140 | 0 | 0 | 001 | --- | 0269.00 | -.00 | 42 | 61 | 62 | 63 | 62 | 62 | 62 | 62 | 62 | 62 | 62 | 62 | 62 | 62 | 62 | 62 | 62 | 62 | 63 | 63 |
| 023922 | 217149 | 2 | 2 | 141 | 0 | 0 | --- | 0 | 01 | .00 289.00 | 43 | 61 | 62 | 63 | 62 | 62 | 62 | 62 | 62 | 62 | 62 | 62 | 62 | 62 | 62 | 62 | 62 | 62 | 63 | 63 |
| 024159 | 218431 | 2 | 2 | 142 | 0 | 0 | 001 | --- | 0269.00 | -.00 | 43 | 61 | 62 | 63 | 62 | 62 | 62 | 62 | 62 | 62 | 62 | 62 | 62 | 62 | 62 | 62 | 62 | 62 | 63 | 63 |
| 024435 | 219714 | 2 | 2 | 143 | 1 | 0 | --- | 0 | 01 | .00 289.00 | 42 | 61 | 62 | 63 | 62 | 62 | 62 | 62 | 62 | 62 | 62 | 62 | 62 | 62 | 62 | 62 | 62 | 62 | 63 | 63 |
| 024702 | 220996 | 2 | 2 | 144 | 0 | 0 | 001 | --- | 0269.00 | -.00 | 43 | 61 | 62 | 63 | 62 | 62 | 62 | 62 | 62 | 62 | 62 | 62 | 62 | 62 | 62 | 62 | 62 | 62 | 63 | 63 |
| 024948 | 222279 | 2 | 2 | 145 | 1 | 0 | --- | 0 | 01 | .00 289.00 | 43 | 61 | 62 | 63 | 62 | 62 | 62 | 62 | 62 | 62 | 62 | 62 | 62 | 62 | 62 | 62 | 62 | 62 | 63 | 63 |
| 025210 | 223562 | 2 | 2 | 146 | 0 | 0 | 001 | --- | 0269.00 | -.00 | 43 | 61 | 62 | 63 | 62 | 62 | 62 | 62 | 62 | 62 | 62 | 62 | 62 | 62 | 62 | 62 | 62 | 62 | 63 | 63 |
| 025446 | 224844 | 2 | 2 | 147 | 0 | 0 | --- | 0 | 01 | .00 289.00 | 43 | 61 | 62 | 63 | 63 | 62 | 62 | 62 | 62 | 62 | 62 | 62 | 62 | 62 | 62 | 62 | 62 | 62 | 63 | 63 |
| 025732 | 226127 | 2 | 2 | 148 | 1 | 0 | 001 | --- | 0269.00 | -.00 | 42 | 61 | 62 | 63 | 62 | 62 | 62 | 62 | 62 | 62 | 62 | 62 | 62 | 62 | 62 | 62 | 62 | 62 | 63 | 63 |
| 030007 | 227409 | 2 | 2 | 149 | 0 | 0 | --- | 0 | 01 | .00 289.00 | 43 | 61 | 62 | 63 | 62 | 62 | 62 | 62 | 62 | 62 | 62 | 62 | 62 | 62 | 62 | 62 | 62 | 62 | 63 | 63 |

**Fig. E-6. Television data tabular display**

To compensate for individual bit errors, a program was written to permit individual elements to be replaced from punched card input data. The information locating the elements for this replacement was gathered by noting the discrepancies listed by a comparison program that compared the identical pictures from the first and second playbacks. The replaced element was determined manually by assuming a value based on the value of the surrounding elements or by using the most likely value from one of the two playbacks.

Decommutation of the element information was accomplished by referencing the data to the detected television PN sequence. In the process of ground communication of the data from the DSIF sites to the SFOF, the spacecraft data stream was encoded into teletype characters. If a teletype character was deleted or inserted because of transmission difficulties, the number of bits between PN sequence would be altered. Therefore, as demonstrated in Fig. E-7, the decommutation could be in error.

In Fig. E-7 the correct values are 51, 52, 50, and 49. Assuming a 1-bit shift, the decommutated values would

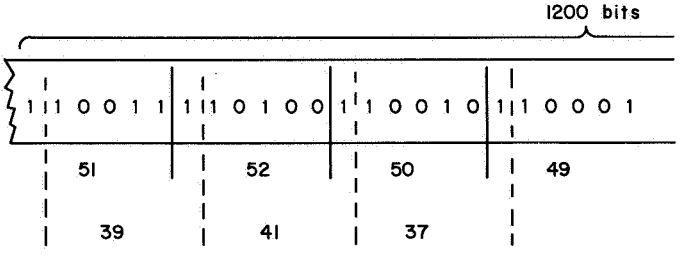


**Fig. E-7. Television data decommutation**

be 39, 41, 37, etc. Because of the gross mismatch with neighboring data, this anomaly was described as "torn lines." Figure E-8a shows Picture 1 with torn lines.

In the initial release of *Mariner IV* pictures, torn lines were removed by the process of line averaging. A *Ranger* program permitted a specified rectangular area to be replaced by the average of the vertical elements on the lines above and below the specified location. If more than one element was to be replaced, the interpolated rather than average value was inserted. Figure E-8b shows the results of such processing of Picture 1.

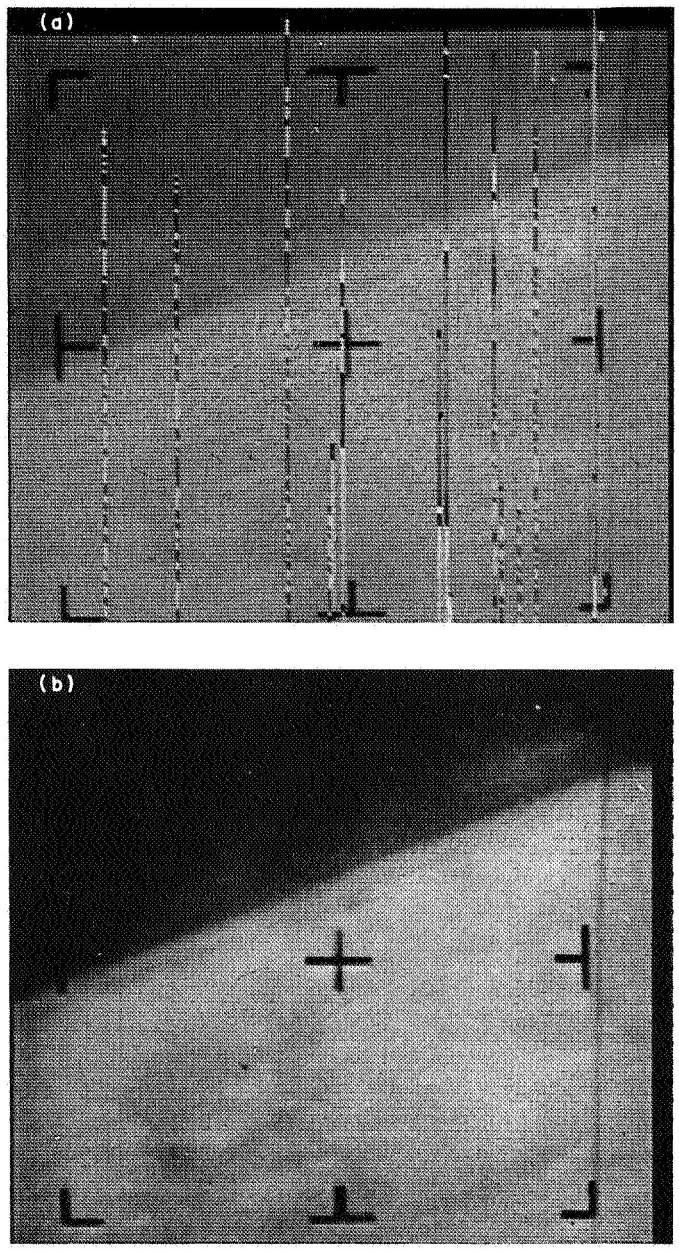


**Fig. E-8. *Mariner IV* Picture 1: (a) with "torn lines," (b) with "torn lines" removed and contrast enhanced**

Included in the reformatting program previously described was a capability to replace whole lines from punched card input or to shift the data for a line a given number of bits and redecommutate the result. This latter method was unsuited for the purpose of correcting garbled lines, because the garbling condition often occurred several times in a line in a nesting sequence. The simpler and more reliable approach was to replace the entire line based on data from the second playback. In no case was a line garbled in both playbacks, confirming the ground origin of the anomaly.

The DSIF-station-recorded magnetic tapes and the teletype punched paper tape were scheduled for processing by the described 7094 programs in order to provide the television experimenters with the most complete and correct data stream. The intention was to demodulate the magnetic tapes using the SFOF Telemetry Processing Station and directly read the data into the 7044–7094 processing system. Similarly, the paper tape was to have been read from the SFOF Communications Center into the 7044–7094 system. By manual selection of the better data, a merge was to have been accomplished, using the line replacement technique described. However, the excellent quality control effected on the real-time processing permitted all bit errors and garbled lines to be corrected, using only the real-time processed data. Therefore, station-recorded data were never processed.

### B. Computer Processing

The real-time 7044 processing of television data was operational several months prior to the required time and did not cause any difficulties during its operational period. The various aspects of the 7094 processing were carried out by several programmers. The separate parts were checked by each cognizant programmer, using self-generated simulated data. The integration into the SFOF processing system was completed a week or two prior to encounter, but was not verified because of the lack of sufficient TV data for testing through entry into the SFOF data processing system. A limited set of simulated TV data afforded some confidence in the operating readiness of the programs and permitted their release for flight data processing support.

The computer processing of the television data was accomplished by a coordinated operations team that included computer operators trained for the TV programs,

the cognizant TV programmers and their supervisor, and quality control personnel in addition to the SFOF operations personnel. For the first playback, each of the first three pictures was processed immediately after being totally received, whereas the remaining pictures were processed daily, one or two at a time. Computer processing time for each picture was approximately 1 hr. Except for Pictures 1 through 9 of the first playback, reprocessing of television data was minimized, with only occasional redundant processing.

The conversion of the electrical signal to an optical image by the video-to-film recorder was treated as a unified system, careful consideration being given to the type of film used and to laboratory control of the developing process. In conjunction with Eastman Kodak Company of Rochester, New York, SO-337 film and a Bi-Mat processing technique were developed to match the dynamic characteristics of the recorder and to minimize differences between processing runs. The recorded image data on the magnetic tape was used to modulate the intensity of the scanning beam of the recorder. Geometric control of the scanning beam was accomplished by preset selection of the format size and precision timing circuits. To provide dynamic calibration, the 64 shades of electronically generated gray were recorded on film by the recorder before and after each recording of a *Mariner* picture. To further calibrate each film-developing operation, an optical gray wedge was added, just prior to each developing, on the unexposed leader accompanying each run. Each of the developed optical gray wedges was measured by a photodensitometer to assure the constancy of the developing parameters. Each picture was processed by the highly trained recorder operating team as received from the 7094 processing. Recorder and film processing of each picture required approximately1.5 hr.

Negatives and transparent positives of the film image were forwarded to the JPL Photography Department, where conventional photographic printing techniques were used to produce enlarged copies of the television images of Mars. In order to readily identify the location of picture elements, the *Ranger* program, used to produce the magnetic tape formatted for the VF recorder, inserted "hash marks" for every 5 elements in the vertical and horizontal directions along the four edges of a picture. In addition, a title block was included to identify the mission, the picture number, and the camera number, and to provide other useful information, such as the processing data, the source of the data, and any special processing incorporated.

To compensate for the contrast emphasis inserted at one end of the photometric scale by the recorder, the 64's complement of data was calculated, processed, and converted to film images for selected pictures. As a further aid to human interpretation, contrast enhancement was provided by noting the range of intensity values in the tabular listing and expanding the scale of included values to encompass the entire 64-level dynamic range of the recorder. This was a controlled means of contrast enhancement accomplished in normal photography by printing on high-contrast paper. The first photographs released to the public incorporated these aids.

Approximately 9 weeks prior to encounter, John H. Morecroft of JPL proposed real-time processing and image display of *Mariner IV* TV data by using a PDP-7 computer and the Space Science Video Processing Laboratory. The real-time teletype data stream was entered into the PDP-7, where control characters were removed and identification of television data was accomplished. The output of the PDP-7 was routed to a digital-to-analog converter, a slow scan monitor, and a scan converter. This system permitted viewing of the image as it was being received, recording of the image using a Polaroid camera, and evaluation of various processing techniques for contrast enhancement and removal of the photometric distortion.

# Appendix F
# Haze Studies

## I. Presence of Haze

The first photograph of Mars taken by *Mariner IV* showed the bright limb of the planet and the "sky" area beyond the limb (see Appendix H). Instead of fading out to complete darkness, the "sky" area remained nearly 30% as bright as the planet, even at a height of 150 km above the planet. Some haze was also present in Pictures 19 through 22, taken at and beyond the terminator, but was here less than 10% as bright as the planet. In the photographs taken between the limb and the terminator, the haze could not be measured because of the absence of a known black reference. It seemed likely that some haze was present in all of the photographs because of their very low contrast. It was necessary to investigate the cause of this haze since it was known that its presence in the photographs would seriously affect the accuracy of photometric measurements of the Martian surface and the interpretation of its features.

The possible sources of haze or veiling glare in the photographs include:

(1) Scattering by dust or clouds in the Martian atmosphere.

(2) Degradation of TV camera telescope by condensation of some outgassing product from the spacecraft.

(3) Malfunction of the camera electronics system.

(4) Etching or blistering of the optical surfaces.

(5) Pitting by micrometeoroids.

A number of experimental tests were made to try to determine the actual cause of the haze.

### A. Electronics

To test whether the background haze in the *Mariner IV* photographs may have been produced by some malfunction in the camera electronics, the camera was turned on several weeks after the Mars encounter, and photographs of black space were recorded at each of the four gain settings and transmitted to earth. In these photographs the video signal was at the proper "black" level, indicating that the camera electronics were working properly at the time of the encounter and that the haze was in fact related to the presence of Mars and was due either to atmospheric scattering or to scattering of Martian surface light in the optical system.

### B. Collimator with Side Light

Initial "haze" tests utilized a *Mariner*-type television camera viewing a 22.5-cm-focal-length collimator containing a resolution chart and with its exit aperture surrounded by a diffuse white reflector. The collimator light level was set to a typical Mars brightness (about 0.6 lambert), and the white reflector was side-illuminated with a 1000-W flood lamp. To produce a haze level equal to that found in Picture 1 required a diffuse side-light level such that all resolution was lost. Since features were seen on the Martian surface, and since a brightness of 2.5 lamberts (four times that of Mars) was required to obtain the effect, this approach was discarded.

The second set of tests was conducted with the simulated "Martian surface" plaster model based on features seen in Pictures 7 through 15. Viewing this model through a semi-mirror and introducing diffuse light by reflection in the semi-mirror, the contribution of the haze to the total light seen at Mars could be estimated. Tests were made under lighting conditions similar to those of Pictures 1, 7, 11, and 15. By visually comparing several test pictures with the corresponding flight picture, the following rough estimates were made:

| Picture | Haze contribution to apparent brightness,% |
|---|---|
| 1 | 39 |
| 7 | 43 |
| 11 | 34 |
| 15 | 50 |

These estimates assume that the surface slopes used in the model are a true representation of slopes on Mars. If Mars has smaller slopes, the haze contribution is reduced.

### C. Side-light and Mirror Degradation Tests

The purpose of these studies was to determine whether the haze was due to light scattering in the optics and, if so, to derive haze functions for the optics that could be applied to the video data to correct the brightness and the contrast of the photographs. Under optical conditions closely simulating those existing during encounter, numerous attempts were made to produce scattered light in the optics approximately equal to the amount of haze found in the photographs at the limb and at the terminator.

The approach taken in the studies was, first, to measure how much scattered light was produced by a "clean" optical system, and then to simulate various possible degradations of the optics to determine what effect each would have on veiling glare. The tests were of two basic categories: (1) those designed to determine the light-scattering characteristics of the optics under various conditions, and (2) those designed to simulate the lighting situation during encounter to find out whether any arrangement could produce haze duplicating that which is seen in the *Mariner* photographs. Because the resolution of the photographs appeared normal and the video level (brightness) was within the expected limits, consideration could be given only to those optics modifications that would produce the required amount of veiling glare without simultaneously producing a great loss in resolution or causing a drastic change in the apparent "speed" of the optics. Also, any such modification had to simulate a condition of the optics that actually could have occurred sometime between launch and encounter with Mars.

Some of the possible causes of veiling glare that were studied are:

(1) Direct (nonimaged) light from outside the camera field of view striking the vidicon faceplate because of inadequate light shielding or baffling.

(2) Increased reflectivity caused by degradation of the dull black interior surfaces of the optical system by micrometeoroid erosion or by condensation of outgassed products on the surfaces.

(3) Pitting of the mirrors by micrometeoroids.

(4) Possible blistering of the electroless Kanigen nickel-nickel phosphorus coating on the mirrors after long exposure in a high vacuum.*

(5) Coating of the filters in the shutter or vidicon faceplate by outgassed products such as polyurethane, which was carried in the vidicon electronics system.

(6) Coating of the primary and secondary mirrors by outgassed products.

(7) Fluorescence of the color filters in the camera.

## II. Optical System Tests

The tests performed on the optical system were the following:

### A. Collimated Point Source Test

The purpose of this test was to measure photoelectrically the amount of light introduced in the image plane of the optical system from a collimated light beam as a function of the angle of the beam with the optical axis. The setup for the test consisted of the *Mariner* television optical system including shutter and filters, a photomultiplier photometer mounted behind the optical system to measure the light intensity in the image plane, and a concentrated arc lamp and collimating lens to illuminate the front of the optical system. The size of the arc in the concentrated arc lamp was small enough to be considered a point source. The arc lamp was placed in the focal plane of a 30-cm $f/2.5$ Aero Ektar aerial camera lens, which produced a parallel beam of light approximately 12 cm in diameter—large enough to illuminate fully the front of the optical system. The arrangement is shown in Fig. F-1, except that the pinhole mask shown was not

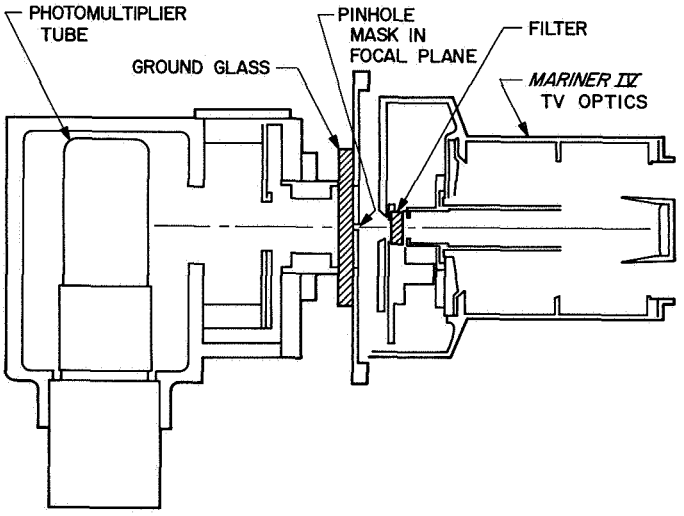


**Fig. F-1. Arrangement of TV optics and photomultiplier for veiling glare and simulated Mars transparency scan tests**

*Blistering of the aluminum reflecting (mirror) surfaces could have been due to the basic construction of the telescope mirrors. These mirrors were made of beryllium metal overcoated with Kanigen (nickel-nickel-phosphorus), a hard alloy. The precision optical reflecting surface was ground and polished on the thin Kanigen coating, and this coating was further coated with a conventional aluminum reflecting film and a silicon monoxide protective layer.

When Kanigen is deposited on beryllium, it forms monatomic hydrogen, which may be absorbed excessively by the beryllium metal. Since it is uncertain whether the *Mariner IV* telescope mirrors were heated to more than 129°C, there is a possibility that hydrogen remained entrapped in the beryllium and escaped through the Kanigen and aluminum films during the seven-month-long trip through the deep space vacuum. If this occurred, the aluminum reflecting surface could have blistered and given rise to scattered light and veiling glare in the image. Samples of Kanigen on beryllium mirrors were held in an ion chamber at $10^{-9}$ mm Hg for several months, under temperature variations from −120 to +149°C, but blistering was not observed. However, there was some chipping of aluminum at the edges.

used for this test. The photomultiplier and optics were mounted on a nodal slide in a manner that allowed them to be rotated as a unit about a vertical axis.

The collimated beam was aligned with the axis of the optical system by putting a piece of ground glass in the focal plane of the optical system and positioning the concentrated arc lamp and the optical system so that the image of the arc was centered in the shutter aperture. The photomultiplier was then mounted in position behind the optical system. Photomultiplier readings were taken at 1-deg intervals as the angle between the collimated beam of light and the axis of the optical system was varied from 0 to 30 deg by rotating the nodal slide. The photomultiplier measured the total amount of light in the image plane.

### B. Veiling Glare Test

The purpose of this test was to measure photoelectrically the veiling glare in the image plane of the television optics as a function of the angular diameter of the illuminated source at which the optics were aimed. Photographic tests of this kind were also used to verify the photoelectric data. The test setup (Fig. F-2) consisted of a light box with various circular masks to vary the size of the light source, the 30-cm Aero Ektar lens used as a collimator, and the photomultiplier–TV optics arrangement. This arrangement consisted of the TV optical system with shutter and filters, a pinhole mask in the focal plane, a piece of ground glass behind the pinhole, and the photomultiplier positioned behind the ground glass. As in the collimated point source test, the photomultiplier and TV optics were mounted on a nodal slide which allowed them to be rotated as a unit around a vertical axis. The light box was uniform in brightness within 5% across the area of the largest mask.

One of the circular masks was positioned on the light box, and a 1.5-mm-square piece of black felt was placed on the light box opal glass in the center of the mask. With the photomultiplier and pinhole mask removed, the optics with the ground glass in the focal plane were aligned so that the square piece of felt was centered in

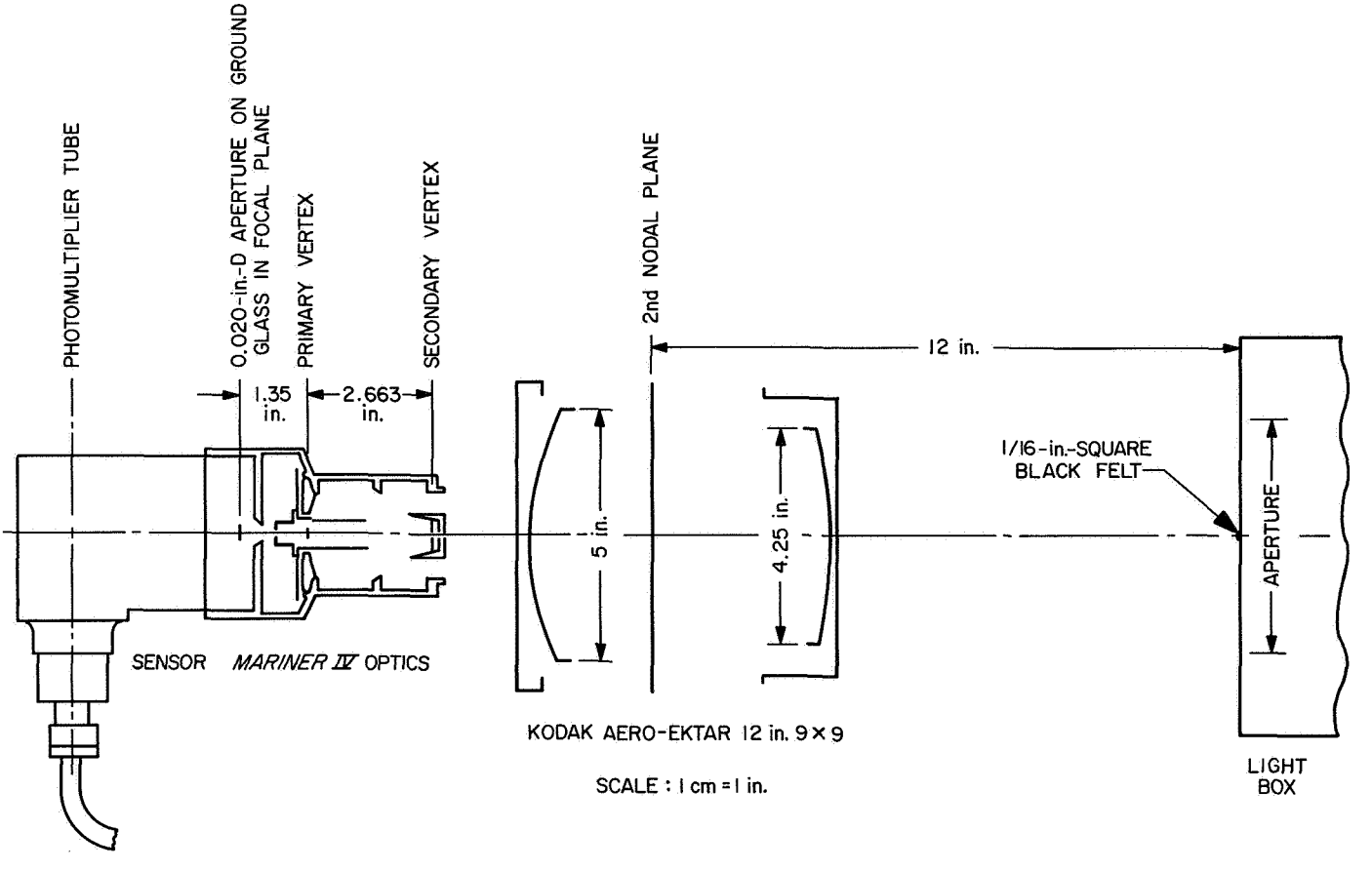


**Fig. F-2. Veiling glare tests**

the field of view. Small adjustments in focus were made by moving the Aero Ektar lens slightly. With the image of the black felt in the center of the field, the 0.5-mm-diameter pinhole mask was placed in front of the ground glass in the focal plane and centered over the image of the black felt spot. As the optics were rotated around the axis of the nodal slide, the pinhole mask would scan across the image of the black spot.

Photomultiplier readings were made of the relative brightness of the image of the black spot, and of the light box to either side of the black spot, for each of six masks. The linear and angular diameters of these masks, as seen by the TV optics through the collimating lens, are given below:

| | |
|---|---|
| 12.5 cm | 23.5 deg |
| 10 | 18.9 |
| 5 | 9.5 |
| 2.5 | 4.8 |
| 1 | 1.8 |
| 6 | 1.2 |

The 1-cm (1.8-deg) mask was slightly larger than the field of view through the shutter aperture.

Figure F-3 presents the important results of the veiling glare tests. The stray light curve for clean optics showed that the TV optical system was adequately shielded for stray light, since the maximum stray light was only 6% with a bright source 23.5 deg in diameter, the approximate maximum angular diameter of Mars as seen from the spacecraft. (As seen from *Mariner IV*, the Martian disc was, of course, not fully illuminated.) Rounded blisters on the mirrors produced a maximum of 29% stray light in the image; shallow blisters produced 63% stray light. Although this is a considerable amount of stray light, the test did not reproduce the illumination conditions that *Mariner IV* experienced but is essentially a "worst case" situation. From the curves in Fig. F-3, it can be seen that most of the stray light came from a solid angle less than 10 deg in diameter or 5 deg from the axis of the optical system.

The thin, shallow blisters produced more stray light than rounded blisters because, in a closed-tube Cassegrain system, the mirrors are well shielded from light incident at large angles with the axis.

### C. Photographic Tests

These tests, including direct photographic photometry of the image, were originally intended to provide the

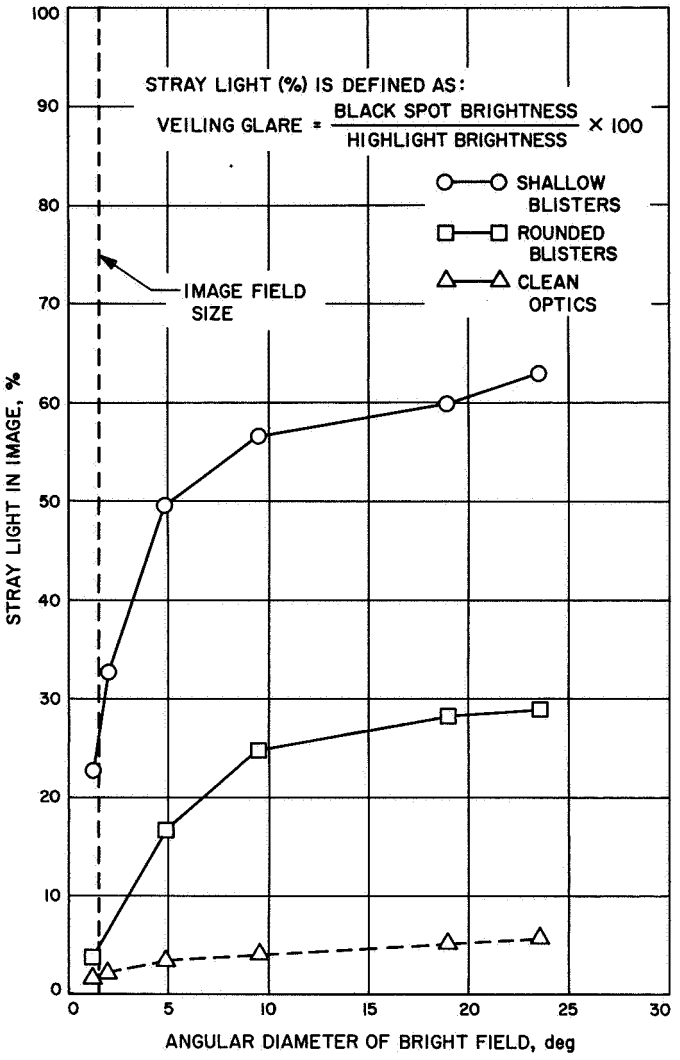


**Fig. F-3. Stray light in image as a function of the diameter of the bright source at which the optical system is pointed**

image brightness and contrast data for the veiling glare tests and the Mars simulation tests. However, owing to the difficulty and time involved in obtaining the photographic image data, the photographic technique was used to verify the accuracy of the photomultiplier technique. The test setup was the same as that for the veiling glare tests, except that the photomultiplier was replaced by a roll film holder. In addition, a timing circuit was connected to the light box and used to expose the film for the proper length of time. The procedure for the veiling glare tests was to center the image of the black spot in the optics field of view and then focus the image on the ground glass by moving the Aero Ektar lens. The film holder was designed so that the ground glass could be placed in the same plane that the film occupied in the film holder.

For each mask size an exposure was made on film. At the beginning and end of the film roll, a small calibrated step wedge was placed on the film roll in the optics image plane and exposed by turning on the light box for the same exposure as was given in the test. The photographic data agreed with the photomultiplier data within about 10%.

Using the photographic photometric technique, tests were also made on the veiling glare arising in the telescope from outgassing of paints and plastics, such as polyurethane, in the space vacuum and their redeposition on the telescope mirrors and light shields. These materials introduced some veiling glare, but not nearly enough to explain that which was actually encountered by *Mariner IV*.

### D. Mars Simulation Transparency Scan Tests

The purpose of this test was to simulate as closely as possible the optical conditions seen by the television camera during encounter with Mars. In order to simulate Mars optically as the television camera saw it, a photographic transparency of Mars was mounted over a uniformly illuminated light box and viewed by the camera through a large lens so as to appear to be at an infinite distance. (The lens itself introduced a negligible amount of scattered light.) The Mars transparency was made by photographing a 30-cm-diameter, hand-painted globe, illuminated by a spot lamp placed 6 meters away. The globe of Mars was positioned so that the subillumination point on the globe was at the subsolar point on Mars during encounter. The globe was then photographed with a Questar telescope from about 21 meters. The subcamera point on the Mars globe was on a perpendicular from the spacecraft trajectory through the center of the planet. A black-and-white Mars transparency, made from the negative, was then taped onto the opal glass on the light box. A black cardboard mask, with a cutout shaped like the Mars globe image on the transparency, was placed on the transparency so that all light from the box was blacked out except for the Mars image. Five small felt squares were placed on the light box, approximately along the line followed by the camera field of view.

The collimating lens was then focused using the same technique as in the veiling glare tests. The pinhole mask was aligned so that, as the optics were rotated about the nodal slide axis, the pinhole scanned all five of the black spots. The ground glass and the photomultiplier were mounted as shown in Fig. F-2. Photomultiplier readings were then taken as the optical system was rotated and the transparency was scanned. Readings were taken at the limb in 1-deg increments, starting at 4 deg off the limb. The photomultiplier and optics were scanned across each of the black reference spots across the transparency. Readings were taken of the brightness of each black spot and the area on either side of it.

The Mars transparency test showed that a clean optical system, under simulated conditions of the *Mariner IV* encounter with Mars, gives a high-contrast image with very little background veiling glare. During these tests the only optical degradations that produced enough veiling glare to approach that seen in the first *Mariner IV* photograph were shallow simulated blisters on both mirrors.

### E. Mars Simulation Mask Scan Tests

Because of the difficulty of simulating accurately the relative brightness profile of Mars across the area scanned by *Mariner IV* with the transparency of the Mars globe, it was decided to remove the transparency from the light box, leaving only the outlining mask in place. This gave a "worst case" simulation of a uniformly bright planet. The test setup was identical to the one used in the Mars transparency tests except that the transparency was removed. The small pieces of black felt were placed at intervals across the mask area of the light box so that they would be scanned by the optics as they were rotated on the nodal slide. The test procedure was the same as that used in the Mars simulation tests. Both scanning methods were used: rotating the optics and photomultiplier as a unit and pointing the optics at an area and then scanning the image with a pinhole mask attached to the photomultiplier.

The clean optical system produced very little veiling glare beyond the limb: a maximum of 4% of the limb brightness. On the other hand, the optics with blistered mirrors not only produced considerable veiling glare beyond the limb (a maximum of 32.4%), but produced a great loss in image brightness. The brightness of the limb (bright area) with blistered mirrors was only 35.5% of the limb brightness with clean optics. In comparing the effect of the simulated blisters with the effect of optics coated with clear spray-on lacquer (Krylon) it was found that the Krylon produced nearly the same veiling glare as the blisters but did not cause as great a loss in image brightness.

### F. Visual Resolution Test

The purpose of this test was to measure whether degradation of the optics affected resolution as well as contrast.

The test, which was made with an Air Force target, employed a clean, nondegraded optical system and a degraded system. No significant loss in high-contrast resolution was observed.

## III. General Conclusions

1. A clean *Mariner IV* television optical system could not have produced the haze. In none of the tests conducted did the clean optical system produce more than a few percent (maximum of 6%) veiling glare. The veiling glare at the limb in the Mars simulation tests was only 4%.

2. It is quite doubtful that any abrasion or coating of the black interior surfaces of the optical system could have produced the haze. In none of the tests that simulated increased reflectivity of the black interior surfaces was there enough stray light produced to account for the haze.

3. Sufficient pitting of the mirrors (e.g., by micrometeoroid impacts) could have produced considerable veiling glare. However, the micrometeoroid count experienced by *Mariner IV* appears to be far too low to explain the veiling glare encountered.

4. Only two simulated optical system degradations were found that produced enough veiling glare in the tests to equal the amount of haze shown in the first *Mariner IV* photo. One of these was simulated blistering of the mirror surfaces; the other was coating of the mirrors with a thin coat of lacquer to simulate space debris deposited on the optical surfaces.

The simulated blisters were shallow (rather flat in cross section) and covered from 40 to 50% of both mirrors. They produced 63% veiling glare with the optical system pointed at the center of a bright source having a 23.5-deg angular diameter. In the Mars simulation mask tests, with the optical system pointed at the limb, the veiling glare or haze at the limb was 32%, which was slightly greater than *Mariner IV* Picture 1.

Lacquer mist sprayed on the mirrors to simulate possible condensed materials produced 26% veiling glare at the limb in the Mars simulation mask test, but produced only a 15% loss in light at the center of the mask. This proved that it is possible to degrade the mirrors enough to produce considerable veiling glare without a great overall loss in image brightness.

# Appendix G
# TV Interpretation Studies

## I. Pre-encounter

During the period between launch and the return of TV picture data from Mars, the scientific team responsible for evaluation of the pictures became familiar with the capabilities and limitations of the spacecraft TV system. The problem of interpreting pictures of an unknown planetary surface led to laboratory and field tests to provide the specialized photo-interpretive data necessary to evaluate the encounter photographs more precisely.

Although the pictures returned from Mars were to be quantitatively analyzed, using the digital numbers representing the observed brightness of the planet, well-balanced pictures of moderate contrast are required for subjective interpretation of the surface and to provide clues as to the most interesting areas to examine among the 40,000 numbers comprising each picture.

As the magnitude of this problem became better understood, the initial proposal to carry out TV photography of local terrain from elevated ground sites and/or aircraft was discarded in favor of controlled laboratory studies. The pre-encounter activities were divided into four general categories:

(1) TV system selection

(2) Laboratory tests

(3) Field tests

(4) Presentation optimization

### A. TV System Selection

A TV subsystem was required that could closely simulate the flight subsystem (MC-4) in sensitivity, color response, and geometrical characteristics. The subsystem selected was a hybrid consisting of electronics from the prototype system and a proof-test-model (PTM) camera head of an early mechanical design with especially selected vidicon tube and color filters of the flight type. This subsystem (P-2) exhibited response characteristics within a few percent of those of the flight subsystem (Fig. G-1). The camera had provision for mounting of various optics. In addition to the 305mm, T8, Cassegrain telescope, 28, 55, and 100mm refracting lenses were used in lab studies to provide varying scale factors for each test. Additional flexibility of operation was provided by changing the exposure time circuit from fixed two-speed (80 and 200 msec) to continuously variable from 80 msec to 1.60 sec.

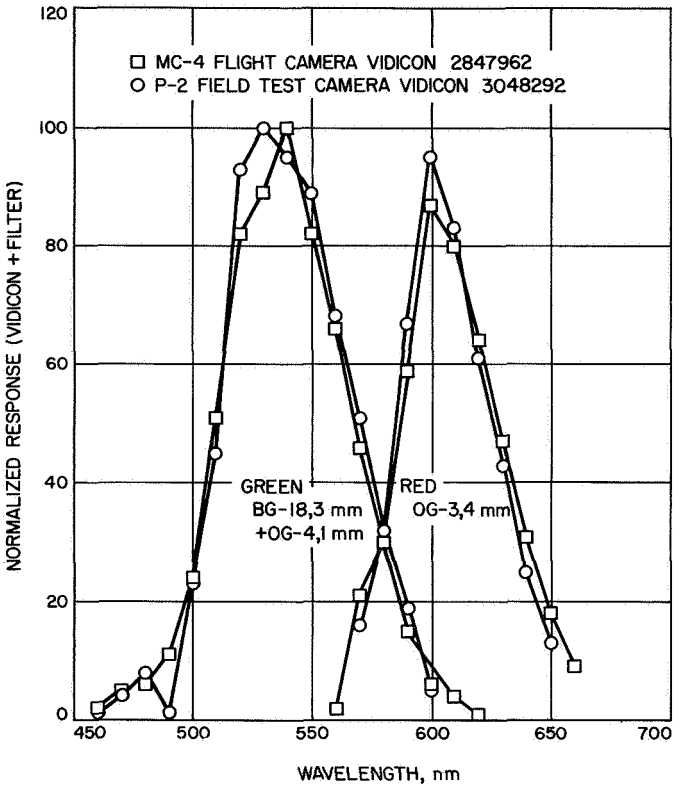


**Fig. G-1. Spectral response of flight field test TV camera system**

### B. Laboratory Tests

Tests were performed to determine detectability thresholds of simple simulated topographical features (e.g., slopes and edges characteristic of faulting and mountain forming activities) and variations in color and albedo typical of contiguous terrains of differing composition or age. Combinations of both were also studied.

Quantitative data were obtained from simple step models painted in grey shades to simulate Martian light-and-dark area reflectivities ($\rho = 0.18$ and 0.07, respectively) as shown in Fig. G-2. The models were illuminated by a 750-W spotlight at geometries analogous to those anticipated at encounter. Models were mounted on a three-degree-of-freedom platform and oriented to desired

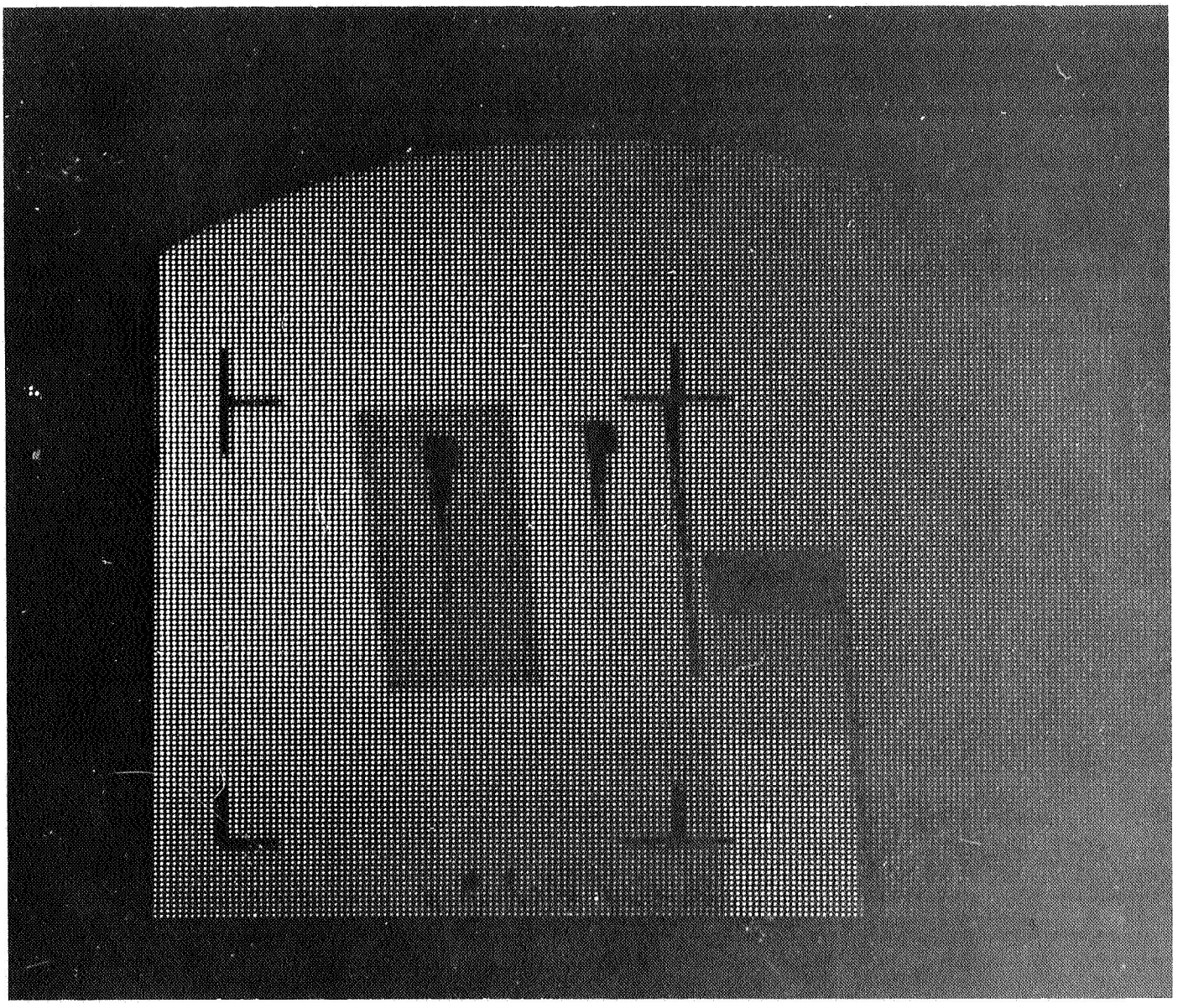

**Fig. G-2. Step/edge model**

positions relative to the TV camera and the light source (Fig. G-3). As at encounter, a constant phase angle of 60 deg was maintained.

Scale factor and subjective evaluation studies were made using U.S. Army Map Service topographical relief maps painted suitably to simulate terrain as seen from high altitudes (Fig. G-4). By proper choice of optics, equivalent ground resolution could be simulated for judging the detectability of terrestrial formations under the conditions of the Mars encounter.

### C. Field Tests

Field operations at the Mt. Wilson Observatory were conducted during the March 1965 opposition in order to directly check the sensitivity and the color filter selections by actually photographing Mars. The TV system was coupled to the 60-in. Mt. Wilson reflector in folded Cassegrain configuration, and direct TV pictures were taken of the planet. To compensate for the difference in the optics (the 60-in.-telescope Cassegrain focus is $f/16$), the variable exposure time was used and most pictures were taken at 800 msec. On the night of March 20, 1965, when

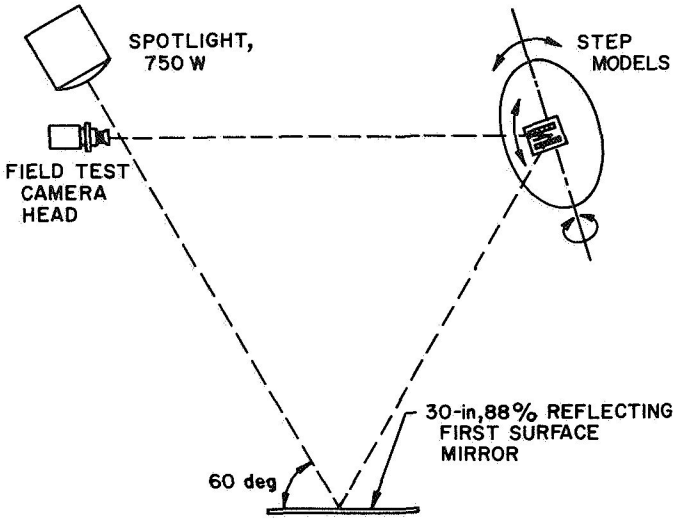


**Fig. G-3. Laboratory setup for model studies**

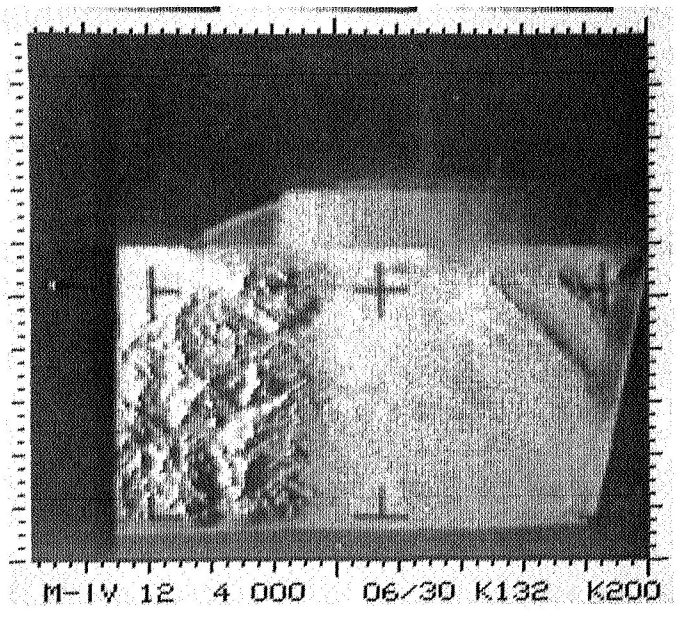


**Fig. G-4. Terrain model of the Bakersfield (California) area (also shown is a linear grey step chart providing a check of system gamma during model studies)**

reasonable seeing and very good atmospheric transparency were experienced, more than 60 pictures of Mars were obtained, and the video signals recorded on magnetic tape. Later, at JPL, the data were digitized and played back into the PDP-4 (programmed data processor) and 35mm negatives were obtained from the video processor (Fig. G-5). Analysis of the digitized video indicated a 15% difference between red and green pictures, the signal being greater for the green filter. These results very closely matched the calculated and measured responsitivity to the 3000°K light source used for flight system calibration. In addition, the apparent brightness of the disc was within a factor of 2 of that expected (536 ft-lamberts) without consideration of the absolute atmospheric transparency (estimated at 60–80%), and well within the self-adjustment range of the flight camera.

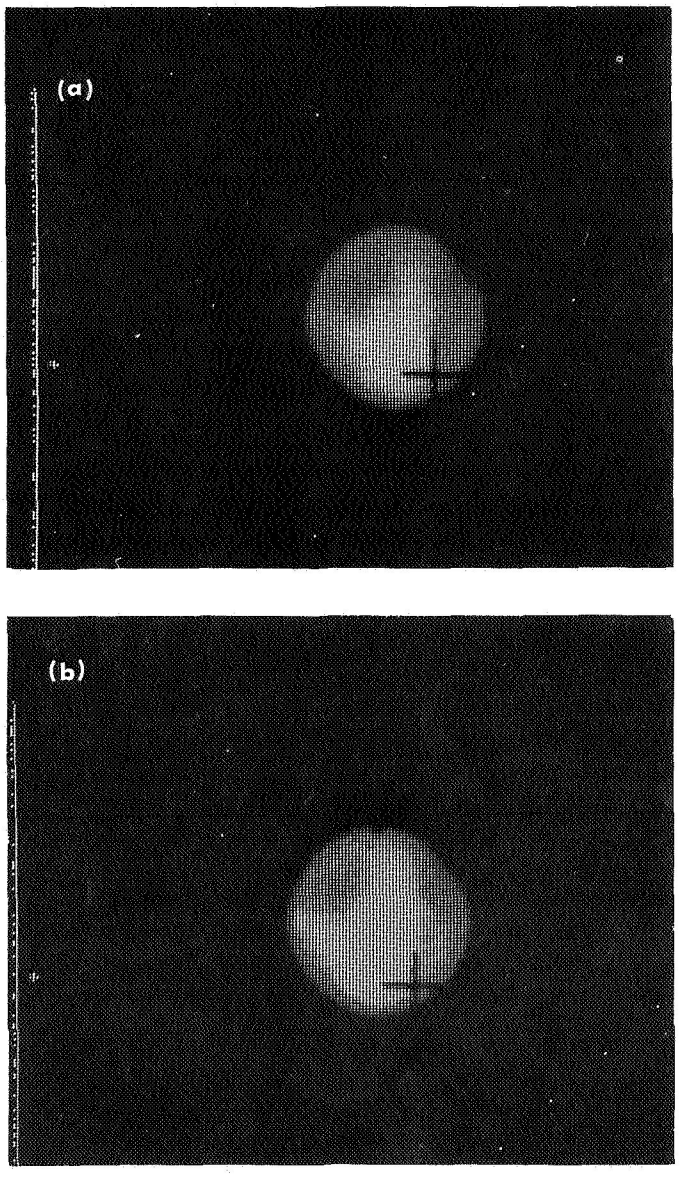


**Fig. G-5. Mt. Wilson 60-in.-reflector, full aperture, 800-msec exposure, March 20, 1965, Mars date June 15, central meridian 40 deg, south at top, magnitude −0.9 (a) Green, 540 nm, (b) Red, 600 nm**

### D. Presentation Optimization

Encounter pictures were received in digital form. After being decoded by a computer, these were imaged by the video data processor onto 35mm film. The film was exposed by a cathode-ray tube (CRT) beam that was intensity-modulated by a voltage proportional to the digital level as it scanned the 200 × 200 element raster.

Laboratory and field test TV picture data were recorded on magnetic tape. Real-time check prints were made from a time lapse cinerecording of the TV monitor display. The magnetic tape recorded data were digitized during playback, and after suitable computer processing were processed by the VFC system in the same manner as flight data.

To enhance the interpretability of encounter pictures, various parameters of the VFC system and the computer operations required optimization. The 200 × 200 element raster leaves large spaces between dots (elements) on a 35mm format. To provide smoother appearing pictures, the scan format size was decreased and the CRT beam defocused slightly. Additional smoothing could be accomplished by interpolation between elements to derive a 400 × 400 element picture. To ensure that all of the data in the picture can be seen, the computer can also invert the numerical data allowing the film to be exposed more linearly, and the gamma was adjusted to provide lower but more linear contrast (i.e., $\gamma = 1.0$, cf. $\gamma = 1.5$). The result was a picture showing the scene as photographed—that is, as continuous data without the interruptions between dots (Fig. G-6).

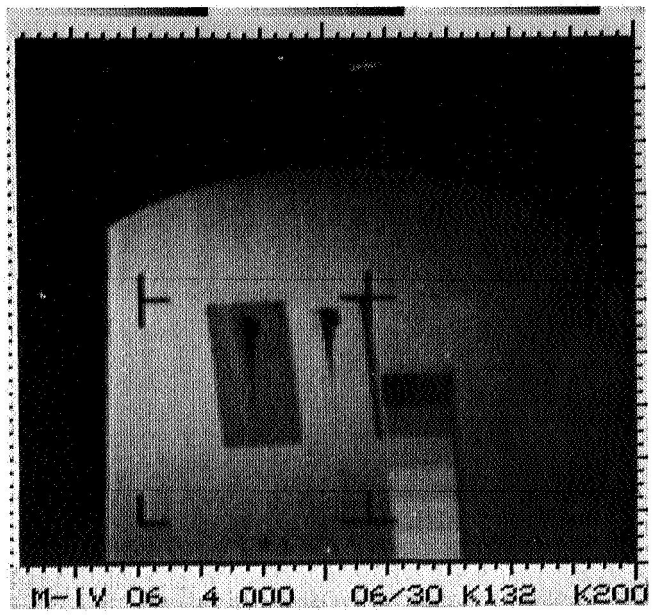


**Fig. G-6. VFC system processed model study picture with optimized operation (cf. Fig. G-2)**

## II. Postencounter

After the receipt of encounter data, the model studies were continued to further refine the interpretability of the TV pictures. Based on data from the flight pictures, a model was constructed (Fig. G-7) and installed in the lab setup shown in Fig. G-3. The model was fabricated by dropping steel and plastic spheres from various heights into semisolidified plaster which was predyed to give a reflectivity of approximately 20%. This model was photographed at encounter geometries and at varying scale factors so that visual crater detectability as a function of depth-to-diameter ratio could be determined. The model was also viewed with added diffused light in order to investigate the haze seen in the flight pictures (see Appendix F).

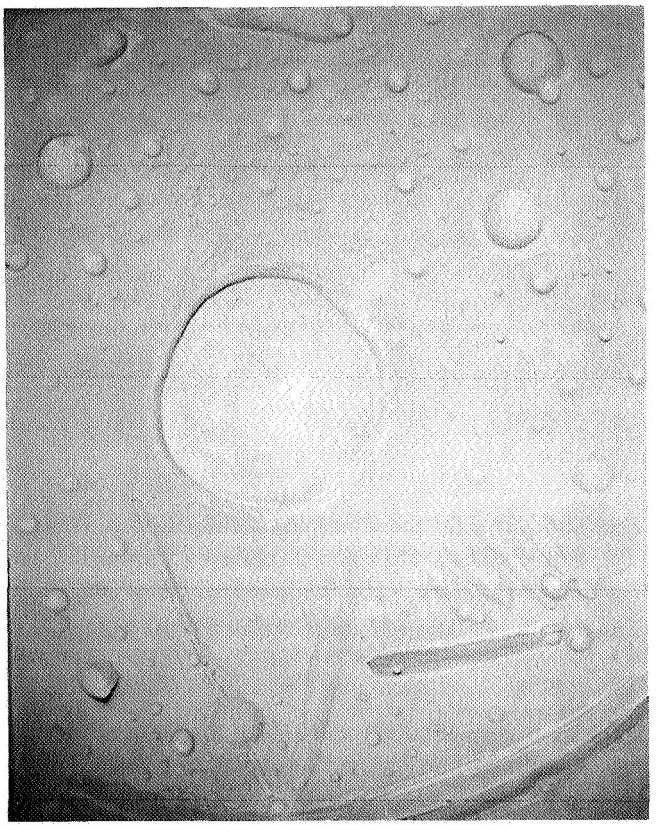

**Fig. G-7. Martian topography, simulated model**

# Appendix H

## Martian Slopes and Surface Roughness

### I. Introduction

The magnitudes and topographic scales of slopes are of direct interest both for improving our understanding of the present conditions and past history of the Martian surface, and for planning future planetary probes. Information on slopes at a scale larger than a few kilometers may be derived from the *Mariner IV* pictures, while doppler radar studies provide some slope information down to a scale of a few meters. All available information indicates that the Martian terrain is quite smooth relative to the upland areas of the moon. The implications of this conclusion to the understanding of Martian surface processes are considered in Appendix I.

Two different kinds of topographic data have been obtained from the calibrated *Mariner IV* intensities. First, large-scale slopes have been calculated directly from the intensity values in profiles across craters where the direction of maximum slope was clearly evident. Second, the 2- to 3-km intensity "roughness" has been separated into albedo and topographic contributions and average slope estimates made on this basis for the general land surface away from conspicuous topographic features.

### II. Direct Computation of Slope and Elevation Profiles

If a level surface of albedo $a$ is observed at an altitude angle $\varepsilon$ to the horizontal and azimuth $A_\varepsilon$, and illuminated by the sun from an altitude angle $i$ at azimuth $A_i$, the apparent intensity per unit solid angle will be

$$I(0,a) = I_0 aq(\varepsilon, i, \Delta A_{i\varepsilon}) \sin i \tag{H-1}$$

where $\Delta A_{i\varepsilon} = A_i - A_\varepsilon$, $q(\varepsilon, i, \Delta A_{i\varepsilon})$ is a function which describes the scattering properties of the surface, and $I_0$ is the solar radiation intensity intercepted by a surface normal to the direction of the sun. In the case of a perfectly diffusely reflecting surface, $q(\varepsilon, i, \Delta A_{i\varepsilon})$ is constant, and in the case of the moon it can be reduced to $f(\alpha)$, where $\alpha$ is the phase angle. The surface of Mars evidences an intermediate photometric function to the extent that some limb-darkening is observed. However, we shall be concerned with cases where $\varepsilon$ varies only rather slightly from that of a level surface. Hence, we shall consider $q(\varepsilon, i, \Delta A_{i\varepsilon})$ to be constant across a given crater. Then

$$I(0,a) = I_0 aq(\varepsilon) \sin i \tag{H-2}$$

The intensity at a point where the slope of the surface is $s$ radians, and the surface normal lies in the vertical plane including the direction to the sun, can be written as

$$I(s,a) = I_0 aq(\varepsilon) \sin(i - s) \tag{H-3}$$

$$= I(0,a) \frac{\sin(i-s)}{\sin i} \tag{H-4}$$

if the albedo is unchanged from that of the adjacent level surface. Finally, if the normal is at an azimuth $A_g$ to the sun azimuth, then

$$I(s,a) = \frac{I(0,a)(\sin i \cos s - \cos i \sin s \cos \Delta A_{g\varepsilon})}{\sin i} \tag{H-5}$$

where $\cos \Delta A_{g\varepsilon} = \cos(A_g - A_\varepsilon)$.

Using the above relationships, Clyde Chadwick, a graduate student in planetary science at Caltech, developed a computer routine for the computation of slope profiles and, by integration, relative elevation profiles. In his routine, the slope at each point of a profile is obtained by solution of the quadratic equation

$$as^2 + bs + c = 0 \tag{H-6}$$

where

$$a = \left[\frac{I(s,a)}{I(0,a)} \sin i\right]^2 - \cos i \cos \Delta A_{g\varepsilon}$$

$$b = 2 \sin i \cos i \cos \Delta A_{g\varepsilon}$$

$$c = \left[\frac{I(s,a)}{I(0,a)} \sin i\right]^2 - \sin^2 i$$

In order to ensure the requisite two-dimensional symmetry, contour maps were prepared of the intensity at each (line-element) point in the area of the crater. Diametrical profiles through the crater were then selected where two-dimensional symmetry was clear (i.e., where the intensity contours intersected the profile

normally). Slopes were computed for each point in the profile, and then topographic profiles were generated by integration of the slopes in serial fashion from one end of the profile to the other. A range of values of level intensity $I(0, a)$ was used in each profile. This range included the intensities of the nearly level surfaces at each end of a profile as well as the intensity values for apparently flat portions of the crater floor. This variation was necessary because a slight change in assumed albedo—and therefore level intensity—produces a slight systematic increase or decrease in all slopes, i.e., a tilt. Hence considerable experimentation was necessary in order to avoid any conspicuous uniform tilt of the profile. Figure H-1 illustrates the procedure. However, in some cases it was found that the particular level intensity value which removed tilt of the surrounding terrain on the two sides of the crater resulted in conspicuous systematic tilts of part of the interior of the profile. Such a result can easily arise from variations in albedo across the crater. In some cases these variations could be detected in the original printout intensity data (see Part II of this report), when the data were contoured and the profiles computed. In others, the transition between differing albedo regions was not abrupt enough to be detected in this way, and some

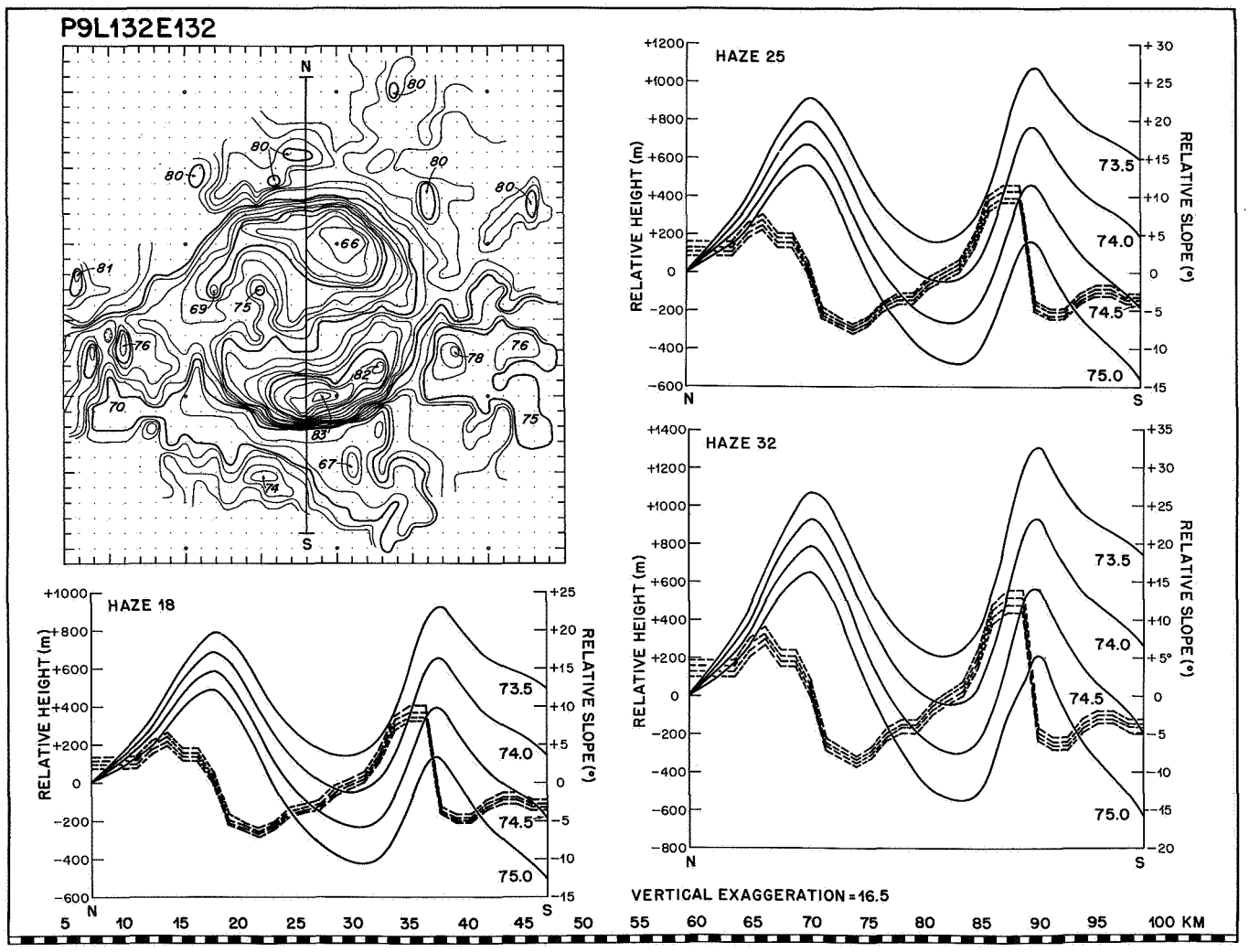


**Fig. H-1. Parametric variation of haze and level intensity values**

**The maximum and minimum possible values of haze, estimated in Section III of this report, merely vary the maximum slopes from about 10 to 15 deg. None of the level intensities used removes the obvious "tilt" in the section. Examination of the contoured intensity data shows that the level intensity at the north end of the section is about 10% greater than that of the south. Hence some adjustment must be made for this change, either abrupt or gradual, in order to generate a topographic profile which is not obviously tilted. However, the relative relief of the crater may be estimated satisfactorily even from a tilted profile.**

distortion still remains. It should be noted, however, that albedo variations are only a secondary source of error in estimation of slopes, since much of the crater relief is restricted to relatively short distances, especially near the crater wall. Hence the estimates of general relief derived from the slope profiles are, in general, not likely to be significantly in error from undetected albedo variations.

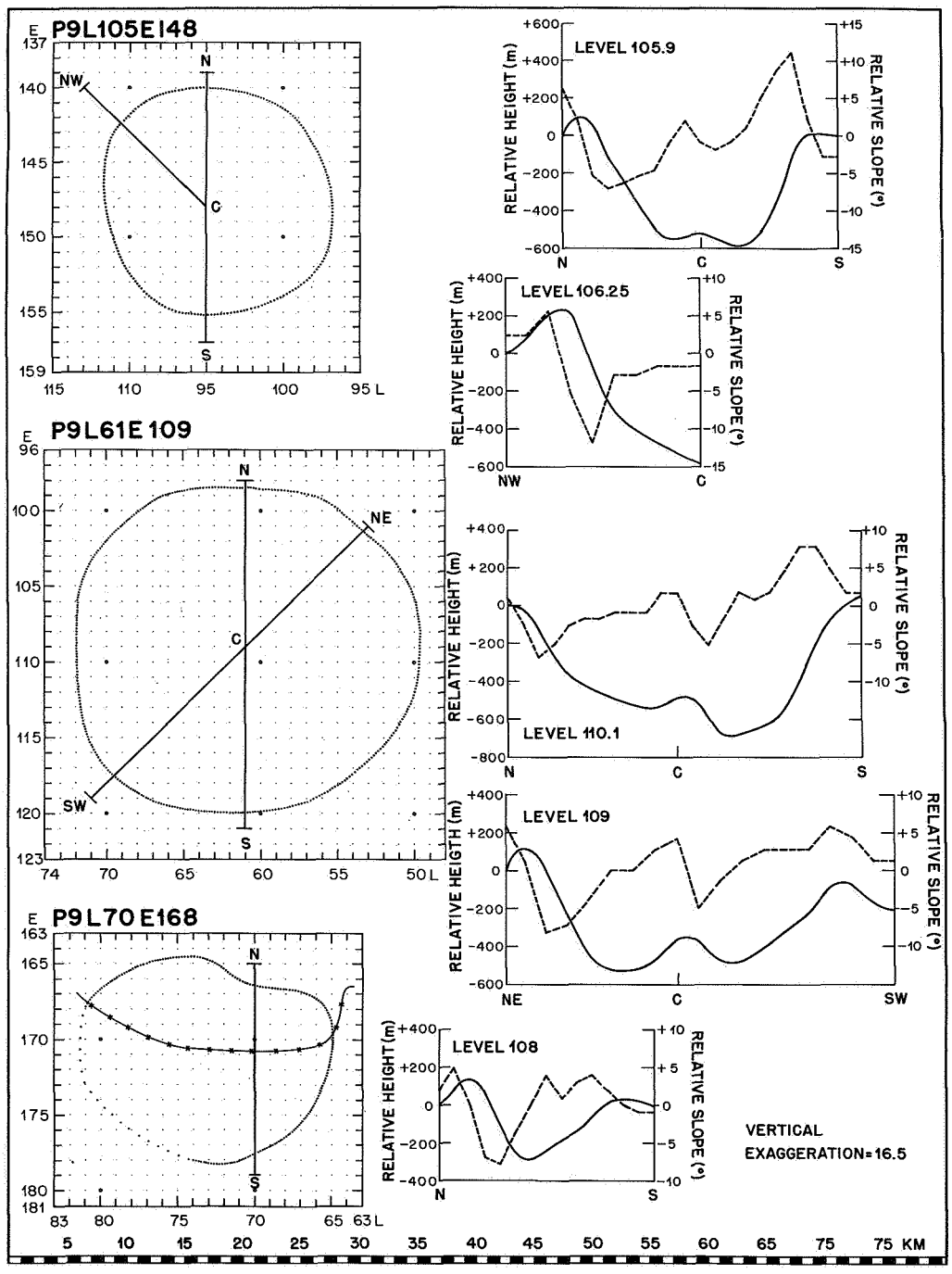


**Fig. H-2. Profiles of selected craters in Picture 9**

Haze value used is 30; level intensities are as indicated. The slight asymmetry in L70 E168, and probably that in L61 E109, reflects slight variations in albedo across these craters.

One other possible source of error arises from the general haze and glare intensity which is, of course, included in the intensity printouts. The effects of a variation of haze intensity were evaluated. Overcorrection of the intensity, by subtraction from both $I(0, a)$ and $I(s, a)$ of too large an estimated haze intensity, results in excess sharpening of relief, while undercorrection results in artificial smoothing of relief. Fortunately, both upper and lower limits of the haze can be determined independently (see Section III-C). The value used in the profiles published here is, in every case, the average of the two limits.

Symbols used herein (Figs. H-1 through H-5) are defined as follows:

Height ——————

Slope – – – – – – – –

Albedo contrast -x-x-x-x-x-

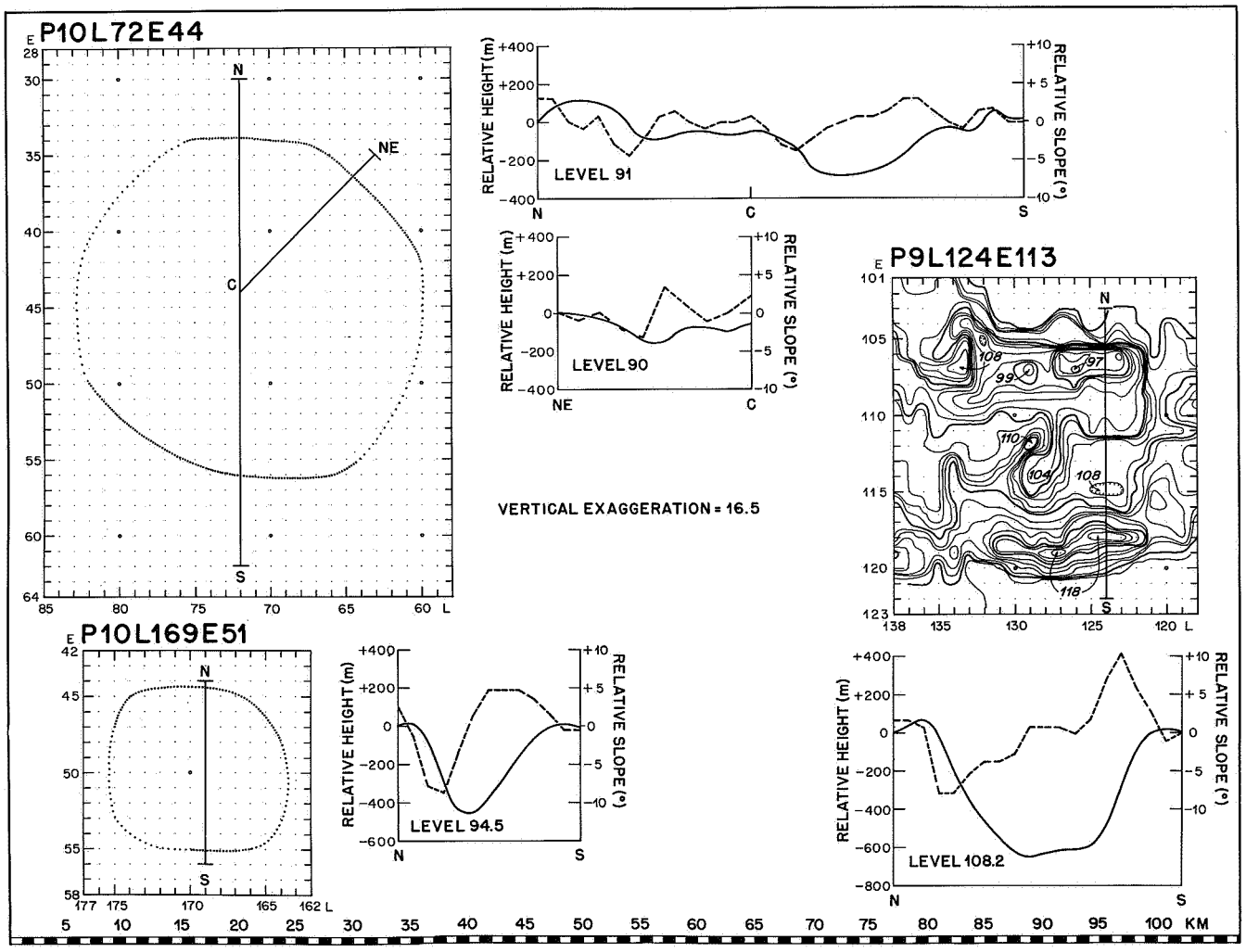


**Fig. H-3. Profiles of selected craters in Pictures 9 and 10**

**Haze value used for Picture 10 is 28; that for Picture 9 is 30. Note complex interior of L72 E44. Slight asymmetry of L169 E51 probably is due to albedo variation. The rectangular structure of L124 E113 is not simply a product of the vidicon scan pattern since the linear intensity contours cut across the scan direction in part and are several elements wide.**

Crater outline

Definite.....

Approximate.....

Haze correction value used* HAZE 25

Level intensity used* LEVEL .091

Location of albedo contrast on section A

Mismatch of slope between two profiles of differing level intensity which have been adjusted to provide continuous elevation profiles

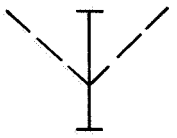

*Values of haze and intensity used in the subsequent illustrations (Figs. H-1 through H-5) were taken from intermediate processed picture data. Numerically, the data here differs systematically from that of Part II of this report as follows:

Red picture data (App. H) × 1.36 = red picture data (Part II)
Green picture data (App. H) × 0.94 = green picture data (Part II)

Such systematic effects do not affect calculated slopes or heights.

Figures H-1 through H-5 present basic Martian topographic data obtained in the manner outlined above. Some interpretive comments are presented in Section II of this report.

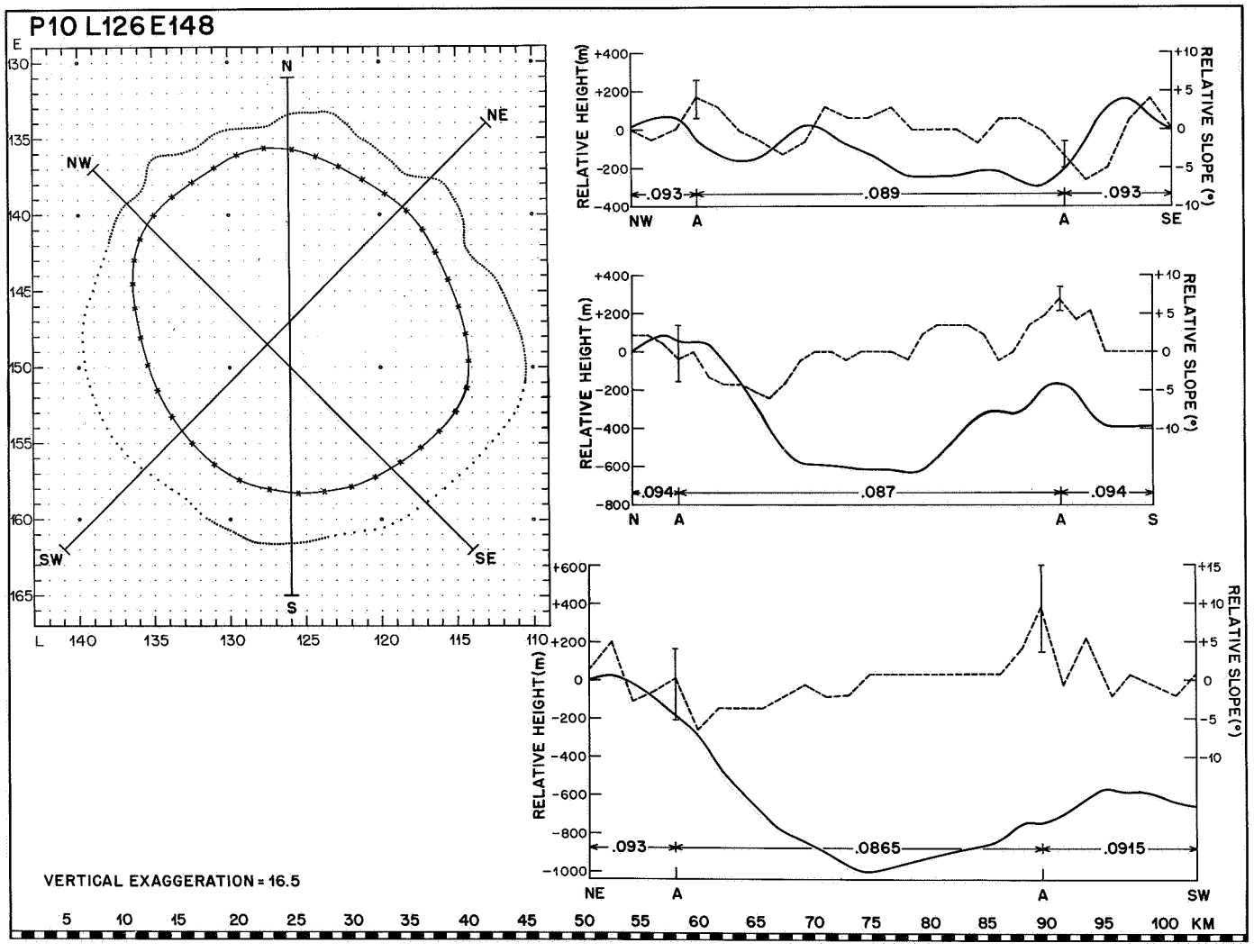


**Fig. H-4. Profiles of Crater P10 L126 E148**

**This crater exhibits both structural and albedo variation across the floor. However, an average albedo of the floor significantly lower than that of the surrounding area is clearly indicated under any circumstances. The large apparent elevation differences between opposite walls on the N–S and NE–SW sections very probably arise from complex albedo variations.**

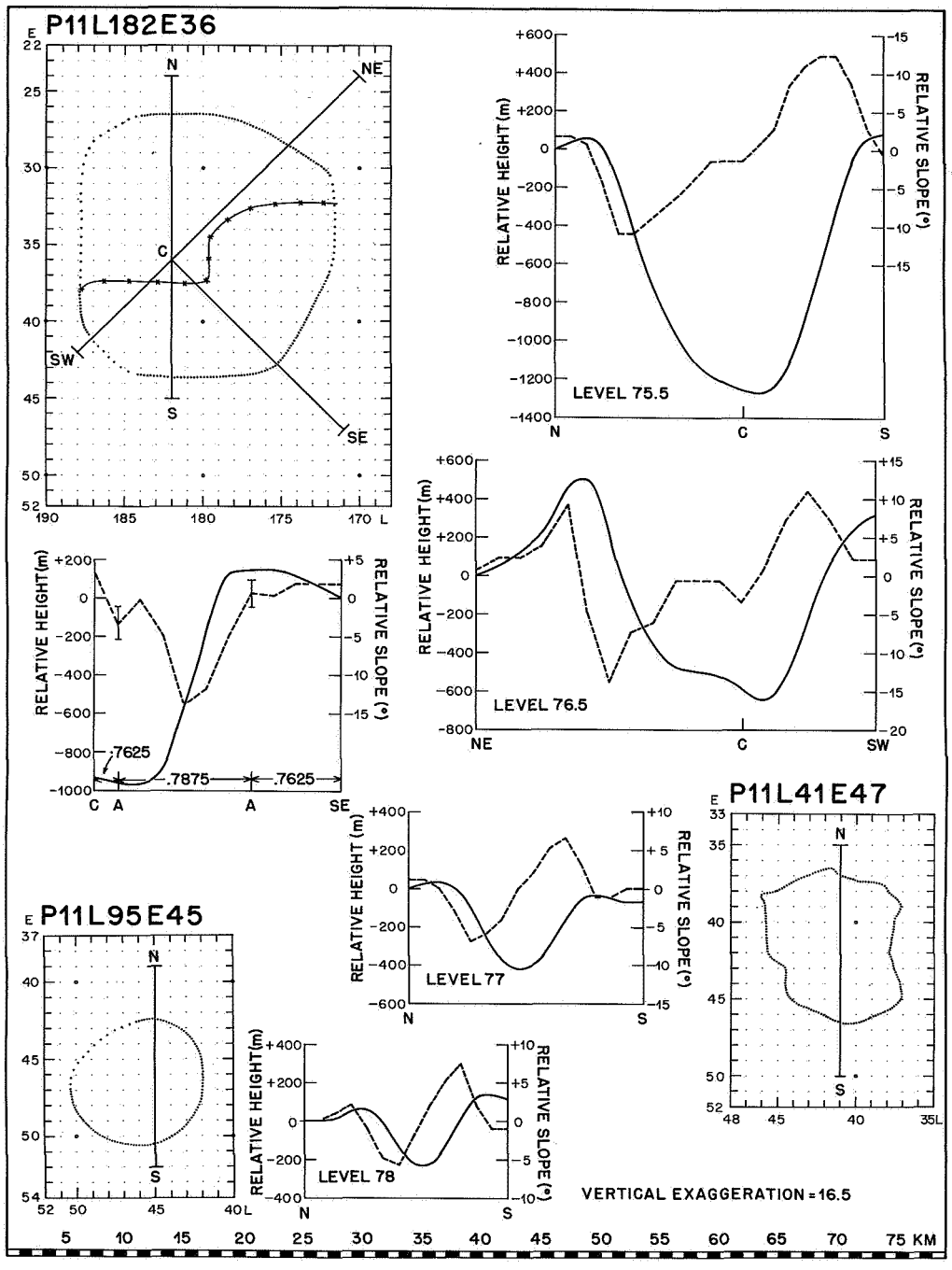


**Fig. H-5. Profiles of selected craters in Picture 11**

**Crater L182 E36 appears to be one of the deepest craters in the *Mariner IV* pictures. The extreme NE rim is probably a result of an uncorrected albedo variation, since the relative relief of 1100 meters on the NE–SW profile is consistent with the other two profiles although the apparent depth is too shallow. Haze value used is 24.**

## III. Statistical Measures of Slopes

The only topographic features present in the *Mariner IV* pictures which provide an unambiguous measure of surface slopes are the craters. Although other features are also seen, it is not possible in any specific instance to distinguish with certainty between surface albedo variations and shading due to oblique illumination of a tilted surface. In spite of this limitation, however, it may still be possible to derive some meaningful information about albedo variations, as well as slopes, on a statistical basis. This question has been studied in several ways, and it seems possible to place useful limits upon the rms albedo fluctuations and upon rms slopes.

Consider a region which possesses a certain rms relative albedo fluctuation $\sigma_A = \langle(\Delta A/a)^2\rangle^{1/2}$, and a certain rms slope fluctuation $\sigma_s = \langle s^2\rangle^{1/2}$, $A$ being the local "albedo" (reflectance at the given angles of illumination and observation) and $s$ being the local slope (in radians) relative to the local horizontal. For simplicity, assume that the surface is Lambertian, so that $I = AI_0 \cos\theta$, where $I$ is the observed intensity, $I_0$ is the intensity of a white Lambertian surface illuminated normally, and $\theta$ is the local zenith angle of the sun. Then a fluctuation $\Delta I/I$ of the intensity is made up of two terms, one due to the albedo fluctuation and the other due to the slope fluctuation:

$$\Delta I/I = \frac{\Delta A I_0 \cos\theta - A I_0 \sin\theta\,\Delta\theta}{A I_0 \cos\theta}$$

$$= \Delta A/A - \tan\theta\,\Delta\theta \qquad \text{(H-7)}$$

If it is then assumed that albedo and slope are statistically uncorrelated, this leads to an rms relative intensity fluctuation $\sigma_I$ equal to

$$\sigma_I^2 = \langle(\Delta I/I)^2\rangle = \sigma_A^2 + \frac{1}{2}\sigma_s^2 \tan^2\theta \qquad \text{(H-8)}$$

where the factor of ½ arises from the fact that only one component of the local slope contributes to a change in the solar illumination angle:

$$\langle(\Delta\theta)^2\rangle = \frac{1}{2}\langle s^2\rangle \qquad \text{(H-9)}$$

From Eq. (H-8) we find, as expected, that albedo fluctuation should dominate near the subsolar point, and slope fluctuations should become more important near the terminator. The phenomenon is well exhibited in lunar photographs of similar phase.

In order to study these effects, the relative intensity fluctuation $\sigma_I$ was measured over square areas of various sizes in the *Mariner IV* pictures; the full picture area and squares 16, 3, and 2 picture elements on a side were used. In the last two cases, averages of $\sigma_I$ over 16 × 16 element squares of the original picture, designated $\langle\sigma_I\rangle$, were also evaluated. For each picture, the minimum and maximum values of $\langle\sigma_I\rangle$ were found by inspection of the 10 × 12 matrix of $\langle\sigma_I\rangle$ values, omitting those values around the edge of the array. Plots of $\langle\sigma_I\rangle_{min}$ and $\langle\sigma_I\rangle_{max}$ vs picture number were next made (Fig. H-6). These plots revealed that $\langle\sigma_I\rangle_{min}$ varied quite smoothly from picture to picture; $\langle\sigma_I\rangle_{max}$ was less systematic in its behavior but was in each case approximately a constant factor times $\langle\sigma_I\rangle_{min}$.

These results suggest that the statistical characteristics of the slope and albedo do not depend as strongly upon

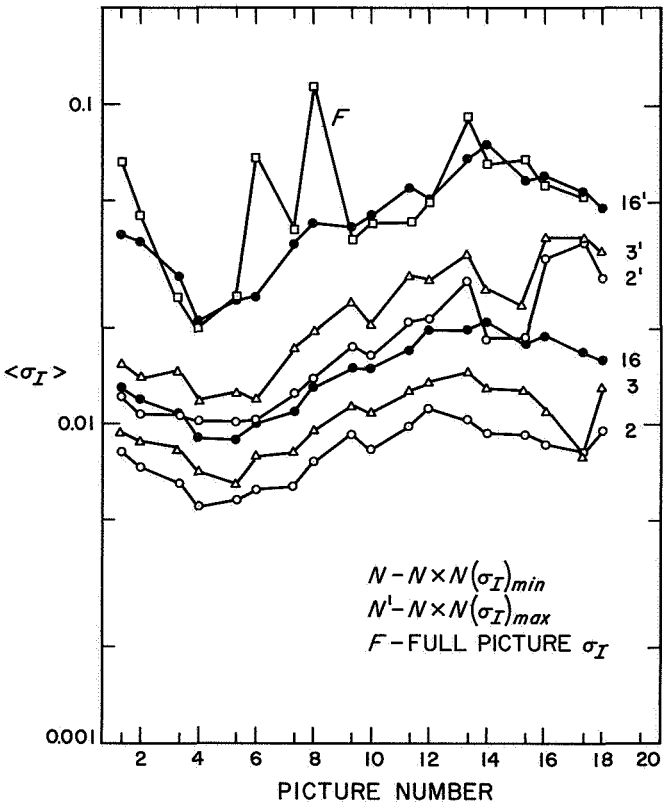


**Fig. H-6. Maximum and minimum intensity fluctuations vs picture number**

**The fluctuations are shown for several different square sample sizes, all averaged over 16 x 16 element squares.**

the gross character of the local surface—i.e., its classification as "desert" or "mare"—as upon the local conditions of solar illumination, time of day, season, etc. This is further borne out in a plot of $\sigma_I^2$ vs $\tan^2\theta$ (Fig. H-7), which shows a rather good linear relation for Pictures 1–13 inclusive. This linear relation was used to estimate $\sigma_A$ and $\sigma_s$.

The quantity $\sigma_I^2$ plotted in Fig. H-7 is a weighted average of the values shown in Fig. H-6. The data were combined as follows: Let $\sigma_N$ be the minimum $\langle\sigma_I\rangle$ for N×N squares, averaged over a 16×16 square, and $\sigma_{N'}$ be the corresponding maximum $\langle\sigma_I\rangle$. (These are the quantities appearing in Fig. H-6.) Then let $R_N$ and $R_{N'}$ be the values of $\sigma_N/\sigma_{16}$ and $\sigma_{N'}/\sigma_{16'}$ averaged over the set of pictures. The observed values of $R_N$ and $R_{N'}$ were:

$$R_2 = 0.60 \pm 0.03 \qquad R_{2'} = 1.13 \pm 0.08$$

$$R_3 = 0.75 \pm 0.02 \qquad R_{3'} = 1.46 \pm 0.15$$

$$R_{16} = 1 \qquad R_{16'} = 3.1 \pm 0.4$$

Each $\sigma_N$ value was divided by its corresponding average ratio $R_N$ to produce a homogeneous set of $\langle\sigma_I\rangle$ suitable for averaging. Two averages were evaluated, one using relative weights $w_2 = w_3 = \frac{1}{4}$, $w_{16} = 1$, and the other using equal weights. Both sets of averages were consistent with the relation

$$\sigma_{16}^2 = (70 + 190\tan^2\theta) \times 10^{-6} \qquad \text{(H-10)}$$

From this equation and Eq. (H-6), we find

$$\sigma_A = 0.008$$
$$\sigma_s = 0.019 \qquad \text{(H-11)}$$

If we take $\sigma_{16}$ and $\sigma_{16'}$, as being representative of the minimum and maximum fluctuations present in the pictures, we find the following approximate limits for $\sigma_A$ and $\sigma_s$:

$$0.01 < \sigma_A < 0.03 \qquad \text{(H-12)}$$

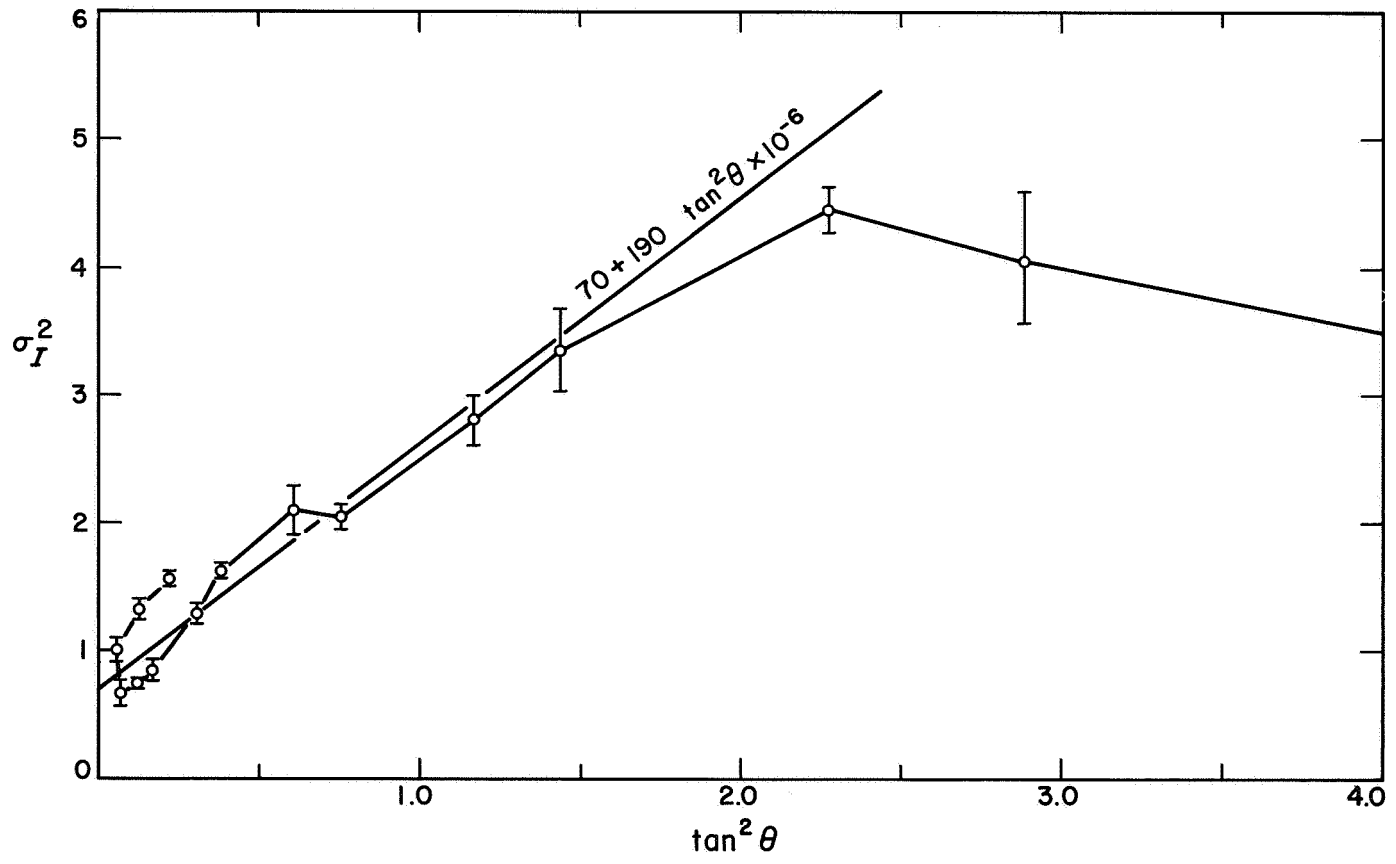


**Fig. H-7. Plot of average variance vs $\tan^2\theta$, where $\theta$ is the solar zenith angle**

and

$$0.02 < \sigma_s < 0.06 \qquad \text{or} \qquad 1° < \sigma_s < 3° \tag{H-13}$$

as representative of the albedo and slope fluctuations, based upon the 16 × 16 averages. (These values must be corrected upward about 25% because of haze in the pictures.)

The rms fluctuations $\sigma_I$ for the full picture area (~190 elements square) were also determined. As seen in Fig. H-6, the variation of $\sigma_I$ with picture number is not as smooth for "full picture" averages as for the smaller areas. In particular, Pictures 6 and 8 had $\sigma_I$ values more than 2½ times greater than normal. Picture 6 is believed to have included a "canal," while Picture 8 was situated near the northern boundary of Mare Sirenum and may have included both "desert" and "mare" features. Pictures 6 and 8 were therefore given very low weight. Values of $\sigma_A$ and $\sigma_s$, obtained from the $\sigma_I$ values for the whole pictures using the same technique as above, were

$$\sigma_A = 0.02 \tag{H-14}$$

$$\sigma_s = 0.05 \qquad \text{or} \qquad \sigma_s = 3° \tag{H-15}$$

These are in good agreement with Eq. (H-12) and (H-13) above.

The linear dependence of $\sigma_I^2$ upon $\tan^2\theta$ breaks down beyond Picture 13. Some evidence of frost deposits around craters was seen in Pictures 13, 14, and 15, and surface detail became systematically less distinct, contrary to expectation. This trend might be explained partly by a departure from Lambert's law due to the presence of obscuring fog or mist, a common phenomenon at this latitude and season, and partly by the progressively poorer intensity discriminability of the camera from Picture 12 onward.

The results obtained in the foregoing analysis may be compared on the one hand with slope measurements on individual craters discussed in Section II of this appendix, and on the other hand with radar results (Ref. 5). Measurements on individual craters yield wall slopes up to about 12 deg (0.21 rad) as a maximum. If we regard the upper limiting $\sigma_s$ value of 0.06 as resulting from 12-deg slopes over a certain fraction of the surface and negligible slopes elsewhere, the fraction of the surface that would have such slopes would be approximately $(0.06/0.21)^2 = 0.08$, which seems reasonable for a cratered area.

The *Mariner IV* results refer only to topographic scales of about 3 km and larger. Information on the surface slopes on a much finer scale is contained in the reflection coefficient and doppler spread of radar reflections from Mars (Ref. 5). In that work it was found that most of the returned 12.5-cm signal was reflected from an area only 4 or 5 deg in radius about the subearth point on Mars. Thus the surface slopes over regions larger than a few wavelengths in size are of about this same magnitude. (The regions giving a quasi-specular reflection must be larger than 10-20 wavelengths, for otherwise the diffraction width of the returned beam would exceed the observed width.) A value of 4–5 deg for the rms slopes on a scale of ≧2 meters seems reasonably consistent with the value of about 3 deg based upon the full-picture averages, which refer to a scale of ≧3 km.

## IV. Pictorial Representation of Surface Roughness

In addition to the statistical characterization of surface slopes discussed above, it is possible also to display pictorially the point-to-point variations of intensity that are related to the slopes. Such a pictorial display potentially contains much more information about the organization of these slopes into structurally meaningful forms such as craters.

In the discussion of the intensity and color calibration of the *Mariner IV* photographs (Section III), it was mentioned that several of the pictures seemed to show relatively large areas having little fluctuation of intensity. The subsequent analysis of the flat-field calibration pictures verified that the vidicon, preamplifier, and encoding circuitry were indeed reproducible to within about 0.2%—a level far below the 1% or so discriminability set by the 6-bit encoding scheme. The observed DN's in a given picture are thus representative of the actual video signal, and the fluctuations of the DN values from point to point may be taken to imply actual intensity variations on Mars.

Consider a small group of picture elements near a given point. The intensities of these elements will have a certain average $I_0$ and a certain standard deviation $\sigma$ about this average. The ratio $\sigma/I_0$ is a simple measure of the point-to-point relative intensity fluctuations of the surface. If we neglect variations in intrinsic reflectivity over small areas (as seems justified in view of the very low value of $\sigma_A$ obtained in the preceding discussion) we may equate point-to-point intensity variations with local

slopes, subject to the limitations set by the basic discriminability of the data encoder and the (small) intrinsic noise level of the electronic system.

The fractional intensity variation (which we designate by $\sigma_I$) was calculated for samples of 4 picture elements in $2 \times 2$ element squares, and of 9 elements in $3 \times 3$ element squares, on an overlapping-sample basis. The calculation was carried out on the calibrated flight pictures with shutter mark and fiducial marks removed, but in the unrectified format. A second calculation was made of the DN fluctuation of $2 \times 2$ element squares, using the original uncalibrated (but edited) digital data. The three versions were in close agreement. Selected results are shown in pictorial form along with the corresponding flight pictures in Section II. In such a "fluctuation plot," zero variation means that all elements in the sample had the same intensity; this is plotted as "black." A value $\sigma_I \geqq 0.03$ is plotted as "white." The relative fluctuation of a $2 \times 2$ sample consisting of three equal DN values and one differing by $\pm 1$ DN is about 0.008, which would be plotted as a 16 on a scale of 0–63.

The general appearance of these "fluctuation plots" is approximately what one would expect: in the corrected pictures the shutter mark and the fiducial marks appear very smooth because of the linear interpolation procedure used in their removal; the limb in Picture 1 appears as a very bright line because of the rapid change of intensity at this boundary; the edges of craters and other features appear bright. The sky area in Picture 1 and all areas of Pictures 16–18 show prominent contours, indicating that the DN values tend to remain constant over considerable areas, and to change by $\pm 1$ unit along relatively well-defined boundaries.

Viewed in closer detail, some of the pictures reveal interesting new information. In Picture 1, the limb seems to show a three-layered structure, the two upper layers being nearly coalesced and distinctly separated from a fainter lower layer. Some of this structure can be seen rather well in Picture 1D (Section II). The significance of this layered appearance is not yet clear.

In the sky, the contoured appearance results from the gradual fall of intensity above the limb combined with the known shading characteristics of the camera system. However, unlike the case of Pictures 12–18, where the appearance of distinct contours arises from a degradation in the discriminability of the system at low light levels, the contours in the sky of the first picture apparently result from a true "smoothness" of the intensity field, since the light intensity is here relatively high. This result in turn lends support to the belief that the intensity variations in the intermediate pictures are characteristic of the Martian surface. Also visible in the sky are the "edges" of the cloudlike features above the surface of the planet.

The planet surface shows a characteristic grainy texture having nearly the same appearance in Pictures 1 through 6. The major part of the field is random in appearance except for narrow edges which delineate the boundaries of the more prominent features. Short groups of bright, connected elements perpendicular to the line scan direction outline the residual harmonic "noise" present in the pictures. Here and there, extended chains of light or dark groups of elements seem to suggest an organization of smooth or rough areas on Mars. However, few of these are sufficiently well defined or extensive as to stand out from the similar lineations to be expected on the basis of chance. Further, although the grainy patterns in overlapping areas are grossly similar, they are often quite different in detail because of the effects of shading in the vidicon tube.

Perhaps the clearest example of an organized smooth area is seen in Picture 9, which shows a quite prominent, gently curving smooth area about 5–10 km wide, running SW–NE in the SE quadrant of the frame. This structure is quite invisible in the ordinary pictures. Picture 7 exhibits a relatively rough region characterized by numerous craters and crater fragments, rather sharply separated from a relatively smooth area running from the SW corner toward the N corner. Other pictures show irregularly shaped regions of greater or lesser smoothness than the average, sometimes with suggestions of structural relationship.

The interiors of the two large craters partially visible in the southern edge of Picture 10 seem unusually rough as compared with the adjacent external areas. On the other hand, a large part of the interior of the large crater in Picture 11 seems unusually smooth. Numerous such relationships are apparent throughout the picture series.

# Appendix I

## Martian Surface Processes

### I. Introduction

The softened appearance, shallow depths, and gentle slopes of many Martian craters suggest that they have been modified to varying degrees by some process or processes of erosion or deposition. The lesser abundance of craters on Mars compared to the lunar uplands, in spite of a meteoroidal flux at Mars estimated as 4 to 25 times larger, supports the above inference. Crater modification and eventual elimination have occurred at a faster rate on Mars than on the moon.

If isostatic readjustments occur with greater facility in the Martian than in the lunar crust, they could account for some of these differences for craters larger than 20–50 km. However, the differences extend to smaller craters, especially in terms of numbers, indicating that much of the crater modification on Mars must be of exogenic origin.

Erosive and blanketing processes possibly acting at present on Mars are discussed, evaluated, and an answer is sought as to why, in sum, they are more effective than processes acting on the moon. Such a discussion is not intended to eliminate consideration of possible secular changes in the Martian environment.

### II. Surface Materials

Before considering processes, it is necessary to formulate a model for the physical state of the material constituting the surface layer of Mars. Limitations of space require that consideration of the many speculations concerning the chemical and lithological nature of this material be omitted, not because they are unimportant, but because they are not directly pertinent to the focus of this discussion.

For the following reasons it has frequently been suggested that a fine-grained layer mantles at least parts of the Martian surface. On numerous occasions, yellowish "clouds" have been observed visually and photographically. Many of the properties of these "yellow clouds" suggest that they are due to wind-carried dust. The large diurnal range in soil temperatures in light-colored areas has been attributed at least partly to low thermal conductivity and interpreted as indicative of a dust mantle. Radar observations (Goldstein, Ref. 5, p. 1715) suggest that these areas are indeed smooth, on a meter scale, and possibly underlain by a pulverized, highly porous material (Ref. 6). However, it is well to recall that a dust mantle for the moon was postulated on the basis of similar evidence. The *Luna 9*, *Surveyors I* and *III* photographs, and experiments demonstrate a high degree of coherence and integrity within the fine-grained lunar surface material, with a modest number of included fragments which look like rock.

*Mariner IV* photographs contribute to a possible understanding of the surface mantle by demonstrating abundant craters on the Martian surface. By analogy with the moon, an impact origin is favored for most, if not all, of these features. Even if some are of explosive volcanic origin, the surrounding terrain would be littered with rubble. Such a rubble would presumably have a considerable matrix of fine particles because of repeated impacting. The fines would far exceed those found in one-shot earthly impact (Shoemaker, Ref. 7, p. 303) or explosion breccias (Roberts, Ref. 8, p. 475). Such a rubble with abundant fines might well display the thermal response and radar properties reported. The possibility that chunks of the rubble become "shock lithified" (Short, Ref. 9, pp. 383–384) is worth consideration.

As a working model for the Martian surface mantle, we favor the idea that it is principally a loose impact rubble, rich in fines owing to repeated impacts, but also containing larger rock fragments. The coherence of this rubble may be less than exhibited by any lunar counterpart because of Martian atmospheric inflences. An exception would be those areas, if any, in which a permafrost exists at the surface.

### III. Martian Surface Environment

Attention is given only those aspects of the environment that influence the production and transportation of fragmental rock debris. These include the atmosphere—as to composition and density; temperature—as to magnitude, range, and frequency of fluctuation; and most importantly, water—as to quantity and state. These factors are discussed in the light of current data and models, recognizing that significant secular changes may have occurred during the life of the planet.

### A. Atmosphere

Recent observations have shifted estimates of atmospheric pressure at the Martian surface to ever lower values. One can only hope that we are not experiencing a "bandwagon" effect. At present, figures between 5 and 10 mb are in vogue, far below the 80–90 mb popular around 1950. Sagan and Pollack (Ref. 10, p. 33) have attempted to push the pendulum the other way by advancing arguments for a pressure as high as 20 mb over the lowest parts of the Martian surface.

At 5–10 mb, most of the Martian atmosphere must be $CO_2$, and the other near-surface ingredients (argon, nitrogen) are quantitatively minor and chemically inert. Oxygen, if ever present at the surface in significant amounts, or produced at a finite rate, has been largely consumed by oxidation or depleted by escape.

### B. Temperature

Calculations based on a model used for study of the behavior of volatiles on Mars (Leighton and Murray, Ref. 11) give a more comprehensive picture, in time and space, of surface and shallow subsurface temperatures than previously available (Hess, Ref. 12, Gifford, Ref. 13). These calculations agree rather well with spot determinations made by radiometric means (Sinton and Strong, Ref. 14, among others). They suggest an average temperature for Mars between −80 and −90°C, considerably lower than most previous estimates but just about at the lower limit set by Lederberg and Sagan (Ref. 15, p. 1474). These differences result in large part from the lower computed nighttime temperatures. Average annual temperatures at 10° latitude intervals are shown in Table I-1. Extreme temperatures range from a minimum of −131°C on the polar caps, reflecting the condensation temperature of $CO_2$, to a maximum of +30°C at 30° south latitude. Annual equatorial extremes are 22 and −112°C. At the south pole, where the cap disappears, annual extremes are −28 and −131°C. The seasonal range of average temperature (Table I-2) is 16°C at the equator and 103°C at the south pole, reasonably close to Smoluchowski's (Ref. 16) estimate of 120°C. The smallest seasonal change in average daily temperature, aside from the constant temperature of the residual north polar cap, is 7°C, and it occurs at 10° south latitude.

Nowhere on the Martian surface is the average annual temperature above 0°C, and temperatures below 0°C occur every night on all parts of the planet. For a period of roughly two months, centered about the northern hemisphere summer solstice, temperatures over the entire surface remain below 0°C. At other seasons temperatures above 0°C are attained for at least a few daylight hours on parts of the Martian surface. This occurs within a zone extending from 70° S to 30° N for intervals ranging from 1 to 10 Martian months, as shown on Fig. I-1. The area between 0° and 10° N is the most favored, with a 10-month interval in which temperatures rise daily

**Table I-1. Calculated average annual temperatures on Mars**

| Latitude | °K | °C |
|---|---|---|
| −90 (south pole) | 160 | −113 |
| −80 | 162 | −111 |
| −70 | 165 | −108 |
| −60 | 173 | −100 |
| −50 | 183 | −90 |
| −40 | 198 | −75 |
| −30 | 204 | −69 |
| −20 | 207 | −66 |
| −10 | 210 | −63 |
| 0 (equator) | 211 | −62 |
| 10 | 210 | −63 |
| 20 | 207 | −66 |
| 30 | 203 | −70 |
| 40 | 196 | −77 |
| 50 | 181 | −92 |
| 60 | 167 | −106 |
| 70 | 155 | −118 |
| 80 | 149 | −124 |
| 90 (north pole) | 144 (polar cap) | −129 |

**Table I-2. Seasonal ranges in average daily temperatures with latitude**

| Latitude | Highest average, °K | Lowest average, °K | | Difference, °C |
|---|---|---|---|---|
| −90 (south pole) | 245 | 141 | polar cap | 103 |
| −80 | 243 | 142 | | 101 |
| −70 | 235 | 142 | | 93 |
| −60 | 232 | 142 | | 90 |
| −50 | 231 | 142 | | 89 |
| −40 | 230 | 160 | | 70 |
| −30 | 229 | 175 | | 54 |
| −20 | 226 | 186 | | 40 |
| −10 | 222 | 194 | | 28 |
| 0 (equator) | 217 | 201 | | 16 |
| 10 | 212 | 205 | | 7 |
| 20 | 210 | 200 | | 10 |
| 30 | 211 | 190 | | 21 |
| 40 | 212 | 173 | | 39 |
| 50 | 212 | 143 | polar cap | 69 |
| 60 | 212 | 143 | | 69 |
| 70 | 210 | 143 | | 67 |
| 80 | 201 | 143 | | 58 |
| 90 (north pole) | 146 (polar cap) | 142 | | 4 |

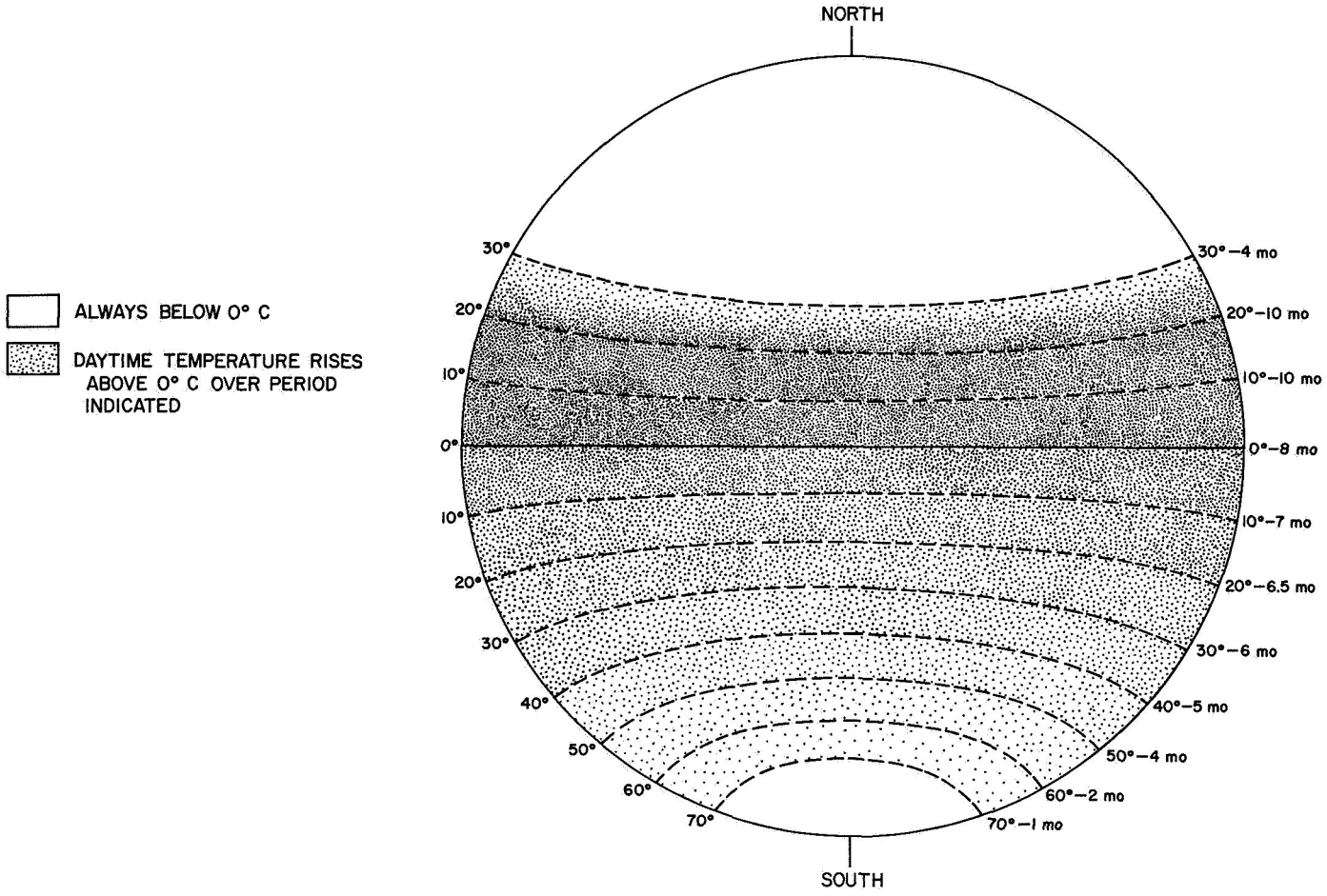


**Fig. I-1. Mars surface temperature**

above 0°C. Poleward of 30° N and 70° S surface temperatures remain below 0°C the year around.

At an estimated water-vapor pressure of $3.7 \times 10^{-4}$ mb, water ice will form only below −83°C. The computations suggest that such temperatures may prevail at shallow depths within the ground poleward of latitudes 40–50° in both hemispheres, thus providing conditions favorable for permafrost to a depth of some tens of meters. It does not follow, of course, that the supply of moisture is necessarily adequate to form any significant amount of subsurface ice.

Diurnal temperature ranges are of special interest with respect to surface processes (Table I-3). The largest diurnal ranges, over 130°C, lie in the 10°–30° south-latitude belt during southern summer solstice, when the planet is nearest the sun. The calculated ranges exceed those earlier derived from radiometric observations because of the lower computed nighttime temperatures.

**Table I-3. Diurnal temperature change at southern hemisphere solstice on Mars**

| Latitude, deg | Range, °C | |
|---|---|---|
| −90 (south pole) | 0 (still some polar cap) | |
| −80 | 97 (still some frost) | |
| −70 | 92 | |
| −60 | 109 | |
| −50 | 119 | |
| −40 | 127 | |
| −30 | 130 | |
| −20 | 132 | |
| −10 | 131 | |
| 0 (equator) | 128 | |
| 10 | 121 | |
| 20 | 115 | |
| 30 | 105 | |
| 40 | 86 | |
| 50 | 0 | polar cap |
| 60 | 0 | |
| 70 | 0 | |
| 80 | 0 | |
| 90 (north pole) | 0 | |

### C. Water

The amount and physical state of water substance in the Martian environment are critical for processes active in the production and transportation of rock debris. Infrared, polarization, and spectroscopic observations have been interpreted as indicative of water on Mars, either as vapor in the atmosphere or as solid on the ground. Estimates of the amount of precipitable water currently in the atmosphere range from as little as 0.007–0.021 mm to as much as 0.15 mm, with the lower values now favored.

With so little vapor, condensation occurs only at temperatures below −80°C, and the product, of course, is solid. The ambient temperatures are so low that ice or frost go directly to vapor as incident radiation increases or temperatures rise. These relationships suggest that liquid water even in minute quantities must be extremely rare or nonexistent on the Martian surface.

Nonetheless it is well to keep an open mind on the possibility that minute quantities of liquid water may be formed through wind-blown ice spicules landing on a sun-warmed surface (Otterman and Bronner, Ref. 17, p. 59), through "skin" or absorption effects of silicate particles (Loomis, Ref. 18, p. 1100; Otterman and Bronner, Ref. 17, p. 59), or by the melting of ice in closed spaces by conducted solar heat or transmitted radiation, as through a clear ice coating. Deliquescence of salts might also yield some liquid moisture (Leighton and Murray, Ref. 11, p. 143; Horowitz, *et al.*, Ref. 19, p. 1504). None of these processes seems particularly significant with respect to the problem at hand.

Geothermal areas could supply moisture either as hydrothermal fluids or by the melting of subsurface ice (Lederberg and Sagan, Ref. 15, p. 1474). However, earth has produced an atmosphere 150 times more massive than that of Mars, presumably by outgassing, and today only a small fraction of 1% of the earth's surface is geothermally active. For this and other reasons, extensive or numerous geothermal areas on Mars seem unlikely.

Masses of ice (Fizeau, Ref. 20, p. 287; Strughold, Ref. 21, pp. 37–38, Ref. 22, pp. 82–86; Urey, Ref. 23, p. 99; Johnson, Ref. 24, p. 1446) or frozen ground (Leighton and Murray, Ref. 11, p. 1446) postulated as underlying the Martian surface cannot supply liquid water to the surface if they have existed for any length of time and no secular change in environment occurs.

It has been recognized for over 30 years and more recently re-emphasized by many investigators that Mars is a very dry planet and that liquid water on its surface is most unlikely. Whether or not this has long been the case remains to be determined.

## IV. Weathering Processes

### A. Mechanical Weathering

Diurnal temperature changes as great as 132°C on Mars suggest the possibility of rock fragmentation by thermal fluctuations. Experiments by Blackwelder (Ref. 25, pp. 107–108) and Griggs (Ref. 26) and observations by Blackwelder (Ref. 27, pp. 137–138), Emery (Ref. 28), Howard (Ref. 29), and Roth (Ref. 30), among others, indicate that changes in excess of 200–300°C are probably required to produce significant rock disintegration on earth. Ryan's analysis (Ref. 31, p. 2557) led to the conclusion that thermal fracturing is not effective on the moon, where temperature fluctuations are even greater than on Mars, although much less frequent. Thus it seems unlikely that the process is effective on Mars, unless fatigue becomes important.

Each day, temperatures pass back and forth across the melting point of ice on those parts of the Martian surface lying between 70° S and 30° N for periods ranging between 1 and 10 Martian months (Fig. I-1). The most favored zone lies between 10° and 20° N, and the highly effective process of freeze and thaw would be more active here than any place on earth, *if there was an adequate supply of liquid water.* On the basis of the preceding discussion and the analysis of Anderson *et al.* (Ref. 32, pp. 320–321), the possibility of liquid water in amounts adequate for significant frost action on the surface of Mars is regarded as remote, Otterman and Bronner (Ref. 17) perhaps dissenting.

### B. Chemical Weathering

Nearly all forms of chemical weathering are promoted by liquid water and restricted by its absence. Under the currently indicated ultradry environment, it is difficult to see how any significant amount of chemical weathering appears on Mars. If disorganized water molecules in transition from the solid to vapor state can participate in chemical reactions with atmospheric gases, such as $CO_2$, or with solid substances, some minor chemical weathering might take place on the Martian surface.

Rea (Ref. 33, p. 235) mentions the possibility of chemical reaction involving water vapor and promoted by high radiation fluxes. The lack of a significant magnetic

field on Mars (Smith *et al.*, Ref. 34, p. 1242) permits solar winds to press closely upon the planet, and the thin atmosphere allows many energetic cosmic and solar particles to reach the surface. These could promote photochemical and lattice reactions (Smoluchowski, Ref. 16, p. 947) that might, in conjunction with thermal changes or other processes, lead to some rock alteration.

In the present state of knowledge, or ignorance, of Mars, it would seem that the formation of craters, whether by meteoroidal impact or explosive volcanism, would far outstrip all weathering processes in producing fragmental material.

## V. Transportation on the Martian Surface

This discussion is most effectively pursued in comparison with the moon. The relative scarcity of Martian craters 10–20 km in diameter, indicated by the "knee" in the integral number distribution (Fig. J-3, App. J), is believed to be real and not an instrumental resolution effect (Hartmann, Ref. 35, pp. 567–569). Therefore, some process or processes of crater erosion or burial more effective on Mars than on the moon are indicated.

As a working model it will be assumed that most of the Martian surface is mantled with an impact rubble, probably rich in fines, and possibly by some debris secondarily derived therefrom. If the environment of Mars is as pictured, fluvial and glacial processes need not be considered. Freeze and thaw is an extremely effective mechanism for transport on slopes, and the thermal regime of Mars is highly favorable in the 10° S to 30° N latitude belt. However, the lack of an adequate supply of liquid water is fatal. A comparison of erosive processes possibly at work on the moon and Mars (Table I-4) suggests that particular attention should be given to pelting, wind, and thermal creep.

**Table I-4. Martian erosion**

| | |
|---|---|
| **Abrasion** | |
| Eolian | Minimal (< moon) |
| Flying impact debris | Strong (≦ moon) |
| **Transportation** | |
| Meteoroidal impact | High (> moon) |
| Micrometeorite pelting | < Moon |
| Freeze–thaw | Nil (no liquid water) |
| Electrostatic hopping | < Moon |
| Eolian | > Moon |
| Thermal creep | > Moon |

### A. Pelting

Meteoroidal impacts produce a curtain of flying particles, both primary and secondary, that effect considerable abrasion and transport. The blanket of impact debris so formed also obscures craters by burial. These are probably the principal processes of crater modification on the moon (Shoemaker, Ref. 36, pp. 66–68), although Gold (Ref. 37, pp. 116–117) may still favor the movement of dust.

Most investigators accept a greater meteoroidal flux at Mars than at the moon, although the magnitude of the difference is not agreed upon. The Martian atmosphere, although thin, exerts a retarding influence on flying particles produced by impact, and it reduces the spectrum of micrometeorite particles impacting the Martian surface. Nonetheless, this atmospheric influence probably does no more than balance the higher meteoroidal flux. Pelting could be just as effective in crater modification on Mars as on the moon. Below a certain critical diameter (Shoemaker, Ref. 36, p. 67), which might be larger on Mars than on the moon because of the greater meteoroidal flux, Martian craters should be at least as abundant as lunar craters if pelting were the only significant modifying influence. Since they are not (Fig. J-3, App. J), other erosional processes or a significant secular change in environment is indicated for Mars.

### B. Eolian Processes

Wind is usually regarded as an important, if not the most effective, agent of transportation and erosion on Mars. This idea, not endorsed by everyone (Hess, Ref. 38, p. 292; Tombaugh, Ref. 39, p. 10), is based in part on the yellow clouds, presumed to be dust, which episodically obscure parts or most of the Martian disc. Wind transports dust by suspension and sand grains by traction, impact creep, and saltation (hopping). If the surface of Mars is mantled by a repeatedly pounded impact rubble, an adequate source of sand- and dust-sized particles presumably exists. The problem is whether or not Martian wind velocities are adequate to pick up and transport this material.

Fine dust is not easily picked up by wind unless dislodged by some other agent (Bagnold, Ref. 40, pp. 90–92). Saltating (hopping) grains are one of the best ways of dislodging dust (Gifford, Ref. 41, p. 439), and saltation is the most effective mode of sand transport (Bagnold, Ref. 40, p. 37) as well as the chief agent of eolian abrasion. If saltation occurs, the other processes and modes of transportation become effective, but without it they

are severely restricted. Therefore, attention is focused on the problem of moving grains by eolian saltation on Mars.

There is an ideal particle size for transport with minimal wind velocity. On earth, this ideal particle is about 0.1 mm in diameter, and the wind velocity required to move it by traction is about 4.5 m/sec (10 mph) (Bagnold, Ref. 40, pp. 6, 90; Ryan, Ref. 42, p. 3763). On Mars, owing primarily to the lower air density, the ideal particle averages about 0.7 mm (Gifford, Ref. 41, p. 438), and the velocity required to move it, assuming ideal conditions of surface roughness and a 25-mb atmosphere, is about 40 m/sec (90 mph) (Ryan, Ref. 42, p. 3765). Extrapolation to an atmospheric pressure of 10 mb indicates required velocities in excess of 90 m/sec (200 mph) (Rea, Ref. 33, p. 219). Gifford's (Ref. 13, p. 439) lower figures are based on a calculation of earthly velocities less by a factor of 2–4 than that suggested by the empirical data of Bagnold (Ref. 40, p. 6). All these values are for movement by traction; requirements for saltation may be a little higher.

Observation of cloud movement on the limbs and across the disc of Mars suggest average velocities of 8–12.5 m/sec (18–28 mph), with extremes perhaps as great as 25–38 m/sec (55–85 mph). Velocities at the ground surface are probably lower, and under any circumstances hardly appear adequate to move sand grains. Leovy's theoretical analyses (Ref. 43, p. 21) suggest the possibility of zonal wind velocities in the neighborhood of 22–45 m/sec (50–100 mph) at the ground surface, but even these may not be adequate at atmospheric pressures of less than 25–30 mb, and their frequency and duration are unknown.

If the yellow clouds are truly dust—a reasonable but unproved assumption—they might be caused by local dust devils (Neubauer, Ref. 44) or represent debris blasted into the air by meteoroidal impact (Öpik, Ref. 45, pp. 22, 24; Ref. 46, p. 26). Dust settles out of the air as a blanket of uniform thickness which mantles topographic features, softening but not wholly obscuring them until the dust thickness becomes very great.

The thought of wind action on Mars is appealing, but it appears for the present that a reserved attitude toward its effectiveness as a modifier of Martian craters is in order. Even if wind is effective, significant abrasion of crater features (Öpik, Ref. 46, p. 256; Ref. 47, p. 95) seems unlikely; burial by wind drifted sand is more likely, and mantling by dust is the most likely mechanism of topographic modification.

### C. Thermal Creep

If much of the Martian surface is mantled by dry, loose impact rubble, and if frozen ground exists only poleward of 40–50° latitude, possibilities are good that debris moves slowly down slopes and fills depressions by the process of thermal creep. Even in areas of frozen ground, removal of ice in summer by sublimation to depth of a few tens of centimeters would permit some movement.

It is known from general observations (Sharpe, Ref. 48, pp. 28, 31) and simple experiments (Moseley, Ref. 49; Davison, Ref. 50) that unattached fragments of material move downslope by alternate expansion and contraction through temperature change. The creep of individual rock blocks by this process on a 17-deg slope under modest natural temperature changes can exceed 0.5 in./yr (Davison, Ref. 50, p. 235). The extreme temperature regime on Mars, with diurnal fluctuations up to 132°C (Table I-3), suggests that this process could be even more effective there than on earth. Davison (Ref. 50, p. 237) long ago recognized the potential of thermal creep in the lunar environment, but it should be more effective on Mars owing to a daily rather than a monthly temperature cycle.

Thermal creep can presumably act on slopes down to essentially 0 deg inclination. It should be effective on rubble-constituted features but not on bedrock exposures, unless some other process is fragmenting the rock. It merits consideration as a process that may be the principal means of modifying Martian craters.

Vibrations set up in the Martian crust by meteoroidal impacts or intrinsic seismic events could also cause downhill creep of loose surface rubble. To the degree that they occur, they would supplement and enhance the process of thermal creep.

## VIII. Conclusion

At least two processes of transportation, wind and thermal creep, may currently be more effective on the Martian surface than any combination of crater-modifying processes acting on the moon. Wind action is appealing because the yellow clouds are supposedly dust, but proof that wind velocities at the Martian surface are adequate to produce significant eolian transportation is lacking. The present Martian environment is highly favorable for thermal creep, and if the Martian surface is mantled with impact rubble, this could be the principal process currently modifying Martian craters.

A question now arises as to how far into the past the current surface environment of Mars can be projected. Has the Martian environment long been as it is now, has it undergone slow evolution, or has it experienced major episodic change? Opinions on these matters differ. Strughold (Ref. 22, p. 82) thinks Mars previously had oceans, but Tombaugh (Ref. 39, p. 12) says Mars never had oceans or enough water to effect erosion. Others (Sagan, Ref. 51, p. 284; Sagan *et al.*, Ref. 52, p. 59; Binder and Cruikshank, Ref. 53, p. 8; Binder, Ref. 1, p. 1054) favor antecedent conditions of heavier atmosphere, more water, oxidation, and erosion, but Öpik (Ref. 47, p. 94; Ref. 46, p. 263) thinks such conditions may have existed only briefly, in a very early stage of the planet's history, and Salisbury (Ref. 54, p. 292) is of a similar mind.

If the surface processes discussed herein, especially thermal creep, are effective on Mars, there may be no basis to the argument (Anders and Arnold, Ref. 55, p. 1496) that the degree of crater modification displayed requires a secular or episodic change in environment, although the possibility of such change is not excluded. Present conditions, with perhaps only minor secular change, may have prevailed far back into the evolutionary history of the planet, and large craters on the surface of Mars may indeed be billions of years old.

PRECEDING PAGE BLANK NOT FILMED.

# Appendix J
# Crater Frequency Distribution and Age Implication

## I. Instrumental Limitations to the Recognition of Craters

Two fundamental aspects of any imaging system will ultimately limit the recognition of topographic detail in the scene being viewed. The sensitivity with which light intensity variations from the object can be distinguished from noise arising in the sensor and in subsequent processing systems will place a limit on the smallness of variation of slopes which can be recognized in the scene. Secondly, photographic grain, TV reading beam size, optical diffraction, and other sources of angular blurring will ultimately limit the spatial resolution and hence limit the minimum size of objects which can be recognized. In general, the two limitations are relatively independent, except near the resolution limit.

Inasmuch as one of the principal scientific results of the *Mariner IV* television experiments is the estimation of the density of craters larger than 3–4 km on the part of the Martian surface viewed, a considerable effort has been made to understand the instrumental limitations to this task inherent in the *Mariner IV* camera and readout system itself. Appendix H included a discussion of the measurement of slopes from the calibrated intensities and also presented some data. From these it can be seen that the minimum detectable slope in Pictures 7–12 is generally in the range of 1–2 deg. Hence, craters whose slopes–when averaged over several kilometers distance–do not display as much as 1–2 deg maximum slope in at least the rim areas usually cannot be identified with certainty. Indeed the distribution of vertical profiles of the Martian craters is skewed to the low relief extreme, as compared to the moon, and significant increases in apparent crater density were produced with each substantial improvement in reconstruction of the original light intensity distribution. Further substantial increases will presumably be obtained when these same areas are photographed in the future under more favorable lighting conditions and with equipment with even greater discriminability. It should be remembered that lunar photographs used for crater counts and other topographical analyses normally have been acquired at a sun elevation angle of 5–15 deg in order to maximize shadow delineation as well as variation of light intensity produced by differences in slope. Pictures 7–12 of the *Mariner* data, on the other hand, correspond to elevation angles of 40 to over 60 deg. *No shadows are present.*

Hence it is necessary to understand the angular resolution of the *Mariner* camera system independently of the intensity discrimination discussed above. This has been accomplished in two ways. First, the conventional sine wave response measurements were carried out. The results are shown in Fig. J-1a. The sine wave response measurements imply little size dependence of recognizable space frequencies above about 6 lines (10 km). The relevance of these measurements to the recognition of craters involves knowledge of the spatial frequency spectrum associated with craters, under the lighting conditions of Pictures 7–12.

To develop some further understanding of this problem, a model simulation was conducted in 1966. At JPL, Clayton LaBaw prepared a plaster of paris surface in which a wide range of crater-like depressions had been produced (Fig. J-2). The surface was painted with low albedo, diffusely reflecting paint, and the model was photographed with the prototype TV camera system at the same phase angle and viewing angle as Pictures 7–11. Digital recording capability was not available for these tests, so the TV display was produced simply by Polaroid photography of a laboratory oscilloscope screen. There could not be the same enhancement of these model pictures as characterized those presented in Section II of this report. On the other hand, no disturbing haze is present and, most important, the model craters generally are far steeper than those of Mars (note the shadow in Fig. J-2). The results of this simulation are summarized in Fig. J-1b. The strong dependence on lighting is, of course, prominent, but it is clear that the only *systematic* dependence on crater diameter is below 6–10 km. Above that size, variations in detectability also exist, due to the low slopes of some craters, but are not correlated with size. Hence, this imperfect, but still relevant, simulation reinforces the results of the sine wave response study. Significant variations in apparent abundance of craters of diameter greater than 10 km cannot be ascribed to diminishing resolution of the *Mariner* camera but must reflect genuinely lower abundance, or at least systematically smoother topography. The actual crater counts from *Mariner* photographs, summarized in Fig. J-3, indeed show a striking change in relative abundance below 20 km. On the basis of the foregoing, we consider this to be a genuine property of the Martian surface.

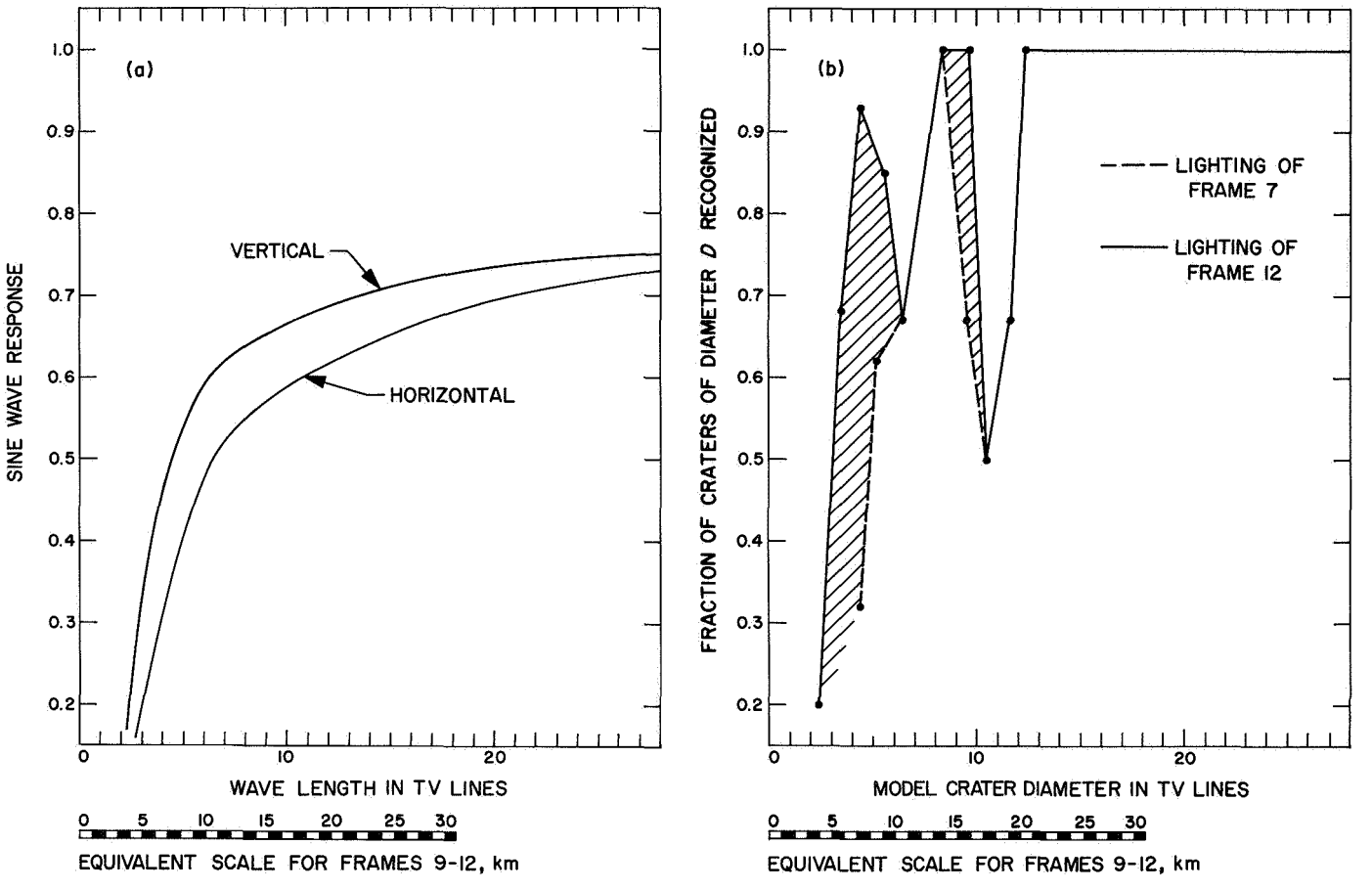


**Fig. J-1. (a) Sine wave response of *Mariner IV* television system, (b) results of simulation study of model shown in Fig. J-2**

**Note that no systematic correlation of crater recognizability with crater diameter was encountered above 10-km simulated diameter.**

## II. Tabulation of Crater Counts

The procedure for identifying craters and other Martian features recorded in the *Mariner* pictures was based initially on a series of transparent work sheets prepared by R. P. Sharp and B. C. Murray. These, in turn, were the basis for four separate phases of review and modification of the ACIC illustrations prepared in Flagstaff, Arizona. Finally, R. B. Leighton made an independent crater count using the calibrated, sharpened, and enhanced pictures. Hence, the counts presented here are the result of independent analyses within the experimentor team as well as lengthy iteration with the highly qualified ACIC group in Flagstaff, heavily experienced in lunar mapping and charting.

The counts were subdivided at each stage into "definite," "probable," and "possible" categories, reflecting the degree of rim preservation and hence ease of recognition. The least certain category was assigned in case of disparity between individual results. Such a system must inevitably be somewhat subjective. However, the experimentors expect that at least 50% of those in the "possible" category, 90% of those in the "probable" category, and 99% of those in the "definite" category will eventually be confirmed by subsequent investigations.

Although some craters are evident in all the pictures, only Pictures 7–12 were used as a basis for estimation of crater density on the Martian surface. The selection was therefore based on the most useful third of the daytime pictures from the point of view of numbers of recognizable features. The breakdown of the counts from Pictures 7–12 is shown in Table J-1, and the surface areas for all useful frames are given in Table J-2.

Inasmuch as the question of maximum surface density of craters is of importance to an understanding of the

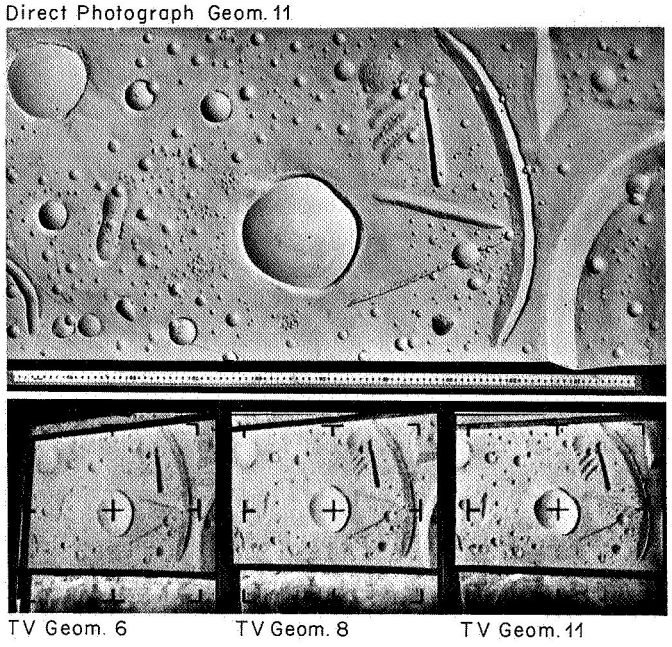


**Fig. J-2. Direct and TV photographs of simulation model**

**Note that most craters evident in TV pictures are delineated by shadows, a condition not encountered in the actual *Mariner* flight pictures. The craters in the model are generally much steeper than those photographed by *Mariner IV*.**

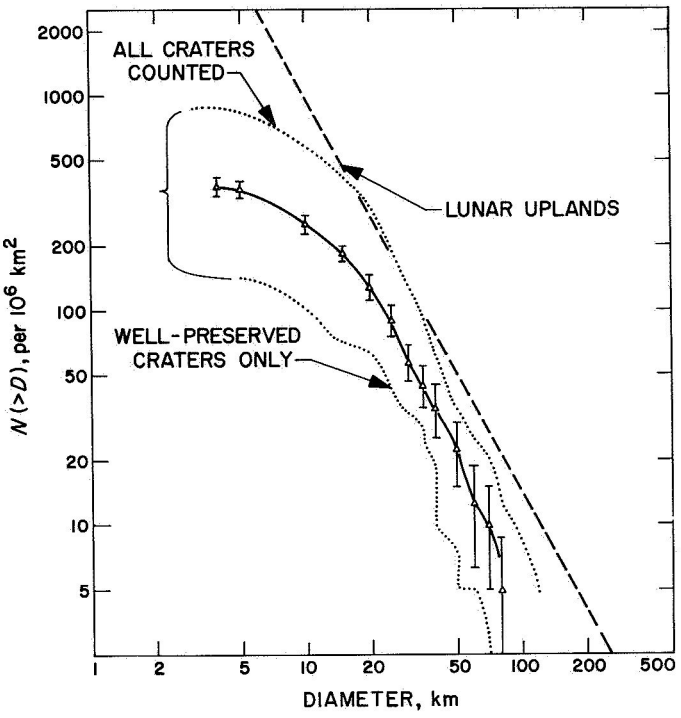


**Fig. J-3. Integral crater frequency plot of craters recognized in Pictures 7–12**

**The upper and lower dotted lines give liberal (75% certainty) and conservative limits (99%). The solid line includes the definite and probable categories, estimated to be 90% certain. The error bars are based on statistical fluctuation only. The lunar upland curve (dashed) is based on data of Trask (Ref. 59).**

**Table J-1. Integral crater count data, Pictures 7–12**

| Number greater than diameter *D* | | | | |
|---|---|---|---|---|
| *D*, km | Definite | Probable | Possible | All |
| 5 | 57 | 149 | 126 | 332 |
| 10 | 41 | 102 | 89 | 232 |
| 15 | 28 | 74 | 63 | 165 |
| 20 | 25 | 51 | 47 | 123 |
| 25 | 17 | 36 | 28 | 81 |
| 30 | 13 | 23 | 16 | 52 |
| 35 | 11 | 18 | 10 | 39 |
| 40 | 7 | 14 | 4 | 25 |
| 50 | 2 | 9 | 3 | 14 |
| 60 | 2 | 5 | 3 | 10 |
| 70 | 1 | 4 | 3 | 8 |
| 80 | 1 | 2 | 2 | 5 |
| 90 | 1 | 2 | 1 | 4 |
| 100 | 1 | 2 | 1 | 4 |
| 125 | 1 | 0 | 1 | 2 |
| 175 | 1 | 0 | 1 | 2 |
| 200 | 0 | 0 | 0 | 0 |
| **Number greater than 5 km** | | | | |
| **Pictures** | **Definite** | **Probable** | **Possible** | **All** |
| 7, 8 | 18 | 45 | 50 | 113 |
| 9, 10 | 19 | 64 | 45 | 128 |
| 11, 12 | 20 | 40 | 31 | 91 |
| | 57 | 149 | 126 | 332 |

**Table J-2. Area of pictures (km²)**

| Pictures | Total | Overlap | Net |
|---|---|---|---|
| 3, 4 | $32.5 \times 10^4$ | $3.34 \times 10^4$ | $29.2 \times 10^4$ |
| 5, 6 | $20.71 \times 10^4$ | $1.68 \times 10^4$ | $19.0 \times 10^4$ |
| 7, 8 | $16.41 \times 10^4$ | $1.56 \times 10^4$ | $14.8 \times 10^4$ |
| 9, 10 | $14.11 \times 10^4$ | $1.42 \times 10^4$ | $12.7 \times 10^4$ |
| 11, 12 | $13.2 \times 10^4$ | $1.10 \times 10^4$ | $12.1 \times 10^4$ |
| 13, 14 | $12.4 \times 10^4$ | $1.28 \times 10^4$ | $11.1 \times 10^4$ |
| 15, 16 | $13.41 \times 10^4$ | $1.19 \times 10^4$ | $12.2 \times 10^4$ |

minimum age of large topographic features on the Martian surface, it is important to note that even the selection of Pictures 7–12 leads to a lower crater frequency distribution than would be obtained from 9 and 10 alone. Figure J-3 shows these results in graphical form. The lower dotted line corresponds to "definite" only and the upper one to "definite" plus "probable" plus "possible." The solid line corresponds to "definite" plus "probable." The error bars refer only to the expected statistical fluctuation.

Three principal features of the integral crater frequency curve are evident:

(1) In the 20- to 60-km size range, the slope of the curve approximates that for the moon, and the absolute abundance of the Martian craters (upper limiting curve) approaches that of the lunar uplands.

(2) In the largest size classes, there is an apparent dearth of Martian craters. This may, in reality, reflect the limited areas covered by the individual *Mariner* pictures.

(3) Below 20 km, there is a genuinely lower abundance and/or systematic change to smoother craters on Mars.

## III. Age Implication of Martian Craters

An initial estimate, based on brief preliminary inspection of *Mariner IV* photos, suggesting that features on the cratered surface of Mars "must be very ancient—perhaps 2 to $5 \times 10^9$ years old" (Leighton *et al.*, Ref. 56) produced subsequent expressions of sharply diverging views. An immediate reaction was that the surface features of Mars must be much younger, on the order of a few million to 800 million years old at most because of the proximity of Mars to the asteroid belt (Anders and Arnold, Ref. 55, p. 1495; Witting, *et al.*, Ref. 57, p. 1498; Baldwin, Ref. 58, p. 1499). Subsequently, Opik (Ref. 47, p. 100; Ref. 46, p. 261), Binder (Ref. 1, p. 1053), and Hartmann (Ref. 35, p. 570) advanced counter arguments suggesting an age between 3 and 4.5 billion years for the larger craters recognizable on Mars.

These differing views are not surprising considering the small amount of direct observational data and the relatively large amount of speculative thinking involved in their formulation. Estimates of the maximum possible age of Martian surface features involve some or all of the following considerations, among others: (1) an initial assumption that the craters are mostly if not wholly of impact rather than volcanic origin, (2) knowledge or assumptions of size distribution within the population of impacting bodies, (3) knowledge or assumptions of the flux of meteoroidal bodies in the vicinity of Mars, the moon, and earth, (4) assumptions concerning the temporal variations or lack of same in this meteoroidal flux, (5) the age of the bodies comprising the solar system, (6) the age of the maria on the moon, and (7) assumptions or theories concerning processes of erosion and deposition modifying and obscuring craters on the moon and Mars.

Some of the data, assumptions, theories, and speculations involved are on a firmer basis than others. For example, a date of 4.5 to 4.7 billion years for an event that probably played an important part in creating solar system bodies has been confirmed in several different ways. However, a second date important in many of the estimates of Martian-surface antiquity, specifically the age of the maria of the moon, is much less certain. On the basis of crater number and sizes and estimates of the meteoroidal flux population, the ages of lunar maria have been variously estimated at 3 to nearly 4.5 billion years. These ages are currently under critical scrutiny and may be revised sharply downward because of a possible gross underestimation of the density of the cometary and meteoroidal flux (E. M. Shoemaker, personal communication). However, no one, for the moment at least, seems to question that the heavily cratered lunar uplands are comprised in large part of features which originated near the beginning of the solid history of the moon, at least 4.5 billion years ago. The arguments made herein concerning the antiquity of Martian features are framed principally in comparison with the lunar uplands rather than the maria.

It was recognized from the beginning that the *Mariner IV* photos showed that part of the surface of Mars viewed to be more like the lunar uplands than the lunar maria. Further studies, including those described in this report, show this similarity to be much greater than initially thought. It appears that the Martian surface surveyed by *Mariner IV* is closely analogous except for a pervasive and greater modification of its features by some process or processes of erosion and deposition.

It seems to be generally accepted that the characteristics of the lunar upland surface cannot have been generated within any reasonably acceptable time period through bombardment by the presently assumed meteoroidal flux. For that reason, the uplands are interpreted as largely the product of an initial intense bombardment in the earliest phases of lunar development when interplanetary space was presumably much more heavily populated with meteoroidal debris than during the last few billion years.

Insofar as this argument is valid for the moon, it should also apply to Mars. If any of this primarily bombarded surface is preserved on Mars, then at least some of its surface features have an antiquity approaching 4.5 billion years. Even if the surface of Mars preserves none of these primary features, many of its larger craters must still have a very great antiquity because of their abundance. This is so because of meteoroidal fluxes postulated for Mars; even the high values of Anders and

Arnold (Ref. 55, p. 1494) would require several billion years to produce the number of relatively large craters now recognized on the *Mariner IV* photos.

The cumulative plot of Martian craters shown in Fig. J-3 essentially parallels a similar plot for lunar upland craters down to a crater diameter of 20 km, where it diverges with lower slope. The fact that the two curves are not coincident down to the 20-km diameter is probably a product of greater crater modification on Mars by erosion and deposition. The departure from parallelism at 20 km more certainly represents the actual elimination of Martian craters by the modifying processes, whatever they may be.

The possibility that the meteoroidal flux at Mars may be higher than previously estimated, on the basis of new thinking about higher possible fluxes at the moon, remains to be evaluated. However, since the increased flux values presumably involve cometary bodies, it may be possible that the Martian atmosphere, even though highly attenuated, at least partly shields that planet, just as our atmosphere shields the earth.

On the basis of more detailed study and analysis of the *Mariner IV* photos, our initial belief that many of the topographic features on the Martian surface have an antiquity that may be measured in billions of years remains unchanged.

PRECEDING PAGE BLANK NOT FILMED.

# Appendix K

## Unenhanced Version of the Pictures

Since the initial acquisition of the *Mariner* pictures, several versions have been prepared and some have been released. All of the released versions have been enhanced in one way or another to emphasize special aspects of the pictorial information. This appendix is included to demonstrate Mars as it would appear to an observer at the focal plane of the camera during the picture taking sequence.

These pictures, shown in Fig. K-1, are a calibrated, unenhanced set prepared to maintain the correct relative brightness throughout. Two important characteristics are noticeable. First, the "haze" in Picture 1 is very bright at great distances from the limb. At 150 km the sky brightness is approximately one-half that of the surface. Second, the contrast in all pictures is very low. Without enhancement, the familiar features in Pictures 7 through 11 are barely discernible.

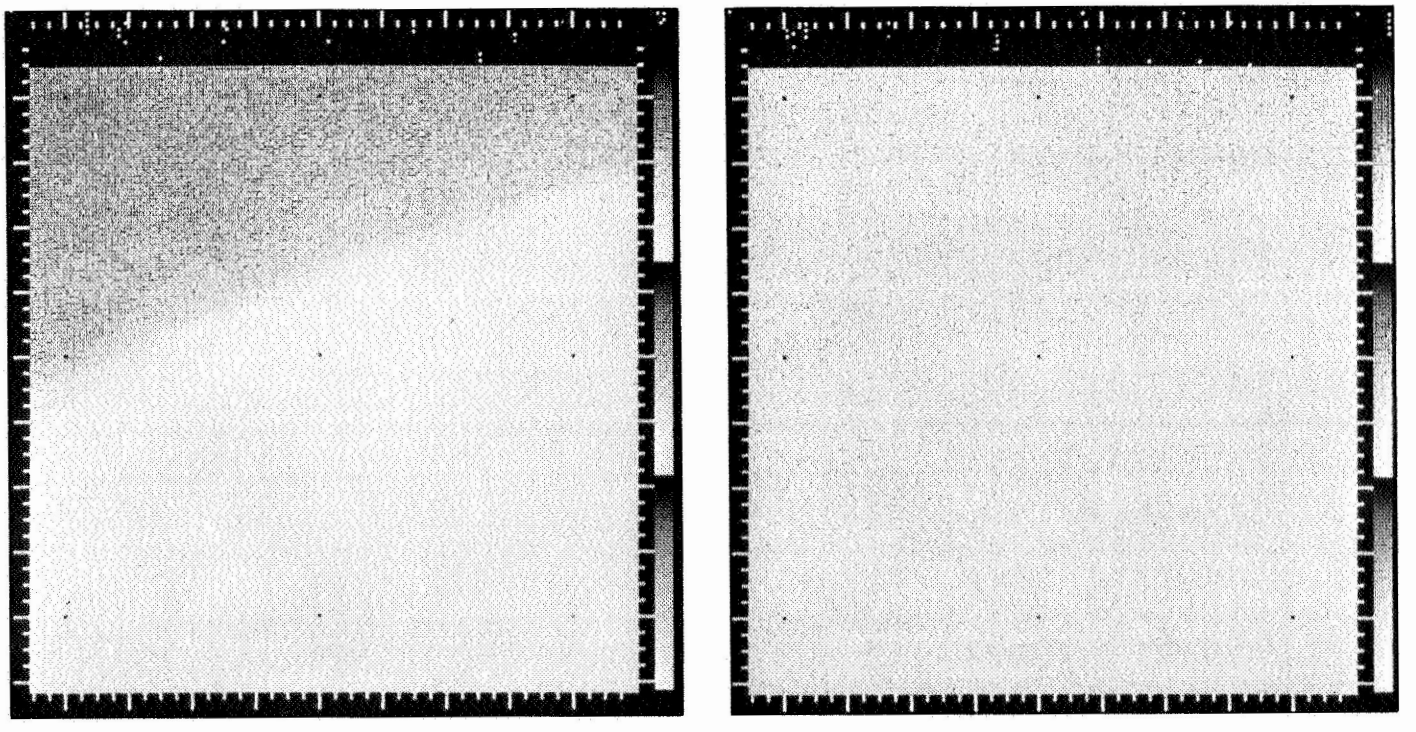

Picture 1 Picture 2

Fig. K-1. Pictures 1–18: calibrated, unenhanced

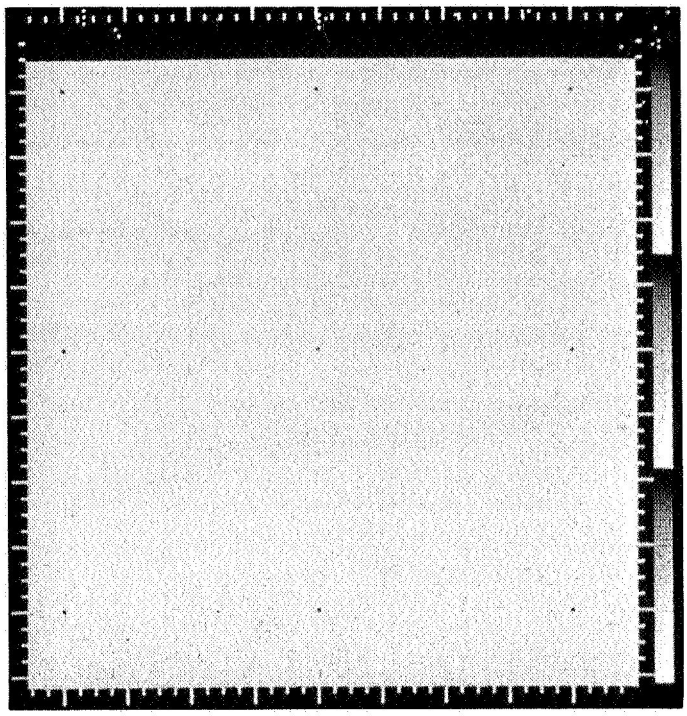

Picture 3

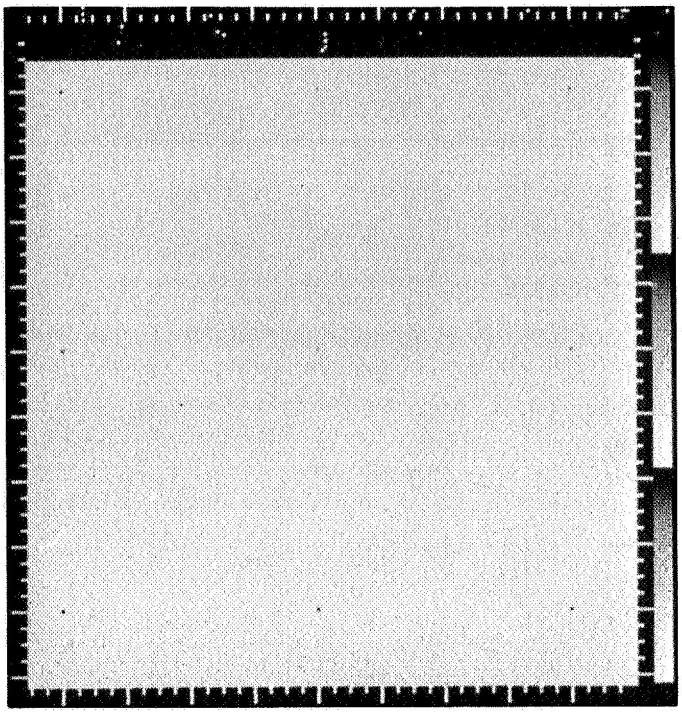

Picture 5

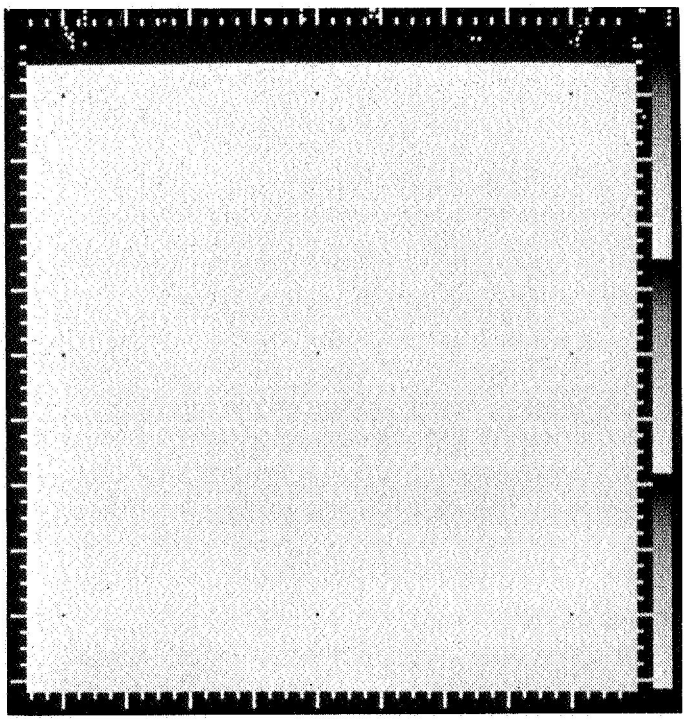

Picture 4

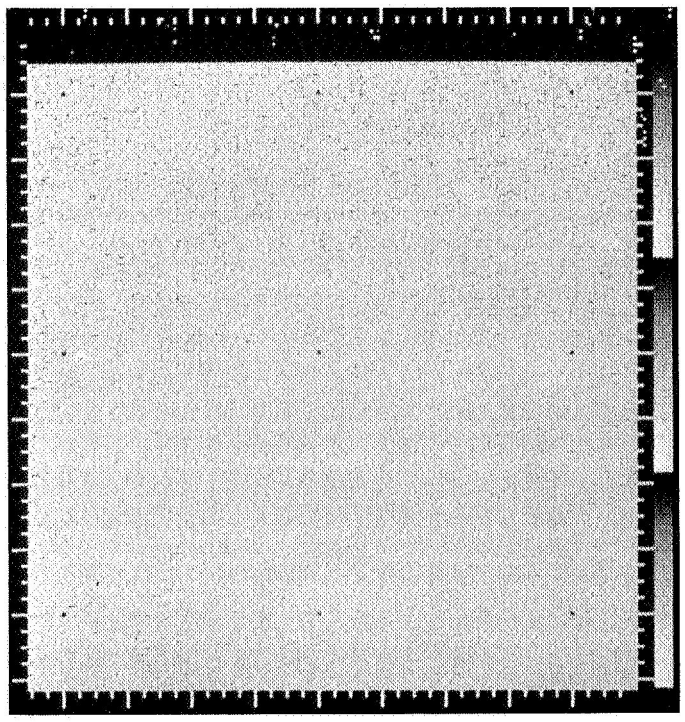

Picture 6

Fig. K-1 (contd)

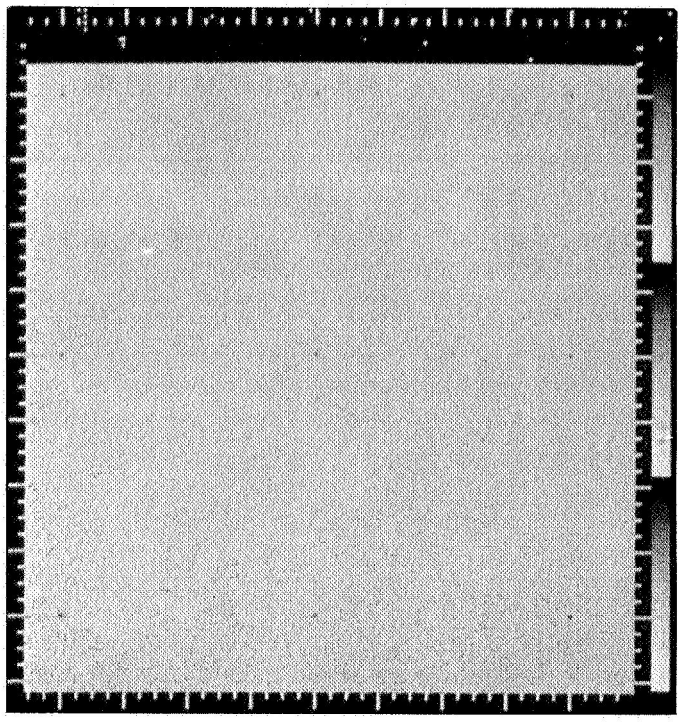

Picture 7

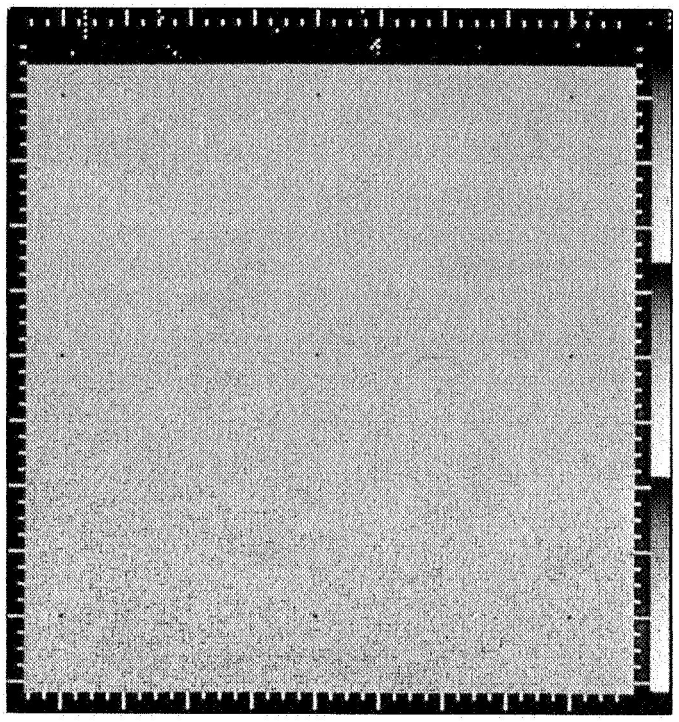

Picture 9

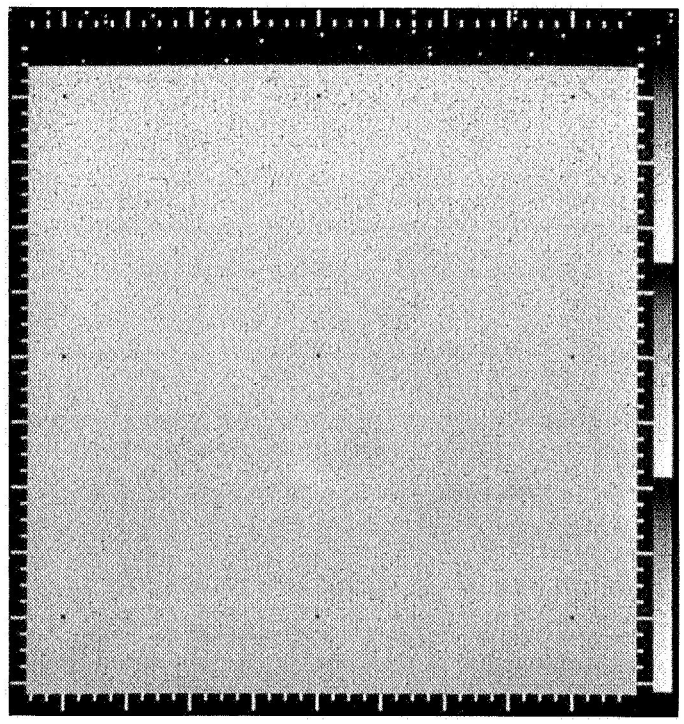

Picture 8

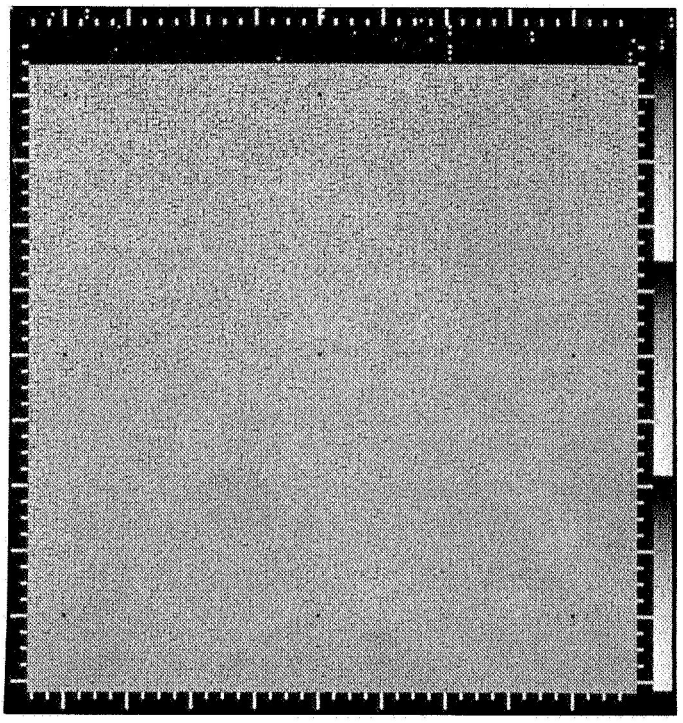

Picture 10

Fig. K-1 (contd)

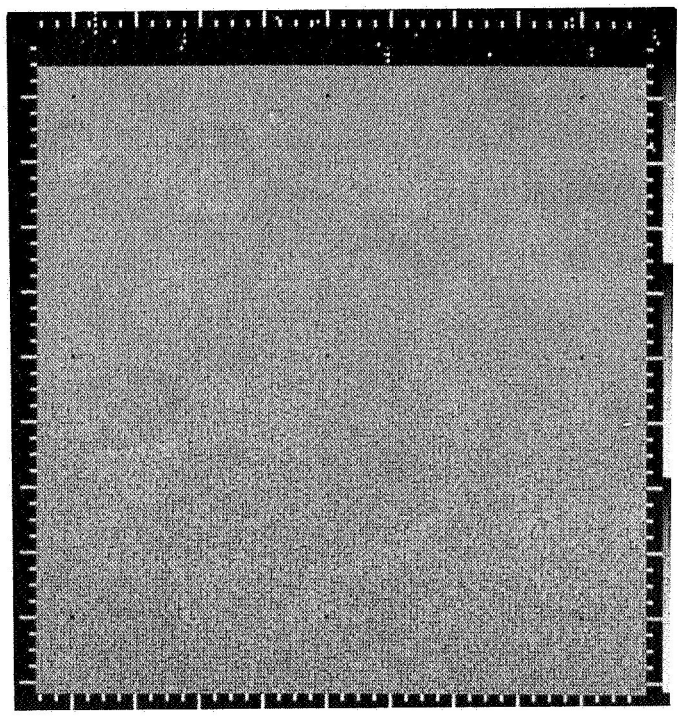

Picture 11

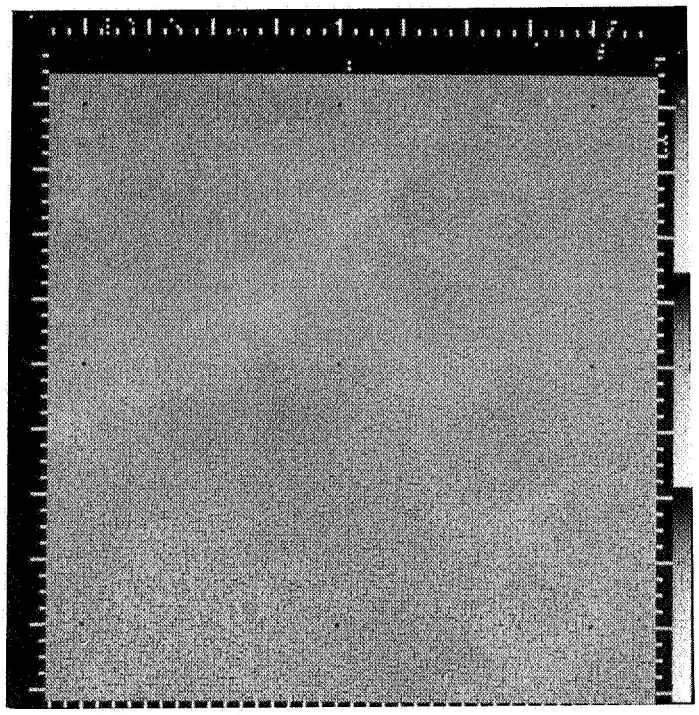

Picture 13

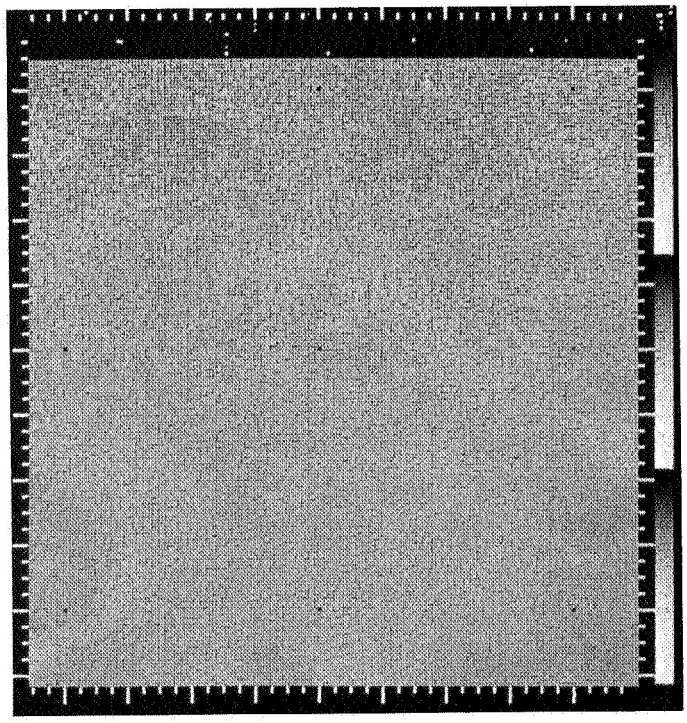

Picture 12

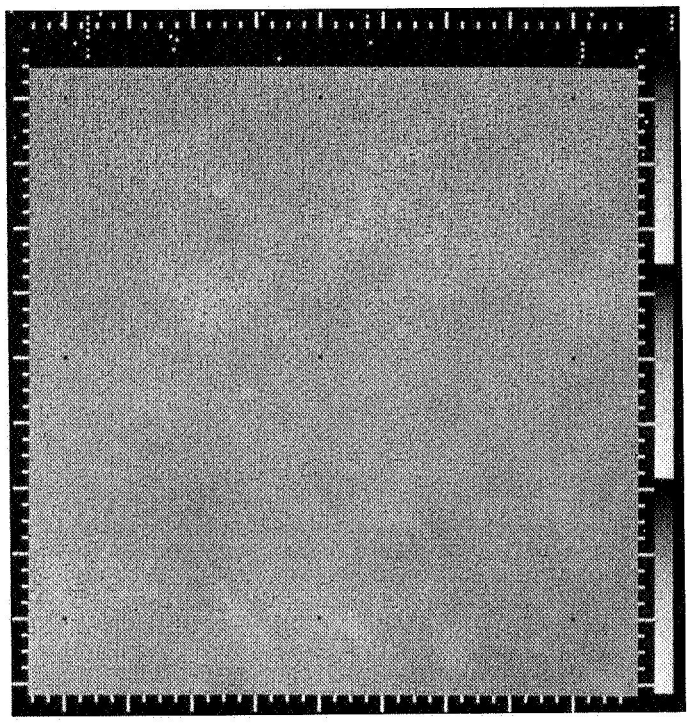

Picture 14

Fig. K-1 (contd)

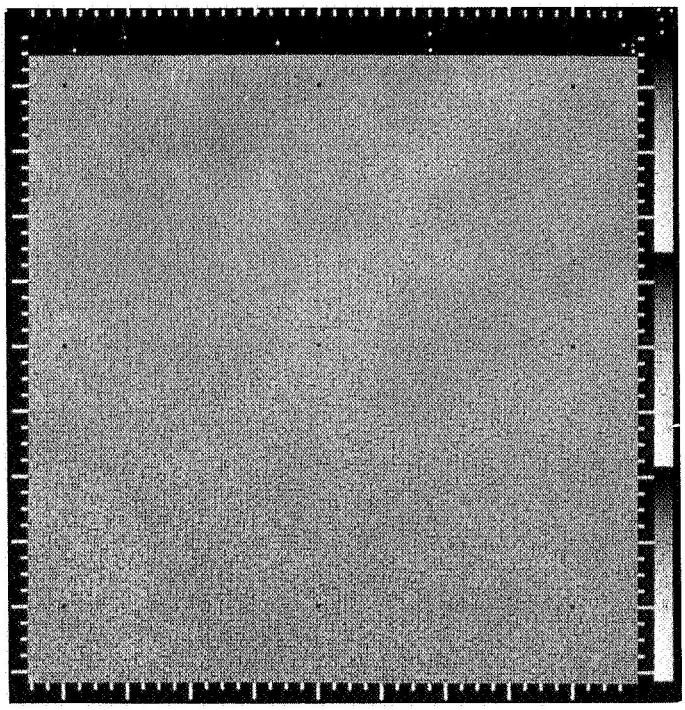

Picture 15

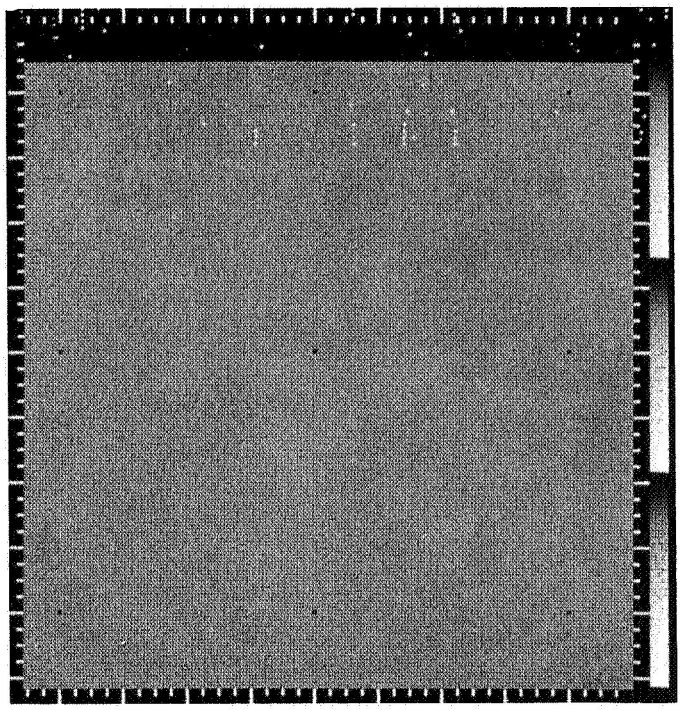

Picture 17

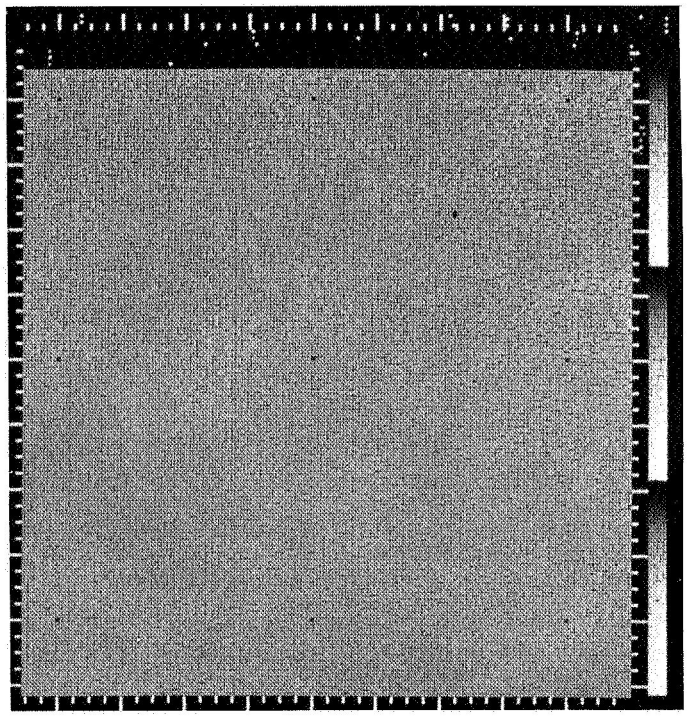

Picture 16

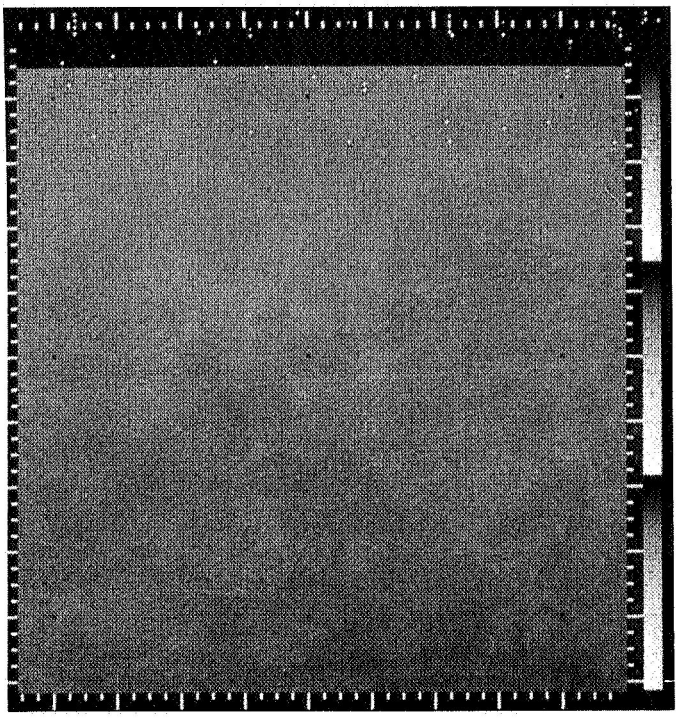

Picture 18

Fig. K-1 (contd)

PRECEDING PAGE BLANK NOT FILMED.

## References


1. Binder, A. B., "Mariner IV: Analysis of Preliminary Photographs," *Science*, Vol. 152, pp. 1053–1055, 1966.
2. Allen, C. W., *Astrophysical Quantities*, 2nd ed., p. 169, University of London, The Athlone Press, 1963.
3. Guerin, P., "Continuous Spectrophotometry," from *Physics of the Planets*, a collection of papers presented at the 11th International Colloquium on Astrophysics, Liege, July 1962.
4. de Vaucouleurs, G., *Geometric and Photometric Parameters of the Terrestrial Planets*, NASA Memorandum RM-4000-NASA, p. 62, Washington, D.C., March 1964.
5. Goldstein, R. M., "Mars: Radar Observations," *Science*, Vol. 150, pp. 1715–1717, 1965.
6. Sagan, C., and Pollock, J. B., "Radio and Radar Evidence on the Structure and Composition of the Martian Surface," *Proceedings of the Caltech–JPL Lunar and Planetary Conference, September 13–18, 1965*, Technical Memorandum 33-266, pp. 255–256, Jet Propulsion Laboratory, Pasadena, Calif., 1966.
7. Shoemaker, E. M., "Impact Mechanics at Meteor Crater, Arizona," in *The Moon, Meteorites and Comets*, pp. 301–336, edited by G. P. Kuiper and B. M. Middlehurst, University of Chicago Press, Chicago, Ill., 1963.
8. Roberts, W. A., "Shock–A Process in Extraterrestrial Sedimentology," *Icarus*, Vol. 5, pp. 459–477, 1966.
9. Short, N. M., "Shock-Lithification of Unconsolidated Rock Materials," *Science*, Vol. 154, pp. 382–384, 1966.
10. Sagan, C., and Pollack, J. B., *Elevation Differences on Mars*, Special Report 224, Smithsonian Institution Astrophysical Laboratory, Washington, 1966.
11. Leighton, R. B., and Murray, B. C., "Behavior of Carbon Dioxide and Other Volatiles on Mars," *Science*, Vol. 153, pp. 136–144, 1966.
12. Hess, S. L., "Some Aspects of the Meteorology of Mars," *J. Meteorol.*, Vol. 7, pp. 1–13, 1950.
13. Gifford, F. A., "The Surface Temperature Climate of Mars," *Astrophys, J.*, Vol. 123, pp. 154–161, 1956.
14. Sinton, W. M., and Strong, John, "Radiometric Observations of Mars," *Astrophys, J.*, Vol. 131, pp. 459–469, 1960.
15. Lederberg, J., and Sagan, C., "Microenvironments for Life on Mars," *Proc. Nat. Acad. Sci. U.S.A.*, Vol. 48, pp. 1473–1475, 1962.
16. Smoluchowski, R., "Is There Vegetation on Mars?" *Science*, Vol. 148, pp. 946–947, 1965.
17. Otterman, J. O., and Bronner, F. E., "Martian Wave of Darkening: A Frost Phenomenon?" *Science*, Vol. 153, pp. 56–60, 1966.
18. Loomis, A. A., "Some Geologic Problems of Mars," *Bull. Geol. Soc. Am.*, Vol. 76, pp. 1083–1104, 1965.

## References (contd)


19. Horowitz, N. H., Sharp, R. P., and Davies, R. W., "Planetary Contamination. I. The Problems and the Agreements," *Science*, Vol. 155, pp. 1501–1505, 1967.

20. Fizeau, H. L., *L'Astronomie*, p. 287, August 1888.

21. Strughold, Hubertus, "The Ecological Profile of Mars, Bioastronautical Aspect," in *Exploration of Mars, Advances in Astronautical Sciences*, Vol. 15, American Astronautical Society, edited by G. W. Morgenthaler, 1963.

22. Strughold, Hubertus, "A Subsurface Marine Biosphere on Mars?" *Astronaut. Aeronaut.*, Vol. 3, pp. 82–86, 1965.

23. Urey, H. C., *The Planets, Their Origin and Development*, Yale University Press, New Haven, Conn., 1952.

24. Johnson, F. S., "Atmosphere of Mars," *Science*, Vol. 150, pp. 1445–1448, 1965.

25. Blackwelder, Eliot, "The Insolation Hypothesis of Rock Weathering," *Am. J. Sci.*, Vol. 213, pp. 97–113, 1933.

26. Griggs, D. T., "The Factor of Fatigue in Rock Exfoliation," *J. Geol.*, Vol. 44, pp. 783–796, 1936.

27. Blackwelder, Eliot, 'Fire as an Agent in Rock Weathering," *J. Geol.*, Vol. 35, pp. 134–140, 1927.

28. Emery, K. O., "Brush Fires and Rock Exfoliation," *Am. J. Sci.*, Vol. 242, pp. 506–508, 1944.

29. Howard, A. D., "An Observation Bearing on the Problem of Exfoliation," *J. Geol.*, Vol. 58, pp. 155–156, 1950.

30. Roth, E. S., "Temperature and Water Content as Factors in Desert Weathering," *J. Geol.*, Vol. 73, pp. 454–468, 1965.

31. Ryan, J. A., "The Case Against Thermal Fracturing at the Lunar Surface," *J. Geophys. Res.*, Vol. 67, pp. 2549–2558, 1962.

32. Anderson, D., Haffrey, E. S., and Low, P. F., "Frost Phenomena on Mars," *Science*, Vol. 155, pp. 319–322, 1967.

33. Rea, G. D., *The Atmosphere and Surface of Mars—a Selective Review*, Technical Memorandum 33-266, pp. 209–266. Jet Propulsion Laboratory, Pasadena, Calif., 1966.

34. Smith, E. J., Davis, Leverett, Coleman, P. J., and Jones, D. E., "Magnetic Field Measurements Near Mars," *Science*, Vol. 149, pp. 1241–1242, 1965.

35. Hartmann, W. K., "Martian Cratering," *Icarus*, Vol. 5, pp. 565–576, 1966.

36. Shoemaker, E. M., "Preliminary Analysis of the Fine Structure of the Lunar Surface in Mare Cognitum," in *The Nature of the Lunar Surface*, edited by W. H. Hess, D. H. Menzel, and J. A. O'Keefe, pp. 23–77, The Johns Hopkins Press, Baltimore, Md., 1966.

37. Gold, T., "The Moon's Surface," in *The Nature of the Lunar Surface*, edited by W. H. Hess, D. H. Menzel, and J. A. O'Keefe, pp. 107–121, The Johns Hopkins Press, Baltimore, Md., 1966.

## References (contd)


38. Hess, S. L., "A Meteorological Approach to the Question of Water Vapor on Mars and the Mass of the Martian Atmosphere," *Pub. Astron. Soc. Pac.*, Vol. 60, pp. 288–302, 1948.

39. Tombaugh, C. W., "The Absence of an Aqueous Morphology on Mars and Some Geologic Consequences," *Icarus* (in press).

40. Bagnold, R. A., *The Physics of Blown Sand and Desert Dunes*, Methuen and Co., Ltd., London, 1941.

41. Gifford, F. A., "A Study of Martian Yellow Clouds That Display Movement," *Monthly Weather Rev.*, Vol. 92, pp. 435–440, 1964.

42. Ryan, J. A., "Notes on the Martian Yellow Clouds," *J. Geophys. Res.*, Vol. 69, pp. 3759–3770, 1964.

43. Leovy, Conway, "Some Aspects of the Circulation of Mars," manuscript, 1966.

44. Neubauer, F. M., "Thermal Convection in the Martian Atmosphere," *J. Geophys. Res.*, Vol. 71, pp. 2419–2426, 1966.

45. Öpik, E. J., "Mars and the Asteroids," *Irish Astron. J.*, Vol. 1, pp. 22–24, 1950.

46. Öpik, E. J., "The Martian Surface," *Science*, Vol. 153, pp. 255–265, 1966.

47. Öpik, E. J., "Mariner IV and Craters on Mars," *Irish Astron. J.*, Vol. 7, pp. 92–104, 1965.

48. Sharpe, C. F. S., *Landslides and Related Phenomena*, Columbia University Press, New York, 1938.

49. Moseley, Henry, "On the Descent of a Solid Body on an Inclined Plane When Subjected to Alternations of Temperature," *London, Edinburgh, and Dublin Phil. Mag. and J. Sci.*, Vol. 37, 4th Ser., pp. 99–118, 1869.

50. Davison, Charles, "Notes on the Movement of Scree-Material," *Geol. Soc. London, Quart. J.*, Vol. 44, pp. 232–238, 1888.

51. Sagan, C., "High-Resolution Planetary Photography and the Detection of Life," *Proceedings of the Caltech–JPL Lunar and Planetary Conference, September 13–18, 1965*, Technical Memorandum 33-266, pp. 279–287, Jet Propulsion Laboratory, Pasadena, Calif., 1966.

52. Sagan, Carl, Phaneuf, J. P., and Ihnat, Michael, "Total Reflection Spectrophotometry and Thermogravimetric Analysis of Simulated Martian Surface Materials," *Icarus*, Vol. 4, pp. 43–61, 1965.

53. Binder, A. B., and Cruikshank, D. P., "The Composition of the Surface Layer of Mars," manuscript, 1966.

54. Salisbury, J. W., "The Light and Dark Areas of Mars," *Icarus*, Vol. 5, pp. 291–298, 1966.

55. Anders, E., and Arnold, J. R., "Age of Craters on Mars," *Science*, Vol. 149, pp. 1494–1496, 1965.

56. Leighton, R. B., *et al.*, "Mariner IV photography of Mars: initial results," *Science*, Vol. 149, pp. 627–630, 1965.

## References (contd)


57. Witting, J., Narin, F., and Stone, C. A., "Mars: Age of its Craters," *Science*, Vol. 149, pp. 1496–1498, 1965.

58. Baldwin, R., "Mars: An Estimate of the Age of its Surface," *Science*, Vol. 149, pp. 1498–1499, 1965.

59. Trask, M. J., section in *Ranger VIII and IX. Part II. Experimenters' Analyses and Interpretations*, Technical Report 32-800, pp. 252–263, Jet Propulsion Laboratory, Pasadena, Calif., March 15, 1966.